Titre: Title:	Development of a Seismic Design Procedure of Tailings Impoundments Reinforced With Waste Rock Inclusions
Auteur: Author:	Ali Reza Zafarani
Date:	2022
Type:	Mémoire ou thèse / Dissertation or Thesis
Référence: Citation:	Zafarani, A. R. (2022). Development of a Seismic Design Procedure of Tailings Impoundments Reinforced With Waste Rock Inclusions [Thèse de doctorat, Polytechnique Montréal]. PolyPublie. https://publications.polymtl.ca/10452/

URL de PolyPublie: PolyPublie URL:	https://publications.polymtl.ca/10452/
Directeurs de recherche: Advisors:	Samuel Yniesta, & Michel Aubertin
Programme: Program:	Génie minéral

POLYTECHNIQUE MONTRÉAL

affiliée à l'Université de Montréal

Development of a seismic design procedure of tailings impoundments reinforced with waste rock inclusions

ALI REZA ZAFARANI

Département des génies civil, géologique et des mines

Thèse présentée en vue de l'obtention du diplôme de *Philosophiæ Doctor*

Génie minéral

Août 2022

POLYTECHNIQUE MONTRÉAL

affiliée à l'Université de Montréal

Cette thèse intitulée:

Development of a seismic design procedure of tailings impoundments reinforced with waste rock inclusions

présenté par **Ali Reza ZAFARANI**

en vue de l'obtention du diplôme de *Philosophiæ Doctor*

a été dûment acceptée par le jury d'examen constitué de :

Carlos OVALLE, président
Samuel YNIESTA, membre et directeur de recherche
Michel AUBERTIN, membre et codirecteur de recherche
Benoit COURCELLES, membre
Mamadou FALL, membre externe

DEDICATION

To Shadi and my parents

ACKNOWLEDGEMENTS

I would like to express my deepest gratitude to my advisor, Prof. Samuel Yniesta, for his excellent guidance, patience, and providing me with an excellent atmosphere for doing research. I would like to thank my co-advisor, Prof. Michel Aubertin, whose timely advice, meticulous scrutiny, and scientific approach have helped me to a very great extent in achieving different accomplishments throughout my Ph.D. I would also like to thank Prof. Michael James for his contributions to the project before his departure from RIME.

I would like to thank Abtin Jahanbakhshzadeh, who as a good friend, was always willing to help and give his best suggestions. Many thanks to Carlos Contreras, for helping and supporting me with numerical simulations. I thank profusely Karim Essayad and Akram Deiminiat for their support during my study period.

Finally, I would like to thank my family. They were always supporting me and encouraging me with their best wishes and stood by me through good and bad times.

RÉSUMÉ

La stabilité sismique des installations de stockage de résidus est une préoccupation majeure pour le secteur minier, car ces installations ont été sujettes à des défaillances dans les zones sismiquement actives. La stabilité sismique des parcs à résidus est largement influencée par les propriétés des résidus, qui sont généralement constitués d'un matériau silteux de faible plasticité dans un état lâche et saturé. La génération de pressions interstitielles excessives pendant un tremblement de terre peut entraîner une réduction des contraintes effectives, ce qui provoque une perte de résistance des résidus et la rigidité associées (c'est-à-dire la liquéfaction), ce qui peut provoquer la défaillance d'un parc à résidus. De meilleures méthodes d'analyse des parcs à résidus existants, ainsi que des stratégies de conception appropriées, sont essentielles pour minimiser les défaillances et les dommages qui en découlent. Les inclusions de roches stériles (IRS/WRI) sont l'une des techniques qui peuvent être utilisées pour améliorer la stabilité statique et dynamique des parcs à résidus en raison de leur plus grande rigidité, résistance et conductivité hydraulique par rapport aux résidus.

Des études antérieures utilisant des modèles physiques et des simulations numériques ont montré que l'utilisation des IRS dans un parc à résidus peut accélérer la dissipation des pressions interstitielles excessives et améliorer la stabilité géotechnique des parcs à résidus. Cependant, certaines lacunes subsistent en ce qui concerne l'étude du comportement sismique des parcs à résidus et l'effet des IRS sur leur réponse sismique. Des directives de conception et des méthodologies d'optimisation sont nécessaires pour mieux intégrer cette méthode de co-disposition dans la conception des parcs à résidus. Ainsi, il est nécessaire de mieux quantifier l'effet de divers paramètres, tels que la configuration des IRS (c'est-à-dire la largeur et l'espacement) et la géométrie du parc à résidus, comme la pente et la hauteur en aval, sur différents indicateurs de performance de la stabilité sismique d'un parc à résidus. Les directives de conception devraient également prendre en compte la réponse sismique des parcs à résidus soumis à une variété de mouvements du sol représentatifs des caractéristiques des aléas sismiques anticipés, ce qui est un autre aspect qui n'a pas été évalué de manière adéquate auparavant.

L'objectif principal du présent projet de recherche était donc de développer une méthode pour optimiser la conception des inclusions de roches stériles dans un parc à résidus afin d'assurer sa

stabilité sismique. Pour atteindre cet objectif principal, une approche de modélisation numérique pour simuler le comportement sismique des parcs à résidus avec et sans IRS a été développée en utilisant le code FLAC Version 8.00. Diverses simulations ont ensuite été effectuées pour étudier comment certaines caractéristiques, telles que l'inclinaison de la pente aval du parc, la hauteur du modèle et la configuration des IRS, affectent le comportement sismique du modèle. La pente aval variait entre 7H:1V et 12H:1V, la hauteur du parc à résidus était comprise entre 20 m et 50 m, la largeur des inclusions était comprise entre 12 et 25 m, et l'espacement entre 55 et 155 m. Les résultats ont indiqué que la réponse sismique du modèle est plus influencée par l'épaisseur du parc à résidus que par la pente aval pour les conditions considérées dans les simulations. De plus, l'effet de la configuration des IRS sur la réponse sismique est moins perceptible dans les parcs à résidus de faible épaisseur en raison de déplacements horizontaux plus faibles que dans les parcs à résidus plus épais.

En plus des effets géométriques (c.-à-d. la pente en aval, la hauteur et la configuration des IRS), les effets des mesures d'intensité (MI) du mouvement du sol sur la stabilité sismique des parcs à résidus ont également été étudiés dans le cadre de l'étude paramétrique numérique afin d'élaborer des directives de conception pour l'utilisation des IRS. Dix enregistrements différents de mouvements du sol provenant des bases de données NGA-West2 et NGA-East ont été utilisés pour évaluer la réponse sismique et la stabilité des parcs à résidus avec et sans inclusion de stériles. Des différences significatives entre les réponses du système à la fin de mouvements du sol avec certains MI comparables, ont mis en évidence la nécessité d'identifier le MI (ou les MI) optimal qui présente la meilleure corrélation avec les indicateurs de performance. Les résultats de l'analyse de régression ont montré qu'une combinaison de l'intensité du spectre de la vitesse, VSI (MI_1) et de l'accélération maximale du sol, PGA (MI_2) avait la plus grande efficacité globale pour les cas évalués.

Dans la dernière étape de cette recherche, en utilisant les résultats de l'étude paramétrique numérique, une procédure systématique a été proposée pour évaluer le déplacement induit par la liquéfaction des parcs à résidus renforcés par des inclusions de roches stériles. Un modèle de performance (relation multi-paramètres) a été utilisé pour relier le niveau de déplacement aux caractéristiques du parc à résidus, y compris l'inclinaison de la pente, la hauteur, l'indice de densité des résidus, aux mesures d'intensité optimale des secousses sismiques et la configuration des IRS.

Les résultats montrent qu'en général, les résultats des simulations et les estimations fournies par le modèle de performance (équation) concordent.

Les praticiens peuvent utiliser l'approche simplifiée proposée pour évaluer la performance sismique des parcs à résidus. La procédure doit cependant être utilisée en conjonction avec les résultats des analyses dynamiques non linéaires spécifiques au projet. La méthode proposée devrait également aider à développer des modèles de prédiction déterministes et probabilistes pour évaluer la stabilité sismique des parcs à résidus.

ABSTRACT

The seismic stability of tailings storage facilities is a major concern for the mining industry, as tailings impoundments have been prone to failure in seismically active areas. The seismic stability of tailings impoundments is largely influenced by the properties of tailings, which usually consist of low plasticity silty material in a loose and saturated state. The development of excess pore water pressures during an earthquake may reduce the effective stresses and induce a loss in shear strength and stiffness (i.e., liquefaction), which might cause an impoundment to fail. Improved methodologies for analyzing the stability of existing tailings impoundments, as well as proper design strategies, are essential to minimize failures and the ensuing damage. Waste rock inclusions (WRI) is one of the techniques that can be used to improve the static and dynamic stability of tailings impoundments due to their higher stiffness, strength, and hydraulic conductivity compared to tailings.

Previous studies using physical models and numerical simulations have shown that the use of WRI in a tailings facility can accelerate the dissipation of excess pore pressures and improve the geotechnical stability of tailings impoundments. However, a few gaps still remain regarding the seismic behavior of tailings impoundments and the effect of WRI on their seismic response. Design guidelines and optimization methodologies are needed to better integrate this co-disposal method in the design of tailings impoundments. To develop such guidelines, it is necessary to better quantify the effect of various parameters, such as WRI configuration (i.e., width and spacing) and impoundment geometry, such as downstream slope and height, on different performance indicators of the seismic stability of tailings impoundments. Design guidelines should also consider the seismic response of impoundments under a variety of ground motions representative of the anticipated earthquake characteristics, which is another aspect that has not been adequately evaluated previously.

The primary objective of the current research project was therefore to develop a method to optimize the design of waste rock inclusions in a tailings impoundment to ensure its seismic stability. To attain this primary objective a numerical modeling approach for simulating the seismic behavior of tailings impoundments with and without WRI was developed using the code FLAC (Fast Lagrangian Analysis of Continua) Version 8.00. Various simulations were then conducted to

investigate how selected characteristics, such as the downstream slope inclination of the impoundment, height of the model, and configuration of WRI affect the seismic behavior of the model. The downstream slope was varied between 7H:1V and 12H:1V, the height of the impoundment was between 20 m and 50 m, the width of the inclusions was between 12 and 25 m, and the spacing was between 55 and 155 m. Results indicated that the seismic response of the model is more influenced by the thickness of the tailings deposit than by the downstream slope for the conditions considered in the simulations. Moreover, the effect of the WRI configuration on seismic response is less noticeable in impoundments with smaller tailings thickness due to lower horizontal displacements than in impoundments with a thicker tailings deposit.

In addition to the geometry effects (i.e., downstream slope, height, and WRIs' configuration), the effects of intensity measures (IMs) of the ground motion on the seismic stability of tailings impoundments were also investigated as part of the numerical parametric study in order to develop design guidelines for WRI. Ten different ground motion records from the NGA-West2 and NGA-East databases were used to assess the seismic response and stability of tailings impoundments with and without waste rock inclusions. Significant differences between the responses of the system at the end of ground motions with similar PGA and Arias Intensity highlighted the necessity of identifying the most sensitive, or optimum IM (or IMs) that correlate best with the performance metrics. The regression analysis results showed the vector-valued IMs composed of Velocity Spectrum Intensity, VSI (IM_1) and Peak Ground Acceleration, PGA (IM_2) had the highest overall efficiency for the cases evaluated.

In the final step of this research, using the results of the numerical parametric investigation, a systematic procedure was proposed for assessing liquefaction-induced displacement of tailings impoundments reinforced with waste rock inclusions. A performance model (multi-parameter relationship) was employed to link the level of displacement to tailings impoundment characteristics including the slope inclination, height, tailings density index, optimum intensity measurements of earthquake shaking, and WRI configuration. The results show that in general, the simulation results and the estimations provided by the performance model (equation) matched.

Practitioners can use the proposed simplified approach to evaluate the seismic performance of tailings impoundments. The procedure should, however, be used in conjunction with the results of project-specific nonlinear dynamic analyses. The suggested method should also help develop

deterministic and probabilistic prediction models for assessing the seismic stability of tailings impoundments.

TABLE OF CONTENTS

LIST OF TABLES

LIST OF FIGURES

LIST OF SYMBOLS AND ABBREVIATIONS

A_{loop} Area of the hysteresis loop (-)

a_h Horizontal pseudo-static acceleration (m/s^2)

AI Arias Intensity (m/s)

a_{rms} Root-mean-square acceleration (m/s^2)

ASI Acceleration spectrum intensity (m/s^2)

$a(t)$ Acceleration time history (m/s)

a_v Coefficient of compressibility (-)

a_v Vertical pseudo-static acceleration (m/s^2)

c Cohesion (kPa)

c' Effective cohesion (kPa)

CAV Cumulative absolute velocity (m/s)

C_c Compression index (-)

C_I Characteristic intensity (-)

CDA The Canadian Dam Association

CDV Critical displaced volume (m^3)

C_{GD} Modulus degradation factor (-)

C_r Recompression index (-)

CRR Cyclic resistance ratio (-)

$CRR_{Mw=7.5}$ Normalized cyclic resistance ratio for an earthquake of magnitude 7.5 (-)

CSR Cyclic stress ratio (-)

C_U Coefficient of uniformity (-)

D_{10} Grain diameter by 10% passing (mm)

D_{60} Grain diameter by 60% passing (mm)

D_{5-95} Significant duration (s)

D_r Relative density (-)

DSS Direct Simple Shear

e Void ratio (-)

e_{crit} Void ratio at the critical state (-)

e_d Void ratio of loose soil (-)

e_l Void ratio of loose soil (-)

e_{min} Minimum void ratio (-)

e_{max} Maximum void ratio (-)

Fp Predominant frequency (Hz)

FLAC Fast Lagrangian Analysis of Continua

FLS Flow Liquefaction Surface

G Gravity acceleration (m/s^2)

G_0 Shear modulus coefficient (-)

G_{max} Maximum shear modulus (kPa)

G_{tan} Tangent shear modulus (kPa)

G_{sec} Secant shear modulus (kPa)

H Tailings height (thickness) (m)

H_i Initial height of the nodal point (m)

H_I Housner's spectral intensity (m)

h_{p0} Contraction rate parameter (-)

ICOLD International Commission on Large Dams

I_d Density Index (-)

$I_{d,CS}$ Density index at critical state (-)

IMs Intensity Measures

K Bulk modulus (kPa)

k_h Horizontal pseudo-static coefficient (-)

k_{sat} Saturated hydraulic conductivity (m/s)

k_v Vertical pseudo-static coefficient (-)

M Critical stress ratio (-)

M^d Relative state parameter index (-)

m_v Coefficient of volume change (-)

M_w Magnitude (-)

n^b Boundary parameter (-)

$(N_1)_{60}$ Corrected number of blows of the standard penetration test (-)

p' Mean effective stress (kPa)

p_A Atmospheric pressure (kPa)

PGA Peak ground acceleration (m/s^2)

PGV Peak ground velocity (m/s)

PTL Phase Transformation Line

Q Critical state parameter (-)

q Deviatoric stress (kPa)

R Critical state parameter (-)

r_u Excess pore water pressure ratio (-)

RIME The Research Institute on Mines and Environment

S Edge-to-edge spacing between inclusions (m)

S_1 Spacing between the starter dike and the edge of the closest inclusion (m)

s_a Acceleration spectra (m/s^2)

s_v Velocity spectra (m/s)

S_{pv} Pseudo velocity spectrum (m/s)

SAR_x Average normalized horizontal displacement of the downstream slope (-)

SMA Sustained maximum acceleration (m/s^2)

SMV Sustained maximum velocity (m/s)

S_{max} Spacing between the starter dike and the edge of the farthest waste rock inclusion (m)

SSL Steady State Line

S_{su} Shear strength at steady state (kPa)

T Dominant period of response spectrum (s)

t_d Relative duration (s)

t_f Ground motion duration (s)

t_5 Time at 5% of Arias intensity (s)

t_{95} Time at 95% of Arias intensity (s)

USCS Unified Soil Classification System

V_r Volume ratio (-)

v_{rms} Root-mean-square velocity (m/s)

$v(t)$ Velocity time history (m/s)

VSI Velocity spectrum intensity (m)

W Width of inclusions (m)

W Potential landslide mass (m)

WRI/IRS Waste Rock Inclusions

W_D	Dissipated energy (-)
w_0	Initial water content (-)
w_l	Liquid limit (-)
w_p	Plastic limit (-)
w_{opt}	Optimum water content (-)
W_s	Maximum strain energy (-)
W_{vs}	Volume-Spacing index (-)
X_{disp_i}	Horizontal displacement (m)
φ’	Effective internal friction angle (˚)
φ	Angle of internal friction in total stresses (˚)
$\gamma_{d\ max}$	Maximum dry unit weight after compaction (kN/m^3)
τ	Shear strength (kPa)
γ_w	Unit weight of water (kN/m^3)
μ_w	Dynamic viscosity of water (Pa s)
σ'_1	Maximum principal stress (kPa)
σ'_3	Minimum principal stress (kPa)
γ	Shear strain (-)
ξ	Damping (-)
ϕ'_{cv}	Constant volume internal friction angle (˚)
υ	Poisson ratio (-)
γ_{dry}	Dry unit weight (kN/m^3)
ξ_{min}	Small-strain damping (-)
σ_ε	Standard deviation of residuals (-)

ζ Proficiency index (-)

θ Downstream slope inclination angle of the impoundment (˚)

LIST OF APPENDICES

CHAPTER 1 INTRODUCTION

The economic and environmental damage caused by a dike breach on mining facilities and on local ecosystems and inhabitants can be disastrous. Overtopping, earthquakes and foundation instability are the three most common reasons of these failures (ICOLD, 2001; Aubertin et al. 2002, 2011; Davies, 2002; Azam and Li, 2010; Santamarina et al., 2019). The seismic stability of tailings impoundments is greatly influenced by the properties of the tailings, which are composed for hard rock mines of low plasticity silty material in a loose and saturated state, the response of the retention dikes, and their interactions during and immediately following the earthquake. During an earthquake, tailings may lose strength due to the development of excess pore water pressures that reduce the effective stresses and related shear strength and stiffness, potentially leading to impoundment failure due to tailings liquefaction. Numerous case studies have been published in which a seismic event may have resulted in the failure of a tailings impoundment owing to liquefaction (Finn, 1985, 1993, 1998; ICOLD, 2001; Gens and Alonso, 2006).

Improved methods for characterizing existing tailings impoundments and appropriate design strategies are required to prevent failures and the resulting damage. Among the available techniques, waste rock inclusions (WRI) can be constructed in tailings impoundments to improve the static and dynamic stability of tailings impoundments due to their higher stiffness, strength, and hydraulic conductivity compared to tailings (Aubertin et al. 2002a, 2021). These WRI improve tailings strength and impoundment lateral resistance by accelerating drainage and tailings consolidation. Tailings impoundments with WRI are generally built by placing waste rock in specified positions prior to tailings deposition (Figure 1.1), discharging slurry tailings from the crest of the external dikes and inclusions, and raising the external dikes and inclusions ahead of the next tailings hydraulic deposition (James et al. 2013, 2017; Aubertin et al. 2021). Typically, WRI constructed on mine sites have a crest width of 12 to 25 meters and a length of several hundred meters. They are built in stages with 2 to 3 m raises, constructed in parallel with the raising of the external dikes, before a new stage of tailings deposition. WRI improve mine waste management by reducing the amount of waste rock deposited in piles on the surface and increasing the stability of tailings facilities (James and Aubertin, 2010, 2012; James et al., 2013, 2017). Previous and recent studies using physical models (Pépin et al., 2012; Saleh-Mbemba and Aubertin, 2019, 2021) and numerical simulations (James, 2009; James and Aubertin, 2012; Jaouhar et al., 2013; Ferdosi

et al., 2015a; Aubertin et al., 2019; Jahanbakhshzadeh and Aubertin, 2020) have shown that the use of WRI in a tailings facility can accelerate the dissipation of excess pore pressures and improve the geotechnical stability of tailings impoundments under static and seismic conditions. The WRI technique has been applied at the Canadian Malartic mine tailings storage facility (Figure 1.1), primarily to accelerate drainage and consolidation of tailings and to create cells in the impoundment.

Figure 1.1: WRI in the Canadian Malartic mine tailings storage facility (photo taken September 2020)

Design guidelines are required for tailings impoundments that apply this relative new co-disposal process. The optimization of this technique for seismic loading conditions specifically requires a thorough investigation of various aspects that influence the behavior of a tailings facility with WRI. Encouraging results from previous studies indicated that WRI can significantly improve the seismic response and stability of tailings impoundments that would otherwise be unstable without reinforcement. However, there is a need to investigate more thoroughly the effect of various influence factors, such as WRI configuration (i.e., width and spacing), on different metrics of seismic stability of a tailings impoundment. Furthermore, the impact of impoundment geometry, such as downstream slope and height, as well as material properties on the seismic response of reinforced tailings impoundments has never been investigated. Design guidelines should also consider the seismic response of impoundments under a variety of ground motions representative

of the anticipated earthquake characteristics, which is another aspect that has not been thoroughly evaluated previously.

1.1 Objectives

The primary objective of the current research project is to develop a method to optimize the design of waste rock inclusions in a tailings impoundment to ensure its seismic stability.

To attain this primary objective, there are several secondary objectives and tasks that have been completed in the course of the doctoral research project. These include:

- Developing a numerical modeling approach for simulating the seismic behavior of tailings impoundments with and without WRI;
- Investigating the effect of the waste rock inclusions configuration (i.e., spacing and width) on the seismic behavior of the impoundment using various indicators;
- Assessing the impact of impoundment geometry, particularly the downstream slope and height, on seismic behavior and stability of the impoundment;
- Evaluating the efficacy of various seismic intensity measures (IMs) that reflect ground motion characteristics to provide relevant performance indicators for the numerical evaluation of seismic behavior of tailings impoundment;
- Quantifying the effect of tailings density (and related properties) on the seismic response of the system;
- Developing a design correlation model that links the performance indicators to the parameters investigated.

1.2 Content of the thesis

This introduction chapter includes a description of the study with the main objectives and components of this research. Chapter 2 presents a review of the literature on the properties of mine wastes, and on the main construction methods for tailings facility. Some previous work on the use of WRI in tailings facilities and numerical analyses of various scenarios are also presented. The chapter also discusses different methods of evaluating the liquefaction potential in contractive,

cohesionless material such as tailings from hard rock mines. Finally, the basic concept and formulation of the UBCSAND and PM4Sand constitutive models for numerical modeling of tailings dynamic behavior are described and compared briefly.

Chapters 3, 4 and 5 are presented in the form of three papers submitted to peer-reviewed journals.

- Chapter 3 presents the results of numerical dynamic analyses of the seismic behavior of tailings impoundments with and without waste rock inclusions. A parametric analysis investigates the effects of the downstream slope, impoundment height, and loading conditions on the overall response and seismic stability of the system. The critically displaced volume of tailings and the horizontal displacement of the downstream slope are used to evaluate the influence of each parameter individually. The results are used to develop correlations that estimate the downstream slope displacement as a function of the impoundment geometry and waste rock inclusions configuration.
- Chapter 4 presents a numerical parametric investigation to assess the effect of different intensity measurements (IMs) of the ground motion on the seismic response of tailings impoundments with and without waste rock inclusions reinforcement. Statistical analyses are carried out to determine the predictability of the influence of IMs based on the criteria of efficiency, practicality, and proficiency. Based on the numerical results, an earthquake performance model is developed, which correlates the downstream slope displacement to the best correlated seismic parameters that characterize the intensity of the ground motions.
- Chapter 5 presents a simplified approach to develop a correlation equation that relates the horizontal displacement of the downstream slope of reinforced tailings impoundments to a variety of independent parameters, including the downstream slope inclination, impoundment height, optimal seismic intensity measures, tailings density index, and WRI configuration. The effects of each parameter on seismic stability (i.e., horizontal displacement) are discussed individually before presenting and analyzing the proposed relationship. The predictability of the developed equation in terms of normal distribution of residuals is assessed using regression analysis. The results are employed to develop guidelines for using waste rock inclusions in tailings impoundments to ensure seismic stability.

Chapter 6 synthetizes Chapter 3, 4 and 4, and presents a general discussion of the research findings and the interactions between the various aspects of the investigation.

Chapter 7 includes the main conclusions and recommendations. The appendices include additional results and information.

CHAPTER 2 LITERATURE REVIEW

2.1 Mine wastes management

Mine waste management techniques have recently progressed as a result of the numerous failures of storage facilities. While it is still vital to improve design and operational plans in the mining industry, this alone is insufficient to mitigate failure risks, so proper technical and operational management is required (Vick,1990; Aubertin et al., 2002a; Bussiere, 2007). In this regard, it is acknowledged that a mining waste storage facility is no longer considered temporary and may need to be constructed to be geotechnically and environmentally stable following the mine closure (Barrera et al., 2015; Aubertin et al. 2016). The following section will discuss the principles of mine waste management that must be adopted into the mining operations plan.

2.1.1 Mine wastes disposal

The mine wastes disposal plan generally refers to the method used for producing, transporting, discharging, and retaining mine waste products (mainly waste rock, tailings and process waters). The disposal strategy, which is part of the management practices, should be determined in accordance with the following criteria (Aubertin et al. 2002b; ANCOLD, 2012):

- Type of mining and milling process
- The final volume of the wastes
- The waste physical and chemical characteristics
- The nature of the available disposal area
- The local climate
- Environmental impacts (during operation and upon closure)

The amount and characteristics of the different wastes generated at various phases of the mining operation must be evaluated in details to ensure the efficiency of the chosen mine wastes management strategy. Mining wastes volumes and characteristics can vary widely depending on the geographical, geological, hydrological, and climatological characteristics (Chevrel et al., 2001; Aubertin et al., 2002b).

2.2 Mine wastes

2.2.1 Tailings

Tailings are comprised of crushed rocks and concentrator-processed fluids that remain after the extraction of metals during the mining and milling process (Aubertin et al., 1996; Younger and Wolkersdorfer, 2004; Bussière, 2007; Lottermoser, 2011). The term 'tailings' refers to the waste produced by ore processing (or dressing) at a variety of mines, including those for aluminum, coal, oil sands, precious and base metals, iron, and uranium. Tailings are classified into several categories based on the characteristics of the parent rock, the mineral compositions, and the mode of milling and deposition. Soft-rock tailings, fine tailings, coarse tailings, and hard-rock tailings are the typical classifications for tailings based on parent rock properties (Vick, 1990). Most tailings are a mix of fines (particles smaller than 75 µm) and sands (particles larger than 75 µm but smaller than 4.75 mm). The fines portion, sometimes referred to as "slimes", often dominates the tailings behavior, particularly for soft rock tailings where these are comparable to that plastic silt or clay (Vick, 1990). Many modern mines produce almost only fine tailings, where the amount of sand is minimal. Fine particles (silt or clay size) generally have the greatest influence on the engineering behavior of (most) tailings, including their sedimentation-consolidation characteristics. The term 'coarse tailings' is sometimes used for the products of iron, oil sands, uranium, gypsum, and phosphate mining, although some of these operations also contain a large proportion of fine particles (e.g., oil sands of Alberta). Hard-rock tailings are mostly produced by base and precious metal operations such as lead-zinc, copper, gold, silver, molybdenum, and nickel mines, and other similar operations. Hard-rock tailings are a mixture of sand and non-plastic slimes. The sand fraction often dominated the overall behavior of hard rock tailings in older operations, but improvement in the milling extraction processes has led to the production of finer tailings over the last 2-3 decades (i.e., tailings with more than 50-70% of fine particles; Aubertin et al., 2002a,b; Bussière, 2007). The focus of this study is on hard-rock tailings, notably those from the Canadian Malartic mine (Abitibi, QC) that have been characterized extensively over the last 12 years or so (Bussière, 2007; L-Bolduc, 2012; Boudrias, 2018; Essayad and Aubertin, 2021). The hydro-geotechnical properties of these (and similar) tailings, as well as different methods of deposition, will be outlined in the following.

2.2.2 Waste rock

The surrounding host rock must be extracted in open-pit or underground mines to reach and extract ore in a mining operation. Typically, these host rocks are not valuable, and the waste rock produced by blasting is stored on the mine site in surface waste rock piles to decrease transportation costs (Aubertin et al., 2002a; Bussière, 2007). Waste rocks from hard rock mines are made up of angular particles with a very wide granulometry that ranges from small particles (silt) to blocks up to one meter in diameter (Aubertin et al., 2008). Different construction techniques are used to raise waste rock piles and their hydro-geotechnical properties and behavior depend on the construction method and on waste rock characteristics, as will be discussed in this chapter. Both tailings and waste rock can also be returned in the mine as backfill, but this aspect is not considered here (Thomas et al., 1979; Aubertin et al., 2002a; Sivakugan et al., 2006).

2.2.3 Wastewater

Wastewater is stored in tailings impoundments and includes mine water, process water, and water circulated through tailings, concentrate, or ore. Retaining water in a tailings storage facility could be for operational or environmental reasons. This increases the risk of a rupture and the associated effects (contamination). When a breach occurs in a tailings impoundment, pond water, retained tailings, and other waste materials could discharge from the impoundment and contaminate the environment (CDA, 2019).

2.3 Mine wastes storage methods

Mining operations around the globe generate billions of tonnes of wastes each year. Mine wastes storage methods are a source of concern for the industry and society because these wastes can include pollutants that can seep on the surface and through the soils and groundwaters and contaminate the ecosystems (Aubertin et al. 2002b; Bussière et al., 2004; Plante et al., 2012).

Mine wastes can include solids and liquids, and they may also contain leaching metals and acid-generating minerals. Contaminated mine waters necessitate treatment for secure disposal, with continuous monitoring (Aubertin et al., 2002b).

Waste rock piles and tailings impoundments are the two main kinds of surface storage facilities, and these are described in the following section.

2.3.1 Tailings disposal methods

2.3.1.1 Conventional methods

Tailings are usually transported as slurry and deposited in designated areas known as tailings impoundments in conventional methods of tailings disposal. Geometrical characteristics of impoundments are determined by topographic, climatic, geotechnical, and geochemical factors. The tailings are retained by dikes (and natural topographic features) which are commonly composed of coarse tailings or waste rocks. There is no global database of all tailings impoundments. There are an estimated 18,000 impoundments, of which 3,500 are active (Davies and Lighthall, 2001; Davies, 2002; Lottermoser, 2011).

During the initial years of mining, a starter dike constructed of local soils or waste rock is used to retain the tailings impoundment. The produced tailings are then added in the ponds generally from the top of the starter dike. There are three standard methods to raise the height of the dike which are presented in Figure 2.1 (Vick,1990; Aubertin and Chapuis, 1991; Aubertin et al., 2002b, 2011): the upstream, downstream and centerline methods.

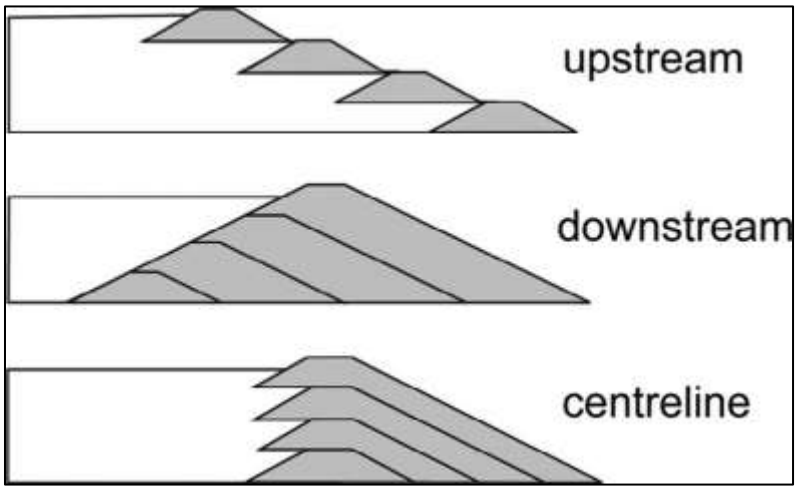

Figure 2.1: Schematic illustrations of upstream, downstream and centreline sequentially raised tailings dikes (redrawn after Vick, 1990).

The upstream raise method is a relatively simple and economical construction method. This method is suitable for areas relatively dry climate and low seismic risk. There are however many well-known disadvantages to this technique, which include (Vick, 1990; Aubertin et al., 2002a):

- Significant risk of geotechnical instability;
- Maximum dike height and rate of rise are both limited;
- Close monitoring of material response and settlement is required (complexity of management)

The downstream construction method generally leads to safer and more reliable dikes compared to the upstream method. This method is better suited for seismically active locations and also when there is a need to maintain an elevated water level in the long term (for reactive tailings). This technique also allows the construction of zoned dikes with different materials (selected and compacted) to better control water seepage (i.e., impervious core, filters, drain, etc.). There are disadvantages to the downstream raised technique, which include:

- A substantial volume of material is required for construction;
- It is much more expensive compared to other methods;

The centerline approach is a compromise between the two previous methods. When compared to the upstream method, this method has greater stability and lead to improved stability. Less material is required than for the downstream method, so it is less costly. In general, this method is adaptable to a wide range of scenarios. Some of the main limitations of this method are:

- Usually necessitates the use of hydrocyclones to separate the coarse and fine fractions when tailings are used as construction material, but there is not enough sandy fraction in many cases;
- Higher costs than the upstream method, with a large amount of material required.

2.3.2 Waste rock piles

Waste rock piles are commonly used to store the extracted rock that is not economical to process at the mill. There are a variety of considerations to take into account when deciding where to place waste rock piles, including geological, geotechnical, hydrogeological and hydrological aspects

(Aubertin et al., 2002a; Aubertin et al., 2013) as well as operational, topographic, earthquake (Fourie, 2008; Blight, 2010; Hawley and Cunning, 2017) and climatic ones (Maknoon and Aubertin, 2021). The waste rock pile selection process can be challenging when considering all of the relevant factors (Hustrulid et al., 2000).

The waste rock pile construction method should be chosen as a function of the geography of the area, foundation conditions, available equipment, and overall pile design criteria (Piteau Associates Engineering Ltd., 1991). The construction method affects the waste rock pile characteristics, such as the degree of compaction and segregation, which could have an impact on water flow in the pile (Morin et al., 1991; Fala et al., 2003).

2.4 Hydro-geotechnical properties of hard rock tailings

2.4.1 Geotechnical properties of hard rock tailings

The mineralogy, grain size, method of deposition, age, and thickness of the deposited tailings inside the impoundments all influence their behavior and properties. With conventional tailings disposal processes, hard rock tailings are transported as a slurry to the impoundment where they are discharge. The slurry pumping approach causes particle segregation and the loss of homogeneity (Vick, 1990; Aubertin et al.2002a; Bussière,2007). The water content and porosity of the deposit is initially high, and the density index of the tailings is low, as a result of the disposal procedure.

Table 2.1 summarizes the main hydro-geotechnical properties of tailings reported by different sources. Some variations in property values, such as those relating to consolidation and hydraulic conductivity, can be attributable to particle size, and to different types of testing and different techniques of specimen preparation. The next sections discuss these various properties in further detail, particularly those of Canadian Malartic mine tailings.

Table 2.1: Typical geotechnical characteristics of hard rock mine tailings (reported by various authors).

Properties	**Units**	**Qiu et Sego (2001)**	**Bussière (2007)**		**L-Bolduc (2012)**	**Contreras Romero (2013)**	**Essayad (2015)**	**Grimard (2018)**
Origin		Hard rocks	Canada	Québec	Canadian Malartic mine			
Relative density (D_r)	-	2.6-4.5	2.6 to 2.9 (Quartz) 2.9 to 4.5 (sulphide)		2.75	2.73	2.76	2.69
Effective internal friction angle (φ')	°	33	30 to 42		-	36.8	-	38
Effective cohesion (c')	kPa	0	0		-	0	-	0
Angle of internal friction in total stresses (φ)	°	-	14 to 25		-	-	-	-
Cohesion (c)	kPa		0 to 100		-	-	-	-
Grain diameter by 10% passing (D_{10})	µm	5	1 to 4	0.9 to 6	1.3 to 3	2.2 to 3	4.6	3.8
Grain diameter by 60% passing (D_{60})	µm	54	10 to 50	10 to 80	18 to 19	20 to 25	37	44.6
Coefficient of uniformity (C_U)	-	11	8 to 18	10 to 30	6 to 15	8 to 9	7	11.8
Liquid limit (w_l)	%	-	<40		-	-	-	-
Plastic limit (w_p)	%	-	0 to 15		-	-	-	-
Clays size fraction (< 2 µm)	%	5.3	5 to 14	4 to 20	7 to 13	7 to 9	3 to 5	5.9
Fraction of fine particles (< 75 µm)	%	81.3	70 - 97	60 - 100	100	100	95	79
Unified classification (USCS)	-	ML	ML	ML/SM	ML	ML	ML	ML
Optimum water content (w_{opt}) (compaction)	%	-	10 - 20		16.2 - 16.5	15- 16.1	-	12.7 - 13.0
Maximum dry unit weight after compaction ($\gamma_{d\ max}$)	kN/m^3	-	14.6 - 20.1		16.8 - 17.0	17.7 - 17.4	-	18.54
Minimum void ratio (e_{min})	-	-	-		0.59 - 0.61	0.54 - 0.56	-	0.45
Maximum void ratio (e_{max})	-	-	-	-	-	1.60 - 1.51	-	1.53

Compression index(C_c)	-	0.08 - 0.15	0.05 - 0.3		0.003 - 0.31	0.05- 0.42	0.02 - 0.56	0.042 - 0.087
Recompression index(C_r)	-	-	0.003 - 0.03		-	-	0.013 - 0.024	0.01 - 0.020
Coefficient of compressibility (a_v)	MPa^{-1}	-	-		0.09 - 22	0.14 - 0.34	0.09 - 180	0.08 - 0.3
Coefficient of volume change (m_v)=a_v/(1+e_0)	MPa^{-1}	0.29 - 163	-		0.43-11	-	0.06 - 92	0.05 - 0.18
Coefficient of consolidation (C_v)	cm^2/s	0.004 - 0.025	0.001 - 0.1	0.1 - 100	0.01 - 3	0.063 - 0.77	0.02 - 6.6	0.95 - 2.6
Saturated hydraulic conductivity (k_{sat})	cm/s	$3x10^{-5}$ - $7x10^{-5}$	10^{-2}- 10^{-4}	10^{-4} - 10^{-6}	$1x10^{-5}$ - $4x10^{-5}$	-	$9x10^{-6}$ - $1x10^{-4}$	-

Grain size distribution

Tailings grain size distribution is highly variable as it depends on individual processing conditions. In the case of the Canadian Malartic mine, 95% to 100% of tailings produced in the early years of operation were made of fine particles (< 75 µm) (L-Bolduc, 2012; Poncelet, 2012; Contreras Romero, 2013; Jahanbakhshzadeh and Aubertin, 2022), but these became coarser later (Grimard, 2018). On average, tailings from gold mines in Quebec contain between 70% and 97% of fine particles (Bussière, 2007).

Figure 2.2 shows various grain size distributions for Quebec hard rock mine tailings (Bussière 2007) and for the Canadian Malartic mine tailings (L-Bolduc, 2012; Contreras Romero, 2013; Essayad, 2015; Grimard, 2018). Figure 2.2(a) shows that the particle size of the hard rock tailings varies from one mine to another, with D_{10} and D_{60} typically varying respectively between 0.9 and 6 µm and between 10 and 80 µm. The differences between the grain size curves can be explained in part by the different comminution methods used to extract the ore (Bussière, 2007). The value of uniformity coefficient ($C_U = \frac{D_{60}}{D_{10}}$) varies between 10 to 30 for these granulometric curves (Figure 2.2a). It should be noted that even though the calculation of C_U is more applicable for coarse-grained soil, it will be shown later in this chapter that this parameter is important for tailings when

evaluating a variety of geotechnical parameters, such as saturated hydraulic conductivity (Aubertin et al., 1996).

In the case of Canadian Malartic mine tailings, the particle size has evolved over the years, becoming somewhat coarser between 2011 to 2016 (for samples characterized at Polytechnique; Figure 2.2 (b), (c), (d) and (e)). The D_{10} varied between 1 and 5 µm while D_{60} was between 18 µm and 42 µm, respectively. The gradation curves obtained by L-Bolduc (2012) showed a percentage of clay size particles (< 2 µm) up to 13%, while it was 3% and 5.9% for Essayad (2015) and Grimard (2018), respectively. The tailings characterized by Grimard (2018) included 21% of sand (> 75 µm), while the gradation curves presented by L-Bolduc (2012) and Contreras Romero (2013) did not contain any sand particles. The coarser grain size distribution was attributed to modifications to the milling process to improve the efficiency of gold extraction.

Relative density (D_r) and void ratio (e)

The relative density of tailings is determined by the mineralogical composition of the parent rock. According to Bussière (2007), the relative density of tailings ranges between 2.6 and 2.9 for ore predominantly extracted from quartz veins, and between 2.9 and more than 4.5 when the ore is mostly in sulphide veins. The measured relative density of tailings at the Canadian Malartic mine is typically between 2.69 and 2.76 (L-Bolduc, 2012; Poncelet, 2012; Contreras Romero, 2013; Essayad, 2015; Grimard, 2018).

Sangrey et al. (1978) and Bjelkevik (2005) also performed extensive tests to determine the physical properties of tailings, and they reported a relative density of hard rock tailings from 2.6 to 2.8. Aubertin et al. (1996) reported values ranging from 2.78 to 2.87. Wijewickreme et al. (2005) obtained relative densities of 3.36 to 3.42 for 20 samples of copper, gold, and zinc tailings. James (2009) reported an average D_r value of 3.88 for tailings from the LaRonde polymetallic mine (Abitibi, Quebec).

The tailings void ratio (e) varies with different parameters, including grain size, particle shape, stress state, and deposit age. The in-place void ratio (e_0) in the laboratory might vary greatly depending on the specimen reconstitution procedure and the initial water content (w_0) (Aubertin et al., 1996; Blight, 2010; Bussière, 2007; Poncelet, 2012; Essayad et al., 2016). Vibrating table tests (ASTM D-4253-16) or modified Proctor tests are commonly used to determine the minimum void

ratio (e_{min}), which is the densest state of the tailings (ASTM D1557-12). Proctor test results show that the minimum void ratio (e_{min}) for tailings from the Canadian Malartic mine is between 0.45 and 0.6 (Jahanbakhshzadeh and Aubertin, 2022). According to Vick (1990), the in-situ void ratio of hard rock tailings varies between 0.6 and 0.9 depending on the confining pressure.

Index properties

Vick (1990) and Aubertin et al. (1996) reported that hard rock tailings are commonly non-plastic, with a low (near zero) plasticity index. According to Bussière (2007), the liquid limit of hard rock tailings is typically less than 40%, while the plastic limit is typically less than 15%. Qiu and Sego (2001) studied the basic properties of four different mine tailings (copper mine tailings from Kennecott Mining, gold mine tailings from Echo Bay's Lupin Mines, coal wash plant tailings from the Coal Valley Mine of Luscar Sterco Ltd., and oil sand composite tailings (CT) from Syncrude Canada Ltd). Except for the coal wash tailings, the tailings were non-plastic based on their basic physical properties. The relative density, liquid and plastic limits, and relative density of the copper tailings were all within the ranges proposed by Mittal and Morgenstern (1975) and Volpe (1979). The plastic limits for the copper, gold, and CT tailings were the same as the value presented by Aubertin et al. (1996).

Shear strength parameters

The shear strength τ (kPa) of soils and similar materials is commonly expressed using the Mohr-Coulomb equation (Holtz and Kovacs 1991; Ishihara 1996; Mitchell and Soga, 2005), expressed as a function of the normal effective stress σ'_N (kPa), the effective internal friction angle, φ' (˚), and the effective intrinsic cohesion c' (kPa):

$$\tau = \sigma'_N \tan(\varphi') + c' \quad (2.1)$$

According to Aubertin et al. (2011), the effective internal friction angle (φ') of tailings for the coarse fraction (sand) is typically between 33 ° and 42 °, while it is usually between 30 ° and 37 ° for the fine fraction. These values are similar to those reported for Canadian Malartic mine tailings (L-Bolduc, 2012; Poncelet, 2012; Contreras Romero, 2013; Essayad, 2015; Grimard, 2018; Jahanbakhshzadeh and Aubertin, 2022). Bussière (2007) reported that hard rock mine tailings have the effective internal friction angle of 30 ˚to 42 ˚ and a cohesiveness (c') close to zero. It was also

mentioned by Bussière (2007) that the effective internal friction angle (φ') of the tailings can be up to 6 ° higher than that of natural soils, of the same particle size, due to the particle angularity.

Vick (1990) demonstrated that the undrained (total stress) internal friction angle of tailings (φ) is lower than the drained friction angle (φ') and ranges from 14 ˚ to 25 ˚. Vick (1990) also reported that the undrained cohesion of tailings, *c*, can range anywhere from 0 to 100 kPa. According to Jahanbakhshzadeh and Aubertin (2002), for normally consolidated tailings, the undrained shear strength S_u is close to $0.22\sigma'_v$ (the effective vertical stress). However, for over-consolidated tailings (with OCR > 1; Vick, 1990), the value of Su/σ'_v can increase. For liquefied tailings, the Su/σ'_v ratio is usually decreased to between 0.10 and 0.12 (e.g., James et al. 2011; Contreras, 2022).

James (2009) used a series of direct shear tests to determine the strength parameters of the relatively coarse-grained Laronde Gold Mine tailings. According to this study, the average effective internal friction angle was 36.6° and was influenced by the confining stress variation (100 to 400 kPa).

Hu et al. (2016) performed CU and CD triaxial testing on Yuhezhai iron tailings as well as CU tests on Bahuerachi copper tailings. The results of the triaxial tests were used to compute the friction angle and cohesion of fine and coarse tailings. The findings indicated that the effective internal friction angle of coarse-grained tailings is greater than that of fine-grained tailings for both iron and copper tailings. The values of φ' of coarse iron tailings are comparable to coarse copper tailings, but those of fine iron tailing are less for fine copper tailings.

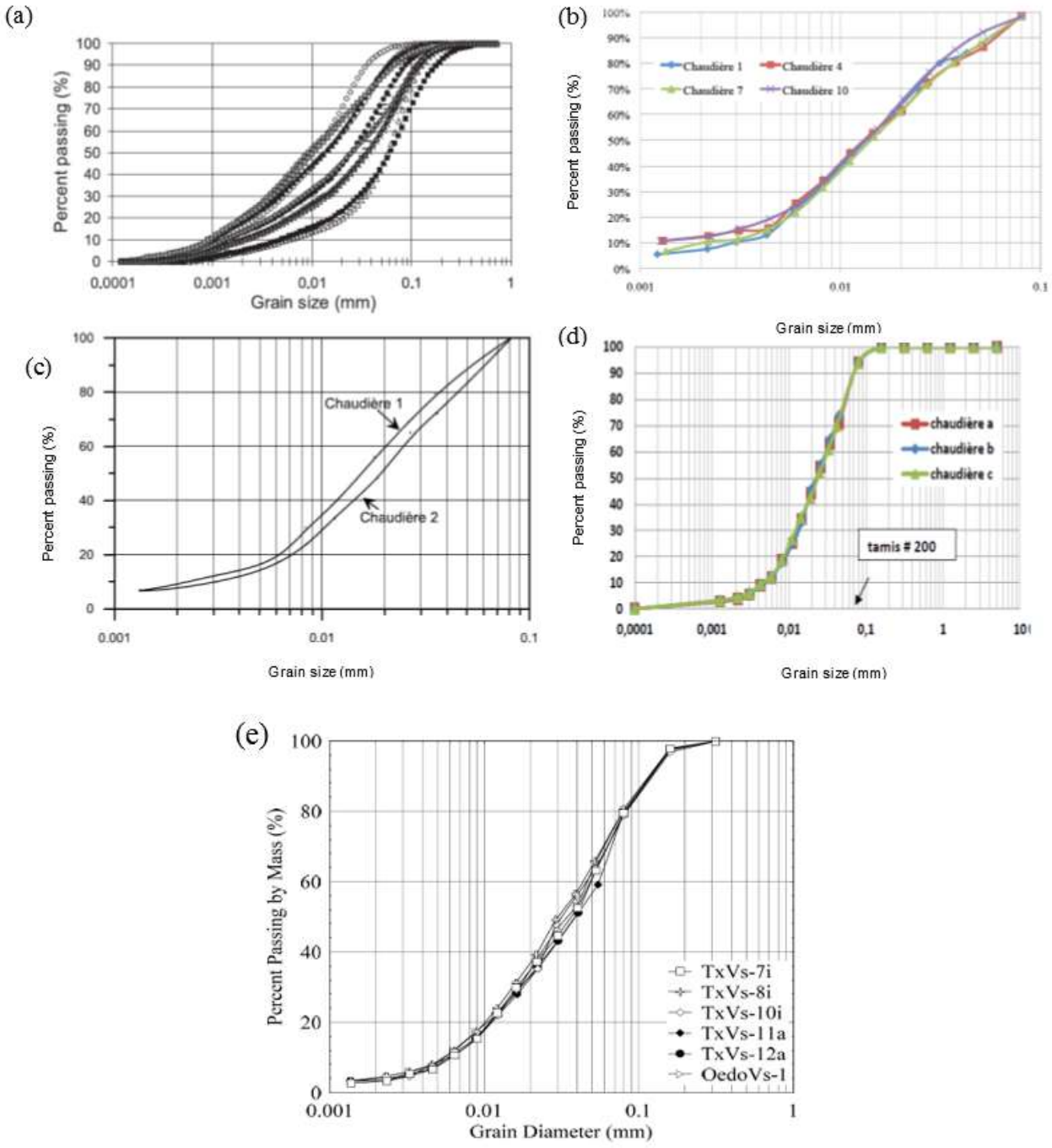

Figure 2.2: Tailings grain size distribution for: (a) various hard rock mines (adapted from Bussière, 2007); Canadian Malartic mine according to (b) L-Bolduc (2012); (c) Contreras Romero (2013); (d) Essayad (2015); (e) Grimard (2018)

2.4.2 Hydrogeological properties of hard rock tailings

Conventional tailings typically show a difference in their horizontal and vertical hydraulic conductivity due to the deposition method, the presence of particles of varying size and consolidation rate. Horizontal hydraulic conductivity in-situ can be 10 to 100 times greater than vertical hydraulic conductivity (Vick, 1990; Aubertin et al., 2002a, 2011).

Vick (1990) indicated that the saturated hydraulic conductivity of hard rock mine is commonly between 5×10^{-7} cm/s for silts with low plasticity and 1×10^{-4} cm/s for sands with up to 30% fines by weight. Aubertin et al. (1996) and Chapuis and Aubertin (2003) showed experimental results and demonstrated that the Hazen and Kozeny Carman relationships are not directly applicable for estimating the saturated hydraulic conductivity of tailings. Aubertin et al. (1996) proposed the following equation to estimate the saturated hydraulic conductivity of tailing material, based on laboratory measurements.

$$k_{sat}[cm/s] = 1962\ \frac{e^{5.16}}{1+e} {C_U}^{1/3} D_{10}^2 \tag{2.2}$$

Where e is void ratio, C_U is the uniformity coefficient, D_{60} and D_{10} are diameters corresponding to 60% and 10% passing on the cumulative grain-size distribution curve (cm), respectively.

Mbonimpa et al. (2002) generalized formula (2.2) for estimating of k_{sat} of a variety of soils and tailings as follows:

$$k_{sat}[cm/s] = C_G(\frac{\gamma_w}{\mu_w})({C_U}^{\frac{1}{3}} {D_{10}}^2)(\frac{e^{3+x}}{1+e}) \tag{2.3}$$

Where C_G is constant equal to 0.1 (for the selected units), γ_w is the unit weight of water (9.81 kN/m^3), μ_w is the dynamic viscosity of water (1×10^{-3} Pa), e is the void ratio, x is approximately equal to 2 for soils and tailings with low plasticity index.

According to the review presented by Bussière (2007), the typical value of saturated hydraulic conductivity of fine grain tailings (ML) is between 1.0×10^{-4} and 1.0×10^{-6} cm/s and the value for coarse grain tailings (SM) is between 1.0×10^{-2} and 1.0×10^{-4} cm/s (see also Aubertin et al., 2011). The typical saturated hydraulic conductivity of tailings from a Canadian Malartic mine is near to 10^{-5} cm/s (L-Bolduc, 2012; Essayad, 2015).

Hu et al. (2016) showed that the average saturated hydraulic conductivity of coarse iron tailings and the coarse copper tailings are 1.0×10^{-4} and 2.1×10^{-3} cm/s, respectively. They observed that the hydraulic conductivity of fine-grained tailings increases as the void ratio increases, and that the tested fine copper tailings had a higher hydraulic conductivity than fine iron tailings.

2.4.3 Consolidation properties of hard rock tailings

Bussière (2007) reported results from consolidation tests on undisturbed and remoulded hard rock tailings. The compression index C_c of the tested specimens varied from 0.05 to 0.54 and the recompression index, C_r, were about 5 to 20% of the C_c value. The coefficient of consolidation, c_v, is almost equal for undisturbed and remoulded specimens, with a value between 4.3×10^{-3} and 3.7×10^{-1} cm^2/s. Aubertin et al. (2011) noted that for tailings with a high proportion of fine particles (<75 μm), C_c typically varies between 0.10 and 0.30, while it varies between 0.05 and 0.15 for a high proportion of coarse (sandy) particles.

The coefficient of compressibility (a_v) of Canadian Malartic mine tailings was shown to be highly variable by L-Bolduc (2012), Contreras Romero (2013), and Essayad (2015); this is expected because this parameter strongly depends on the effective stress level and initial void ratio. The minimum compressibility coefficient is near 0.09 MPa^{-1} while the maximum value can sometimes reach 180 MPa^{-1}. The corresponding coefficient of volume compressibility (m_v) varies between 0.06 and 163 MPa^{-1} for these tailings (L-Bolduc, 2012; Essayad, 2015).

Stone et al. (1994) conducted a series of experiments on tailings from an Australian gold mine to measure the consolidation coefficient in the laboratory. The results showed that the laboratory-measured values were half of those determined by in-situ measurements. They indicated that the variation was mainly due to the deposition of tailings with varying gradation and degree of consolidation (i.e., different grain sizes and void ratios).

Qiu and Sego (2001) performed a series of consolidation tests to assess the behavior of tailings over an effective stress ranging from 0.5 to 100 kPa. The compression index, C_c for copper tailings was comparable to values reported in the literature (Volpe 1979; Vick 1990). The C_c values for gold tailings were lower than those reported by Stone et al. (1994) (C_c = 0.75), but higher than

those reported by Williams and Morris (1990) (C_c = 0.2). They concluded that discrepancies were due in part to different initial void ratios (0.6–1.0) and clay content.

2.5 Hydro-geotechnical properties of waste rocks

Waste rocks are made up of a wide variety of particle sizes, ranging from silt to boulders with a maximum size of 0.5 to 1.0 m (Azam et al., 2009) and a coefficient of uniformity (C_U) of 20 or higher (Barbour et al., 2001; Aubertin et al., 2002a; Gamache-Rochette, 2004). Figure 2.3 illustrates the range of grain size distributions of waste rock that have been investigated (laboratory or in-situ) and reported in the literature. The majority of the grain size is in the sand and gravel range (from 75 µm to about 5-10 cm). Some of the characteristics of coarse rock aggregates such as waste rock (i.e., hardness and brittleness), are usually controlled by the parent rock, while others are related to the grain size distribution, density (porosity), and grain crushing under high stresses. The grain size of waste rocks is sometimes reduced by crushing in underground mines to aid transportation. The size range influences rock aggregate crushing strength (McDowell and Bolton, 1998; McDowell and Amon, 2000; Alonso et al., 2012; Ovalle et al., 2014). The shape of waste rock particles, including their angularity, may change during the various stages of mine processing. Due to material heterogeneity, segregation, and the presence of large boulders, precise grain size distributions of waste rock in waste rock piles are difficult to evaluate (Fala, 2008). However, multiple approaches such as sampling and laboratory measurements, in-situ determination, and image analysis can be employed to estimate the range size of course rockfill materials such as waste rock (McLemore et al., 2009; Hu et al., 2011; Ovalle et al., 2013).

Table 2.2 presents a summary of the hydro-geotechnical properties of waste rocks as reported by various studies over the years.

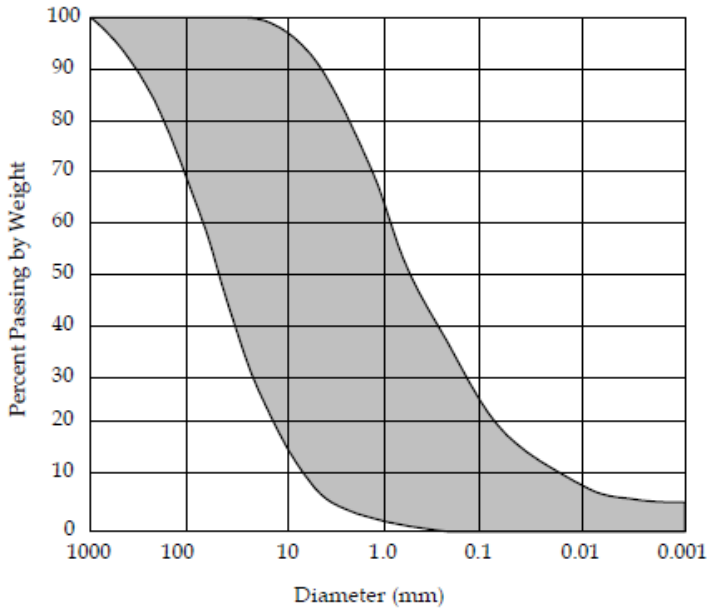

Figure 2.3: Range of grain size distribution curves reported in the literature (adapted from Gamache-Rochette, 2004).

Table 2.2: Typical geotechnical characteristics of waste rock material (reported by various authors).

Properties	**Units**	**Average range**	**Reference**
Relative density (D_r)	-	2.1-3.7	Kesimal et al. (2004); Bussière et al. (2011)
Angle of internal friction in effective stresses (φ')	°	33-45	Aubertin et al. (2002a); Barton (2008); Azam et al. (2009); McLemore et al. (2009); Maknoon (2016); Ovalle et al. (2020)
Effective cohesion (c')	kPa	0-10	MacLemore et al. (2009)
Grain diameter by 10% passing (D_{10})	mm	0.008-6	Nichols (1987); Aubertin et al. (2002a); Azam et al. (2007); Anterrieu et al. (2010); Lessard (2011); Bussière et al.
Grain diameter by 60% passing (D_{60})	mm	1-80	

Coefficient of uniformity (C_U)	-	More than 20 Can be more than 200	(2011); L-Bolduc (2012); Peregoedova (2012)
Silt size fraction (< 80 μm)	%	Between 0% to 10%	
Dry density (ρ_d)	kg/m^3	1500-2500	Williams (2000); MacLemore et al. (2009)
Saturated hydraulic conductivity (k_{sat})	cm/s	10^{-3}-10^{-1}	Aubertin et al. (2011); Bussière et al. (2011); Peregoedova (2012)
Young's modulus (E)	MPa	50-150	Anbazhagan et al. (2010); Maknoon (2016)

According to published studies by various authors, the typical internal friction angle, which governs the shear strength of waste rock (under effective stresses), can range between 21 º (for softer rock) and 62 º, with typical values for hard rocks ranging between 33 º and 45 º (Sherard et al. ,1963; Leps, 1970; Aubertin et al., 2002a; Azam et al., 2009; Maknoon, 2016; Ovalle et al., 2020). However, grain size, mineralogy, particle shape, and stress levels can all have an impact on the shear strength of waste rock (Barton, 2008; Holtz et al., 2010; Aubertin, 2013; Ovalle et al., 2020).

In the absence of cohesive (clayey) minerals, the effective cohesion, c', of dry or saturated waste rock from hard rock mining is usually near to zero (Aubertin, 2013). However, under unsaturated conditions, an apparent cohesion may appear; but it should be ignored in stability analyses for pile construction (Aubertin, 2013; Maknoon and Aubertin, 2021).

The saturated hydraulic conductivity, k_{sat}, depends on the particle size of waste rock material. The values of k_{sat} can be measured in laboratory (usually on a truncated grain size) and in-situ or be estimated by predictive models such as the Kozeny-Carman (KC) equation (Chapuis and Aubertin, 2003) and the Kozeny-Carman modified KCM model (Mbonimpa et al., 2002). The range of saturated hydraulic conductivity reported in the literature for waste rock material varies between 10^{-7} to 1 cm/s (Bussière and Aubertin,1999; Morin et al., 1991; Li, 2000; Barbour et al., 2001; Lessard, 2011; Peregoedova, 2012; Martin et al. 2019).

2.6 Liquefaction

2.6.1 Liquefaction mechanism

Soil liquefaction is generally defined as a loss of shear strength caused by the generation of excess porewater pressure under static or dynamic loading. This condition, which typically occurs within saturated, contractive, cohesionless soils, is associated with a state of near-zero (or very low) effective stress that can result in excessive deformation under gravity or external loading (Holtz and Kovacs, 1981; Seed and Idriss, 1982; Kramer, 1996; Youd et al., 2001). This relatively simple definition does not, however, reveal the full complexity of the liquefaction phenomenon. Indeed, the mechanisms of pore pressure generation depend on many factors including the type of soil, initial state, and loading conditions (Idriss and Boulanger, 2007, 2008; Boulanger and Idriss, 2014).

2.6.1.1 Critical state line

The initial state of a soil has a significant effect on its susceptibility to liquefaction. The state of the material should be compared with the critical state condition to evaluate the tendency of the material to dilate or contract upon loading (Jefferies and Been, 2015). A soil is in a critical state when it deforms without changing the volume during shearing under constant deviatoric and mean effective stresses (Holtz and Kovacs 1981; Been et al., 1985). The critical-state line (CSL) is a set of points that describes the relationship between void ratio (e) and effective confining pressure (p') under the critical state condition.

Figure 2.4 shows the stress-strain behavior of a typical sand material under loose and dense initial conditions. The samples are loaded in a conventional triaxial cell under drained conditions with a controlled strain. The results indicate that by increasing the deviatoric stress the initial void void ratio of the loose (e_l) and dense (e_d) sample converges to the critical void ratio (e_{crit}) as defined by Casagrande, (Holtz and Kovacs, 1991). Theoretically, the critical void ratio for the loose (e_{cl}) and the dense state (e_{cd}) should be the same (e_{crit}). The disparity is occasionally attributable to a lack of precision in measuring the final void ratio or to the non-uniform distribution of stresses and strains within the sample (Hirschfeld, 1963). There is a state from which excessive deformations at constant volume can appear. The critical state (or critical void ratio) line is the locus of void ratio-ultimate deviatoric stress conditions $(\sigma_1\text{-}\sigma_3)_{ultimate}$ achieved after shearing a soil to large strain.

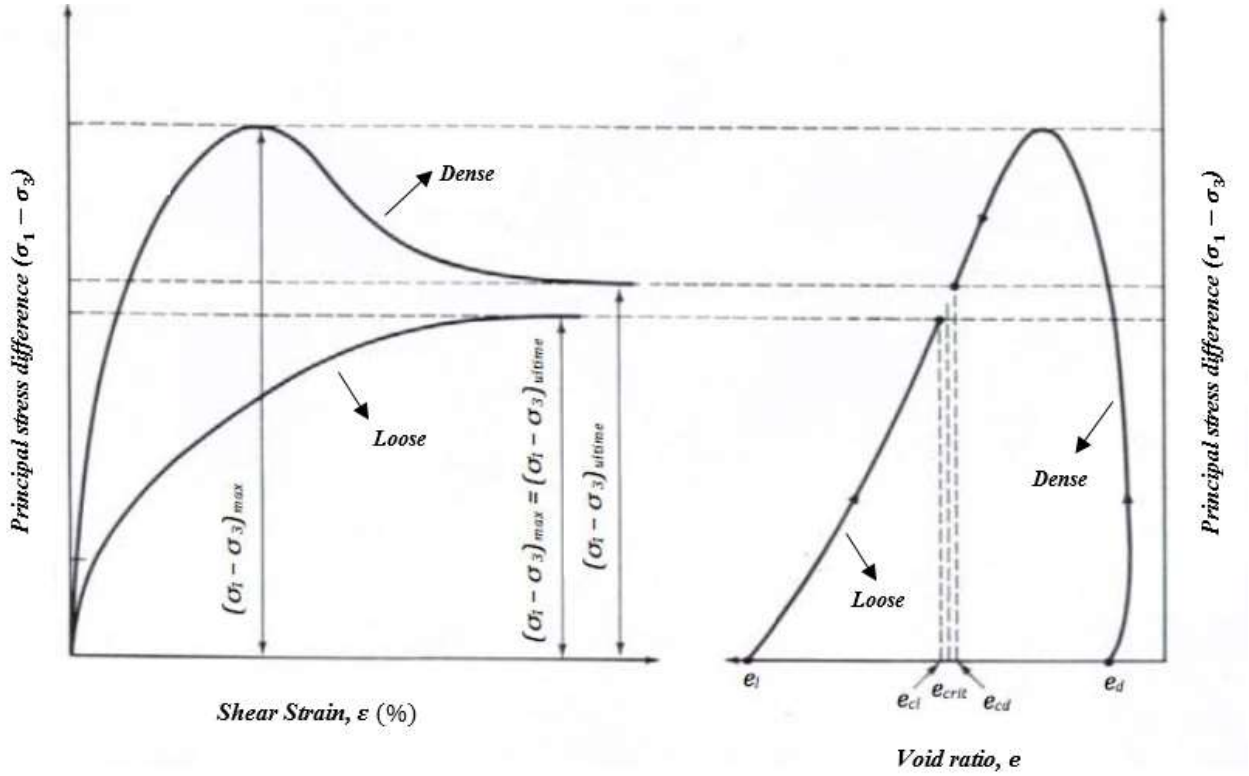

Figure 2.4: Stress-strain behavior during triaxial tests under drained conditions on loose and dense samples of a typical sand (adapted from Holtz and Kovacs, 1991)

Figure 2.5 shows the critical state line for a typical sandy material. A soil that is looser than the critical state has a tendency to contract under shearing, whereas a soil that is denser than the critical state has a tendency to dilate during shearing and will typically exhibit lower deformations under cyclic loading. Figure 2.5 indicates that under undrained loading, contractive (loose) soils generate positive excess pore water pressures that reduce the effective stress until the critical state condition is reached. Under the same loading conditions, dilative (dense) soils generate negative excess pore water pressure changes with an increase in effective stress (Holtz and Kovacs, 1981).

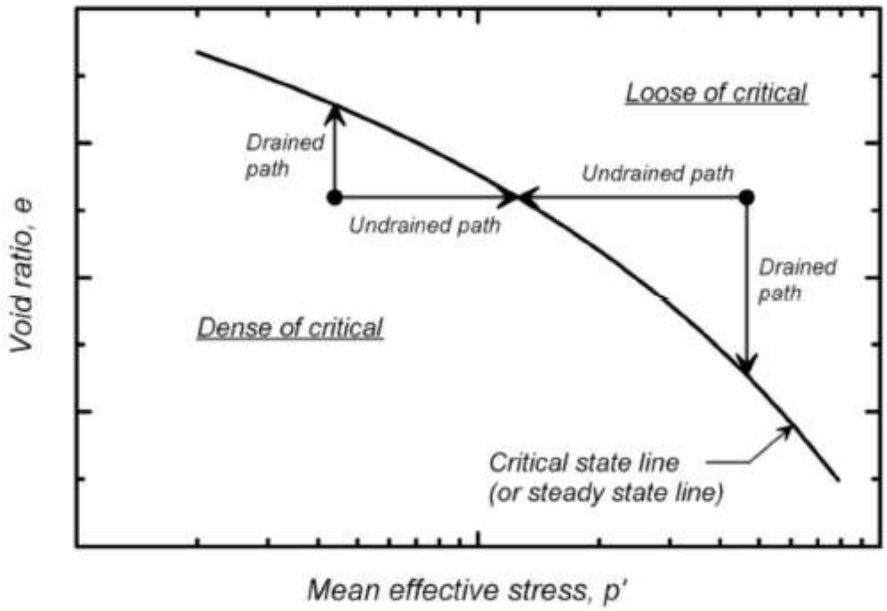

Figure 2.5: Critical State Line for sand (CSL) (adapted from Kramer, 1996)

2.6.1.2 Initiation of liquefaction

Liquefaction can occur as a result of monotonic or cyclic loads on a loose soil in an undrained condition. The initiation of liquefaction is usually defined from the generated excess pore water pressure or when the induced shear strain reaches amplitudes greater than 3% (Seed and Lee, 1966). The initiation of liquefaction may differ depending on the type of loading. The mechanics of liquefaction initiation under monotonic and cyclic loads are presented in the following.

Monotonic loading

Figure 2.6 illustrates how a loose soil behaves differently under drained and undrained conditions. Situation A represents the behavior of drained loose soil, whereas Situation B shows the behavior of the same soil in an undrained condition. According to this graph, the deviatoric stress (σ_1-σ_3) applied to loose soil in the drained case increases until it reaches a plateau, whereas in the undrained situation, deviatoric stress increases until it reaches a maximum, at which point the soil becomes unstable, leading to a decrease in strength and a rapid increase in axial deformation.

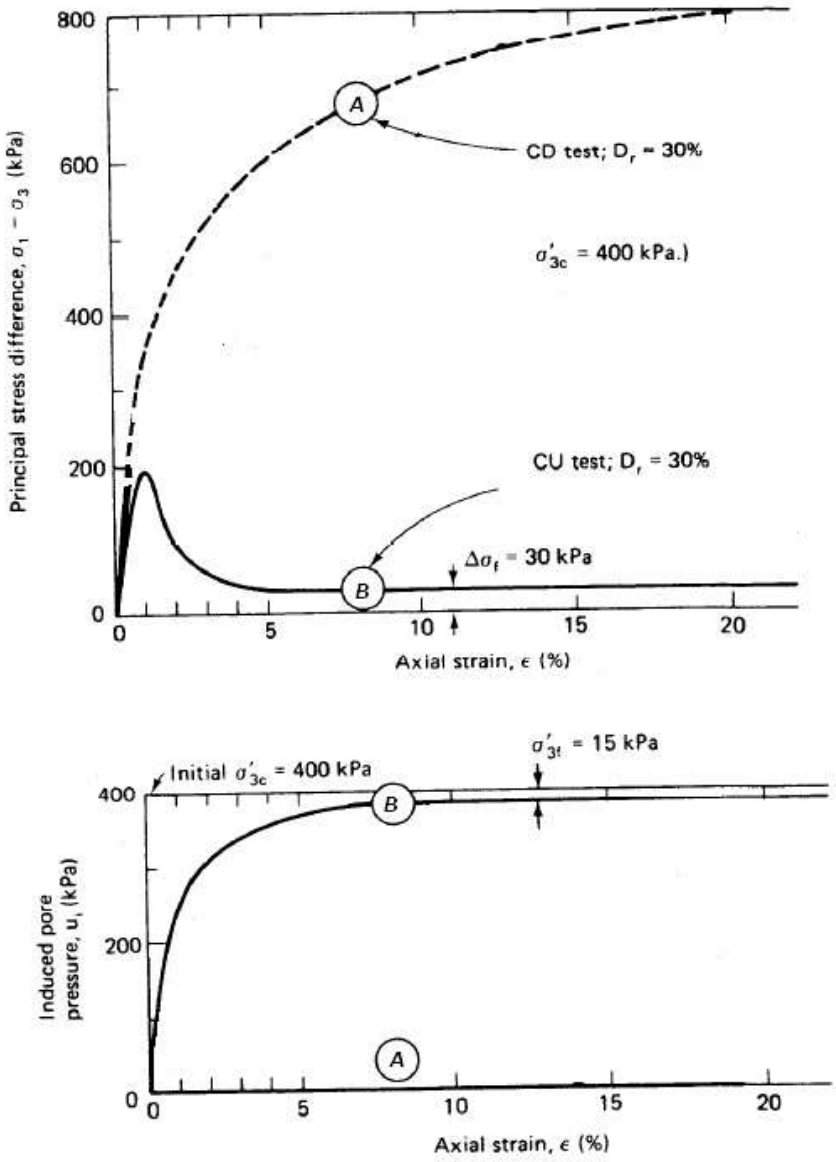

Figure 2.6: Comparison of drained and undrained isotropically consolidated tests of loose soil (after Casagrande, 1975 and Castro, 1969; figure adapted from Holtz and Kovacs, 1991)

Figure 2.7 illustrates the typical undrained behavior of loose, medium-dense, and dense sand materials. For each density state, the phase transformation (PTL) and steady state (SSL) lines can be identified using the stress paths shown in Figure 2.7a. In the case of loose sand, the start of shear (Point A) results in a reduction in mean stress ($p = (\sigma'_1 + 2\sigma'_3)/3$, kPa), while deviatoric stress

(q = $\sigma'_1 - \sigma'_3$, kPa) increases to the point of maximum soil strength. From this point, p' and q begin to decrease to reach the limit state or effective stress near zero which represents liquefaction condition (Point B'' and C''). Dense sand shows a decrease in p' from the initiation of the shear (Point A) until the dilatant behavior (phase transformation line) starts (Point B). Then, p' increases until the soil reaches the limit (critical) state (Point C).

The stress-strain behavior in the undrained state, as shown in Figure 2.7b, can be used to determine whether the soil has a hardening behavior (dense state) or a softening behavior (loose state). The term "strain hardening" refers to the process of increasing soil strength by increasing strain up to a plateau (known as the limit or critical state (Point C)); the term "softening" refers to the process of decreasing stress with deformation beyond the maximum value of resistance until reaching the residual resistance that corresponds to the limit (or critical state (Point B'' and C'')) in the post-peak phase.

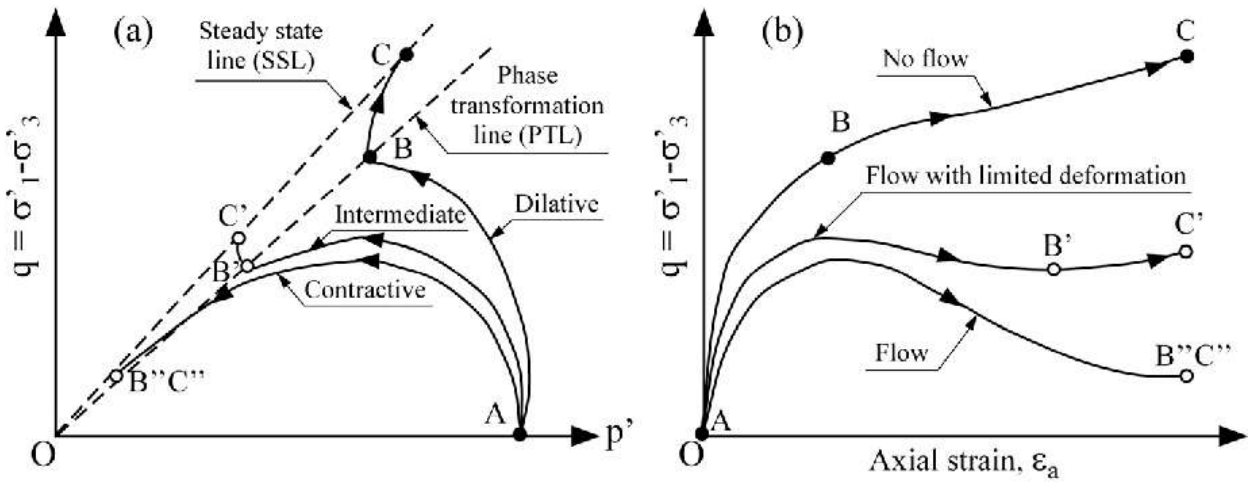

Figure 2.7: Untrained response of samples of loose, medium dense, and dense sand in terms of (a) stress path, and (b) stress-deformation response (Kamata et al., 2009)

Grimard (2018) has investigated the undrained response of tailings from Canadian Malartic Mine (in the Abitibi region of Quebec, Canada). In this study, the specimens were consolidated isotopically in the triaxial cell to effective confining stresses of 50, 100, 200, 400 and 600 kPa with consolidated void ratios varied from 0.63 at 50 kPa to 0.52 at 600 kPa. The behavior of tailings were assessed through strained-controlled undrained, monotonic compression tests. Figure 2.8

presents the undrained monotonic test results in terms of (a) deviatoric stress ($\sigma_d = \sigma'_1 - \sigma'_3$), (b) effective major principal stress (σ'_1), (c) pore water pressure (u), and (d) the effective minor principal stress (σ'_3) versus the axial vertical strain (ε_{ax}). At axial strains of less than 1%, all of the specimens show contractive behavior as indicated by a sudden increase in the σ_1, σ_d, and u. However, at higher strains (2% to 2.5%), the behavior becomes dilative (i.e., pore water pressure starts to decrease) until the critical state is reached. These results confirm that the sample showed overall dilative behavior (i.e., no risk of static liquefaction) except for a small strain range (1%).

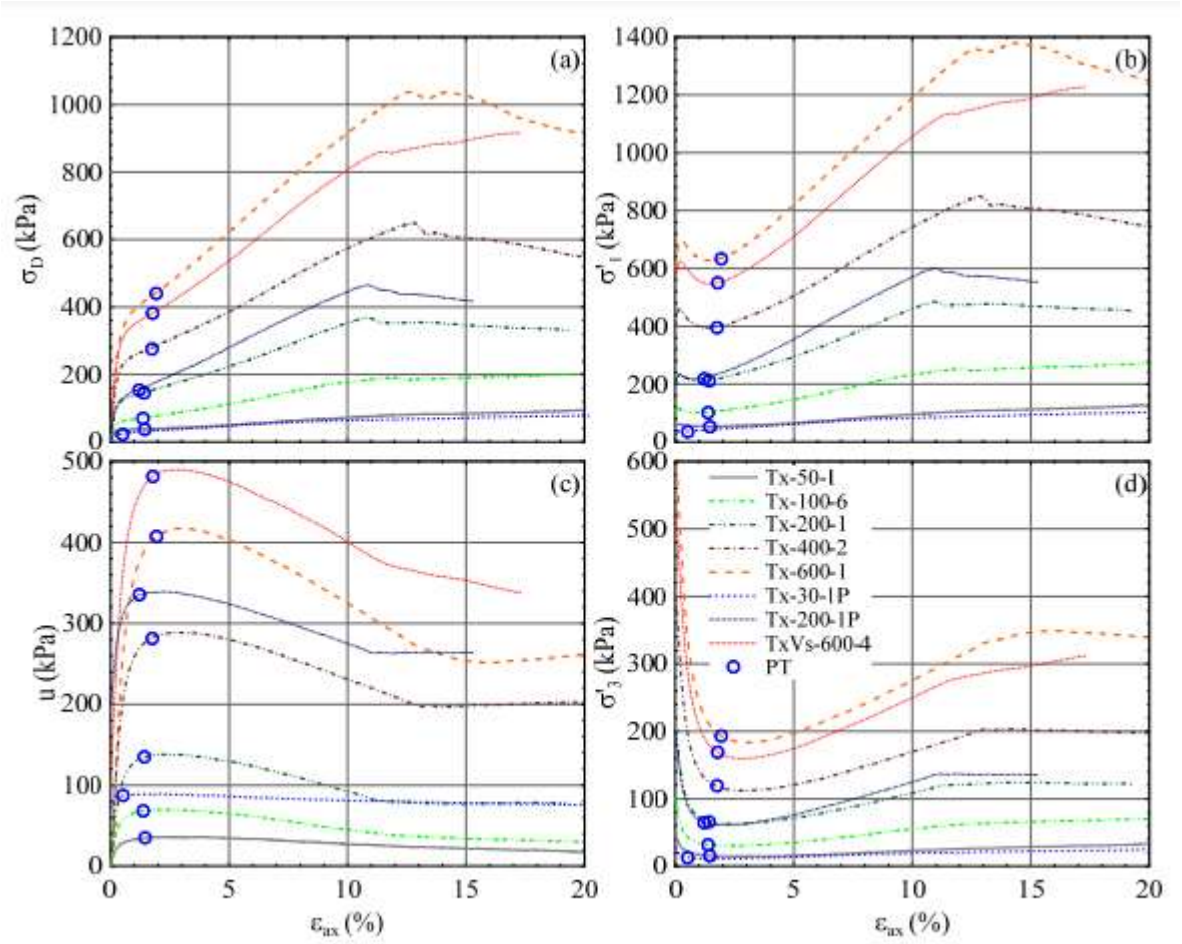

Figure 2.8: Monotonic undrained tests results on tailings from Canadian Malartic Mine in terms of (a) Deviatoric stress, σ_d, vs axial strain, ε_{ax}; (b) Effective major principal stress, σ'_1, vs axial strain; (c) Pore water pressure, u, vs axial strain; and (d) Effective minor principal stress, σ'_3, vs axial strain. The (blue) circles show phase transformation (PT) (Grimard, 2018).

Figure 2.9 illustrates the average critical state line obtained from similar studies on tailings from the Canadian Malartic Mine (Contreras, 2013; Archambault-Alwin, 2017; Grimard, 2018), presented in terms of density index (I_d) as a function of mean effective stress (P'). The results of these studies show that the critical state for the tailings under study is reached for an axial strain between 9% and 16.5%.

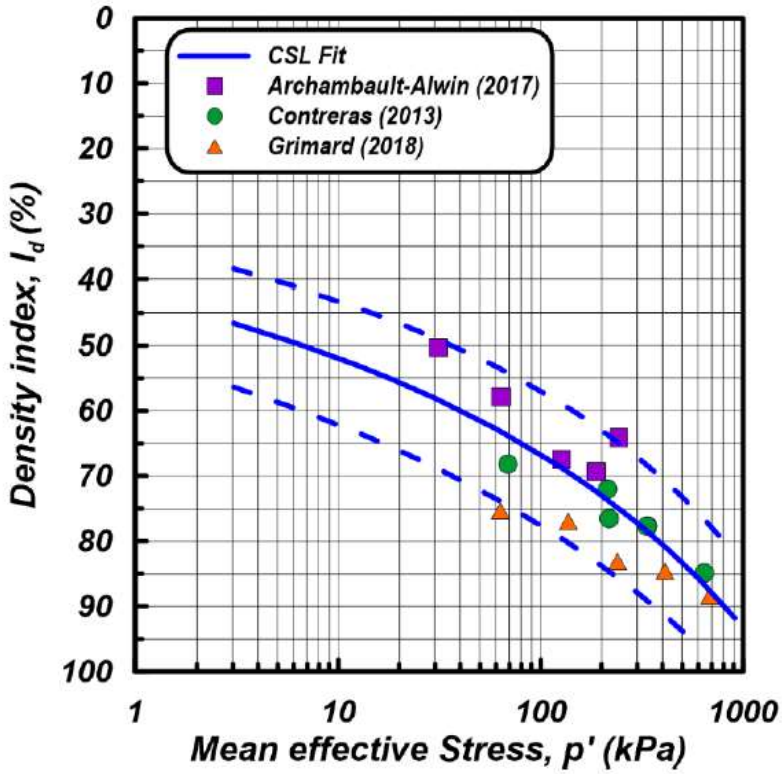

Figure 2.9: Average Critical State Line (CSL) with one standard deviation range, obtained from monotonic tests on hard rock tailings (Contreras et al., 2022a)

Cyclic loading

Granular soils can liquefy under both static and cyclic loading conditions. When a saturated granular soil cannot dissipate the excess pore pressure generated by loading due to low permeability or a high loading rate, there is a decrease in effective stress that favors the development of shear deformation (Kramer, 1996). The initiation of liquefaction is independent of the type of loading (Vaid and Chern, 1985). Therefore, monotonic or cyclic loading can lead to the steady state boundary in a contractive soil. In Figure 2.10, a soil is loaded in both static monotonic (path AB) and cyclic (path AD) types, with an initial static shear at point A. Both types of loading

get the soil to the flow liquefaction surface (FLS) at different stress levels (points B and D, respectively), but once on the FLS, both stress paths move towards the limit state point (Point C), where excessive deformation can occur at constant stresses (Kramer, 1996).

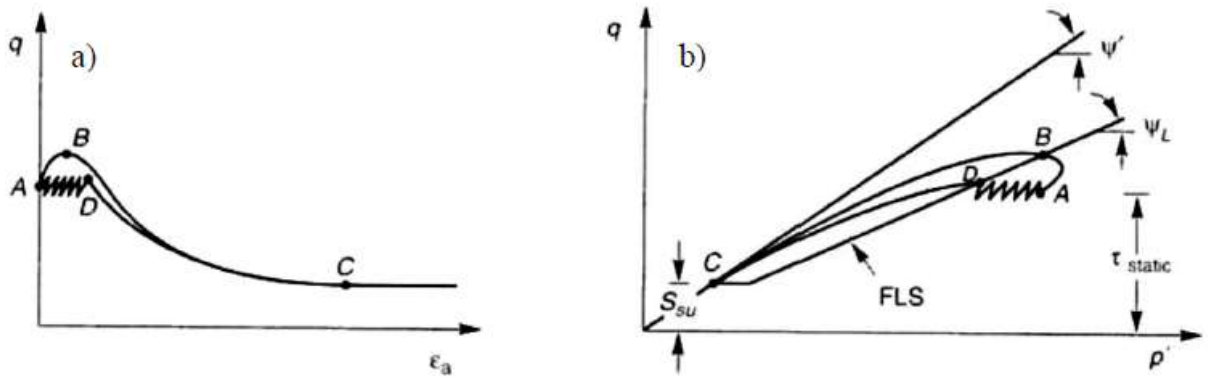

Note:S_{su} is the shear strength at steady state

Figure 2.10: Undrained response of sand material under monotonic and cyclic loading conditions in terms of (a) stress-deformation response (b) stress path (adapted from Kramer, 1996)

Results of a cyclic triaxial compression test for loose sand (contractive) is shown in Figure 2.11. The density index, I_D, was 38%, and the confining pressure, σ_3, was equal to 100 kPa. The axial deformation of the samples (Figure 2.11a) is small, almost zero for the first few loading cycles. However, once the soils reached the FLS (see Figure 2.10) after 10 cycles, the axial strain increased dramatically to over 20% and the pore water pressure increased to a value of Δu equal to the initial effective confining pressure, $\sigma'_{v,0}$ (Figure 2.11b), leading to zero effective stress and high deformation (Holtz and Kovacs, 1991).

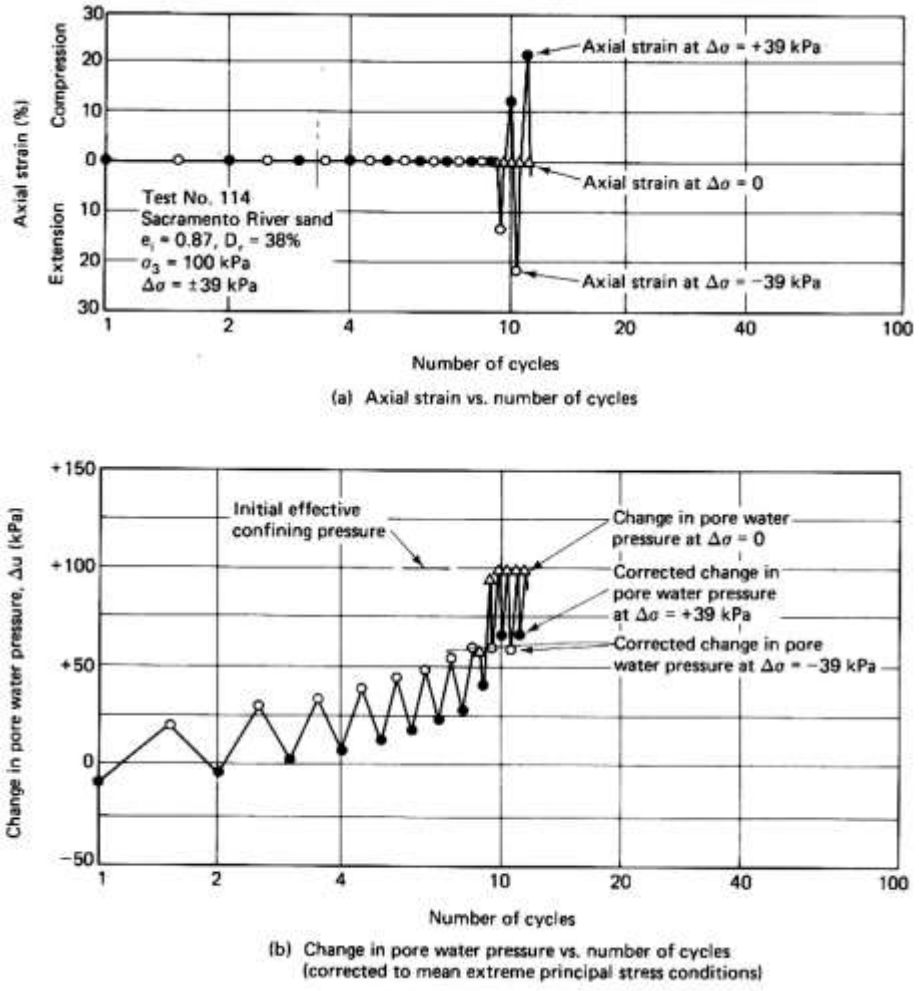

Figure 2.11: Cyclic triaxial compression test results of loose sand (from Holtz and Kovacs, 1981)

The initial state of the soil has a significant impact on the cyclic response of the granular material. Generally, when granular soils are subjected to cyclic stress, the soil may undergo sudden deformations and a significant loss of strength. However, if the soil responds by gradually developing deformations and a loss of strength, this type of behavior can be attributed to cyclic mobility. In general, the differences between these two types of behavior are determined by the initial density of a soil. The effect of the density on the undrained cyclic response of sand is indicated in Figure 2.12. In this figure, the cyclic triaxial test results are presented in terms of deviatoric stress–axial strain curves and effective stress paths, for the loose (Figure 2.12a), medium-dense (Figure 2.12b) and dense (Figure 2.12c) sand. The loose sand sample (Figure 2.12a)

indicated flow liquefaction and showed relatively modest axial strain during the initial cycles of loading. However, the results show a significant softening and a sudden development of axial strain (i.e., liquefaction) after a couple of cycles. The liquefaction failure mechanism is characterized by cyclic mobility and recovery of stiffness due to strain hardening for the medium-dense and dense materials. The decrease of shear stiffness between cycles caused permanent deformations to accumulate slowly for these samples (Figure 2.12b and c). The mean effective stress, *p'*, gradually decreased as the strain increased, and the stress path proceeded in the direction of the origin of the axes.

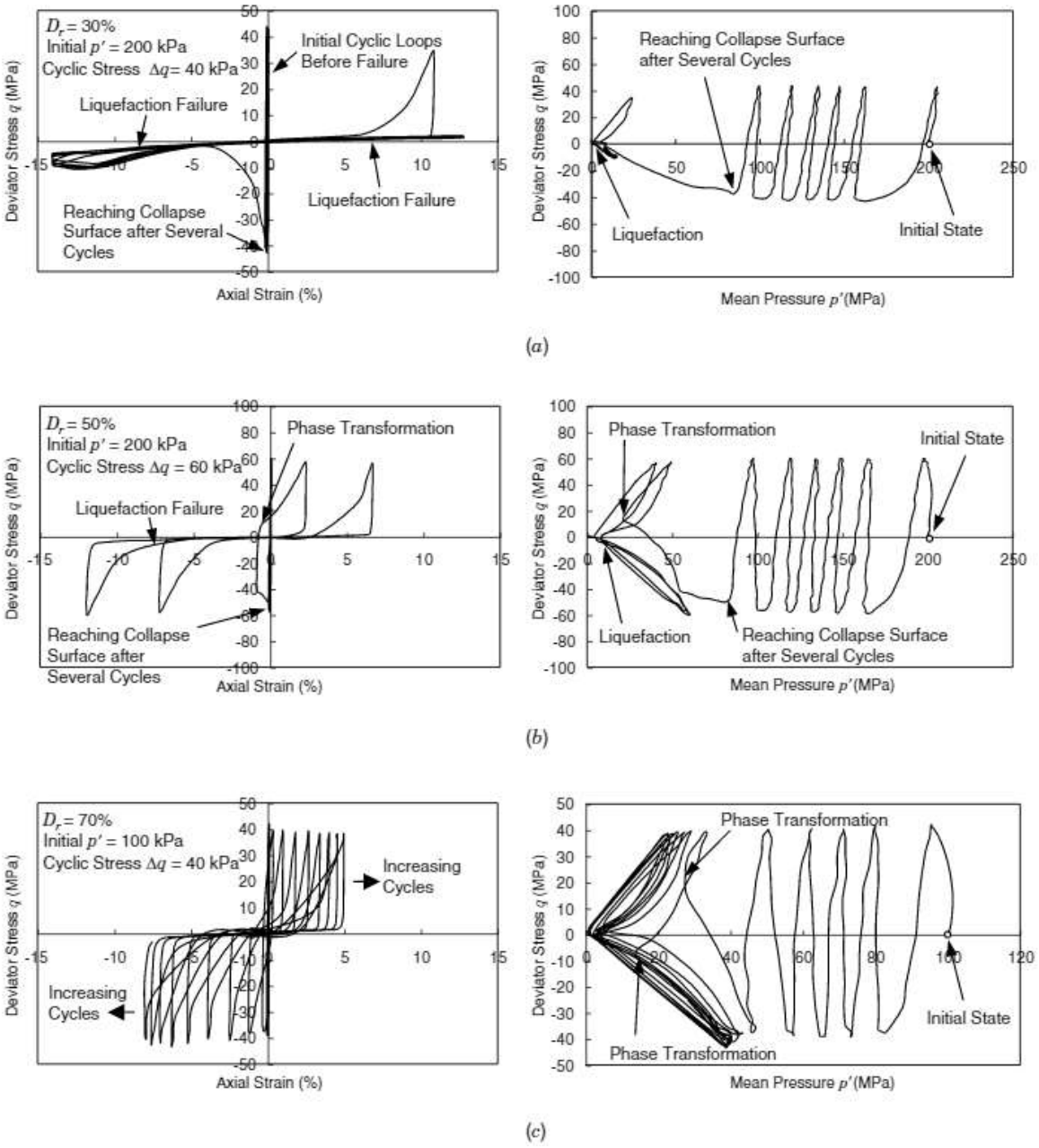

Figure 2.12: Cyclic responses of Toyoura sand in terms of deviatoric stress–axial strain curves and effective stress paths for (a) loose sand; (b) medium-dense sand; (c) dense sand (adapted from Mitchell and Soga, 2005)

2.6.2 Dynamic characteristics of soils

The initial shear modulus, shear modulus reduction, and damping increment with shear strain are the main dynamic properties of tailings and waste rock that must be determined to conduct seismic behavior analysis. This section discusses these dynamic characteristics of soils.

2.6.2.1 Shear modulus and damping ratio

The shear stress (τ) - strain (γ) behavior of a soil element subjected to cyclic loading, shown in Figure 2.13, demonstrates a hysteresis loop for each cycle of loading (Kramer, 1996). The inclination of the loop is determined by the stiffness and is specified at any point by a tangent shear modulus, G_{tan}. The secant shear modulus, G_{sec}, can be used to approximate the average value of G_{tan} (Kramer, 1996):

$$G_{sec} = \frac{\tau_c}{\gamma_c} \tag{2.4}$$

Where τ_c and γ_c are the corresponding shear stress and shear strain at the given (selected) condition, respectively; G_{sec} and τ_c have same units (typically kPa) and γ_c is dimensionless.

The area of the loop in Figure 2.13 depends on the energy dissipation during cyclic loading, which is described by the damping ratio, ξ (Kramer, 1996):

$$\xi = \frac{W_D}{4\pi W_s} = \frac{1}{2\pi}\frac{A_{loop}}{G_{sec}\gamma_{cyc}^2} \tag{2.1}$$

Where W_D, W_s and A_{loop} are the dissipated energy, the maximum strain energy, and the area of the hysteresis loop, respectively. W_D, W_s, A_{loop} and G_{sec} have consistent units so the damping ratio, ξ, is a dimensional.

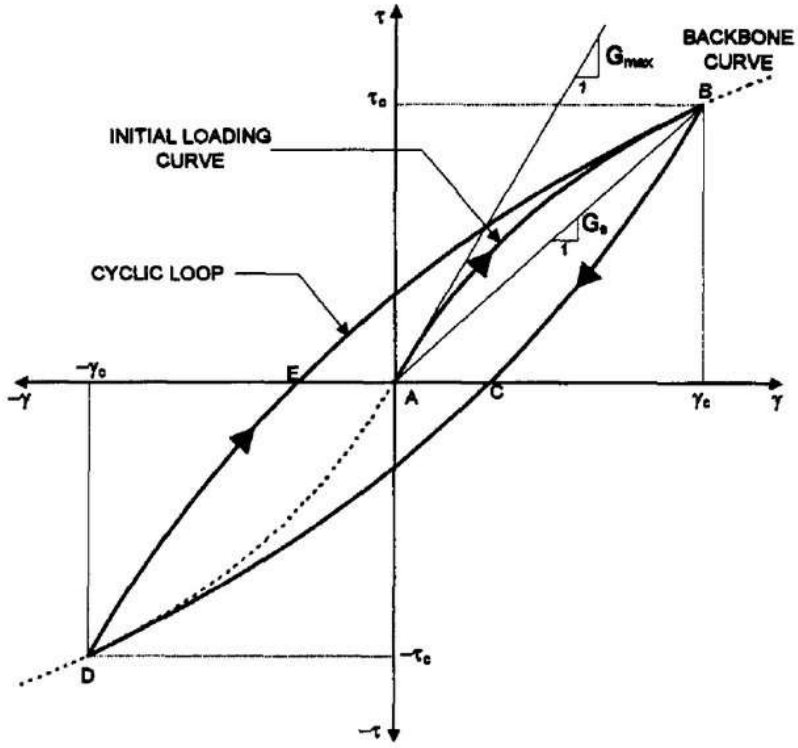

Figure 2.13: Hysteretic stress-strain relationship at different strain amplitudes (Kramer, 1996)

The locus of points corresponding to the tips of hysteresis loops during cyclic loading tests is commonly called the backbone curve. The slope of the backbone curve at the origin corresponds to the highest value of shear modulus, G_{max}, known as the maximum or low-strain shear modulus. As the shear strain increases during cyclic loading, the modulus ratio ($\frac{G_{sec}}{G_{max}}$) decreases (from 1.0 to near zero) and the damping, ξ increases. The variation of modulus ratio versus the shear strain is described by the modulus reduction curve (Figure 2.14). The backbone and modulus reduction curves can be obtained based on drained and undrained cyclic loading tests (Kramer, 1996).

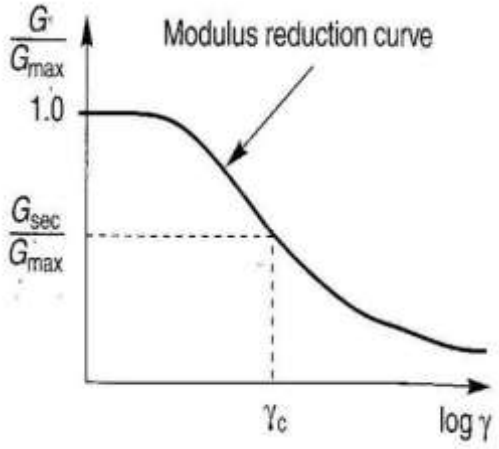

Figure 2.14: Schematic evolution of the shear modulus ratio during cyclic loading tests (Kramer, 1996)

Figure 2.15 shows the influence of strain on the reduction of shear modulus and the increase in damping through stress-strain hysteresis loops generated under undrained cyclic loading for a typical sand. The shear modulus and damping change progressively for each stage, as shown in this figure, and closely follow the backbone loading curve presented in Figure 2.13(Szilvágyi et al., 2016).

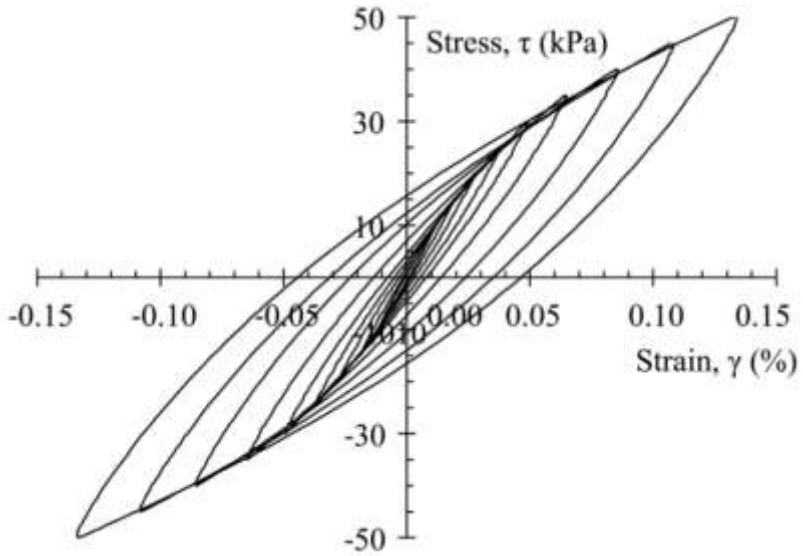

Figure 2.15: Stress-strain hysteresis loops for a typical sand (Szilvágyi et al., 2016)

The values of shear modulus, G_{max} can be obtained by several methods including (Seed and Idriss, 1982; Seed et al., 1984; Kramer, 1996; Ishihara, 1993; Towhata, 2008):

- Determination of stress-strain relationship from laboratory testing (cyclic triaxial compression tests, cyclic simple shear tests, cyclic direct shear tests, and cyclic torsional shear tests).
- Forced vibration tests.
- Free vibration tests.
- In-situ measurement of shear wave velocities.
- Analysis of ground response during earthquake ground motions.

2.6.2.1.1 Effect of various parameters on modulus reduction and damping ratio

Several studies have investigated the impact of various parameters on the reduction of the modulus ratio for granular soils, including plasticity, confining pressure, void ratio, and grain size distribution (Seed and Idriss, 1970; Kokushu et al., 1980; Troncoso and Verdugo, 1985; Dobry and Vucetic, 1987; Ishibashi and Zhang,1993; Ishihara, 1996; Kramer, 1996).

Zen et al. (1978) and Kokushu et al. (1982) investigated the effect of plasticity on the modulus reduction curve. According to their findings, the degradation rate of shear modulus in low plasticity soils is faster than in highly plastic soils (Figure 2.16). The influence of plasticity index and void ratio on modulus reduction was also studied for soils by Dobry and Vucetic (1987) and Sun et al. (1988). They observed that the effect of the plasticity index on the reduction of the modulus was more important than the effect of the void ratio.

The influence of confining pressure on soil modulus reduction was investigated by Ishibashi (1992). Figure 2.17(a) shows the effect of confining pressure on modulus reduction in non-plastic soils, while Figure 2.17(b) illustrates the effect in plastic soils with a plasticity index of 50. This investigation demonstrated that confining pressure has a considerable influence on non-plastic soils but has a much more limited (negligible) effect on highly plastic soils.

Troncoso and Verdugo (1985) investigated the effect of silt (fines) content on shear modulus of tailings. They observed that as silt content increased, the reduction in shear modulus at a given level of shear strain increased.

Kokusho (1980) used reconstituted samples of crushed, round, and alluvial gravel to investigate the behavior of different gravelly soils. Their findings indicate that crushed rock has a higher modulus reduction rate compared to round and alluvial gravel.

James (2009) conducted a series of cyclic tests on hard rock mine tailings. The results of that study showed that the modulus reduction of the tailings fit fairly well with the curves proposed by Seed et al. (1984) for clean sands (Figure 2.18).

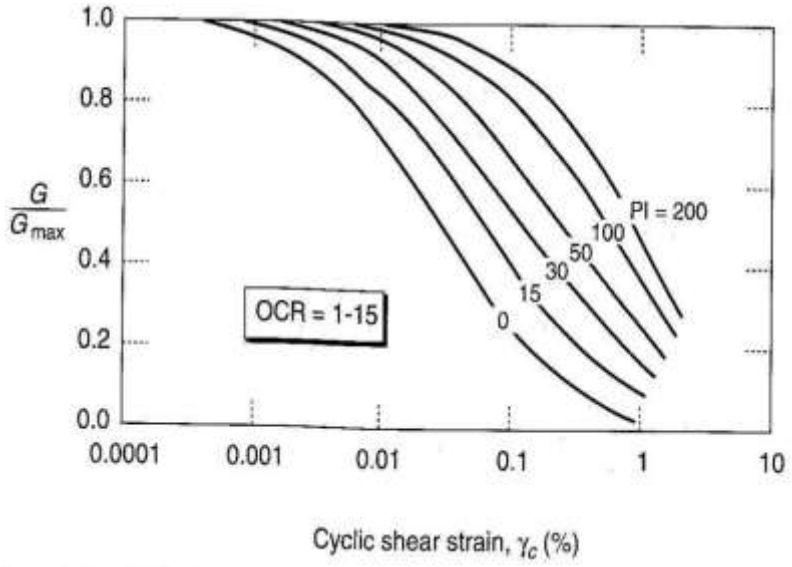

Figure 2.16: Modulus reduction curves for fine-grained soils with different plasticity (Index PI) (after Vucetic and Dobry, 1991).

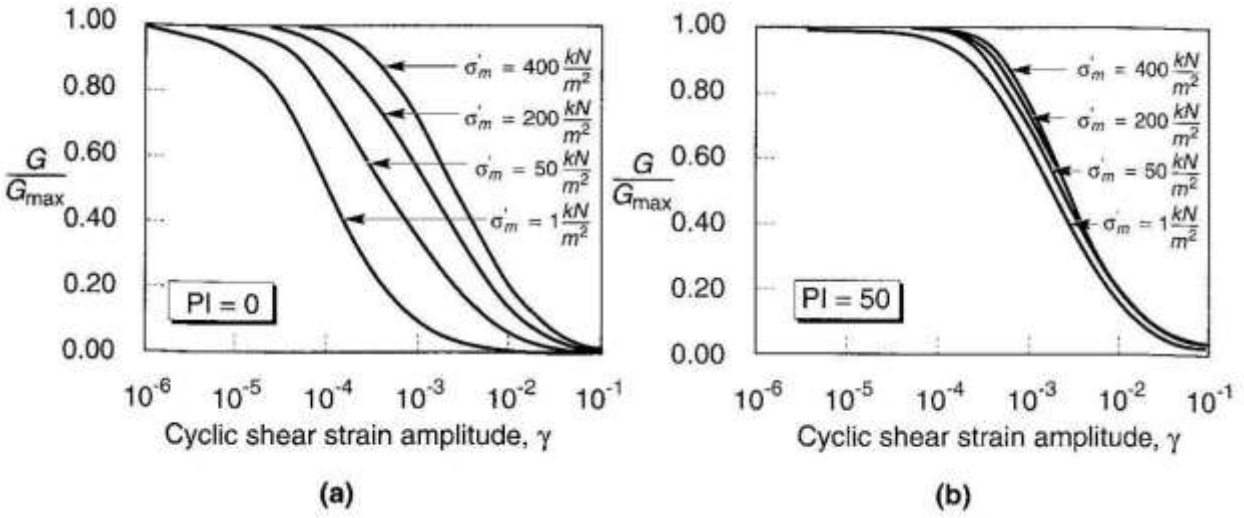

Figure 2.17: Influence of mean effective confining pressure on modulus reduction curves for (a) a non-plastic (PI=0) soil, and (b) a plastic (PI=50) soil (after Ishibashi, 1992).

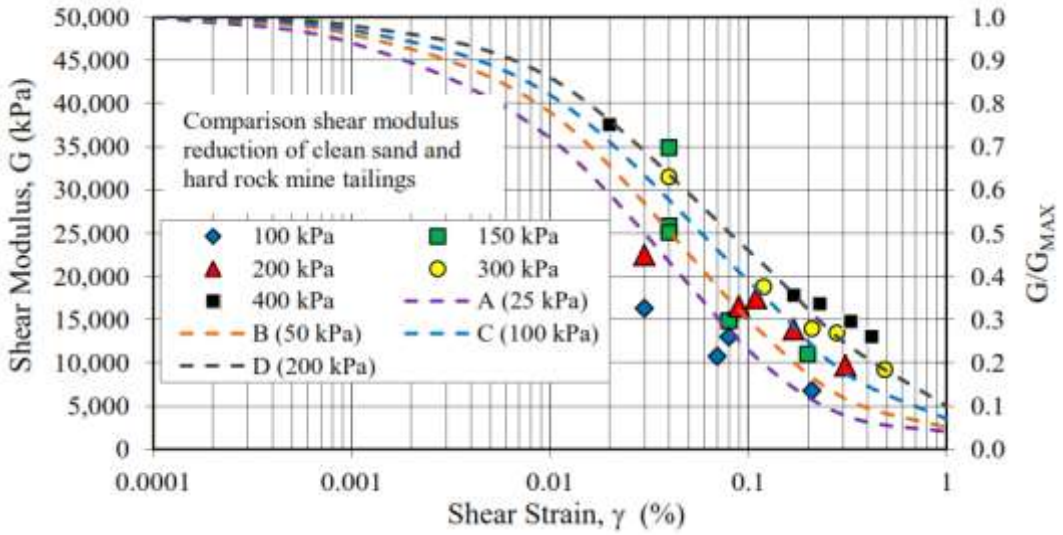

Figure 2.18: Shear modulus reduction in hard rock mine tailings and for clean sands (from James et al., 2011)

Several studies have investigated the effect of different parameters on the damping ratio, ξ such as plasticity, and confining pressure (Ishibashi and Zhang,1993; Ishihara, 1996; Kramer, 1996). Figure 2.19 shows the results of some of these investigations. The results indicate that damping ratios are lower for soils with high plasticity indices than soils with low plasticity indices (Figure 2.19a). Moreover, the findings show that the damping ratio for low plastic soils such as sands

decreases by decreasing the confining stress (Figure 2.19b). However, Kokusho et al. (1982) had shown that the effect is limited for the high plastic soils.

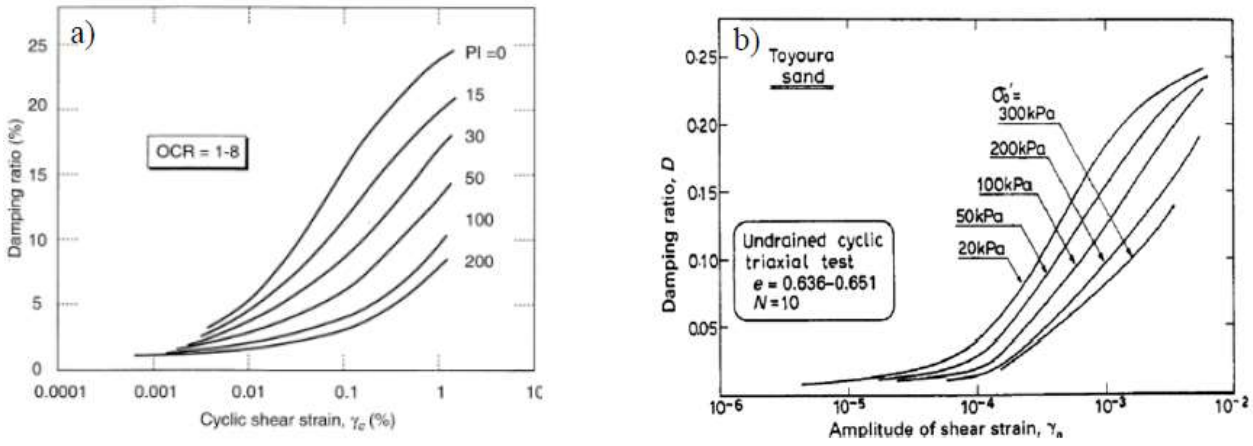

Figure 2.19: Effect of the (a) plasticity index (PI) and (b) confining stress on the damping ratio (Kramer, 1996; Ishihara, 1996) Rupture mechanisms of tailings impoundments

2.6.3 Tailings impoundment failure

The possibility of tailings impoundment failure is an issue that the mining industry has to deal with throughout the life of a mine and after closure. The stability of this type of structure is crucial, as the historical failure rate has historically been around ten times that of conventional water retention dikes (Davies, 2002; Azam and Li, 2010; Roche et al. 2017). Rupture mechanisms of past events provide important insights in order to assess the risks of existing structures, but they need to be properly understood. According to historical records (ICOLD 2001; Bowker and Chambers 2017; Roche et al. 2017; Rana et al., 2021), the majority of failures were caused by slope instabilities, overtopping, internal and external erosion, seismic event, and foundation instabilities. The records show that the slope instability and overtopping, followed by seismic events are the primary causes of the majority of ruptures (Roche et al., 2017; Santamarina et al., 2019; Rana et al., 2021).

Common characteristics of failures in tailings impoundments that have failed by seismic action include (Blight, 2010; Jamiolkowski et al., 2010):

- The presence of a large pond in the impoundment that may apply extra force to the external impoundment dike;

- An exterior dike formed of loose, poorly compacted or uncompacted tailings sand that is contractive and potentially liquefiable when subjected to shear stress (Geremew at al., 2012);
- Inadequate separation of the sand used to build the retaining dike from the silts stored within the impoundment, possibly with weak lenses of silt included in the dike; and
- Dikes usually built (at least partially) by upstream deposition over the impounded silts.

2.6.3.1 Some important failure cases

Some of the notable failure cases of tailings impoundments under dynamic loading conditions are summarized here:

- The El Cobre (Antiguo) failure, which occurred in Chile in March 1965, was an example of a flow failure triggered by an earthquake (Dobry and Alvares, 1967). Upstream hydraulic filling was used to construct the dike. The dam was around 33 meters high at the time of the failure, with a downstream slope of 35˚ to 40˚. The epicentre of the 7.5 magnitude La Ligua earthquake that caused the dam to break was 70 kilometers away from the site, with a focal point at 61 kilometers below the surface (Blight, 2010). 1.9×10^6 m^3 of total tailings storage flowed down a dry valley over a distance of 12 km during and after this earthquake. A small town in the path of the flood was completely devastated, with 300 people killed.
- On January 14, 1978, the Izo-Ohshima-Kinkai earthquake of magnitude 7.0 generated maximum horizontal accelerations of approximately 0.25g at the Mochikoshi Mine site. Dike 1 constructed by the upstream method failed within 10 seconds of the main shaking. The tailings flow reached the Mochikoshi River, contaminating the downstream Kano River. The next day, Dike 2 failed 5.5 hours after the secondary shaking of magnitude 5.8. The failure of Dike 2 is attributed to the rising water table due to the liquefaction of tailings and the pore pressures generated by the primary and secondary shaking. The failure of Dike 2 caused a flow of 3,000 m^3 of tailings over a distance of 240 m (Ishihara, 1984).
- The Tapo Canyon tailings impoundment failed on January 17, 1994, as a result of the earthquake in Northridge, California. The liquefaction of the impounded tailings caused the failure (Harder and Stewart, 1996). A significant volume of liquefied tailings was released

from the impoundment, which displaced hundreds of meters downstream. The incident resulted in significant financial losses for the owner of the tailings storage facility as well as the downstream water-treatment facility damaged by the tailings flow.

- The Las Palmas tailings impoundment failed on February 27, 2010 as a result of the M8.8 Maule Chile earthquake. The earthquake continued for one minute and had a maximum acceleration of 0.94 (g) at a station in the Chilean city of Angol. The ground motion caused the saturated tailings to liquefy, which led to a flow failure that extended up to 350 m in a downstream direction.

Based on these and other failure case histories, when an earthquake of sufficient magnitude occurs, a failure typically emerges as follows (Blight, 2010):

- The cyclic loading generates a pore pressure buildup that causes a reduction in the stiffness of the tailings mass. The most common consequence of this reduction is the action of additional earth pressure and seepage forces that increase the level of deformation.
- Liquefied tailings and wastewater may overtop the crest of the confining dike;
- The upstream slope of the dike may be displaced into the impoundment when drawn down, and the dike may fracture;
- The downstream slope of the dike may fail, as a result of strain-softening followed by erosion;

The assessment of the dynamic stability of tailings impoundments should evaluate (Pirulli et al., 2017):

- The liquefaction potential of the materials of the impoundment such as retained tailings and foundation and the rate of excess pore water pressure generation in these materials (Verdugo et al., 2017).
- Deformation of the starter dike and external slopes, which should be evaluated to be in the acceptable range given the ground motion characteristics.
- The induced lateral loads on retaining dikes and downstream side slope due to the horizontal shaking.

- The post-seismic instability caused by strength loss of the material and dissipation of excess pore water pressure (Contreras, 2022).

2.7 Improving the seismic stability of tailings impoundments

A drainage and reinforcing system may be used to mitigate liquefaction in sands, non-plastic silts, and silty sands. Sand drains and stone columns are frequently used in this system. Various researchers (Sasaki and Taniguchi, 1984; Adalier et al., 2003; and Martin et al., 2004) have conducted laboratory testing, site investigations, and numerical simulations to determine the efficiency of such systems. The reinforcement and draining system may include gravel and sand drains, stone columns, and high modulus columns. These methods are briefly detailed in the following section.

Aubertin et al. (2002) investigated methods for improving geotechnical stability of tailings impoundment under static and seismic loading. These strategies include lowering the water table level in the impoundment, reducing the initial water content and/or densifying the tailings, and adding inclusions as a reinforcing and drainage system in the impoundment. The latter will also be described in the following.

2.7.1 Gravel and sand drains

The following are some of the effects and advantages of adding stone columns in sand and silt deposits for liquefaction control (Adalier et al. 2003):

- Soil densification
- Dissipation of excess pore water pressure during the shaking
- Decreasing the shear strains by increasing the stiffness of the soil and consequently limiting the generation of excess pore water pressure.

Seed and Brooker (1977) investigated the potential drainage capacity of gravel drains and proposed a method for stabilizing liquefiable sand deposits. Their results indicate that the effective radius and distance of gravel drains can be determined based on the excess pore water pressure development in the liquefiable deposit.

Shaking table experiments were used by Saski and Tanighuchi (1982) to assess the performance of gravel drains in liquefiable soils. The model (box) was 12 meters in length, 3 meters in depth, and 2 meters in width. Their main findings is summarized here:

- The rate of development of excess pore water pressure was slower near gravel drains than at locations farther from the drains. The effective radius of the drains was approximately 50 cm in various tests.
- The gravel drains reduced the excess pore water pressure generated at the end of the shaking and improved the post-seismic behavior of the models..
- Numerical simulations were conducted using the two-dimensional finite element program "SADAP," and the numerical analysis findings supported the efficacy of the gravel drains.

The high modulus column technique (jet grouting) was developed to improve the seismic stability of soil deposits, These columns, like stone columns, increase the rigidity of the soil and reduce shear strains. The drainage capacity during and after the dynamic motion, however, is limited due to the low hydraulic conductivity of the columns. More specifically, Martin et al. (2004) investigated the performance of jet-grouted columns during the 1999 Kocaeli earthquake (M=7.4, Turkey), based on a case study conducted on a remediated parking lot for a shopping mall. The results revealed that there were no significant deformations in the jet-grouted area; these indicated that jet groutingmay increase the stiffness of the foundation while limiting shear stresses and pore water pressure development during an earthquake.

Paramasivam et al. (2018) investigated the effect of prefabricated vertical drains on soil seismic response using centrifuge modeling. The drains had a substantial impact on the settlement, duration, and dissipation of excessive pore pressures, even if the results showed that acceleration was amplified in the foundation layer. Howell et al. (2012) assessed the improvements in settlement reduction and excess pore pressure dissipation by comparing the behavior of a soil region treated with prefabricated drains and a region without treatment. The results showed that drains play a critical role in improving the response of the soil in terms of excess pore water prssure dessipation. Olarte et al. (2017) investigated the seismic response of structures on saturated soil using three distinct mitigation techniques, including soil densification, prefabricated vertical drains, and

ground reinforcement with structural walls. In this study, the effects of each technique on the behavior of the soil and the foundation before, during, and after the shaking were investigated.

2.7.2 Waste rock inclusions

The method of co-disposal of tailings and waste rock inclusions (Aubertin et al. 2002) in the impoundment is based on the principles of gravel columns, which are known to be an efficient method of ground improvement and have been used to improve the behavior of soft and loose soils for decades (Barksdale, 1987). Figure 2.20 shows a tailings impoundment with waste rock inclusions (WRI). Rows of waste rock are placed within the impoundment prior to each dike raising, along designated routes to divide impoundment into interconnected cells (James, 2009; James and Aubertin, 2012; James et al., 2013).

The following are the key advantages of using WRI in tailings impoundment (James et al. 2013, 2017; Aubertin et al. 2021):

- Improving the geotechnical stability of the tailings impoundment by reducing the shear strains and dissipating the excess pore pressure generated by an earthquake;
- Increase the consolidation rate;
- Controlling the water table and lowering the pore pressure within the tailings impoundment.

Under static loading, the waste rock columns increase drainage and consolidation rate and hence increase the stability of the consolidated tailings. It can also reduce settlement locally through stress transfer from softer tailings to the more rigid columns. One of the most essential aspects to take into account for stability, as well as for improving tailings drainage and consolidation, is the spacing between inclusions (Jaouhar at al., 2011, 2013; L-Bolduc and Aubertin 2014; Saleh Mbemba 2016). A recent study on this aspect showed that the rate of dissipation of excess pore pressure increases with the presence of inclusions up to nearly twice the thickness of the tailings (Saleh Mbemba et al., 2019). In another study, Saleh Mbemba and Aubertin (2021) investigated the evolution of the tailings void ratio and volumetric water content, as well as the amount of water transferred to waste rock, considering also fine particles migration at the interface between the two materials under static condition. For various imposed conditions, the experimental results were used to show how waste rock inclusion can influence tailings consolidation by reducing porewater

pressures with increased water drainage. The results of the physical model testing program and numerical simulations show how horizontal water transfer to waste rock can increase the tailings consolidation rate. The tests also indicated that the level of tailings that migrated towards the waste rock was relatively small and had no effect on the rate of PWP dissipation. Essayad (2021) investigated the migration of fine tailings particles in waste rock under various conditions and analyze the effect on drainage capacity under static loading. The effect of hydraulic gradient, initial solid percentage of tailings, waste rock size, degree of saturation and macroporosity were experimentally evaluated in this study using large diameter instrumented column tests and field observations. The results of the migration tests indicate that the retention of tailings in the pores of the waste rock is low and that the effect of tailings migration on the hydraulic conductivity of the waste rock is limited. The experimental data show that tailings migration and retention do not have a significant effect on the overall drainage capacity of waste rock used as inclusions.WRI also increase the overall stiffness and strength and thus contribute to the increased factor of safety against dike failure (Jahanbakhshzadeh and Aubertin, 2020).

Various studies in recent years have investigated the effect of waste rock inclusions on the dynamic stability of tailings impoundment (James,2009; James and Aubertin, 2012; Pépin et al., 2012a, 2012b; Ferdosi et al., 2015a, 2015b; Aubertin et al., 2019; Jahanbakhshzadeh et al., 2019; Zafarani et al., 2020; and Contreras et al., 2020). The results of these investigations showed that WRI can significantly improve the seismic response of tailings impoundments by reducing shear strain and dissipating excess pore water pressure generated by the earthquake (post-seismic).

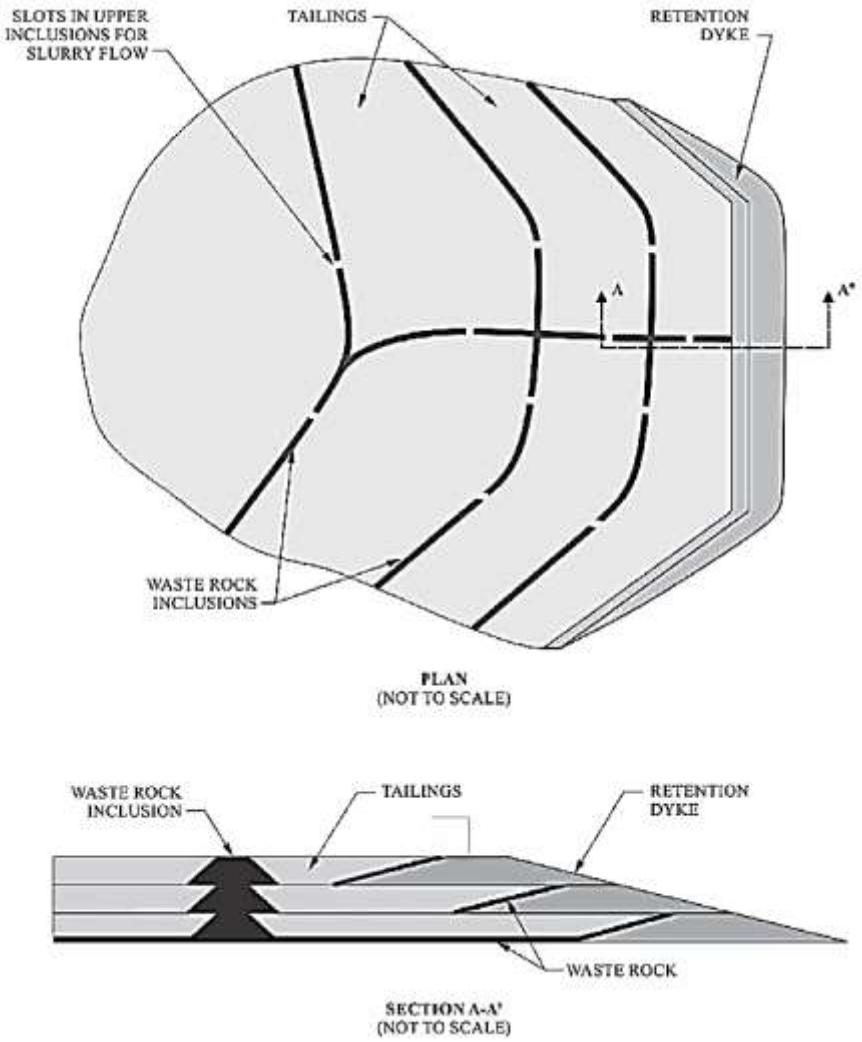

Figure 2.20: Schematic of a tailings impoundment with waste rock inclusions (James et al., 2012)

James (2009) used numerical modeling to assess the dynamic behavior of tailings impoundments with and without waste rock inclusions (FLAC, Version 5). He used the UBCSAND model version 904a developed by Beaty and Byrne (1998) for modeling tailings behavior; this constitutive model is described below. The model was calibrated using cyclic simple shear test results, and then used to simulate conceptual reinforced and conventional tailings impoundments. The main outcomes from James (2009) simulations can be summarized as follow:

- The liquefaction behavior of the tailings can be simulated using the FLAC software and the UBCSAND model (904a) (Figure 2.21);

- Compared with conventional tailings impoundments, the displacements in reinforced tailings impoundments were reduced by an order of magnitude during and after shaking;
- The effectiveness of WRI was found to be due to their stiffness rather than their drainage capacity in numerical simulations of reinforced tailings impoundments subjected to short term dynamic loading due to earthquakes;
- The volume of tailings that would be discharged if the impoundment failed can be reduced by the addition of WRI.

Pépin et al. (2012a, 2012b) analyzed the performance of sand inclusion in tailings under cyclic loading on a shaking table. The applied sinusoidal loading in this study had a 1 Hz frequency and three varied peak ground accelerations (PGA) of 0.12g, 0.17g, and 0.35g. Pépin (2009) (also Pépin et al. 2012a, and 2012b) observed that inclusions reduced the increase in pore water pressure when compared to tests without inclusions. In addition, the rate of excess pore water pressure in physical models with an inclusion was lower than in models without inclusions.

Ferdosi (2014) conducted additional numerical simulations using FLAC (Version 6) to evaluate the dynamic response of tailings impoundments with and without waste rock inclusions. The UBCSAND (Beaty and Byrne, 1998) model version 904aR was used as a constitutive model in these simulations. The shaking table test results from Pépin et al. (2012a, 2012b) were used to validate the model. The following are the major findings from this numerical study:

- Excess pore water pressure generation in seismic table testing is fairly well predicted by the UBCSAND (904aR) model. However, as shown in Figure 2.22, the rate of excess pore water pressure development in the simulation was higher than in the laboratory at the lower levels of tailings.
- Waste rock inclusions can improve the seismic response and stability of the tailings impoundment, which would be unstable without inclusions.
- The average normalized horizontal displacements of the downstream slope of impoundment can be used to classify the responses of various WRI configurations (this approach will also be used in the Thesis).

- Analyses of high- and low-frequency ground motions show that the predominant frequency content of earthquakes has a significant impact on the response of reinforced tailings impoundments. Generally, low-frequency earthquakes result in higher tailings displacement than high-frequency ground motions; this aspect is also investigated in this Thesis.

- Post-shaking evaluations for various waste rock inclusion configurations indicate a relationship between impoundment post-shaking stability and the average normalized horizontal displacements of the downstream slope and horizontal nodal velocity at the end of shaking. A horizontal nodal velocity greater than approximately 20 cm/s at the end of the shaking seems indicative of an unstable condition.

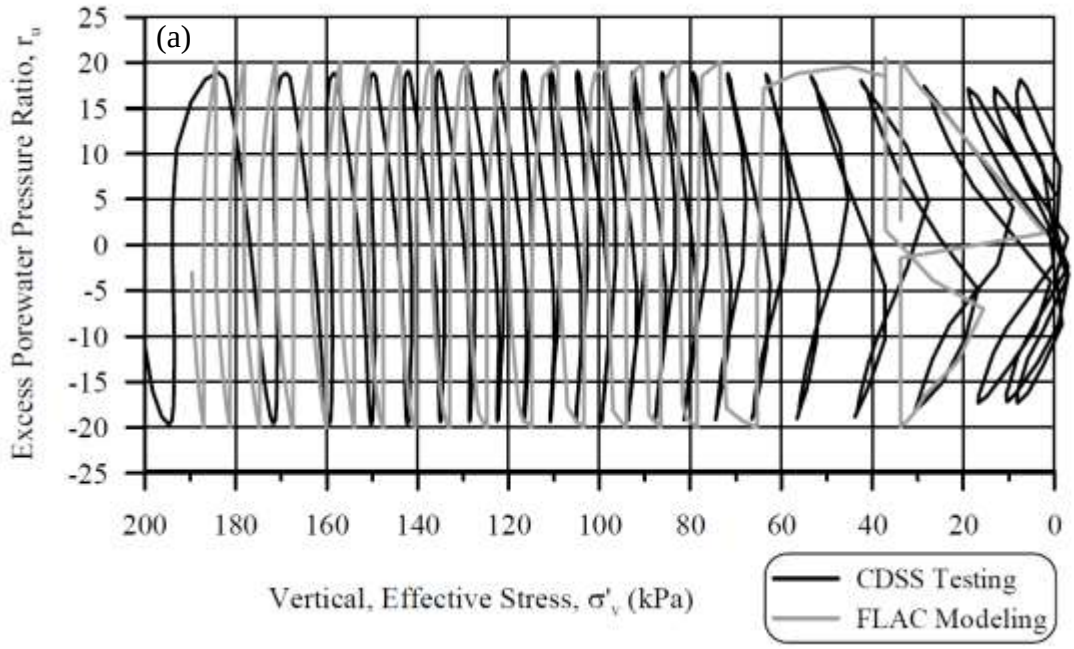

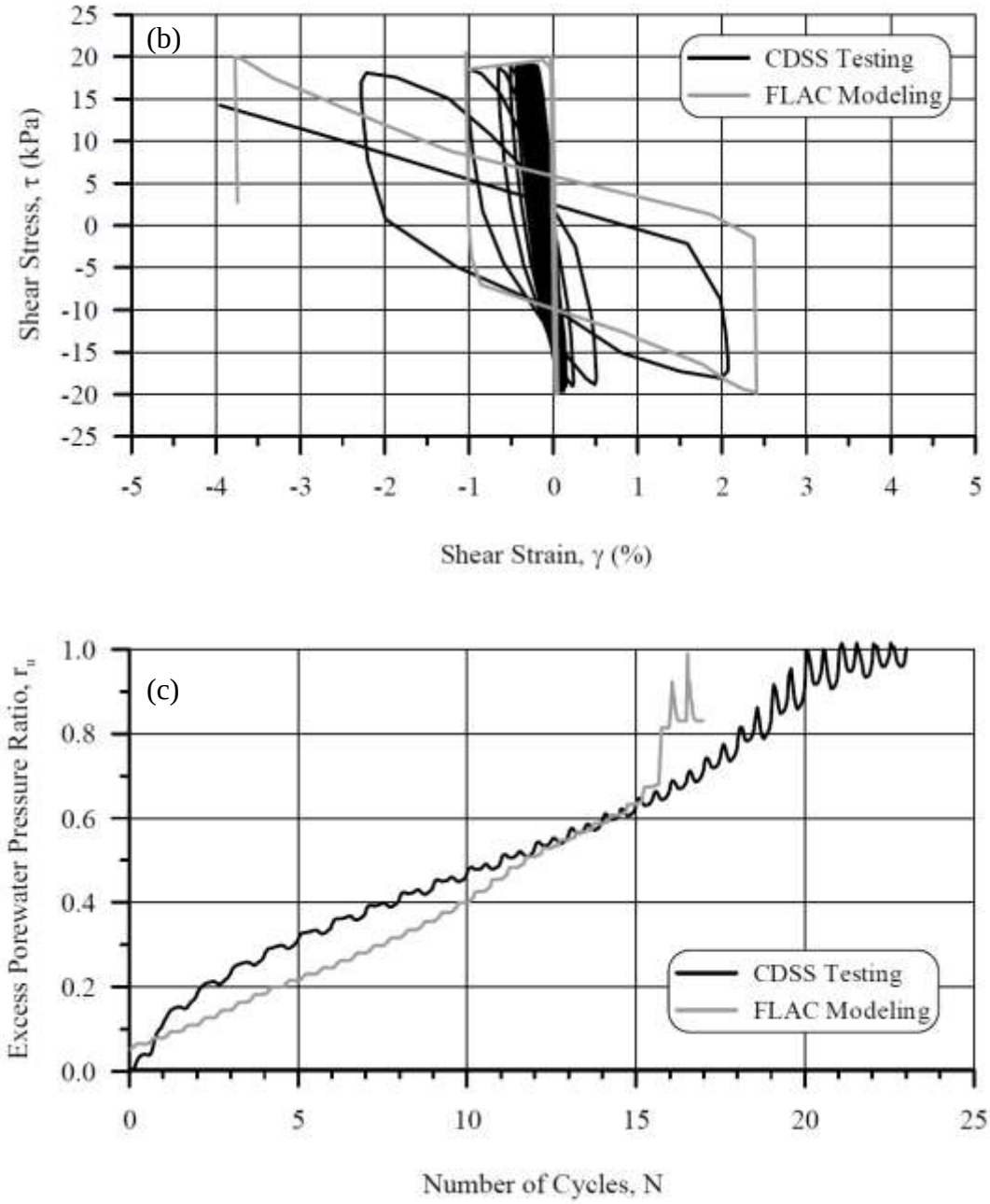

Figure 2.21 (a) Normal stress v. shear stress for CDSS test and FLAC simulation (b) Shear strain v. shear stress for CDSS Test and FLAC (c) Number of cycles v. excess porewater pressure ratio for CDSS Test and FLAC (James, 2009)

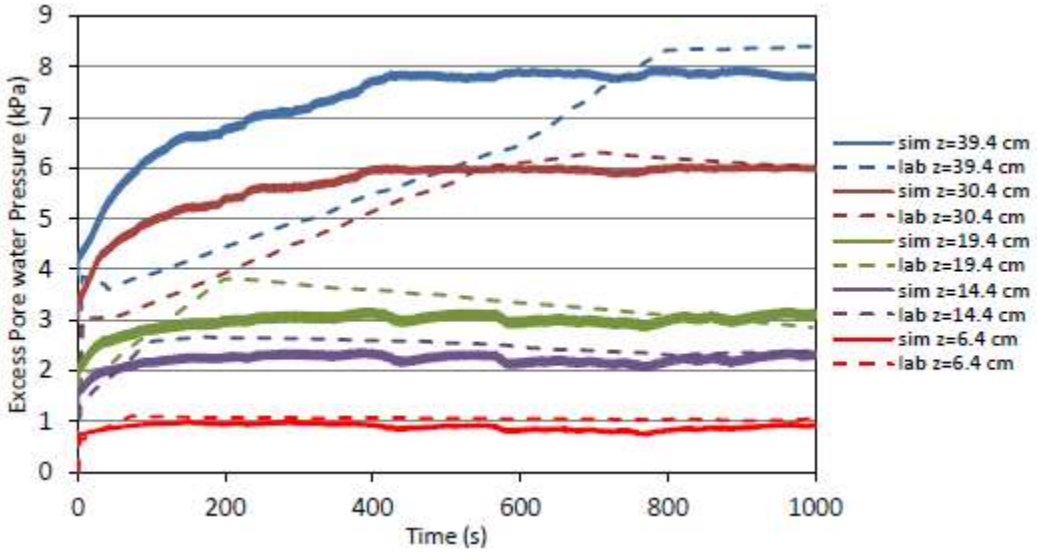

Figure 2.22: The results of the generated excess pore water pressure measured during shaking table test and simulated with the UBCSAND model in FLAC, considering a small value of stiffness proportional damping for zones in which shear strain is less than 0.015% (Ferdosi et al., 2015(a))

2.8 Methodology for seismic analysis of tailings impoundments

The methods of analysis for seismic stability of embankments can be classified into three main types (CDA, 2007; Jibson 2011): pseudo-static, permanent-displacement and stress-deformation analysis. The pseudo-static and permanent-displacement methods, summarized below, cannot predict or simulate excess pore water pressure generation and strength loss of the material; they only evaluate the seismic stability of impoundments regardless of the liquefaction potential of the material.

2.8.1 Pseudo-static analysis

The pseudo-static approach is a type of limit equilibrium analysis in which horizontal and vertical inertial forces are added to the static forces acting on the mass of the embankment's slope to simulate earthquake loading and determine a factor of safety.

The pseudo-static method has many disadvantages and limitations (Kramer, 1996), including the concept that earthquake loading can be represented by a constant, unidirectional body force (which

deemed to be a conservative assumption in some cases). The inertial horizontal and vertical forces are defined as follows (Kramer, 1996):

$$F_h = \frac{a_h W}{g} = k_h W \quad (2.5)$$

$$F_v = \frac{a_v W}{g} = k_v W \quad (2.6)$$

Where a_h and a_v are horizontal and vertical pseudo-static accelerations, respectively. W is the weight of a potential landslide mass; k_h and k_v are dimensionless horizontal and vertical pseudo-static coefficients, and g is the acceleration due to the gravity.

Seed and Idriss (1970) indicated that if the soil does not develop excessive pore pressures during shaking and the embankment is initially constructed to withstand an inertia force of approximately 0.1 or 0.15 g without yielding, a pseudo-static analysis is all that is required to ensure acceptable performance. However, the pseudo-static approach is not applicable when pore water pressure builds up or when significant strength loss occurs as a result of seismic loading (such as liquefaction).

2.8.2 Permanent displacement analysis

Several methods for estimating the deformation of embankment dams have been developed Newmark (1965) conceptualized the volume as a hard block sliding over an inclined surface. The yield acceleration defined in this approach is the minimum acceleration required to overcome the basal resistance. The portions of the ground motion's acceleration-time history that exceed the yield acceleration are integrated to obtain the velocity-time history. Yield acceleration is defined as the average acceleration above which a sliding mass undergoes permanent displacement, obtained from the velocity-time history (integrated). The seismic performance is evaluated in this approach based on the total displacement, which is influenced by the amplitude, frequency and duration of the motion (Kramer, 1996).

Makdisi and Seed (1978) proposed a model in which the block is considered flexible rather than rigid to be able to account for the deformations caused by seismic stress. They calibrated their model using a small number of strong motion data (Jibson, 2011). This approach is a "decoupled" technique, where the dynamic response and plastic deformations are considered separately. In

contrast, the "coupled" permanent displacement method models both the sliding mass's dynamic response and the permanent displacement simultaneously. This method, however, is unable to take into account the effect of excessive pore water generation. Therefore, it is not recommended to be used in cases where significant pore pressure development occurs during seismic motion (Bray and Travasarou, 2007; Jibson, 2011).

2.8.3 Stress-deformation analysis

Dynamic numerical analysis is one of the most advanced techniques for determining the potential for embankment deformation and failure under cyclic stress (Armstrong et al., 2013; Meisheng et al., 2011). This method of analysis can take into account the complete geometry of the modelled structure and simulate the non-linear stress-strain behavior of materials. While stress-strain analyses include information obtained from seismic motion, such as strains and displacements, stress state, and the generation of excess pore pressures, they do have significant limitations (Jibson, 2011). For instance, to ensure the simulations are reliable, the input ground motions should be selected and scaled in accordance with the seismic hazard of the region. Such simulations are only as accurate as the constitutive model and related parameters employed in the investigation. A suitable constitutive model should be considered to model the excess pore water pressure and stress-strain behavior at various stages of the modeling process, and the model should be carefully calibrated using field observations and laboratory experiments that may not be easily available. Such constitutive models concentrating on cyclic behavior are presented in various publications (e.g., Potts and Zdravkovic, 1999; Jefferies and Been, 2015). Most of these constitutive models are developed based on finite-element and finite-difference methods and implemented into two widely used software in geotechnical engineering such FLAC and PLAXIS (Itasca, 2021; Plaxis, 2021).

Fast Lagrangian Analysis of Continua (FLAC)

Numerous finite difference and finite element software packages have been developed or updated in recent years to simulate the dynamic response of earth structures, including liquefaction (Itasca, 2021; Plaxis, 2021).

The commercially available and commonly used code FLAC (Fast Lagrangian Analysis of Continua) Version 8.00 (Itasca, 2016), which is based on finite difference method, was chosen for

this research project due to its ability to implement the UBCSAND and PM4Sand constitutive models (discussed later). Additionally, FLAC is adaptable to meet specific project requirements with user-defined models and a reasonably open design that enables modification of a large number of characteristics. In particular, a built-in programming language (FISH) can be used to modify the functionality of the software, and constitutive models can be added to FLAC as dynamic linked libraries (DLLs) from the database or developed by the user.

There are three steps in each dynamic numerical simulation in FLAC. The primary step is to define the model geometry, the meshing, the boundary conditions, constitutive models, and the material properties. In the second step, the numerical model is run to establish the static conditions, which include the initial state of the stresses, strains, and pore water pressures under mechanical and hydraulic equilibrium. In the final step, earthquake loading is applied to the base of the model. In the last step, stresses from the static phase are used as initial conditions for the dynamic analysis and earthquake loading is applied at the base of the model. The constitutive models of the various materials are changed at this step to more accurately represent their seismic behavior. The formulation and necessary parameters of several of the constitutive models are described in the following sections.

2.9 Constitutive models for numerical dynamic analysis

As indicated above, the pseudo-static and permanent displacement methods have serious limitations in evaluating the geotechnical response under earthquake loading, including liquefaction displacements (since they do not account for the potential for excess pore water pressure development and subsequent loss of shear strength). Dynamic numerical simulations are the best tool for analyzing the seismic behavior of tailings impoundments. However, the validity of the results of dynamic numerical simulations is largely determined by the constitutive model (and related parameters) used to simulate tailings seismic behavior. There are numerous constitutive models have been developed and applied to evaluate the response of liquefiable soil. Laboratory tests, centrifuge testing, and information from case histories have all been used to evaluate the response and validity of the models (Byrne,1991; Arduino and Macari, 2001a, 2001b; Byrne, 2003; Imam et al. 2005; Yang and Ling, 2005).

The UBCSAND (Beaty and Byrne, 2011) model has been evaluated for simulating tailings in recent years by a few researchers (Seid-Karbasi and Byrne, 2004; James, 2009; Ferdosi, 2014). In these studies, the model was calibrated for tailings based on cyclic direct simple shear testing (CDSS). More recently, the PM4SAND (Boulanger and Ziotopoulou, 2017) model has been calibrated for simulating the cyclic behaviour of tailings, based on experimental results obtained on the tailings from the Canadian Malartic mine (Contreras et al., 2022). These models are described in the following sections.

2.9.1 UBCSAND model (Beaty and Byrne, 2011)

Byrne et al. (1995) developed the UBCSAND model to investigate the behavior of sandy-like material under seismic loading. The mechanism of the UBCSAND model for seismic simulations is based on the model designed for static liquefaction prediction in the CANLEX (Canadian Liquefaction Experiment) project by Puebla et al. (1997) and Puebla (1999). Static liquefaction occurs when a loose granular material, such as sand or silty sand, is loaded and cannot drain under static conditions.

The first version of the UBCSAND model, UBCSAND904a, was released in 2002 for use in numerical dynamic analyses. The UBCSAND model for seismic analysis has the same fundamental formulation as the UBCSAND model for static liquefaction (published by Puebla et al. (1997) and Puebla (1999)). However, the shear mechanism hardening behavior differs throughout the UBCSAND static and dynamic liquefaction models.

Although the model was used to simulate earth dams and tailings by multiple researchers (Bryne et al., 2003; Seid-Karbasi and Byrne, 2004; Byrne et al., 2004; Yang et al., 2004; James, 2009), the distributed model has certain limitations. For instance, when there were large initial shear stresses, the UBCSAND904a model could not simulate the excess pore water pressure development (Beaty and Byrne, 2011). Figure 2.23 illustrates the incremental stress ratio versus plastic shear strain for UBCSAND904a model. The UBCSAND904a model responds elastically during unloading-reloading cycles and cycles of unloading-reloading maintain elastic as long as the direction of stress ratio does not change. As a result, throughout these cycles, plastic volumetric strains are not produced.

Beaty and Byrne (2011) modified the UBCSAND904a model into the UBCSAND904aR model based on the findings. The updated model generates an unloading-reloading response that is composed of elastic unloading and plastic reloading responses, as shown in Figure 2.24. When there are considerable initial shear stresses, the updated model can capture plastic strains and excess pore water pressure. However, the UBCSAND904aR, cannot estimate plastic strains under isotropic triaxial compression or when the stress vector is in the direction of the constant stress ratio line.

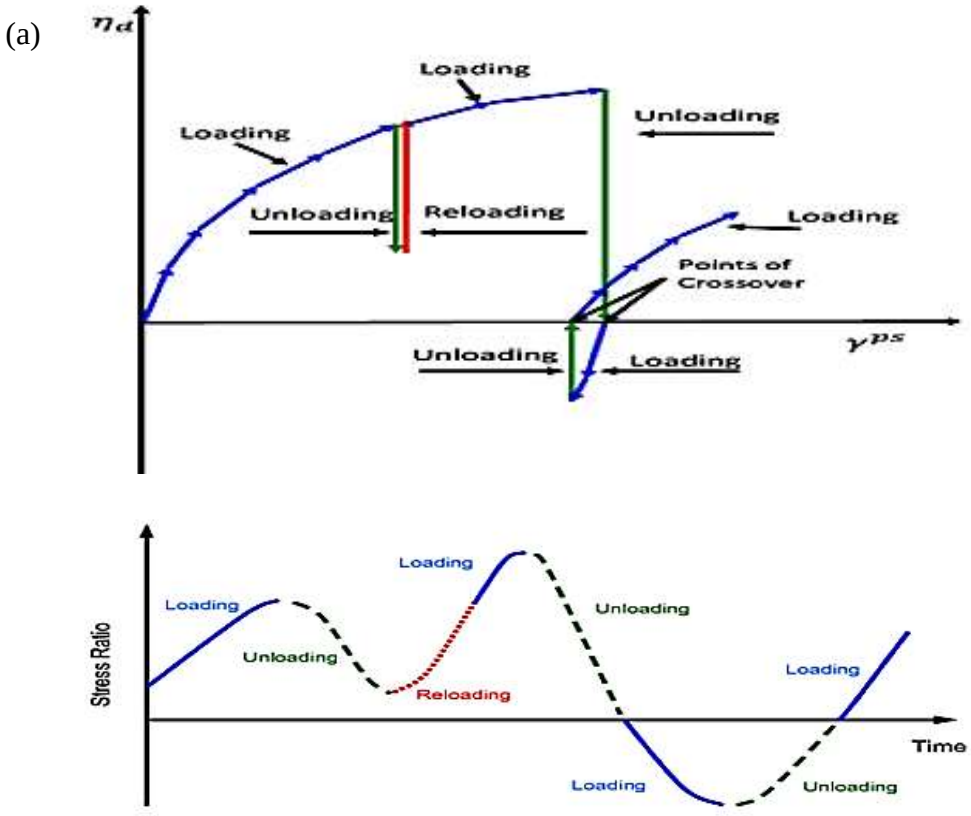

Figure 2.23 (a): Incremental stress ratio ($\eta_d = \frac{(\Delta\sigma_1 - \Delta\sigma_3)}{(\Delta\sigma'_1 + \Delta\sigma'_3)}$) versus plastic shear strain (γ^{ps}) for UBCSAND904a. (b) Stress ratio ($\eta = \frac{(\sigma_1 - \sigma_3)}{(\sigma'_1 + \sigma'_3)}$) history showing loading, unloading, and reloading (after Beaty and Byrne, 2011)

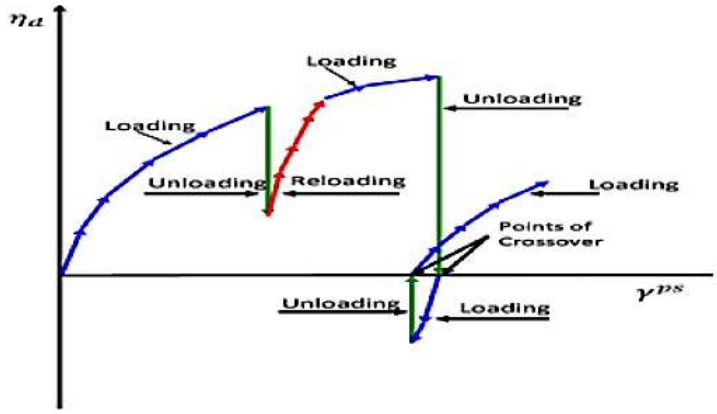

Figure 2.24: Incremental stress ratio versus plastic shear strain for UBCSAND904aR (after Beaty and Byrne, 2011)

2.9.2 PM4Sand model (Boulanger and Ziotopoulou, 2017)

The PM4Sand model is a critical-state compatible, stress-ratio based, bounding surface plasticity model for sand that is based on Manzari and Dafalias (1997) model, further developed by Dafalias and Manzari (2004). The Dafalias and Manzari (2004) model has been modified to increase its ability to estimate liquefaction-induced ground deformations during earthquakes. The model consists of three primary parameters that need to be calibrated based on the soil properties, and 21 secondary parameters that can be changed from their default values to obtain a material-specific calibration if detailed information is available. The critical state curve used in this constitutive model is defined from the density index (I_d) according to the relationship of Bolton (1986). This relationship can capture the influence of fine particle content and plastic consistency on the critical state curve (Carraro et al., 2009). The calibration of the PM4Sand model for hard-rock tailings presented in Contreras (2022) is used in the present research. The formulation of the PM4SAND is described in following sections.

Critical state line

The critical state line is determined by the PM4Sand model using the Bolton (1986) relationship, which is based on the measurement of the density index (or relative density D_R) at the critical state as shown by the following equation:

$$I_{d,CS} = \frac{R}{Q - \ln\left(100\frac{p}{p_A}\right)} \quad (2.7)$$

Where R and Q are fitting parameters, P is the mean effective stress, p_A is atmospheric pressure and $I_{d,CS}$ is the density index at the critical state. The R and Q fitting parameters in the Bolton relation are among secondary input parameters of the PM4Sand model. Boulanger and Ziotopoulou (2017) adopted the values of Q=10 and R=1.5 for the calibration of sand material based on the simple shear (DSS) test results. However, the Q and R values may increase for soils with higher fine content such as tailings (Carraro et al. 2009; Robertson, 2018).

Relative state parameter index

The model incorporates a relative state parameter index which compares the density index (I_d) to the density index at the critical state ($I_{d,CS}$) as follows:

$$\xi_R = I_{d,CS} - I_d \quad (2.8)$$

A positive value represents a soil state that is denser than critical, whereas a negative value represents a state that is looser than critical (and thus prone to excess porewater pressure generation).

Critical surface in stress space

The ultimate stress condition that the soil reaches during shear loading is known as the critical surface. The critical stress ratio, M, is defined in this model regardless of the shear mode:

$$M = 2\sin(\phi'_{cv}) \quad (2.9)$$

Where ϕ'_{cv} is the constant volume or critical state internal friction angle.

Dilatancy surface

The dilatancy surface represents a stress state where the volumetric response of the soil changes from contraction to dilatation during shear. This surface is determined by the relative state parameter index in the following way:

$$M^d = Mexp(-n^d \xi_R) \quad (2.10)$$

Where n^d is a material property which controls the ratio of stress at which contraction to dilation occurs, which is often called the phase transformation.

Bounding surface

The bounding surface (M^b) defines the initiation of softening and the progression of the soil towards the critical state. The following equation is used to compute the stress ratio for the bounding surf ace (M^b):

$$M^b = Mexp(n^b \xi_R) \tag{2.11}$$

Where n^b is a material property which controls the rate at which the bounding surface approaches the critical state surface. If the soil is on the critical state (ξ_R = 0), the bonding and dilatancy surfaces overlap with the critical state ($M = M^b = M^d$).

A schematic illustration of different surfaces of PM4Sand is shown in Figure 2.25. In this figure, α is a variable showing the currant stress ratio of yield surface and it is called the back-stress ratio.

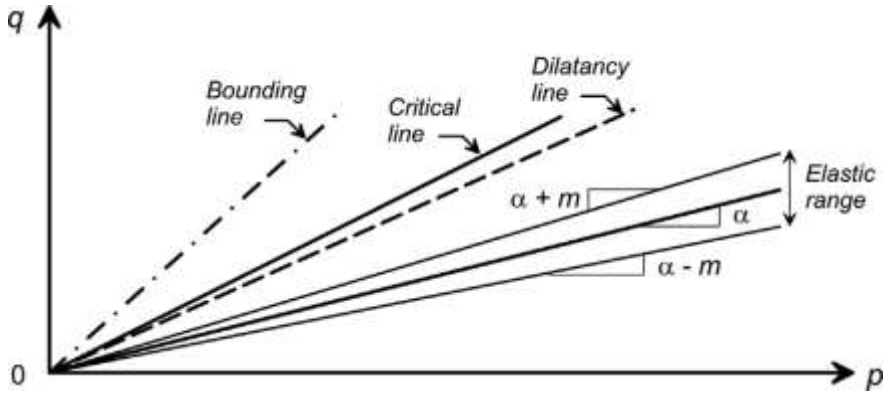

Figure 2.25: schematic illustration of different surfaces used by PM4Sand (Boulanger and Ziotopoulou, 2017)

Elastic response

The shear modulus is defined based on the mean effective stress, p' by the following equation:

$$G = G_0 p_A (\frac{p'}{p_A})^{1/2} C_{SR} \tag{2.12}$$

Where G_0 is the shear modulus coefficient, and C_{SR} is a factor that accounts for stress ratio effects which is defined by the following equation:

$$C_{SR} = 1 - C_{SR,0} \cdot (\frac{M}{M^b})^{m_{SR}} \tag{2.13}$$

According to Boulanger and Ziotopoulou (2017) calibration examples, the model works well with $C_{SR,0}$ = 0.5 and m_{SR} = 4, which keeps the effect of stress ratio on elastic modulus limited at low stress ratios but allows it to increase to a 60% reduction when the stress ratio is on the bounding surface.

2.9.2.1 Primary parameters of the PM4SAND model in FLAC

Density index (I_D)

The common form of the correlation between density index (I_D) and SPT number is as follows:

$$I_D = \sqrt{\frac{(N_1)_{60}}{C_d}} \tag{2.14}$$

Where I_D is expressed as a ratio. Idriss and Boulanger (2008), adopted a value of $C_d = 46$ in development of their liquefaction triggering correlations based on published data and past relationships.

For correlation between density index and CPT, Idriss and Boulanger (2008), similarly reviewed available relationships and proposed the following expression:

$$I_D = 0.456\left(\frac{q_{c1N}}{C_{dq}}\right)^{0.264} - 1.063 \tag{2.15}$$

For which they adopted C_{dq}= 0.9.

Shear modulus coefficient (G_0)

The shear modulus coefficient is the constant controls the elastic (or small strain) shear modulus. The correlation between shear modulus coefficient (G_0) and SPT number is defined as follows: (Boulanger and Ziotopoulou, 2015)

$$G_0 = 167\sqrt{(N_1)_{60} + 2.5} \tag{2.16}$$

This expression produces G_o values of 476, 677, and 890 for the typical I_D values of 35%, 55%, and 75%, respectively.

Contraction rate parameter (h_{p0})

Contraction rate parameter is a primary variable that adjusts the contraction rates and hence can be adjusted to obtain a target cyclic resistance ratio (CRR), as commonly estimated based on CPT or SPT penetration resistances and liquefaction correlations. Calibration of this parameter should be performed last because its value can depend on the values assigned to other parameters (Boulanger et al., 2011).

2.9.2.2 PM4Sand model calibration

The calibration of the PM4Sand model for hard-rock tailings from a gold mine of the province of Quebec presented in Contreras (2022) is used in the present study. Consolidation and compression tests are used to define some of the model parameters, while monotonic triaxial and direct simple shear tests are used to define the critical state line. The characterization results showed that the calibrated model can reasonably simulate monotonic behavior and offers an excellent fit of the cyclic strength curves observed in the lab at various confining pressures and density indices. Table 2.3 presents the PM4Sand calibrated parameters provided in Contreras (2022); the original paper by Boulanger and Ziotopoulou includes a detailed discussion of each input parameter (2017).

Table 2.3: List of input parameters of the PM4Sand model (Contreras, 2022)

Parameter identification	Symbol	Default value [range]	Calibrated value
Density index (D_r in original publication)	I_d	r	Var
Shear modulus coefficient	G_o	r	502.5
Contraction rate parameter	h_{po}	r	0.55
Plastic modulus ratio	h_o	f(I_d)	NA
Minimum void ratio	e_{min}	0.5	0.49
Maximum void ratio	e_{max}	0.8	1.1

Bounding parameter	n^b	0.5	0.7
Dilatancy parameter	n^d	0.1	NA
Dilatancy parameter	A_{do}	f(M, ξ_r, ϕ'_{cv})	NA
Fabric term	z_{max}	f(ξ_r) [0.7 ; 20]	NA
Fabric growth parameter	c_z	250	150
Strain accumulation rate factor	c_ε	f(I_d) [1 ; 5]	NA
Critical state friction angle	ϕ'_{cv}	33	35
Poisson ratio	υ_o	0.3	NA
Modulus degradation factor	C_{GD}	2.0	2.5
Factor to reduce the rotated dilatancy surface	C_{DR}	f(I_d)	NA
Plastic modulus factor	$C_{k\alpha f}$	f(I_d) [4 ; 35]	NA
Critical state line parameter	Q	10	12.7
Critical state line parameter	R	1.5	5.4
Size of the yield surface	m	0.01	NA
Minimum value for F_{sed}	$F_{sed,min}$	f(I_d)	NA

Mean effective stress for reconsolidation strains	$P'_{sed,o}$	$-p_a/5$	NA
plastic shear strength ratio used to compute c_{hg}	cr_{hg}	0.005	NA
Plastic shear strength at initialization	c_{hg}	$cr_{hg} \cdot p'$	NA

r- required specific values for primary input parameters

NA – Not Applicable, indicates that the default value was used

Figure 2.26 compares the simulation results of cyclic tests performed by Contreras (2022) on samples with a density index of 90% under vertical effective stresses of 50 kPa, 100 kPa, 300 kPa, and 500 kPa to experimental results in terms of cyclic strength curves. It should be noted that the cyclic strength curves are defined as the number of cycles required to reach an excess pore-water pressure ratio, r_u of 0.9, for a given vertical effective stress, at a certain cyclic stress ratio (CSR). The results indicate that the simulated curves closely match the experimental curves, demonstrating that the model with calibrated parameters can represent the cyclic behaviour of tailings (Contreras, 2022 and Contreras et al., 2022a). The cyclic strength curve with a lower density index (I_d of 60%) under vertical effective stresses of 100 kPa is also shown in Figure 2.26. The results confirms that the model with calibrated parameters represents a realistic behavior, with cyclic strength curves that are compatible with the range of curves from other research with lower density indices (James et al., 2011; Poncelet, 2012; Contreras 2013), displayed in the figure with dashed lines.

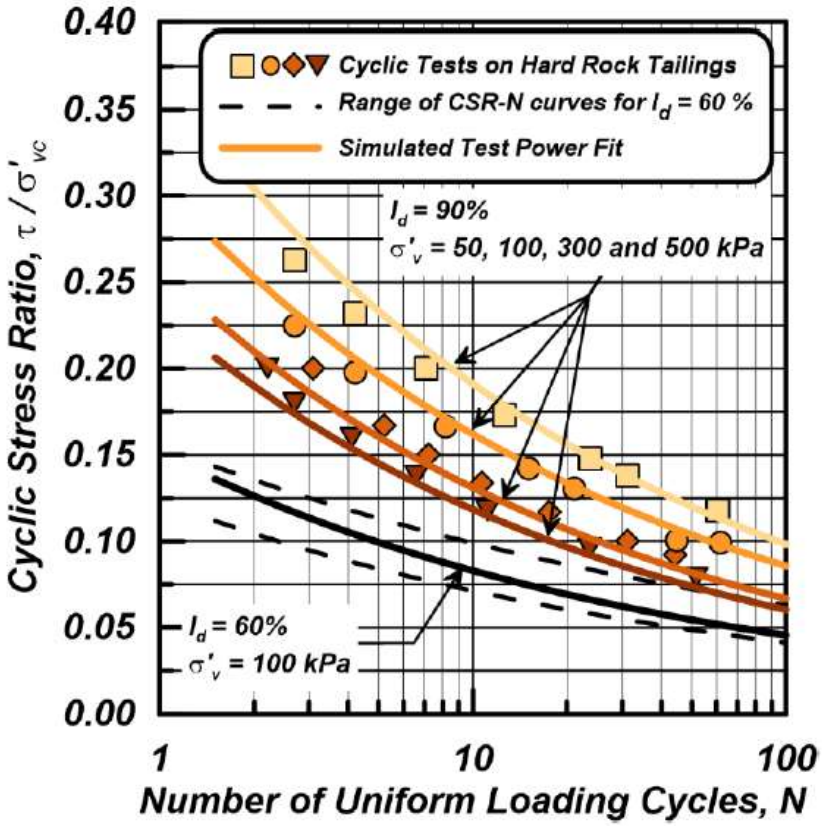

Figure 2.26: Comparison of cyclic strength curves CSR Vs N_{liq} from laboratory data and PM4Sand simulations at effective stress of 50kPa to 500kPa and a I_d of 90%; and effective stress of 100kPa for I_d of 60% (Contreras et al., 2022a)

Figure 2.27 compares the simulation and laboratory testing results of one of the tests performed by Contreras (2022), with σ'_v 100 kPa and CSR of 0.167, in terms of the (a) shear strain, (b) pore water pressure ratio r_u, (c) stress path and (d) stress-strain curve. The results show that the calibrated PM4Sand model is generally in good agreement with the cyclic behavior of tailings (Contreras, 2022; Contreras et al., 2022a). These results show that the calibrated model is capable of capturing the cyclic mobility behavior of the tailings as indicated by the cumulated shear strain upon liquefaction.

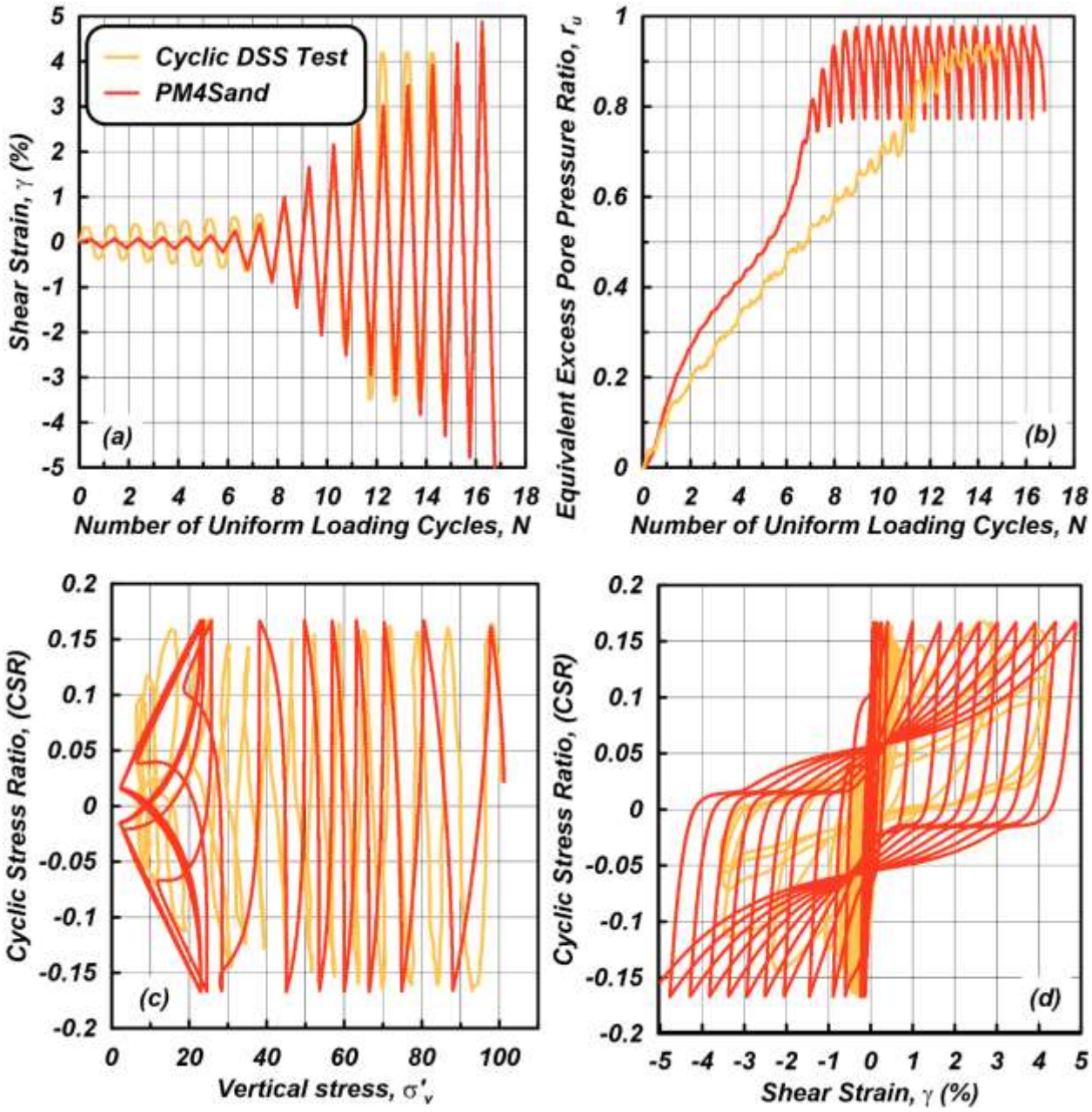

Figure 2.27: Comparison laboratory vs. simulated behaviour of tailings at σ'_v of 100 kPa, CSR of 0.167 and a I_d of 90% a) γ vs N b) CSR Vs γ c) r_u Vs N and d) CSR Vs σ'_v (Contreras, 2022; Contreras 2022a)

2.9.3 Comparing the seismic response of the UBCSAND and PM4Sand models

Carey and Kutter (2017) compared the response of four different constitutive models (UBCSAND, PM4Sand, PDMY02 (pressure dependant multi yield), and Manzari-Dafalias 2004) in predicting

the undrained behavior of uniformly graded sands with density index around 50%. One of the objectives of this study was to compare a consistent set of results showing that the implementations of each model behave in the manner predicted, as well as to highlight fundamental differences in behavior for the models. The selected models were subjected to a cyclic direct simple shear testing (CDSS) plan that included an initial vertical effective stress of 100 kPa followed by a cyclic stress. The cyclic stress ratios (CSRs) ranged from 0.05 to 0.55 in 0.05 increments for 11 runs per model. The cyclic loading ends when the shear strain reached 3% or after 40 loading cycles.

The results of this study for UBCSAND and PM4Sand model are shown in Figure 2.28 and Figure 2.29, respectively. In these figures σ'_{vc} is initial vertical effective stress equal to 100 kPa, σ'_{v} is current vertical effective stress, τ is current shear stress, and γ is shear strain.

The UBCSAND model in Figure 2.28b reached a stabilized hysteretic behavior during undrained cyclic loading, with no ongoing decrease in effective stress or increase in the amplitude of the cyclic shear strains with additional cycles of loading. As a result, many of the 40 loading cycles applied are indistinguishable from one another because they coincide exactly on the previous cycle. On the other hand, the PM4Sand model (Figure 2.29b) enables the strain to develop without stabilization in a repeating stress-strain loop.

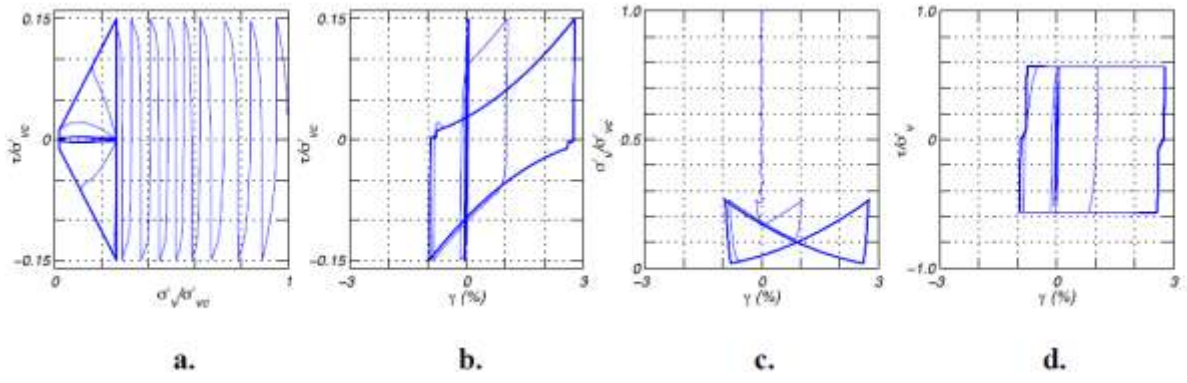

Figure 2.28: UBCSAND response to stress-ratio controlled cyclic loading with σ'_{vc}=100 kPa, and CSR=0.15 (Carey and Kutter, 2017)

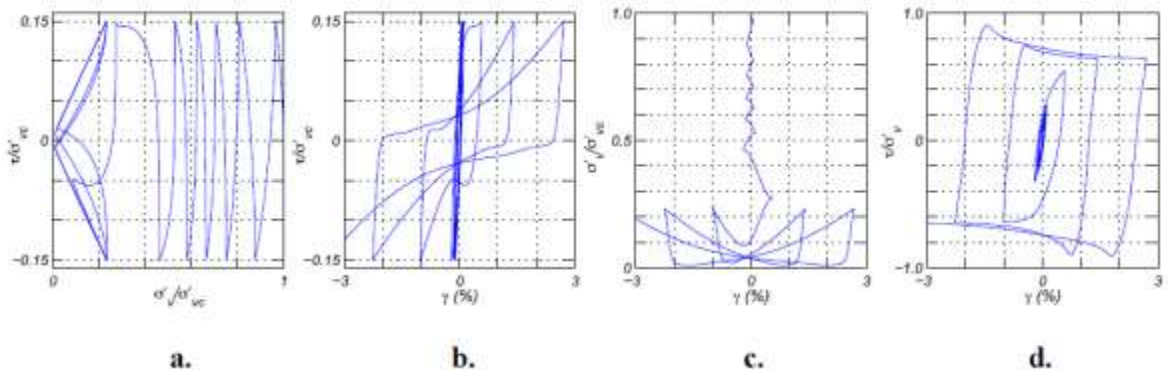

Figure 2.29: PM4 response to stress-ratio controlled cyclic loading with σ'_{vc}=100 kPa, and CSR=0.15 (Carey and Kutter, 2017)

Anthi and Gerolymos (2019) developed a methodology for calibrating the material properties of UBCSAND and PM4Sand, referred to as element-test based calibration process. Calibration is performed by best matching the response in terms of shear strength curve (i.e., CRR versus uniform cycles required to trigger the liquefaction) and shear modulus reduction and damping ratio curves. They ran simulations in both FLAC and PLAXIS software to compare the results. Figure 2.30 shows the modulus ratio reduction and damping ratio increase as a function of shear strain for a density index I_d = 60, 50, 40, and 30% in the developed calibration. In comparison to PM4Sand, the UBCSAND shows more linear behavior throughout a wide range of shear strain. In terms of the damping curve, UBCSAND in FLAC produces higher damping ratios than the Seed and Idriss suggested curves (1970). The high damping ratio in the UBCSAND under large strains could be related to the elastic response of the model during unloading and stress reversal.

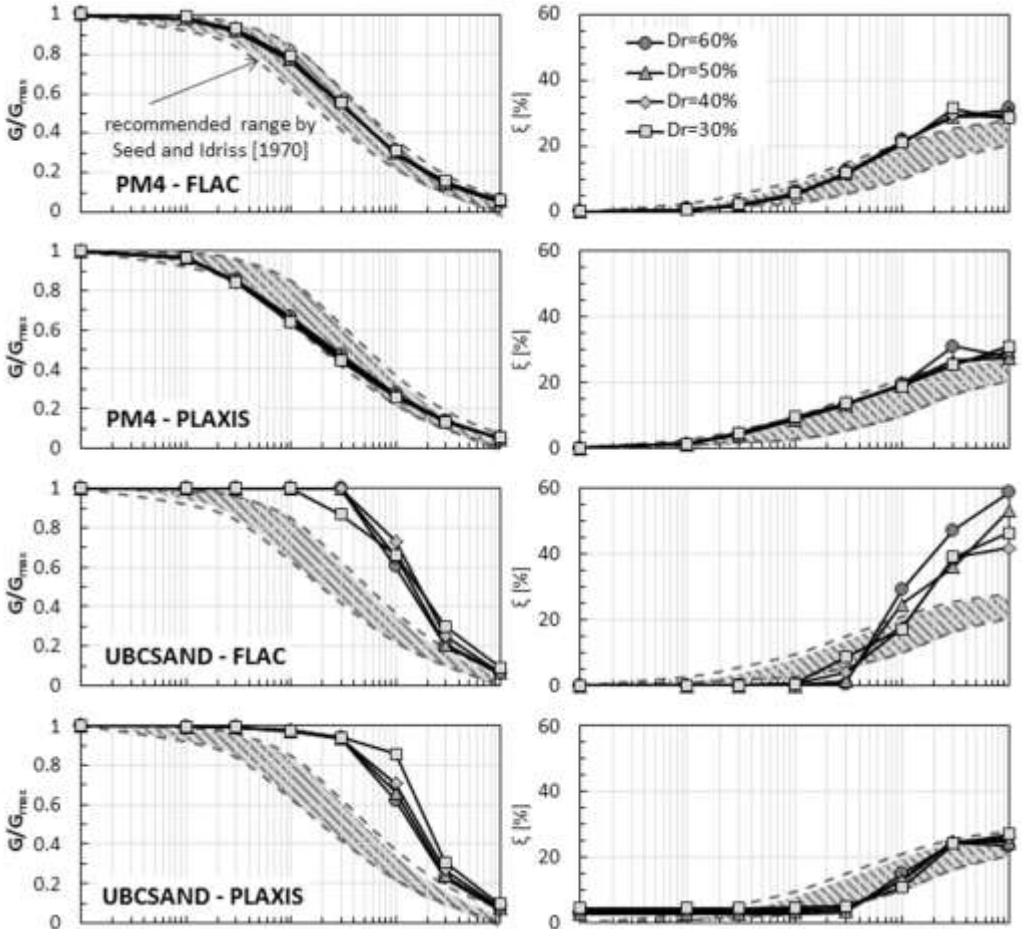

Figure 2.30: Shear modulus reduction and damping ratio curves for the density index (I_d = 60%, 50%, 40%, 30%) obtained by simulating drained cyclic DSS tests with UBCSAND and PM4Sand model, with σ'_{v0}=100 kPa and K_0=1 (Anthi and Gerolymos, 2019)

2.9.4 Final remarks on the constitutive model selection

Table 2.4 summarizes the differences between the UBCSAND and PM4Sand models based on various aspects. The PM4Sand model was chosen in this research project to simulate the cyclic behavior of tailings material considering the results of previous studies and taking into account two major limitations of the UBCSAND model in predicting the cyclic behavior of single element sands, i.e., strain locking-up and damping ratio misestimation. The calibrated parameters of the PM4Sand model for hard-rock tailings obtained by Contreras et al. (2022), which are based on extensive laboratory tests and field studies, are used in the dynamic simulations.

Table 2.4: Comparison of the UBCSAND and PM4Sand (Carey and Kutter, 2017; Tran, 2018; Anthi and Gerolymos, 2019)

Factor	**UBCSAND**	**PM4Sand**
Elastoplastic formulation	To evolve the primary yield surface, the hardening law employs a restrict hyperbolic law.	The distance between the yield surface and the bounding surface determines the hardening law, with additional parameters controlling it.
	The model is not based on critical state theory.	Critical state theory is used in the formulations of the model. As a result, the model can simply change its behavior by shifting its state position in regard to the critical state.
Cyclic response	The model shows a stabilize hysteretic behaviour after certain cycles with no more increasing in pore water pressure and shear strain development. Furthermore, the model is simulating high damping ratio at large strains.	The model simulates continuous development of pore water pressure and shear strain under high number of cycles
Input parameters	9 input parameters that are easily calibrated using laboratory or field tests	Three primary and 21 secondary input parameters, a lengthy calibration procedure requiring soil response in various states under drained and undrained conditions

CHAPTER 3 ARTICLE 1: A DYNAMIC NUMERICAL INVESTIGATION TO ASSESS THE OPTIMAL CONFIGURATION OF WASTE ROCK INCLUSIONS FOR SEISMIC STABILITY OF TAILINGS IMPOUNDMENTS

Ali Reza Zafarani[1*], Samuel Yniesta[1] and Michel Aubertin[1]

[1]Department of Civil, Geological and Mining Engineering, Polytechnique Montréal, C.P. 6079, Centre-ville, Montréal, QC H3C 3A7, Canada.

*Corresponding Author; email: ali-reza.zafarani@polymtl.ca

This article was submitted to Canadian Geotechnical Journal in November 2021

Abstract

A large number of tailings impoundments are constructed with retaining dikes built using the upstream-raised construction method due to its relative simplicity and cost-effectiveness. However, the stability of such impoundments is a concern, as these have been prone to failure. The use of waste rock inclusions (WRI) in tailings impoundment was proposed to improve the stability of impoundments, particularly for upstream-raised dikes under seismic loading. This paper presents the results of numerical dynamic analyses of the seismic behavior of tailings impoundments reinforced with waste rock inclusions. The effects of the downstream slope, height of the impoundment, and loading conditions on the overall response and seismic stability are investigated through a parametric study. The effect of each parameter is evaluated individually using two performance indicators: the critically displaced volume of tailings and the horizontal displacement of the downstream slope. The analyses are used to develop equations to estimate the displacement of the downstream slope as a function of geometry of the impoundment and waste rock inclusions configuration.

Key Words: Tailings impoundments; dynamic numerical simulations; Waste rock inclusions; seismic stability; parametric study

3.1 Introduction

Hard-rock mine tailings produced by mining operations are usually deposited in surface impoundments as a slurry. These impoundments are commonly constructed using retaining dikes made (at least in part) of granular materials such as waste rocks and coarse-grained tailings. The seismic stability of tailings impoundments depends on the performance of the retaining dikes, the behavior of the relatively loose tailings, and the interaction between the two. Under dynamic loading, excess pore water pressure may build up in the compressible tailings, and they may undergo reduced stiffness and strength loss associated with liquefaction (Holtz and Kovacs, 1981; Seed and Idriss, 1982). The liquefied tailings may then impose additional loading on the retaining dikes, which could lead to failure of the impoundment (Gens and Alonso, 2006).

Aubertin et al. (2002) proposed that the waste rock inclusion (WRI) method of co-disposal could be used to improve the static and dynamic stability of tailings impoundments. This method mainly consists of placing rows of waste rock along predetermined locations in the impoundment and raising the waste rock inclusions with each raise of the retaining dikes. The effects of waste rock inclusions on the seismic response of tailings impoundments have been studied in recent years using laboratory testing, physical modeling and numerical dynamic simulations (James, 2009; James and Aubertin, 2012; Pepin et al., 2012; Ferdosi 2015; Jahanbakhshzadeh et al., 2019). The results of these studies have shown that waste rock inclusions can significantly improve the seismic response and stability of the tailings impoundment, and the overall geo-environmental performance of the tailings disposal facility (James et al. 2013, 2017; Aubertin et al. 2021). However, design guidelines and optimization methodologies are needed to better integrate this co-disposal method in the design of tailings impoundments. This aspect is addressed in great details in this study for tailings impoundments constructed with upstream dikes by assessing the response of the models during and after ground motions, for various conditions including different WRI configurations, downstream slope and thickness of tailings, and ground motion characteristics (i.e., peak ground acceleration). Moreover, the seismic response of tailings impoundments reinforced with WRI needs to be evaluated using representative performance indicators. These metrics should evaluate the response in terms of the mechanisms leading to liquefaction and the deformation during and after the ground motion, for various conditions. In this study the key performance indicators

selected to assess the seismic response of reinforced impoundments are the volume of liquefied tailings, critically displaced volume, and average horizontal displacement of downstream slope. A description of the numerical modeling procedure is provided before presenting and analyzing the main results. The effects of the downstream slope of the retaining dikes, tailings thickness in the impoundment, and peak ground acceleration (PGA) are evaluated based on performance indicators. This analysis also includes the variation trends for the critically displaced volume of tailings and the average horizontal displacement of the external slope for various dikes and WRI configurations. The simulation results are used to develop a design approach to optimize the configuration of waste rock inclusions in tailings impoundments.

3.2 Numerical modeling procedure

The seismic behavior of tailings impoundments is analyzed using nonlinear dynamic numerical analysis, which has been shown to be a powerful and useful method to assess the evolving stress state and the deformation of embankments under cyclic loading (e.g., Seid-Karbasi and Byrne, 2004; Castillo et al., 2006; James, 2009; Meisheng et al., 2011; Armstrong et al., 2013; Ferdosi et al., 2015; Salam et al., 2021). This type of analysis can consider the complex geometry of the tailings impoundment and simulate the non-linear stress-strain behavior of the materials. However, the reliability of such simulations depends heavily on the accuracy of the constitutive model used in the analysis (e.g., Ferdosi et al., 2015).

A number of finite difference and finite element software packages developed over the years are capable of simulating the dynamic response of earth structures, and the triggering of liquefaction. FLAC (Fast Lagrangian Analysis of Continua) Version 8.00 (Itasca, 2016), which is based on the finite difference method, is used in this study in part because of the built-in constitutive models and the good results obtained in earlier investigations (Moriwaki et al. ,1998; Seid-Karbasi and Byrne, 2004; Piao et al., 2006; James, 2009; Ferdosi et al., 2015). FLAC also allows the use of advanced models implemented through a user-defined model option, such as the PM4Sand constitutive model (Boulanger and Ziotopoulou,2017) applied here.

This section presents a short description of the procedure used to perform the numerical simulations. The simulation results then serve to assess the performance of the impoundments

based on excess porewater pressures development, and the pattern and magnitude of deformations. Key outcomes are presented and discussed in the subsequent sections.

3.2.1 Analysis steps

Each numerical simulation consists in three steps. The first step is to set up the model and define its geometry, the meshing, the boundary conditions, and the material properties. The second step consists in running the numerical model to establish the static conditions, including the initial state of stresses, strains and pore water pressures under mechanical and hydraulic equilibrium. In this stage the soils are modeled using the Mohr-Coulomb elasto-plastic model, except the bedrock which was considered linearly elastic. Long term (steady-state) static conditions are simulated here, so sequential raising of the impoundment is not considered; the model is created in a single placement of material, followed by application of the gravity.

In the last step, stresses from the static phase are used as initial conditions for the dynamic analysis, by applying earthquake loading at the base of the model. In this stage, the constitutive models of the different materials are changed to better simulate their behavior under seismic loading, as described in subsequent sections.

3.2.2 General model geometry

In the present study, the upstream-raised dike construction method is used for the representative tailings impoundment, with different heights and external slopes. Figure 3.1 presents the general model geometry and distribution of material zones of the impoundment reinforced with waste rock inclusions, being considered for the parametric study. The starter dike and dikes raises are composed of waste rock (as is the case at various hard rock mines, such as the Canadian Malartic mine in Abitibi, QC; James et al. 2017; Aubertin et al. 2021). The dike raises are 2 m high with a side slope that ranges from 1.5H/1V to 4H/1V depending on the height and global slope of the model; the crest width and height of the starter dike are 19 m and 10 m, respectively. The impoundment model extends up to 140 m away from the upper dike crest, following a parametric study indicating that the analysis results are not affected by a wider model. A 5-m-thick layer of hard bedrock is added beneath the impoundment.

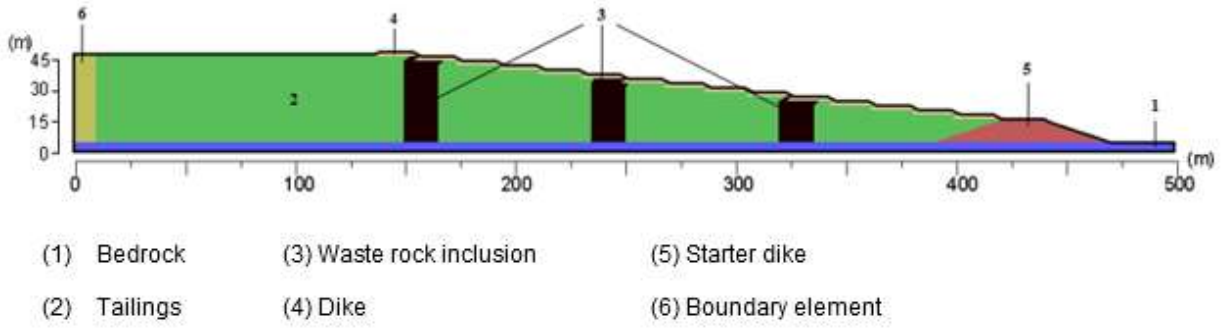

Figure 3.1:Conceptual model of a tailings impoundment with 3 waste rock inclusions with a width of 16 m and spacing 70 m

3.2.3 Meshing and boundary conditions

FLAC uses quadrilateral elements, and their size was set so that it would not exceed a tenth of the wavelength of the highest frequency component of the input wave that contains appreciable energy (Kuhlemeyer and Lysmer 1973). This guideline was followed and satisfied with an element size of 1 m by 1 m in the core of the model, which ensured that ground motions frequencies up to 25 Hz are realistically transmitted through the model. The mesh size was refined with smaller elements down to 0.5 m in the zones where higher deformations and stresses were expected (mostly under the dikes).

The mechanical and fluid boundary conditions applied to the models during the static phase of the analysis consist of fixed horizontal displacement on both sides, vertical displacements fixed at the base and a fixed zero pore water pressure at the surface of the tailings and on the right side of the model (i.e., surface of dikes).

For the dynamic analyses, the boundary conditions were modified as a free field on the sides and the application of a ground motion at the base of the model in the form of applied horizontal accelerations. However, a free field boundary condition cannot be used directly with the PM4Sand model (Boulanger and Ziotopoulou, 2017), used here for the tailings, so the free field boundary condition on the left side of the impoundment is applied through a series of vertical elements modeled with the elastoplastic Mohr-Coulomb constitutive model (for both static and dynamic

analyses). The fluid boundary conditions of the static phase were retained during the dynamic analyses.

3.2.4 Ground water

The water level within active tailings impoundments is often kept at or above the surface of the tailings. This is advantageous when there is a need to control oxygen ingress, but it creates unfavorable geotechnical conditions (Aubertin et al. 2002, 2016). The groundwater level within the impoundment was assumed to be at the surface of the tailings for all the simulations, which can be considered as a realistic worst-case scenario for the seismic stability. The hydrostatic pressures and seepage conditions resulting from the elevated water table are calculated in FLAC during the static stage; a typical pore water distribution and phreatic surface in the model during this stage are shown in Figure 3.2.

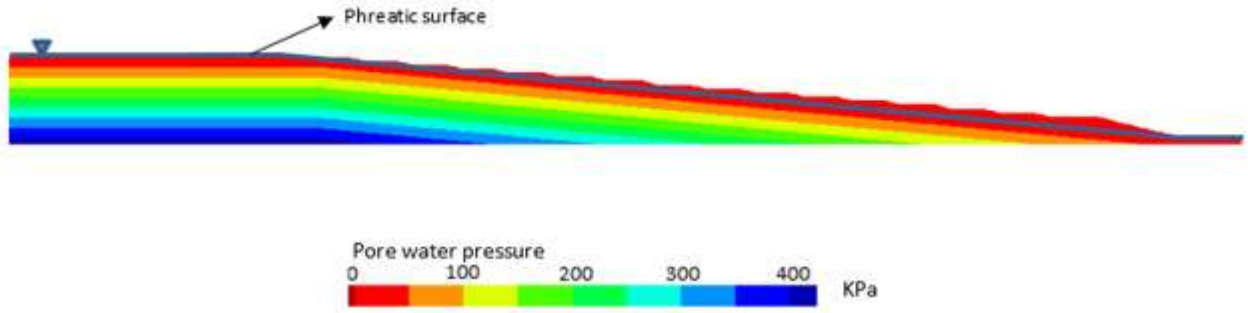

Figure 3.2: Pore water pressure distribution at the end of the static analysis, and position of the phreatic surface in the impoundment model

3.2.5 Material properties and constitutive models

As indicated above, the elastoplastic Mohr-Coulomb model is used to simulate the behavior of all materials in the static phase, except for the bedrock which was considered linearly elastic. The constitutive models of the different zones are then changed during the dynamic phase to better model the seismic behavior of the various materials. For the tailings, the PM4Sand model (Boulanger and Ziotopoulou,2017) was used to capture their cyclic liquefaction behavior, while the elastoplastic Mohr-Coulomb model with the hysteretic Sigmoidal model-sig3 (Itasca, 2016) option was assigned to waste rocks for the raised dikes and starter dike.

3.2.5.1 Hydro-geotechnical properties

The hydro-geotechnical properties of tailings material such as unit weight, porosity and hydraulic conductivity are highly influenced by the method of deposition, age and height of the deposit inside the impoundments. Various investigations have been conducted on the properties of hard rock mine tailings either from field or laboratory tests (e.g., Vick, 1990; Aubertin et al. 2002, 2011; Bussière 2007; L-Bolduc, 2012; Poncelet, 2012; Contreras Romero, 2013; Grimard et al., 2021). Previous investigations performed by James (2009), Poncelet (2012), Contreras (2013), and Essayad and Aubertin (2021) on hard rock tailings from the Quebec region indicate that the average density index (I_D) of consolidated tailings is about 60% for vertical effective stresses of 100 to 400 kPa. Based on these investigations, a value of 60% was adopted here for the consolidated tailings in the impoundment.

The in-situ saturated hydraulic conductivity, k_{sat}, of tailings is influenced by the density index (porosity) and grain size of the tailings inside the impoundment. A k_{sat} value of 5.8×10^{-8} m/s was used for the numerical simulation of the tailings based on experimental measurements reported for similar tailings (Mbonimpa et al., 2002; Bussière, 2007; Essayad, 2015).

The dry unit weight γ_d of the waste rock material (20 kN/m^3) and the porosity (0.25) are based on typical values reported in Peregoedova et al. (2013), Essayad et al. (2018), and Martin and Aubertin (2019). The saturated hydraulic conductivity of waste rock, k_{sat}, depends on the particle size and density. A value of 10^{-3} m/s is adopted here for the saturated hydraulic conductivity of the waste rock material forming the inclusions and raised dikes (based on data from the same sources as γ_d). The properties of the starter dike are similar, except for the porosity and saturated hydraulic conductivity which are 0.2 and 10^{-2} m/s, respectively.

The hydro-geotechnical properties of bedrock material such as γ_d and k_{sat} are based on values reported by Goodman (1989) and Wyllie and Mah (2004).

3.2.5.2 Mohr-Coulomb model

The linear elastic perfectly plastic Mohr-Coulomb model is used for all the materials to compute the static stress conditions, except for the bedrock which was considered linearly elastic. The input parameters needed are the cohesion, the internal friction and dilatancy angle, and a combination of

two isotropic elastic properties (for instance shear and bulk moduli). All the material properties for the static phase are listed in Table 3.1.

The average shear modulus, *G*, of the tailings is based on in-situ shear wave velocity measurements and estimated average in-situ density (Grimard et al., 2021). The typical effective internal friction angle of hard rock mine tailings is close to 35° based on direct shear testing at confining stresses between 100 kPa and 500 kPa (e.g., James 2009; Poncelet, 2012; Grimard, 2018). A Poisson ratio, υ, of 0.3 is used for tailings, based on the following relationship with the effective friction angle (Duncan and Bursey, 2013; Falaknaz et al. 2015a, 2015b; Yang et al. 2018):

$$\upsilon = \frac{1-sin\,\varphi'}{2-sin\,\varphi'} \tag{3.1}$$

The shear and bulk moduli of waste rock material are defined according to two relationships proposed for granular materials by Seed et al. (1984) and Rollins et al. (1998):

$$G = 55000.(0.6.\sigma'_v)^{0.5} \tag{3.2}$$

$$K = 2.3833.G \tag{3.3}$$

Where σ'_v is the effective vertical stress in kPa. Minimum values of 3.1×10^5 kPa and 7.4×10^5 kPa are considered for shear and bulk moduli, respectively (James, 2009).

Dilation angle of granular material during shear has been shown to be related to its density index and confining pressure (Vaid et al., 1981). Nevertheless, this value is generally assumed to be constant when using the Mohr-Coulomb elasto-plastic model. Before failure, a positive dilatancy ($\psi > 0$) tends to increase the mean effective stress under undrained loading, which also increases the shear strength of the material. Thus, it is conservative to consider a zero dilation angle (corresponding to a constant volume upon yielding) when using the Mohr-Coulomb model to investigate the stability of earth structures.

Table 3.1: Material properties for the static phase simulations

Properties	Tailings	Dikes (WRI)	Starter dike	Bedrock
Constitutive model	Elasto-plastic, Mohr-Coulomb	Elasto-plastic Mohr-Coulomb	Elasto-plastic Mohr- Coulomb	Elastic
Dry unit weight, $\boldsymbol{\rho_{dry}}(\frac{\boldsymbol{kN}}{\boldsymbol{m^3}})$	16.5	20	20	22
Effective internal friction angle, $\boldsymbol{\varphi'}$(°)	35	45	45	-
Effective cohesion, $\boldsymbol{c'}(\boldsymbol{kPa})$	0	0	0	-
Dilation angle, ψ(°)	0	0	0	-
Porosity, $\boldsymbol{n}$	0.4	0.25	0.2	0.1
Shear Modulus, $\boldsymbol{G}$ $(\boldsymbol{kPa})$	$113*10^3$	Varied[1]	$3.1*10^5$	$13.46*10^6$
Bulk Modulus, $\boldsymbol{K}$ $(\boldsymbol{kPa})$	$300*10^3$	Varied[1]	$7.4*10^5$	$29.16*10^6$
Hydraulic conductivity, $\boldsymbol{k_{sat}}(m/s)$	$5.8*10^{-8}$	10^{-3}	10^{-2}	$5*10^{-8}$

[1] Equations [3.2] and [3.3]

3.2.5.3 PM4Sand model

The PM4Sand model (Boulanger and Ziotopoulou, 2017) is a critical-state compatible, stress-ratio based, bounding surface plasticity model developed for sand, which is based on the model of

Manzari and Dafalias (1997) and extended by Dafalias and Manzari (2004). Previous work had shown that cohesionless tailings from hard rock mines typically behave similarly to sandy soils (James et al., 2012). The PM4Sand model includes three primary parameters that need to be calibrated based on the experimental soil properties, and 21 secondary parameters that can be adjusted from their default values to obtain a material-specific calibration if detailed information is available about the soil's behavior.

The calibration of the PM4Sand model for hard-rock tailings presented in Contreras et al. (2021) is used in the present study. Primary and secondary parameters of the PM4Sand model were calibrated based on laboratory cyclic tests and field investigations. Special care was taken to ensure that the model yielded accurate cyclic resistance curves (CRR vs number of cycles to trigger liquefaction). Calibration was verified by comparing simulated stress-strain curves and pore pressure response with laboratory test results. Table 3.2 presents the PM4Sand parameters used for the tailings in the dynamic simulation stage that differ from the default values provided in Boulanger and Ziotopoulou (2017).

Table 3.2: Calibrated PM4Sand model parameters for tailings (Contreras et al., 2021)

Parameter identification	Symbol	Calibrated value
Density index (D_r in original publication); Primary	I_d	0.6
Shear modulus coefficient; Primary	G_o	502.5
Contraction rate parameter; Primary	h_{po}	0.55
Minimum void ratio	e_{min}	0.49
Maximum void ratio	e_{max}	1.1
Bounding parameter	n^b	0.7

Fabric growth parameter	c_z	150
Critical state friction angle	φ'_{cv}	35
Modulus degradation factor	C_{GD}	2.5
Critical state line parameter	Q	12.7
Critical state line parameter	R	5.4

3.2.5.4 Hysteretic Sigmoidal model-Sig3

Upon cyclic loading, the Mohr-Coulomb model would result in unrealistic damping at both low and high strains (Itasca, 2016). Up until the yielding point, the unloading curve would be perfectly linear, therefore resulting in zero hysteretic damping, while upon unloading past yielding the damping would be higher than observed in laboratory tests. To solve this shortcoming of the Mohr-Coulomb model, a hysteretic damping scheme is suggested for simulations with FLAC, where the shape of the unloading curve is modified to give more realistic damping. Such hysteretic damping scheme is not intended to be a full constitutive model, but should rather be used as a complement to one of the nonlinear models. Among the different hysteretic models implemented in FLAC, the Hysteretic Sigmodial model-sig3 (Itasca, 2016) is used here to introduce hysteretic damping for the material modelled with the Mohr-Coulomb model (i.e., waste rock inclusions, raised dikes, starter dike, boundary element). This Sigmoidal model is defined with three specific non-dimensional parameters *a*, *b*, and x_0. The value of these parameters is provided by Itasca (2016) for sands and clays. Ferdosi (2015) calibrated this model based on the degradation curves of a gravelly soil provided by Rollins et al. (1998), and obtained the corresponding values for parameters, *a*, *b* and x_0: 1.02, -0.698 and -1.45, respectively.

3.2.6 Viscous damping

At low strains, hysteretic damping of the nonlinear constitutive models is essentially zero. Mass and stiffness- proportional Rayleigh damping (Rayleigh and Lindsay 1945) is used to introduce small-strain damping. The mass-proportional and stiffness-proportional damping constants are set so that the target small-strain damping, ξ_{min} (i.e., 2%) is matched at a given predominant frequency

(f_{min}) taken as the mean frequency of the system. This is estimated based on the Fourier analysis of the free vibration response of the model with elastic properties (Kishi et al., 1987). The same damping approach was taken for the bedrock so that this layer does not amplify nor attenuate the motion.

3.3 Parametric numerical investigation

Various simulations were conducted to investigate the influence of specific characteristics on seismic behavior, including the downstream slope angle of the impoundment, height of the model, and maximum acceleration of the input motion. The effect of these characteristics is studied through a total of 100 numerical simulations by assessing their impact on three performance indicators: the critically displaced volume of tailings (*CDV*), the deformation of the impoundment crest, and the normalized horizontal displacement of the downstream slope.

3.3.1 Geometry of the impoundments

The impoundment with a downstream slope of 8H:1V and a height of 40 m under a seismic motion with maximum horizontal acceleration (PGA) of 3.04 m/s^2 is defined as the reference case. In the parametric study, the downstream slope ranges between 7H:1V and 12H:1V, the height of the impoundment varies between 20 m and 50 m, and the maximum acceleration of the ground motion goes from 1.21 (m/s^2) to 4.87 (m/s^2). The simulated seismic response of the various models is compared to the reference case and the effect of each characteristic and parameter is investigated individually by evaluating their influence on specific model response quantities.

3.3.2 Seismic loading

The recording of the M_w 6.93 Loma Prieta 1989 earthquake from the NGA-West2 database (Ancheta et al. 2013) at station RSN810, situated at a distance of 18.41 km from the surface projection of the rupture plan, is used as the input ground motion. Figure 3.3 shows the response spectrum of the record. The recording is characterized by medium frequencies (i.e., average frequency of 6.5 Hz), with a *PGA* of 4.70 m/s^2, an Arias Intensity, *AI*, of 2.7 m/s, and a significant duration ($D_{5\text{-}95}$) of 13.72 s (PEER, 2019). The Loma Prieta record was chosen for this study because of its medium frequency content. The Loma Prieta recording is scaled at four different levels of

*PGA (*1.21 m/s^2, 2.04 m/s^2, 3.04 m/s^2 and 4.87 m/s^2) to assess the effect of the peak ground acceleration (*PGA*) on the seismic response of the models. The associated parameters of the scaled ground motions are presented in Table 3.3.

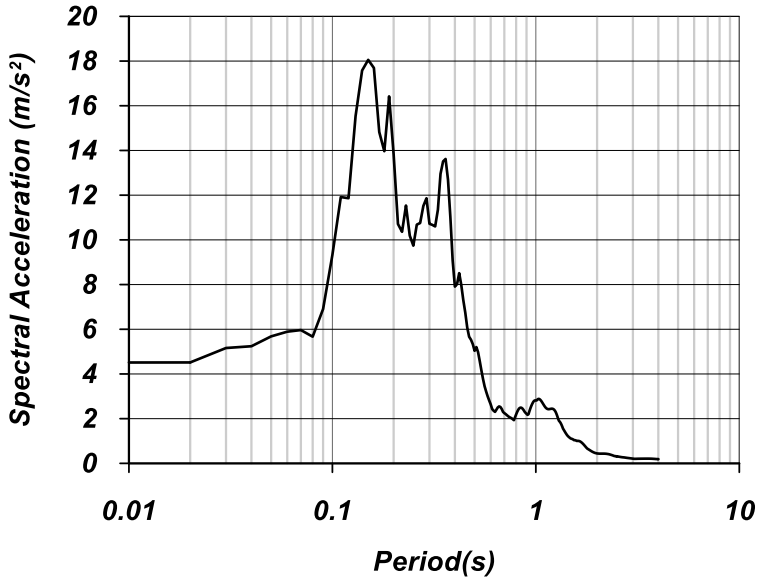

Figure 3.3: Response spectrum of Loma Prieta (record RSN810) ground motion (Adapted from PEER 2019)

Table 3.3: Input ground motions parameters

Event	Loma Prieta (Base)	E_1-Loma (Scaled)	E_2- Loma (Scaled)	E_3-Loma (Scaled)	E_4-Loma (Scaled)
Arias Intensity (m/s)	2.7	0.19	0.54	1.2	3.09
Significant duration (D_{5-95})	13.72	13.72	13.72	13.72	13.72
M_w	6.93	-	-	-	-
PGA (m/s^2)	4.7	1.21	2.04	3.04	4.87

Average frequency (Hz)	6.5	6.5	6.5	6.5	6.5

3.3.3 Configuration of the waste rock inclusions

The effect of waste rock inclusions (WRI) configuration on the seismic response of the tailings impoundments is evaluated using different width *W* (m) and edge-to-edge spacing *S* (m) for the WRI, using values based on field applications (Aubertin et al. 2021). The width of the inclusions ranges from 12 to 25 m and spacing from 55 to 155 (m). The combinations of width, spacing, height, slope, and seismic loading considered for this parametric study are listed in Table A_1 in Appendix A.

3.4 Main results and analysis

3.4.1 Representative dynamic responses

Figure 3.4a and Figure 3.4b show the effective vertical stress contours of an unreinforced model with an external downstream slope of 8H:1V, for a height of 40 m (reference case) under static loading (Figure 3.4a) and at the end of the input motion E_3-Loma (Figure 3.4b). The contours indicate that most of the tailings experienced considerable excess pore water pressure following shaking. The induced dynamic shear stress and the generation of excess pore water pressure lead to reduced effective stress and stiffness and consequently large deformations. As shown in Figure 3.4b the vertical effective stresses within the tailings are less than 100 kPa at the end of shaking, which are significantly lower than those before shaking (Figure 3.4a). The most common consequence of this reduction of effective stress is the action of additional earth pressure and seepage forces on retaining dikes and downstream side slope.

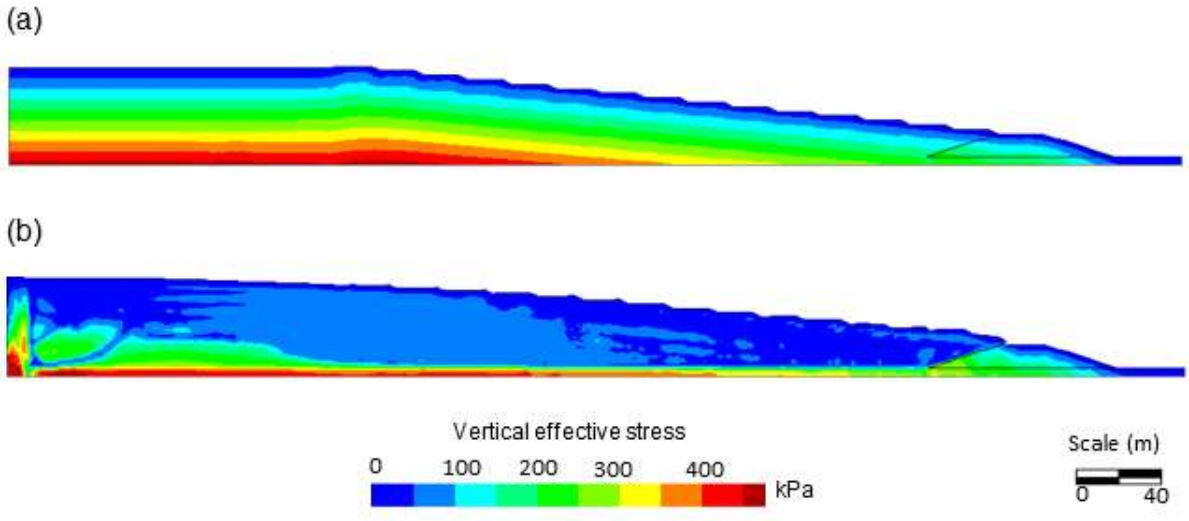

Figure 3.4: Contours of effective vertical stress of the unreinforced model with a height of 40 m and external slope of 8H:1V (a) under static loading and (b) at the end of E_3-Loma earthquake

3.4.2 Performance indicators

The response of the various model impoundments is quantified with two performance indicators: the critically displaced volume of tailings (*CDV*) and the horizontal displacement of the downstream slope. These indicators are described in the following.

3.4.2.1 Critically displaced volume of tailings

Jibson (2011) reported that horizontal displacement exceeding 100 cm are likely to cause critical landslide movements. Ferdosi et al. (2015) used a similar displacement value to analyse the seismic response of tailings impoundments in terms of the critically displaced volume (*CDV*). The authors are also using the same *CDV*, defined as the percentage volume of tailings (over the total volume) displaced horizontally more than 100 cm to analyse simulation results.

3.4.2.2 Horizontal displacement of the downstream slope

The horizontal displacement is computed at the end of shaking at each nodal point along the downstream slope of tailings impoundment. These values are used to evaluate the effect of waste rock inclusions' configuration on the seismic response of the impoundment. The normalized horizontal displacement at each nodal point is then calculated by dividing its horizontal

displacement at the end of shaking by its initial height above the bedrock layer. Using the approach described in Ferdosi et al. (2015), the average value of the normalized horizontal displacement of all the nodal points along the downstream slope (SAR_x) can be defined by the following equation:

$$\mathrm{SAR_x} = \mathrm{Average}\left(\frac{\mathrm{X_{disp_i}}}{\mathrm{H_i}}\right) \tag{3.4}$$

Where X_{disp_i} is the horizontal displacement at nodal point *i* along the downstream slope at the end of the shaking, and H_i is the initial height above the bedrock layer at said nodal point.

3.4.3 Influence of slope on the response of the system

The effect of the downstream slope of the impoundment on the seismic behavior of the unreinforced models was evaluated by simulating the behavior of impoundments without inclusion with an external slope of 7H:1V, 8H:1V, 10H:1V and 12H:1V, for a height of 40 m under the E_3-Loma ground motion.

Figure 3.5 presents the critically displaced volume (*CDV*) of these unreinforced impoundments. As expected, an increase in the downstream slope causes an increase in the *CDV* of the model. The applied ground motion causes about 75% of the impoundment's volume of the model with a downstream slope of 7H:1V (Figure 3.5a) to displace critically and induces a general failure which stopped the simulation after 17 seconds due to non-convergence (caused by the excessive deformation of at least one element). The seismic response of the impoundment with a downstream slope of 12H:1V (Figure 3.5d) shows that 58% of the model's volume is displaced more than 100 cm at the end of the motion, indicating that a decrease in the downstream slope leads to a decrease in *CDV* of tailings. Nonetheless, the *CDV* of the 12H:1V impoundment is still significant and would most likely lead to high deformations and potential failure of the unreinforced impoundment. Increasing the downstream slope from 12H:1V to 10H:1V does not change significantly the *CDV* (i.e., 60%), but further increment of the slope to 8H:1V leads to a marked increase in the *CDV* up to 70%.

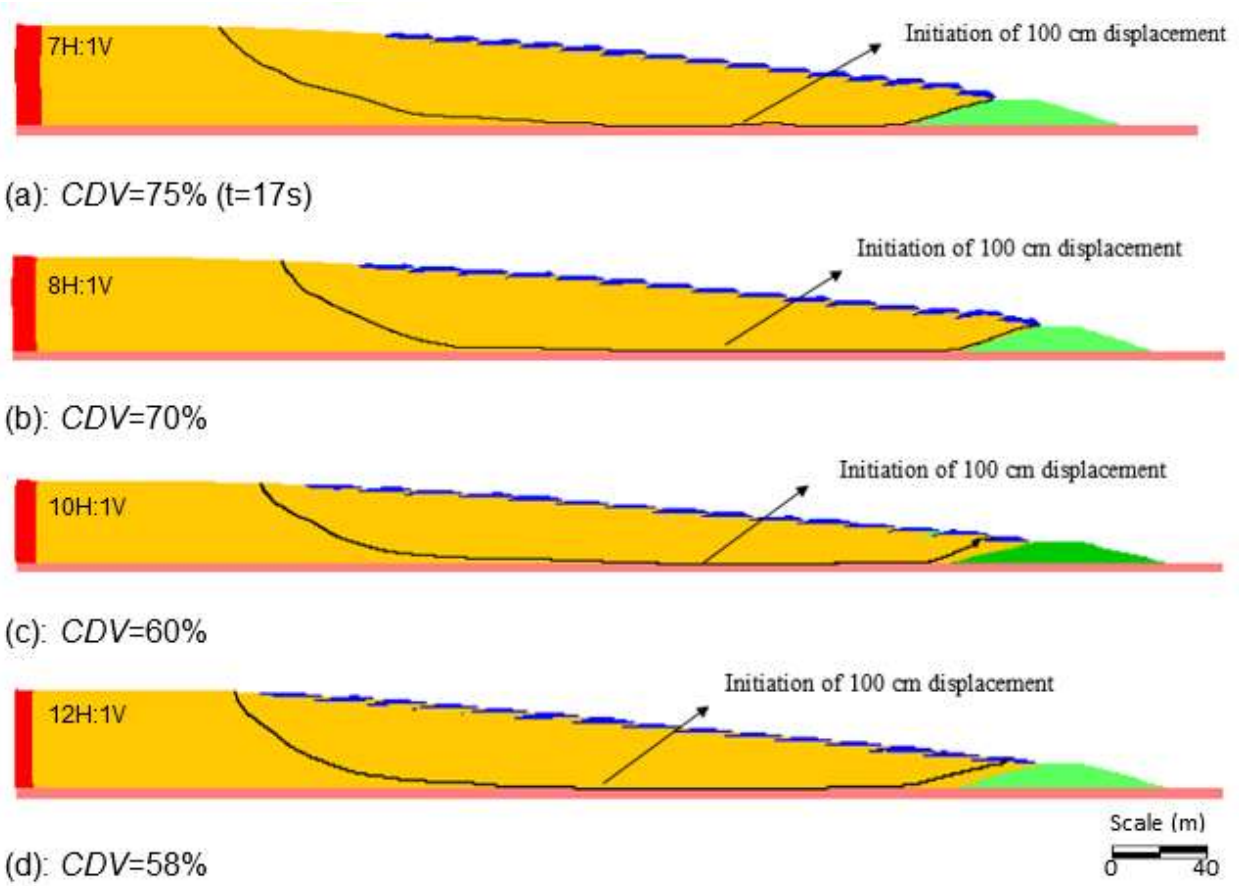

Figure 3.5: Critically displaced volume under the E_3-Loma earthquake of the unreinforced models with a height of 40 m and external slope of (a) 7H:1V (at t=17 s), (b) 8H:1V (Final), (c) 10H:1V (Final), and (d) 12H:1V (Final)

The maximum horizontal displacement of the impoundment's crest was computed during the E_3-Loma ground motion to assess the seismic stability of the dike crest zone of the unreinforced models. Figure 3.6 shows the contours of the maximum horizontal displacement of the unreinforced models shown in Figure 3.5. The downstream side of impoundment with slope of 7H:1V is displaced about 10.5 m after 17 seconds of the ground motion for the E_3-Loma earthquake, at which point the simulation stopped because of a lack of convergence. The dike crest zone of this simulated impoundment (shown in close-up) is displaced up to 8 m, which is a very large deformation that may cause failure. The displacements for a slope of 8H:1V are similar to the model with slope of 7H:1V, but the simulation reached the end of the earthquake motion. The impoundments with downstream slopes of 10H:1V and 12H:1V experience somewhat reduced

crest displacements under the same ground motion, i.e. 5.5 m and 3.5 m respectively; the corresponding contours of the horizontal displacement (Figure 3.6c and Figure 3.6d) indicate that such gentler slope angles lead to lower displacements throughout. Note that the displacements shown here would still cause significant straining that would likely lead to failure of the impoundment.

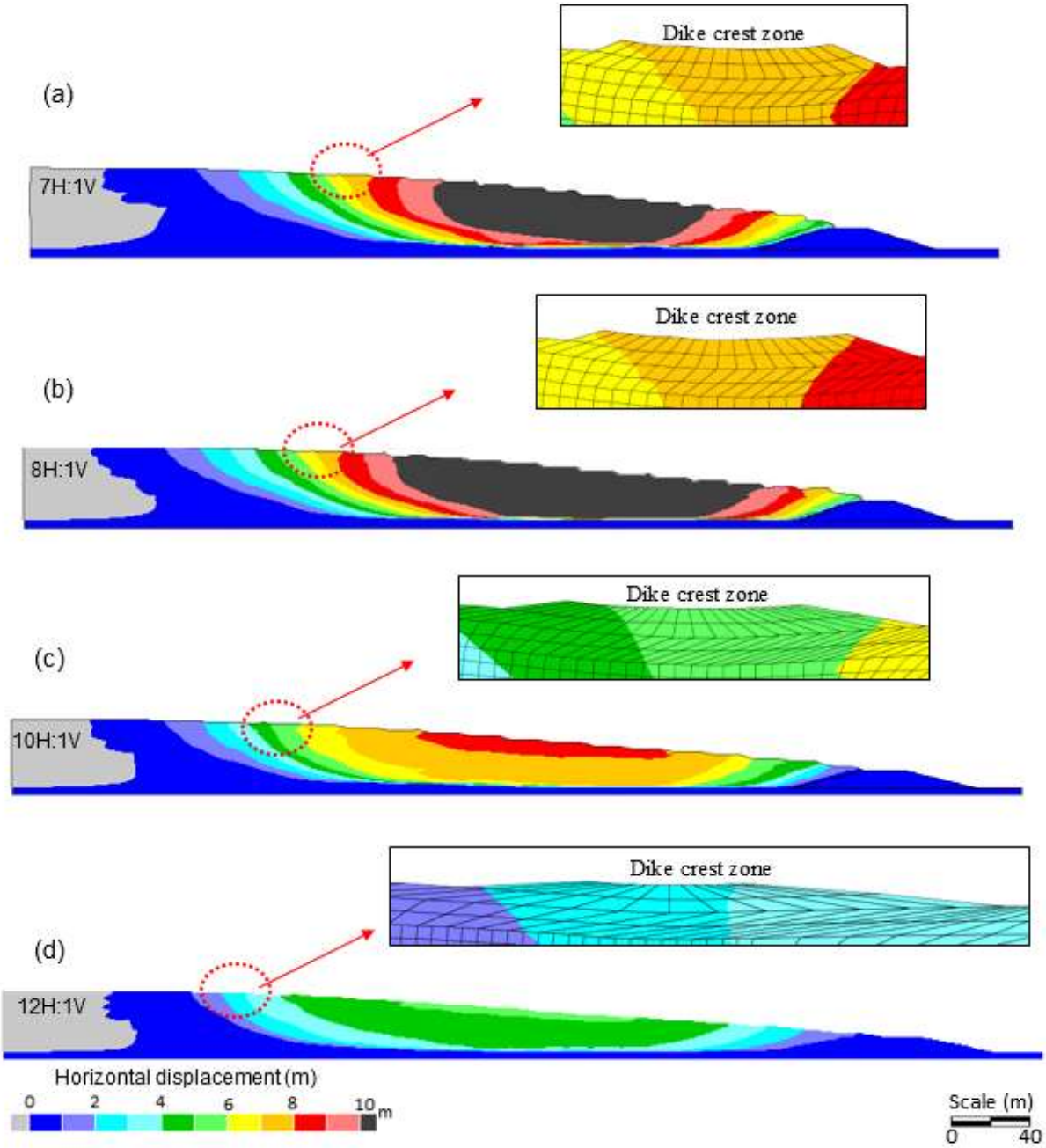

Figure 3.6: Contours of the horizontal displacement of the simulated unreinforced impoundment models with a height of 40 m and slopes of (a) 7H:1V (at t=17 s), (b) 8H:1V (Final), (c) 10H:1V (Final), and (d) 12H:1V (Final), under the E_3-Loma earthquake

The effect of the downstream slope of the model on the *CDV* and maximum horizontal displacement of reinforced tailings impoundments with a height of 40 m is illustrated in Figure 3.7

for the models with an external slope of (a) 7H:1V, (b) 8H:1V, (c) 10H:1V, and (d) 12H:1V. Each of these models, loaded with the E_3-Loma ground motion, includes three 16-m wide waste rock inclusions. Figure 3.7(a) indicates that 35% of the reinforced impoundment with a slope of 7H:1V is displaced critically at the end of the motion, compared to 75% for the case without inclusions in Figure 3.6(a). The maximum horizontal displacement of the downstream side of the reinforced model with the shallowest slope of 12H:1V is about 1.5 m at the end of the motion, compared to about 6 m without the WRI. Moreover, as seen in the close-up, the crest zone of this dike is displaced less than 1 m, as opposed to 3.5 m without reinforcement, which demonstrates the positive impact of the waste rock inclusions on the seismic behavior of the impoundment. Figure 3.7(c) shows that the maximum horizontal displacement of the impoundment with a slope of 10H:1V is also 1.5 m at the end of the earthquake, similarly to 12H:1V model. Increasing the slope to 8H:1V leads to a maximum horizontal displacement close to 2 m. These results indicate that the seismic response of the models with shallow slopes (i.e., 10H:1V and 12H:1V) are similar, while increasing the slope angle produces somewhat larger horizontal displacements, despite the smaller spacing between the WRI. These results can be attributed to the fact that there is a higher volume of liquefied tailings under the steeper slopes. Moreover, the higher static stress below steeper slopes such as 7H:1V and 8H:1V can increase the potential for liquefaction of the tailings compared with shallow slopes (i.e., 10H:1V and 12H:1V), as shown in laboratory testing (Idriss and Boulanger 2008). In all cases, the presence of WRI reinforcement significantly reduces the displacements compared to unreinforced impoundments. This trend has been obtained for all the other configurations of the waste rock inclusions as well.

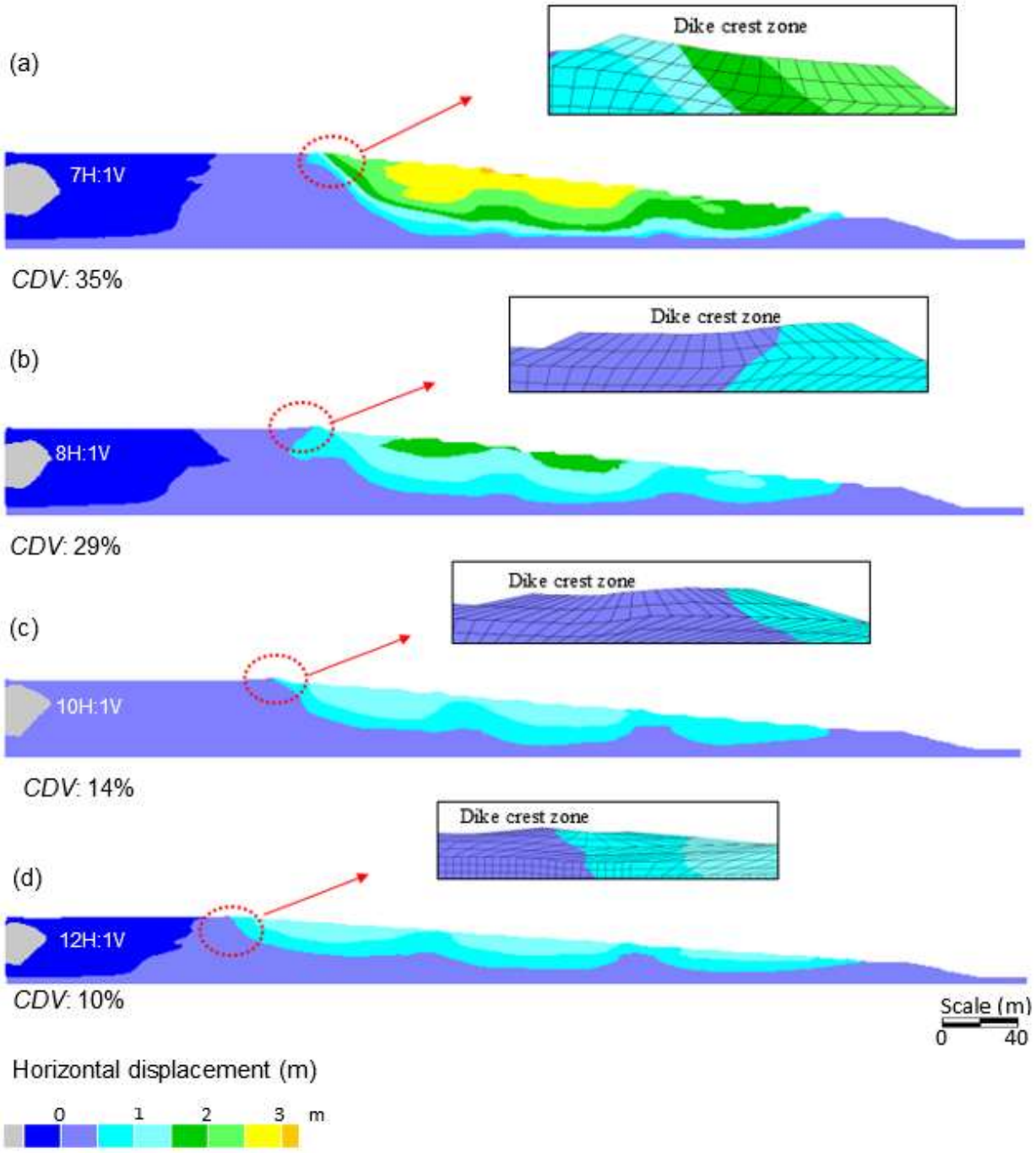

Figure 3.7: Final contours of horizontal displacements of reinforced impoundment models with a height of 40 m, for WRI having a width of 16 m, with a (a) spacing of 60 m, slope 7H:1V (b) spacing 70 m, slope 8H:1V (c) spacing 90 m, slope 10H:1V (d) spacing 121 m, slope 12H:1V

The average value of the normalized horizontal displacements along the downstream slope (SAR_x) was computed to evaluate the effect of the dike and inclusions configuration on the behavior of the impoundment. Figure 3.8 illustrates the variation of the SAR_x as a function of a non-dimensional volume-spacing index W_{vs} defined by:

$$W_{vs} = V_r \cdot (1 - \frac{S_1}{S_{max}}) \quad (3.5)$$

where V_r is the volume ratio of the WRI and the tailings ($\frac{\text{Volume of WRI}}{\text{Volume of tailings in the impoundment under the slope}}$), S_1 is the spacing between the starter dike and the edge of the closest inclusion, and S_{max} is the spacing between the starter dike and the edge of the farthest waste rock inclusion in the model.

Results of simulations are presented in Figure 3.8 for the four downstream slope angles (i.e., 7H:1V, 8H:1V, 10H:1V, and 12H:1V), with trendlines. It should be noted that this analysis of the results with the trend lines is only applicable to reinforced models, as many simulations of unreinforced models, such as the one shown in Figure 3.6a (with slope of 7H:1V and height of 40 m), were stopped during the ground motion due to high deformation and a lack of convergence. As seen in the figure, an increase in the volume of inclusions in the impoundment is associated with a decrease in SAR_x. These results illustrate how the WRI configuration influences the seismic response of the tailings impoundment in terms of horizontal displacement of the downstream slope. The effect of the inclusions on the value of SAR_x for shallower downstream slopes of 12H:1V and 10H:1V is limited, while it is much more noticeable for the two steeper slopes (i.e., 8H:1V, 7H:1V). This can be seen in Figure 3.8 by comparing the slope of the variation trend lines of SAR_x versus W_{vs} for various external slopes. For example, for an impoundment with an external slope of 7H:1V the SAR_x value decreases from about 23% to less than 5% with an increase of 0.14 in the volume-spacing index W_{vs}. The reduction of SAR_x for the models with downstream slope of 12H:1V is much less significant (from 7% to 4%) for the same increase in the W_{vs} value. In general, the values of SAR_x of the models with higher W_{vs} values become close to each other, indicating that there is an optimum configuration beyond which adding more waste rock has little effect on the displacements. These results also confirm the effect of waste rock inclusions in reducing the horizontal displacement of the models, particularly for those with steep external slopes (i.e., 7H:1V and 8H:1V).

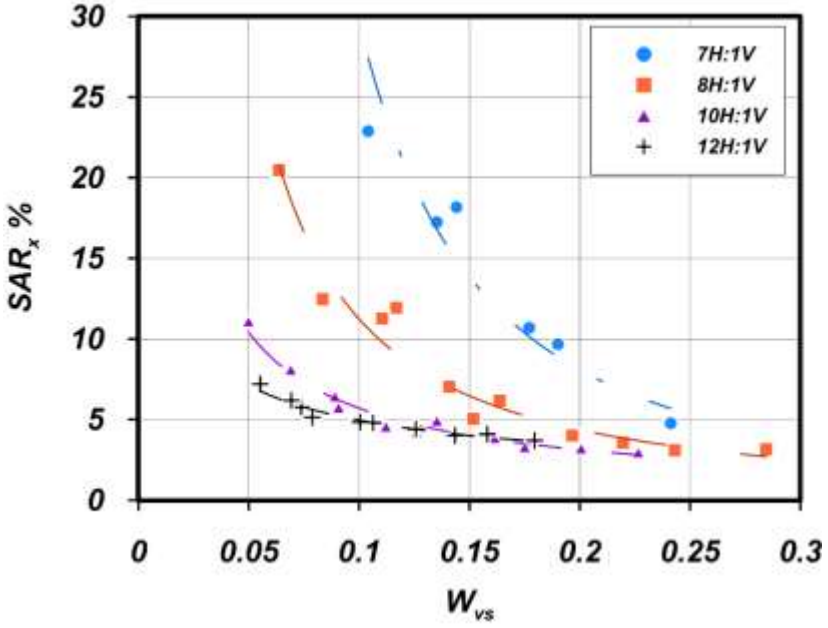

Figure 3.8: Variation of the SAR_x value as a function of volume-spacing index, W_{vs} for the reinforced impoundment models with a height of 40 m and downstream slopes of 7H:1V, 8H:1V, 10H:1V, and 12H:1V

The excess pore water pressure ratio (r_u) within the reinforced impoundment at the end of E_3-Loma earthquake is presented on Figure 3.9 for the models with an external slope of (a) 7H:1V, (b) 8H:1V, (c) 10H:1V, and (d) 12H:1V. The simulation results indicate that the tailings between the waste rock inclusions are for the most part liquefied (r_u> 0.9) at the end of shaking. Hence, the addition of waste rock inclusions and variation of the downstream slope of the impoundment do not affect significantly the generation of excess pore water pressure in the tailings except at the immediate vicinity of the waste rock. These results are consistent with those of previous studies conducted with the UBCSand model (James, 2009; Ferdosi et al. 2015). This confirms that the stability improvement due to the inclusions arises from the increased lateral stiffness and strength of the added waste rock, rather than the increased drainage during the earthquake. Dissipation of excess pore water pressures is however accelerated by the WRI after the dynamic loading, contributing to the post-seismic stability (Contreras et al., 2020).

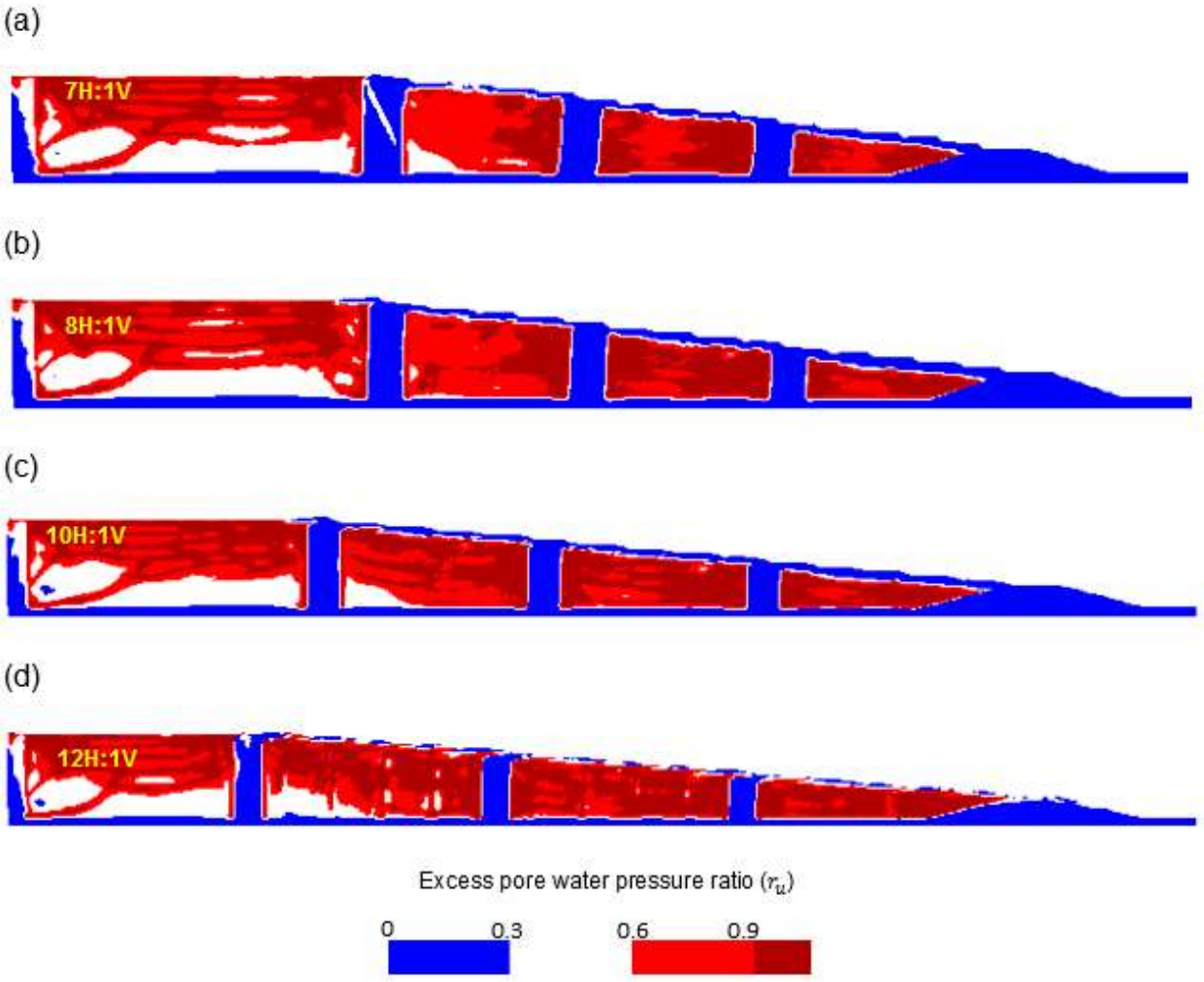

Figure 3.9: Final distribution of excess pore water pressure ratio (r_u) of reinforced models with a height of 40 m and WRI having a width of 16 m, for a (a) spacing of 60 m, slope 7H:1V (b) spacing of 70 m, slope 8H:1V(c) spacing of 90 m, slope 10H:1V (d) spacing of 121 m, slope 12H:1V under the E_3-Loma earthquake

3.4.4 Effect of height and inclusions width

The effects of the height of the impoundment (or tailings thickness) and inclusions width on the various reinforced tailings impoundments under the E_3-Loma ground motion are illustrated in Figure 3.10 using the critically displaced volume, *CDV*. The legends in Figure 3.10 provide the configuration of the WRIs; the four numbers correspond to the width of each inclusion, the spacing between WRIs, the height of the impoundment, and the downstream slope of the external dikes.

The three configurations presented here are comparable, although the spacing between WRIs differs due to the height difference.

The results indicate that the area of the impoundment displaced by more than 100 cm for the models with a height of 40 m (Figure 3.10a) is relatively smaller than for the models with a height of 50 m (Figure 3.10b). The contours of *CDV* for all the configurations for the 40 m-high impoundments are limited to the zone under the downstream slope. However, for two configurations with a height of 50 m (i.e., 12-70-50-8H, 16-70-50-8H), the *CDV* extends beyond the crest of the downstream slope.

For configuration 12-80-40-8H, 45% of the total impoundment volume (i.e., the entire zone under the downstream slope) is displaced critically. Increasing the width of the inclusions from 12 m to 16 m decreases the *CDV*, which is then limited to the top half of the downstream slope. Further increasing the width of the inclusions to 20 m yields in an even lower critically displaced volume (i.e., 9%).

The *CDV* contours for configuration 12-70-50-8H in Figure 3.10b show that 60% of the impoundment volume is displaced critically at the end of the motion. By increasing the width of the inclusions from 12 m to 16 m (16-70-50-8H), the *CDV* decreases by 5%, a reduction that is less pronounced compared to the models with a height of 40 m. Further increasing the width of the WRIs to 20 m (20-65-50-8H) causes a reduction of the critically displaced volume by a factor of 2.6 compared to configuration 16-70-50-8H. These results indicate that increasing the width of WRIs reduces the horizontal displacements; however, this effect appears to be less significant for the thicker tailings deposit.

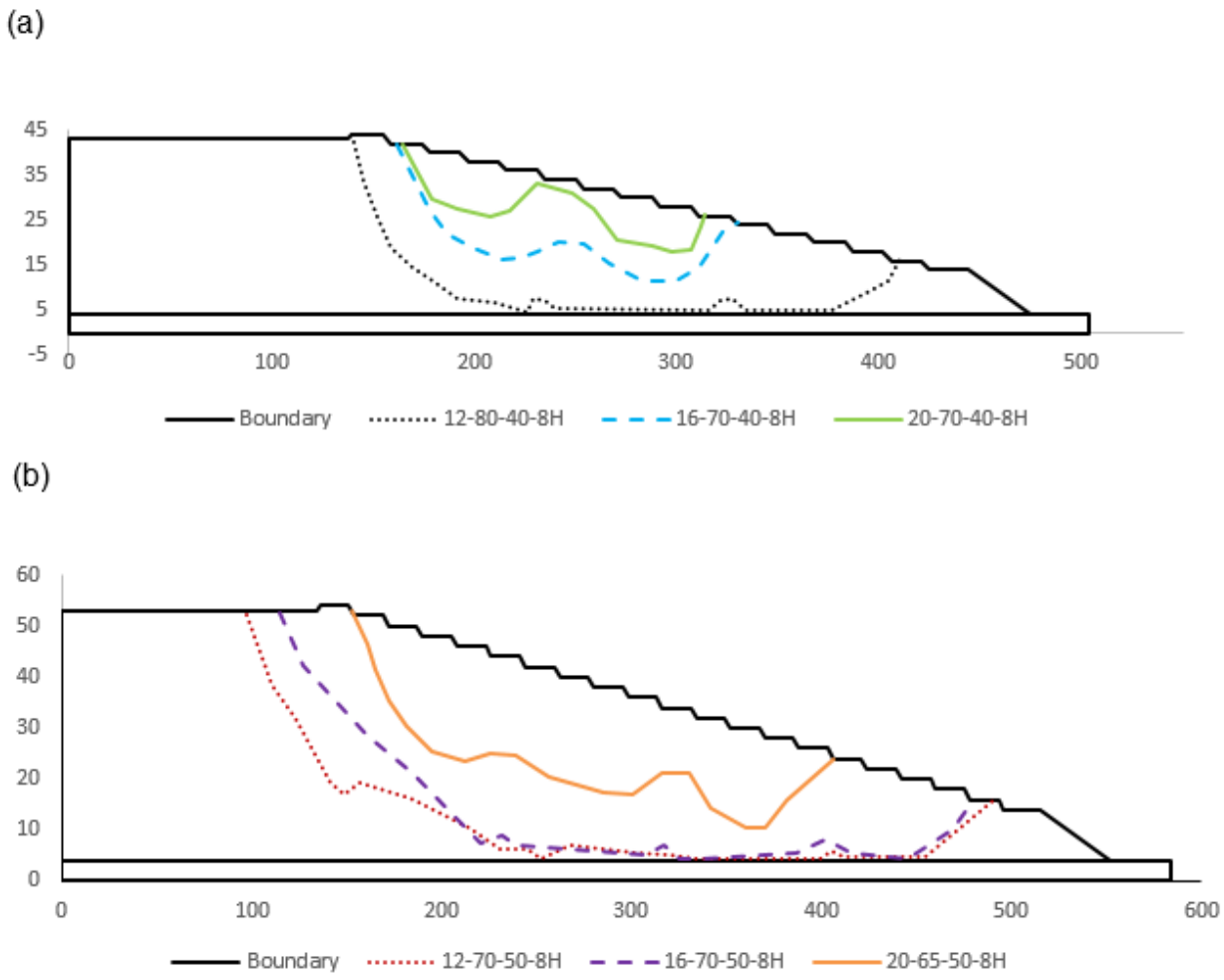

Figure 3.10: Volume of the simulated critically displaced tailings within the reinforced impoundments at the end of the ground motion, for a slope of 8H:1V, and a height (a) of 40 m, and (b) 50 m. The WRI and dikes configurations are given in the inserted captions (see text for details)

Figure 3.11 shows the variation of the SAR_x versus spacing-volume index W_{vs} for various configurations of WRI with impoundment heights of 20 m, 30 m, 40 m, and 50 m, for a downstream slope of 8H:1V. Simulations results indicate that the value of the maximum horizontal displacement increases as the thickness of the tailings increases. This is due to the fact that as the thickness increases, the volume of liquefied tailings increases proportionally. This increase results in additional earth pressure and seepage forces, which increase the level of deformation. However,

the variation of SAR_x values computed for the configurations with heights of 20 m and 30 m is relatively small and remains almost constant, due to the low horizontal displacements. However, increasing the height of the impoundment model to 50 m leads to much higher displacements, with SAR_x increasing by a factor of 6 for the model with the lesser reinforcement (i.e., lowest W_{vs}). As illustrated in Figure 3.11, the SAR_x variation trend line for models with a 50 m height with a steep slope is reduced from 30% to 7.32% with a 0.13 increase in the volume-spacing index value (W_{vs}). The variation trend line for models with a height of 40 m shows a similar pattern, with the SAR_x value decreasing from about 20% to 4% with a 0.14 increase in W_{vs} and remaining essentially constant at higher W_{vs} values. In general, the difference in SAR_x values for models with different heights with volume-spacing indexes greater than about 0.2 is less than 3%. These results further highlight how WRI may impact the response of impoundments with thicker tailings by reducing horizontal displacements. The variations of SAR_x shown in Figure 3.11 also indicate that thickness of the tailings deposit has a higher influence on the seismic response of the impoundment compared with the downstream slope (for the configurations considered here).

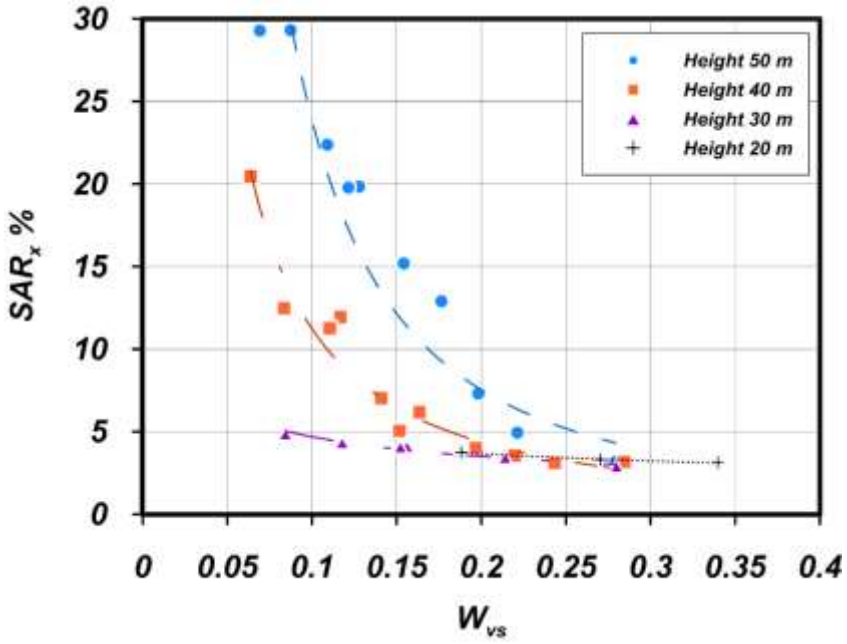

Figure 3.11: Variation of the SAR_x value as a function of volume-spacing index, W_{vs} for the reinforced impoundment models with a downstream slope of 1:8 and heights of 20 m,30 m, 40 m, and 50 m

3.4.5 Effect of PGA on the seismic response of the reinforced impoundment

The effect of the peak horizontal ground acceleration (PGA) of the selected input ground motions on the seismic response of the tailings impoundment with waste rock inclusions was also investigated through additional simulations. Figure 3.12 shows the variation trend of the *CDV* versus W_{vs} for the E_2-Loma, E_3-Loma, and E_4-Loma (see Table 3.3) ground motions. Simulation results indicated that the maximum horizontal displacement of all the models with different configurations of the waste rock inclusion under the E_1-Loma earthquake is less than 100 cm at the end of the motion, and therefore *CDV* is always zero for E_1-Loma.

As expected, for the three levels of the PGA, the value of *CDV* tends to decrease when the volume of waste rock inclusions in the impoundment increases. However, when the volume of inclusions is relatively small (i.e., lower values of W_{vs}), *CDV* does not vary much between the stronger ground motions E_3-Loma and E_4-Loma because the impoundment sustains large displacements indicative of a general failure.

The variation of the SAR_x as a function of the volume spacing index, W_{vs} for four levels of the PGA is presented in Figure 3.13. The value of SAR_x is relatively constant for different WRI configurations under the smallest ground motion, with PGA of 1.21 m/s^2. The results indicate that the level of deformation is low, and that the impoundment would remain stable. The variation of the SAR_x under the E_2-Loma earthquake shows that an increase in the PGA level, from 1.21 m/s^2 to 2.05 m/s^2, leads to a major increase in the horizontal displacement of the impoundments, especially for the smallest volume of waste rock inclusions. By further increasing the PGA level from 2.05 m/s^2 to 3.04 m/s^2, the SAR_x increases by factor of 2 for the model with the lowest value of W_{vs}. The values of the SAR_x of the models with low volume of the waste rock inclusions under the E_3-Loma and E_4-Loma are much closer to each other, compared with the two other ground motions. For these more severe ground motions, the larger waste rock inclusions seem to be providing the greatest improvement of seismic stability, as the normalized displacement decreases more significantly with an increasing volume of inclusions.

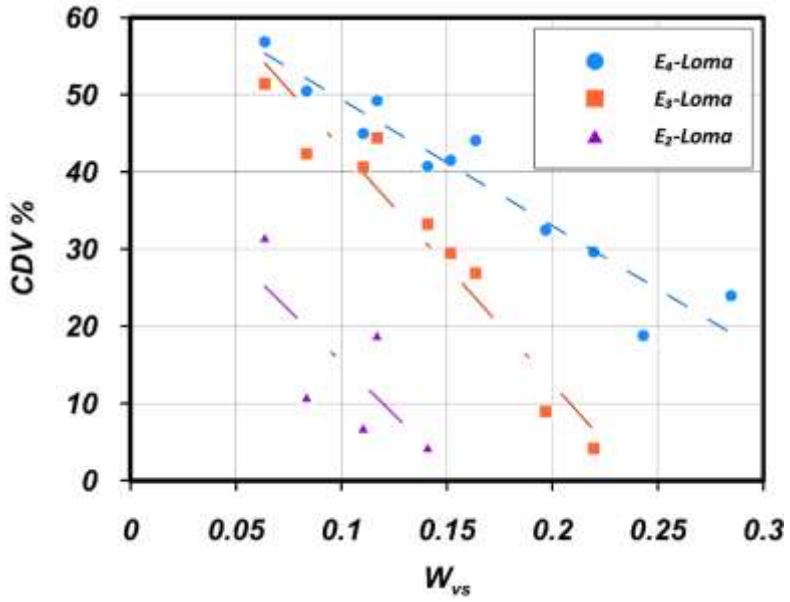

Figure 3.12: Variation of the CDV% as a function of the volume-spacing index, W_{vs} for the ground motions of E_2-Loma, E_3-Loma, and E_4-Loma with different PGA levels (see details in Table 3.3)

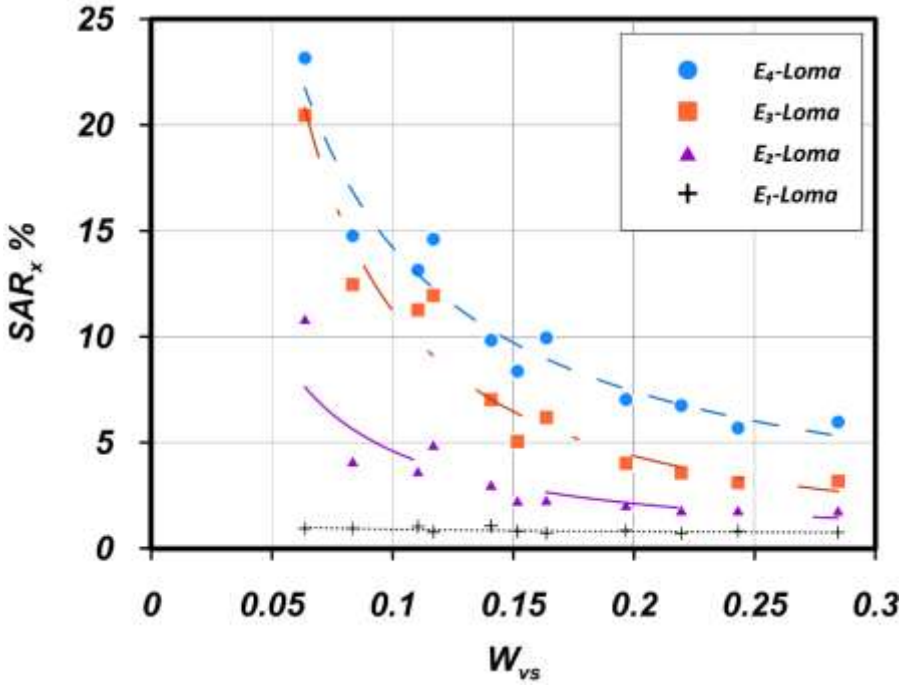

Figure 3.13: Variation of the (SAR_x) versus volume- spacing index, W_{vs} for different ground motions

3.5 Discussion

The seismic behavior of tailings impoundments with and without waste rock inclusions was simulated using FLAC. The results presented above show the effects of the downstream slope, height of the impoundment, and earthquake loading conditions on the seismic stability, based on two performance indicators: the (normalized) critically displaced volume (*CDV*) of tailings and normalized horizontal displacement of the downstream slope (SAR_x). It should be noted that the analysis of the performance indicators is only applicable to reinforced models, as many simulations of unreinforced models were stopped during the ground motion due to high deformation. However, in seismic regions, unreinforced impoundments built with the upstream method should not be used.

The consistency of the results and the generated trend lines obtained from the various simulations for the two indicators indicate that the *CDV* and SAR_x can be used to quantify the effect of each parameter. However, the use of *CDV* is restricted to models with a horizontal displacement of at least 100 centimeters, so this excludes some of the simulated cases. This is the case for example for the models with external slope of 8H:1V and height of 20 m, or the reinforced models under the E_1-Loma earthquake where the horizontal displacement is less than 1 m at the end of the ground motions; in such instances, SAR_x is the only indicator used here to evaluate the seismic response of the models. Additional indicators are investigated as part of ongoing research to compare the response of models with smaller displacements (and shear strains).

Given the novelty of the co-disposal method, design guidelines and prediction equations for the optimal configuration of waste rock inclusions in tailings impoundments subjected to seismic loading are required so this promising technology becomes more widely used in practice (Aubertin et al. 2021). The relationships presented above can be useful in engineering practice to assess the seismic stability of tailings impoundments in a deterministic or probabilistic framework. Additional work is underway to assess and quantify the response of impoundments under a variety of ground motions reflecting various degrees of seismic loading (Contreras et al., 2020; Zafarani et al., 2021).

In addition to the effect of seismic loading, the impact of the material property must also be investigated, to be addressed in the design guidelines. The value of density index for the tailings (I_d = 60%) used in the simulations presented here is higher than the values reported for different

sites, which typically vary between 40% and 70% (e.g., Vick, 1990; Aubertin et al., 2002, 2011; James 2009; Poncelet 2012; Contreras 2013, 2021; Boudrias 2018; Essayad and Aubertin 2021). Evaluating the effect of tailings with lower density indexes on the seismic response of reinforced and unreinforced models is thus also part of ongoing research.

Finally, plane strain simulations were used, but the tailings impoundments are 3D structures. The performance of available constitutive models in 3D at the start of the project were not yet satisfying, and a 2D analysis of a representative cross section of the impoundment was considered a good approximation. However, future work will include 3D modeling of the seismic behaviour of the tailings impoundments to study how it would differ from 2D analysis.

3.6 Conclusion

The seismic behavior of tailings impoundments, with and without waste rock inclusions, has been evaluated based on dynamic numerical simulations performed with FLAC (Version 8.00, Itasca, 2016). The linear elastic perfectly plastic Mohr-Coulomb model is used to analyze the static loading conditions for all the material zones in the numerical models. The constitutive models of the different zones are changed for the dynamic analysis phase to better simulate the seismic response of the materials. The Mohr-Coulomb elasto-plastic model with the hysteretic Sigmoidal model-sig3 option is used to simulate the seismic behavior of waste rock inclusions, dikes (including starter dike), and boundary structural element added to laterally confine the impoundment models. The PM4Sand model (Boulanger and Ziotopoulou,2017) is used to simulate the dynamic behavior of the tailings.

The effects of the downstream slope, height of the impoundment, and PGA level of the ground motion on the overall response and seismic stability were investigated, considering four downstream slopes (7H:1V, 8H:1V, 10H:1V, and 12H:1V), four heights of the tailings impoundment (20 m, 30 m, 40 m, and 50 m), and four levels of PGAs (1.21 m/s^2, 2.04 m/s^2, 3.04 m/s^2, and 4.87 m/s$^{2)}$. The seismic response of the impoundments is evaluated with two performance indicators: the (normalized) critically displaced volume of tailings (*CDV*) and the average (normalized) horizontal displacement of the downstream slope (*SARx*).

Results of the unreinforced impoundments with four inclinations of the downstream slope show that a significant volume of tailings is displaced critically during the E_3-Loma ground motion. The crest zone of the simulated impoundments becomes unstable, indicating that the ground motion could cause the failure of unreinforced impoundments. Adding reinforcement (i.e., WRI) improves the seismic response of the models significantly. For instance, only 35% of the reinforced impoundment with slope of 7H:1V is displaced critically at the end of the motion compared to 75% for the unreinforced case (without inclusion). Results also indicate that an increase in the size (volume) of WRIs leads to a decrease in the value of normalized horizontal displacement of downstream slope (i.e., SAR_x), with a more significant impact for the steeper slopes (8H:1V and 7H:1V).

Results of the models with different heights indicate that, as expected, higher (thicker) impoundments induce larger volumes of critically displaced tailings. For example, the critically displaced volume for the 40 m high models occurs entirely under the downstream slope, while for most configurations with a height of 50 m the critically displaced volume extends beyond the downstream zone. Increasing the volume of WRI in the impoundments decreases the *CDV*. This beneficial effect however appears less pronounced for impoundments with a height of 50 m, due to higher excess pore water pressure ratios and larger deformations.

The seismic response of reinforced impoundments under the four levels of PGA shows that the maximum horizontal displacement of all configurations of the waste rock inclusion under the lower ground motion (with a PGA of 1.21 m/s^2 , E_1-Loma) is less than 100 cm at the end of the motion; as the impoundment is deemed stable, the effect of waste rock inclusion configuration is limited. For the three other levels of PGA, *CDV* decreases when the volume of waste rock inclusions in the impoundment increases. The variation of the SAR_x versus W_{vs} shows that an increase in the PGA level from 1.21 m/s^2 to 2.05 m/s^2 raises the horizontal displacement for the impoundments with a low volume of the waste rock inclusions. The effect of WRIs on the improvement of seismic stability is even more pronounced for larger PGA levels of 3.04 m/s^2 and 4.87 m/s^2; as shown by a value of SARx that decreases significantly with an increasing volume of inclusions.

The results and analysis presented here can be very useful to assess the optimal configuration of WRI and ensure the stability of tailings impoundments constructed with upstream dikes.

3.7 Acknowledgements

The authors acknowledge the financial support from NSERC and from the industrial partners of the Research Institute on Mines and the Environment (RIME UQAT-Polytechnique; http://rime-irme.ca/en).

3.8 References

Ancheta, T. D., Darragh, R. B., Stewart, J. P., Seyhan, E., Silva, W. J., Chiou, B. S., and Donahue, J. L. 2013. Peer NGA-West2 database.

Armstrong, R. J., Boulanger, R. W., and Beaty, M. H. 2013. Liquefaction effects on piled bridge abutments: Centrifuge tests and numerical analyses. Journal of geotechnical and geoenvironmental engineering, 139(3), 433-443.

Aubertin, M., Mbonimpa, M., Jolette., D., Bussière, B., Chapuis, R.P., James, M., Riffon, O. 2002. Stabilité géotechnique des ouvrages de retenue pour les résidus miniers: problèmes persistants et méthodes de contrôle. Défis and Perspectives : Symposium sur l'environnement et les mines, Rouyn-Noranda, Développement Économique Canada/Ministère des Ressources Naturelles du Québec/CIM. Comptes-Rendus sur CD-ROM.

Aubertin, M., Bussière, B., James, M., Martin, V., Pépin, N., Mbonimpa, M., and Chapuis, R.P. 2011. Vers une mise à jour des critères de stabilité géotechnique pour la conception des ouvrages de retenue de résidus miniers. Symposium sur les Mines et l'Environnement, Rouyn-Noranda, Québec, 6-9 Novembre 2011

Aubertin, M., James, M., Maknoon, M., and Bussière, B. 2013. Recommandations pour améliorer le comportement hydrogéotechnique des haldes à stériles. GeoMontreal 2013-Geosciences for Sustainability, 66th CGS Conference, Montreal, QC, 8 p.

Aubertin, M., Bussière, B., Pabst, T., James, M., Mbonimpa, M., 2016. Review of reclamation techniques for acid generating mine wastes upon closure of disposal sites. Conference Geo-Chicago pp. 343-358. 10.1061/9780784480137.034.

Aubertin, M., Jahanbakhshzadeh, A., and Yniesta, S. 2019. The effect of waste rock inclusions on the seismic stability of a tailings impoundment. Proceedings of 7th International Conference on Earthquake Geotechnical Engineering.

Aubertin, M., Jahanbakshzadeh, A., Saleh-Mbemba, F., Yniesta, S. and Pednault, C. 2021. General guidelines for the design and construction of waste rock inclusions in tailings impoundment. Paper presented at the 74th Canadian Geotechnical Conference (Geo Niagara 2021), Niagara Falls, Ontario.

Blight, G. E. 2009. Geotechnical engineering for mine waste storage facilities. CRC Press.

Boudrias, G. 2018. Évaluation numérique et expérimentale du drainage et de la consolidation de résidus miniers à proximité d'une inclusion de roches stériles. Master thesis, Ecole Polytechnique de Montreal.

Boulanger, R. W., and Ziotopoulou, K. 2017. PM4Sand (Version 3): A sand plasticity model for earthquake engineering applications. Center for Geotechnical Modeling Report No. UCD/CGM-15/01, Department of Civil and Environmental Engineering, University of California, Davis, Calif.

Bussière, B. 2007. Hydro-Geotechnical properties of hard rock tailings from metal mines and emerging geo-environmental disposal approaches. Canadian Geotechnical Journal, 44(9): 1019-1052

Bussière, B., and Aubertin, M. 1999. Clean tailings as cover material for preventing acid mine drainage: an in situ experiment. In Proceedings of Conference Mining and the Environment II, September 13–17, Sudbury, Canada, (vol. 1, p. pp 19–28).

Castillo, J., Hallman, D., Byrne, P., and Parra, D. 2006. Non-linear dynamic analysis of heap leach pad under high phreatic levels. In Proceedings of FLAC and Numerical Modeling and Geomechanics, Madrid, Spain, 29-31 May 2006. Itasca Consulting Group, Inc., Minneapolis MN, pp. 187-194.

Contreras Romero, C. A. 2013. Comportement dynamique du sol pulvérulent « résidus miniers ». M.Sc., thesis, Department of Civil, Geological, and Mining Engineering, Ecole Polytechnique de Montreal, Montreal, QC.

Contreras Romero, C. A., Yniesta, S., and Aubertin, M. 2020. Seismic and post-seismic stability of tailings impoundments, considering the effect of reinforcement inclusions. Proc. 73rd Canadian Geotechnical Conference (GEOVirtual 2020).

Contreras Romero, C. A., Yniesta, S., Jahanbakhshzadeh, A., and Aubertin, M. 2021. Calibration of the PM4Sand Model for Hard-Rock Mine Tailings Based on Laboratory and Field Tests. Submitted to the Canadian Geotechnical Journal.

Dafalias, Y. F., and Manzari, M. T. 2004. Simple Plasticity Sand Model Accounting for Fabric Change Effects. Journal of Engineering Mechanics, Vol. 130, No. 6, pp 622-634.

Duncan J.M., and Bursey A. 2013. Soil modulus correlations. In Foundation Engineering in the Face of Uncertainty: Honoring Fred H. Kulhawy, 321-336. ASCE.

Essayad, K. 2015. Development of experimental protocols for the characterization of saturated and unsaturated tailings consolidation from columns compression tests (text in French), Master thesis, Ecole Polytechnique de Montreal.

Essayad, K., Pabst, T., Aubertin, M. and Chapuis, R.P. 2018. An experimental study of the movement of tailings through waste rock inclusions. Paper presented at the 71st Canadian Geotechnical Conference (GeoEdmonton 2018), Edmonton, Alberta.

Essayad, K, and Aubertin, M. 2021. Consolidation of hard rock tailings under positive and negative pore-water pressures: Testing procedures and experimental results. Canadian Geotechnical Journal, 58(1), 49-65.

Falaknaz, N., Aubertin, M., and Li, L. 2015a. Evaluation of the stress state in two adjacent backfilled stopes within an elastoplastic rock mass. Geotech Geol Eng. doi:10.1007/s10706- 015-9868-6

Falaknaz, N., Aubertin, M., and Li, L. 2015b. Numerical investigation of the geomechanical response of adjacent backfilled stopes. Can Geotech J 52(10):1507–1525

Ferdosi, B. 2015. A numerical investigation of the seismic response of tailings impoundments reinforced with waste rock inclusions. Ph.D. Thesis, Ecole Polytechnique de Montreal.

Ferdosi, B., James, M., and Aubertin, M. 2015. Effect of waste rock inclusions on the seismic stability of an upstream raised tailings impoundment: a numerical investigation. Canadian Geotechnical Journal, 52(12): 1930-1944.

Gens, A., and Alonso, E. E. 2006. Aznalco'llar Dam Failure. Part 2: Stability Conditions and Failure Mechanism. Gèotechnique 56, No. 3, 185-201

Goodman, R. E. 1989. Introduction to Rock Mechanics. John Wiley and Sons Inc.

Grimard, L.P. 2018. Une étude en laboratoire sur la réponse des résidus miniers aux charges compressives non drainées et aux pertes de confinement avec caractérisation par vitesse des ondes de cisaillement. (Mémoire de maîtrise, École Polytechnique de Montreal, QC).

Grimard, L. P., Karray, M., James, M., and Aubertin, M. 2021. Consolidation characteristics of hydraulically deposited tailings obtained from shear wave velocity (V s) measurements in triaxial and oedometric cells with piezoelectric ring-actuator technique (P-RAT). Canadian Geotechnical Journal, 58(2), 281-294.

Holtz, R. D., Kovacs, W. D., and Sheahan, T. C. 2010. An introduction to geotechnical engineering (second editione éd.): Pearson.

Itasca Consulting Group, Inc. (Itasca). 2016. FLAC – Fast Lagrangian Analysis of Continua. Version 8.00. [computer software and user manual]. Minneapolis MN: Itasca Consulting Group, Inc.

Jahanbakhshzadeh, A., Aubertin, M., Yniesta, S. and Zafarani, A. 2019. On the seismic response of tailings dikes constructed with the upstream and center-line methods. Paper presented at the 72nd Canadian Geotechnical Conference (GEO 2019), St. John's.

James, M. 2009. The use of waste rock inclusions to control the effect of liquefaction in tailings impoundments. Ph.D. Thesis, Department of Civil, Geological, and Mining Engineering, Ecole Polytechnique de Montreal, Montreal, QC.

James, M., and Aubertin, M. 2009. The use of waste rock inclusions in tailings impoundments to improve geotechnical and environmental performance. In Proceedings, Tailings and Mine Waste 2009, Banff, Alta. pp. 233–245.

James, M., and Aubertin, M. 2010. On the dynamic response of tailings and the stability of tailings impoundments for hard rock mines. Geotechnical News, 23(3), 39-43.

James, M., and Aubertin, M. 2012. The use of waste rock inclusions to improve the seismic stability of tailings impoundments. GeoCongress 2012, Okland, 22-25 March 2012. American Society of Civil Engineers, pp. 4166-4175.

James, M., Aubertin, M., and Bussière, B. 2013. On the use of waste rock inclusions to improve the performance of tailings impoundments. 18th International Conference on Soil Mechanics and Geotechnical Engineering, Paris, France, pp. 735-738.

James, M., Aubertin, M., Bussière, B., Pednault, C., Pépin, N., and Limoges, M. 2017. A research project on the use of waste rock inclusions to improve the performance of tailings impoundments. Geo Ottawa, Ottawa, ON. p. 8.

Jibson, R., W. 2011. Methods for assessing the stability of slopes during earthquakes-A retrospective. Engineering Geology 122 (2011) 43–50

Kishi, N., Nomachi, S.G., Matsuoka, K. G., Kida, T. 1987. Earthquake engineering. Japan society of civil engineering, proceeding of JSCE, No. 386/ I- 8, Vol. 4, No. 2, pp 259 - 267

Kuhlemeyer, R. L., and Lysmer, J. 1973. Finite element method accuracy for wave propagation problems. Journal of Soil Mechanics and Foundations Division, 99 (Tech Report).

L-Bolduc, F. 2012. Étude expérimentale et numérique de la consolidation des résidus et des effets d'inclusions drainantes. Mémoire de maîtrise, École Polytechnique de Montréal.

L-Bolduc, F., and Aubertin, M. 2014. A numerical investigation of the influence of waste rock inclusions on tailings consolidation, Canadian Geotechnical Journal, 51(9): 1021-1032.

Leps, T. M. 1970. Review of shearing strength of rockfill. Journal of the Soil Mechanics and Foundations Division, 96(4), 1159-1170.

Maknoon, M. 2016. Slopes stability analyses of waste rock piles under unsaturated conditions following large precipitations. Ph.D. Thesis. Ecole Polytechnique de Montreal.

Manzari, M. T., and Dafalias, Y. 1997. A Critical State Two-Surface Plasticity Model for Sands. Geotechnique, Vol. 47, No. 2, pp 255-272.

Martin, V., and Aubertin, M. 2019. An assessment of hydrogeological properties of waste rock using infiltration tests and numerical simulations. Paper presented at the 72nd Canadian Geotechnical Conference (GEO 2019), St. John's.

Mbonimpa, M., Aubertin, M., Chapuis, R. P., and Bussiere, B. 2002. Practical pedotransfer functions for estimating the saturated hydraulic conductivity. Geotechnical and Geological Engineering, 20(3): 235-259.

Meisheng, F., and Laigui, W. 2011. A tailings dam dynamic stability study based on numerical simulation. In 2011 International Conference on Consumer Electronics, Communications and Networks (CECNet) (pp. 1002-1005). IEEE.

Moriwaki, Y., Tan, P. and Ji, F. 1998. Seismic Deformation Analysis of the Upper San Fernando Dam Under the 1971 San Fernando Earthquake. Proceedings of Geotechnical Earthquake Engineering III, Seattle WA, USA (pp. 854-865). New York: ASCE.

Pacific Earthquake Engineering Research Center (PEER), 2019. Earthquake and station details. Consulted on September 2019. https://ngawest2.berkeley.edu/

Piao, R. P., Rippe, A. H., Myers, B. and Lane, K. W. 2006. Earth Dam Liquefaction and Deformation Analysis using Numerical Modeling. Proceedings of GeoCongress 2006: Geotechnical Engineering in the Information Age, Atlanta GA, USA (on CD ROM). Reston VA: ASCE.

Pépin, N., Aubertin, M., James, M. 2012. Seismic Table Investigation of the Effect of Inclusions on the Cyclic Behavior of Tailings. Canadian Geotechnical Journal, 49(4): 416-426.

Peregoedova, A. 2012. Étude expérimentale des propriétés hydrogéologiques des roches stériles à une échelle intermédiaire de laboratoire. M.Sc.A. thesis, Département des génies civil, géologique et des mines, École Polytechnique de Montréal, QC.

Peregoedova, A., Aubertin, M., and Bussière, B. 2013. Laboratory measurement and prediction of the saturated hydraulic conductivity of mine waste rock. In GeoMontreal 2013: Geosciences for Sustainability, 66th CGS Conference, Montréal, QC.

Poncelet, N. 2012. Élaboration et implément d'un protocole de laboratoire pour l'étude du potential de liquéfaction de résidus miniers. M.Sc. Thesis unpublished. Ecole Polytechnique Montréal PQ, Canada.

Rayleigh, J. W. S. and Lindsay, R. B. 1945. The theory of sound, Dover Publications, New York.

Roche, C., Thygesen, K., and Baker, E. (Eds.). 2017. Mine Tailings Storage: Safety Is No Accident, A UNEP Rapid Response Assessment. United Nations Environment Programme and GRID-Arendal, Nairobi and Arendal.

Rollins, K. M., Evans, M. D., Diehl, N. B., and III, W. D. D. 1998. Shear modulus and damping relationships for gravels. Journal of Geotechnical and Geoenvironmental Engineering, 124(5), 396-405.

Salam, S., Xiao, M., Khosravifar, A., and Ziotopoulou, K. 2021. Seismic stability of coal tailings dams with spatially variable and liquefiable coal tailings using pore pressure plasticity models. Computers and Geotechnics, 132, 104017.

Saleh Mbemba, F. 2016. Évaluation du drainage, de la consolidation et de la dessiccation des résidus miniers fins en présence d'inclusions drainantes. Thèse de doctorat, Département civil, géologie et Mine, Université de Polytechnique de Montréal, Montréal, QC.

Seed, H. B., and Idriss, I. M. 1982. Ground Motions and Soil Liquefaction During Earthquakes. Berkeley CA: Earthquake Engineering Research Institute.

Seed, H.B., Wong, R.T., Idriss, I.M. and Tokimatsu, K. 1984. Dynamic moduli and damping factors for dynamic analysis of cohesionless soils. Report No. UCB/EERC-84/14, Earthquake Engineering Research Center, Berkeley, CA.

Seid-Karbasi, M., and Byrne, P. M. 2004. Embankment dams and earthquakes. Hydropower and Dams, 2: 96-102.

Sherard, J.L., Woodward, R. T., Gizienski, S. F., and Clevenger, W. A. 1963. Earth and Earth-rock Dams. New York: John Wiley and Sons, Inc.

Vaid, Y. P., Byrne, P. M., and Hughes, J. M. C .1981. Dilation Angle and Liquefaction Potential. Journal of the Geotechnical Division, ASCE, Vol. 107, No. GT7.

Wyllie, D., C., and Mah, C., W. 2004. Rock Slope Engineering. London and New York: Spon Press.

Yang, P., Li, L. and Aubertin, M. 2018. Theoretical and Numerical Analyses of Earth Pressure Coefficient along the Centerline of Vertical Openings with Granular Fills. Applied Sciences, 8(10), 11 pages.

Zafarani, A., Yniesta, S., Aubertin, M. 2020. Effect of height and downstream slope on the seismic behavior of tailings impoundments reinforced with waste rock inclusions. Proc. 73rd Canadian Geotechnical Conference (GEOVirtual 2020). p. 8.

Zafarani, A., Yniesta, S., Aubertin, M. 2021. On the selection of ground motion intensity measures to evaluate the seismic stability of tailings impoundments. Paper presented at the 74th Canadian Geotechnical Conference (Geo Niagara 2021), Niagara Falls, Ontario.

3.9 Appendix A. The combinations of width, spacing, height, slope, and ground motion considered in this study

Table A_1: Waste rock inclusions configurations

Simulation Identification*	Impoundment height(m)	Downstream slope (xH:1V)	Width of the WRI (m)	Space between WRI (m)	Number of WRI
0-0-40-8H-E_1, E_2, E_3, and E_4-Loma	40	8	Without WRI		NA
12-55-40-8H- E_1, E_2, E_3, and E4-Loma	40	8	12	55	4
12-80-40-8H- E_1, E_2, E_3, and E4-Loma	40	8	12	80	3
12-120-40-8H- E_1, E_2, E_3, and E_4 -Loma	40	8	12	120	2
16-50-40-8H- E_1, E_2, E_3, and E_4-Loma	40	8	16	50	4
16-70-40-8H- E_1, E_2, E_3, and E_4-Loma	40	8	16	70	3
16-110-40-8H- E_1, E_2, E_3, and E_4-Loma	40	8	16	110	2
20-50-40-8H- E_1, E_2, E_3, and E_4-Loma	40	8	20	50	4
20-70-40-8H- E_1, E_2, E_3, and E_4-Loma	40	8	20	70	3
20-115-40-8H- E_1, E_2, E_3, and E_4-Loma	40	8	20	115	2
25-60-40-8H- E_1, E_2, E_3, and E_4-Loma	40	8	25	60	3
25-110-40-8H- E_1, E_2, E_3, and E_4-Loma	40	8	25	110	2
0-0-40-7H-E_3-Loma	40	7	Without WRI		NA
12-65-40-7H-E_3-Loma	40	7	12	65	3
16-60-40-7H-E_3-Loma	40	7	16	60	3

16-100-40-7H-E_3-Loma	40	7	16	100	2
20-56-40-7H-E_3-Loma	40	7	20	56	3
20-100-40-7H-E_3-Loma	40	7	20	100	2
25-100-40-7H-E_3-Loma	40	7	25	100	2
0-0-40-10H-E_3-Loma	40	10	Without WRI		NA
12-70-40-10H-E_3-Loma	40	10	12	70	4
12-90-40-10H-E_3-Loma	40	10	12	90	3
12-140-40-10H-E_3-Loma	40	10	12	140	2
16-60-40-10H-E_3-Loma	40	10	16	60	4
16-90-40-10H-E_3-Loma	40	10	16	90	3
16-140-40-10H-E_3-Loma	40	10	16	140	2
20-60-40-10H-E_3-Loma	40	10	20	60	4
20-90-40-10H-E_3-Loma	40	10	20	90	3
20-140-40-10H-E_3-Loma	40	10	20	140	2
25-80-40-10H-E_3-Loma	40	10	25	80	3
25-130-40-10H-E_3-Loma	40	10	25	130	2
0-0-40-12H-E_3-Loma	40	12	Without WRI		NA
12-90-40-12H-E_3-Loma	40	12	12	90	4
12-90-40-12H-E_3-Loma	40	12	12	90	3
16-86-40-12H-E_3-Loma	40	12	16	86	4
16-121-40-12H-E_3-Loma	40	12	16	121	3

16-186-40-12H-E_3-Loma	40	12	16	186	2
20-82-40-12H-E_3-Loma	40	12	20	82	4
20-117-40-12H-E_3-Loma	40	12	20	117	3
20-182-40-12H-E_3-Loma	40	12	20	182	2
25-110-40-12H-E_3-Loma	40	12	25	110	3
25-150-40-12H-E_3-Loma	40	12	25	150	2
0-0-20-8H-E_3-Loma	20	8	Without WRI		NA
12-50-20-8H-E_3-Loma	20	8	12	50	2
16-37-20-8H-E_3-Loma	20	8	16	37	2
20-33-20-8H-E_3-Loma	20	8	20	33	2
0-0-30-8H-E_3-Loma	30	8	Without WRI		NA
12-55-30-8H-E_3-Loma	30	8	12	55	3
12-85-30-8H-E_3-Loma	30	8	12	85	2
16-50-30-8H-E_3-Loma	30	8	16	50	3
16-85-30-8H-E_3-Loma	30	8	16	85	2
20-50-30-8H-E_3-Loma	30	8	20	50	3
20-80-30-8H-E_3-Loma	30	8	20	80	2
0-0-50-8H-E_3-Loma	50	8	Without WRI		NA
12-70-50-8H-E_3-Loma	50	8	12	70	4
16-70-50-8H-E_3-Loma	50	8	16	70	4
16-95-50-8H-E_3-Loma	50	8	16	95	3

16-155-50-8H-E_3-Loma	50	8	16	155	2
20-65-50-8H-E_3-Loma	50	8	20	65	4
20-95-50-8H-E_3-Loma	50	8	20	95	3
20-150-50-8H-E_3-Loma	50	8	20	150	2
25-60-50-8H-E_3-Loma	50	8	25	60	4
25-90-50-8H-E_3-Loma	50	8	25	90	3
25-140-50-8H-E_3-Loma	50	8	25	140	2

Note: The first number represents the inclusion width (m), the second number is edge-to-edge spacing (m), the third number is the impoundments height (m), the fourth number is the downstream slope(xH:1V), and the fifth is the ground motion based on the Table 3.3

CHAPTER 4 ARTICLE 2: COMPARISON AND SELECTION OF GROUND MOTION INTENSITY MEASURES TO EVALUATE THE SEISMIC RESPONSE OF TAILINGS IMPOUNDMENTS

Ali Reza Zafarani[1*], Samuel Yniesta[1] and Michel Aubertin[1]

[1]Department of Civil, Geological and Mining Engineering, Polytechnique Montréal, C.P. 6079, Centre-ville, Montréal, QC H3C 3A7, Canada.

*Corresponding Author; email: ali-reza.zafarani@polymtl.ca

This article was submitted to Canadian Geotechnical Journal in March 2022

Abstract

Ground motions are commonly defined using a combination of peak and spectral accelerations, but other Intensity Measures *(IMs*) can be used to characterize the intensity of motions. In the present study, the results of a numerical parametric investigation are used to assess the impact of different *IM*s on the seismic response of tailings impoundments with and without waste rock inclusions reinforcement. The simulation results are used to investigate the efficacy of the *IM*s to provide relevant performance metrics in the evaluation of the seismic behavior of impoundments. Regression analyses are performed to assess predictability of the *IM*s impact based on the efficiency, practicality, and proficiency criteria. The statistical regression analyses show that velocity-related *IM*s (such as velocity spectrum intensity, *VSI,* and peak ground velocity, *PGV*) appear to be the most efficient, practical and proficient scalar (single) intensity measures. However, some modelling results show relatively low efficiency. This indicates that a vector-valued *IM*, which combines two distinct measures, would be preferable to enhance efficiency of the models. The combination of *VSI* and *PGA* yields the optimal efficiency for the conditions considered here and is therefore recommended to define the ground motion *IMs* for performance assessment models aimed at tailings impoundment analysis.

Key Words: Seismic loading; Optimum intensity measures; Cyclic loading; Tailings impoundments; Waste rock inclusions; Seismic stability

4.1 Introduction

The expansion of mining operations has resulted in an increase in the number and size of tailings impoundments in Canada and around the world. Several cases of tailings impoundment failure over the last few decades suggest that both the static and seismic stability of these geotechnical structures could be improved with the appropriate tools and techniques (Davies, 2002; Aubertin et al. 2002, 2011, 2021; Azam and Li, 2010; Santamarina et al., 2019). The seismic stability of a tailings impoundment is influenced by the performance of the retention dikes, the behaviour of the retained tailings, and their interactions during and shortly after an earthquake. Dynamic loading may result in a reduction of stiffness and strength in the tailings as a consequence of the generation of excess pore water pressure, a process known as liquefaction (Holtz and Kovacs, 1981; Seed and Idriss, 1982), which may impose additional loading on the retaining dikes and cause failure (Gens and Alonso, 2006; James 2009; Ferdosi 2014).

Waste rock inclusions (WRI) can be used to increase the static and dynamic stability of tailings impoundments, owing to their higher stiffness, strength, and hydraulic conductivity in comparison to tailings (Aubertin et al. 2002, 2021). These WRI accelerate drainage and tailings consolidation, improve the tailings strength, and increase lateral resistance of the impoundment.

Previous investigations demonstrate that waste rock inclusions can greatly improve the seismic response and stability of tailings impoundments that could be unstable in the absence of reinforcement (e.g., James, 2009; Pepin et al., 2012; Ferdosi et al., 2015a; 2015b; Jahanbakhshzadeh et al., 2019; Zafarani et al., 2020, 2021; Contreras et al., 2020). The simulation results also show that the configuration of the inclusions, downstream slope, and tailings thickness all have a substantial impact on the seismic response of reinforced impoundments (Zafarani et al., 2021).

Given the relative novelty of this method, design guidelines for the optimal configuration of waste rock inclusions in tailings impoundments subjected to static and seismic loadings are required for this technology to become widely used in practice (Aubertin et al. 2021). In this regard, the seismic

response of impoundments should be assessed and quantified under a variety of ground motions reflecting the anticipated seismic loading characteristics. Different intensity measurements (*IM*s) can be used in performance-based earthquake analyses to define the seismic loading and related seismic demand.

This paper presents the results of a dynamic numerical parametric investigation that evaluates the seismic stability of tailings impoundments, including cases with WRI reinforcement, using 13 potential *IM*s for ten ground motion recordings from the NGA-West2 (Ancheta et al. 2013) and NGA-East (Goulet et al. 2014) databases. The numerical results are used to develop a seismic performance model which relates the downstream slope displacement with the best correlated parameters characterizing the intensity of the ground motions. Linear regression analyses are employed to correlate the downstream slope displacement with various intensity measures (*IM*s). Optimum scalar and vector *IM*s are determined based on efficiency, proficiency and practicality criteria. The corresponding relationships can be used in engineering practice to assess the seismic response and stability of tailings impoundments in a deterministic or probabilistic framework.

4.2 Numerical modeling

The seismic behaviour of tailings impoundments is simulated using the finite-volume software FLAC (Fast Lagrangian Analysis of Continua) Version 8.00 (Itasca, 2016). There are two phases in numerical modelling: a static and a dynamic analysis. The static analysis defines the initial stresses, strains, and pore water pressures under mechanical and fluid equilibrium. The static phase stresses are employed as initial conditions for the dynamic analysis. Before applying an earthquake loading (from the recording) at the base of the model, the constitutive models of the various materials are changed to better capture their cyclic behaviour under seismic loading, as described in the following sections.

4.2.1 Model geometry

The upstream-raised design approach is considered in this study aimed at analyzing the response of a typical tailings impoundment, with and without WRI, and to assess the effect of seismic loading level on its stability. The modelled impoundment investigated here is 40 metres high with a downstream slope of 8H:1V. The starter dike and dike raises are made of waste rock. The

impoundment lies on a 5-m-thick layer of hard bedrock. Each dike raise is 2 metres high, with a 15-meter crest width and side slopes of 2H:1V. The crest width and height of the starter dike are 19 m and 10 m, respectively. The impoundment model extends up to 140 metres from the crest, based on a parametric study which indicated that the simulation results are not affected by using a wider model. The simulations use a discretized model with a basic element size of 1 m by 1 m. This mesh size ensures the accurate transmission of ground motion frequencies of up to 25 Hz (Kuhlemeyer and Lysmer ,1973). However, in the zones where higher deformations and stresses are expected (i.e., under the dikes), the mesh size is refined with smaller elements (down to 0.5 m). A parametric study, not presented here for the sake of brevity, indicated that a mesh with elements smaller than 0.5 m showed no difference in the response of the model, but increased significantly the computation time. An example of a conceptual model geometry and material zone distribution for a tailings impoundment with two 12-m wide inclusions with 120-m edge-to-edge spacing is shown in Figure 4.1. Models with various configurations of WRI have also been considered elsewhere (Zafarani et al. 2021; Zafarani, 2022).

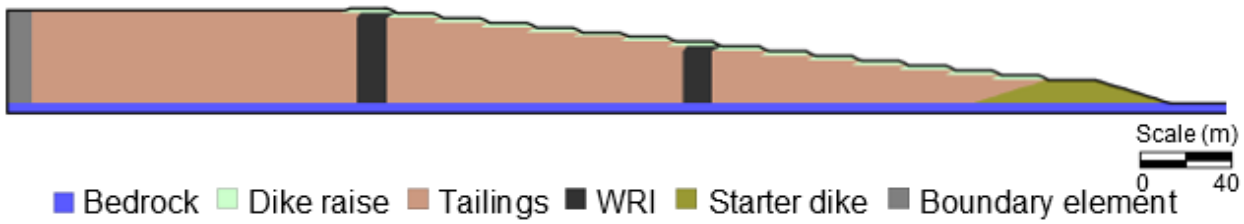

Figure 4.1: Conceptual model of a reinforced tailings impoundment with two 12-m wide inclusions with 120-m edge-to-edge spacing

4.2.2 Boundary conditions

The mechanical and fluid boundary conditions imposed to the model for the static phase of the analysis are: fixed horizontal displacements on both sides of the impoundment, fixed vertical displacements at the base, and a fixed zero pore water pressure at the tailings surface and on the dikes along the right side of the model. The phreatic surface is located at the top of the

impoundment as the water level within active tailings impoundments is frequently at or above the tailings surface. This also represents a critical case scenario for dynamic stability analysis.

The boundary conditions are updated during the dynamic analysis by adding a free field boundary on the sides of the model and applying a ground motion at the base in the form of horizontal accelerations. However, as a free field boundary condition cannot be applied directly to the PM4Sand constitutive model (Boulanger and Ziotopoulou, 2017), which is used for the tailings, the free field boundary condition on the left side of the impoundment is applied via the addition of a boundary element modeled using the elastoplastic Mohr-Coulomb constitutive model in both static and dynamic analyses. The fluid boundary conditions of the static phase are kept during the dynamic analyses.

4.2.3 Material Properties

4.2.3.1 Static loading phase

Static stress conditions are calculated using the linear elastic perfectly plastic Mohr-Coulomb constitutive model, except for the bedrock layer which was considered linearly elastic. The required input parameters are the cohesion, internal friction angle and dilatancy angle, as well as two isotropic elastic properties (for instance shear and bulk moduli). Table 4.1 lists all material properties used for the static phase.

The process of deposition, age, and height of the deposit inside the impoundments can have a significant impact on the hydro-geotechnical characteristics of tailings, such as unit weights, porosity, and hydraulic conductivity. The tailings properties adopted here are based on numerous studies conducted on hard rock mine tailings in the Abitibi region of Quebec (e.g., Bussière 2007; James 2009; Poncelet 2012; Contreras 2013; Essayad 2015; Saleh Mbemba 2016; Grimard 2018; Boudrias 2018). A k_{sat} value of 5.8×10^{-8} m/s is used for the numerical simulation of the tailings; this value was obtained from experimental measurements of similar tailing materials (Aubertin et al. 1996; Mbonimpa et al., 2002; Bussière, 2007; Essayad, 2015). The tailings average shear modulus, *G*, is calculated using in-situ shear wave velocity measurements and an approximation of in-situ density (Grimard et al., 2021). A Poisson ratio, υ, of 0.3 is used for tailings; this value is

obtained from the K_o-consistency relationship with the internal friction angle ($\upsilon = \frac{1-\sin\varphi'}{2-\sin\varphi'}$; e.g., Frederico and Elia, 2009; Duncan and Bursey, 2013; Falaknaz et al. 2015).

The dry unit weight and internal friction angle of waste rock are based on typical values reported for hard rock mines (e.g., Aubertin et al., 2013; Maknoon, 2016; Essayad et al., 2018). The shear and bulk moduli (kPa) of waste rock are defined using the following relationships provided by Seed et al. (1984) and Rollins et al. (1998) for granular materials:

$$G = 55000.(0.6.\sigma'_v)^{0.5} \quad (4.1)$$

$$K = 2.3833.G \quad (4.2)$$

where σ'_v is the effective vertical stress (kPa). Minimum values of 3.1×10^5 kPa and 7.4×10^5 kPa are considered for shear and bulk moduli, respectively (James, 2009).

The dry unit weight (γ_d = 20 kN/m^3) and porosity (n = 0.25) of the waste rock material is also based on typical average values. The saturated hydraulic conductivity, k_{sat}, of waste rock is influenced by particle size and density. The range of k_{sat} for waste rock reported in the literature extends from 10^{-9} to 10^{-1} m/s, but k_{sat} values are typically close to 10^{-3} m/s for hard rock mines (Peregoedova, 2012; Essayad et al., 2018; Martin et al. 2019); a value of 10^{-3} m/s is thus selected here for the saturated hydraulic conductivity of the waste rock material.

The starter dike has similar material properties to waste rock inclusions except for its porosity and saturated hydraulic conductivity, which are set at n = 0.2 and k_{sat} = 10^{-2} m/s, respectively.

The hydro-geotechnical properties of this foundation material, such as dry unit weight and k_{sat}, are based on values reported by Goodman (1989) and Wyllie and Mah (2004).

Dilation angle of granular material during shear is uniquely related to its relative density and confining pressure (Vaid et al., 1981), but this angle is typically considered to be constant when the Mohr-Coulomb elasto-plastic model is used. A positive dilatancy angle ($\psi > 0$) tends to increase the mean effective stress and shear strength prior to failure. Thus, it is conservative to adopt a zero dilation angle (ψ = 0) when assessing the stability of earth structures with the Mohr-Coulomb model (as is the case when considering the critical state).

Table 4.1: Material properties for the static phase simulations

Properties	Tailings	Dikes (WRI)	Starter dike	Bedrock
Constitutive model	Elasto-plastic, Mohr-Coulomb	Elasto-plastic Mohr-Coulomb	Elasto-plastic Mohr-Coulomb	Elastic
Dry unit weight, $\gamma_{dry}(\frac{kN}{m^3})$	16.5	20	20	22
Effective friction angle, $\varphi'(°)$	35	45	45	-
Effective cohesion, $c'(kPa)$	0	0	0	-
Dilation angle, $\psi(°)$	0	0	0	-
Porosity, n	0.4	0.25	0.2	0.1
Shear Moduli, G (kPa)	$113*10^3$	Varied[1]	$3.1*10^5$	$13.5*10^6$
Bulk Moduli, K (kPa)	$300*10^3$	Varied[1]	$7.4*10^5$	$29.2*10^6$
Hydraulic conductivity, $k_{sat}(m/s)$	$5.8*10^{-8}$	10^{-3}	10^{-2}	$5*10^{-8}$

[1] Equations [4.1] and [4.2]

4.2.3.2 Dynamic phase

Once the initial (static) stresses are determined, the constitutive model of the main material zones is modified to simulate the dynamic behaviour of the impoundment. Waste rock inclusions, starter dike and raised dikes, and boundary element are all modeled using the Sigmoidal model-Sig3 (Itasca, 2016). The default values for granular materials are adopted for the boundary element, while the calibrated values obtained by Ferdosi et al. (2015a) are used for the WRI and dikes. In

addition, mass and stiffness- proportional Rayleigh damping (Rayleigh and Lindsay, 1945) is employed to introduce small-strain damping. The mass-proportional and stiffness-proportional damping constants are chosen so that the target small-strain damping, ξ_{min} (i.e., 2%), is matched at the predominant frequency (f_{min}) taken as the mean frequency of the system.

The seismic behaviour of tailings is simulated using the PM4Sand model (Boulanger and Ziotopoulou, 2017). This constitutive model is a critical-state compatible, stress-ratio based, bounding surface plasticity model developed for sandy soils. Three primary and 21 secondary parameters are included in the model. The calibrated parameters of the PM4Sand model for hard-rock tailings presented in Contreras et al. (2022), based on extensive laboratory experiments and field studies, are used in the dynamic simulations. For the sake of conciseness, the calibrated parameters are not presented here; further information can be found in Contreras (2022).

4.3 Parametric study

This numerical parametric study investigates the influence of different *IM*s on the seismic behavior and stability of tailings impoundments, with and without waste rock inclusions. A total of 120 numerical simulations were conducted to assess the correlations between the *IM*s and various performance indicators such as the critically displaced volume of tailings and the normalized horizontal displacement of the downstream slope.

4.3.1 Intensity measures (IMs)

Over the last few decades, extensive research has focused on determining the optimum *IM*s for predicting structural response due to ground motions (e.g., Shome and Cornell, 1999; Baker and Cornell, 2005; Luco and Cornell, 2007; Tothong and Luco, 2007). An analysis of *IM*s is conducted here to identify the most appropriate (optimum) measures for evaluating the seismic response of tailings impoundments. Thirteen different ground motion intensity measures have been used to analyze earthquake-induced displacements, as presented in Table 4.2. The four *IM*s that only reflect the maximum amplitude of the ground motion are referred to herein as the "peak" category of *IM*s. The "compound" *IM* can be used to characterise amplitude and duration of a ground motion. The third category with five *IM*s, termed "spectrum" *IM*s, is used to describe the amplitude and

frequency of ground motion. Finally, the "integral" category includes *IM*s influenced by the three main ground motion characteristics, i.e., amplitude, frequency, and duration.

Table 4.2: Intensity Measures (IMs) considered for the numerical simulations

Type	IMs (identification, source)	Definition or formula
Peak	Peak ground acceleration, *PGA* (Kramer, 1996)	$PGA = \max \lvert a(t) \rvert$
	Peak ground velocity, *PGV* (Kramer, 1996)	$PGV = \max \lvert v(t) \rvert$
	Sustained maximum acceleration, *SMA* Sustained maximum velocity, *SMV* (Nuttli, 1979)	Third highest absolute value of acceleration/velocity in the time-history.
Compound	Ratio of *PGV* over *PGA* (Kramer, 1996)	$\frac{PGV}{PGA} = \frac{\max \lvert v_{(t)} \rvert}{\max \lvert a_{(t)} \rvert}$
Integral	Arias Intensity, *AI* (Arias, 1970)	$AI = \frac{\pi}{2g} \int_0^{tf} a^2(t) dt$
	Cumulative absolute velocity, *CAV* (Kramer, 1996)	$CAV = \int_0^{tf} \lvert a(t) \rvert dt$
	Root-mean-square acceleration, a_{rms} (Housner and Jennings, 1964)	$a_{rms} = \sqrt{\frac{1}{t_d} \int_{t_5}^{t_{95}} a^2(t) dt}$

	Root-mean-square velocity, v_{rms} (Housner and Jennings, 1964)	$v_{rms} = \sqrt{\frac{1}{t_d}\int_{t_5}^{t_{95}} v^2(t)dt}$
	Characteristic intensity, C_I (Park et al., 1985)	$C_I = {a_{rms}}^{1.5}.(t_{95} - t_5)^{0.5}$
Spectrum	Acceleration spectrum intensity, *ASI* (Housner, 1952)	$ASI = \int_{0.1}^{0.5} s_a(\xi = 5\%, T)dT$
	Velocity spectrum intensity, *VSI* (Housner, 1952)	$VSI = \int_{0.1}^{0.5} s_v(\xi = 5\%, T)dT$
	Housner's spectral intensity, H_I (Housner, 1952)	$H_I = \int_{0.1}^{2.5} S_{pv}(\xi = 5\%, T)\,dT$

Definition of symbols: $a(t)$ and $v(t)$ are acceleration and velocity time histories, in m/s^2 and m/s, respectively; t_f is duration of a ground motion in seconds; t_d is the relative duration ($t_d = t_{95} - t_5$) in seconds; t_5 and t_{95} are times at which 5% and 95% of Arias intensity of the motion are reached in seconds, respectively; T is the dominant period of response spectrum in seconds, defined as the period of maximum spectral acceleration (Rathje at al., 1998).; s_a and s_v are the acceleration and velocity spectra, in m/s^2 and m/s, respectively; S_{pv} is the pseudo velocity spectrum in m/s; and ξ is the damping ratio.

4.3.2 Input ground motions

Ten earthquake ground motions were selected to investigate the impact of seismic loading on the geotechnical response of tailings impoundments. Table 4.3 identifies the ground motions from the NGA-West2 (Ancheta et al. 2013) and NGA-East (Goulet et al. 2014) databases. Ground motions 1-6 have been amplitude-scaled to assess the impact of intensity level on horizontal displacements. The intensity of ground motion 10 (Mineral) is lower than the other motions to evaluate the effect of a less severe excitation.

Table 4.3: Input ground motion parameters (Ancheta et al. 2013; Goulet et al. 2014)

#	Earthquake	M_W	PGA (m/s^2)	AI (m/s)	F_p (Hz)	PGV (m/s)	VSI (m)	ASI (m/s)	CAV (m/s)
1	Northridge	6.69	3.23	2.04	4.55	0.35	1.6	2.9	15.35
2	Saguenay	5.9	4.38	2.05	25	0.08	0.3	1.63	12.52
3	E_1-Loma Prieta	6.93	1.21	0.19	6.5	0.06	0.24	1.18	3.25
4	E_2-Loma Prieta	6.93	2.04	0.54	6.5	0.10	0.41	1.99	5.48
5	E_3-Loma Prieta	6.93	3.04	1.20	6.5	0.15	0.61	2.95	8.15
6	E_4-Loma Prieta	6.93	4.87	3.09	6.5	0.25	0.98	4.73	13.06
7	Au Sable Forks	4.99	1.96	0.47	6.25	0.06	0.22	1.50	5.60
8	Cape Mendocino	7.01	3.68	1.71	1.79	0.09	2.5	2.95	10.62
9	San Fernando	6.61	3.13	0.7	3.13	0.17	0.66	2.71	7.60
10	Mineral	5.74	1.02	0.05	12.5	0.04	0.17	0.43	1.30

Note: M_w is the moment magnitude; and F_p is the predominant frequency of a ground motion

4.3.3 WRI configurations

The influence of waste rock inclusion configuration on the seismic response of tailings impoundments is investigated using variable width, *W* (m), and edge-to-edge spacing, *S* (m), of

waste rock inclusions. The width of WRI ranges from 12 (m) to 25 (m), while their edge-to-edge spacing ranges from 50 (m) to 120 (m). The width and spacing combinations that are considered for this parametric analysis are listed in Table 4.4. It should be noted that all models have a height of 40 m and a downstream slope of 8H:1V.

Table 4.4: Waste rock inclusion configurations in the tailings impoundment models

Simulation Identification	Width (m)	Spacing (m)	Number of WRI
0-0	Without WRI		0
12-55	12	55	4
12-80	12	80	3
12-120	12	120	2
16-50	16	50	4
16-70	16	70	3
16-110	16	110	2
20-50	20	50	4
20-70	20	70	3
20-115	20	115	2
25-60	25	60	3
25-110	25	110	2

4.4 Numerical results and analysis

4.4.1 Performance indicators

The numerical simulation results give the distribution of pore water pressures, stresses, strains and displacements. Each tailings impoundment response is also assessed here using specific indicators to facilitate the comparison between the different cases and establish relationships with the various *IMs*.

The simulated response of the various impoundment models is quantified in the following sections with two performance indicators: the critically displaced volume of tailings (*CDV*) and the normalized horizontal displacement of the downstream slope *(SAR_x)*.

4.4.1.1 Critically displaced volume of tailings

According to Jibson (2011), horizontal displacements exceeding 100 cm are likely to result in significant slope movements. Similarly to previous studies on the dynamic response of tailings impoundments (e.g., Ferdosi et al. 2015a, 2015b), the critically displaced volume (*CDV*) of tailings is defined here as the percentage of the tailings volume displaced horizontally by more than 100 cm.

4.4.1.2 Horizontal displacement of the downstream slope

To quantify the response of impoundments, the horizontal displacement at each nodal point calculated along the downstream slope of the tailings impoundment is taken at the end of ground motion. The normalized horizontal displacement at each nodal point is then determined by dividing the horizontal displacement at the end of the shaking by the initial height above the bedrock layer. The following equation, adapted from Ferdosi et al. (2015a), defines the average value of the normalized horizontal displacement of all nodal points along the downstream slope (SAR_x):

$$SAR_x = Average\left(\frac{X_{disp_i}}{H_i}\right) \tag{4.3}$$

Where X_{disp_i} is the horizontal displacement a nodal point *i* along the downstream slope at the end of the shaking, and H_i is the initial height above the bedrock layer at the same nodal point.

4.4.2 Influence of seismic loading characteristics

4.4.2.1 Unreinforced tailings impoundment

The effect of seismic intensity measures on the response of the unreinforced model is illustrated in Figure 4.2 showing the contours of maximum horizontal displacements of an impoundment without WRI at the end of the Au Sable Forks (Figure 4.2a) and the E_2-Loma Prieta (Figure 4.2b) ground motions. These two ground motions have similar *PGA*, *AI*, and F_p (but differ for other *IM*s – see below). The simulation results indicate that the Au Sable Forks ground motion lead to significantly less horizontal displacements compared to E_2-Loma Prieta. The horizontal displacement contours in Figure 4.2a show that the SAR_x value is around 3.5 and that the impoundment would remain stable under the Au Sable Forks ground motion, with no critically displaced volume (80 cm of maximum displacement). However, 47 percent of the impoundment displaced more than 100 cm at the end of the E_2-Loma Prieta ground motion (Figure 4.2b) and the downstream slope of the impoundment is unstable with a SAR_x value of 25.

This significant difference in response for two ground motions with similar values of *PGA*, *AI*, and F_p demonstrates the importance of identifying the most appropriate (optimum) *IM* (or *IMs*) that best correlates with the overall seismic behavior, reflected here in the selected performance indicators. For instance, the *PGV* and *VSI* values of the E_2-Loma Prieta ground motion are approximately twice as high as those of the Au Sable Forks ground motion, which could explain the difference in response observed in Figure 4.2. Thus, it is necessary to identify which *IM*s minimize the variability of the simulated seismic response of the system. Employing optimum *IM*s leads to less variability, and hence a higher degree of confidence in the simulated seismic response of the impoundment model. The optimum *IM*s evaluation approach is detailed in the followings.

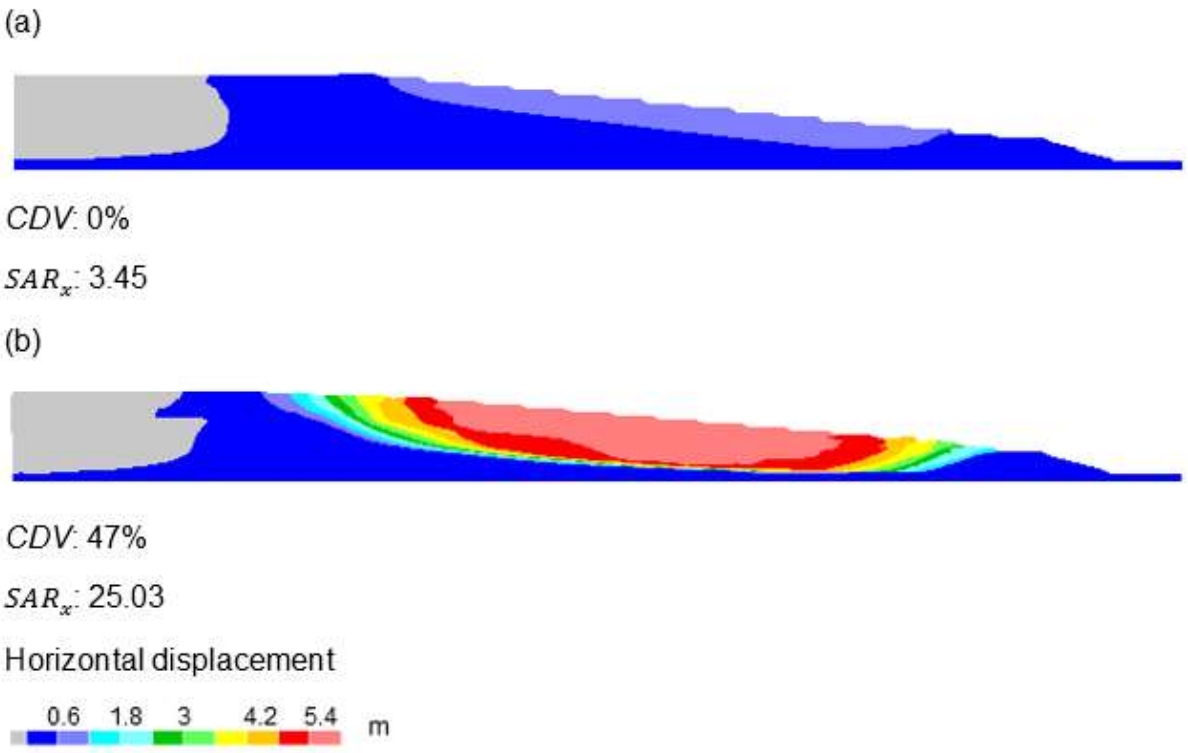

Figure 4.2: Contours of horizontal displacements of the unreinforced impoundment model with a height of 40 m and an external slope of 8H/1V at the end of (a) Au Sable Forks, and (b) E_2-Loma Prieta ground motions

4.4.2.2 Reinforced tailings impoundment

The effect of reinforcement with waste rock inclusions on the seismic response of the impoundment is illustrated in Figure 4.3 as an example, considering three 12-m wide inclusions with an edge-to-edge spacing of 80 m, under the (a) Au Sable Forks and (b) E_2-Loma Prieta ground motions. Comparing the maximum horizontal displacement contours of reinforced (Figure 4.3) and unreinforced (Figure 4.2) models demonstrates that adding the stiff WRI greatly reduced the final horizontal displacement, by a factor of 2.7 for the Au Sable Forks event and by a factor of 5 for the E_2-Loma Prieta case.

The simulation of excess pore water pressure development within the reinforced impoundment showed that waste rock inclusions have a limited effect on the earthquake-induced excess pore water pressure in the tailings, except in the immediate vicinity of the inclusions (Zafarani, 2022).

This is in accordance with other simulations conducted recently (James, 2009; Ferdosi et al., 2015a, 2015b; Zafarani et al., 2020, 2021), which confirm that the higher lateral stiffness, rather than increased drainage, is the driving mechanism for the improved behaviour of tailings impoundments with WRI during most earthquakes. Inclusions can also play a major role in the post-shaking phase by accelerating the dissipation of EPWP generated by seismic loading (Contreras, 2022), but this aspect is not addressed here.

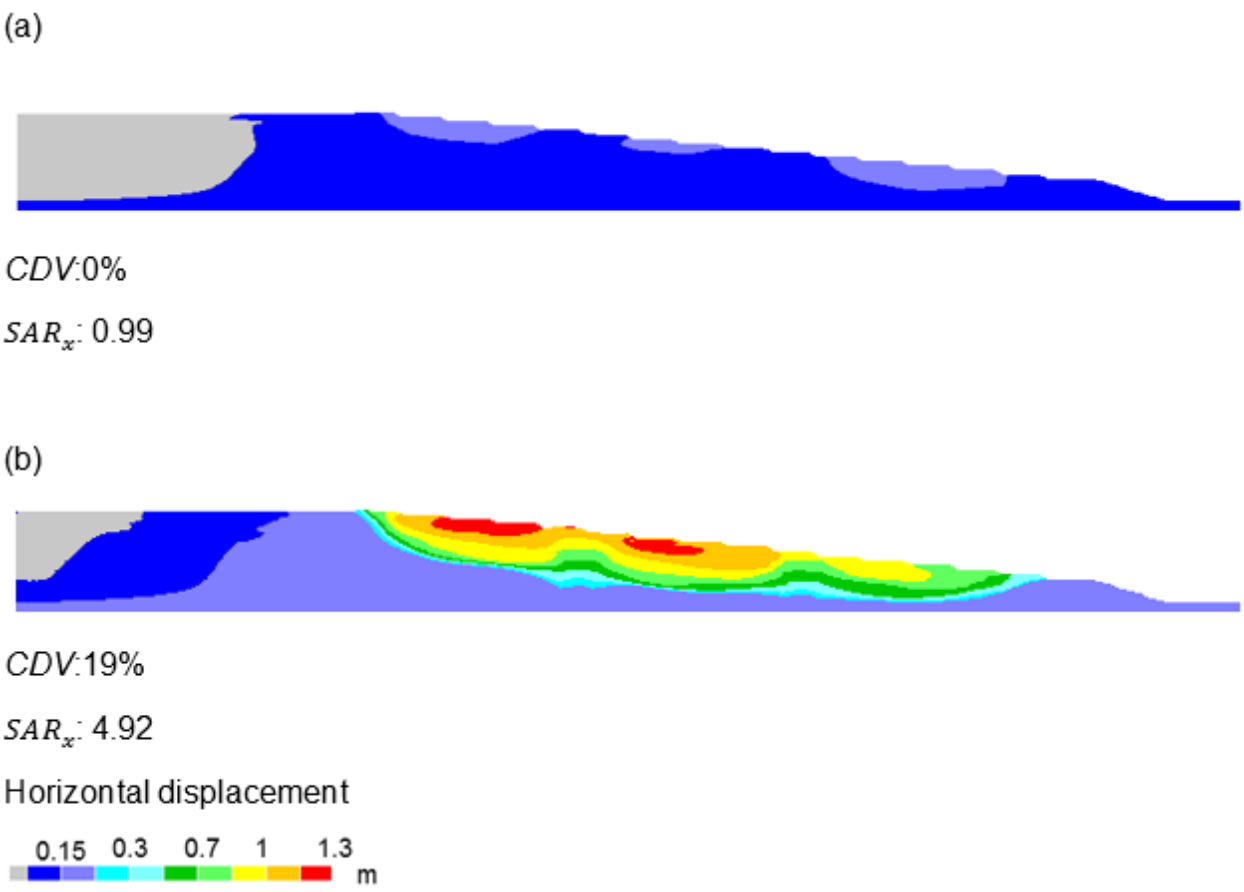

Figure 4.3: Horizontal displacements of a reinforced impoundment model with three 12-m wide WRI, and spacing of 80 m at the end ground motions for the (a) Au Sable Forks and (b) E_2-Loma Prieta seismic events

The average value of the normalized horizontal displacement along the downstream slope (SAR_x) is calculated to determine the effect of the WRI configuration on the seismic behaviour of a

reinforced impoundment. Figure 4.4 shows the variation trendlines of SAR_x as a function of the non-dimensional volume-spacing index W_{vs} defined by:

$$W_{vs} = V_r \cdot (1 - \frac{S_1}{S_{max}}) \quad (4.4)$$

where V_r is the volume ratio of the WRI and the tailings under the slope (Volume of WRI/Volume of tailings in the impoundment under the slope), S_1 is the spacing between the starter dike and the edge of the closest inclusion, and S_{max} is the spacing between the starter dike and the edge of the farthest waste rock inclusion in the model.

Results of simulations presented in Figure 4.4 are for the earthquake ground motions presented in Table 4.3. As seen in the figure, an increase in the volume of inclusions in the impoundment is generally associated with a decrease in SAR_x. The effect of W_{vs} on the value of SAR_x for ground motions with lower intensities (i.e., Mineral, E_1-Loma Prieta, Au Sable Forks, and Saguenay), is limited but the impact is much more noticeable for records with higher intensities (such as Cape Mendocino and Northridge).

The SAR_x values for most configurations under the San fernando and E_3-Loma Prieta ground motions are similar. Both ground motions have similar values of *PGA*, *PGV*, *VSI*, and *ASI*, which indicates that one or more of these *IM*s correlate well with SAR_x, and that other *IM*s, such as *AI*, F_p and *CAV*, do not affect significantly the response of the system.

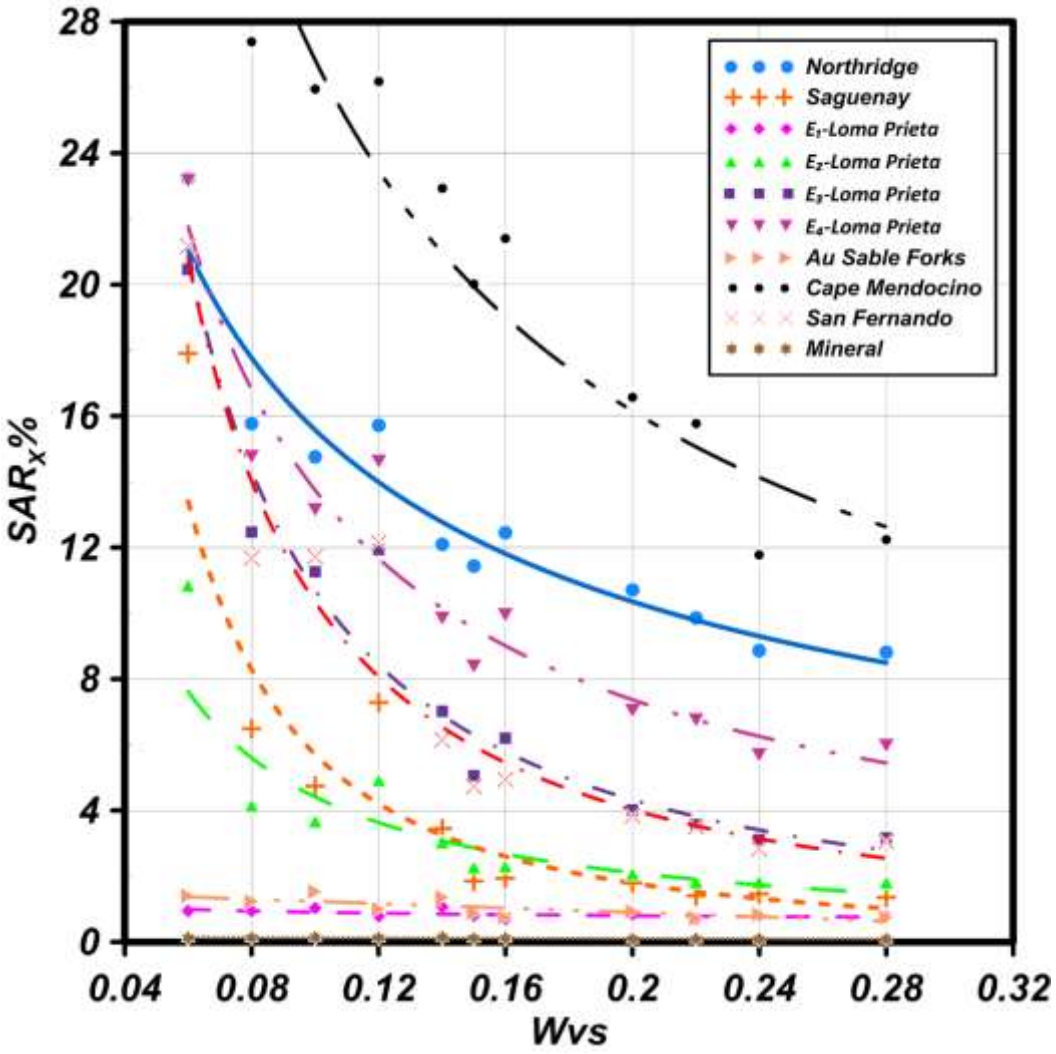

Figure 4.4: Variation of SAR_x as a function of the volume-spacing index, W_{vs} for the reinforced impoundment models under the ground motions presented in Table 4.3

4.4.3 Optimum scalar IMs evaluation approach

A power law equation can be used to represent the relationship between the seismic performance indicator (represented by SAR_x) and seismic demand (represented by *IM*s).

$$SAR_x = a\,.\,(IM)^b \tag{4.5a}$$

Equation 4.5a can then be rearranged in the following log-normal form to perform linear regressions (Cornell and Jalayer, 2002; Rezaeian and Der Kiureghian, 2010):

$$ln(SAR_x) = a + b\,.\ ln(IM) \quad (4.5b)$$

Where coefficient *a* and exponent *b* in Eq. (4.5 a) are defined with a regression analysis based on Eq. 4.5b.

The optimum *IM*s for the seismic stability evaluation of tailings impoundments can be determined by efficiency (Shome and Cornell, 1999), practicality (Nielson, 2007), and proficiency indicators (Padgett et al., 2008). The next sections present and discuss the evaluation of these indicators to identify the optimum *IMs*.

4.4.3.1 Efficiency analyses

The efficiency of an *IM* is a key metric that evaluates the degree of uncertainty with which performance of the system can be estimated for a given *IM* (Chen et al., 2015). A more efficient *IM* generally yields less dispersion in the seismic performance (i.e., SAR_x) of the simulated model (Travasarou and Bray, 2003).

The standard deviation of residuals, σ_ε, known as the dispersion term in a regression analysis, is used here as the first efficiency criteria for the optimum *IM* (Shome and Cornell, 1999), with a higher value of σ_ε indicating a lower efficiency. The standard deviation of residuals, σ_ε can be determined as follows:

$$\sigma_\varepsilon = \left(\frac{\sum[\ln(SAR_{x-sim}) - (a + b\,.\ ln(IM)]^2}{n}\right)^{\frac{1}{2}} \quad (4.6)$$

where n is the number of simulations and SAR_{x-sim} is the normalized horizontal displacement of all the nodal points along the downstream slope computed from the simulation results using Eq.(4.3). The *IM* is considered as extremely efficient if σ_ε is less than 0.2, highly efficient if σ_ε is between 0.2-0.3, acceptable if σ_ε is between 0.3-0.4, and usually inefficient when σ_ε is higher than 0.4 (Hu and Liu, 2019).

Figure 4.5 shows the values of the standard deviation of residuals for the considered *IM*s and different impoundment model configurations with waste rock inclusions. The legend in this figure gives the configuration of the waste rock inclusions: the first number is the width of the inclusions and the second is the spacing between the inclusions (in meters). The majority of the calculated values of σ_ε are between 0.4 and 1.1, indicating that all of the candidate *IM*s have a limited

efficiency. *VSI* and *PGV* are the *IM*s with the lowest values of σ_ε for all the configurations of WRI. In particular, *VSI* has a σ_ε between 0.14 and 0.63, which is the smallest among all *IM*s, while *PGV* has a σ_ε between 0.24 to 0.71 and comes in as the second best. The σ_ε values of *SMA* and a_{rms} are between 0.84 and 1.08, implying that these *IM*s have an extremely weak correlation or no correlation with the SAR_x.

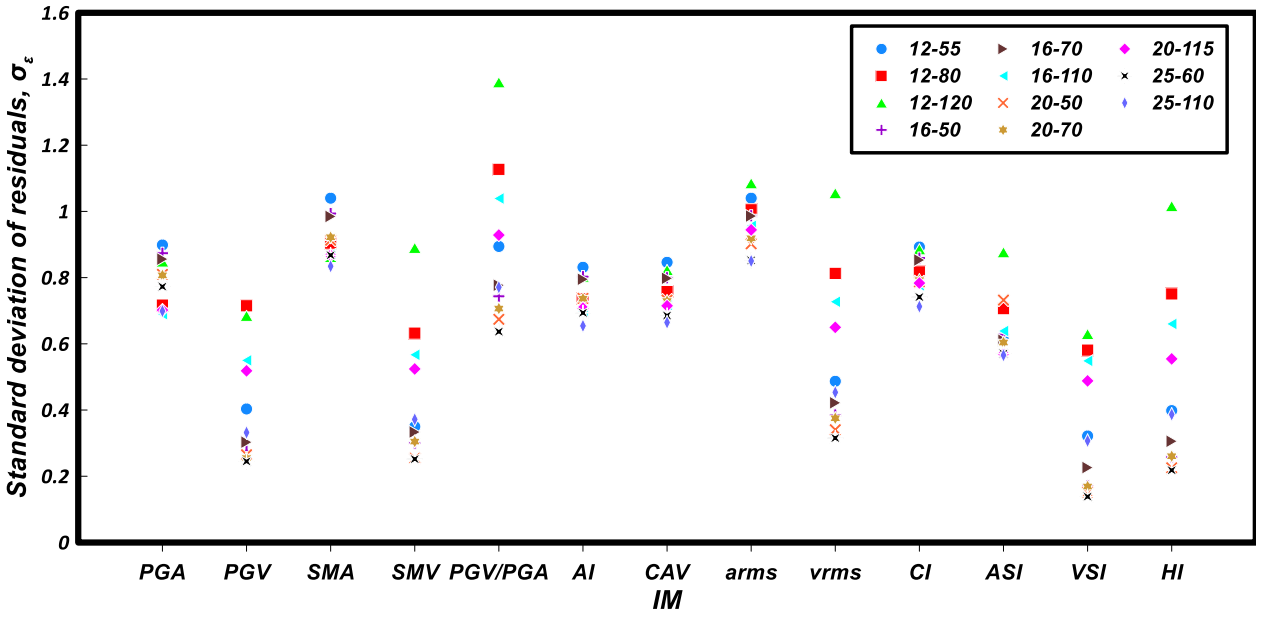

Figure 4.5: Standard deviation of residuals, σ_ε obtained from the seismic performance relationship (Eq.4.5) for the candidate IMs and various configurations of the WRI (identified in the inserted legend)

The coefficient of determination (R^2) is another predictor employed here for assessing the efficiency of the regression line given by Eq. (4.5). It is a measure of the proportion of variance for the dependent variable (SAR_x) that can be explained by the independent variable (*IM*) in the regression equation. A value of 1.0 means that the relationship perfectly fits the data, as opposed to a value of 0.0 that indicates that the equation does not represent the data. An increase in R^2 is associated with a reduced dispersion in the data, which quantifies the efficiency of the *IM*.

The R^2 values of the candidate *IM*s for impoundments with various WRI configurations are displayed in Figure 4.6, with the same legend as in Figure 4.5. It is observed that the coefficient of

determination for *VSI* varies between 0.78 and 0.97, and exhibits a noticeable advantage over the other *IM*s considered here. The R^2 value of *PGV* and *SMV* are the second highest with values between 0.61 and 0.94. The *PGV/PGA* and a_{rms} have the lowest values of R^2, hence showing the least efficiency among *IM*s.

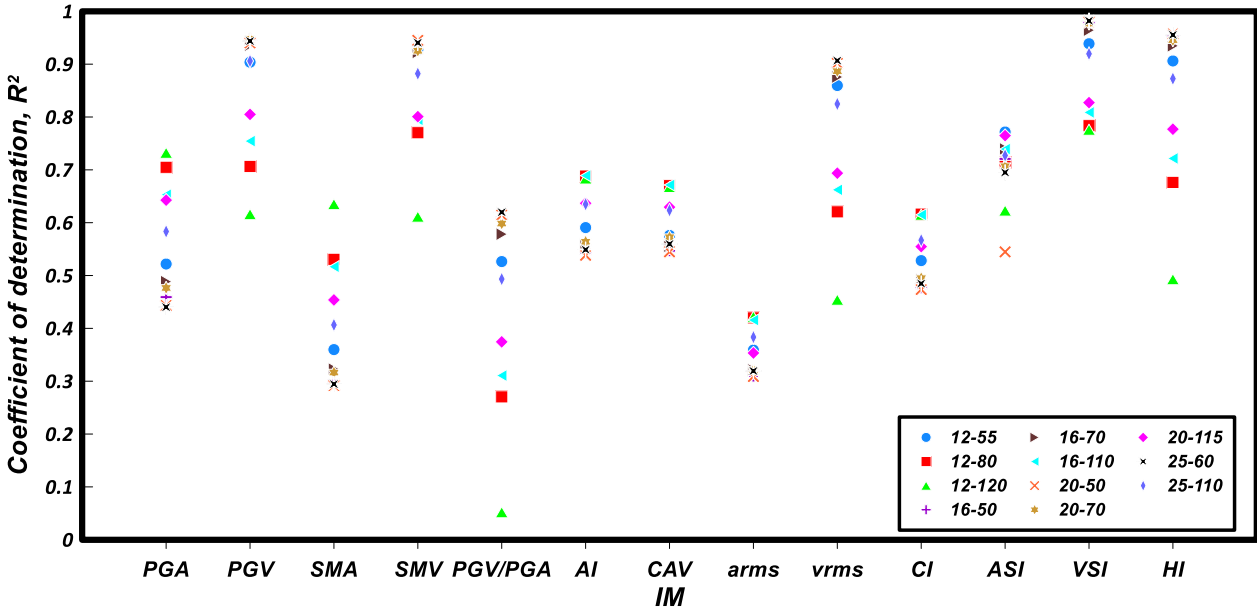

Figure 4.6: Coefficient of determination, R^2 obtained from the seismic performance relationship (Eq.4.5) for the candidate IMs and various configurations of the WRI (identified in the inserted legend)

4.4.3.2 Practicality analyses

To characterize the sensitivity of a given *IM* to the seismic performance indicator (SAR_X), the regression parameter *b* in Eq. (4.5b), or the exponent in Eq. 4.5a, is used to define practicality, based on Nielson (2005). Practicality indicates whether the *IM* has any direct correlation to relevant engineering measurements such as SAR_x. The assumption is that a greater value of *b* corresponds to a more sensitive relationship and to a more practical *IM*. Results indicate that the coefficients for *PGV*, *SMV*, V_{rms}, and *VSI* are all higher compared to other *IM*s. Therefore, these four *IM*s are deemed more practical, with *VSI* having the highest *b* value, ranging from 1.14 to 1.40. Indicators *PGV* (*b* =1.06 ~1.41) and *SMV* (*b* =1.1 ~1.38) are the second and third most practical *IM*s,

respectively based on this analysis, while *AI* and *PGV/PGA* are the least practical *IM*s for predicting the SAR_x value. More details on the comparison of the practicality (represented by exponent *b* of Eq. (4.5a)) for the considered *IM*s and WRI configurations can be found in Zafarani (2022).

4.4.3.3 Proficiency analyses

Padgett et al. (2008) introduced an integrated index ζ, called proficiency, for evaluating the performance of *IM*s. The proficiency index combines the efficiency (σ_ε) and the practicality (*b*) parameters and avoid improper selection of an *IM* based exclusively on a single indicator. In the following, the proficiency index is calculated as follows:

$$\zeta = {}^{\sigma_\varepsilon}/_{b} \tag{4.7}$$

The lower the value of ζ is, the more proficient is the *IM*. According to the results, the *IM*s that have lower ζ values are *PGV*, *SMV*, and *VSI*; *VSI* has the best proficiency with the lowest values of ζ, from 0.12 to 0.46, and *PGV* is the second most proficient *IM*, with ζ values between 0.22 and 0.61. The variation of ζ values obtained for the candidate *IM*s and various configurations of the WRI can be found in Zafarani (2022).

According to the efficiency (Figure 4.5 and Figure 4.6), practicality, and proficiency indicators, *VSI* and *PGV* are the IMs with the lowest dispersion and the highest correlation with the seismic response of tailings impoundment expressed in terms of horizontal displacements. These two velocity-related *IM*s might perform better than other *IM*s because the simulated response of the impoundment models is heavily influenced by the liquefaction of the tailings. This is in accordance with other studies showing that velocity-related *IM*s are well correlated to the occurrence of liquefaction (e.g., Midorikawa and Wakamatsu 1988; Kostadinov and Yamazaki 2001; Kostadinov and Towhata 2002).

However, the value of σ_ε for four configurations of WRI are higher than 0.4 for *VSI* and *PGV*, indicating that even the best candidate *IM*s have a relatively low level of efficiency. The efficiency of the correlation between SAR_x and velocity-related *IM*s can be improved by adding a second *IM*, and defining vector *IM*s. The procedure for selecting the second optimum *IM* is described in the following section.

4.4.4 Evaluation of the optimum vector IMs

A vector-valued *IM* composed here of two *IM*s, can be a more efficient and accurate choice than a scalar *IM* to reduce variability in the simulated seismic response of the system (Fotopoulou and Pitilakis, 2015).

The most appropriate (optimum) vector *IM*s are identified here using the efficiency, practicality and proficiency of the individual (scalar) *IM*s, the correlation coefficient between the combined *IM*s, and the overall efficiency of the vector *IM*s. While *VSI* and *PGV* are the most optimum scalar *IM*s, *VSI* is selected here as the first component (IM_1) of the various vector-valued *IMs* considered, based on the overall efficiency, practicality, and proficiency shown in the previous sections. Similar to the optimum scalar *IM* evaluation approach, a linear equation in the log-normal form is used to represent the relationship between SAR_x (seismic performance indicator) and vector-valued *IM* as follows:

$$ln(SAR_x) = a + b\,.\;ln(VSI) + c\,.ln(IM_2) \tag{4.8}$$

Where IM_2 is the second component of the vector *IM; a*, *b* and *c* are the corresponding regression parameters.

4.4.4.1 Correlation analysis

The correlation coefficient is widely used to assess the relational degree of two variables. In this study, correlation analysis outlined by Baker and Cornell (2005) is applied to detect the relational degree between *VSI* (IM_1), and other candidate *IM*s (IM_2) presented in Table 4.2. Such correlation between related *IM*s should be minimized to avoid redundancy in the model simulations. The expression of the correlation coefficient between the *IM*s is as follows (Baker and Cornell ,2005):

$$\rho_{VSI,IM_2} = \frac{\sum_{i=1}^{n}(VSI_i-\overline{VSI})(IM_{2i}-\overline{IM_2})}{\sqrt{\sum_{i=1}^{n}(VSI_i-\overline{VSI})^2\sum_{i=1}^{n}(IM_{2i}-\overline{IM_2})^2}} \tag{4.9}$$

Where ρ_{VSI,IM_2} is the correlation coefficient between *VSI* and IM_2. VSI_i and IM_{2i} are the *i*th observation of *VSI* and IM_2, respectively. $\overline{VSI}$ and $\overline{IM_2}$ are their sample mean, and *n* is total number of records. The correlation coefficient, ρ_{VSI,IM_2} varies between 0 and 1.0. Smaller correlation coefficients between *IM*s indicate that the two *IM*s contain more complementary information about

the ground motion, resulting in a lower variability and minimizing biased error in displacement prediction (Rathje and Saygili, 2008). The two *IM*s are considered to have an extremely weak correlation if ρ_{VSI,IM_2} is between 0-0.2, weak correlation if ρ_{VSI,IM_2} is between 0.2-0.4, moderate correlation if ρ_{VSI,IM_2} is between 0.4-0.6, strong correlation if ρ_{VSI,IM_2} is between 0.6-0.8, and extremely strong correlation if ρ_{VSI,IM_2} is more than 0.8. The correlation analysis shows that the values of ρ_{VSI,IM_2} for *PGA* and a_{rms} are below 0.4. Thus, these two *IM*s show the weakest correlation with *VSI*, with *PGA* having the lowest correlation coefficient ($\rho_{VSI,PGA}$=0.32). *SMA*, *CI*, *AI*, and *ASI* all lead to ρ_{VSI,IM_2} values between 0.4 and 0.6, indicating a moderate correlation with *VSI*. According to the results, *CAV* has a strong correlation with *VSI*, while *SMV*, *PGV*/*PGA*, V_{rms}, *PGV*, and *HI* have an extremely strong correlation, which was expected given that they are velocity-based *IM*s similarly to *VSI*.

4.4.4.2 Efficiency analysis of vector IMs

The standard deviation of residuals (σ_ε) and the coefficient of determination (R^2) are both employed to evaluate the overall efficiency of the vector-valued *IM*s considered here. To avoid the possible biased error in regression analysis mentioned above, only *IM*s with weak (i.e., *PGA* and a_{rms}) and moderate (i.e., *SMA*, *CI*, *AI*, and *ASI*) correlations with the IM_1 (*VSI*) are evaluated to identify the optimum vector *IM*.

Figure 4.7 illustrates the standard deviation of residuals for the aforementioned *IM*s and for various WRI configurations. The results indicate that there is a significant improvement in the efficiency, in terms of σ_ε , given by the vector *IM* compared to the corresponding scalar *IM* (Figure 4.5). In particular, using the *PGA* in combination with *VSI* leads to a σ_ε lower than 0.4 (high efficiency threshold) for all configurations of WRI, indicating that the efficiency of *PGA* is the most appropriate as the second component of the vector *IM*. *AI* with a σ_ε between 0.07 and 0.52 would be the second most efficient IM_2, but the overall efficiency of a vector *IM* composed of *VSI* and *AI* is too low, as indicated by the σ_ε values above 0.4 for a few of the configurations (such as 20-115, 16-110, 12-120, and 12-80).

The coefficient of determination (R^2) is also used to evaluate the efficiency of vector *IM*s. Figure 4.8 illustrates the R^2 values of vector-valued *IM*s, for which the second component (IM_2) has a

weak and moderate correlation with *VSI* (IM_1). It is seen that the addition of the second component of the *IM* improves R^2 values significantly for all configurations of WRI. For example, the R^2 value of a vector *IM* composed of *VSI* and *PGA* varies between 0.9 and 0.99, which is higher than the scalar *IM* of *VSI* with R^2 values between 0.78 and 0.97 and much higher than for *PGA* with a R^2 value between 0.44 and 0.73 (Figure 4.6). These values of R^2 are the highest among all vector valued *IM*s and as a result, a vector *IM* composed of *VSI* and *PGA* is deemed the most efficient in terms of the coefficient of determination. Results in Figure 4.8 show that, a vector *IM* combining *VSI* and *AI*, with R^2 values between 0.84 and 0.99, could be considered as the second most efficient vector-valued *IM*.

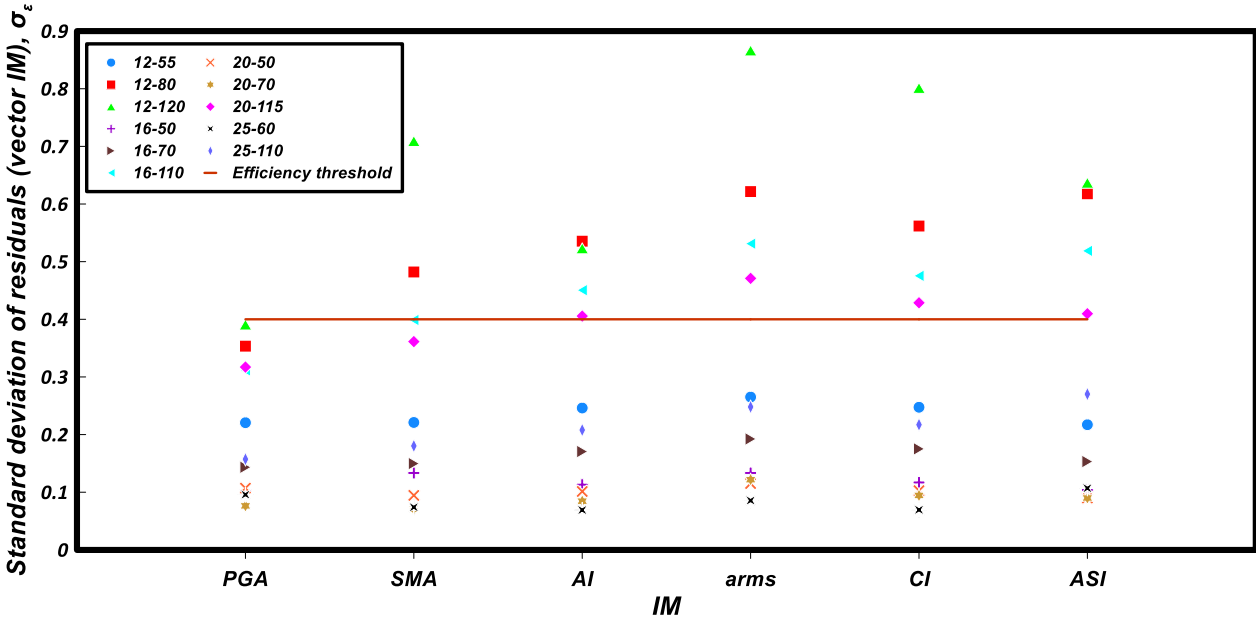

Figure 4.7: Standard deviation of residuals, σ_ε of weak and moderate correlated vector-valued IMs with various configurations of WRI; the horizontal line (at 0.40) represents the level for a good correlation.

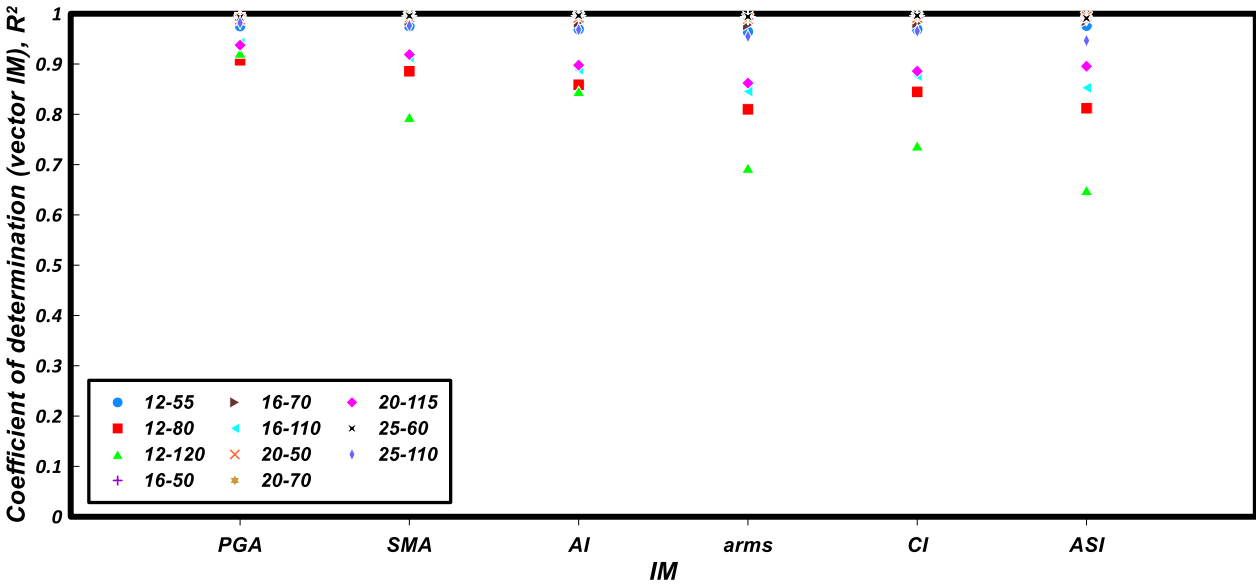

Figure 4.8: Coefficient of determination, R^2 of weak and moderate correlated vector-valued IMs with various configurations of WRI

4.5 Discussion

The liquefaction risk and consequences on a geotechnical structure must be evaluated over a range of ground motions characterized by appropriate intensity measures (*IM*s), as indicated by a performance-based earthquake engineering (PBEE) framework. Many existing approaches for determining liquefaction triggering (e.g., Seed and Idriss 1971; Youd et al. 2001; Seed et al. 2003; Idriss and Boulanger 2008) rely on the use of a ground motion *IM* that may not be optimum in terms of variability of the seismic response. This paper investigates the influence of various ground motion *IM*s on the seismic response of tailings impoundment through dynamic numerical simulations, which is an aspect that has not yet been evaluated in such details before (to the authors knowledge). The main goal is to identify *IM*s (for input ground motions) that minimize variation in the seismic response of the system. The approach should be useful to improve probabilistic modelling to assess the seismic stability of tailings impoundment.

The seismic behavior of tailings impoundments, with and without waste rock inclusions, was evaluated through a numerical parametric study based on 10 ground motion records from the NGA-West2 (Ancheta et al. 2013) and NGA-East (Goulet et al. 2014) databases. Results are provided

for an impoundment with a downstream slope of 8H:1V and a height of 40 m as the reference case. Ongoing parametric study is conducted on additional geometries with the downstream slope ranges between 7H:1V and 12H:1V, and the height of the impoundment varies between 20 m and 50 m (Zafarani, 2022). The simulation and analysis results presented above are used to assess the representativity of different *IM*s in terms of two performance indicators (*CDV*, SAR_x) for the impoundment response. The performance indicators analysis is applied here to reinforced models, as most simulations of unreinforced models were stopped due to excessive deformation during ground motion.

The capability of different *IM*s is assessed using a seismic performance analysis which relates the average normalized horizontal displacement of the downstream slope (SAR_x) with *IM*s. The linear regression analysis results show that over all thirteen *IM*s considered, *VSI* predicted SAR_x with the lowest uncertainty based on efficiency, practicality and proficiency criteria. However, *VSI* alone does not fully satisfy the minimum acceptable efficiency (i.e., σ_ε= 0.4) for some of the WRI configurations. The relatively low correlations obtained for some cases may be due to limitations of the performance indicators used to quantify the seismic response of the system. Ongoing research is conducted on additional performance indicators, such as the evolution of excess pore pressure ratio (Chen et al., 2015; Kramer and Mitchell, 2006), to determine their correlations with the candidate scalar and vector *IM*s (Zafarani, 2022).

The use of a vector valued *IM* can better reflect the effect of the most critical aspects of ground motions on the seismic-induced displacements, such as amplitude, frequency content, and duration. The advantages gained by using a vector *IM* should be evaluated in tandem with the complexities associated with computing the joint annual probability of occurrence of the pairs of ground motion parameters (Travasarou and Bray, 2003).

This investigation of *IM*s focussed specifically on the response of tailings impoundments reinforced with waste rock inclusions. The relative novelty of this co-disposal technique requires guidelines for their optimal design. The ongoing work thus aims at developing correlation equations to establish the most appropriate (optimal) configurations of waste rock inclusions in tailing impoundments subjected to seismic loading. Such engineering tools are needed so that this promising technology can be employed in practice more widely (Aubertin et al. 2021). The seismic

analysis conducted here for selecting the optimum intensity measures can be beneficial in engineering practice to analyze the response of tailings impoundments in a deterministic or probabilistic framework.

In addition to the influence of intensity measures, the impact of other factors, such as material properties, tailings thickness and geometry of the dikes, must also be evaluated and addressed to apply design guidelines. Evaluating the effect of such factors on the seismic response of reinforced and unreinforced models is also part of ongoing work (Zafarani, 2022).

Despite the advances from this study, some additional limitations should be mentioned. For instance, plane strain simulations were employed here, as is the case in the vast majority of similar geotechnical engineering projects. As the efficiency of available constitutive and numerical 3D models is quickly improving, future research can also consider three-dimensional modeling of the seismic behaviour of tailings impoundments to investigate how it affects the response of the tailings storage facilities. Other aspects may also be addressed in complementary investigations, including for example non-uniform distribution of material properties and the effect of sequential deposition on pore water pressures and loading history of the tailings in the impoundment.

The conclusions obtained from this investigation related to specific geometries and tailings properties, and may not apply to other types of tailings impoundment (e.g., downstream and centreline raised dikes), foundations, or stratigraphy. The constitutive model used to simulate seismic response has some limitations that could affect the results. The number of ground motions used in the parametric investigation was also limited given the large size of each model and the computing time. Additional variation in tailings geotechnical properties, geometry, and ground motion properties, as well as validation of numerical results using various constitutive models against physical models such as centrifuge tests, are required prior to developing a probabilistic prediction model.

4.6 Conclusion

This paper presents the results of a numerical parametric investigation to evaluate the effects of ground motion intensities on the seismic stability of tailings impoundment. Many existing approaches for evaluating the liquefaction potential of tailings rely on the use of a ground motion

IM that may not be optimum in terms of variability of the seismic response. Understanding the effects of ground motion characteristics on the simulated seismic response of models, as well as determining the optimum *IM*s to select and scale input motions generally leads to results within a narrow confidence interval so that a given degree of confidence can usually be achieved with fewer calculations.

The seismic response and stability of tailings impoundments, with and without waste rock inclusions, has been evaluated using 10 different ground motion records. The simulations are conducted with FLAC (Version 8.00, Itasca, 2016). The PM4Sand model (Boulanger and Ziotopoulou, 2017) is employed to capture the dynamic behavior of low plasticity tailings.

The improvement of seismic stability due to WRIs in impoundments is assessed under various levels of intensity measure. Thirteen different ground motion intensity measures (*IM*s) are assessed here to quantify the ground motions and evaluate the variability in the simulated response in terms of performance indicators. Each tailings impoundment response is assessed using specific indicators to facilitate the comparison between the different cases and establish relationships with the various *IM*s. The two performance indicators adopted are the (normalized) critical displaced volume of tailings (*CDV*) and the average (normalized) horizontal displacement of the downstream slope (SAR_x).

An optimum *IM* was determined by the seismic model, which captures the relationship between seismic performance as defined by SAR_x and seismic demand associated with various *IM*s. Regression analyses are performed to assess the potential of predictability of the *IM*s based on the efficiency, practicality, and proficiency criteria. Based on the results, velocity-related *IM*s (i.e., *VSI* and *PGV*) appear to be the most efficient, practical and proficient scalar intensity measures. However, some modelling results show relatively low efficiency for all scalar *IM*s considered here. To improve the efficiency and reduce variability in the seismic response of the model a vector-valued *IM* is considered here.

The most appropriate (optimum) vector *IM*s are determined by considering the efficiency, practicality and proficiency of the scalar *IM*s, the correlation coefficient between the combined *IM*s, and the overall efficiency of the vector *IM*s. The combination of *VSI* and *PGA* yields the optimum efficiency for the conditions considered here. More details on the optimum vector *IM*s

evaluation approach, including the efficiency and correlation analysis of the combination of various *IM*s with *VSI* can be found in Zafarani (2022).

Based on the results presented here, it is recommended that performance models for tailings impoundments being used by practitioners be considering the seismic loading in the form of *VSI* and *PGA*, and also that these parameters be considered in the ground motion selection process. The presented work is also being used to create design guidelines for waste rock inclusions in tailings impoundments for practitioners, where the seismic loading will be considered in based on *VSI* and *PGA*.

4.7 Acknowledgements

The authors acknowledge the financial support from NSERC and from the industrial partners of the Research Institute on Mines and the Environment (RIME UQAT-Polytechnique; http://rime-irme.ca/en).

4.8 References

Akkar S, Bommer JJ. 2010. Empirical equations for the prediction of PGA, PGV, and spectral accelerations in Europe, the Mediterranean Region, and the Middle East. Seismol Res Lett 81:195–206.

Ancheta, T. D., Darragh, R. B., Stewart, J. P., Seyhan, E., Silva, W. J., Chiou, B. S., and Donahue, J. L. 2013. Peer NGA-West2 database.

Arias., A. 1970. A measure of earthquake intensity. In: Hansen RJ (ed) Seismic design for nuclear power plants. MIT Press, Cambridge MA, pp 438–483

Aubertin, M., Bussière, B. and Chapuis, R.P. 1996. Hydraulic conductivity of homogenized tailings from hard rock mines. Canadian Geotechnical Journal, 33(3), 470-482

Aubertin, M., Mbonimpa, M., Jolette., D., Bussière, B., Chapuis, R.P., James, M., Riffon, O. 2002. Stabilité géotechnique des ouvrages de retenue pour les résidus miniers: problèmes persistants et méthodes de contrôle. Défis and Perspectives : Symposium sur l'environnement et les mines, Rouyn-Noranda, Développement Économique Canada/Ministère des Ressources Naturelles du Québec/CIM. Comptes-Rendus sur CD-ROM.

Aubertin, M., Bussière, B., James, M., Jaouhar, E.M., Martin, V., Pépin, N., Mbonimpa, M. and Chapuis, R.P. 2011. Vers une mise à jour des critères de stabilité géotechnique pour la conception des ouvrages de retenue de résidus miniers. Proc. Symposium sur l'environnement et les mines, Rouyn-Noranda, QC, CIM, CD Rom.

Aubertin, M., James, M., Maknoon, M., and Bussière, B. 2013. Recommandations pour améliorer le comportement hydrogéotechnique des haldes à stériles. GeoMontreal 2013-Geosciences for Sustainability, 66th CGS Conference, Montreal, QC, 8 p.

Aubertin, M., Jahanbakshzadeh, A., Saleh-Mbemba, F., Yniesta, S. and Pednault, C. 2021. General guidelines for the design and construction of waste rock inclusions in tailings impoundment. Paper presented at the 74th Canadian Geotechnical Conference (Geo Niagara 2021).

Azam, S., and Li, Q. 2010. Tailings dam failures: a review of the last one hundred years. Geotechnical News, 28(4), 50-54.

Baker, J. W., and Cornell, C. A. 2005. Vector-valued ground motion intensity measures for probabilistic seismic demand analysis. Blume Center Technical Rep. #150, Stanford Univ., Stanford, CA.

Boore DM, Atkinson GM. 2008. Ground-motion prediction equations for the average horizontal component of PGA, PGV, and 5%-damped PSA at spectral periods between 0.01 s and 10.0 s. Earth Spectra 24:99–138.

Boudrias, G. 2018. Évaluation numérique et expérimentale du drainage et de la consolidation de résidus miniers à proximité d'une inclusion de roches stériles. Master thesis, Ecole Polytechnique de Montreal.

Boulanger, R. W., and Idriss, I. M. 2004. Evaluating the potential for liquefaction or cyclic failure of silts and clays (p. 131). Davis, California: Center for Geotechnical Modeling.

Boulanger, R. W., and Ziotopoulou, K. 2017. PM4Sand (Version 3): A sand plasticity model for earthquake engineering applications. Center for Geotechnical Modeling Report No. UCD/CGM-15/01, Department of Civil and Environmental Engineering, University of California, Davis, Calif.

Bora, S. S., Scherbaum, F., Kuehn, N. et al. 2015. Development of a response spectral ground motion prediction equation (GMPE) for seismic-hazard analysis from empirical fourier spectral and duration models. Bull Seismol Soc Am 105:2192–2218.

Bradley, B. A. 2012. Empirical correlations between cumulative absolute velocity and amplitude-based ground motion intensity measures. Earth Spectra 28:37–54.

Bussière, B., and Aubertin, M. 1999. Clean tailings as cover material for preventing acid mine drainage: an in situ experiment. In Proceedings of Conference Mining and the Environment II, September 13–17, Sudbury, Canada, (vol. 1, p. pp 19–28).

Bussière, B. 2007. Hydro-Geotechnical properties of hard rock tailings from metal mines and emerging geo-environmental disposal approaches. Canadian Geotechnical Journal, 44(9): 1019-1052

Chen, Z. X., Cheng, Y., Xiao, Y., Lu, L., and Yang, Y. 2015. Intensity measures for seismic liquefaction hazard evaluation of sloping site. Journal of Central South University, 22(10), 3999-4018.

Contreras Romero, C. A. 2013. Comportement dynamique du sol pulvérulent « résidus miniers ». M.Sc., thesis, Department of Civil, Geological, and Mining Engineering, Ecole Polytechnique de Montreal, Montreal, QC.

Contreras Romero, C. A. 2022. Détermination de la stabilité sismique et post-sismique des parcs à résidus miniers avec et sans inclusions de roches stériles pour des aléas faibles, intermédiaires et élevés des régions minières de l'est du Canada. Thèse de doctorat, Département civil, géologie et Mines, École Polytechnique de Montréal, Québec, Canada. In preparation.

Contreras Romero, C. A., Yniesta, S., Jahanbakhshzadeh, A., and Aubertin, M. 2022. Calibration of the PM4Sand Model for Hard-Rock Mine Tailings Based on Laboratory and Field Tests. Submitted to the Canadian Geotechnical Journal.

Contreras Romero, C. A., Yniesta, S., and Aubertin, M. 2020. Seismic and post-seismic stability of tailings impoundments, considering the effect of reinforcement inclusions. Proc. 73rd Canadian Geotechnical Conference (GEOVirtual 2020).

Cornell, A., and Jalayer, F. 2002. Factored nonlinear displacement demand estimation methods for probability-based safety assessment. ASCE Journal of Structural Engineering 2002;128(4): 526–533

Davies, M. P. 2002. Tailings impoundment failures - Are geotechnical engineers listening. Geotechnical News, BiTech Publications, Vancouver, 20(3), 31-36.

Duncan, J. M., and Bursey, A. 2013. Soil modulus correlations. In Foundation Engineering in the Face of Uncertainty: Honoring Fred H. Kulhawy (pp. 321-336).

Esposito, S., Iervolino, I. 2011. PGA and PGV spatial correlation models based on European multievent datasets. Bulletin of the Seismological Society of America 101:2532–2541.

Essayad, K. 2015. Development of experimental protocols for the characterization of saturated and unsaturated tailings consolidation from columns compression tests (text in French), Master thesis, Ecole Polytechnique de Montreal.

Essayad, K., Pabst, T., Aubertin, M. and Chapuis, R.P. 2018. An experimental study of the movement of tailings through waste rock inclusions. Paper presented at the 71st Canadian Geotechnical Conference (GeoEdmonton 2018), Edmonton, Alberta.

Falaknaz, N., Aubertin, M., Li, L. 2015. Evaluation of the stress state in two adjacent backfilled stopes within an elastoplastic rock mass. Geotech Geol Eng. doi:10.1007/s10706-015-9868-6

Federico, A., and Elia, G. 2009. At-rest earth pressure coefficient and Poisson's ratio in normally consolidated soils. Proc. 17th International Conference on Soil Mechanics and Geotechnical Engineering, Alexandria, Egypt.

Ferdosi, B. 2014. A numerical investigation of the seismic response of tailings impoundments reinforced with waste rock inclusions. Ph.D. Thesis, Ecole Polytechnique de Montreal.

Ferdosi, B., James, M., and Aubertin, M. 2015a. Effect of waste rock inclusions on the seismic stability of an upstream raised tailings impoundment: a numerical investigation. Canadian Geotechnical Journal, 52(12): 1930-1944.

Ferdosi, B., James, M., and Aubertin, M. 2015b. Investigation of the effect of waste rock inclusions configuration on the seismic performance of a tailings impoundment. Geotechnical and Geological Engineering, 33(6), 1519-1537.

Fotopoulou, S. D., Pitilakis, K. D. 2015. Predictive relationships for seismically induced slope displacements using numerical analysis results. Bulletin of Earthquake Engineering 13(11):3207–3238

Gens, A. and Alonso, E. E. 2006. Aznalco'llar Dam Failure. Part 2: Stability Conditions and Failure Mechanism. Gèotechnique 56, No. 3, 185-201

Goodman, R. E. 1989. Introduction to Rock Mechanics. John Wiley and Sons Inc.

Goulet, C. A., et al. 2014. PEER NGA-east database. Berkeley, CA: Pacific Earthquake Engineering Research Center

Grimard, L.P. 2018. Une étude en laboratoire sur la réponse des résidus miniers aux charges compressives non drainées et aux pertes de confinement avec caractérisation par vitesse des ondes de cisaillement. (Mémoire de maîtrise, École Polytechnique de Montreal, QC).

Grimard, L. P., Karray, M., James, M., and Aubertin, M. 2021. Consolidation characteristics of hydraulically deposited tailings obtained from shear wave velocity (V s) measurements in triaxial and oedometric cells with piezoelectric ring-actuator technique (P-RAT). Canadian Geotechnical Journal, 58(2), 281-294.

Holtz, R. D., Kovacs, W. D., and Sheahan, T. C. 1981. An introduction to geotechnical engineering (Vol. 733). Englewood Cliffs: Prentice-Hall.

Housner, GW.1952. Intensity of ground motion during strong earthquakes. Second technical report. August 1952, California Institute of Technology Pasadena, California

Housner, G.W. and Jennings, P.C. 1964. Generation of artificial earthquakes. Proceedings of American Society of Civil Engineers 90, 113–150

Hu, J., and Liu, H. 2019. Identification of ground motion intensity measure and its application for predicting soil liquefaction potential based on the Bayesian network method. Engineering Geology, 248, 34-49.

Itasca Consulting Group, Inc. (Itasca). 2016. FLAC – Fast Lagrangian Analysis of Continua. Version 8.00. [computer software and user manual]. Minneapolis MN: Itasca Consulting Group, Inc.

Jahanbakhshzadeh, A., Aubertin, M., Yniesta, S., and Zafarani, A. 2019. On the seismic response of tailings dikes constructed with the upstream and center-line methods. Paper presented at the 72nd Canadian Geotechnical Conference (GEO 2019), St. John's.

James, M. 2009. The use of waste rock inclusions to control the effect of liquefaction in tailings impoundments. Ph.D. Thesis, Department of Civil, Geological, and Mining Engineering, Ecole Polytechnique de Montreal, Montreal, QC.

James, M., and Aubertin, M. 2009. The use of waste rock inclusions in tailings impoundments to improve geotechnical and environmental performance. In Proceedings, Tailings and Mine Waste 2009, Banff, Alta. pp. 233–245.

James, M., Aubertin, M. and Bussière, B. 2013. On the use of waste rock inclusions to improve the performance of tailings impoundments. In proceedings of the 18th International Conference on Soil Mechanics and Geotechnical Engineering, Paris, France, 1: 735-738.

James, M., Aubertin, M., Bussière, B., Pednault, C., Pépin, N., and Limoges, M. 2017. A research project on the use of waste rock inclusions to improve the performance of tailings impoundments. Geo Ottawa, Ottawa, ON. p. 8.

Jibson, R., W. 2011. Methods for assessing the stability of slopes during earthquakes-A retrospective. Engineering Geology 122 (2011) 43–50

Kenney, J. F. and Keeping, E. S. Root Mean Square. 1962. 3rd ed. Princeton, NJ: Van Nostrand, pp. 59-60.

Kishi, N., Nomachi, S.G., Matsuoka, K. G., Kida, T. 1987. Earthquake engineering. Japan society of civil engineering, proceeding of JSCE, No. 386/ I- 8, Vol. 4, No. 2, pp 259 – 267

Kostadinov M.V., Yamazaki F. 2001. Detection of soil liquefaction from strong motion records. Earthquake Engineering and Structural Dynamics 30:173–193. doi:10.1002/1096 9845(200102)30:2\173:AID-EQE3[3.0.CO;2-7

Kostadinov M.V., Towhata I. 2002. Assessment of liquefaction inducing peak ground velocity and frequency of horizontal ground shaking at onset of phenomenon. Soil Dynamics and Earthquake Engineering 22:309–322. doi:10.1016/S0267-7261(02)00018-0

Kramer, S.L. 1996. Geotechnical Earthquake Engineering, New Jersey, Prentice Hall

Kramer, S. L., and Mitchell, R. A. 2006. Ground motion intensity measures for liquefaction hazard evaluation. Earthquake Spectra, 22(2), 413-438.

Kuhlemeyer, R. L., and Lysmer, J. 1973. Finite element method accuracy for wave propagation problems. Journal of Soil Mechanics and Foundations Division, 99 (Tech Report).

L-Bolduc, F. 2012. Étude expérimentale et numérique de la consolidation des résidus et des effets d'inclusions drainantes. Mémoire de maîtrise, École Polytechnique de Montréal.

Luco, N., Cornell, A. C. 2007. Structure-specific scalar intensity measures for near-source and ordinary earthquake ground motions. Earthquake Spectra 2007; 23:357–392.

Maknoon, M. 2016. Slopes stability analyses of waste rock piles under unsaturated conditions following large precipitations. Ph.D. Thesis. Ecole Polytechnique de Montreal.

Martin, V., and Aubertin, M. 2019. An assessment of hydrogeological properties of waste rock using infiltration tests and numerical simulations. In proceedings of 72nd Canadian Geotechnical Conference (GeoStJohn's 2019),

Mbonimpa, M., Aubertin, M., Chapuis, R. P., and Bussiere, B. 2002. Practical pedotransfer functions for estimating the saturated hydraulic conductivity. Geotechnical and Geological Engineering, 20(3): 235-259.

Midorikawa S., Wakamatsu K. 1988. Intensity of earthquake ground motion at liquefied sites. Soils Found 28:73–84. doi:10.3208/sandf1972.28.2_73

Nielson, B. G., and DesRoches, R. 2007. Seismic fragility methodology for highway bridges using a component level approach. Earthquake Engineering and Structural Dynamics, Vol. 36, No. 6, pp. 823-839, DOI: 10.1002/Eqe.655.

Nuttli, O. W. 1979. Seismicity in the central United States, Geological Society of America 4, 67–93.

Padgett, JE, Nielson, BG, DesRoches, R. 2008. Selection of optimal intensity measures in probabilistic seismic demand models of highway bridge portfolios. Earthquake Engineering and Structural Dynamics 37: 711–725.

Park, Y., and Ang A. 1985. Mechanistic Seismic Damage Model for Reinforced Concrete. Journal of Structural Engineering, 111(4): 722–739.

Pépin, N., Aubertin, M., James, M. 2012. Seismic Table Investigation of the Effect of Inclusions on the Cyclic Behavior of Tailings. Canadian Geotechnical Journal, 49(4): 416-426.

Peregoedova, A. 2012. Étude expérimentale des propriétés hydrogéologiques des roches stériles à une échelle intermédiaire de laboratoire. M.Sc.A. thesis, Département des génies civil, géologique et des mines, École Polytechnique de Montréal, QC.

Poncelet, N. 2012. Élaboration et implément d'un protocole de laboratoire pour l'étude du potential de liquéfaction de résidus miniers. M.Sc. Thesis unpublished. Ecole Polytechnique Montréal PQ, Canada.

Rathje, E.M. and Saygili, G. 2008. Probabilistic Seismic Hazard Analysis for the Sliding Displacement of Slopes: Scalar and Vector Approaches. Journal of Geotechnical and Geoenvironmental Engineering, ASCE, 134(6), 804- 814.

Rathje EM., Abrahamson NA., Bray JD. 1998. Simplified frequency content estimates of earthquake ground motions. Journal of Geotechnical and Geoenvironmental Engineering 124(2):150–159

Rayleigh, J. and Lindsay, R. 1945. The Theory of Sound. Dover Publications, Inc., Dover.

Rezaeian, S., and Der Kiureghian, A. 2010. Simulation of synthetic ground motions for specified earthquake and site characteristics. Earthquake Engineering and Structural Dynamics, 39(10), 1155-1180.

Rollins, K. M., Evans, M. D., Diehl, N. B., and III, W. D. D. 1998. Shear modulus and damping relationships for gravels. Journal of Geotechnical and Geoenvironmental Engineering, 124(5), 396-405.

Saleh Mbemba, F. 2016. Évaluation du drainage, de la consolidation et de la dessiccation des résidus miniers fins en présence d'inclusions drainantes. Thèse de doctorat, Département civil, géologie et Mine, Université de Polytechnique de Montréal, Montréal, QC.

Santamarina, J. C., Torres-Cruz, L. A., and Bachus, R. C. 2019. Why coal ash and tailings dam disasters occur. Science, 364(6440), 526-528.

Seed, H. B. and Idriss, I. M. 1982. Ground Motions and Soil Liquefaction During Earthquakes. Berkeley CA: Earthquake Engineering Research Institute.

Seed, H.B., Wong, R.T., Idriss, I.M. and Tokimatsu, K. 1984. Dynamic moduli and damping factors for dynamic analysis of cohesionless soils. Report No. UCB/EERC-84/14, Earthquake Engineering Research Center, Berkeley, CA.

Shome, N. and Cornell, C. A. 1999. Probabilistic seismic demand analysis of nonlinear structures. PhD Thesis. Stanford University, California.

Tothong, P., Luco, N. 2007. Probabilistic seismic demand analysis using advanced intensity measures. Earthquake Engineering and Structural Dynamics 2007, 36: 1837–1860

Travasarou, T., and Bray, J. D. 2003. Optimal ground motion intensity measures for assessment of seismic slope displacements. In 2003 Pacific Conference on Earthquake Engineering, Christchurch, New Zealand, Feb.

Vaid, Y. P., Byrne, P. M., and Hughes, J. M. O. 1981. Dilation angle and liquefaction potential.

Wyllie, D., C., and Mah, C., W. 2004. Rock Slope Engineering. London and New York: Spon Press.

Zafarani, A. 2022. Using numerical modeling with dynamic loading to develop a procedure for the optimal design of waste rock inclusions in tailings impoundments. Ph.D. Thesis. Ecole Polytechnique de Montreal. In preparation.

Zafarani, A., Yniesta, S., Aubertin, M. 2020. Effect of height and downstream slope on the seismic behavior of tailings impoundments reinforced with waste rock inclusions. Paper presented at the 73rd Canadian Geotechnical Conference (GEOVirtual 2020).

Zafarani, A., Yniesta, S., Aubertin, M. 2021. On the selection of ground motion intensity measures to evaluate the seismic stability of tailings impoundments. Paper presented at the 74th Canadian Geotechnical Conference (Geo Niagara 2021), Niagara Falls, Ontario.

Zhang, C., Zhong, Z., and Zhao, M. 2020. Study on Ground Motion Intensity Measures for Seismic Response Evaluation of Circular Tunnel. In IOP Conference Series: Earth and Environmental Science (Vol. 455, No. 1, p. 012164). IOP Publishing.

CHAPTER 5 ARTICLE 3: NUMERICAL PROCEDURE AND DESIGN GUIDELINES FOR SEISMIC STABILITY OF TAILINGS IMPOUNDMENTS WITH WASTE ROCK INCLUSIONS

Ali Reza Zafarani[1*], Samuel Yniesta[1] and Michel Aubertin[1]

[1]Department of Civil, Geological and Mining Engineering, Polytechnique Montréal, C.P. 6079, Centre-ville, Montréal, QC H3C 3A7, Canada.

*Corresponding Author; email: ali-reza.zafarani@polymtl.ca

This article was submitted to Journal of Geotechnical and Geological Engineering in July 2022

Abstract

The geotechnical stability of tailings storage facilities (TSFs) during earthquakes is a major concern for the mining industry, as these have been prone to failure in seismically active areas. Waste rock inclusions (WRI) can be used to improve the geotechnical behavior of tailings impoundments by increasing the rate of consolidation and drainage of the tailings and providing lateral reinforcement. Considering the relative novelty of this co-disposal method, there is a need to develop guidelines and optimization strategies for this method as part of the design of tailings impoundment. In this paper, the results of a dynamic numerical investigation are used to develop functional relationships, leading to a correlation equation, for the optimal configuration of waste rock inclusions in tailings impoundments subjected to seismic loading. The effects of the downstream slope of upstream dikes, height of the impoundment, intensity measures (*IM*s) of seismic loadings, configuration of WRI and tailings properties are investigated for representative conditions. The effect of each parameter is evaluated using a performance indicator representing the horizontal displacement of the downstream slope. Regression analyses are performed to assess the reliability of the developed equation in terms of normal distribution of residuals. The statistical regression analyses based on numerical simulations of the impoundment response show that the proposed global equation represents well the liquefaction-induced horizontal displacement of the downstream slope of the impoundment for the conditions considered here. The general analysis procedure is relevant for

different types of impoundment while the specific relationship proposed here should be of great interest for the design of tailings impoundment reinforced with waste rock inclusions.

Key Words: Seismic loading; earthquake intensity measures; Tailings impoundments; Waste rock inclusions; Seismic behavior; Stability

5.1 Introduction

Failure of storage tailings facilities (TSFs) often leads to a fast-moving mudflow that can reach several miles downstream, and which may cause disastrous consequences (Davies, 2002; Aubertin et al. 2002b, 2011, 2021; Azam and Li, 2010; Santamarina et al., 2019). Major tailings dike failures have been attributed to a variety of causes and factors, including overtopping due to water mismanagement, failure of foundation soils, and static liquefaction of the tailings causing a reduction of stiffness and strength (e.g., Zhang et al. 2004, Blight, 2010; Kramer and Wang, 2015; Robertson et al., 2018). Seismic stability has also been a concern following events reported over the years (Tapo Canyon, 1994 (Harder and Stewart, 1996); Las Palmas, 2010 (Moss et al., 2019); Fundão, 2015 (Morgenstern et al., 2016)

To increase the static and dynamic stability of tailings impoundments, a co-disposal strategy incorporating waste rock and tailings has been proposed and developed (Aubertin et al. (2002b; 2021)). This technique involves the addition of waste rock inclusions (WRI) placed in tailings impoundments, along predetermined locations. Under static conditions, WRI can accelerate the consolidation rate of tailings and increase their shear resistance (Jaouhar at al., 2011, 2013; L-Bolduc and Aubertin, 2014; Saleh Mbemba et al. 2019, 2021), while also improving the stability of external slopes (Jahanbakhshzadeh and Aubertin, 2021). Dynamic loading conditions have been studied using laboratory testing, physical modeling, and numerical simulations to investigate the effects of waste rock inclusions on the seismic response of tailings impoundments (e.g., James, 2009; Pepin et al., 2012; Ferdosi et al., 2015a; 2015b; Jahanbakhshzadeh et al., 2019; Zafarani et al., 2020, 2021, 2022a; Contreras et al., 2020; Contreras, 2022). These studies have indicated that WRI can improve the stability of the impoundment during and after an earthquake. Additionally, recent numerical investigations show that the configuration of the inclusions, the downstream slope, the thickness of the tailings, and the intensity of the ground motion all have a significant effect on the seismic response of reinforced impoundments (Zafarani et al., 2020; 2021; 2022a,b).

In light of the relative novelty of this method, an optimization methodology is needed for the design of tailings impoundment with WRI. In this paper, dynamical numerical analyses are used to establish specific relationships that lead to a correlation equation that can be used to establish the configurations of waste rock inclusions in tailings impoundments subjected to seismic loading. Numerical simulations are performed to assess and quantify the effects of the downstream slope, height of the impoundment, intensity of the ground motion (through the use of different intensity measures (*IM*s)), WRI configuration, and tailings properties. The influence of each factor is evaluated individually using a performance indicator that represents the horizontal displacement of the downstream slope. The reliability of the developed equation in terms of normal distribution of residuals is assessed using regression analyses. The correlations are used to develop a design framework to optimize the configuration of waste rock inclusions in tailings impoundments.

5.2 Numerical investigation procedure

The numerical parametric analysis was conducted using FLAC version 8.00 (Itasca 2016) for two stages: static and dynamic loading conditions. Each numerical model is first used to simulate the hydro-geotechnical response and to determine pore water pressures and initial stresses under static (equilibrium) conditions. The static phase stresses are then used as initial conditions for the dynamic analysis. Prior to applying the earthquake loading at the base of the FLAC model, the constitutive models of the different materials are modified to more accurately simulate their cyclic response under seismic loading, as described in the following sections. More details on the parametric study procedure, including the numerical simulation set up, material properties selection, and ground motion selection are included in Zafarani (2022).

5.2.1 Model geometry and boundary conditions

The effects of the downstream slope angle (θ), height of the impoundment model (H), and width, W (m), and edge-to-edge spacing, S (m), of waste rock inclusions are investigated through numerical simulations. The effect of these parameters is assessed using more than 180 numerical simulations to evaluate their effect based on the normalized horizontal displacement of the downstream slope. Table 5.1 lists the simulation characteristics and configurations used in the parametric analysis, which are based on conditions commonly encountered with hard rock tailings

impoundments built with upstream dikes (e.g., Vick, 1990; Aubertin et al. 2002a,b, 2011, 2021; Jahanbakhshzadeh and Aubertin, 2022). The downstream slope varies between 7H:1V (θ = 8.13˚) and 12H:1V (θ = 4.76˚), the height of the impoundment ranges between 20 m and 50 m, the width of the inclusions varies between 12 (m) to 25 (m) and spacing between 55 (m) to 155 (m).

Figure 5.1 shows the geometry and material zone distribution of the reference case with a downstream slope of 8H:1V (θ = 7.12˚) and a height of 40 m, which includes two 12-m wide waste rock inclusions with a 120-m edge-to-edge spacing. The foundation of the impoundment consists of a 5-m-thick layer of hard bedrock. The dike rises and starter dike are composed of waste rock. The starter dike has a crest width of 19 m and a height of 10 m. Each dike raise is 2-metre high, with a 15-metre crest width and a 2H:1V side slope. The side slope of the dikes varies from 1.5H/1V to 4H/1V in the numerical analyses, depending on the height and global slope of the impoundment. The basic element size is 1 m by 1 m, determined using Kuhlemeyer and Lysmer's (1973) recommendation to achieve consistent transmission of ground motion frequencies up to 25 Hz. However, the mesh size is refined with smaller elements (down to 0.5 m) in zones where higher deformations and stresses are expected (e.g., under the dikes).

During the static phase of the analysis, the numerical model is subjected to fixed horizontal displacements on both sides, fixed vertical displacements at the base, and a fixed zero pore water pressure at the surface of the tailings and on the right side of the modelled impoundment (i.e., surface of dikes). The phreatic surface is considered at the top of the impoundment since the water level in active tailings impoundments is often at or above the surface of the tailings. This also represents a worst-case scenario for dynamic stability analysis. The boundary conditions for the dynamic analyses were adjusted to include a free field boundary on the sides and the application of ground motion at the base of the model in the form of applied horizontal accelerations. However, because a free field boundary condition cannot be applied directly to the PM4Sand model (Boulanger and Ziotopoulou, 2017), which is used for the tailings, the free field boundary condition on the left side of the impoundment is applied across a series of vertical elements modeled using the elastoplastic Mohr-Coulomb constitutive model (for both static and dynamic analyses). The fluid boundary conditions of the static phase were kept for the dynamic analyses. The seismic response of the various models is compared to a reference case, and the effect of each parameter on the performance indicator is addressed individually.

Table 5.1: Parameters considered in the parametric study

Parameter	Description	Values Used	Reference Case
θ	Downstream slope inclination angle of the impoundment (˚)	7H:1V (8.13˚), 8H:1V (7.12˚), 10H:1V (5.71˚), 12H:1V (4.76˚)	8H:1V (7.12˚)
H	Tailings thickness (m)	20 (m), 30 (m), 40 (m), 50 (m)	40 (m)
W	Width of the WRI (m)	12 (m), 16 (m), 20 (m), 25 (m)	12 (m)
S	Edge-to-edge spacing between WRI (m)	Between 55 (m) to 155 (m)	120 (m)

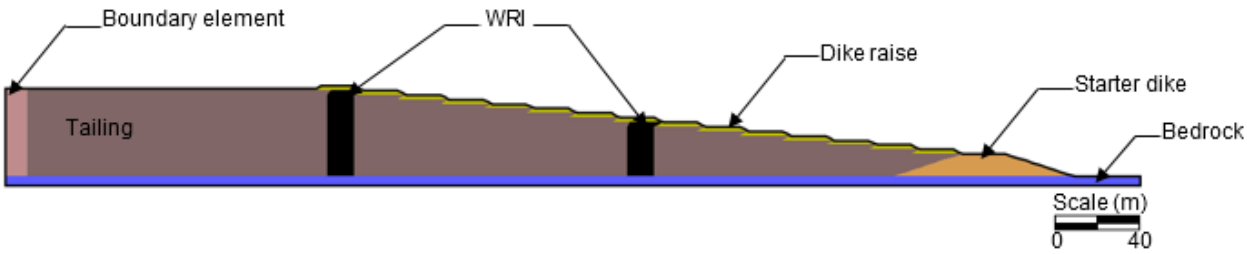

Figure 5.1: Reference case model for the tailings impoundment with a height of 40 m and external slope of 8H:1V (7.12˚) with two 12-m wide waste rock inclusions with 120-m edge-to-edge spacing

5.2.2 Material properties and constitutive models

5.2.2.1 Static analyses

The static stress distribution is calculated using the linear elastic perfectly plastic Mohr-Coulomb model for all materials, except for the bedrock which was considered linearly elastic. The material properties for the static phase are given in Table 5.2 (see further details in Zafarani 2022).

Hydro-geotechnical properties of tailings such as unit weight, density and porosity, and hydraulic conductivity are greatly influenced by the grain size distribution, method of deposition, age, and thickness (height) of the deposit within impoundments. Many studies on the characteristics of hard rock mine tailings have been undertaken using field and laboratory experiments (e.g., Vick, 1990; Aubertin et al. 1996, 2002a, 2002b, 2011, 2021; Bussière, 2007; L-Bolduc, 2012; Poncelet, 2012; Contreras Romero, 2013; Grimard et al., 2021; Jahanbakhshzadeh and Aubertin, 2022). Investigations on hard rock tailings from the western Quebec mining region by James (2009), Poncelet (2012), Contreras (2013), and Essayad and Aubertin (2021) indicate that the density index (I_d) of normally consolidated tailings typically varies between 40% and 70%, for vertical effective stresses less than about 400 kPa. The effect of the tailings density index on the seismic response of the model is taken into account in this numerical investigation. Based on these studies, two representative values of 60% and 53% were considered for the density index of normally consolidated tailings in the impoundment. The tailings saturated hydraulic conductivity, k_{sat}, is a function of the density index (or porosity) and particle size distribution. For the numerical modeling of the tailings values of k_{sat} of 5.8×10^{-8} m/s and 7.5×10^{-8} m/s were used for the density index of 60% and 53%, respectively, based on experimental measurements and predictive models for these and similar tailings (e.g., Mbonimpa et al., 2002; Bussière, 2007; Essayad, 2015). The shear modulus, G, of tailings is defined based on in-situ shear wave velocity measurements and estimated in-situ density (Grimard et al., 2021). An average Poisson ratio, υ, of 0.3 is used for tailings with a density index of 60% and 53%; this value was obtained from the K_o-consistency relationship with the internal friction angle (Frederico and Elia, 2009; Duncan and Bursey, 2013; Falaknaz et al. 2015; Yang et al. 2018).

The dry unit weight (20 kN/m^3) and saturated hydraulic conductivity (10^{-3}m/s) of the waste rock in the inclusions and raised dikes are based on typical values published for hard rock mines (e.g., Aubertin et al., 2013; Peregoedova et al., 2013; Maknoon, 2016; Essayad et al., 2018; Martin and Aubertin, 2019). The shear and bulk moduli of waste rock are determined using the following equations proposed for granular materials by Seed et al. (1984) and Rollins et al. (1998), as a function of the effective vertical stress σ'_v (kPa):

$$G = 55000.(0.6.\sigma'_v)^{0.5} \quad (5.1)$$

$$K = 2.3833.G \quad (5.2)$$

Minimum values of 3.1×10^5 kPa and 7.4×10^5 kPa are considered for shear and bulk moduli, respectively based on previous studies (e.g., James 2009; Ferdosi et al 2015a; 2015b). The starter dike material has comparable properties, with the exception of its porosity and saturated hydraulic conductivity, which are 0.2 and 10^{-2} m/s, respectively. The hydro-geotechnical parameters of bedrock layer are based on values provided by Goodman (1989) and Wyllie and Mah (2004).

Previous studies have shown that the dilation angle (ψ) of granular material under shear is proportional to its density index and confining pressure (Vaid et al., 1981). For a non-associated flow rule, the value of ψ is typically much smaller than the value of the internal friction angle. When employing the Mohr-Coulomb elasto-plastic model to evaluate the behavior and stability of soil structures it is generally conservative to adopt a zero dilation angle (corresponding to the critical state).

Table 5.2: Material properties for the static phase analysis

Properties	Tailings		Dikes (WRI)	Starter dike	Bedrock
Density index (I_d)	60%	53%	-	-	-
Dry unit weight, $\gamma_{dry}(\frac{kN}{m^3})$	16.5	16	20	20	22
Effective friction angle, $\boldsymbol{\varphi'}$(°)	35	34.5	45	45	-
Effective cohesion, $\boldsymbol{c'(kPa)}$	0	0	0	0	-
Dilation angle, ψ(°)	0	0	0	0	-
Porosity, $\boldsymbol{n}$	0.4	0.45	0.25	0.2	0.1

Shear Moduli, $\boldsymbol{G}$ ($\boldsymbol{kPa}$)	$113*10^3$	$115*10^3$	Varied[1]	$3.1*10^5$	$13.5*10^6$
Bulk Moduli, $\boldsymbol{K}$ ($\boldsymbol{kPa}$)	$300*10^3$	$305*10^3$	Varied[1]	$7.4*10^5$	$29.2*10^6$
Hydraulic conductivity, $\boldsymbol{k_{sat}}(m/s)$	$5.8*10^{-8}$	$7.51*10^{-8}$	10^{-3}	10^{-2}	$5*10^{-8}$

[1] Equations [5.1] and [5.2]

5.2.2.2 Dynamic analyses

The PM4Sand model (Boulanger and Ziotopoulou, 2017) is used to simulate the seismic behavior of tailings. This constitutive model is a critical-state compatible, stress-ratio based, bounding surface plasticity model developed for sand, based on the Dafalias and Manzari (2004) model. The density index, I_d (or relative density D_r in Boulanger and Ziotopoulou, 2017), shear modulus coefficient, G_0, and contraction rate parameter, h_{p0}, are the three primary parameters in the PM4Sand model. Calibration of the primary parameters is required, based on field and experimental soil conditions. The model includes 21 secondary parameters that, can also be adjusted from their default values to provide a material-specific calibration, depending on the information (data) available. The calibration of the PM4Sand model for hard-rock tailings provided by Contreras (2022) is applied in this investigation. The PM4Sand model primary and secondary parameters were determined using laboratory cycling testing results and field measurements, for density indexes ranging from 40% to 89%. Contreras (2022) has validated the calibration by comparing modeled stress-strain curves and pore pressure response to laboratory test data. Table 5.3 presents the values used to model the dynamic behavior of tailings; only the parameters that vary from the default calibration published by Boulanger and Ziotopoulou (2017) are listed here; more details can be found in Contreras et al. (2022).

Table 5.3: PM4Sand model parameters for the tailings (Contreras et al., 2022)

Parameter identification	Symbol	Calibrated value
Density index (D_r in Boulanger and Ziotopoulou (2017)); Primary parameter	I_d	0.6, 0.53
Shear modulus coefficient; Primary parameter	G_o	502.5
Contraction rate parameter; Primary parameter	h_{po}	0.55
Minimum void ratio	e_{min}	0.49
Maximum void ratio	e_{max}	1.1
Bounding surface parameter	n^b	0.7
Fabric growth parameter	c_z	150
Critical state friction angle (°)	φ'_{cv}	35
Modulus degradation factor	C_{GD}	2.5
Critical state line parameter	Q	12.7
Critical state line parameter	R	5.4

5.2.2.3 Damping parameters

For the materials simulated with the Mohr-Coulomb elasto-plastic model, the Hysteretic Sigmodial model-sig3 implemented in FLAC (Itasca, 2016) is also applied to induce hysteretic damping (i.e., waste rock inclusions, raised dikes, starter dike, boundary element). This Sigmoidal model is defined by three non-dimensional parameters: *a*, *b*, and x_0. Ferdosi (2015) calibrated this model using Rollins et al. (1998) degradation curves for a gravelly soil and obtained the following values for *a*, *b*, and x_0: 1.02, -0.698, and -1.45.

Hysteretic damping of nonlinear constitutive models is nil at low strains. To incorporate small-strain damping, mass and stiffness-proportional Rayleigh damping (Rayleigh and Lindsay, 1945) is used. The corresponding mass and stiffness-proportional damping constants have been selected to match the desired small-strain damping, ξ_{min} (i.e., 2%), at a given predominant frequency (f_{min}), which is considered the system's mean frequency. This is computed using a Fourier analysis of the free vibration response of the model with elastic properties (Kishi et al., 1987). The bedrock was assigned the same damping parameters so that it does not amplify or attenuate the motion.

5.2.3 Input earthquake ground motions

Ten earthquake ground motion recordings from the NGA-West2 (Ancheta et al. 2013) and NGA-East (Goulet et al. 2014) databases, included in Pacific Earthquake Engineering Research Center (PEER) Strong Motion Database, (2019), were selected to analyze earthquake-induced response of the impoundments, with an emphasis on horizontal displacements. The response spectra of these records are shown in Figure 5.2, and Table 5.4 identifies their corresponding characteristics. Ground motions 1 through 6 have been amplitude-scaled to assess the effect of intensity level on the horizontal displacements. Ground motion 10 (Mineral) has a lower intensity than the other movements, so the effect of a less severe ground motion on the system can be evaluated. The recordings are characterized by predominant frequencies (F_p) ranging from 1.79 Hz to 25 Hz, peak ground acceleration (PGA) ranging from 1.02 m/s^2 to 4.87 m/s^2, and velocity spectrum intensity (VSI) ranging from 0.17 m to 2.5 m.

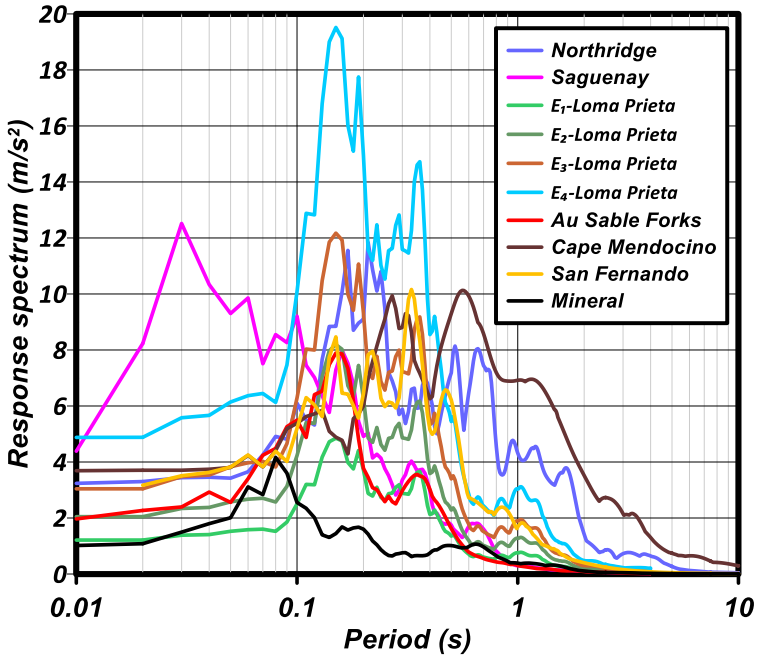

Figure 5.2: Response spectra of the input ground motions (PEER Strong Motion Database, 2019)

Table 5.4: Input ground motion parameters (Ancheta et al. 2013; Goulet et al. 2014)

#	Earthquake	M_W	PGA (m/s^2)	VSI (m)	PGV (m/s)	F_p (Hz)
1	Northridge	6.69	3.23	1.6	0.35	4.55
2	Saguenay	5.9	4.38	0.3	0.08	25
3	E_1-Loma Prieta	6.93	1.21	0.24	0.06	6.5
4	E_2-Loma Prieta	6.93	2.04	0.41	0.10	6.5
5	E_3-Loma Prieta	6.93	3.04	0.61	0.15	6.5
6	E_4-Loma Prieta	6.93	4.87	0.98	0.25	6.5

7	Au Sable Forks	4.99	1.96	0.22	0.06	6.25
8	Cape Mendocino	7.01	3.68	2.5	0.09	1.79
9	San Fernando	6.61	3.13	0.66	0.17	3.13
10	Mineral	5.74	1.02	0.17	0.04	12.5

Definition of symbols: M_w is the moment magnitude; *PGA* is peak ground acceleration ($PGA = \max |a(t)|$, where $a(t)$ is acceleration time history in m/s^2); *VSI* is velocity spectrum intensity($VSI = \int_{0.1}^{0.5} s_v(\xi = 5\%, T)dT$, where s_v is velocity spectra in m/s, ξ is damping ratio, T is the dominant period of response spectrum in seconds); and *PGV* is Peak ground velocity ($PGV = \max |v(t)|$, where $v(t)$ is velocity time history in m/s).

5.2.4 Performance indicator

The seismic response of each model is quantified using specific performance indicators to facilitate the comparison between the different cases and establish correlations with the different parameters. In this paper, the impoundment's behavior is assessed using the average value of the normalized horizontal displacement of all nodal points along the downstream slope (SAR_x), defined by the following equation:

$$SAR_x = Average\left(\frac{X_{disp_i}}{H_i}\right) \tag{5.3}$$

Where X_{disp_i} represents the horizontal displacement along the downstream slope at a nodal point *i* at the end of the shaking, and H_i defines the initial height above the bedrock layer at the same node.

5.3 Development of correlations

The effects of the downstream slope, height of the impoundment, intensity of seismic loading, configuration of WRI, and tailings density index on the seismic behavior of the unreinforced and reinforced models were quantified using the results of the numerical simulations. The effect of each parameter is assessed individually using SAR_x, based on Eq. (5.3), which represents the average (normalized) horizontal displacement of the downstream slope. The numerical results are

combined to develop a performance function that links the value of SAR_x, to the influence factors investigated. The performance of the developed relationship is evaluated using regression analysis in terms of normal distribution of residuals. The performance function development is detailed in the followings.

5.3.1 Slope inclination and tailings thickness

The effects of the external slope inclination and height of the tailings impoundment on the seismic behavior of the unreinforced and reinforced models were evaluated by simulating the behavior of impoundments with and without WRI with an external slope inclination angle (θ) ranging from 8.13° (7H:1V) to 4.76° (12H:1V) and heights (H) between 20 m and 50 m, under the E_3-Loma ground motion. The initial density index of tailings was maintained at 60% in these simulations.

The non-dimensional volume-spacing index, W_{vs}, was used to assess the effect of the inclusions' configuration on the seismic response of the impoundment; this index is defined by the following relationship:

$$W_{vs} = V_r \cdot (1 - \frac{S_1}{S_{max}}) \tag{5.4}$$

where V_r is the volume ratio (Volume of WRI/Volume of tailings under the external slope of the impoundment), S_1 is the spacing between the starter dike and the edge of the closest inclusion, and S_{max} is the spacing between the starter dike and the edge of the farthest waste rock inclusion in the model. The additional WRI have equal edge-to-edge spacing, which is determined based on the desired configuration.

The average value of the normalized horizontal displacements along the downstream slope (SAR_x) has been calculated to evaluate the effect of geometric characteristics on the seismic behavior of the impoundment., i.e., the slope inclination, height of the impoundment and inclusions configuration.

Simulations results with trend lines are presented in Figure 5.3 for the unreinforced and reinforced models with W_{vs} ranging between 0.07 and 0.23. The results presented in Figure 5.3a, for different inclination angles, show that the WRI can significantly reduce the horizontal displacement of the downstream slope. As an example, SAR_X is 44% for the case without inclusions and a slope

inclination of 7.12°, while it is 21% for the model with the lowest volume of WRI (W_{VS}=0.07); the reduction is even more pronounced for larger volume of waste rock. Note that some of the simulations of unreinforced and reinforced models with low volume of WRI (W_{Vs} values of 0.07, 0.09 and 0.11) stopped before the end of the ground motion due to high deformation and a lack of convergence. These configurations would lead to impoundment general failure due to high magnitude of deformation (more than 10 m horizontal displacement); these results are not included in Figure 5.3. This figure shows non-linear trendlines that, in general, show a decrease in SAR_x with an increase in the volume of inclusions (W_{Vs}) in the impoundment. However, the slope of the variation trend lines is steeper for the lower values of W_{vs}. The inclusions have a lesser effect on the value of SAR_x for the shallower downstream slope inclinations of 4.76˚ and 5.71˚, but they have a more significant effect for the two steeper slopes (i.e., 8.13˚ and 7.12˚). For example, for W_{vs} = 0.07, the SAR_x value decreases from about 23% to 11% with a decrease of downstream slope inclination from 7.12° to 5.71°, while the reduction of SAR_x for the impoundment models with W_{vs} = 0.23 is much less significant (from 5% to 3%) for the same decrease in slope inclination. This indicates that there is an optimal configuration of WRI beyond which adding more waste rock has a limited influence on the displacements. The same tendencies have also been observed in previous investigations conducted with the UBCSand model by Ferdosi et al. (2015a; 2015b) (see also Zafarani et al., 2020, 2022a).

The effects of impoundment height and WRI configuration on the seismic behavior of tailings impoundments subjected to the E_3-Loma ground motion are illustrated in Figure 5.3b, based on the variation of the SAR_x as a function of the impoundment heights of 20 m, 30 m, 40 m, and 50 m, for a spacing-volume index (W_{vs}) ranging from 0.07 to 0.23 and a downstream slope inclination of 7.12˚. The results indicate that for the various configurations with heights of 20 m and 30 m, the change in SAR_x is small due to the modest horizontal displacements. However, increasing the impoundment height to 40 m results in substantially higher displacements, with SAR_x increasing up to 20% for the model with the least reinforcement (W_{vs}=0.07). Overall, the change in SAR_x values caused by increasing the height is less pronounced for models with a high volume of reinforcement, such as impoundments with a volume-spacing index of 0.2 and 0.23, compared to less reinforced impoundments (such as Wvs=0.09).

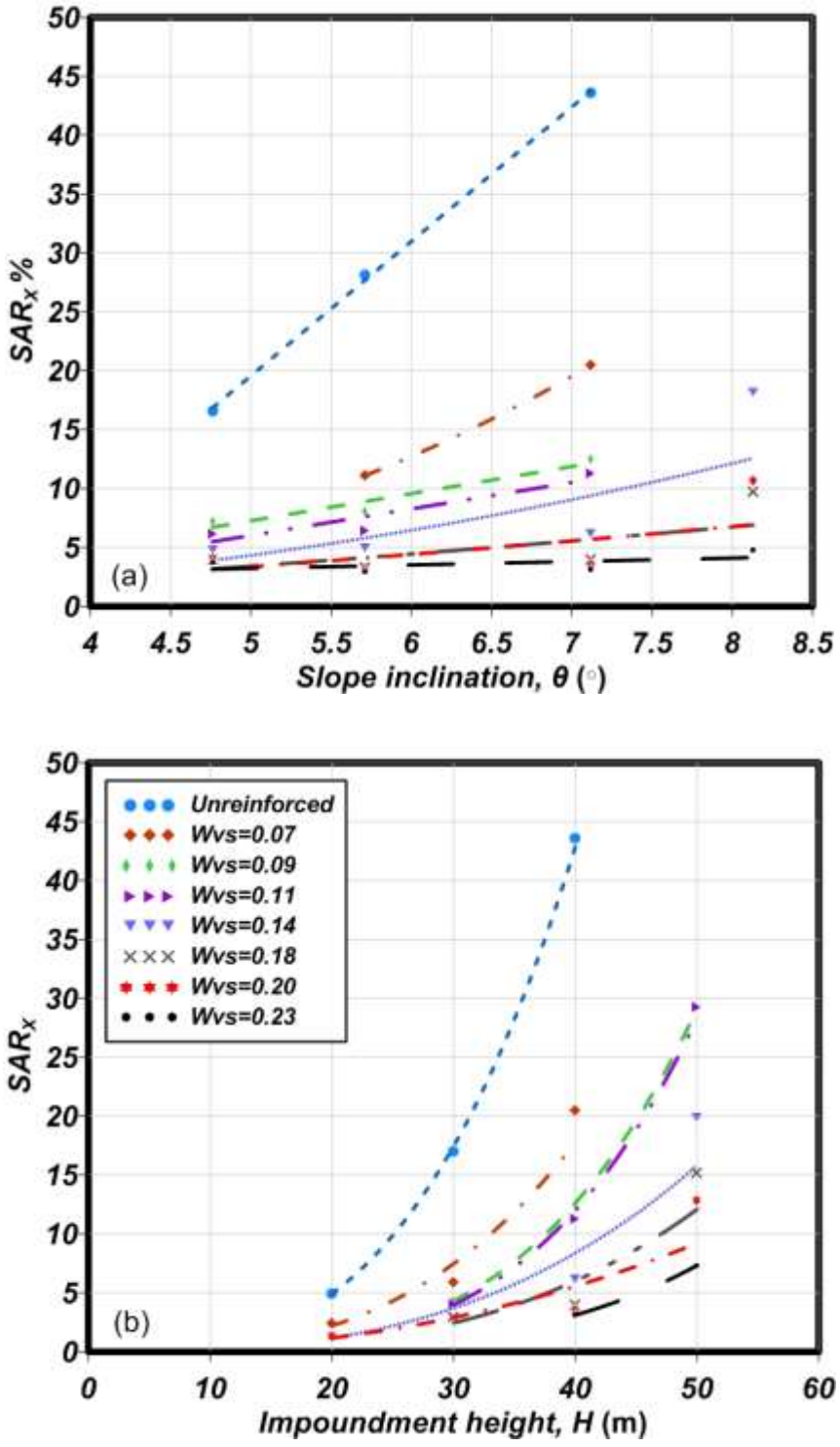

Figure 5.3: Variation of the SAR_x value as a function of (a) downstream slope inclination, θ; (b) impoundment height for the unreinforced and reinforced impoundment models with various configurations of WRI

5.3.2 Seismic loading intensity

Impoundment design should take into account the seismic response of the models under a variety of ground motions that reflect the expected seismic loading characteristics. In performance-based earthquake engineering, different intensity measures (*IM*s) can be employed to quantify seismic loading. An *IM* is considered optimum for the analysis when it leads to low dispersion in the simulated seismic response of the structure (Shome and Cornell, 1999; Chen et al., 2015; Zhang et al., 2020). When optimum *IM*s are used to analyze the seismic behavior of a structure, the results are generally within a limited confidence interval, giving an acceptable (targeted) degree of confidence with fewer calculations (Kramer and Mitchell, 2006).

Zafarani et al. (2022b) investigated various options to determine the optimum *IM*s for simulating the seismic response of tailings impoundments with and without waste rock inclusions. The simulation results and statistical analysis showed that the combination of a velocity related *IM*, such as the velocity spectrum intensity, *VSI* (Housner, 1952), or peak ground velocity, *PGV* (Kramer, 1996), with the commonly used peak ground acceleration, *PGA*, leads to optimum intensity measures. On the basis of these findings, a vector-valued *IM* composed of *VSI* and *PGA* is applied in this investigation to quantify the intensity of the motions presented in Figure 5.2. The velocity spectrum intensity (m) is defined by the following equation:

$$VSI = \int_{0.1}^{0.5} s_v(\xi = 5\%, T)dT \tag{5.5}$$

Where s_v is velocity spectra in m/s, ξ is the damping ratio, and T is the dominant period of response spectrum in seconds.

Figure 5.4 shows the variation trends for SAR_x as a function of the two selected components of the optimum vector *IM* (i.e., *VSI* and *PGA*) for unreinforced and reinforced models, for different earthquake loadings. In this figure, non-linear trend lines show how SAR_x decreases as inclusion volume (W_{Vs}) increases. Unreinforced configurations and models with lower values of W_{Vs}, however, have steeper variation trend line slopes. Simulation results indicate that the level of deformation of all the models under the low intensity earthquakes, such as E_1-Loma Prieta and Mineral recordings, is low (i.e., $SAR_x < 4\%$) and the impoundment model remains stable. The effect of W_{vs} on the value of SAR_x is thus limited for these lower intensities (i.e., *VS I* < 0.3 m, and *PGA*

< 1.5 m/s^2). The effect is however much more pronounced for higher levels of intensity. As seen in Figure 5.4, for the lowest volume of WRI (i.e., W_{vs}=0.07), an increase in *VSI* or *PGA* level leads to a major increase in the normalized horizontal displacement (SAR_x) of the impoundments. Increasing the WRI volume appears to be most beneficial for improving the seismic response at higher *VSI* (Figure 5.4a) and *PGA* (Figure 5.4b) levels, as the value of SAR_x decreases by a greater margin as W_{Vs} increases.

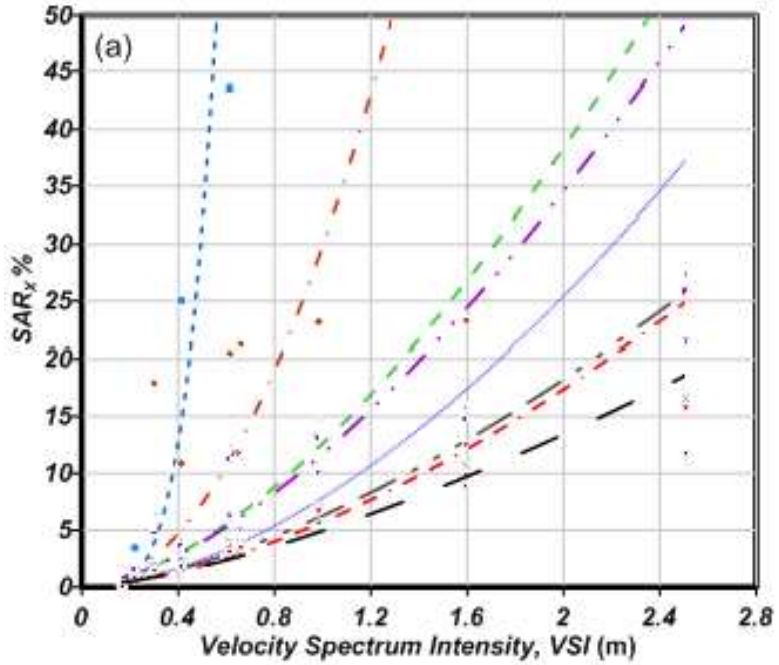

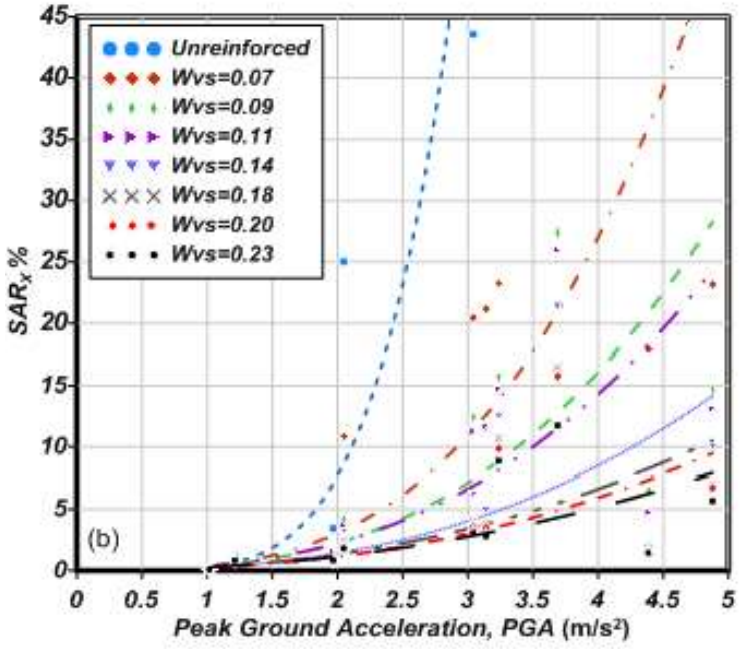

Figure 5.4: Variation of the SAR_x value as a function of (a)Velocity Spectrum Intensity, VSI; (b) Peak Ground Acceleration, PGA, for the unreinforced and reinforced impoundment models with various configurations of WRI

5.3.3 Tailings density

The effect of the density index (I_d) of the tailings (and related strength) on the seismic behavior of the unreinforced and reinforced models was evaluated by simulating the behavior of impoundments retaining tailings with a density index of 60% and 53%. Such increase in the density index leads to an increase in the Cyclic Resistance Ratio (*CRR*), as shown by various experimental results (e.g., Archambault-Alwin, 2017; Contreras, 2022, Jahanbakhshzadeh and Aubertin, 2022). The $CRR_{Mw=7.5}$ values, (i.e., the values of *CRR* to reach liquefaction, defined as an excess pore-water pressure ratio, r_u of 0.95 (Ishihara 1993; Karray et al. 2015) in 15 cycles, were obtained from cyclic strength curves obtained from the simulations of cyclic tests using the calibrated constitutive model. The simulations indicate that under a vertical effective stress of 100 kPa, the value of $CRR_{Mw=7.5}$ is 0.067 and 0.075 for a density index of 53% and 60%, respectively. These values are taken into account in the simulations conducted for developing performance correlations in the following.

5.3.4 Statistical analysis of simulation results

Based on concepts developed to assess liquefaction-induced deformations of earth structures (e.g., Travasarou and Bray, 2003; Bray and Travasarou, 2007; Bray and Macedo, 2018) and on the results of the simulations described above, several functional forms were investigated to correlate the earthquake-induced horizontal displacement of downstream slope of reinforced tailings impoundments (SAR_x) with the various parameters considered in the previous sections. The selected functional form for the proposed relationship can be expressed as:

(5.6)

$$ln(SAR_x) = a_1 + a_2 .\ ln(\theta) + a_3 .ln(H) + a_4 .\ ln(VSI) + a_5 .\ ln(PGA) + a_6.\ ln(W_{vs}) + a_7.\ ln(CRR_{Mw=7.5})$$

Where a_1 to a_7 are coefficients, θ is the slope inclination in degree, H is the tailings thickness in (m), VSI is the velocity spectrum intensity in (m), PGA is the peak ground acceleration in (m/s^2), W_{vs} is the volume-spacing index, and $CRR_{Mw=7.5}$ is the normalized cyclic resistance ratio at an effective stress of 100 kPa for an earthquake of magnitude 7.5.

Regression analyses were performed using the functional form of Eq.(5.6) and the simulation results presented in Figure 5.3 and Figure 5.4 (with additional details provided in Zafarani 2022). The calculated coefficients of Eq. (5.6) are presented in Table 5.5.

Table 5.5: Coefficients of Eq. (5.6)

Coefficient	a_1	a_2	a_3	a_4	a_5	a_6	a_7
Value	-35.867	1.575	0.863	0.985	0.798	-0.995	-11.215

The average normalized horizontal displacement of downstream slope (SAR_x) obtained with this functional relationship (Eq. 5.6) is compared to the SAR_x values obtained in the simulations for all cases in Figure 5.5. This figure indicated that in general, the estimates given by the proposed relationship agree well with the numerical simulations. Based on the results, the equation can

accurately estimate SAR_x. Overall, Eq.(5.6) represents the observed trends given by the simulation results for a wide range of deformations that encompasses key situations for engineering.

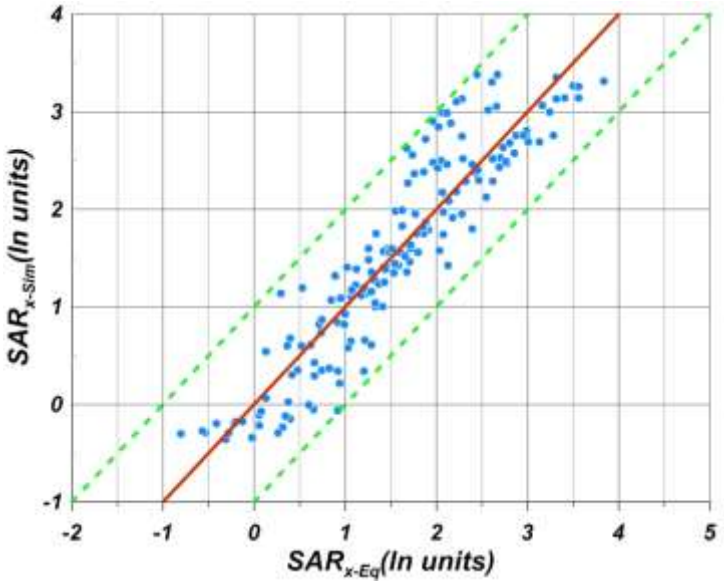

Figure 5.5: Comparison of SAR_x value estimated using Eq. (5.6) and calculated through numerical simulations (Eq.5.3)

A study of residuals is frequently used to evaluate the performance of a regression model and assess any potential bias (Anscombe, 1961; Anscombe and Tukey, 1963; Cook and Weisberg, 1982). The residuals between the simulated (SAR_{x-Sim}) and estimated (SAR_{x-Eq}) values of SAR_x is computing as follows:

$$Residual = \ln(SAR_{x-Sim}) - \ln(SAR_{x-Eq}) \tag{5.7}$$

The main assumptions for the general multiple linear regression model include the normal distribution of residuals with and average value of zero. These assumptions are validated by plotting the residuals as a function of the estimated values (i.e., SAR_{x-Eq}) and independent variables (such as θ, H, etc.). If the selected model is adequate, the residuals have a mean close to 0, and are symmetrically distributed over a horizontal band of points about the origin (Anscombe and Tukey, 1963; Cook and Weisberg, 1982). Positive residuals indicate an under-estimation of the SAR_x, while negative residuals imply an over-estimation. Figure 5.6 shows the calculated

residuals for the specific influence factors (parameters) included in Eq. (5.6), i.e. (a) slope inclination, (b) impoundment height, (c) *VSI*, (d) *PGA*, (e) $CRR_{Mw=7.5}$, and (f) W_{vs}. The 25th and 75th percentiles of the dataset are represented by the box limits, while whiskers limits are specified as 1.5 of the interquartile range (*IQR*), and the mean is represented by a horizontal line across the *IQR*. The variations of SAR_x residuals versus slope inclination and impoundment height show relatively symmetrical distribution of residuals along a thin horizontal band with an average close to 0 for typical downstream slopes of 12H:1V, 10H:1V, and 8H:1V and heights of 30 m and 40 m. However, the results show an unsymmetrical distribution of residuals with an average value of 0.8 (i.e., underestimating tendency) for models with downstream slopes of 7H:1V and heights of 20 m and 50 m. This underestimation for the calculated values with a 20-meter-height is not significant, as it has already been demonstrated that the WRI configuration has a limited influence on their seismic behavior. The simulation results in Figure 5.3 showed a significant magnitude of deformation and variability in the SAR_x values for the steepest slope (7H:1V) and highest tailings elevation (50 m), indicating that these cases could lead to potential failure. This may explain, at least in part, the differences between the SAR_x value obtained from the simulations and from Eq (5.6). The residual plots of *VSI* and *PGA* show high variability in the residuals, with a tendency towards over-predicting SAR_x for a majority of ground motions. The range of residuals appears to meet the normal distribution assumption for E_1-Loma, E_2-Loma, E_3-Loma, Mineral and San Fernando ground motions with an average value close to 0. However, the equation estimates the SAR_x values with greater uncertainty for ground motions with higher intensity levels such as Cape Mendocino, E_4-Loma, Northridge, and Saguenay. This can be associated to the considerable variability in the seismic response under these ground motions, as seen in Figure 5.4. The residuals of SAR_x vs. tailings density index (i.e. through the normalized CRR) and W_{vs} demonstrate no significant systematic bias for various WRI configurations.

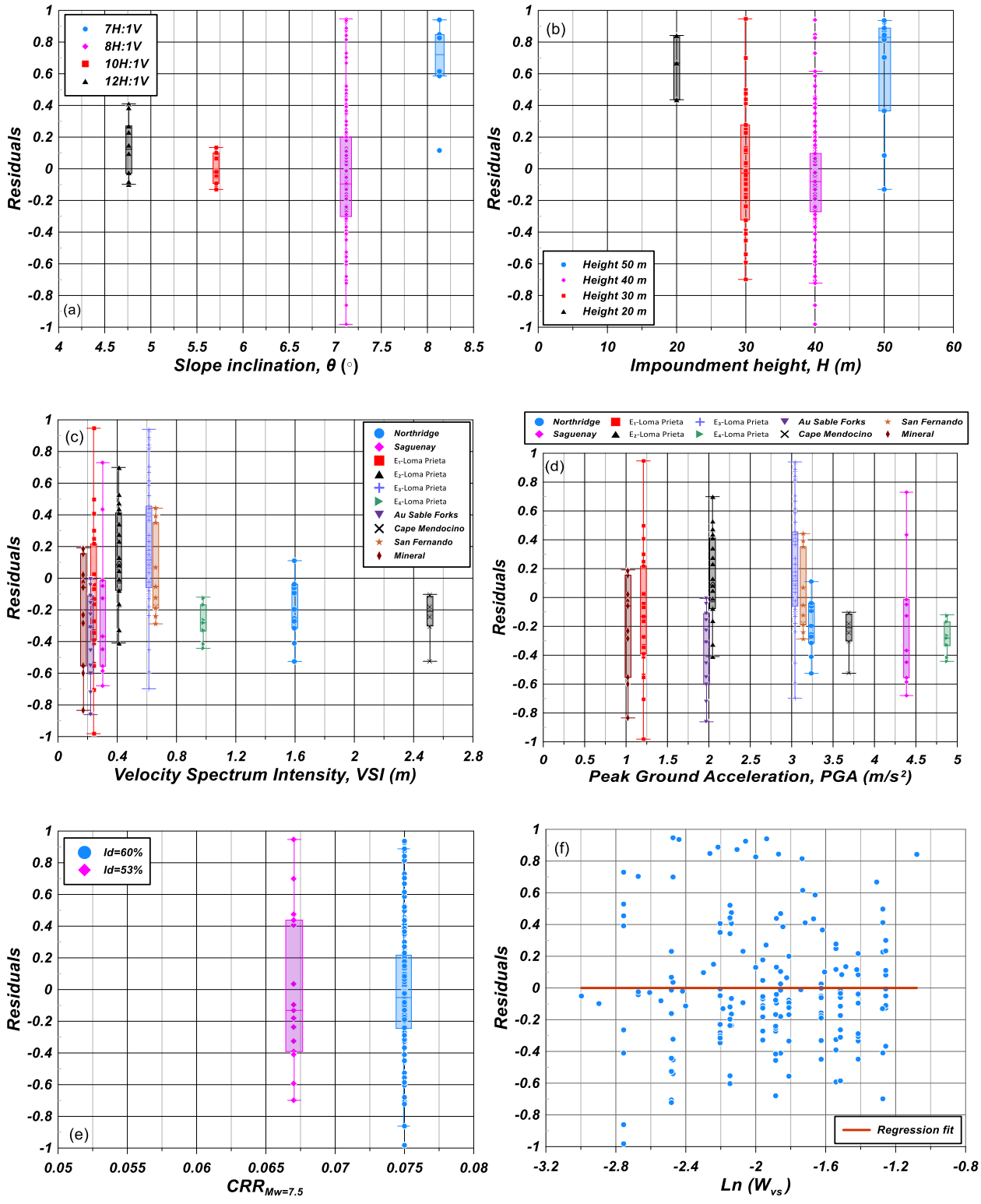

Figure 5.6: Distribution of residuals of Eq. 5.6 versus (a) slope inclination, (b) impoundment height, (c) VSI, (d) PGA, (e) CRR $_{Mw=7.5}$, and (f) W_{vs}

5.4 Analysis and Discussion

The evaluation of the performance and serviceability of tailings impoundments is of primary interest and concern for the mining industry. This assessment should use seismic design principles and screening-level analysis to identify structures that are prone to failure. Screening-level assessments of the seismic behavior of tailings impoundments are typically based on an estimate of earthquake-induced displacements.

Jibson and Michael (2009) applied the California Geological Survey's (2008) recommendations to identify hazard categories based on the magnitude of earthquake-induced permanent displacements. The guidelines suggest that displacements of 0–15 cm are unlikely to lead to substantial landslide movement and damage; displacements of 15–100 cm might be serious enough to cause strength loss and apparent instability; and displacements exceeding 100 cm are very likely to correspond to devastating landslides. Such displacement limits apply mostly to larger, deeper landslides; smaller, shallower landslides are usually induced at considerably lower displacement levels, approximately 2-15 cm (Jibson, 2011). It should be noted that these ranges are provided for landslides in natural slopes. However, these guidelines can be used in more critical projects such as tailings impoundment as preliminary evaluations and screening methods prior to more sophisticated analysis.

To further evaluate the performance of the impoundments with WRI, the calculated values of SAR_x are plotted as a function of the maximum horizontal displacements in Figure 5.7. Based on Jibson and Michael's (2009) and the California Geological Survey's (2008) guidelines, and using the correlation between horizontal displacement and SAR_x shown in Figure 5.7, three levels of downstream horizontal displacement based on SAR_x can be identified: stable ($SAR_x \leq 0.47$), moderate damage ($0.47 < SAR_x \leq 3$), and severe damage ($SAR_x > 3$).

It should be emphasized that these hazard categories based on SAR_x are defined based on the guidelines provided for landslides in natural slopes cases and may not apply directly to tailings impoundments with WRI. The suggested classification should be checked and extended for other situations with results from additional project-specific nonlinear dynamic simulations.

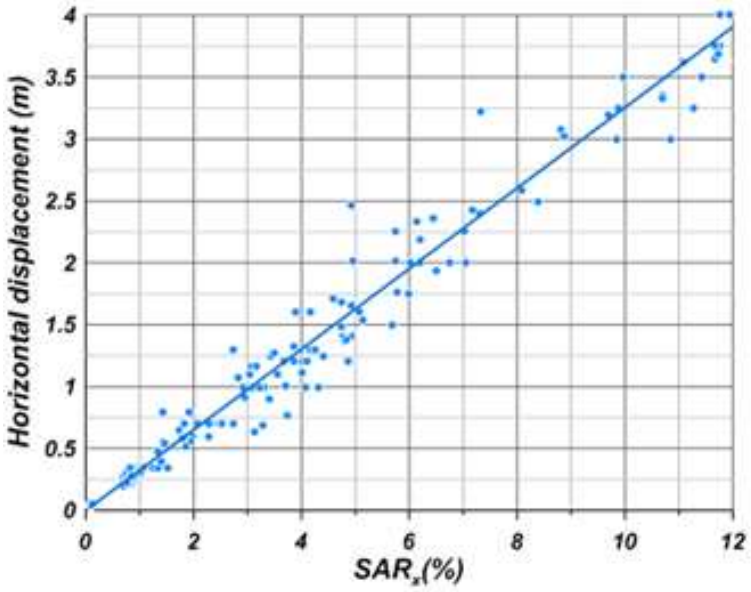

Figure 5.7: Variation of the horizontal maximum displacement as a function of SAR_x with a linear regression

The proposed method for seismic stability of tailings impoundments should be useful in engineering practice to help complement and improve deterministic and probabilistic assessment. It should be recalled however that the analysis of earth structures behavior, particularly for highly nonlinear conditions such as soil liquefaction and its associated lateral displacement, is fraught with uncertainty due to the inherent variability of soil parameters, site conditions, and seismic loadings. The proposed relationship is based on the results of dynamic numerical simulations conducted for a specific set of earthquake ground motions, geometries and material properties, with uniform material conditions or regular configurations involving waste rock inclusions and upstream dikes. Given the novelty of the WRI co-disposal method, and in light of these uncertainties, more work would be needed to further develop probabilistic prediction models for the optimal configuration of waste rock inclusions in tailings impoundments for a wider variety of conditions and properties.

5.5 Conclusion

This paper presents a numerical modelling approach for assessing liquefaction-induced displacement of tailings impoundments reinforced with waste rock inclusions. The methodology is

based on the results of over 180 nonlinear dynamic numerical simulations performed with the FLAC software and the PM4Sand model assigned to tailings. A performance relationship is used to correlate the level of displacement, expressed in terms of the average normalized horizontal displacement of downstream slope (SAR_x), as a function of the characteristics of the tailings impoundment, including slope inclination angle (θ), height (H), tailings density index (I_d), the characteristics of earthquake shaking, and the configuration of the WRI (W_{vs}). The effect of each parameter is evaluated individually and combined to assess the seismic response of the modeled impoundments.

Results of the simulations with different downstream slopes and heights show that the inclusion's configuration have a lesser influence on the seismic response of the model in terms of the SAR_x for the shallower downstream slope compared to the steeper slopes. Similarly, the results show that the effect of WRI is more pronounced for impoundments with a thicker deposit of tailings. The variation trends of the SAR_x versus the selected seismic loading vector *IM* components (i.e., *VSI* and *PGA*) indicate that the amount of deformation under low-intensity earthquakes remains relatively small and models are stable. As a result, the effect of the WRI's configuration on the value of SAR_x is relatively limited at lower intensities, but their reinforcement contribution is much more significantly at higher intensities.

Based on principles of liquefaction-induced deformations of earth structures and simulation results, an equation was developed to relate earthquake-induced horizontal displacement of reinforced tailings impoundments (SAR_x) with different factors of influence (i.e., parameters in the proposed equation). Comparing the estimated and simulated values of SAR_x shows that the estimates provided by the equation are generally consistent and follow the key trends given by the simulation results. The statistical residuals between the simulated and estimated values of SAR_x are used to determine the reliability of the developed equation. These indicate how the model response is affected by slope inclination and impoundment height. The loading parameters (*VSI* and *PGA*) lead to a larger uncertainty for ground motions with higher intensities due to the significant variation in seismic response under these ground motions.

Practitioners can use the proposed simplified approach to evaluate the seismic performance of tailings impoundments. The procedure should, however, be used in conjunction with the results of

project-specific nonlinear dynamic analyses. The suggested method should also help develop deterministic and probabilistic prediction models for assessing seismic stability of tailings impoundments.

5.6 Acknowledgements

The authors acknowledge the financial support from NSERC and from the industrial partners of the Research Institute on Mines and the Environment (RIME UQAT-Polytechnique; http://rime-irme.ca/en).

5.7 References

Ancheta TD, Darragh RB, Stewart JP, Seyhan E, Silva WJ, Chiou B S, Donahue JL (2013) Peer NGA-West2 database.

Anscombe FJ (1961) Examination of residuals. Proceedings 4th Berkeley Symposium. Mathematics, Statistics, Probability 1, 1–36

Anscombe FJ, Tukey JW (1963) Analysis of residuals. Technometrics 5, 141–160

Archambault-Alwin X (2017) Évaluation du comportement dynamique et de la résistance cyclique des résidus miniers. M.Sc.A. thesis, Département des génies civil, géologique et des mines, Polytechnique Montréal, Montréal, QC, Canada.

Aubertin M, Mbonimpa M, Jolette D, Bussière B., Chapuis R, James M, Riffon O (2002a) Stabilité géotechnique des ouvrages de retenue pour les résidus miniers : problèmes persistants et méthodes de contrôle. Défis and Perspectives : Symposium sur l'environnement et les mines, Rouyn-Noranda, Développement Économique Canada/Ministère des Ressources Naturelles du Québec/CIM. Comptes-Rendus sur CD ROM.

Aubertin M, Bussière B, Bernier L (2002b) Environnement et gestion des rejets miniers [CD-ROM Manual]. Montréal: Presses Internationales Polytechnique.

Aubertin M, Bussière B, James M, Martin V, Pépin N, Mbonimpa M, Chapuis RP (2011) Vers une mise à jour des critères de stabilité géotechnique pour la conception des ouvrages de retenue de

résidus miniers. Symposium sur les Mines et l'Environnement, Rouyn-Noranda, Québec, 6-9 Novembre 2011.

Aubertin M, James M, Maknoon M, Bussière B (2013) Recommandations pour améliorer le comportement hydrogéotechnique des haldes à stériles. GeoMontreal 2013-Geosciences for Sustainability, 66th CGS Conference, Montreal, QC, 8 p.

Aubertin M, Jahanbakhshzadeh A, Yniesta S (2019) The effect of waste rock inclusions on the seismic stability of a tailings impoundment. Proceedings of 7th International Conference on Earthquake Geotechnical Engineering.

Aubertin M, Jahanbakshzadeh A, Saleh-Mbemba F, Yniesta S, Pednault C (2021) General guidelines for the design and construction of waste rock inclusions in tailings impoundment. Paper presented at the 74th Canadian Geotechnical Conference (Geo Niagara 2021), Niagara Falls, Ontario.

Azam S, Li Q (2010) Tailings dam failures: a review of the last one hundred years. Geotechnical news, 28(4), pp. 50-54.

Blight GE (2010) Geotechnical engineering for mine waste storage facilities. CRC Press.

Boulanger RW, Ziotopoulou K (2017) PM4Sand (Version 3.1): A sand plasticity model for earthquake engineering applications. Center for Geotechnical Modeling Report No. UCD/CGM-15/01, Department of Civil and Environmental Engineering, University of California, Davis, Calif.

Bray JD, Travasarou T (2007) Simplified procedure for estimating earthquake-induced deviatoric slope displacements. Journal of geotechnical and geoenvironmental engineering, 133(4), pp. 381-392.

Bray JD, Macedo J, Travasarou T (2018) Simplified procedure for estimating seismic slope displacements for subduction zone earthquakes. Journal of Geotechnical and Geoenvironmental Engineering, 144(3), 04017124.

Bussière B (2007) Hydro-Geotechnical properties of hard rock tailings from metal mines and emerging geo-environmental disposal approaches. Canadian Geotechnical Journal, 44(9): 1019-1052

Bussière B, and Aubertin M (1999) Clean tailings as cover material for preventing acid mine drainage: an in situ experiment. In Proceedings of Conference Mining and the Environment II, September 13–17, Sudbury, Canada, (vol. 1, p. pp 19–28).

California Geological Survey (2008) Guidelines for Evaluating and Mitigating Seismic Hazards in California. California Geological Survey Special Publication 117A. 98 pp.

Cook RD, Weisberg S (1982). Residuals and influence in regression. New York: Chapman and Hall.

Chen ZX, Cheng Y, Xiao Y, Lu L, Yang Y (2015) Intensity measures for seismic liquefaction hazard evaluation of sloping site. Journal of Central South University, 22(10), 3999-4018.

Contreras Romero CA (2013) Comportement dynamique du sol pulvérulent « résidus miniers ». M.Sc., thesis, Department of Civil, Geological, and Mining Engineering, Ecole Polytechnique de Montreal, Montreal, QC.

Contreras Romero CA, Yniesta S, Aubertin M (2020) Seismic and post-seismic stability of tailings impoundments, considering the effect of reinforcement inclusions. Proc. 73rd Canadian Geotechnical Conference (GEOVirtual 2020).

Contreras CA (2022) Analyses numériques du comportement et de la stabilité sismique et post-sismique des parcs à résidus miniers, avec et sans inclusions de roche stérile, pour divers aléas relatifs aux régions minières de l'est du Canada. Ph.D. thesis, Civil, Geological and Mining Engineering Department, Polytechnique Montréal, Montréal, QC, Canada

Contreras Romero CA, Yniesta S, Jahanbakhshzadeh A, Aubertin M (2022a) Calibration of the PM4Sand Model for Hard-Rock Mine Tailings Based on Laboratory and Field Tests. Submitted to the Canadian Geotechnical Journal.

Dafalias YF, Manzari MT (2004) Simple Plasticity Sand Model Accounting for Fabric Change Effects. Journal of Engineering Mechanics, Vol. 130, No. 6, pp 622-634.

Davies M (2002) Tailings impoundment failures: are geotechnical engineers listening? Geotechnical News, 20(3), pp. 31-36.

Duncan JM, Bursey A (2013) Soil modulus correlations. In Foundation Engineering in the Face of Uncertainty: Honoring Fred H. Kulhawy, 321-336. ASCE.

Essayad K (2015) Development of experimental protocols for the characterization of saturated and unsaturated tailings consolidation from columns compression tests (text in French), Master thesis, Ecole Polytechnique de Montreal.

Essayad K, Pabst T, Aubertin M, Chapuis RP (2018) An experimental study of the movement of tailings through waste rock inclusions. Paper presented at the 71st Canadian Geotechnical Conference (GeoEdmonton 2018), Edmonton, Alberta.

Essayad K., Aubertin M (2021) Consolidation of hard rock tailings under positive and negative pore-water pressures: Testing procedures and experimental results. Canadian Geotechnical Journal, 58(1), 49-65.

Falaknaz N, Aubertin M, Li L (2015) Numerical investigation of the geomechanical response of adjacent backfilled stopes. Can Geotech J 52(10):1507–1525

Federico A, Elia G (2009) At-rest earth pressure coefficient and Poisson's ratio in normally consolidated soils. Proc. 17th International Conference on Soil Mechanics and Geotechnical Engineering, Alexandria, Egypt.

Ferdosi B (2015) A numerical investigation of the seismic response of tailings impoundments reinforced with waste rock inclusions. Ph.D. Thesis, Ecole Polytechnique de Montreal.

Ferdosi B, James M, Aubertin M (2015a) Investigation of the effect of waste rock inclusions configuration on the seismic performance of a tailings impoundment. Geotechnical Geological Engineering Journal. 33, pp.1519-1537.

Ferdosi B, James M, Aubertin M (2015b) Effect of waste rock inclusions on the seismic stability of an upstream raised tailings impoundment: a numerical investigation. Canadian Geotechnical Journal: 52(12), pp. 1930-1944.

Goodman RE (1989) Introduction to Rock Mechanics. John Wiley and Sons Inc.

Goulet CA et al (2014) PEER NGA-east database. Berkeley, CA: Pacific Earthquake Engineering Research Center.

Grimard LP, Karray M, James M, Aubertin M (2021) Consolidation characteristics of hydraulically deposited tailings obtained from shear wave velocity (Vs) measurements in triaxial and oedometric cells with piezoelectric ring-actuator technique (P-RAT). Canadian Geotechnical Journal, 58(2), 281-294.

Harder LF, Stewart JP (1996) Failure of Tapo Canyon tailings dam. Journal of Performance of Constructed Facilities, ASCE, 10(5): 109–114.

Housner GW, Jennings PC (1964) Generation of artificial earthquakes. In proceedings American Society of Civil Engineers 90, 113–150

Ishihara K (1993) Liquefaction and flow failure during earthquakes. Géotechnique, 43, pp. 351-451.

Itasca Consulting Group Inc (Itasca) (2016) FLAC – Fast Lagrangian Analysis of Continua. Version 8.00. [computer software and user manual]. Minneapolis MN: Itasca Consulting Group, Inc.

Jahanbakhshzadeh A, Aubertin M, Yniesta S, Zafarani A (2019) On the seismic response of tailings dikes constructed with the upstream and center-line methods. Paper presented at the 72nd Canadian Geotechnical Conference (GEO 2019), St. John's.

Jahanbakhshzadeh A, Aubertin M (2022) Main results from an extensive geotechnical characterization of hard rock tailings from an open pit gold mine. In preparation for 75th CGS Conference, GeoCalgary 2022.

James M (2009) The use of waste rock inclusions to control the effect of liquefaction in tailings impoundments. Ph.D. Thesis, Department of Civil, Geological, and Mining Engineering, Ecole Polytechnique de Montreal, Montreal, QC.

James M, Aubertin M (2009) The use of waste rock inclusions in tailings impoundments to improve geotechnical and environmental performance. In Proceedings, Tailings and Mine Waste 2009, Banff, Alta. pp. 233–245.

James M, Aubertin M (2010) On the dynamic response of tailings and the stability of tailings impoundments for hard rock mines. Geotechnical News, 23(3), 39-43.

James M, Aubertin M (2012) The use of waste rock inclusions to improve the seismic stability of tailings impoundments. GeoCongress 2012, Okland, 22-25 March 2012. American Society of Civil Engineers, pp. 4166-4175.

James M, Aubertin M, Bussière B (2013) On the use of waste rock inclusions to improve the performance of tailings impoundments. 18th International Conference on Soil Mechanics and Geotechnical Engineering, Paris, France, pp. 735-738.

James M, Aubertin M, Bussière B, Pednault C, Pépin N, Limoges M (2017) A research project on the use of waste rock inclusions to improve the performance of tailings impoundments. Geo Ottawa, Ottawa, ON. p. 8.

Jaouhar EM, Aubertin M, James M (2011) Effect of mine waste rock inclusions on the consolidation of tailings. In Proceedings, Pan-Am CGS Geotechnical Conference, Toronto.

Jaouhar EM, Aubertin M, James M (2013) The Effect of Tailings Properties on their Consolidation Near Waste Rock Inclusions. Proceedings of the 66th Canadian Geotechnical Conference, Montréal. QC.

Jibson RW, Michael JA (2009) Maps showing seismic landslide hazards in Anchorage, Alaska (p. 3077). Reston, VA, USA: US Geological Survey.

Jibson R, W (2011) Methods for assessing the stability of slopes during earthquakes-A retrospective. Engineering Geology 122 (2011) 43–50

Karray M, Hussien MN, Chekired M (2015) Evaluation of compatibility between existing liquefaction charts in Eastern regions of North America. In Proceedings GeoQuebec 2015, pp. 20-23 September 2015. Canadian Geotechnical Society

Kishi N, Nomachi SG, Matsuoka KG, Kida T (1987) Earthquake engineering. Japan society of civil engineering, proceeding of JSCE, No. 386/ I- 8, Vol. 4, No. 2, pp 259 - 267

Kramer SL (1996) Geotechnical Earthquake Engineering, New Jersey, Prentice Hall

Kramer SL, Mitchell RA (2006) Ground motion intensity measures for liquefaction hazard evaluation. Earthquake Spectra, 22(2), 413-438.

Kramer SL, Wang CH (2015) Empirical model for estimation of the residual strength of liquefied soil. Journal of Geotechnical and Geoenvironmental Engineering, 141(9), 04015038.

Kuhlemeyer RL, Lysmer J (1973) Finite element method accuracy for wave propagation problems. Journal of Soil Mechanics and Foundations Division, 99 (Technical Report).

L-Bolduc F (2012) Étude expérimentale et numérique de la consolidation des résidus et des effets d'inclusions drainantes. Mémoire de maîtrise, École Polytechnique de Montréal.

L-Bolduc F, Aubertin M (2014) A numerical investigation of the influence of waste rock inclusions on tailings consolidation, Canadian Geotechnical Journal, 51(9): 1021-1032.

Maknoon M (2016) Slopes stability analyses of waste rock piles under unsaturated conditions following large precipitations. Ph.D. Thesis. Ecole Polytechnique de Montreal.

Martin V, Aubertin M (2019) An assessment of hydrogeological properties of waste rock using infiltration tests and numerical simulations. Paper presented at the 72nd Canadian Geotechnical Conference (GEO 2019), St. John's.

Mbonimpa M, Aubertin M, Chapuis RP, Bussiere B (2002) Practical pedotransfer functions for estimating the saturated hydraulic conductivity. Geotechnical and Geological Engineering, 20(3): 235-259.

Morgenstern N, Vick SG, Viotti CB, Watts BD (2016) Report on the Immediate Causes of the Failure of the Fundão Dam. Gottlieb Steen and Hamilton LLP, New York

Moss RES, Gebhart R., Frost DJ., Ledezma C (2019) Flow-failure case history of the Las Palmas, Chile, Tailings Dam (No. 2019/01). PEER Report.

Pacific Earthquake Engineering Research Center (PEER) (2019) Earthquake and station details. Consulted in September 2019. https://ngawest2.berkeley.edu/

Pépin N, Aubertin M, James M (2012) Seismic Table Investigation of the Effect of Inclusions on the Cyclic Behavior of Tailings. Canadian Geotechnical Journal, 49(4): 416-426.

Peregoedova A (2012) Étude expérimentale des propriétés hydrogéologiques des roches stériles à une échelle intermédiaire de laboratoire. M.Sc.A. thesis, Département des génies civil, géologique et des mines, École Polytechnique de Montréal, QC.

Peregoedova A, Aubertin M, Bussière B (2013) Laboratory measurement and prediction of the saturated hydraulic conductivity of mine waste rock. In GeoMontreal 2013: Geosciences for Sustainability, 66th CGS Conference, Montréal, QC.

Poncelet N (2012) Élaboration et implément d'un protocole de laboratoire pour l'étude du potential de liquéfaction de résidus miniers. M.Sc. Thesis unpublished. Ecole Polytechnique Montréal PQ, Canada.

Rayleigh JWS, Lindsay R B (1945) The theory of sound, Dover Publications, New York.

Robertson PK (2018) Evaluation of liquefaction in tailings and mine waste: an update. Available from https://www.cpt-robertson.com/publications/ [accessed 13 Mars 2020].

Rollins K M, Evans MD, Diehl NB, III WDD (1998) Shear modulus and damping relationships for gravels. Journal of Geotechnical and Geoenvironmental Engineering, 124(5), 396-405.

Saleh Mbemba F (2016) Évaluation du drainage, de la consolidation et de la dessiccation des résidus miniers fins en présence d'inclusions drainantes. Thèse de doctorat, Département civil, géologie et Mine, Université de Polytechnique de Montréal, Montréal, QC.

Santamarina JC, Torres-Cruz LA, Bachus RC (2019) Why coal ash and tailings dam disasters occur. Science, 364(6440), pp. 526-528.

Seed HB, Wong RT, Idriss IM, Tokimatsu K (1984) Dynamic moduli and damping factors for dynamic analysis of cohesionless soils. Report No. UCB/EERC-84/14, Earthquake Engineering Research Center, Berkeley, CA.

Shome N, Cornell CA (1999) Probabilistic seismic demand analysis of nonlinear structures. PhD Thesis. Stanford University, California.

Travasarou T, Bray JD (2003) Optimal ground motion intensity measures for assessment of seismic slope displacements. In 2003 Pacific Conference on Earthquake Engineering, Christchurch, New Zealand, Feb.

Vaid, YP, Byrne PM, Hughes JMC (1981) Dilation Angle and Liquefaction Potential. Journal of the Geotechnical Division, ASCE, Vol. 107, No. GT7.

Vick SG (1990) Planning, Design, and Analysis of Tailings Dams. BiTech Publishers Limited, Vancouver, BC.

Wyllie DC, Mah CW (2004) Rock Slope Engineering. London and New York: Spon Press.

Yang P, Li L, Aubertin M (2018) Theoretical and numerical analyses of earth pressure coefficient along the centerline of vertical openings with granular fills. Applied Sciences, 8(10), 1721.

Zafarani A, Yniesta S, Aubertin M (2020) Effect of height and downstream slope on the seismic behavior of tailings impoundments reinforced with waste rock inclusions. Proc. 73rd Canadian Geotechnical Conference (GEOVirtual 2020). p. 8.

Zafarani A, Yniesta S, Aubertin M (2021) On the selection of ground motion intensity measures to evaluate the seismic stability of tailings impoundments. Paper presented at the 74th Canadian Geotechnical Conference (Geo Niagara 2021), Niagara Falls, Ontario.

Zafarani A (2022) Using numerical modeling with dynamic loading to develop a procedure for the optimal design of waste rock inclusions in tailings impoundments. Ph.D. Thesis. Polytechnique Montréal. In preparation.

Zafarani A, Yniesta S, Aubertin M (2022a) A dynamic numerical investigation to assess the optimal configuration of waste rock inclusions for seismic stability of tailings impoundments. Submitted to the Canadian Geotechnical Journal.

Zafarani A, Yniesta S, Aubertin M (2022b) Comparison and selection of ground motion intensity measures to evaluate the seismic response of tailings impoundments. Submitted to the Canadian Geotechnical Journal.

Zhang G, Robertson PK, Brachman RWI (2004) Estimating liquefaction-induced lateral displacements using the standard penetration test or cone penetration test. Journal of Geotechnical and Geoenvironmental Engineering, 130(8), 861-871.

Zhang C, Zhong Z, Zhao M (2020) Study on Ground Motion Intensity Measures for Seismic Response Evaluation of Circular Tunnel. In IOP Conference Series: Earth and Environmental Science (Vol. 455, No. 1, p. 012164). IOP Publishing

CHAPTER 6 GENERAL DISCUSSION AND LIMITATIONS

6.1 Synthesis of Chapters 3, 4 and 5

As described in Chapter 1 the primary objective of the current research project was to establish a specific method for optimizing the design of inclusions in a tailings impoundment under seismic loading. To achieve this primary objective, various simulations were conducted to investigate how selected characteristics, such as the downstream slope inclination of the impoundment, height of the model, configuration of WRI (i.e., width and spacing), and maximum acceleration of the input motion affect the seismic behavior of the model (Chapter 3). First, a numerical modeling approach for simulating the seismic behavior of tailings impoundments was developed using the code FLAC (Fast Lagrangian Analysis of Continua) Version 8.00 (Itasca, 2016). The steps of the dynamic numerical modeling which were presented in Chapter 3 are as follows:

- Set up the model and define its geometry, the meshing, the boundary conditions, and the material properties. The present study focusses on tailings impoundments built using the upstream-raised dike construction technique, considering varying elevations and downstream slopes. The impoundment model extends up to 140 m from the crest, based on a parametric study that indicates that adopting a wider model has no effect on the simulation results. The size of quadrilateral elements was set to 1 m by 1 m at the core of the model, ensuring that ground motion frequencies up to 25 Hz are realistically transmitted through the model. In regions where greater deformations and deviatoric stresses were expected (mostly under the dikes), the mesh size was refined down to 0.5 m. A parametric investigation showed that a mesh with elements smaller than 0.5 m did not affect the results, but significantly increased calculation time.

- The numerical model was run to determine the initial state of stresses, strains, and pore water pressures under mechanical and hydraulic equilibrium. The materials (tailings, dikes, waste rock, foundation) are modeled using the Mohr-Coulomb elasto-plastic model at this stage. Long-term (steady-state) static conditions are analyzed, without considering; sequential raising of the impoundment; the model is built in a single placement of material, followed by gravity application;

- In the final step, equilibrium stresses from the static phase are used as initial conditions for the dynamic analysis, with earthquake loading applied at the base of the model. The constitutive models of the various materials are changed for this step to better represent their behavior under earthquake loading. The PM4Sand model (Boulanger and Ziotopoulou, 2017) is used to simulate the dynamic behavior of low plasticity tailings. The calibration of the PM4Sand model parameters for hard-rock tailings presented by Contreras (2022) is used here. Laboratory cyclic tests and field studies were performed to calibrate the primary and secondary parameters of the PM4Sand model for density indexes ranging from 40% to 89 %. Contreras (2022) has validated the parameters by comparing modeled cyclic stress-strain curves and pore pressure response to laboratory test results.

In the parametric study the downstream slope was varied between 7H:1V and 12H:1V, the height of the impoundment was between 20 m and 50 m, the width of the inclusions was between 12 and 25 m, and the spacing was between 55 and 155 m. The recording of the M_w 6.93 Loma Prieta 1989 earthquake from the NGA-West2 database (Ancheta et al. 2013) at station RSN810 was used as the input ground motion for this component of the parametric study. The Loma Prieta recording was then scaled at four different levels of PGA (1.21 m/s^2, 2.04 m/s^2, 3.04 m/s^2, and 4.87 m/s^2) to investigate the influence of peak ground acceleration (PGA) on the seismic response of the models. The influence of each parameter on particular model response indicators was assessed through a total of 100 numerical simulations in this part of the study, presented in Chapter 3. Two specific performance indicators were used to quantify the response of the different models. The critically displaced volume of tailings (*CDV*), based on the volume displaced more than 100 cm, and the average normalized horizontal displacement along the downstream slope (SAR_x) were chosen based on their sensitivity and good correlation with the different WRI configurations. The results of the simulation which were presented in Chapter 3 can be summarized as follows:

- The simulations of unreinforced impoundment models with varying downstream slopes indicated that the applied ground motion caused excessive deformation with a general failure for models with a downstream slope of 7H:1V. Reducing the slope to 12H:1V decreases the maximum horizontal displacement of tailings, but the deformation is still considerable.

- The simulation results of the reinforced impoundments with different downstream slopes showed that WRI can significantly contribute to improving the seismic response of the models by reducing the maximum horizontal displacement. The results indicated that the influence of the inclusions on the value of SAR_x is relatively modest for the shallower downstream slopes of 12H:1V and 10H:1V, but significantly more noticeable for the two steeper slopes of 8H:1V and 7H:1V. In general, the values of SAR_x of the models with a greater volume of WRI tend to become close to one another, which indicates that there is an optimal configuration beyond which adding additional waste rock has little influence on the displacements.

- The contours of the excess pore water pressure ratio (r_u) distribution within the reinforced impoundment with varying external slopes show that the majority of the tailings between the waste rock inclusions are liquefied (r_u >0.9) at the end of the shaking. Waste rock inclusions and variation in the downstream slope thus have little effect on the development of excess pore water pressure in the tailings.

- The variation of SAR_x vs WRI configuration for impoundments with varied heights (or tailings thickness) indicated that SAR_x values computed for configurations with heights of 20 m and 30 m are relatively small and remain practically constant due to the relatively low horizontal displacements. Increasing the height of the impoundment model to 50 m leads to substantially larger displacements, with SAR_x increasing by a factor of 6 for the model with less reinforcement. The variation trend lines also showed that the thickness of the tailings deposit appears to have a greater impact on the seismic response of the impoundment than the downstream slope, for the conditions analyzed here.

- The seismic response of the models under Loma Prieta ground motion scaled at four levels of the PGA showed that the deformation is modest under low intensity ground motion (i.e., PGA=1.21 m/s^2), so the impoundment would probably stay stable. When the PGA level is increased, the extent of deformation increases, and the influence of waste rock inclusions in lowering SAR_x values becomes more prominent. In general, the larger volume of waste rock inclusions provides the greatest improvement in seismic stability for ground motions

of severe intensities (PGA=3.04 and 4.87 m/s^2), since the displacement decreases more considerably.

Following the evaluation of the geometry effect (Chapter 3), the effects of intensity measures (IMs) of the ground motion on the seismic stability of tailings impoundments is investigated as part of the numerical parametric study in Chapter 4 in order to develop design guidelines for using WRI. One of the main objectives here was to identify the most efficient IMs of input ground motions in the evaluation of the seismic response of the system. In this regard regression analyses were used to assess the effect of the 13 different IMs based on the efficiency, practicality, and proficiency criteria. The optimum IMs selection approach is summarized in Chapter 4, with the detailed procedure given in Appendix B. The simulated impoundment investigated here was 40 m high with a downstream slope of 8H:1V. Ten different North America ground motion records from the NGA-West2 (Ancheta et al. 2013) and NGA-East (Goulet et al. 2014) databases were used to assess the seismic response and stability of tailings impoundments with and without waste rock inclusions. The following summarizes the key results presented in Chapter 4:

- The simulation results of the unreinforced and reinforced impoundment at the end of two ground motions with somewhat similar intensity measures, based on the Peak Ground Acceleration (PGA), Arias Intensity (AI), and predominant frequency (F_p), showed significant differences in the response of the system in terms of the horizontal displacement and excess pore water pressure development. This emphasizes the need to identify the most appropriate (optimum) IM (or IMs), which may differ from the ones mentioned above (PGA, AI, Fp), that best correlates with the overall seismic behavior in terms of performance indicators.

- The variation of SAR_x versus WRI configuration for different ground motions showed that the effect of WRIs' configuration on the value of SAR_x for ground motions with lower intensities is modest, but the impact is much more significant for ground motions with higher intensities. The results also indicated that the SARx values were similar for most configurations under the ground motions with similar Velocity Spectrum Intensity (VSI), Peak Ground Velocity (PGV), and Acceleration Spectrum Intensity (ASI) values.

- The regression analysis results showed that VSI and PGV were the IMs with the lowest dispersion and the highest correlation with SAR_x based on efficiency, practicality, and proficiency criteria. However, some configurations lead to a poor level of efficiency. The use of a vector-valued IM was thus considered to improve the efficiency and reduce variability in the seismic response of the system.
- The overall efficiency of the vector-valued IMs composed of VSI (IM_1) and other candidate IMs (IM_2) was evaluated in terms of the variation in the seismic response of the model (i.e., SAR_x). The results showed that the combination of VSI and PGA gives the highest efficiency for the scenarios analyzed.

Chapter 5 presents a systematic approach for assessing liquefaction-induced displacement of tailings impoundments reinforced with waste rock inclusions. Using the results of the numerical parametric investigation presented in Chapters 3 and 4, a systematic procedure was proposed to link the level of displacement in terms of the SAR_x as a function of tailings impoundment characteristics, including the slope inclination (θ), height (H), tailings density index (I_d), the optimum intensity measures of earthquake shaking (i.e., VSI and PGA), and the configuration of the WRI. Based on concepts in liquefaction-induced deformation of earth structures and analysis of the parametric study results described previously, several trial functional forms were investigated to correlate the earthquake-induced horizontal displacement of the downstream slope of reinforced tailings impoundments (SAR_x) with these parameters. The performance of the developed equations is quantified by calculating the residuals between the simulated and estimated SAR_x values. Appendix C provides residual distribution graphs for various trial equations, with the key results summarized in Chapter 5. The characteristics and performance of the selected functional form is summarized as follows:

- Comparing the estimated and simulated values of SAR_x showed that the estimates given by the proposed mathematical relationship follow the right trend and are generally consistent with the simulation results.
- The results showed that, for ground motions of moderate intensity, the VSI and PGA residual plots appear to be free of significant bias. Nonetheless, the proposed equation

leads to SARx values with a greater degree of error for more intense ground motions due to the significant variation in seismic response under these ground motions.

- The residuals of SAR_x versus density index show no systematic bias for various WRI configurations.

The key findings, conclusions, and recommendations that were drawn from these three Chapters were intended to provide design guidelines to better integrate this co-disposal method in the design of tailings impoundments. This research project investigated the seismic behavior of reinforced tailings impoundments in greater detail compared with earlier studies by evaluating the response of models during and after ground motions for various situations, including different WRI configurations, downstream slope and tailings thickness, seismic loading parameters, and material properties. The proposed method for evaluating the seismic stability of tailings impoundments could be beneficial in engineering practice to support and improve stability analyses. However, the results are based on the cases considered here. The provided information, observations, and conclusions should be used with caution to other sites or conditions.

6.2 Limitations

Despite the advances made with this research work, there are several limitations to consider while assessing and interpreting results from numerical simulations such as those provided here; the main ones are as follows:

- The consistency of the data and the generated trend lines for the two indicators suggest that the *CDV* and SAR_x can be used to quantify the effect of each influence factor (parameter). However, since *CDV* is limited to models with a horizontal displacement of at least 100 cm, some of the simulated cases are excluded from the final analysis, and SAR_x is then the only indicator used to quantify the seismic response of the models. An additional performance indicator would be useful to compare the responses of models with smaller displacements and shear strains.
- The performance indicator analysis is only applicable to reinforced models since many simulations of unreinforced models were stopped during ground motion due to high deformation.

- In this study, plane strain simulations were used, while tailings impoundments are three-dimensional structures. At the start of the project, the performance of available constitutive models in 3D was not yet well documented, thus a 2D analysis of a representative cross section of the impoundment was regarded a good approximation. However, future research should consider 3D physical and numerical modeling of the tailings impoundments with WRI (such as centrifuge modeling) to study how it compares to 2D analysis.
- Seismic analyses should be carried out in cases where the tailings contain interlayers that are less pervious (non homogeneity). These layers have been shown to have an impact on pore water pressure dissipation in sand (Malvick et al., 2008). As a result, a thin water layer may form locally, generating localized shear deformation and instability. This issue, and other forms of anisotropy and inhomogeneity, has not been well researched with regard to the dynamic response of tailings impoundment.
- The position of the groundwater level can have a significant impact on the seismic response of tailings impoundments, particularly if part of the tailings is unsaturated as the shear strength of tailings may be increased due to the suction induced in the pores (Narvaez et al. 2014).
- The effect of the soil foundation is not investigated in this study. In cases where the foundation contains weak soil, this aspect may play a significant role and should be included in the seismic stability analyses of the tailings impoundments.
- Evaluation of the consolidation characteristic of tailings and the evolution of pore water pressures during sequential deposition is one of the key aspects of the geotechnical stability of a tailings impoundment. Although self weight consolidation of tailings during deposition in successive layers is not considered in this study, evaluation of this aspect could be useful in understanding the seismic behavior of tailings and evaluating influence parameters.
- The proposed simplified method should improve the deterministic and probabilistic assessment of tailings impoundment seismic stability in engineering practice. However, due to the inherent variability of soil properties, site conditions, and seismic loads, predicting the behavior of earth structures, particularly for highly nonlinear conditions such as soil liquefaction and its corresponding lateral displacement, is fraught with uncertainty. The

main results and related equations are based on the findings of dynamic numerical simulations for a specified set of seismic ground motions and a limited set of geometry and material properties, with no significantly changing local conditions or extremely irregular configurations. Given the novelty of the co-disposal WRI method more study is needed to establish probabilistic prediction models for the optimal design of waste rock inclusions in tailings impoundments with substantially varying characteristics.

CHAPTER 7 CONCLUSION AND RECOMMENDATIONS

The review of current knowledge and practices in mine waste disposal, as well as the seismic evaluation of tailings impoundments, indicated that improved methods for characterizing the stability of existing tailings impoundments and appropriate design strategies are required to prevent failures and the consequent damage. In order to increase the static and dynamic stability of tailings impoundments, Aubertin et al. (2002a) proposed using waste rock inclusions (WRI), which have higher stiffness, strength, and hydraulic conductivity than tailings. Recent research using physical models (Pépin et al., 2012; Saleh-Mbemba and Aubertin, 2020, 2021) and numerical simulations (James, 2009; James and Aubertin, 2012; Jaouhar et al., 2013; L. Bolduc and Aubertin, 2014; Ferdosi et al., 2015; Aubertin et al., 2019; Jahanbakhshzadeh and Aubertin, 2020, 2021) have shown that using WRI in a tailings storage facility can significantly increase the geotechnical behavior and stability of the tailings impoundment. However, design guidelines and optimization methodologies are required to better integrate this co-disposal method in the design of tailings impoundments. This aspect was addressed in greater details in this research project, in comparison to prior research by assessing the response of the models during and after ground motions, for various conditions including different WRI configurations, downstream slope and thickness of tailings, seismic loading characteristics, and material properties. In addition, a systematic procedure is required to link the response of the system to the aforementioned influential parameters. This aspect is investigated in this research by developing a design equation (multi-parameter relationship) relating the magnitude of displacement to key influential parameters such as impoundment height, slope, material properties, seismic loading characteristics, and WRI configuration. Such equations have never existed before for tailings impoundments, and the particular method used to establish them is novel and original.

The key findings, conclusions, and recommendations that were drawn from the various research phases are described in the following sections.

7.1 Conclusion

Chapter 2 (Literature Review) demonstrated the need for effective and practical methods of assessing the liquefaction potential of tailings, evaluating the seismic response and stability of

tailings impoundments, and controlling the consequences of liquefaction on tailings impoundments. A review of the fundamental principles, experimental data, and formulation of various constitutive models for dynamic numerical modeling of sandy-like materials revealed that the PM4Sand model can accurately simulate the behavior of tailings from hard rock mines, as shown by results of cyclic simple shear tests on sands and tailings.

The analyses of the results of parametric numerical simulations on the evaluation of the influence of certain characteristics such as the downstream slope and height of the impoundment model, the configuration of WRI, and the maximum acceleration of the input motion on the seismic response of the conceptual impoundment presented in Chapter 3, and the following conclusions were derived from the analyses:

- The responses of different configurations of WRI can be quantified based on the average normalized horizontal displacement along the downstream slope, SAR_x, and the critically displaced volume of tailings (*CDV*), which represents the volume displaced more than 100 cm.
- The applied ground motion resulted in excessive deformation and general failure for all unreinforced models with different impoundment downstream slopes (for the conditions analyzed here).
- The WRI can significantly improve the seismic response of the models by decreasing the maximum horizontal displacement. The influence of the inclusions on the level of horizontal displacement is more significant for the steeper upstream dikes than for the shallower downstream slopes.
- The waste rock inclusions configuration and variation in the downstream slope have little effect on the development of excess pore water pressure in the tailings.
- The effect of the WRI configuration on seismic response is less noticeable in impoundments with smaller tailings thickness due to lower horizontal displacements than in impoundments with a thicker tailings deposit.
- The seismic response of the model is more influenced by the thickness of the tailings deposit than by the downstream slope for the conditions considered in the simulations.

The impacts of intensity measures (IMs) of ground motion on the seismic response and stability of tailings impoundments are investigated in Chapter 4. The results led to the following conclusions:

- The significant differences between the responses of the system at the end of ground motions with some comparable IMs highlighted the necessity of identifying the most sensitive, or optimum IM (or IMs) that correlate best with the performance metrics.
- The impact of WRI's configuration on the seismic response of the model was limited for ground motions with lower intensities, but the impact was noticeably more pronounced for ground motions with higher intensities.
- The Velocity Spectrum Intensity (VSI) and Peak Ground Velocity (PGV) were identified as the IMs with the highest correlation with SAR_x. However, as the level of the efficiency was low for some configurations, it was deemed necessary to consider a vector-valued IM to increase the level of efficiency and decrease variability in the seismic response of the model.
- The vector-valued IMs composed of Velocity Spectrum Intensity, VSI (IM_1) and Peak Ground Acceleration, PGA (IM_2) had the highest overall efficiency for the cases evaluated. Both IMs are included in the relationship developed between seismic loading and response indicators.

Using the results of the numerical parametric investigation presented in Chapters 3 and 4, a performance model (multi-parameter relationship) was developed in Chapter 5 to link the degree of displacement with the parameters analyzed including the slope inclination, height, tailings density index, optimum intensity measurements of earthquake shaking, and WRI configuration. The key findings can be summarized as follows:

- In general, the simulation results and the estimations provided by the performance model (equation) matched.
- The variability of residuals showed consistency for the typical downstream slopes and heights considered in the simulations.
- The proposed multiparametric relationship showed a very good correlation for ground motions of moderate intensity. The corresponding equation leads to less precise results for

the horizontal displacement for ground motions with higher intensities due to the large variation in seismic response under these ground motions.

- The performance model captured the simulated seismic response of the tailings with various density indexes without systematic error.

7.2 Recommendations for additional research

The following recommendations are provided for further developing the co-disposal concept of using WRI in tailings impoundments:

- The methodology and guidelines proposed here are based on the plane strain (2D) simulations. It would be interesting to carry out three dimensional (3D) numerical modeling of tailings impoundments to determine the effect of WRI on the overall performance of the impoundment under a variety of probable scenarios and compare the results to 2D analyses.
- Reduced-scale physical models such as geotechnical centrifuge modeling of the tailings with and without waste rock inclusions could be performed to quantify interaction between the two materials and validate the numerical simulations, particularly in terms of deformation and pore water pressures.
- In the present research project, the tailings impoundment is assumed to be on level ground with water table at the surface of the impoundment. However, more realistic topography of the mine site with different elevation for water could be taken into account in the numerical simulations to better evaluate the effect of the terrain and water table on the seismic performance of the tailings impoundment with WRI.
- Although the calibration of the PM4Sand model has been validated by experiment studies, it is essential that the model be evaluated against further experiments. An extensive experimental program on various types of tailings should be carried out for this purpose and should include both monotonic (with different confining pressure, densities, loading rates, etc.) and cyclic (triaxial and direct simple shear tests with varying densities, loading frequencies, cyclic stress ratio) testing. Once such a database is available, the model parameters can be thoroughly validated and improved.

- Assessment of the effects of foundation soil type on waste rock inclusions' configuration and overall seismic stability is of great interest and importance. It is recommended to perform simulations with various soil foundation properties and thicknesses. These results would help in the selection of the desired configuration and the analysis of the influence of the foundation on the seismic behavior of tailings impoundments reinforced with WRI.
- The tailings in the impoundment consolidate under their own weight, and they sometimes have a density index profile that increases with time at different depths. However, in some cases the presence of interlayers (non homogeneity) can affect the consolidation characteristic of tailings and the development of pore water pressures. It would be beneficial to analyze and compile numerous measurements of the in-situ density index and investigate the influence of different profiles obtained on the seismic response of the system using numerical simulations.

7.3 Closure

The main objective of this research was to develop seismic design guidelines for tailings impoundments reinforced with waste rock inclusions. The observations, conclusions, and recommendations made in various phases of this study were intended to provide sufficient basis for addressing the primary objective of the project. The results would give a solid foundation for better integrating this co-disposal method into the design of tailings impoundments. The suggested approach for determining the seismic stability of tailings impoundments should be helpful in engineering practice to support and enhance deterministic and probabilistic evaluation. It should be noted, however, that the proposed approach is based on the findings of dynamic numerical simulations performed for a specific set of seismic ground motions, geometries, and material properties, with uniform material conditions or regular configurations involving waste rock inclusions and upstream dikes. The information, observations, and conclusions provided should be transposed to other sites or conditions with caution.

REFERENCES

Adalier, K. and Aydingun, O. 2003. Numerical Analysis of Seismically Induced Liquefaction in Earth Embankment Foundations – Part I: Benchmark Model. Canadian Geotechnical Journal, 40, 753-765.

Akkar S, Bommer JJ. 2010. Empirical equations for the prediction of PGA, PGV, and spectral accelerations in Europe, the Mediterranean Region, and the Middle East. Seismological Research Letters 81:195–206.

Alonso, E.E., Tapias, M., Gili, J. 2012. Scale effects in rockfill behaviour. Géotechnique Letters 2, 155–160

Ancheta, T. D., Darragh, R. B., Stewart, J. P., Seyhan, E., Silva, W. J., Chiou, B. S., and Donahue, J. L. 2013. Peer NGA-West2 database.

ANCOLD. 2012. Guidelines on Tailings Dams- Planning, Design, Construction, Operation and Closure. Australian National Committee on Large Dams (ANCOLD)

Anscombe, F. J. 1961.Examination of residuals. Proc. 4th Berkeley Symposium on Mathematical Statistics Problems 1, 1–36

Anscombe, F. J, Tukey, J. W. 1963. Analysis of residuals. Technometrics 5, 141–160

Anthi, M. and Gerolymos, N., 2019. A Calibration procedure for sand plasticity modeling in earthquake engineering: Application to TA-GER, UBCSAND and PM4SAND. In 7th International Conference on Earthquake Geotechnical Engineering (pp. 17-20).

Archambault-Alwin, X. 2017. Évaluation du comportement dynamique et de la résistance cyclique des résidus miniers. M.Sc.A. thesis, Département des génies civil, géologique et des mines, Polytechnique Montréal, Montréal, QC, Canada.

Arduino, P. and Macari, E. J. 2001a. Implementation of Porous Media Formulation for Geomaterials. Journal of Engineering Mechanics, 127(2), 157-166.

Arduino, P. and Macari, E. J. 2001b. Numerical Analysis of Geomaterials within Theory of Porous Media. Journal of Engineering Mechanics, 127(2), 167-175.

Arias., A. 1970. A measure of earthquake intensity. In: Hansen RJ (ed) Seismic design for nuclear power plants. MIT Press, Cambridge MA, pp 438–483

Armstrong, R. J., Boulanger, R. W., and Beaty, M. H. 2013. Liquefaction effects on piled bridge abutments: Centrifuge tests and numerical analyses. Journal of geotechnical and geoenvironmental engineering, 139(3), 433-443.

Aubertin, M., et Chapuis, R.P. 1991. Considérations hydro-géotechniques pour l'entreposage des résidus miniers dans le nord-ouest du Québec. In Proceedings of the 2ième Conférence Internationale sur la Réduction des Eaux de Drainage Acides, Montréal, Que., 16–18 septembre 1991. MEND-NEDEM, CANMET, Natural Resources Canada, Ottawa, Ont. 3. pp. 1–22.

Aubertin, M., Bussière, B. and Chapuis, R.P. 1996. Hydraulic conductivity of homogenized tailings from hard rock mines. Canadian Geotechnical Journal, 33(3), 470-482

Aubertin, M., Mbonimpa, M., Jolette., D., Bussière, B., Chapuis, R.P., James, M., Riffon, O. 2002a. Stabilité géotechnique des ouvrages de retenue pour les résidus miniers: problèmes persistants et méthodes de contrôle. Défis and Perspectives : Symposium sur l'environnement et les mines, Rouyn-Noranda, Développement Économique Canada/Ministère des Ressources Naturelles du Québec/CIM. Comptes-Rendus sur CD-ROM.

Aubertin, M., Bussière, B., Bernier, L. 2002b. Environnement et gestion des rejets miniers [CD-ROM Manual]. Montréal: Presses Internationales Polytechnique.

Aubertin, M., Fala, O., Molson, J., Chouteau, M., Anterrieu, O., Hernandez, M. A., ... and Lefebvre, R. 2008. Caractérisation du comportement hydrogéologique et géochimique des haldes à stériles. Paper presented at the Symposium 2008 sur l'environnement et les mines, Rouyn-Noranda, QC.

Aubertin, M., Bussière, B., James, M., Martin, V., Pépin, N., Mbonimpa, M., and Chapuis, R.P. 2011. Vers une mise à jour des critères de stabilité géotechnique pour la conception des ouvrages de retenue de résidus miniers. Symposium sur les Mines et l'Environnement, Rouyn-Noranda, Québec, 6-9 novembre 2011

Aubertin, M., James, M., Maknoon, M., and Bussière, B. 2013. Recommandations pour améliorer le comportement hydrogéotechnique des haldes à stériles. GeoMontreal 2013-Geosciences for Sustainability, 66th CGS Conference, Montreal, QC, 8 p.

Aubertin, M., Bussière, B., Pabst, T., James, M., Mbonimpa, M., 2016. Review of reclamation techniques for acid generating mine wastes upon closure of disposal sites. Conference Geo-Chicago pp. 343-358. 10.1061/9780784480137.034.

Aubertin, M., Jahanbakhshzadeh, A., and Yniesta, S. 2019. The effect of waste rock inclusions on the seismic stability of a tailings impoundment. Proceedings of 7th International Conference on Earthquake Geotechnical Engineering.

Aubertin, M., Jahanbakshzadeh, A., Saleh-Mbemba, F., Yniesta, S. and Pednault, C. 2021. General guidelines for the design and construction of waste rock inclusions in tailings impoundment. Paper presented at the 74th Canadian Geotechnical Conference (Geo Niagara 2021), Niagara Falls, Ontario.

Azam, S., Wilson, G. W., Fredlund, D. G., and Van Zyl, D. 2009. Geotechnical characterization of mine waste rock. In Proceedings of the Seventh International Conference Soil Mechanics and Geotechnical Engineering.

Azam, S., and Li, Q. 2010. Tailings dam failures: a review of the last one hundred years. Geotechnical News, 28(4), 50-54.

Baker, J. W., and Cornell, C. A. 2005. Vector-valued ground motion intensity measures for probabilistic seismic demand analysis. Blume Center Technical Rep. #150, Stanford University, Stanford, CA.

Barbour, S. L., Hendry, M. J., Smith, J. L., Beckie, R. D., and Wilson, G. W. 2001. A research partnership program in the mining industry for waste rock hydrology. Workshop Notes (unpublished). NSERC CRD Project. University of Saskatchewan, Canada.

Barksdale, R. D. 1987. Applications of the State of the Art of Stone Columns – Liquefaction, Local Bearing Failure, and Example Calculations. Technical Report No. REMR-GT-7, Washington DC: US Army Corps of Engineers.

Barrera, S., Cacciuttolo, C., and Caldwell, J. 2015. Reassessment of best available tailings management practices. 2015-10-29 (http://www, infomine, com/library/publications/docs/Barre-ra2015, pdf.)

Beaty, M. and Byrne, P. M. 1998. An effective stress model for predicting liquefaction behavior in sand. Proceedings of Geotechnical Earthquake Engineering and soil dynamic III, Seattle, Washington, USA. ASCE Special Publication. 75(1):766-777.

Been, K.and Jefferies, M.G. 1985. A state parameter for sands. Géotechnique 35, pp. 99-112.

Beaty, M.H. and Byrne, P.M. 2011. UBCSAND constitutive model Version 904aR. Document report: UBCSAND Constitutive Model on Itasca UDM Website: http://www.itasca-udm.com/pages/continuum.html.

Bjelkevik, A. 2005. Water cover closure design for tailings dams: state of the art report. Luleå tekniska universitet.

Blight, G. E. 2010. Geotechnical engineering for mine waste storage facilities. CRC Press.

Bolton, M.D. 1986. The strength and dilatancy of sands. Geotechnique, 36, pp. 65-78.

Boore DM., Atkinson GM., 2008. Ground-motion prediction equations for the average horizontal component of PGA, PGV, and 5%-damped PSA at spectral periods between 0.01 s and 10.0 s. Earth Spectra 24:99–138.

Bora SS., Scherbaum F., Kuehn N et al. 2015. Development of a response spectral ground motion prediction equation (GMPE) for seismic-hazard analysis from empirical fourier spectral and duration models. Bulletin of the Seismological Society of America.

Boudrias, G. 2018. Évaluation numérique et expérimentale du drainage et de la consolidation de résidus miniers à proximité d'une inclusion de roches stériles. Master thesis, Ecole Polytechnique de Montreal.

Boulanger, R. W., and Idriss, I. M. 2004. Evaluating the potential for liquefaction or cyclic failure of silts and clays (p. 131). Davis, California: Center for Geotechnical Modeling.

Boulanger, R. W., and Idriss, I. M. 2014. CPT and SPT liquefaction triggering procedures. Report No UCD/GCM.

Boulanger, R. W., and Ziotopoulou, K. 2017. PM4Sand (Version 3): A sand plasticity model for earthquake engineering applications. Center for Geotechnical Modeling Report No. UCD/CGM-15/01, Department of Civil and Environmental Engineering, University of California, Davis, California.

Bowker, L. N., and Chambers, D. M. 2017. In the dark shadow of the supercycle tailings failure risk and public liability reach all time highs. Environments, 4(4), 75.

Bradley BA. 2012. Empirical correlations between cumulative absolute velocity and amplitude-based ground motion intensity measures. Earth Spectra 28:37–54.

Bray, J. D., Travasarou, T. 2007. Simplified procedure for estimating earthquake-induced deviatoric slope displacements. Journal of geotechnical and geoenvironmental engineering, 133(4), pp. 381-392.

Bray, J. D., Macedo, J., Travasarou, T. 2018. Simplified procedure for estimating seismic slope displacements for subduction zone earthquakes. Journal of Geotechnical and Geoenvironmental Engineering, 144(3), 04017124.

Bussière, B. 2007. Hydro-Geotechnical properties of hard rock tailings from metal mines and emerging geo-environmental disposal approaches. Canadian Geotechnical Journal, 44(9): 1019-1052

Bussière, B., and Aubertin, M. 1999. Clean tailings as cover material for preventing acid mine drainage: an in situ experiment. Proceedings of Mining and the Environment conference, September 13–17, Sudbury, Canada, (vol. 1, p. pp 19–28).

Byrne, P. 1991. A Cyclic Shear-Volume Coupling and Pore Pressure Model for Sand. Proceedings of the Second International Conference on Recent Advances in Geotechnical Earthquake Engineering and Soil Dynamics, St. Louis, USA (pp. 47-55). New York: ASCE.

Byrne, P. M., Debasis, R., Campanella, R. G. and Hughes, J. 1995. Predicting Liquefaction Response of Granular Soils from Pressuremeter Tests. Proceedings of the American Society of Civil Engineers national Conventional, San Diego, USA, (pp. 122-135).

Byrne, P. M., Park, S. S. and Beaty, M. 2003. Seismic Liquefaction: Centrifuge and Numerical Modeling. Proceedings of the Third International Symposium on FLAC and FLAC3D numerical Modelling in Geomechanics, Sudbury, Canada (pp. 321-331). Lisse, Netherlands: Balkema.

California Geological Survey. 2008. Guidelines for Evaluating and Mitigating Seismic Hazards in California. California Geological Survey Special Publication 117A. 98 pp.

Canadian Dam Association (CDA). 2007. Dam safety guidelines. Canadian Dam Association (2013 edition).

Canadian Dam Association (CDA). 2019. Technical bulletin: Application of Dam safety guidelines to Mining Dams. Canadian Dam Association (2019 edition).

Carey, T.J. and Kutter, B.L., 2017. Comparison of liquefaction constitutive models for a hypothetical sand. In Geotechnical Frontiers 2017 (pp. 389-398).

Carraro, J.A., Prezzi, M. et Salgado, R. 2009. Shear strength and stiffness of sands containing plastic or non-plastic fines. Journal of Geotechnical and Geoenvironmental Engineering, 135 (9), pp. 1167-1178.

Castillo, J., Hallman, D., Byrne, P., and Parra, D. 2006. Non-linear dynamic analysis of heap leach pad under high phreatic levels. In Proceedings of FLAC and Numerical Modeling and Geomechanics, Madrid, Spain, 29-31 May 2006. Itasca Consulting Group, Inc., Minneapolis MN, pp. 187-194.

Chen, Z. X., Cheng, Y., Xiao, Y., Lu, L., and Yang, Y. 2015. Intensity measures for seismic liquefaction hazard evaluation of sloping site. Journal of Central South University, 22(10), 3999-4018.

Chevrel, S., BRGM, O. F., Kuosmannen, V., GTK, E. F., Belocky, R., GBA, W. A., ... and IGM, L. P. 2001. Hyperspectral airborne imagery for mapping mining-related contaminated areas in various European environments–first results of the MINEO project. In Presented at the Fifth International Airborne Remote Sensing Conference (Vol. 17, p. 20).

Contreras Romero, C. A. 2013. Comportement dynamique du sol pulvérulent « résidus miniers ». M.Sc., thesis, Department of Civil, Geological, and Mining Engineering, Ecole Polytechnique de Montreal, Montreal, QC.

Contreras Romero, C. A. 2022. Analyses numériques du comportement et de la stabilité sismique et post-sismique des parcs à résidus miniers, avec et sans inclusions de roche stérile, pour divers aléas de l'est du Canada. Thèse de doctorat, Département civil, géologie et Mines, Polytechnique Montréal, Québec, Canada.

Contreras Romero, C. A., Yniesta, S., and Aubertin, M. 2020. Seismic and post-seismic stability of tailings impoundments, considering the effect of reinforcement inclusions. Proceedings of 73rd Canadian Geotechnical Conference (GEOVirtual 2020).

Contreras Romero, C. A., Yniesta, S., Jahanbakhshzadeh, A., and Aubertin, M. 2022. Calibration of the PM4Sand Model for Hard-Rock Mine Tailings Based on Laboratory and Field Tests. Submitted to the Canadian Geotechnical Journal.

Cook, R. D., Weisberg, S. 1982. Residuals and influence in regression. New York: Chapman and Hall.

Cornell, A., and Jalayer, F. 2002. Factored nonlinear displacement demand estimation methods for probability-based safety assessment. American Society of Civil Engineers Journal of Structural Engineering 2002;128(4): 526–533

Dafalias, Y. F., and Manzari, M. T. 2004. Simple Plasticity Sand Model Accounting for Fabric Change Effects. Journal of Engineering Mechanics, Vol. 130, No. 6, pp 622-634.

Davies, M. P. 2002. Tailings impoundment failures: Are geotechnical engineers listening? Geotechnical News, BiTech Publisher, Vancouver, 20(3), 31-36.

Davies, M. P. and Lighthall, P. C. 2001. Geotechnical aspects of several recent mine tailings impoundment failures. In Proceedings of the 54th Canadian Geotechnical Conference, Calgary, AB. Canada Geotechnical Society, pp. 321-326.

Dobry, R. and Alvarez, L. 1967. Seismic Failures of Chilean Tailings Dams. Journal of the Soil Mechanics and Foundations Division, 93(SM6), 237-260.

Dobry, R., and Vucetic, M. 1987. Dynamic properties and seismic response of soft clay deposits. Proceedings of International Symposium on Geotechnical Engineering of Soft Soils, Mexico City, Vol. 2, pp. 51-87.

Duncan J.M. and Bursey A. 2013. Soil modulus correlations. In Foundation Engineering in the Face of Uncertainty: Honoring Fred H. Kulhawy, 321-336. American Society of Civil Engineers.

Esposito S, Iervolino I. 2011. PGA and PGV spatial correlation models based on European multievent datasets. Bulletin of the Seismological Society of America 101:2532–2541.

Essayad, K. 2015. Development of experimental protocols for the characterization of saturated and unsaturated tailings consolidation from columns compression tests (text in French), Master thesis, Ecole Polytechnique de Montreal.

Essayad, K., Pabst, T., Aubertin, M. and Chapuis, R.P. 2018. An experimental study of the movement of tailings through waste rock inclusions. Paper presented at the 71st Canadian Geotechnical Conference (GeoEdmonton 2018), Edmonton, Alberta.

Essayad, K. 2021. Évaluation multi-échelle de l'instabilité interne et de la migration des résidus à travers les inclusions de roches stériles. Thèse de doctorat, Département civil, géologie et Mines, Polytechnique Montréal, Québec, Canada.

Essayad, K. and Aubertin, M. 2021. Consolidation of hard rock tailings under positive and negative pore-water pressures: Testing procedures and experimental results. Canadian Geotechnical Journal, 58(1), 49-65.

Fala, O. 2008. Analyses des conditions d'ecoulement non sature dans les haldes à stérile. Ph.D. Thesis, Ecole Polytechnique de Montreal.

Falaknaz N, Aubertin M, Li L. 2015a. Evaluation of the stress state in two adjacent backfilled stopes within an elastoplastic rock mass. Geotechnical and Geological Engineering doi:10.1007/s10706- 015-9868-6

Falaknaz N, Aubertin M, Li L. 2015b. Numerical investigation of the geomechanical response of adjacent backfilled stopes. Canadian Geotechnical Journal 52(10):1507–1525

Federico, A., and Elia, G. 2009. At-rest earth pressure coefficient and Poisson's ratio in normally consolidated soils. Proc. 17th International Conference on Soil Mechanics and Geotechnical Engineering, Alexandria, Egypt.

Ferdosi, B. 2014. A numerical investigation of the seismic response of tailings impoundments reinforced with waste rock inclusions. Ph.D. Thesis, Ecole Polytechnique de Montreal.

Ferdosi, B., James, M., and Aubertin, M. 2015a. Effect of waste rock inclusions on the seismic stability of an upstream raised tailings impoundment: a numerical investigation. Canadian Geotechnical Journal, 52(12): 1930-1944.

Ferdosi, B., James, M., and Aubertin, M. 2015b. Investigation of the effect of waste rock inclusions configuration on the seismic performance of a tailings impoundment. Geotechnical and Geological Engineering, 33(6), 1519-1537.

Finn, W. D. L. 1985. Aspects of Constant Volume Cyclic Simple Shear. Proceedings of Advances in the Art of Testing of Soils Under Cyclic Conditions, Detroit MI, USA (pp. 74-98). New York: American Society of Civil Engineers.

Finn, W. D. L. 1993. Seismic Safety Evaluation of Embankment Dams. Proceedings of the International Workshop on Dam Safety Evaluation, Grindelwald, Switzerland (pp. 91-135). Sutton, UK: Quadrant House.

Finn, W. D. L. 1998. Seismic Safety Evaluation of Embankment Dams - Developments in Research and Practice 1988-1998. Proceedings of Geotechnical Earthquake Engineering and Soil Dynamics III, Seattle WA, USA (Vol. 2, pp. 812-853). Reston VA: American Society of Civil Engineers.

Fotopoulou SD., Pitilakis KD. 2015. Predictive relationships for seismically induced slope displacements using numerical analysis results. Bulletin of Earthquake Engineering 13(11):3207–3238

Fourie, A.B., Mikula, R.J. et al. 2001. Partially Saturated Tailings Sand Below the Phreatic Surface. Géotechnique 51, No. 7, pp. 577-585.

Gamache-Rochette, A. 2004. Une étude de caractérisation en laboratoire et sur le terrain des écoulements de l'eau dans les roches stériles. École Polytechnique de Montréal.

Gens, A. and Alonso, E. E. 2006. Aznalco'llar Dam Failure. Part 2: Stability Conditions and Failure Mechanism. Gèotechnique 56, No. 3, 185-201

Geremew, A., F., Yanful, E., K. 2012. Laboratory Investigation of the Resistance of Tailings and Natural Sediments to Cyclic Loading. Geotechnical and Geological Engineering (2012) 30:431–447

Goodman, R. E. 1989. Introduction to Rock Mechanics. John Wiley and Sons Inc.

Goulet, C. A., et al. 2014. PEER NGA-east database. Berkeley, CA: Pacific Earthquake Engineering Research Center

Grimard, L.P. 2018. Une étude en laboratoire sur la réponse des résidus miniers aux charges compressives non drainées et aux pertes de confinement avec caractérisation par vitesse des ondes de cisaillement. Mémoire de maîtrise, École Polytechnique de Montreal, QC.

Grimard, L. P., Karray, M., James, M., and Aubertin, M. 2021. Consolidation characteristics of hydraulically deposited tailings obtained from shear wave velocity (Vs) measurements in triaxial and oedometric cells with piezoelectric ring-actuator technique (P-RAT). Canadian Geotechnical Journal, 58(2), 281-294.

Harder L. F., Stewart, J. P. 1996. Failure of Tapo Canyon tailings dam. Journal of Performance of Constructed Facilities, ASCE, 10(5): 109–114.

Hawley, M., Cunning, J. 2017. Guidelines for mine waste dump and stockpile design. CSIRO Publishing, Clayton

Hirschfeld, R.C. 1963. Stress – Deformation and Strength Characteristics of Soils. Harvard University, 87 pages.

Holtz, R. D., Kovacs, W. D., and Sheahan, T. C. 1981. An introduction to geotechnical engineering (Vol. 733). Englewood Cliffs: Prentice-Hall.

Holtz, R. D. and Kovacs, W. D. 1991. An Introduction to Geotechnical Engineering. Englewood NJ: Prentice-Hall, Inc.

Housner, GW. 1952. Intensity of ground motion during strong earthquakes. Second technical report. August 1952, California Institute of Technology Pasadena, California.

Housner, G.W. and Jennings, P.C. 1964. Generation of artificial earthquakes, Proceedings American Society of Civil Engineers 90, 113–150

Howell R., Rathje E. M., Kamai, R., Boulanger, R. 2012. Centrifuge modeling of prefabricated vertical drains for liquefaction remediation. Journal of Geotechnical and Geoenvironmental Engineering 138(3):262–271

Hu, J., and Liu, H. 2019. Identification of ground motion intensity measure and its application for predicting soil liquefaction potential based on the Bayesian network method. Engineering Geology, 248, 34-49.

Hustrulid, W. A., McCarter, M. K., Van, Zyl. DJA. 2000. Slope stability in surface mining. Society for Mining Metallurgy, Englewood

Idriss, I. M., and Boulanger, R. W. 2007. SPT-and CPT-based relationships for the residual shear strength of liquefied soils. In Earthquake geotechnical engineering (pp. 1-22). Springer, Dordrecht.

Idriss, I. M., and Boulanger, R. W. 2008. Soil liquefaction during earthquakes. Earthquake Engineering Research Institute Publication, Monograph MNO-12, Earthquake Engineering Research Institute, Oakland.

Imam, S. M. R., Morgenstern, N. R., Robertson, P. K. and Chan, D. H. 2005. A Critical state Constitutive Model for Liquefiable Sand. Canadian Geotechnical Journal, 42, 830-855.

International Commission on Large Dams (ICOLD). 2001. Tailings dams – risk of dangerous occurrences – lessons learnt from past experiences. Paris. Bulletin No. 121.

Ishihara, K. 1984. Post-earthquake failure of a tailings dam due to liquefaction of pond deposit. Paper presented at the International Conference on Case Histories in Geotechnical Engineering, Rolla, Missouri, USA.

Ishihara, K. 1993. Liquefaction and flow failure during earthquakes. Géotechnique, 43, pp. 351-451.

Ishibashi, I. 1992. Discussion to effect of soil plasticity on cyclic response, by M. Vucetic and R. Dobry. Journal of Geotechnical Engineering. American Society of Civil Engineers, Vol. 118, No. 5, pp. 830-832.

Ishihara, K. 1996. Soil behavior in earthquake geotechnics: Kenji Ishihara (vol. 45). New York; Oxford: Clarendon Press.

Ishibashi, I., and Zhang, X. 1993. Unified dynamic shear moduli and damping ratios of sand and clay. Soils and Foundations, Vol. 33, No. 1, pp. 182-191.

Itasca Consulting Group, Inc. (Itasca). 2016. FLAC – Fast Lagrangian Analysis of Continua. Version 8.00. [computer software and user manual]. Minneapolis MN: Itasca Consulting Group, Inc.

Jahanbakhshzadeh, A., Aubertin, M., Yniesta, S. and Zafarani, A. 2019. On the seismic response of tailings dikes constructed with the upstream and center-line methods. Paper presented at the 72nd Canadian Geotechnical Conference (GEO 2019), St. John's.

Jahanbakhshzadeh, A. and Aubertin, M. 2020. The effect of waste rock inclusions on the slope stability of tailings dike. Proceedings of the 73rd Canadian Geotechnical Society Conference, Calgary, Canada.

Jahanbakhshzadeh, A. and Aubertin, M. 2022. Main results from an extensive geotechnical characterization of hard rock tailings from an open pit gold mine. In preparation for 75th CGS Conference, GeoCalgary 2022.

James, M. 2009. The use of waste rock inclusions to control the effect of liquefaction in tailings impoundments. Ph.D. Thesis, Department of Civil, Geological, and Mining Engineering, Ecole Polytechnique de Montreal, Montreal, QC.

James, M., and Aubertin, M. 2009. The use of waste rock inclusions in tailings impoundments to improve geotechnical and environmental performance. In Proceedings, Tailings and Mine Waste 2009, Banff, Alberta. pp. 233–245.

James, M., and Aubertin, M. 2010. On the dynamic response of tailings and the stability of tailings impoundments for hard rock mines. Geotechnical News, 23(3), 39-43.

James, M., and Aubertin, M. 2012. The use of waste rock inclusions to improve the seismic stability of tailings impoundments. GeoCongress 2012, Okland, 22-25 March 2012. American Society of Civil Engineers, pp. 4166-4175.

James, M., Aubertin, M., and Bussière, B. 2013. On the use of waste rock inclusions to improve the performance of tailings impoundments. 18th International Conference on Soil Mechanics and Geotechnical Engineering, Paris, France, pp. 735-738.

James, M., Aubertin, M., Bussière, B., Pednault, C., Pépin, N., and Limoges, M. 2017. A research project on the use of waste rock inclusions to improve the performance of tailings impoundments. Geo Ottawa, Ottawa, ON. p. 8.

Jamiolkowski, M., Carrier, W. D., Chandler, R. J., Hoeg, K., Swierczynski, W., and Wolski, W. 2010. 1st Za Chieh-Moh Distinguished Lecture: The geotechnical problems of the second world

largest copper tailings pond at Zelazny Most, Poland. Geotechnical Engineering Journal of the SEAGS and AGSSEA, 41(1).

Jaouhar, E. M., Aubertin, M., James, M. 2011. Effect of mine waste rock inclusions on the consolidation of tailings. In Proceedings, Pan-Am CGS Geotechnical Conference, Toronto.

Jaouhar, E. M., Aubertin, M., James, M. 2013. The Effect of Tailings Properties on their Consolidation Near Waste Rock Inclusions. Proceedings of the 66th Canadian Geotechnical Conference, Montréal. QC.

Jefferies, M., et Been, K. 2015. Soil liquefaction: a critical state approach. CRC press.

Jibson, R. W., Michael, J. A. 2009. Maps showing seismic landslide hazards in Anchorage, Alaska (p. 3077). Reston, VA, USA: US Geological Survey.

Jibson, R., W. 2011. Methods for assessing the stability of slopes during earthquakes-A retrospective. Engineering Geology 122 (2011) 43–50

Karray, M., Hussien, M. N., Chekired, M. 2015. Evaluation of compatibility between existing liquefaction charts in Eastern regions of North America. In Proceedings GeoQuebec 2015, pp. 20-23 September 2015. Canadian Geotechnical Society.

Kenney, J. F. and Keeping, E. S. 1962. Root Mean Square. 3rd ed. Princeton, NJ: Van Nostrand, pp. 59-60.

Kishi, N., Nomachi, S.G., Matsuoka, K. G., Kida, T. 1987. Earthquake engineering. Japan society of civil engineering, proceeding of JSCE, No. 386/ I- 8, Vol. 4, No. 2, pp 259 – 267

Kokusho, T. 1980. Cyclic triaxial test of dynamic soil properties for wide strain range. Soil and Foundation, Vol. 20, No. 2, pp. 45-60.

Kostadinov M.V., Yamazaki F. 2001. Detection of soil liquefaction from strong motion records. Earthquake Engineering and Structural Dynamics 30:173–193.

Kostadinov M.V., Towhata. 2002. Assessment of liquefaction inducing peak ground velocity and frequency of horizontal ground shaking at onset of phenomenon. Soil Dynamics and Earthquake Engineering 22:309–322. doi:10.1016/S0267-7261(02)00018-0

Kramer, S.L. 1996. Geotechnical Earthquake Engineering, New Jersey, Prentice Hall

Kramer, S. L., and Mitchell, R. A. 2006. Ground motion intensity measures for liquefaction hazard evaluation. Earthquake Spectra, 22(2), 413-438.

Kramer, S. L., Wang, C. H. 2015. Empirical model for estimation of the residual strength of liquefied soil. Journal of Geotechnical and Geoenvironmental Engineering, 141(9), 04015038.

Kuhlemeyer, R. L., and Lysmer, J. 1973. Finite element method accuracy for wave propagation problems. Journal of Soil Mechanics and Foundations Division (Tech Report).

L-Bolduc, F. 2012. Étude expérimentale et numérique de la consolidation des résidus et des effets d'inclusions drainantes. Mémoire de maîtrise, École Polytechnique de Montréal.

L-Bolduc, F., and Aubertin, M. 2014. A numerical investigation of the influence of waste rock inclusions on tailings consolidation, Canadian Geotechnical Journal, 51(9): 1021-1032.

Leps, T. M. 1970. Review of shearing strength of rockfill. Journal of the Soil Mechanics and Foundations Division, 96(4), 1159-1170.

Li, M. 2000. Unsaturated flow and transport observations in large waste rock columns. Communication presented at in Proceedings fifth international conference on acid rock drainage: (p. pp 247-256).

Lottermoser, B. G. 2011. Recycling, reuse and rehabilitation of mine wastes. Elements, 7(6), 405-410.

Luco N, Cornell AC. 2007. Structure-specific scalar intensity measures for near-source and ordinary earthquake ground motions. Earthquake Spectra 2007; 23:357–392.

Makdisi, Faiz I. and Seed, H. Bolton. 1978. Simplified Procedures for Estimating Dam and Embankment Earthquake-Induced Deformations. Journal of the Geotechnical Engineering Division, 104(7), 849-867.

Maknoon, M. 2016. Slopes stability analyses of waste rock piles under unsaturated conditions following large precipitations. Ph.D. Thesis. Ecole Polytechnique de Montreal.

Maknoon, M., and Aubertin, M. 2021. On the Use of Bench Construction to Improve the Stability of Unsaturated Waste Rock Piles. Geotechnical and Geological Engineering, 39(2), 1425-1449.

Malvick, E. J., Kutter, B. L., and Boulanger, R. W. 2008. Postshaking shear strain localization in a centrifuge model of a saturated sand slope. Journal of geotechnical and geoenvironmental engineering, 134(2), 164-174.

Manzari, M. T., and Dafalias, Y. 1997. A Critical State Two-Surface Plasticity Model for Sands. Geotechnique, Vol. 47, No. 2, pp 255-272.

Martin, J. R. II, Olgun, C. G., Mitchell, J. K., and Durgunoglu, H. T .2004. High-modulus Columns for Liquefaction Mitigation. Journal of Geotechnical and Geoenvironmental Engineering, 130(6), 561 571.

Martin, V., and Aubertin, M. 2019. An assessment of hydrogeological properties of waste rock using infiltration tests and numerical simulations. Paper presented at the 72nd Canadian Geotechnical Conference (GEO 2019), St. John's.

Mbonimpa, M., Aubertin, M., Chapuis, R. P., and Bussiere, B. 2002. Practical pedotransfer functions for estimating the saturated hydraulic conductivity. Geotechnical and Geological Engineering, 20(3): 235-259.

McDowell, G.R., Bolton, M.D. 1998. On the micromechanics of crushable aggregates. Géotechnique 48, 667–679

McDowell, G.R., Amon, A. 2000. The application of Weibull statistics to the fracture of soil particles. Soils Found. 40, 133–141

McLemore, V. T., Donahue. K.M., Walsh, P., Tachie-Menson, S., Phillips, E. H., Guitierrez, L. A. F., and Shannon, H. R. 2005. Trench Sampling of the Molycorp Goathill Northrock piles, Questa Rock Pile Stability Study, New Mexico. National Meeting of the American Society of Mining and Reclamation.

Meisheng, F., and Laigui, W. 2011. A tailings dam dynamic stability study based on numerical simulation. In 2011 International Conference on Consumer Electronics, Communications and Networks (CECNet) (pp. 1002-1005). IEEE.

Midorikawa S., Wakamatsu K. 1988. Intensity of earthquake ground motion at liquefied sites. Soils Found 28:73–84. doi:10.3208/sandf1972.28.2_73

Mitchell, K. and Soga, K. 2005. Fundamentals of Soil Behavior. Toronto ON: John Wiley and Sons, Inc.

Mittal, H., and Morgenstern, N.R. 1975. Parameters for the design of tailings dams. Canadian Geotechnical Journal, 12: 235–261.

Morgenstern, N., Vick, S. G., Viotti, C. B., Watts, B. D. 2016. Report on the Immediate Causes of the Failure of the Fundão Dam. Gottlieb Steen and Hamilton LLP, New York

Morin, K. A., Gerencher, E., Jones, C. E., and Konasewich, D. E. 1991. Critical review of acid drainage from waste rock. MEND Report 1.11.1.

Moriwaki, Y., Tan, P. and Ji, F. 1998. Seismic Deformation Analysis of the Upper San Fernando Dam Under the 1971 San Fernando Earthquake. Proceedings of Geotechnical Earthquake Engineering III, Seattle WA, USA (pp. 854-865). New York: ASCE.

Moss, R. E. S., Gebhart, R., Frost, D. J., Ledezma, C. 2019. Flow-failure case history of the Las Palmas, Chile, Tailings Dam (No. 2019/01). PEER Report

Newmark, N. M. 1965. Effects of Earthquakes on Dams and Embankments. Géotechnique, 15(2), 139-160.

Nielson B. G. and DesRoches R. 2007. Seismic fragility methodology for highway bridges using a component level approach. Earthquake Engineering and Structural Dynamics, Vol. 36, No. 6, pp. 823-839, DOI: 10.1002/Eqe.655.

Nuttli, O. W. 1979. Seismicity in the central United States, Geol. Soc. Am. Rev. Eng. Geol. 4, 67–93.

Olarte, J., Paramasivam, B., Dashti, S., Liel, A., Zannin, J. 2017. Centrifuge modeling of mitigation–soil–foundation– structure interaction on liquefiable ground. Soil Dynamics and Earthquake Engineering 97:304 323

Ovalle, C., Dano, C., and Hicher P.-Y. 2013. Experimental data highlighting the role of surface fracture energy in quasi-static confined comminution. International Journal of Fracture 182 (1): 123–130. https://doi.org/10.1007/s10704-013-9833-4.

Ovalle, C., Frossard, E., Dano, C., Hu, W., Maiolino, S., and Hicher, P.-Y. 2014. The effect of size on the strength of coarse rock aggregates and large rockfill samples through experimental data. Acta Mechanica. 225 (8): 2199–2216. https://doi.org/10.1007/s00707-014-1127-z.

Ovalle, C., Linero, S., Dano, C., Bard, E., Hicher, P.-Y. and Osses, R. 2020. Data compilation from large drained compression triaxial tests on coarse crushable rockfill materials. Journal of Geotechnical and Geoenvironmental Engineering, 146(9)

Pacific Earthquake Engineering Research Center (PEER), 2019. Earthquake and station details. Consulted in September 2019. https://ngawest2.berkeley.edu/

Padgett, JE, Nielson, BG, DesRoches, R. 2008. Selection of optimal intensity measures in probabilistic seismic demand models of highway bridge portfolios. Earthquake Engineering and Structural Dynamics 37: 711–725.

Paramasivam, B., Dashti, S., Liel, A. 2018. Influence of prefabricated vertical drains on the seismic performance of structures founded on liquefiable soils. Journal of Geotechnical and Geoenvironmental Engineering 144(10):04018070

Park, Y., and Ang A. 1985. Mechanistic Seismic Damage Model for Reinforced Concrete. Journal of Structural Engineering, 111(4): 722–739.

Pépin, N., Aubertin, M., and James, M. 2009. An investigation of the cyclic behavior of tailings using shaking table tests: effect of a drainage inclusion on pore water development, GeoHalifax2009, pp. 32-39.

Pépin, N., Aubertin, M., James, M., Leclerc, M. 2012a. Seismic simulator testing to investigate the cyclic behavior of tailings in an instrumented rigid box. Geotechnical Testing Journal, 35(3): 469-479.

Pépin, N., Aubertin, M., James, M. 2012b. Seismic Table Investigation of the Effect of Inclusions on the Cyclic Behavior of Tailings. Canadian Geotechnical Journal, 49(4): 416-426.

Peregoedova, A. 2012. Étude expérimentale des propriétés hydrogéologiques des roches stériles à une échelle intermédiaire de laboratoire. M.Sc.A. thesis, Département des génies civil, géologique et des mines, École Polytechnique de Montréal, QC.

Peregoedova, A., Aubertin, M., and Bussière, B. 2013. Laboratory measurement and prediction of the saturated hydraulic conductivity of mine waste rock. *In* GeoMontreal 2013: Geosciences for Sustainability, 66th CGS Conference, Montréal, QC.

Piao, R. P., Rippe, A. H., Myers, B. and Lane, K. W. 2006. Earth Dam Liquefaction and Deformation Analysis using Numerical Modeling. Proceedings of GeoCongress 2006: Geotechnical Engineering in the Information Age, Atlanta GA, USA (on CD ROM). Reston Virginia: American Society of Civil Engineers.

Pirulli, M., Barbero, M., Marchelli, M., and Scavia, C. 2017. The failure of the Stava Valley tailings dams (Northern Italy): Numerical analysis of the flow dynamics and rheological properties. Geoenvironmental Disasters, 4(1), 3.

Piteau Associates Engineering. 1991. Mined rock and overburden piles: investigation and design manual. Prepared for British Columbia Mine Dump Committee and Ministry of Energy and Mines.

Plante, B., Bussière, B., and Benzaazoua, M. 2012. Static tests response on 5 Canadian hard rock mine tailings with low net acid-generating potentials. Journal of Geochemical Exploration, 114, 57-69.

Poncelet, N. 2012. Élaboration et implément d'un protocole de laboratoire pour l'étude du potential de liquéfaction de résidus miniers. M.Sc. Thesis unpublished. Ecole Polytechnique Montréal PQ, Canada.

Potts, D.M. et Zdravkovic, L. 1999. Finite element Analysis in Geotechnical Engineering. Theory. Ed. Thomas Telford.

Puebla, H., Byrne, P.M., and Phillips, R. 1997. Analysis of CANLEX liquefaction embankments: prototype and centrifuge models. Canadian Geotechnical Journal, 34(5): 641-657.

Puebla, H. 1999. A constitutive model for sand and the analysis of the CanLex Embankments. Ph.D. thesis, Civil Engineering Department, University of British Columbia, Vancouver, B. C.

Qiu, Y. and Sego, D. C. 2001. Laboratory Properties of Mine Tailings. Canadian Geotechnical Journal, 38(1), 183-190.

Rana, N. M., Ghahramani, N., Evans, S. G., McDougall, S., Small, A., et Take, W. A. 2021. Catastrophic mass flows resulting from tailings impoundment failures. Engineering Geology, 292, 106262.

Rathje, E.M. and Saygili, G. 2008. Probabilistic Seismic Hazard Analysis for the Sliding Displacement of Slopes: Scalar and Vector Approaches. Journal of Geotechnical and Geoenvironmental Engineering, American Society of Civil Engineering, 134(6), 804- 814.

Rathje EM., Abrahamson NA., Bray JD. 1998. Simplified frequency content estimates of earthquake ground motions. Journal of Geotechnical and Geoenvironmental Engineering 124(2):150–159

Rayleigh, J. W. S. and Lindsay, R. B. 1945. The theory of sound, Dover Publications, New York.

Rezaeian, S., and Der Kiureghian, A. 2010. Simulation of synthetic ground motions for specified earthquake and site characteristics. Earthquake Engineering and Structural Dynamics, 39(10), 1155-1180.

Robertson, P. K. 2018. Evaluation of liquefaction in tailings and mine waste: an update. Available from https://www.cpt-robertson.com/publications/ [accessed 13 Mars 2020].

Roche, C., Thygesen, K., and Baker, E. (Eds.). 2017. Mine Tailings Storage: Safety Is No Accident, A UNEP Rapid Response Assessment. United Nations Environment Programme and GRID-Arendal, Nairobi and Arendal.

Rollins, K. M., Evans, M. D., Diehl, N. B., and III, W. D. D. 1998. Shear modulus and damping relationships for gravels. Journal of Geotechnical and Geoenvironmental Engineering, 124(5), 396-405.

Salam, S., Xiao, M., Khosravifar, A., and Ziotopoulou, K. 2021. Seismic stability of coal tailings dams with spatially variable and liquefiable coal tailings using pore pressure plasticity models. Computers and Geotechnics, 132, 104017.

Saleh-Mbemba, F., Aubertin, M., and Boudrias, G. 2019. Drainage and consolidation of mine tailings near waste rock inclusions. In Sustainable and Safe Dams Around the World. pp. 3296-3305. CRC Press.

Saleh-Mbemba, F. and Aubertin, M. 2021. Physical Model Testing and Analysis of Hard Rock Tailings Consolidation Considering the Effect of a Drainage Inclusion. Geotechnical and Geological Engineering, 39(4), pp. 2777-2798.

Saleh-Mbemba, F. 2016. Évaluation du drainage, de la consolidation et de la dessiccation des résidus miniers fins en présence d'inclusions drainantes. Thèse de doctorat, Département civil, géologie et Mine, Université de Polytechnique de Montréal, Montréal, QC.

Sangrey, D. A., Castro, G., Poulos, S. J. and France, J. W. 1978. Cyclic Loading of Sands, Silts and Clays. Proceedings of the Earthquake Engineering and Soil Dynamics Specialty Conference, Pasadena CA, USA (pp. 836-851). New York: American Society of Civil Engineering.

Santamarina, J. C., Torres-Cruz, L. A., and Bachus, R. C. 2019. Why coal ash and tailings dam disasters occur. Science, 364(6440), 526-528.

Sasaki, Y. and Taniguchi, E. 1982. Shaking Table Tests on Gravel Drains to Prevent Liquefaction of Sand Deposits. Soils and Foundations, 22(3), 1-14.

Seed, H. B., Idriss, I. M. 1970. Soil moduli and damping factors for dynamic response analyses. Report No. EERC 70-10, Earthquake Engineering Research Center, Berkeley, CA.

Seed, H. B., and Booker, J. R. 1977. Stabilization of potentially liquefiable sand deposits using gravel drains. Journal of Geotechnical and Geoenvironmental Engineering, 103(ASCE 13050).

Seed, H. B. and Idriss, I. M. 1982. Ground Motions and Soil Liquefaction During Earthquakes. Berkeley CA: Earthquake Engineering Research Institute.

Seed, H.B., Wong, R.T., Idriss, I.M. and Tokimatsu, K. 1984. Dynamic moduli and damping factors for dynamic analysis of cohesionless soils. Report No. UCB/EERC-84/14, Earthquake Engineering Research Center, Berkeley, CA.

Seed, H. B. and Lee, K. L. 1966. Liquefaction of Saturated Sands during Cyclic Loading. Journal of the Soil Mechanics and Foundation Engineering Division. 92(6). 105-134.

Seid-Karbasi, M., and Byrne, P. M. 2004. Embankment dams and earthquakes. Hydropower and Dams, 2: 96-102.

Sherard, J.L., Woodward, R. T., Gizienski, S. F. and Clevenger, W. A. 1963. Earth and Earth-rock Dams. New York: John Wiley and Sons, Inc.

Shome N. and Cornell CA. 1999. Probabilistic seismic demand analysis of nonlinear structures. PhD Thesis. Stanford University, California.

Sivakugan, N., Rankine, R. M., Rankine, K. J., and Rankine, K. S. 2006. Geotechnical considerations in mine backfilling in Australia. Journal of Cleaner Production, 14(12-13), 1168-1175.

Stone, K. J. L., Randolph, M. F. and Sales, A. A. 1994. Evaluation of Consolidation Behavior of Mine Tailings. Journal of Geotechnical Engineering, 120(30), 473-490.

Sun, J.I., Golesorkhi, R., and Seed, H.B. 1988. Dynamic moduli and damping ratios for cohesive soils. Report No. EERC-88/15, Earthquake Engineering Research Center, University of California, Berkeley.

Szilvágyi, Z., Hudacsek, P., and Ray, R. P. 2016. Soil shear modulus from resonant column, torsional shear and bender element tests. GEOMATE Journal, 10(20), 1822-1827.

Thomas, E., G., Nanteland, J. H., and Notley, K. R. 1979. Fill technology in underground metalliferous mines. International Academic Services, Kingstone, Ontario, Canada

Tothong P, Luco N. 2007. Probabilistic seismic demand analysis using advanced intensity measures. Earthquake Engineering and Structural Dynamics, 2007, 36: 1837–1860

Towhata, I. 2008. Geotechnical Earthquake Engineering. Verlag Berlin Heidelberg: Springer.

Tran, V. 2018. PM4SAND and UBCSAND Constitutive Soil Models for Seismic Soil-Structure Interaction Analysis of an Anchored Sheet Pile Wall System. Paper presented at the 71st Canadian Geotechnical Conference (GeoEdmonton 2018), Edmonton, Alberta.

Troncoso, J. H. and Verdugo, R. 1985. Silt Content and Dynamic Behavior of Tailings Sands. Proceedings of the 11th International conference on Soil Mechanics and Foundation Engineering, San Francisco California, USA (Vol 3., pp. 1311-1314). New York: American Society of Civil Engineering.

Travasarou, T., and Bray, J. D. 2003. Optimal ground motion intensity measures for assessment of seismic slope displacements. Proceedings of the Pacific Conference on Earthquake Engineering, Christchurch, New Zealand, Feb.

Vaid, Y. P., Byrne, P. M., and Hughes, J. M. C. 1981. Dilation Angle and Liquefaction Potential. Journal of the Geotechnical Division, American Society of Civil Engineering, Vol. 107, No. GT7.

Vaid, Y.P. and Chern, J. C. 1983. Mechanism of Deformation During Cyclic Undrained Loading of Saturated Sands. International Journal of Soil Dynamics and Earthquake Engineering, 2 (3), pp.171-177.

Verdugo, R., Peters, G., Valenzuela, L., Campaña, J., Valenzuela, L., Bard, E. 2017. Evaluation of Tailings Dams Subjected to Large Earthquakes. Proceedings of the 19th International Conference on Soil Mechanics and Geotechnical Engineering, Seoul 2017.

Vick, S. G. 1990. Planning, Design, and Analysis of Tailings Dams. BiTech Publishers Limited, Vancouver, BC.

Volpe, R.L. 1979. Physical and engineering properties of copper tailings. In Current geotechnical practice in mine waste disposal. Edited by The Committee on Embankment Dams and Slopes of the Geotechnical Engineering Division. American Society of Civil Engineering, New York, pp. 242–260.

Wijewickreme, D., Sanin, M.V., et Greenaway, G. 2005. Cyclic shear response of fine-grained mine tailings. Canadian Geotechnical Journal, 42(5), pp. 1408–1421.

Williams, D.J., and Morris, P.H. 1990. Engineering properties of Australian coal mine tailings relevant to their disposal and rehabilitation. In Proceedings of the 3rd International Symposium on the Reclamation Treatment and Utilization of Coal Mining Wastes, 3–7 Sept. 1990, Glasgow, pp. 49–56

Wyllie, D., C., and Mah, C., W. 2004. Rock Slope Engineering. London and New York: Spon Press.

Yang, S. and Ling, H. I. 2005. Calibration of Generalized Plasticity Model and its Application to Liquefaction Analysis. Proceedings of the Geo-Frontier 2005Conference, Austin Texas, USA (pp. 483-494). Reston VA: American Society of Civil Engineers.

Yang, P., Li, L. and Aubertin, M. 2018. Theoretical and Numerical Analyses of Earth Pressure Coefficient along the Centerline of Vertical Openings with Granular Fills. Applied Sciences, 8(10), 11 pages.

Youd, T. L., Idriss, I. M., Andrus, R. D., Arango, I., Castro, G., Christian, J. T. et al. 2001. Liquefaction Resistance of Soils: Summary Report from the 1996 NCEER and 1998 NCEER/NSF Workshops on Evaluation of Liquefaction Resistance of Soils. Journal of Geotechnical and Geoenvironmental Engineering, 127(10), 817- 833.

Younger, P. L., and Wolkersdorfer, C. 2004. Mining impacts on the fresh water environment: technical and managerial guidelines for catchment scale management. Mine water and the environment, 23, s2-s80.

Zafarani, A., Yniesta, S., Aubertin, M. 2020. Effect of height and downstream slope on the seismic behavior of tailings impoundments reinforced with waste rock inclusions. Proceedings of 73rd Canadian Geotechnical Conference (GEOVirtual 2020), p. 8.

Zafarani, A., Yniesta, S., Aubertin, M. 2021. On the selection of ground motion intensity measures to evaluate the seismic stability of tailings impoundments. Paper presented at the 74th Canadian Geotechnical Conference (Geo Niagara 2021), Niagara Falls, Ontario.

Zafarani, A., Yniesta, S., Aubertin, M. 2022a. A dynamic numerical investigation to assess the optimal configuration of waste rock inclusions for seismic stability of tailings impoundments. Submitted to the Canadian Geotechnical Journal.

Zafarani, A., Yniesta, S., Aubertin, M. 2022a. Comparison and selection of ground motion intensity measures to evaluate the seismic response of tailings impoundments. Submitted to the Canadian Geotechnical Journal.

Zen, K., Umehara, Y., and Hamada, K. 1978. Laboratory tests and in-situ Seismic survey on vibratory shear modulus of clayey soils with various plasticities. Proceeding 5th Japanese Earthquake Engineering Symposium, pp. 721-728.

Zhang, G., Robertson, P. K., Brachman, R. W. I. 2004. Estimating liquefaction-induced lateral displacements using the standard penetration test or cone penetration test. Journal of Geotechnical and Geoenvironmental Engineering, 130(8), 861-871.

Zhang, C., Zhong, Z., and Zhao, M. 2020. Study on Ground Motion Intensity Measures for Seismic Response Evaluation of Circular Tunnel. In IOP Conference Series: Earth and Environmental Science (Vol. 455, No. 1, p. 012164). IOP Publishing.

APPENDIX A RESULTS OF THE PARAMETRIC STUDY

The models of the unreinforced and reinforced conceptual impoundments were analyzed using 10 different ground motions from the NGA-West2 (Ancheta et al. 2013) and NGA-East (Goulet et al. 2014) databases. The results are summarized in this section for the unreinforced and reinforced models with different downstream slopes, heights, WRIs' configuration, and ground motions.

A1 Representative static responses

The static conditions were established as the initial step in the FLAC analysis by assessing the mechanical and hydraulic stability of the model. Figure A1. 1 shows the representative static response in terms of vertical effective stress for the unreinforced model with a downstream slope of 8H:1V and a height of 40 m. The vertical effective stress at top of the bedrock was calculated analytically as follows:

$$\sigma'_v = 40\ (m).\left(17\frac{kN}{m^3} - 0.75\ .9.81\ \frac{kN}{m^3}\right) = \ 386\ kPa$$

The numerical modeling resulted in vertical effective stresses that were consistent with the analytical estimate and were therefore found to be acceptable.

The static horizontal effective stresses within the impoundment are presented on Figure A1. 2. Within the tailings, these stresses varied from 0 near the surface to about 170 kPa at the bottom. The ratio of the horizontal stresses to the vertical stresses (170 kPa/386 kPa) corresponds to an at-rest pressure coefficient of approximately 0.44. For the tailings:

$$K_0 = 1 - \sin(\varphi) = 1 - \sin(35) = 0.43$$

Considering this, the static horizontal effective stresses within the impoundment are deemed to be reasonable.

The pore water pressure, u, contours under static loading are presented on Figure A1. 3. The porewater pressures varied from about 0 near the surface to just near 400 kPa at the bottom of the model and are indicative of a steady state, hydrostatic condition as determined below:

$$u = 40\ (m).\left(\ 9.81\ \frac{kN}{m^3}\right) = \ 392\ kPa$$

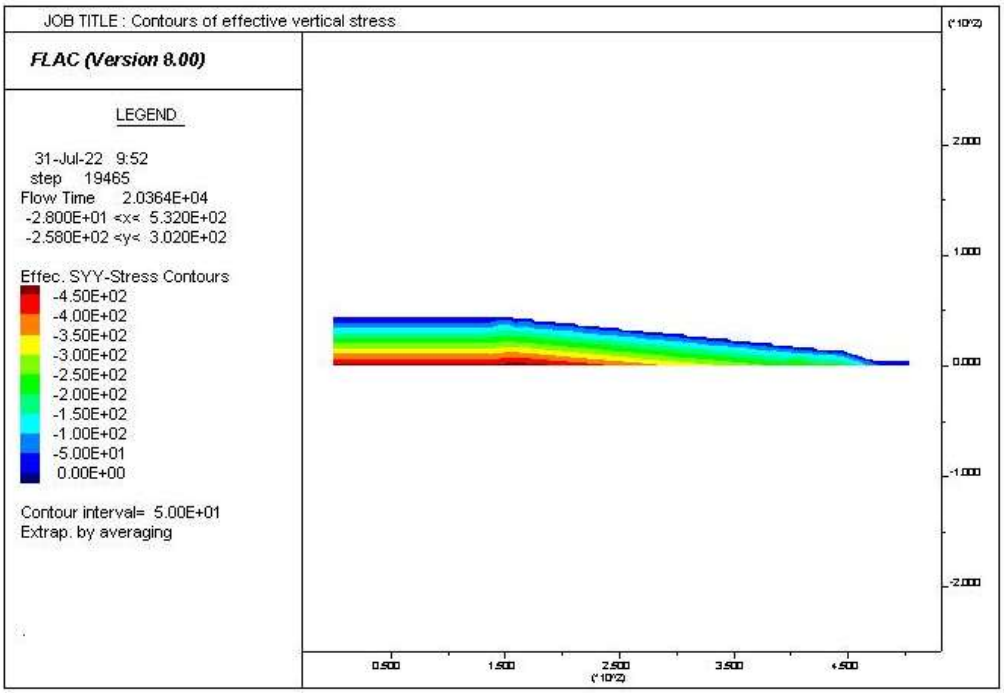

Figure A1. 1: Static vertical effective stresses for the unreinforced model with a downstream slope of 8H:1V and a height of 40 m

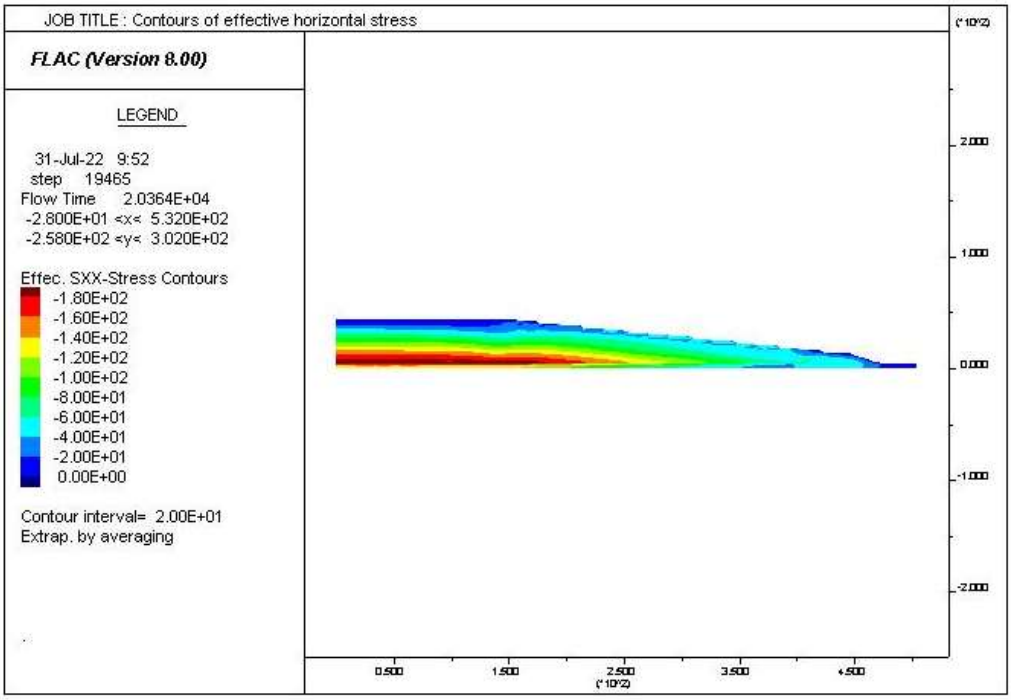

Figure A1. 2: Static horizontal effective stresses for the unreinforced model with a downstream slope of 8H:1V and a height of 40 m

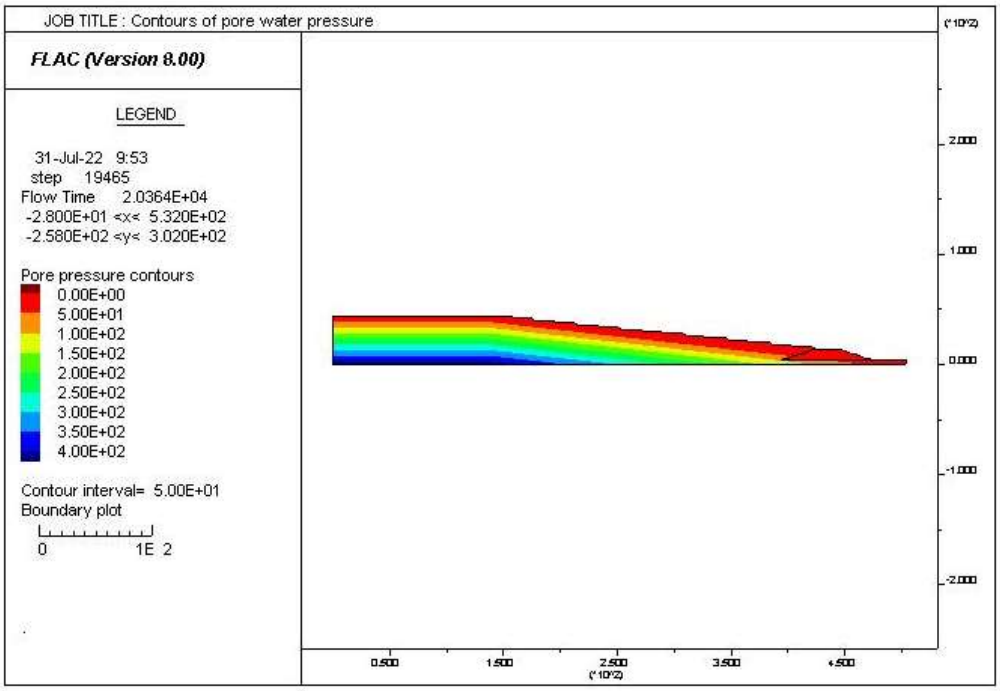

Figure A1. 3: Hydrostatic pore water pressures for the unreinforced model with a downstream slope of 8H:1V and a height of 40 m

A2 Representative dynamic responses

The vertical effective stresses for the unreinforced model with a downstream slope of 8H:1V and a height of 40 m at the end of at the end of E_3-Loma earthquake are shown on Figure A2. 1. Within the tailings, the vertical effective stresses were less than 100 kPa, compared to the 0 to 400 kPa prior to shaking (Figure A1. 1). Figure A2. 2 shows the horizontal effective stresses at the end of shaking. Within the tailings, the horizontal effective stresses were less than 50 kPa, indicating a significant reduction from static levels (Figure A1. 2).

The pore water pressure distribution in the impoundment at the end of shaking is shown on Figure A2. 3. The pore water pressure, u, varied from 0 at the surface of the tailings to just over 800 kPa at the bottom of the tailings and was indicative of high excess pore water pressure development compared to the static loading (0 to 400 kPa).

This excess pore water pressure ratio (ru) contours are shown in Figure A2. 4. The simulation results indicate that the tailings are for the most part liquefied (ru> 0.9) at the end of shaking.

The horizontal deformation of the impoundment at the end of shaking is shown on Figure A2. 5. Maximum deformations of about 10 m occurred on the downstream slope of the dike.

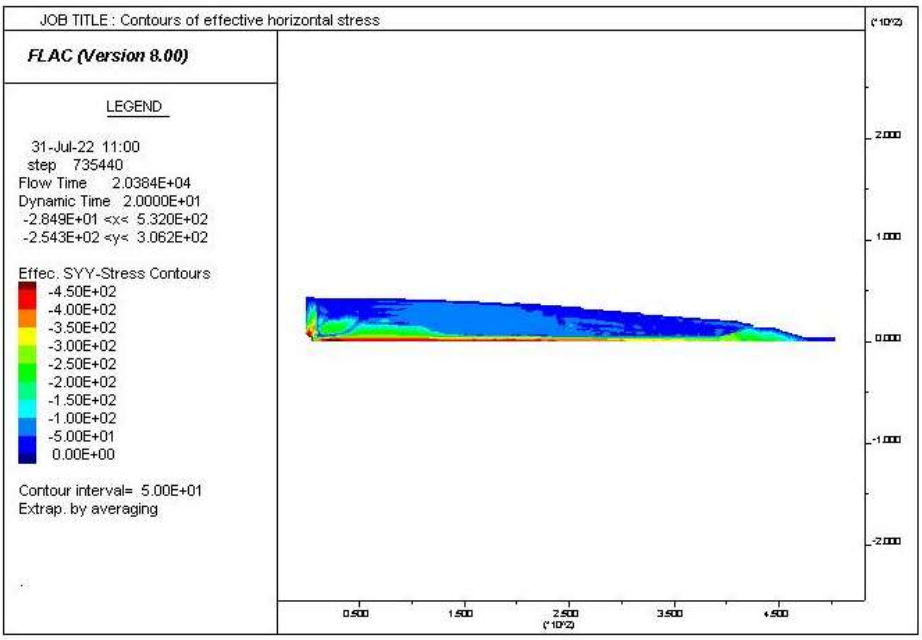

Figure A2. 1: Vertical effective stresses for the unreinforced model with a downstream slope of 8H:1V and a height of 40 m at the end of E_3-Loma earthquake

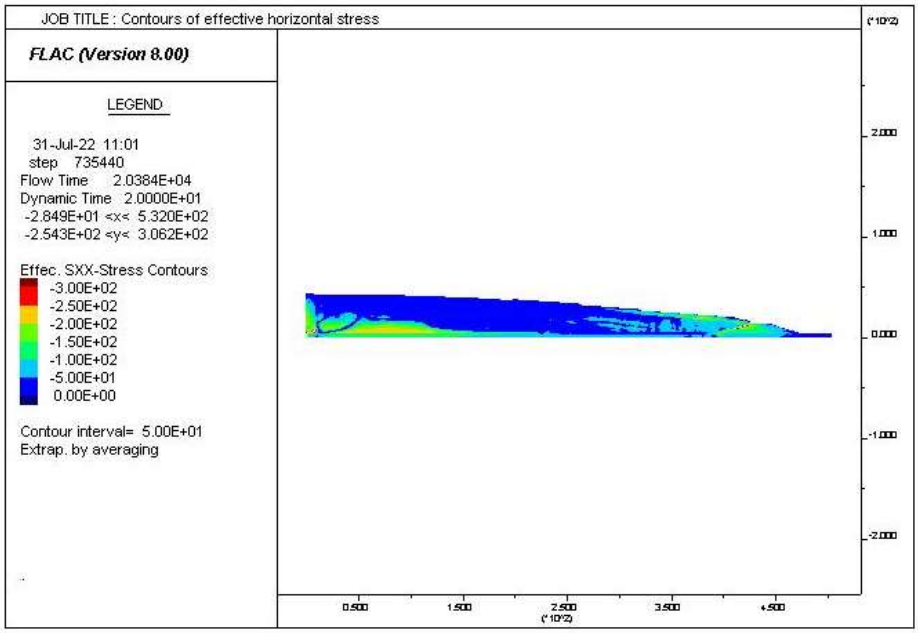

Figure A2. 2: Horizontal effective stresses for the unreinforced model with a downstream slope of 8H:1V and a height of 40 m at the end of E_3-Loma earthquake

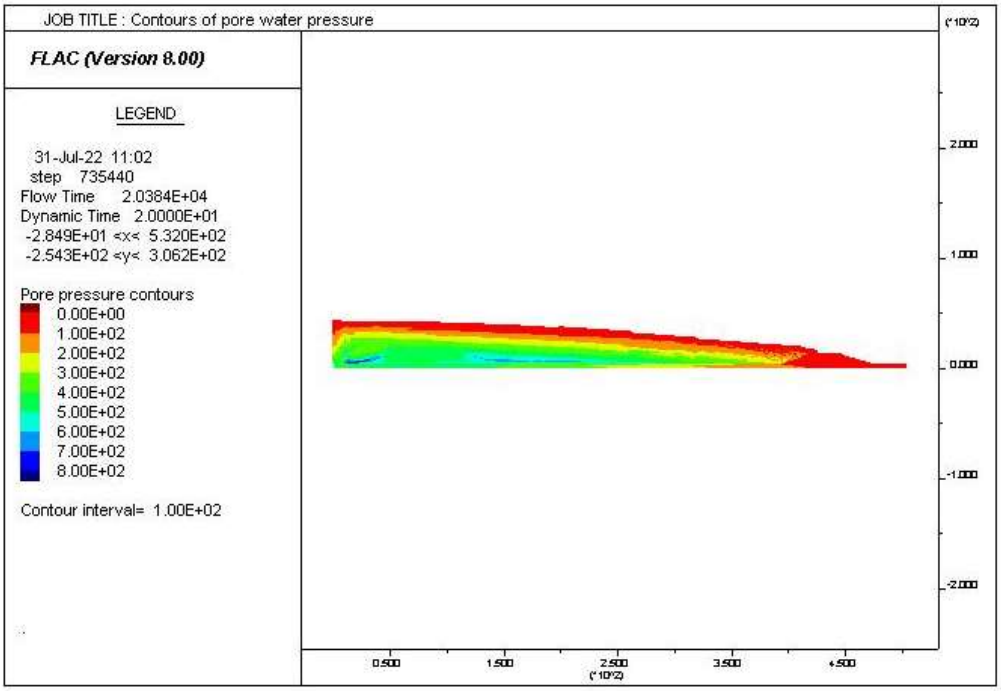

Figure A2. 3: Pore water pressure distribution for the unreinforced model with a downstream slope of 8H:1V and a height of 40 m at the end of E_3-Loma earthquake

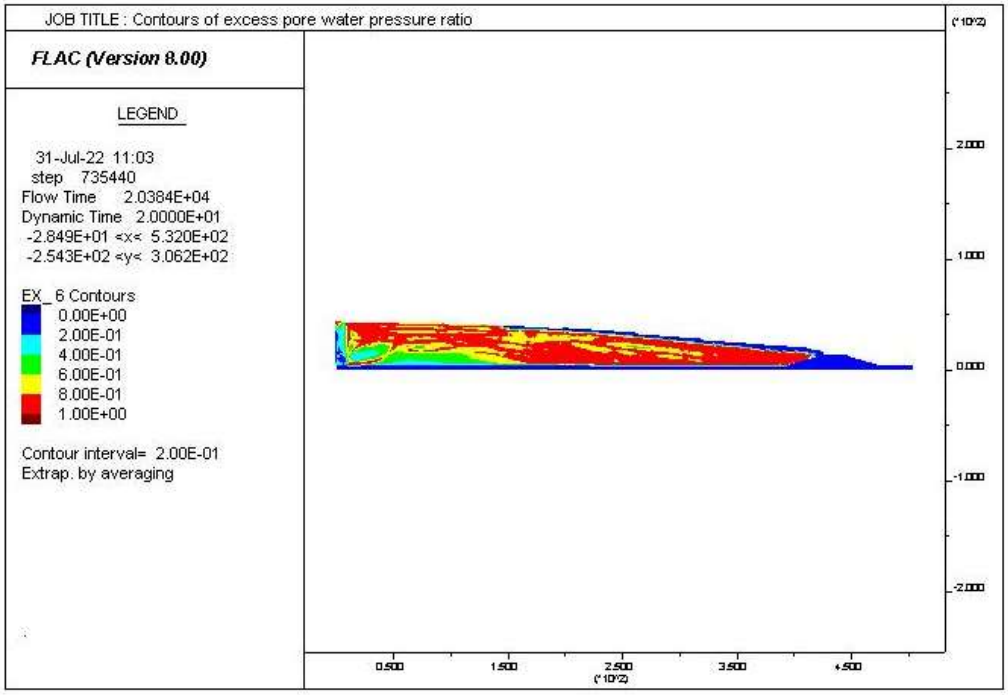

Figure A2. 4: Excess pore water pressure ratio distribution for the unreinforced model with a downstream slope of 8H:1V and a height of 40 m at the end of E_3-Loma earthquake

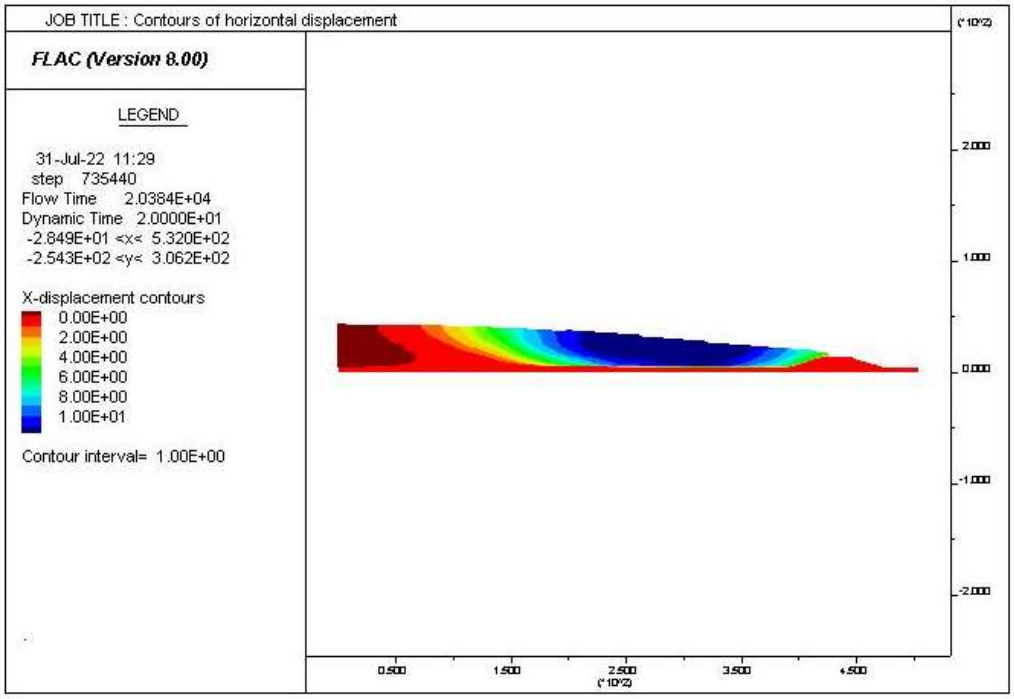

Figure A2. 5: Contours of horizontal displacement for the unreinforced model with a downstream slope of 8H:1V and a height of 40 m at the end of E_3-Loma earthquake

In order to obtain the optimum mesh size the mesh sensitivity analysis is conducted by increasing the mesh element density in the zone with higher magnitude of deformation. As it is shown in Figure A2. 6, the sensitivity analysis is conducted in for the unreinforced model with a downstream slope of 8H:1V and a height of 40 m under the E_3-Loma earthquake in 6 steps (with different elements) and in each step the horizontal displacement of a nodal point at the crest of the dike is plot versus the total elements in that step. Based on this analysis, the value of the horizontal displacement is almost constant for elements number of more than 25300 and increasing the mesh size to 44000 does not change the horizontal displacement remarkably while increasing the running time. Thus the mesh size with 25300 elements is considered as the optimum in this analysis (average value of 1 m by 1 m). This mesh size also ensured that ground motions frequencies up to 25 Hz are realistically transmitted through the model according to the guidelines provided by Kuhlemeyer and Lysmer (1973).

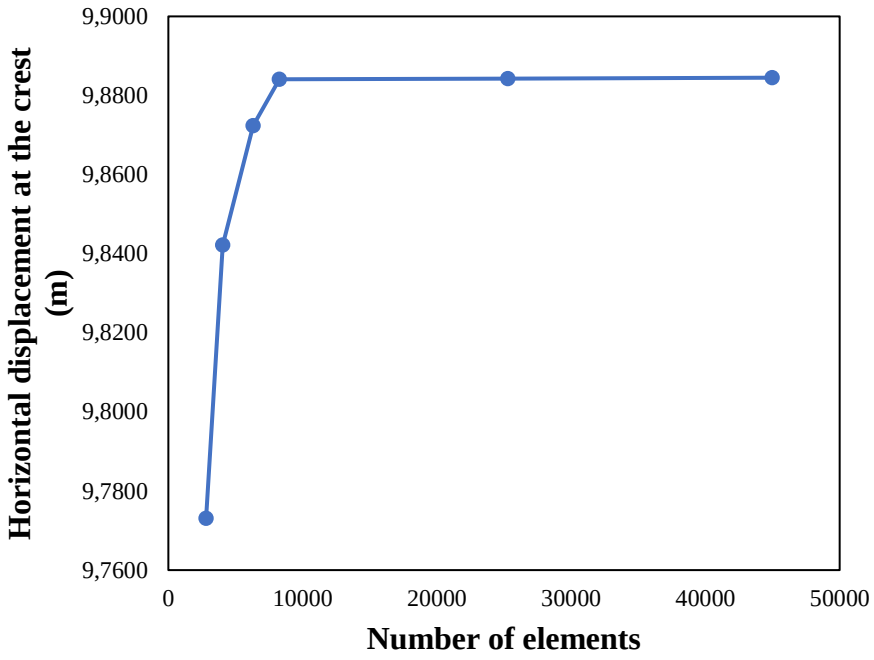

Figure A2. 6: Mesh sensitivity analysis for the unreinforced model with a downstream slope of 8H:1V and a height of 40 m under the E_3-Loma earthquake

A3 Dynamic response of reinforced models

The dynamic response of the reinforced models with different downstream slopes ranges between 7H:1V to 12H:1V, heights ranges between 20 m to 50 m, WRIs' configuration, and ground motions are summarized in this section in terms of excess pore water pressure ratio, r_u, and horizontal displacement at the end of the ground motion. Table A3. 1 summaries the combinations of width, spacing, height, slope, and seismic loading shown in this section.

Table A3. 1: The combinations of width, spacing, height, slope, and seismic loading

Simulation Identification*	Impoundment height(m)	Downstream slope (xH:1V)	Width of the WRI (m)	Space between WRI (m)	Figure No.
12-55-40-8H- E_1, E_2, E_3, and E_4-Loma	40	8	12	55	A3.1 to A3.8
12-80-40-8H- E_1, E_2, E_3, and E_4-Loma	40	8	12	80	A3.9 to A3.16

12-120-40-8H- E_1, E_2, E_3, and E_4 -Loma	40	8	12	120	A3.17 to A3.24
16-50-40-8H- E_1, E_2, E_3, and E_4-Loma	40	8	16	50	A3.25 to A3.32
16-70-40-8H- E_1, E_2, E_3, and E_4-Loma	40	8	16	70	A3.33 to A3.40
16-110-40-8H- E_1, E_2, E_3, and E_4-Loma	40	8	16	110	A3.41 to A3.48
20-50-40-8H- E_1, E_2, E_3, and E_4-Loma	40	8	20	50	A3.49 to A3.56
20-70-40-8H- E_1, E_2, E_3, and E_4-Loma	40	8	20	70	A3.57 to A3.64
20-115-40-8H- E_1, E_2, E_3, and E_4-Loma	40	8	20	115	A3.65 to A3.72
25-60-40-8H- E_1, E_2, E_3, and E_4-Loma	40	8	25	60	A3.73 to A3.80
25-110-40-8H- E_1, E_2, E_3, and E_4-Loma	40	8	25	110	A3.81 to A3.88
12-65-40-7H-E_3-Loma	40	7	12	65	A3.89 and A3.90
16-60-40-7H-E_3-Loma	40	7	16	60	A3.91 and A3.92
16-100-40-7H-E_3-Loma	40	7	16	100	A3.93 and A3.94
20-56-40-7H-E_3-Loma	40	7	20	56	A3.95 and A3.96
20-100-40-7H-E_3-Loma	40	7	20	100	A3.97 and A3.98
25-100-40-7H-E_3-Loma	40	7	25	100	A3.99 and A3.100
12-70-40-10H-E_3-Loma	40	10	12	70	A3.101 and A3.102
12-90-40-10H-E_3-Loma	40	10	12	90	A3.103 and A3.104
12-140-40-10H-E_3-Loma	40	10	12	140	A3.105 and A3.106
16-60-40-10H-E_3-Loma	40	10	16	60	A3.107 and A3.108
16-90-40-10H-E_3-Loma	40	10	16	90	A3.109 and A3.110
16-140-40-10H-E_3-Loma	40	10	16	140	A3.111 and A3.112
20-60-40-10H-E_3-Loma	40	10	20	60	A3.113 and A3.114

20-90-40-10H-E_3-Loma	40	10	20	90	A3.115 and A3.116
20-140-40-10H-E_3-Loma	40	10	20	140	A3.117 and A3.118
25-80-40-10H-E_3-Loma	40	10	25	80	A3.119 and A3.120
25-130-40-10H-E_3-Loma	40	10	25	130	A3.121 and A3.122
12-90-40-12H-E_3-Loma	40	12	12	90	A3.123 and A3.124
12-90-40-12H-E_3-Loma	40	12	12	90	A3.125 and A3.126
16-86-40-12H-E_3-Loma	40	12	16	86	A3.127 and A3.128
16-121-40-12H-E_3-Loma	40	12	16	121	A3.129 and A3.130
16-186-40-12H-E_3-Loma	40	12	16	186	A3.131 and A3.132
20-82-40-12H-E_3-Loma	40	12	20	82	A3.133 and A3.134
20-117-40-12H-E_3-Loma	40	12	20	117	A3.135 and A3.136
20-182-40-12H-E_3-Loma	40	12	20	182	A3.137 and A3.138
25-110-40-12H-E_3-Loma	40	12	25	110	A3.139 and A3.140
25-150-40-12H-E_3-Loma	40	12	25	150	A3.141 and A3.142
12-50-20-8H-E_3-Loma	20	8	12	50	A3.143 and A3.144
16-37-20-8H-E_3-Loma	20	8	16	37	A3.145 and A3.146
20-33-20-8H-E_3-Loma	20	8	20	33	A3.147 and A3.148
12-55-30-8H-E_3-Loma	30	8	12	55	A3.149 and A3.150
12-85-30-8H-E_3-Loma	30	8	12	85	A3.151 and A3.152
16-50-30-8H-E_3-Loma	30	8	16	50	A3.153 and A3.154
16-85-30-8H-E_3-Loma	30	8	16	85	A3.155 and A3.156
20-50-30-8H-E_3-Loma	30	8	20	50	A3.157 and A3.158

20-80-30-8H-E_3-Loma	30	8	20	80	A3.159 and A3.160
12-70-50-8H-E_3-Loma	50	8	12	70	A3.161 and A3.162
16-70-50-8H-E_3-Loma	50	8	16	70	A3.163 and A3.164
16-95-50-8H-E_3-Loma	50	8	16	95	A3.165 and A3.166
20-65-50-8H-E_3-Loma	50	8	20	65	A3.167 and A3.168
20-95-50-8H-E_3-Loma	50	8	20	95	A3.169 and A3.170
20-150-50-8H-E_3-Loma	50	8	20	150	A3.171 and A3.172
25-60-50-8H-E_3-Loma	50	8	25	60	A3.173 and A3.174
25-90-50-8H-E_3-Loma	50	8	25	90	A3.175 and A3.176
25-140-50-8H-E_3-Loma	50	8	25	140	A3.177 and A3.178

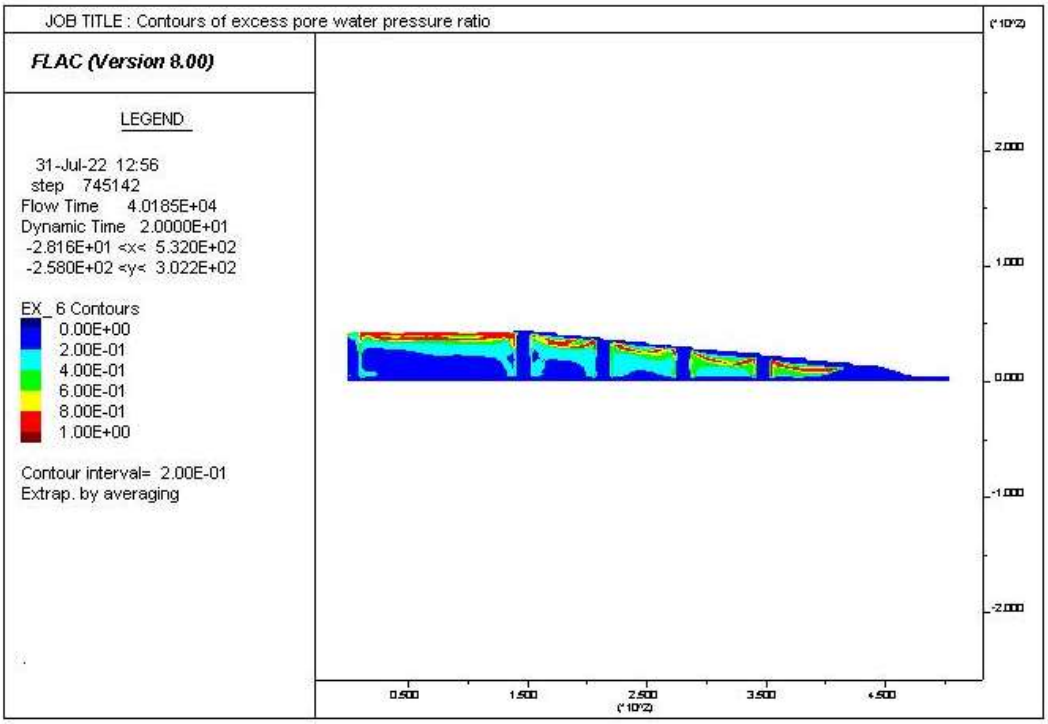

Figure A3. 1: Excess pore water pressure ratio distribution for the 12-55-40-8H- E_1 Loma

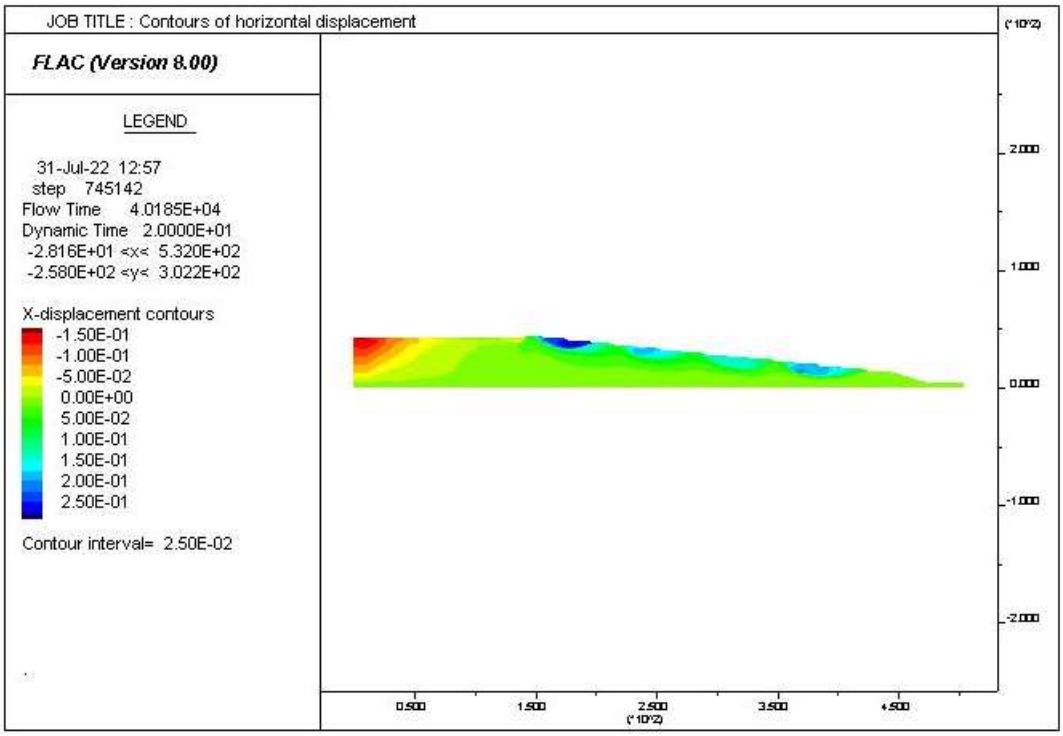

Figure A3. 2: Contours of horizontal displacement for the 12-55-40-8H- E_1 Loma

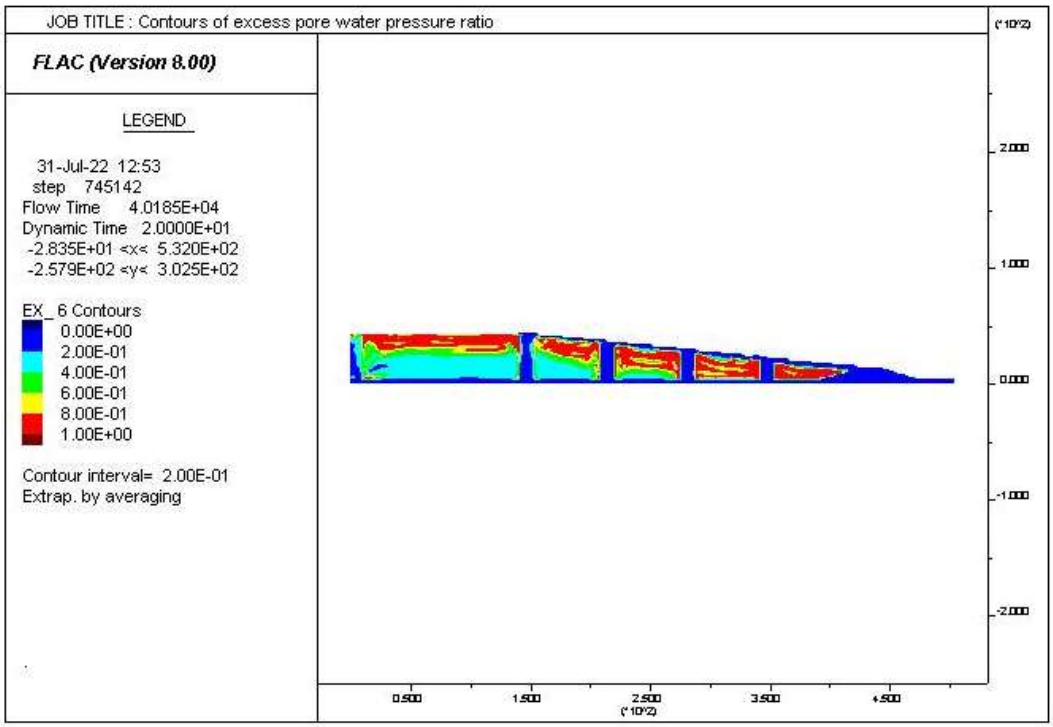

Figure A3. 3: Excess pore water pressure ratio distribution for the 12-55-40-8H- E_2 Loma

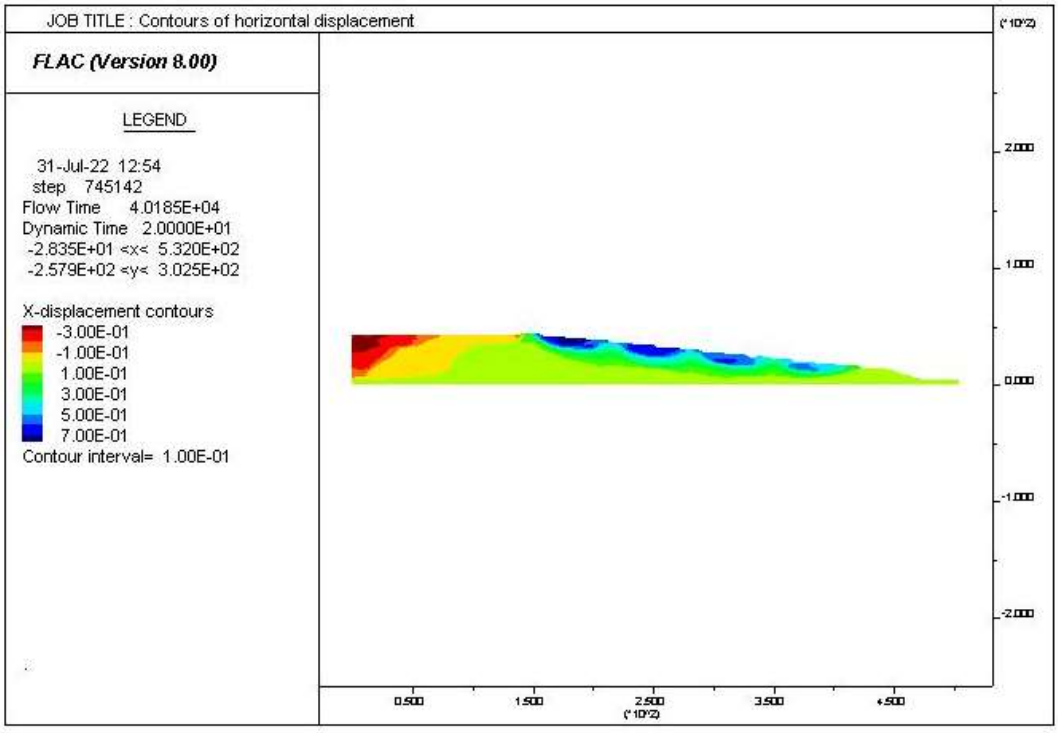

Figure A3. 4: Contours of horizontal displacement for the 12-55-40-8H- E_2 Loma

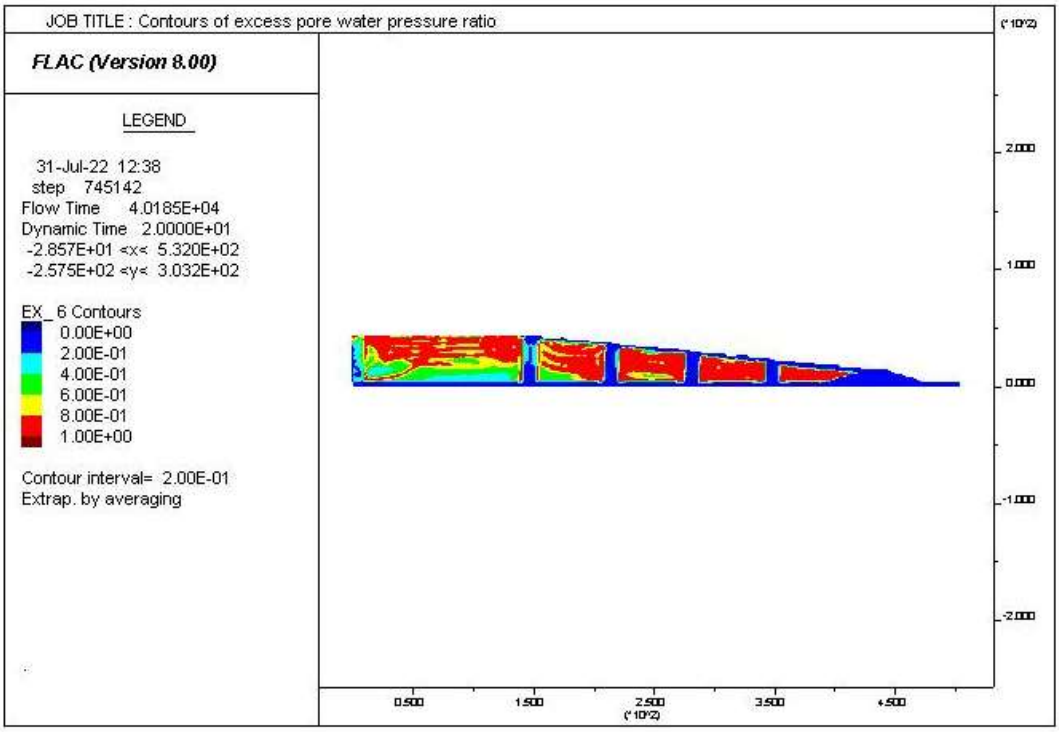

Figure A3. 5: Excess pore water pressure ratio distribution for the 12-55-40-8H- E_3 Loma

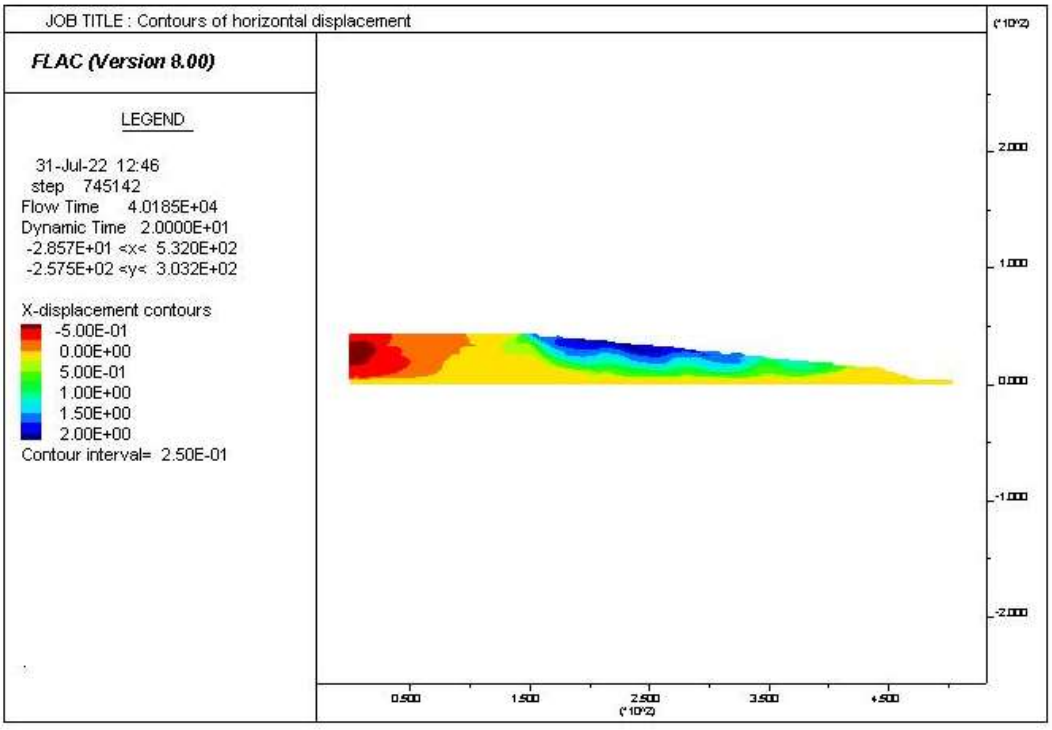

Figure A3. 6: Contours of horizontal displacement for the 12-55-40-8H- E_3 Loma

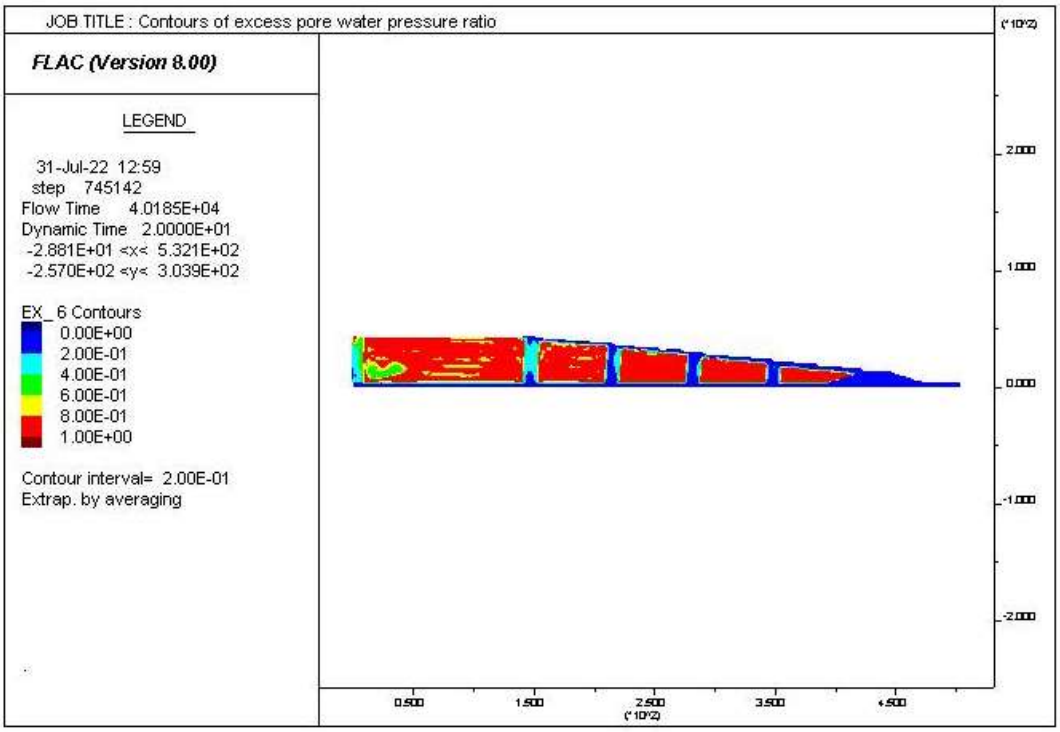

Figure A3. 7: Excess pore water pressure ratio distribution for the 12-55-40-8H- E_4 Loma

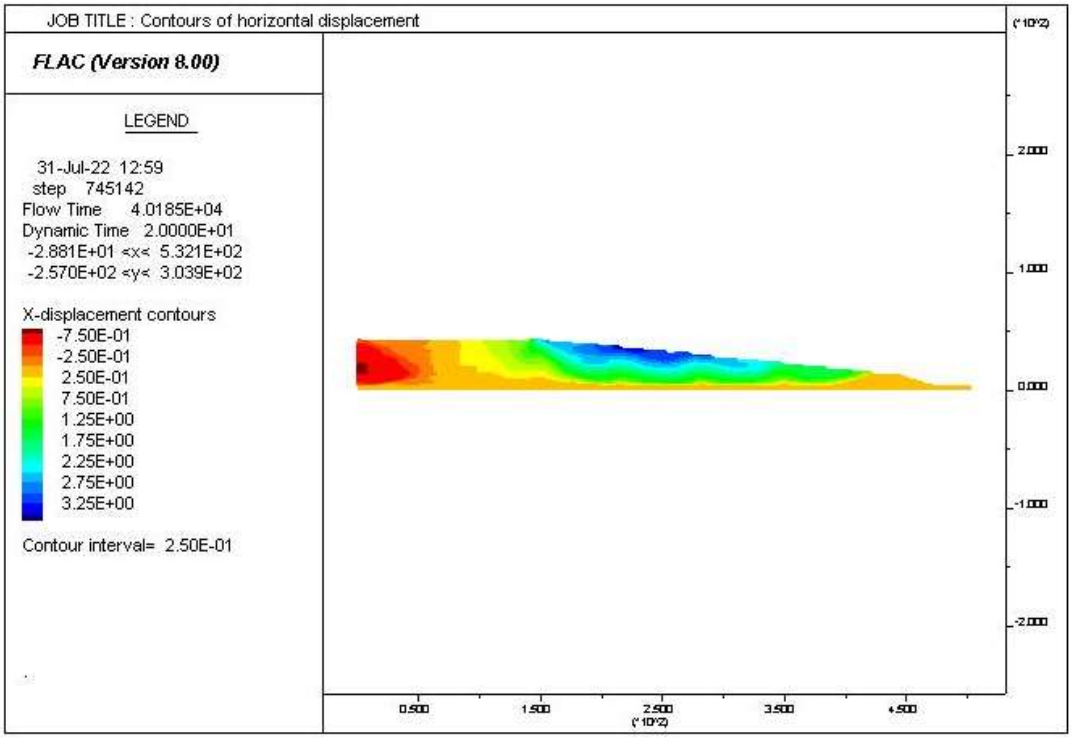

Figure A3. 8: Contours of horizontal displacement for the 12-55-40-8H- E_4 Loma

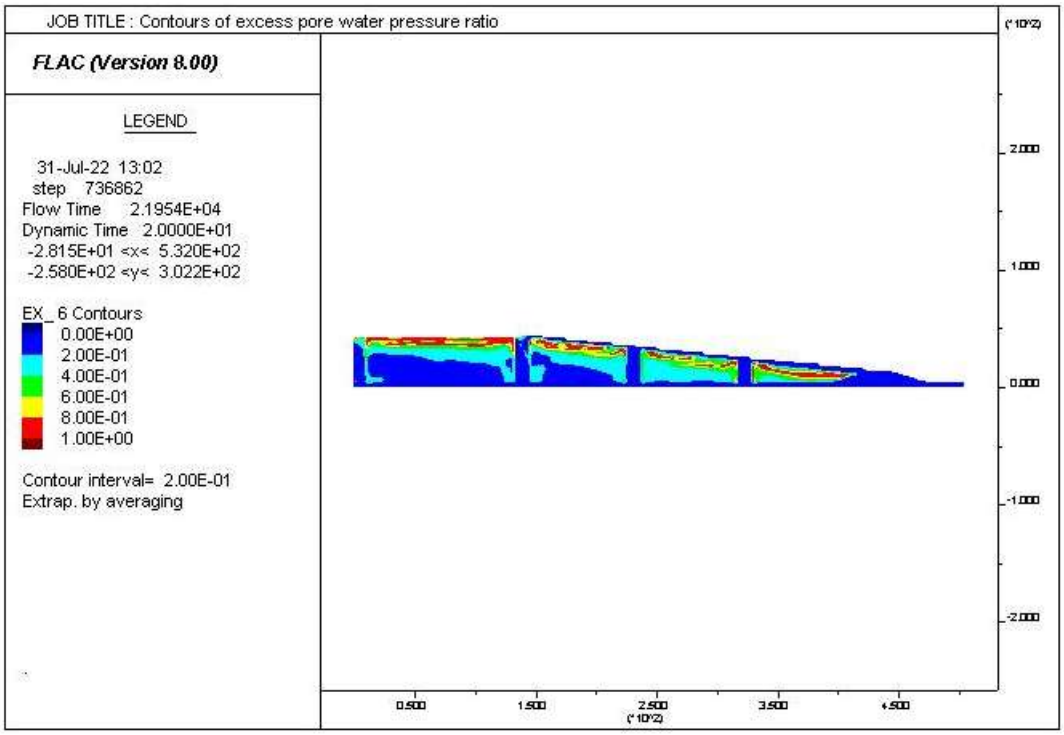

Figure A3. 9: Excess pore water pressure ratio distribution for the 12-80-40-8H- E_1 Loma

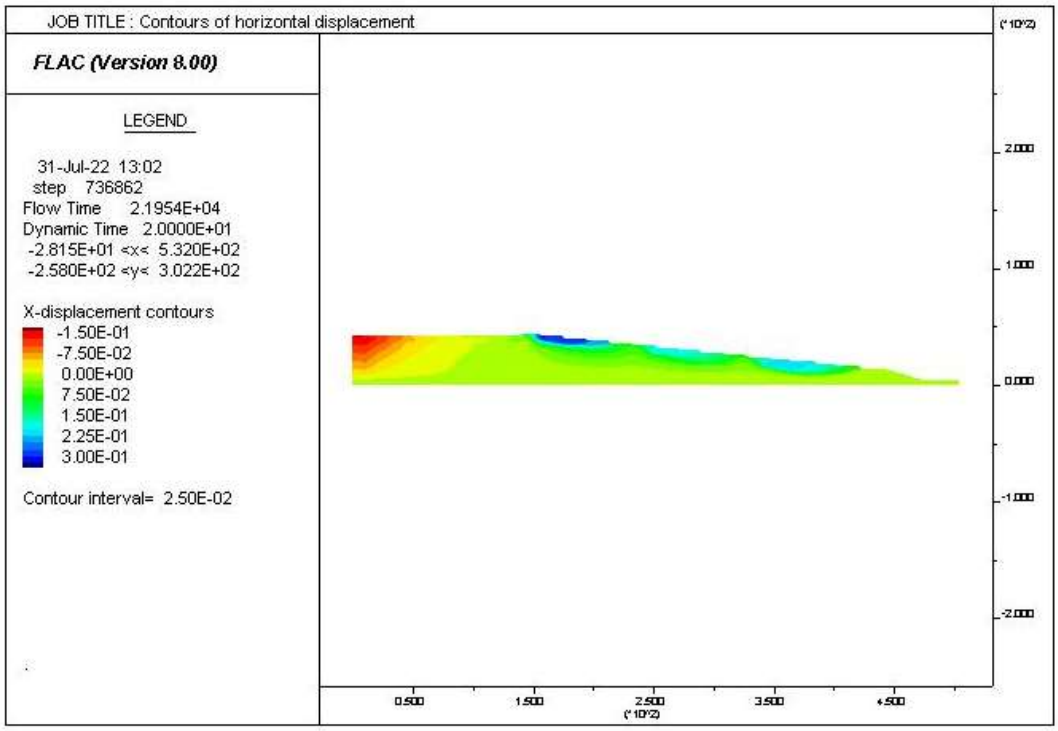

Figure A3. 10: Contours of horizontal displacement for the 12-80-40-8H- E_1 Loma

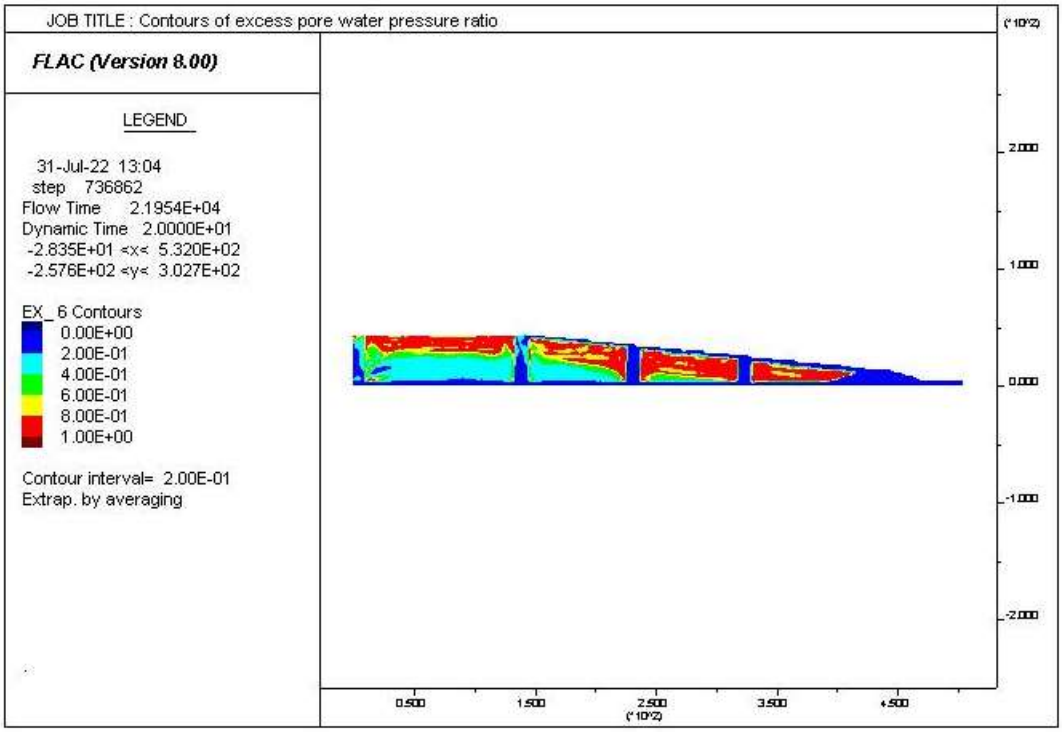

Figure A3. 11: Excess pore water pressure ratio distribution for the 12-80-40-8H- E_2 Loma

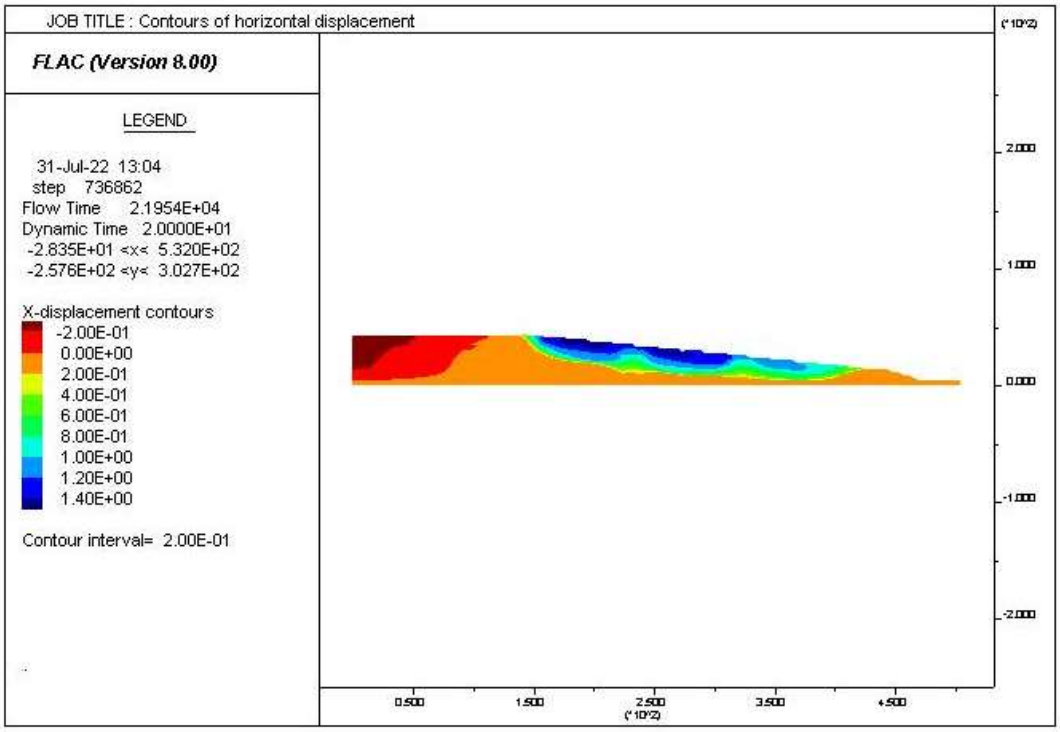

Figure A3. 12: Contours of horizontal displacement for the 12-80-40-8H- E_2 Loma

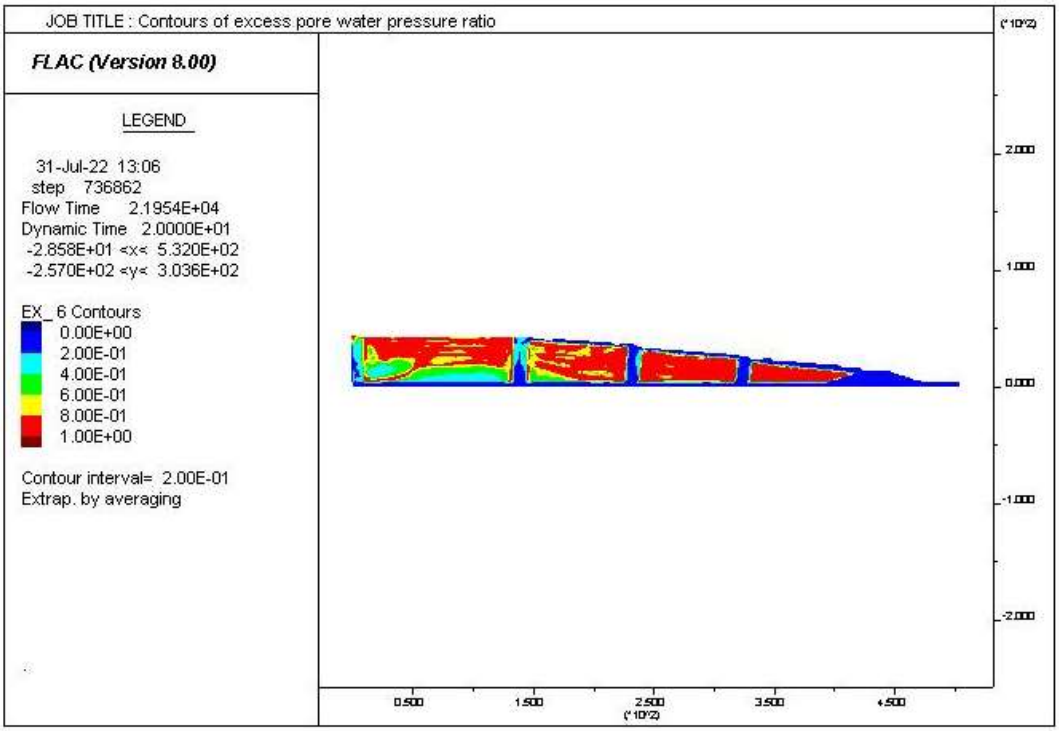

Figure A3. 13: Excess pore water pressure ratio distribution for the 12-80-40-8H- E_3 Loma

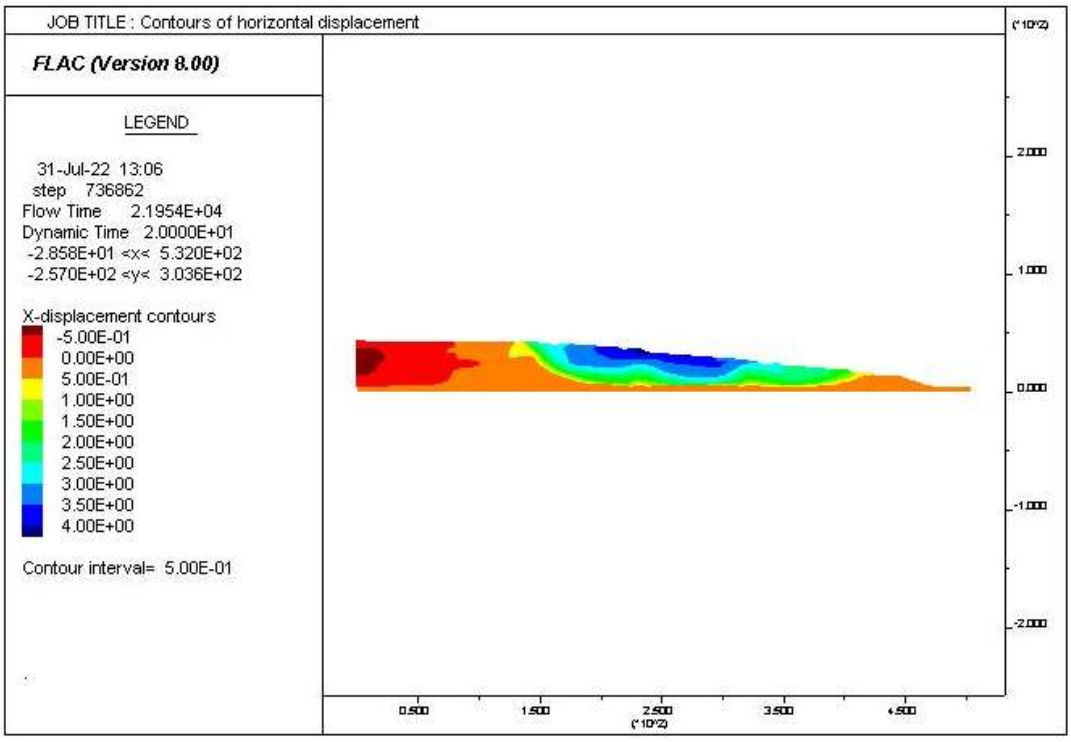

Figure A3. 14: Contours of horizontal displacement for the 12-80-40-8H- E_3 Loma

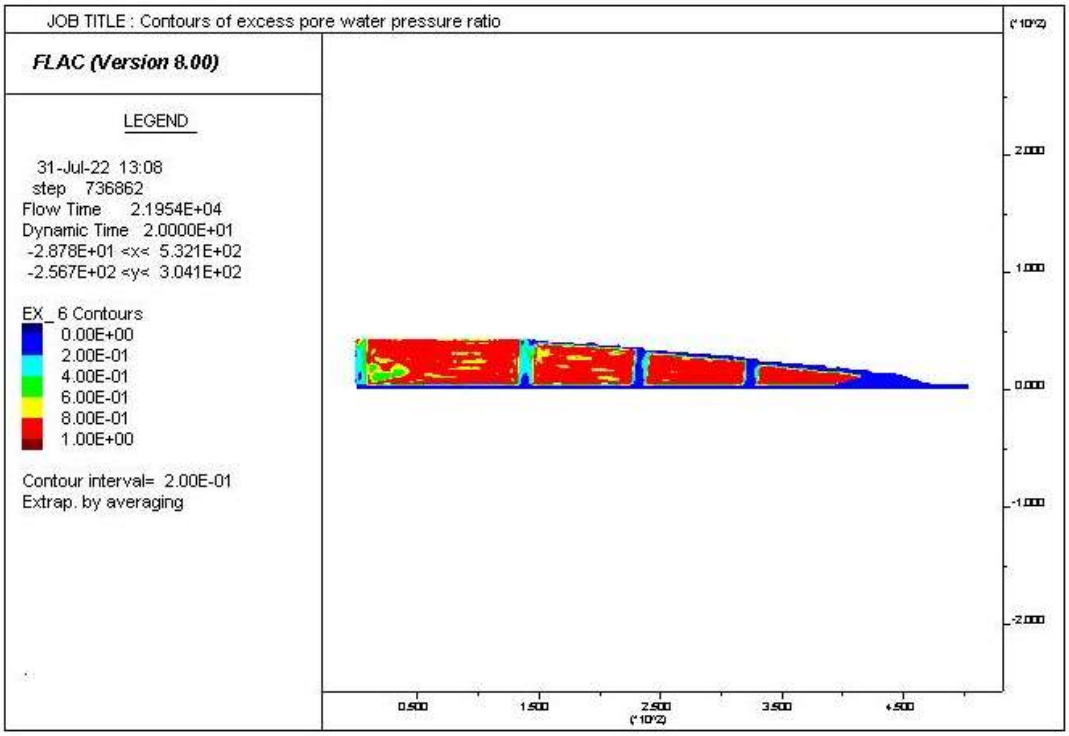

Figure A3. 15: Excess pore water pressure ratio distribution for the 12-80-40-8H- E_4 Loma

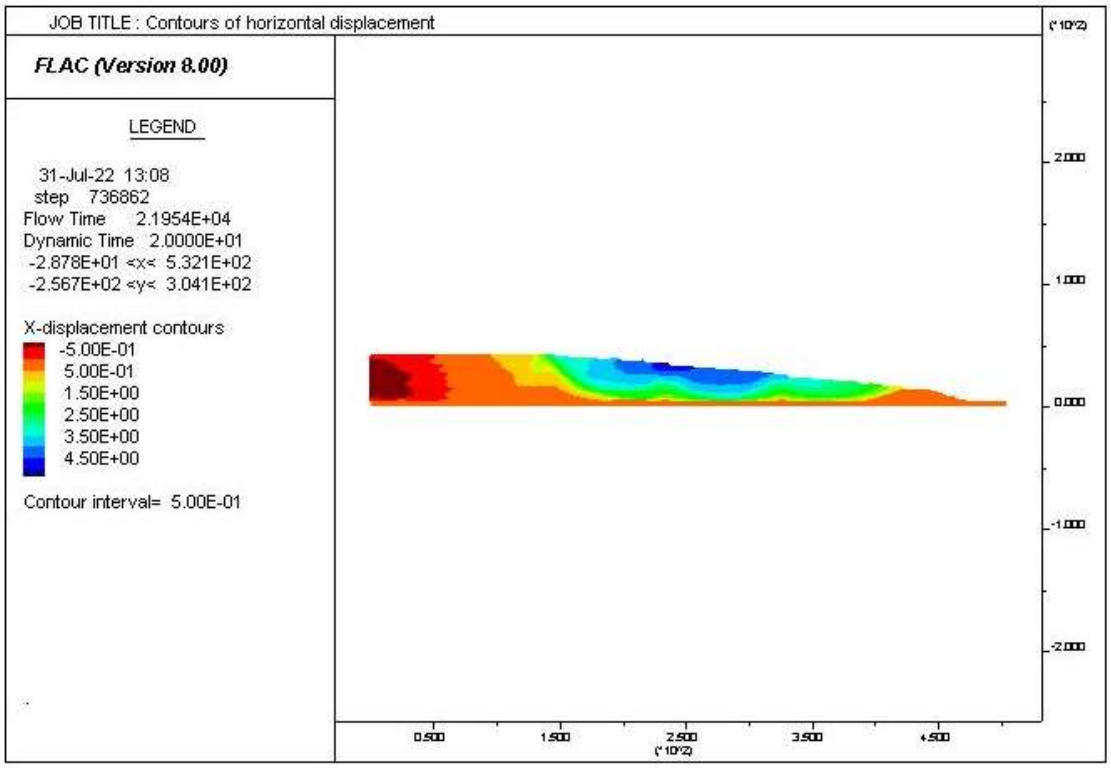

Figure A3. 16: Contours of horizontal displacement for the 12-80-40-8H- E_4 Loma

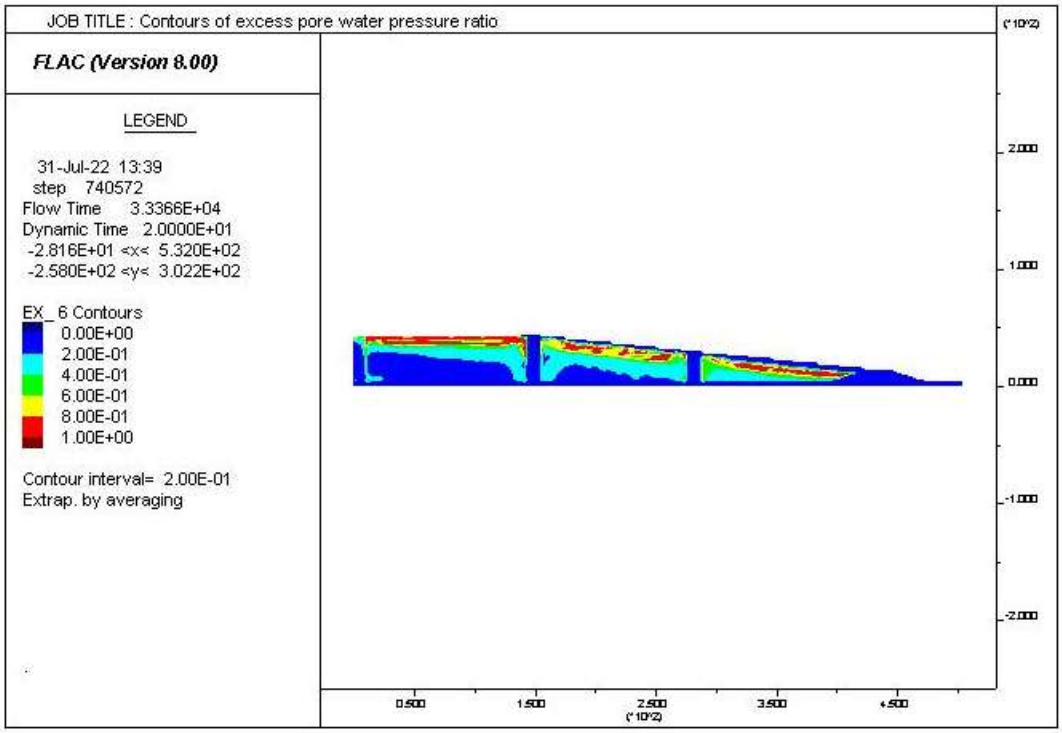

Figure A3. 17: Excess pore water pressure ratio distribution for the 12-120-40-8H- E_1 Loma

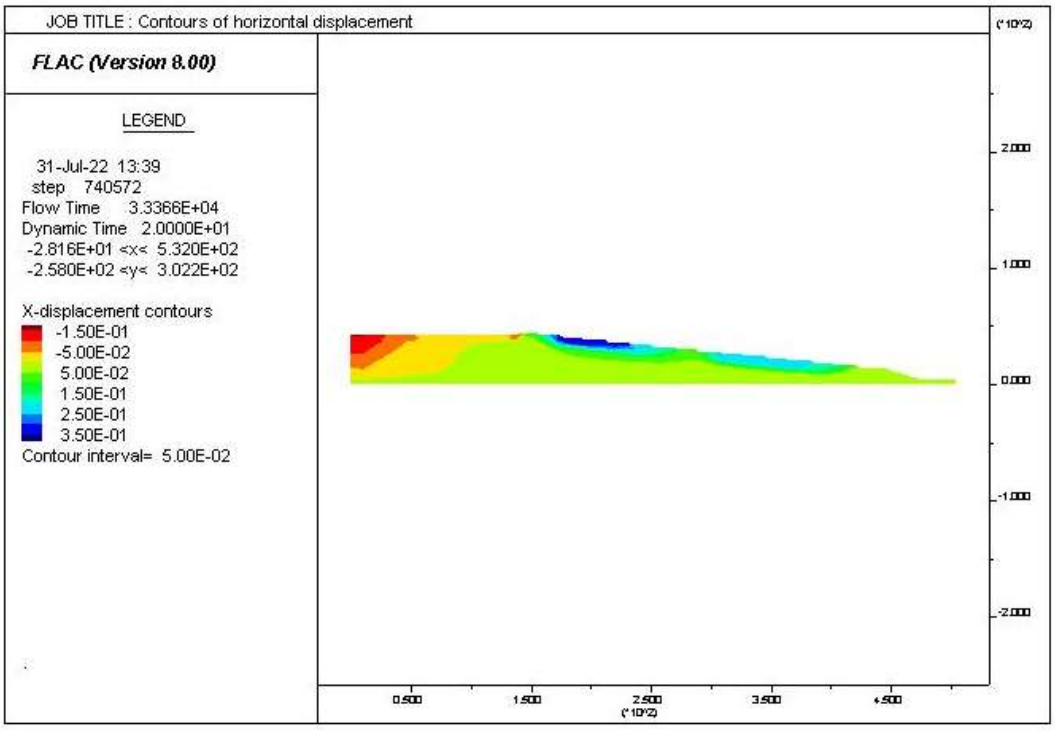

Figure A3. 18: Contours of horizontal displacement for the 12-120-40-8H- E_1 Loma

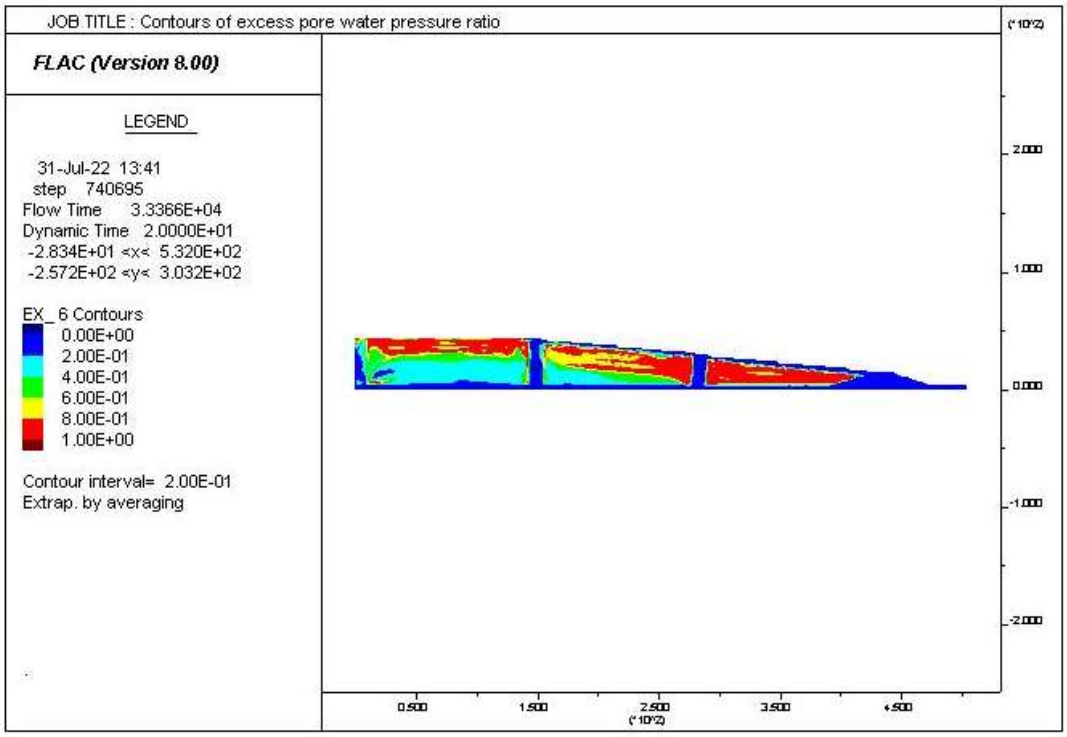

Figure A3. 19: Excess pore water pressure ratio distribution for the 12-120-40-8H- E_2 Loma

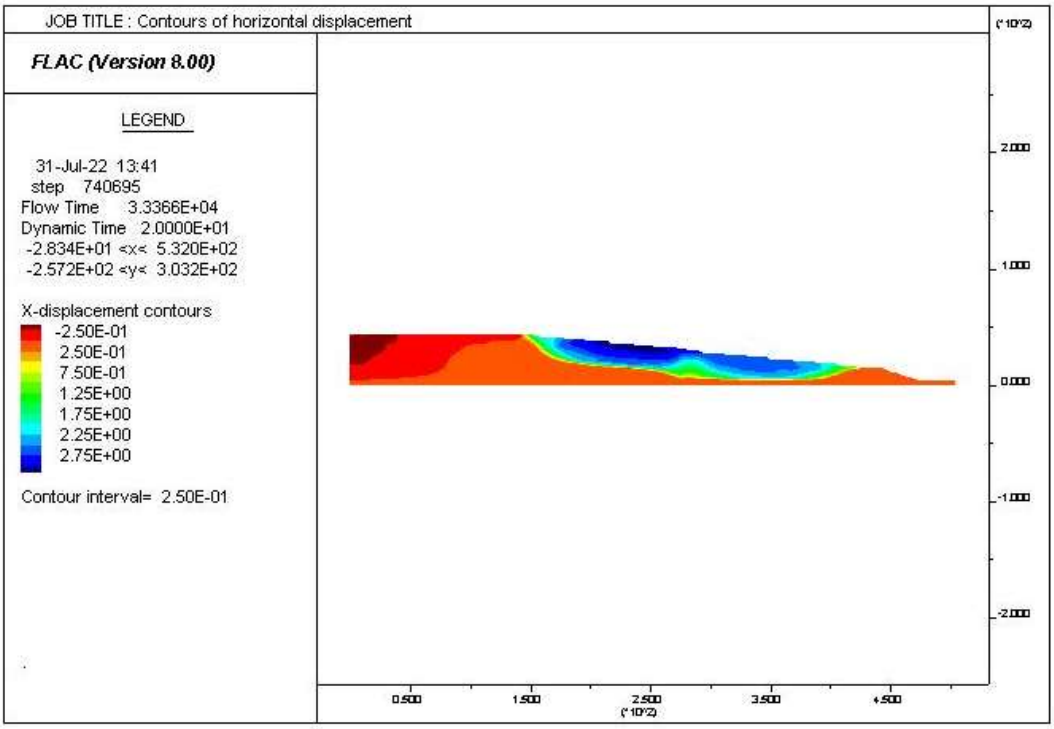

Figure A3. 20: Contours of horizontal displacement for the 12-120-40-8H- E_2 Loma

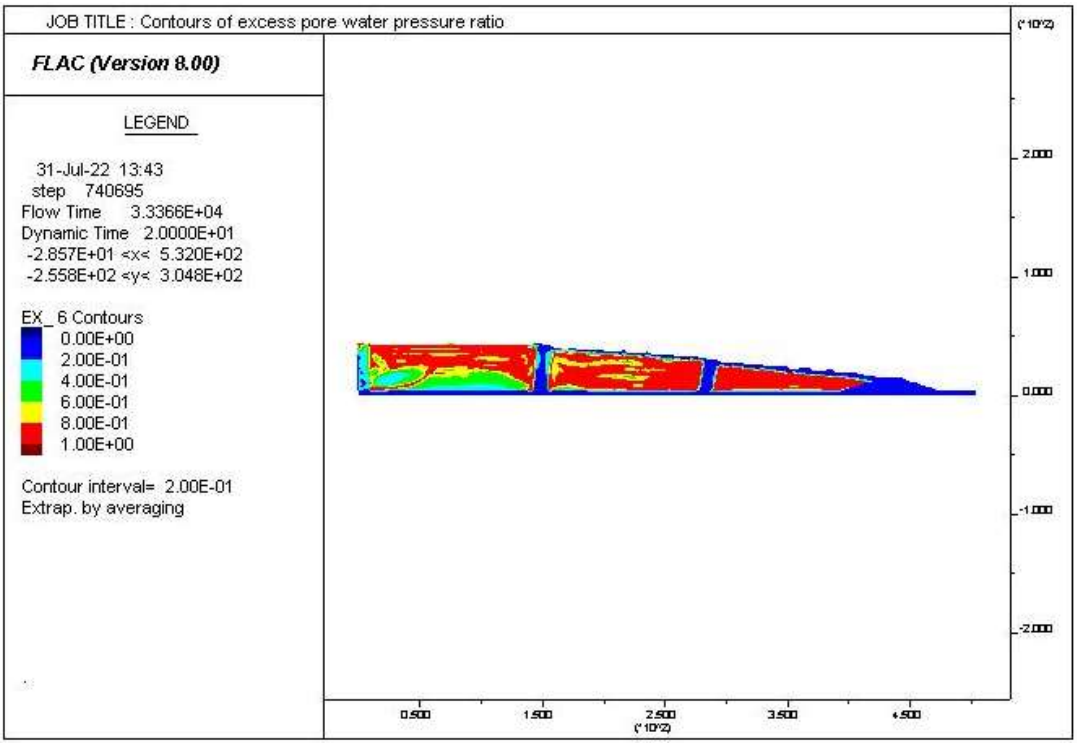

Figure A3. 21: Excess pore water pressure ratio distribution for the 12-120-40-8H- E_3 Loma

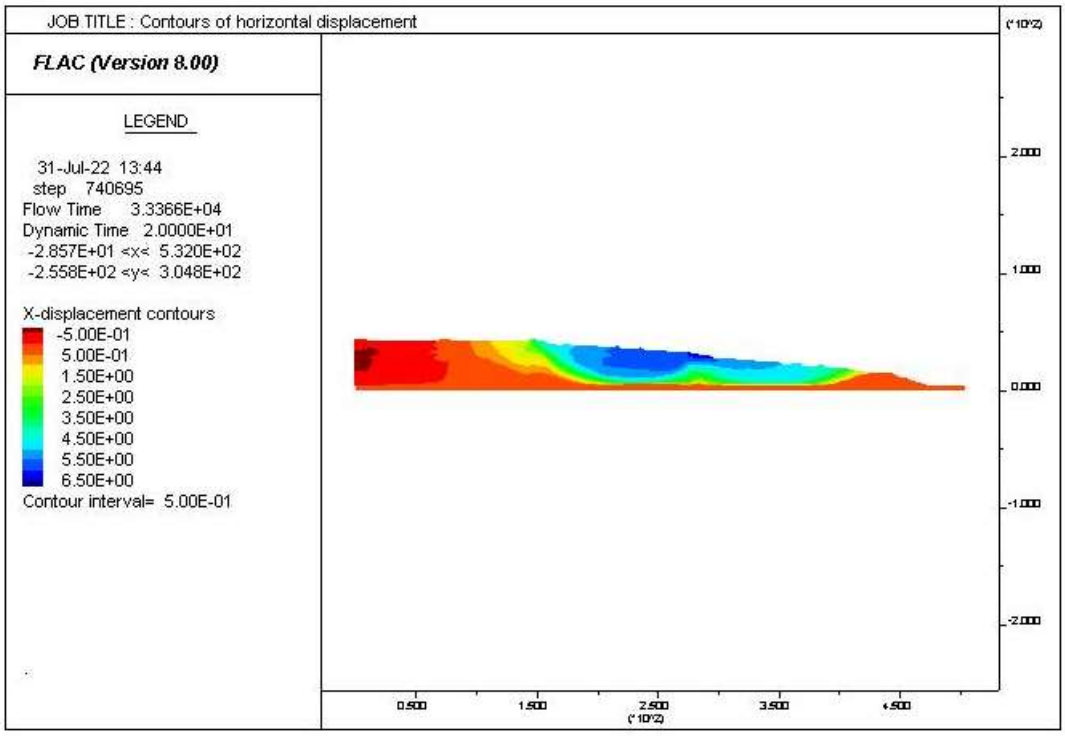

Figure A3. 22: Contours of horizontal displacement for the 12-120-40-8H- E_3 Loma

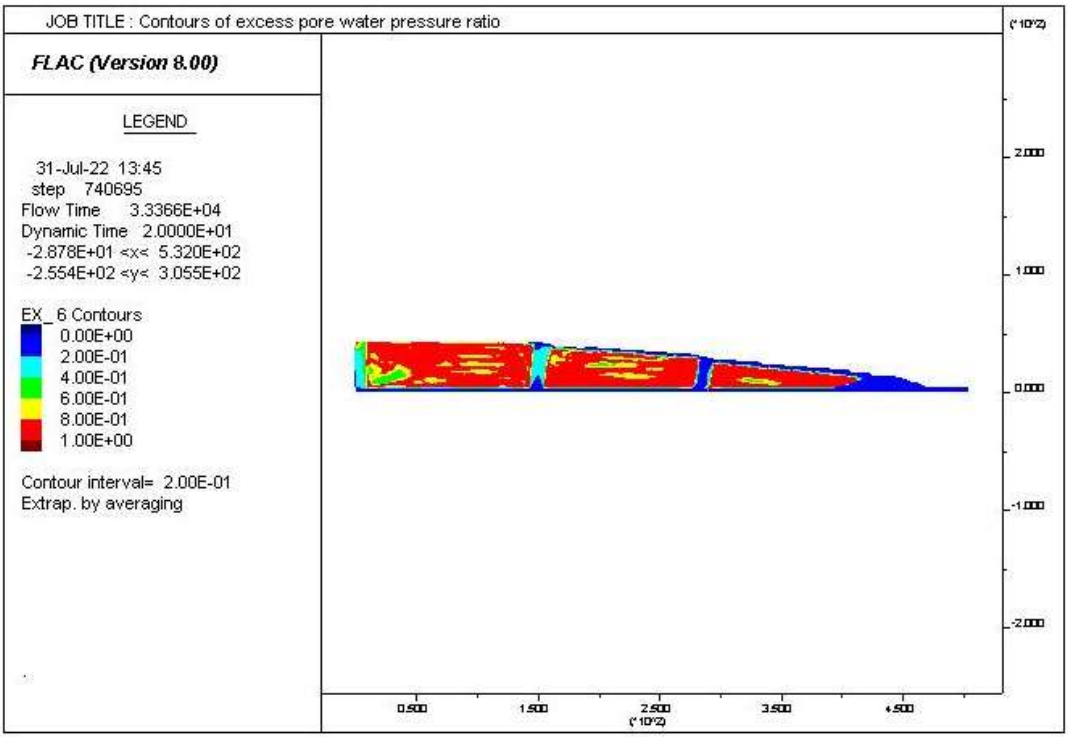

Figure A3. 23: Excess pore water pressure ratio distribution for the 12-120-40-8H- E_4 Loma

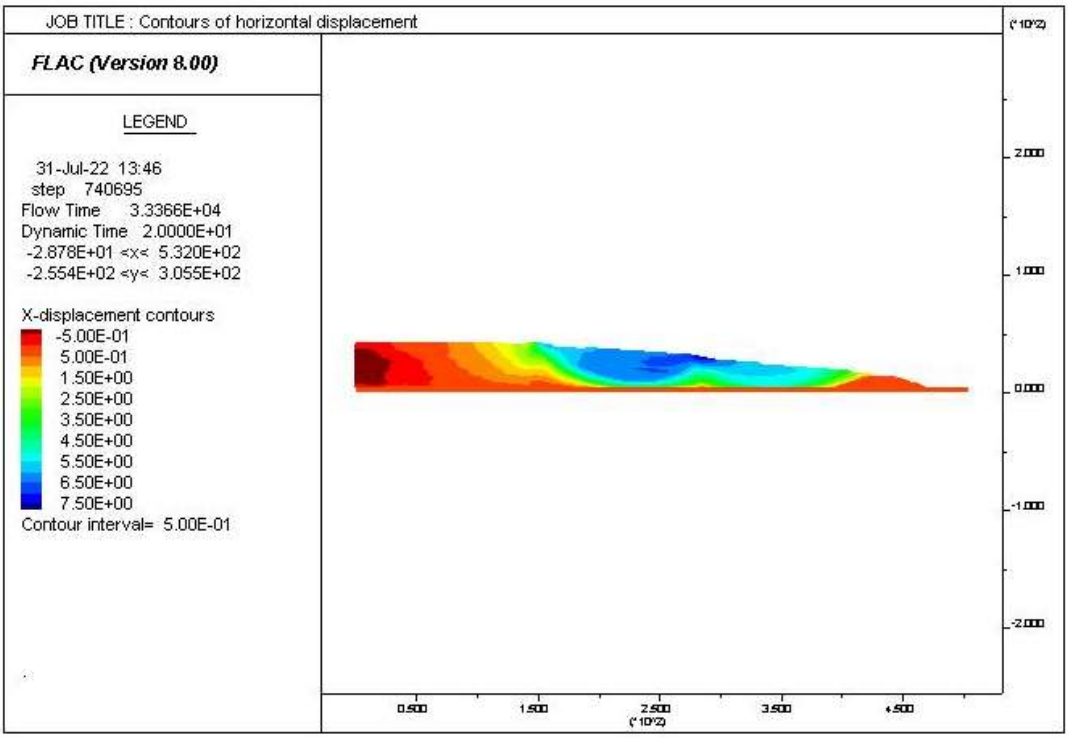

Figure A3. 24: Contours of horizontal displacement for the 12-120-40-8H- E_4 Loma

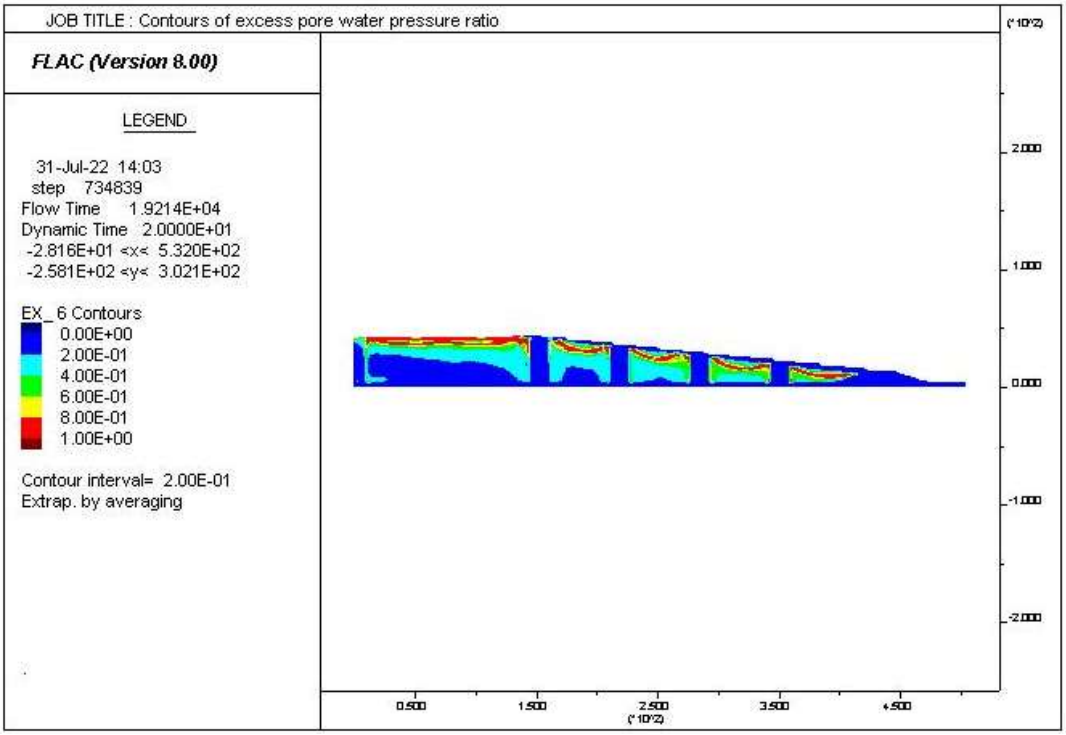

Figure A3. 25: Excess pore water pressure ratio distribution for the 16-50-40-8H- E_1 Loma

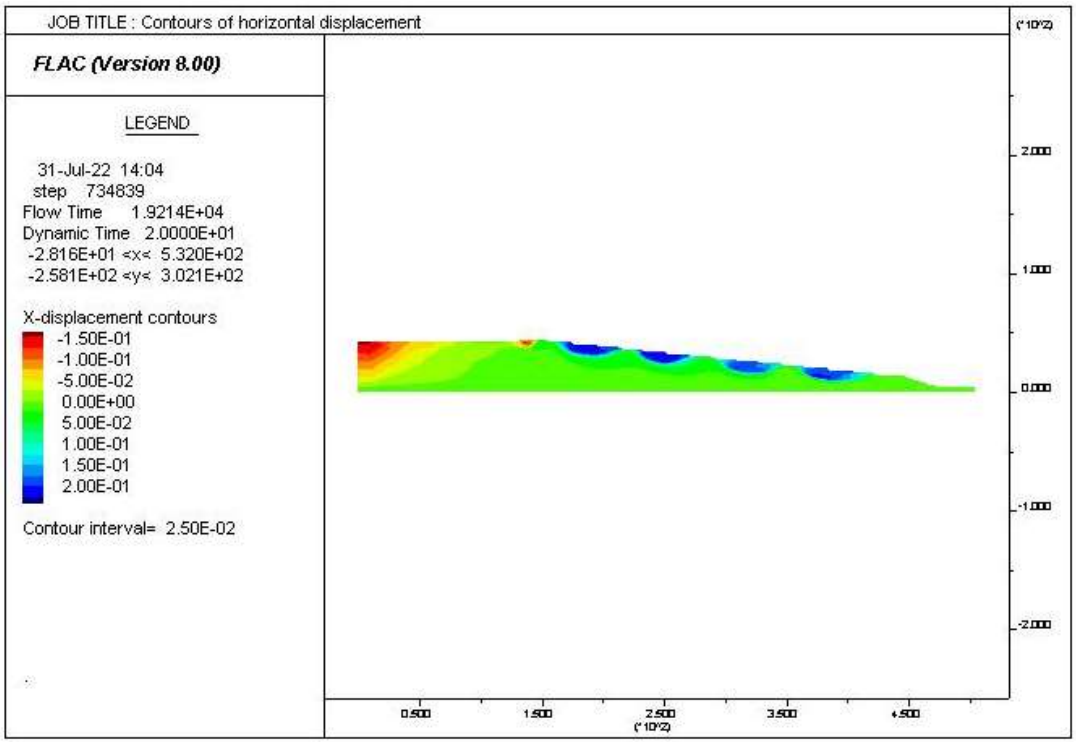

Figure A3. 26: Contours of horizontal displacement for the 16-50-40-8H- E_1 Loma

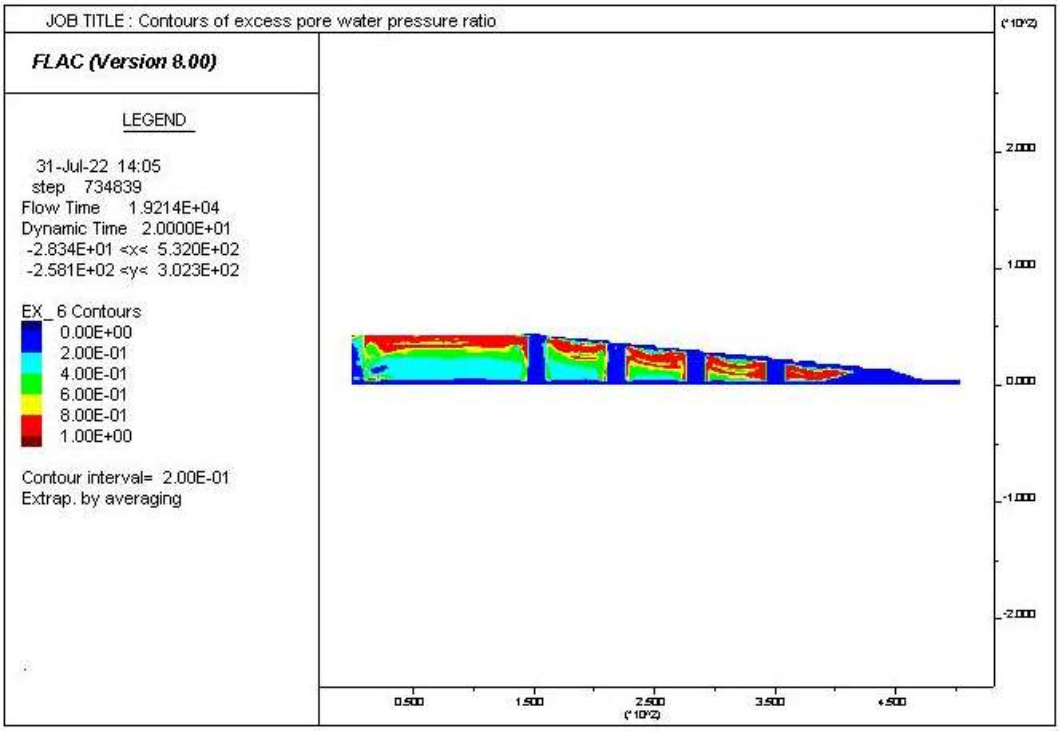

Figure A3. 27: Excess pore water pressure ratio distribution for the 16-50-40-8H- E_2 Loma

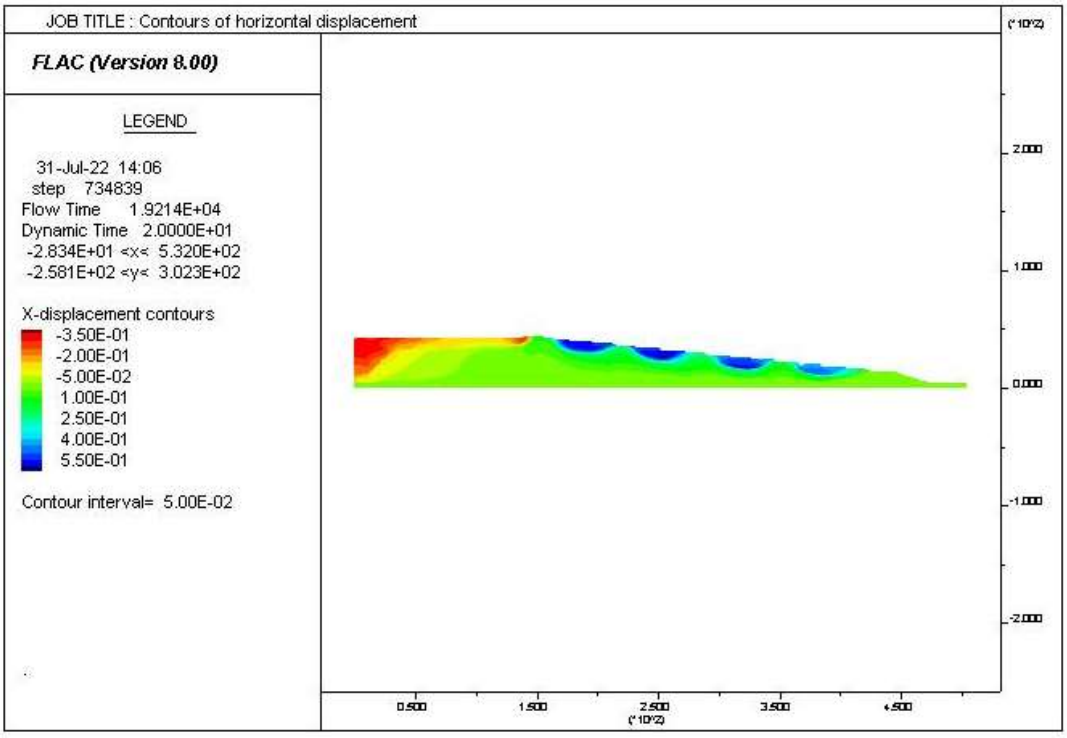

Figure A3. 28: Contours of horizontal displacement for the 16-50-40-8H- E_2 Loma

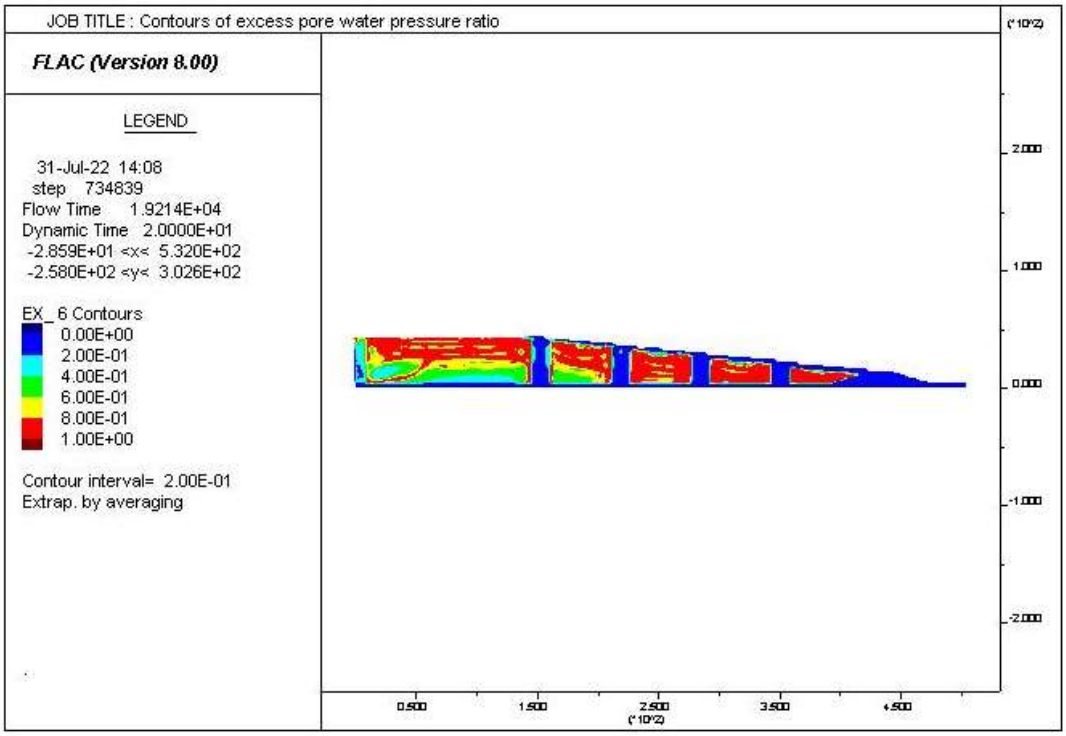

Figure A3. 29: Excess pore water pressure ratio distribution for the 16-50-40-8H- E_3 Loma

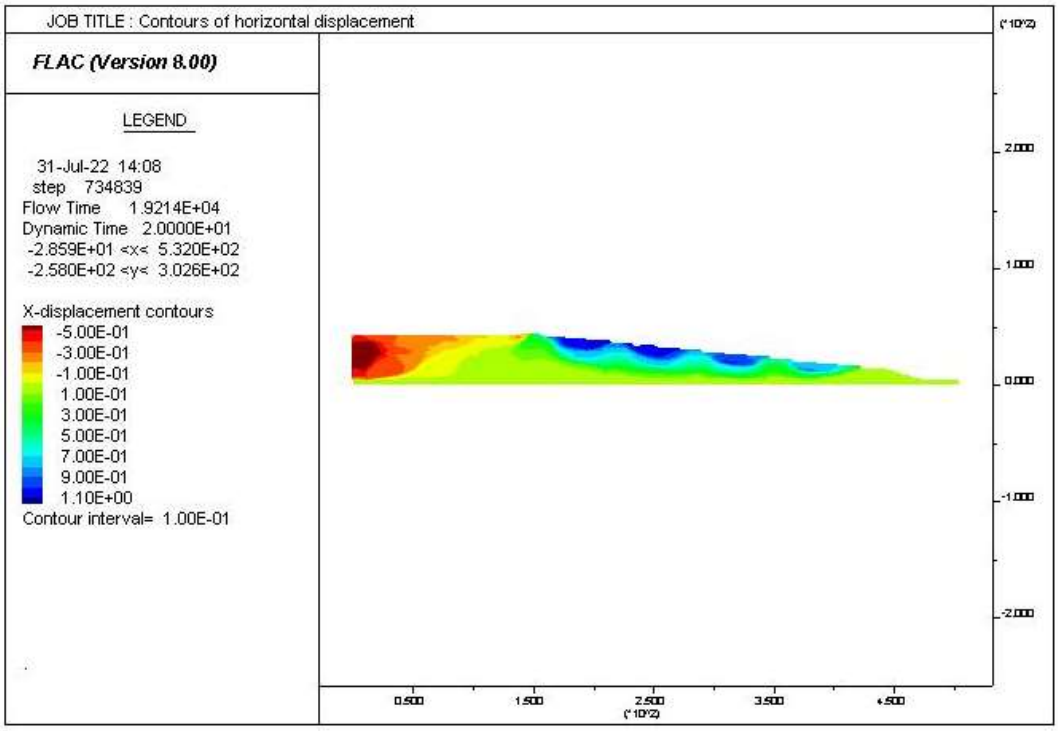

Figure A3. 30: Contours of horizontal displacement for the 16-50-40-8H- E_3 Loma

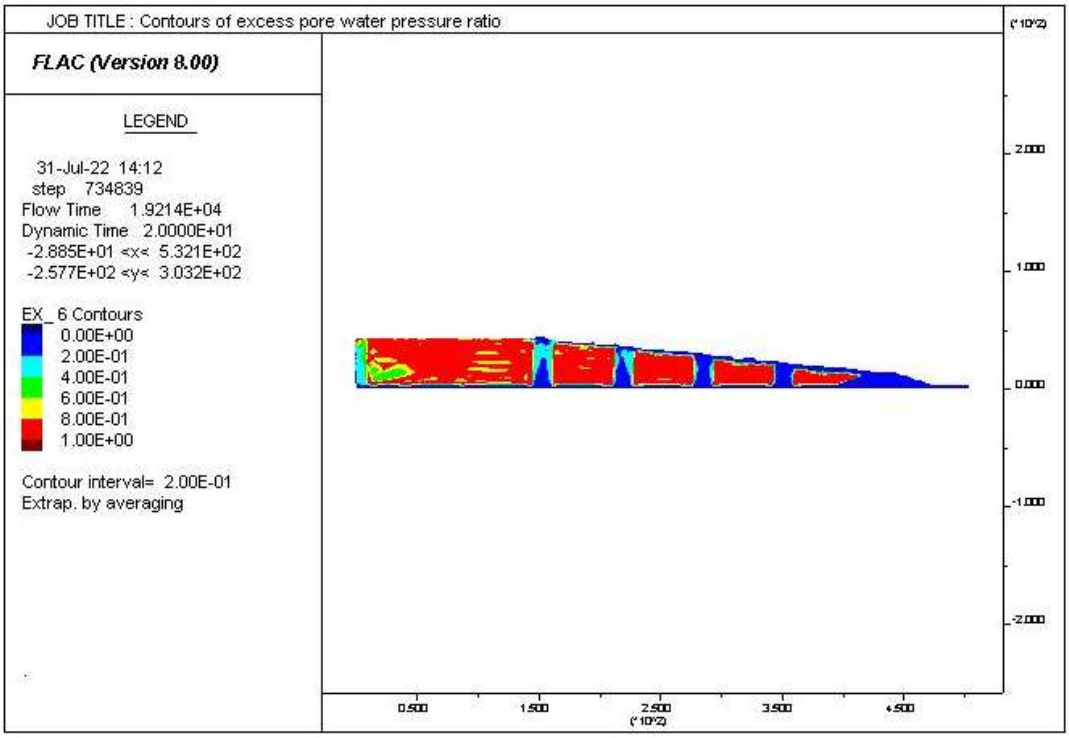

Figure A3. 31: Excess pore water pressure ratio distribution for the 16-50-40-8H- E_4 Loma

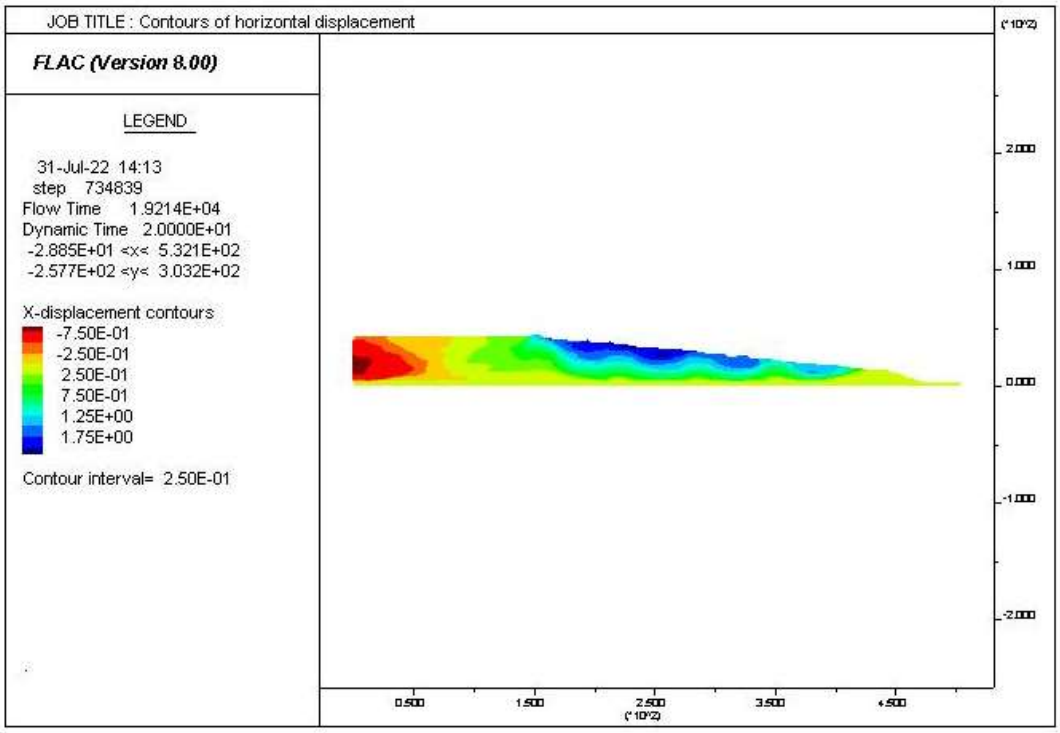

Figure A3. 32: Contours of horizontal displacement for the 16-50-40-8H- E_4 Loma

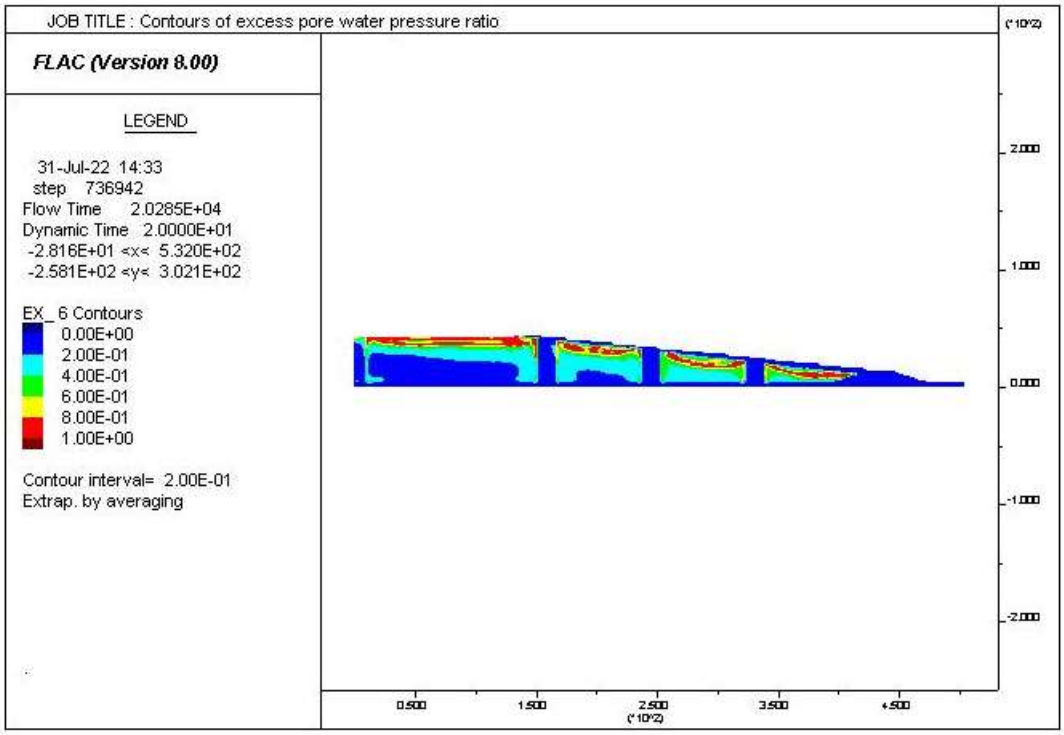

Figure A3. 33: Excess pore water pressure ratio distribution for the 16-70-40-8H- E_1 Loma

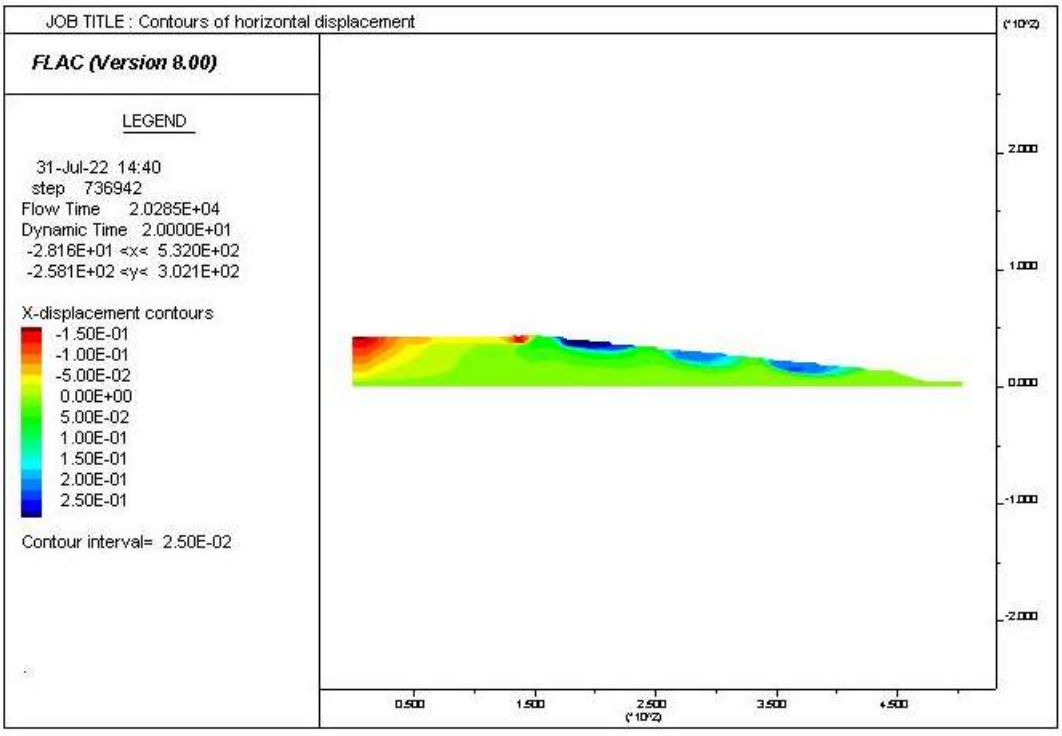

Figure A3. 34: Contours of horizontal displacement for the 16-70-40-8H- E_1 Loma

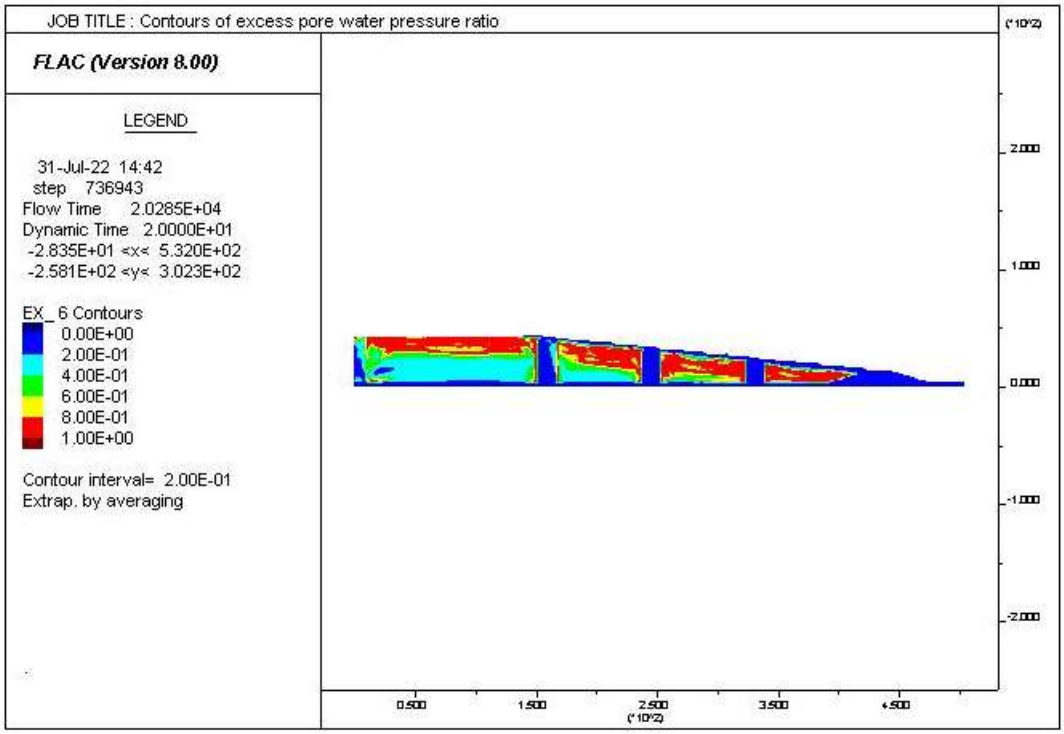

Figure A3. 35: Excess pore water pressure ratio distribution for the 16-70-40-8H- E_2 Loma

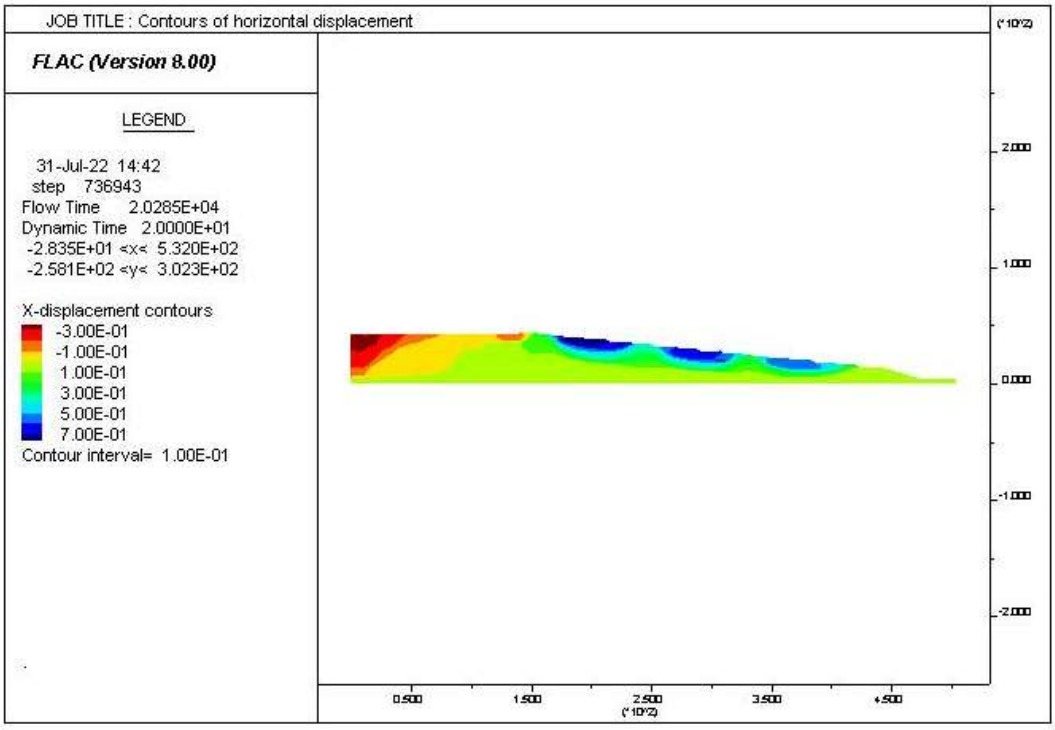

Figure A3. 36: Contours of horizontal displacement for the 16-70-40-8H- E_2 Loma

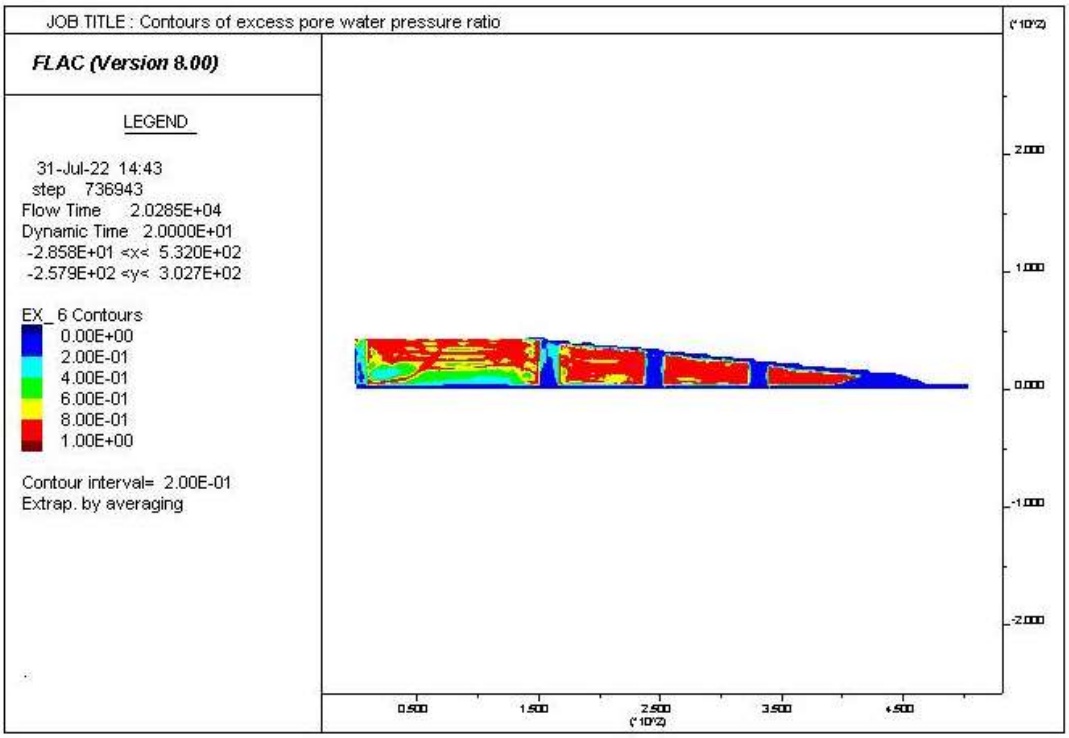

Figure A3. 37: Excess pore water pressure ratio distribution for the 16-70-40-8H- E_3 Loma

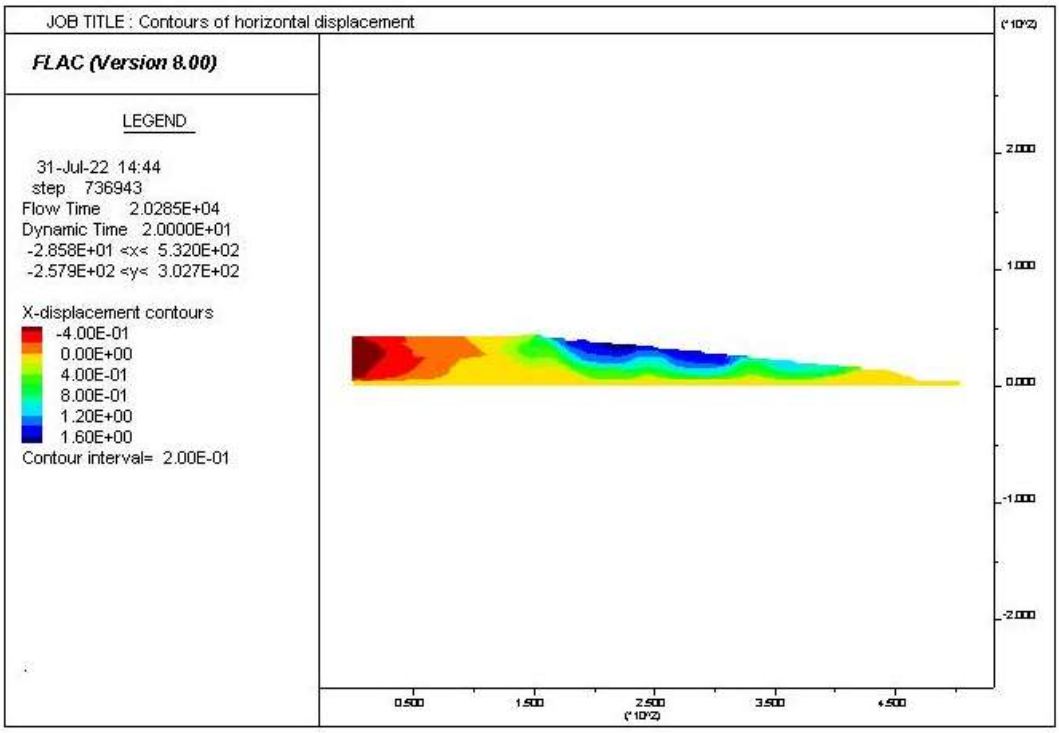

Figure A3. 38: Contours of horizontal displacement for the 16-70-40-8H- E_3Loma

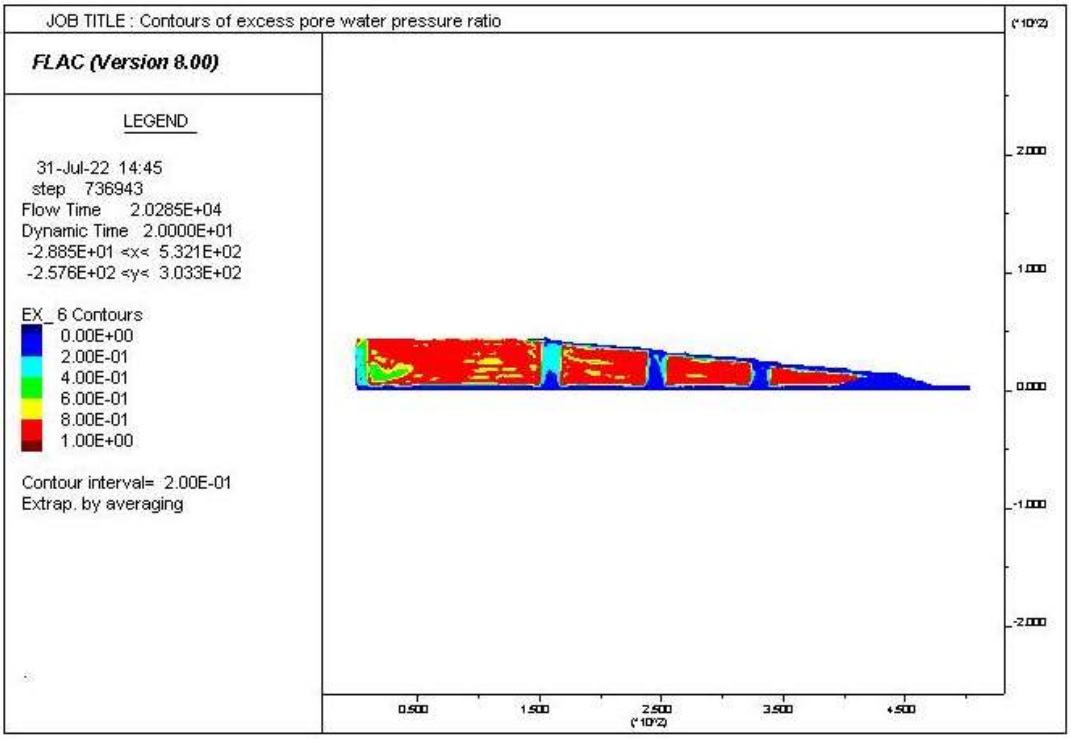

Figure A3. 39: Excess pore water pressure ratio distribution for the 16-70-40-8H- E_4 Loma

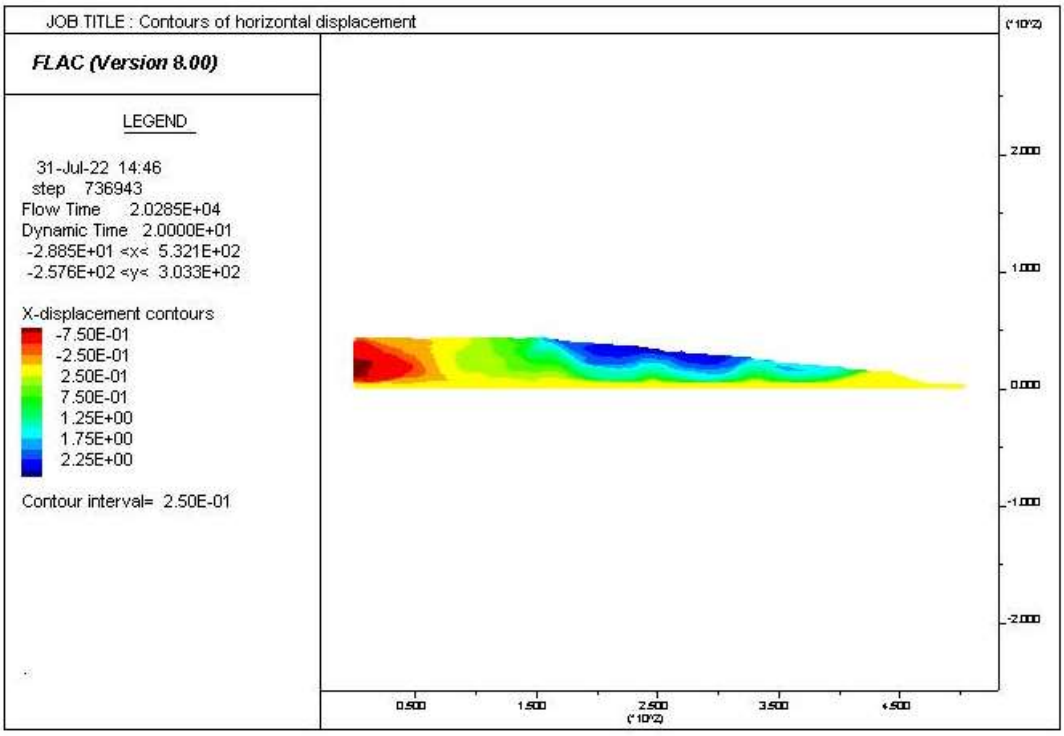

Figure A3. 40: Contours of horizontal displacement for the 16-70-40-8H- E_4Loma

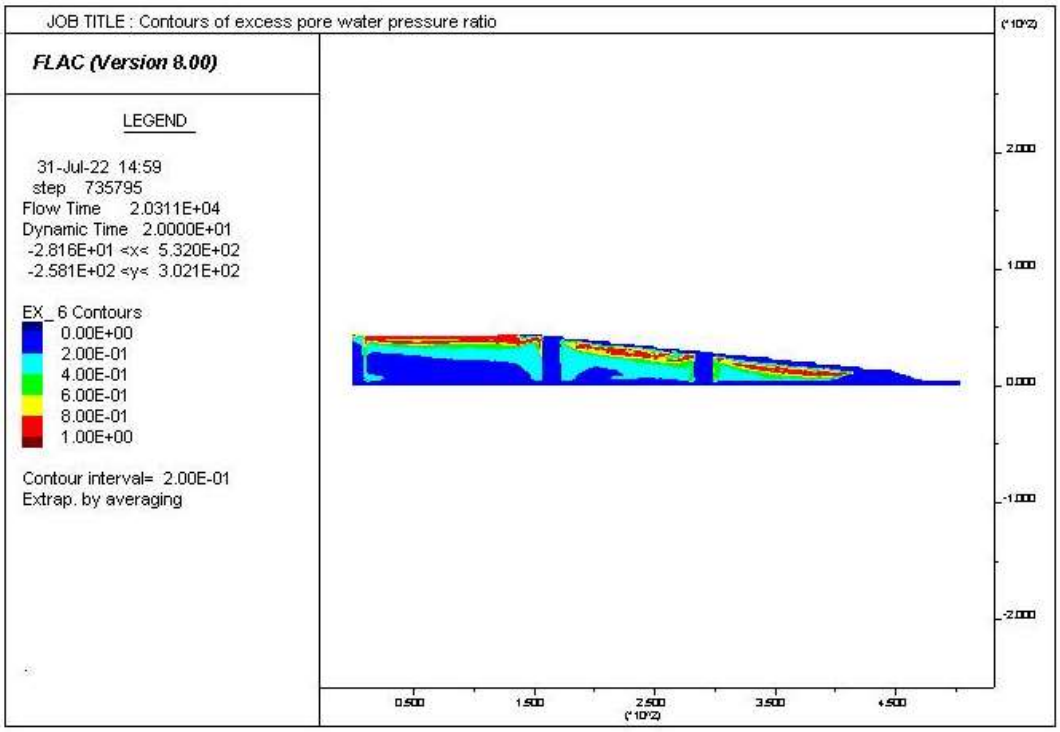

Figure A3. 41: Excess pore water pressure ratio distribution for the 16-110-40-8H- E_1 Loma

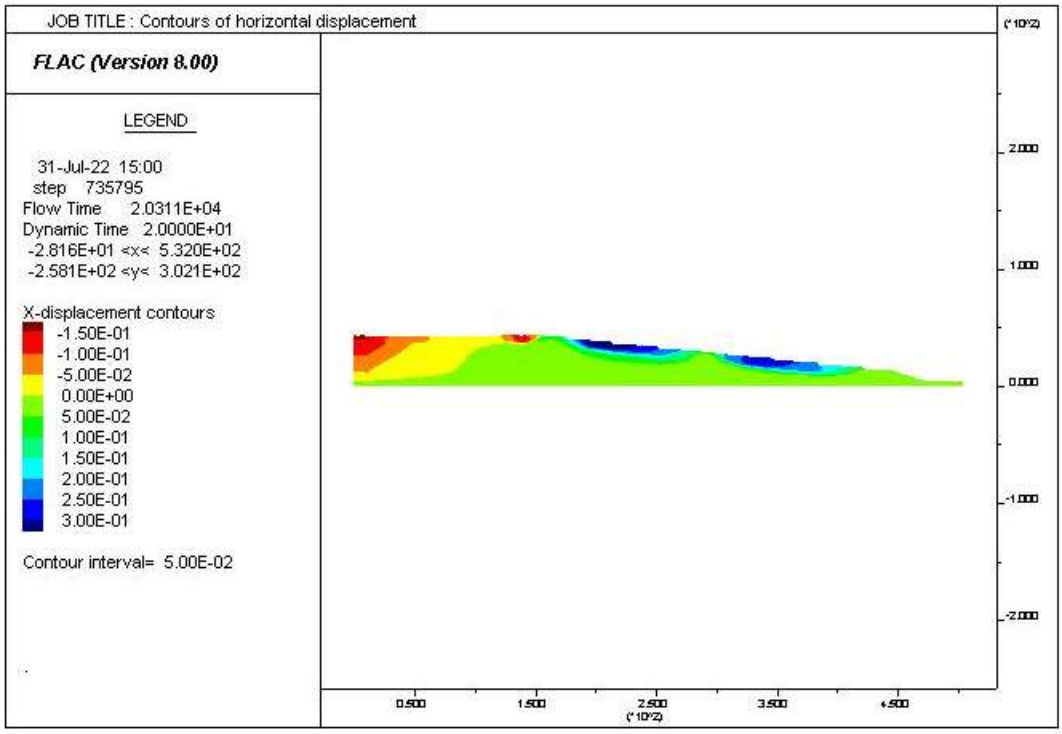

Figure A3. 42: Contours of horizontal displacement for the 16-110-40-8H- E_1Loma

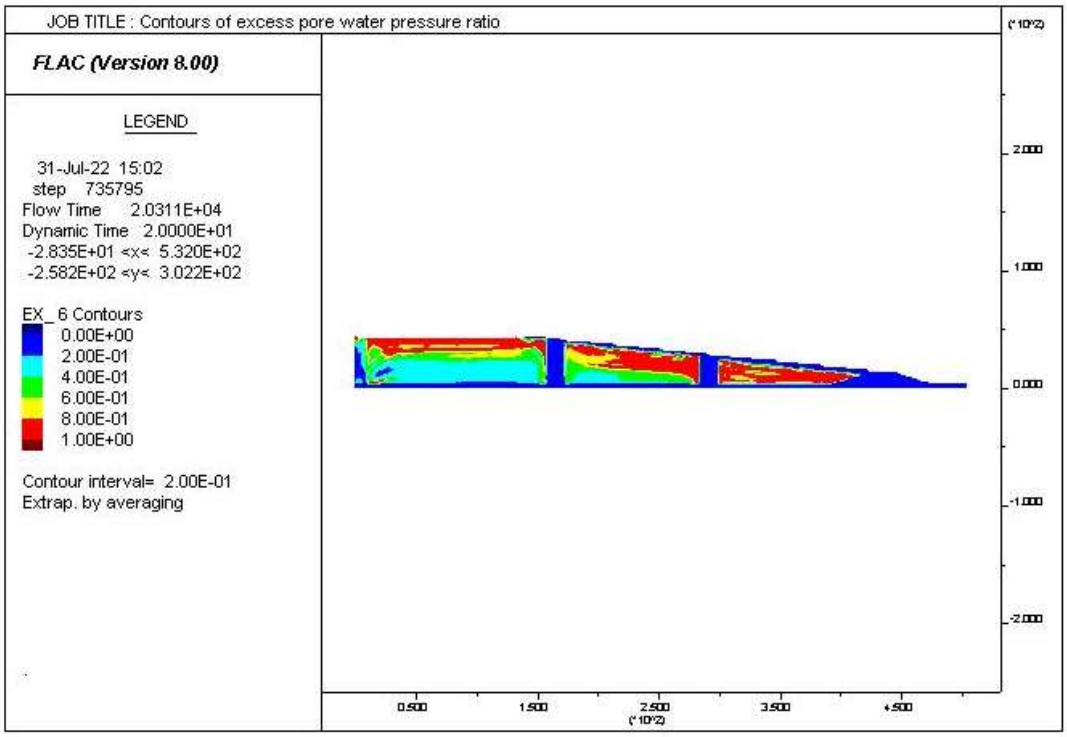

Figure A3. 43: Excess pore water pressure ratio distribution for the 16-110-40-8H- E_2 Loma

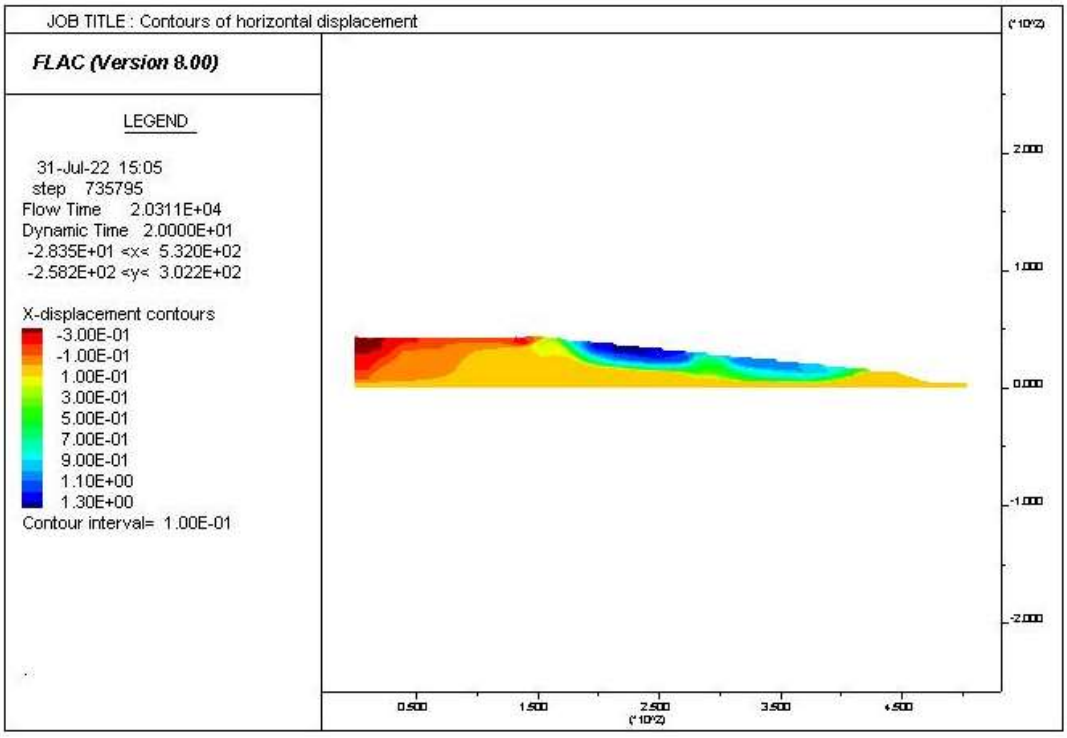

Figure A3. 44: Contours of horizontal displacement for the 16-110-40-8H- E_2Loma

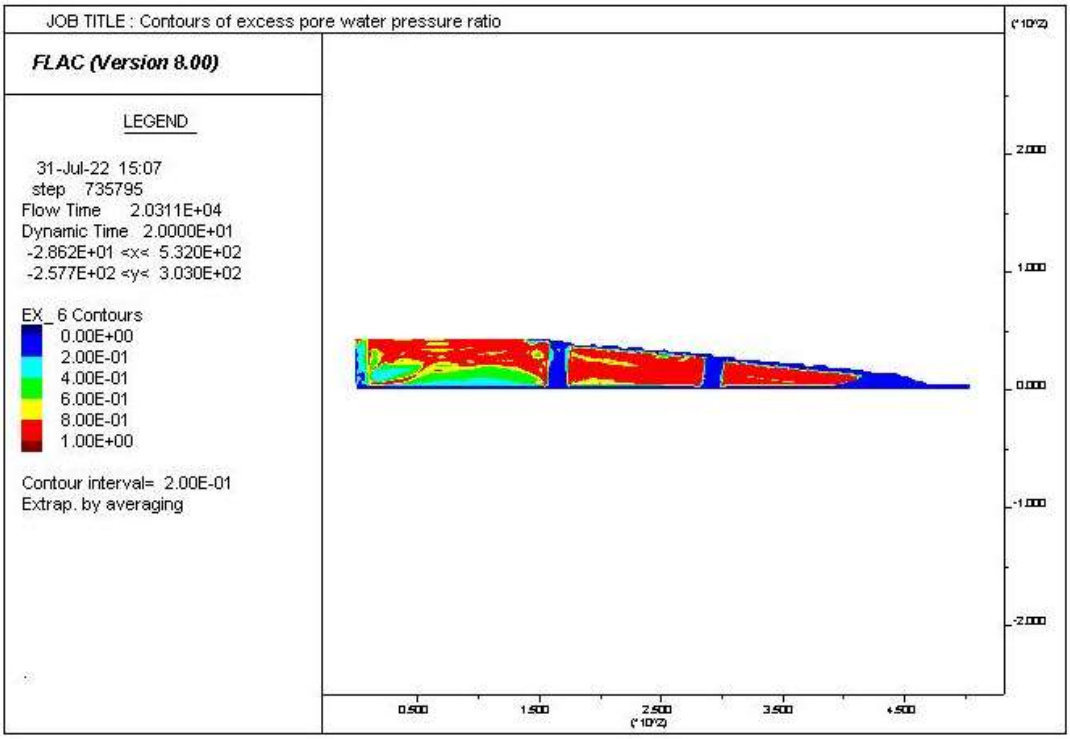

Figure A3. 45: Excess pore water pressure ratio distribution for the 16-110-40-8H- E_3 Loma

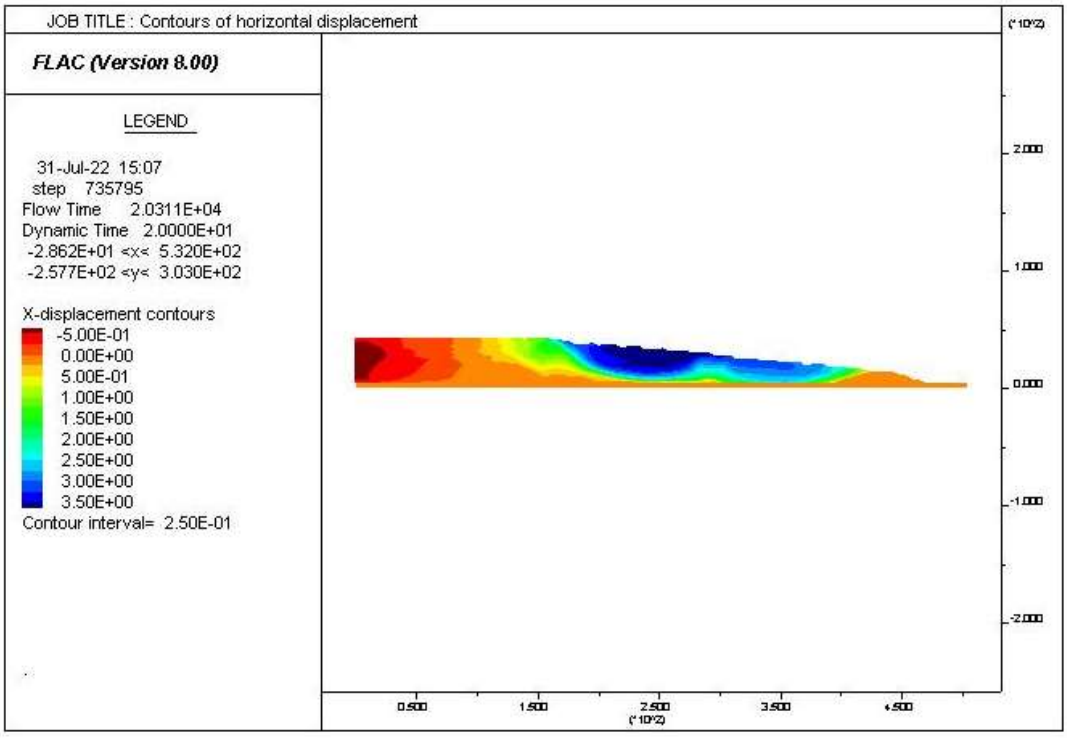

Figure A3. 46: Contours of horizontal displacement for the 16-110-40-8H- E_3Loma

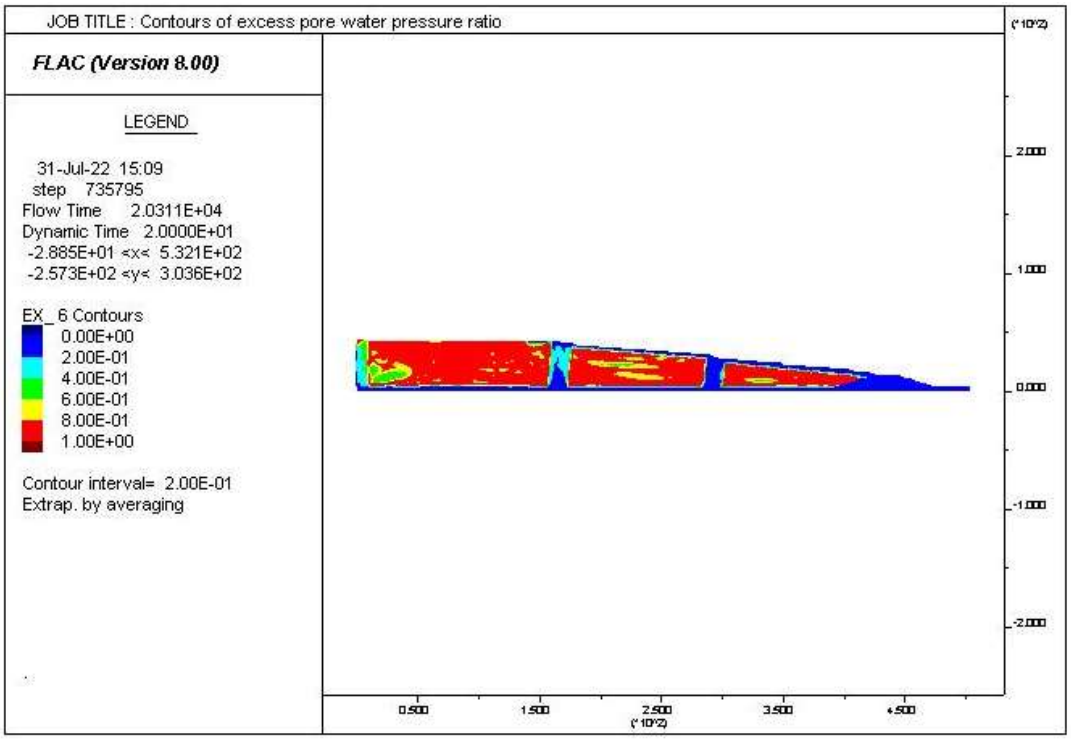

Figure A3. 47: Excess pore water pressure ratio distribution for the 16-110-40-8H- E_4 Loma

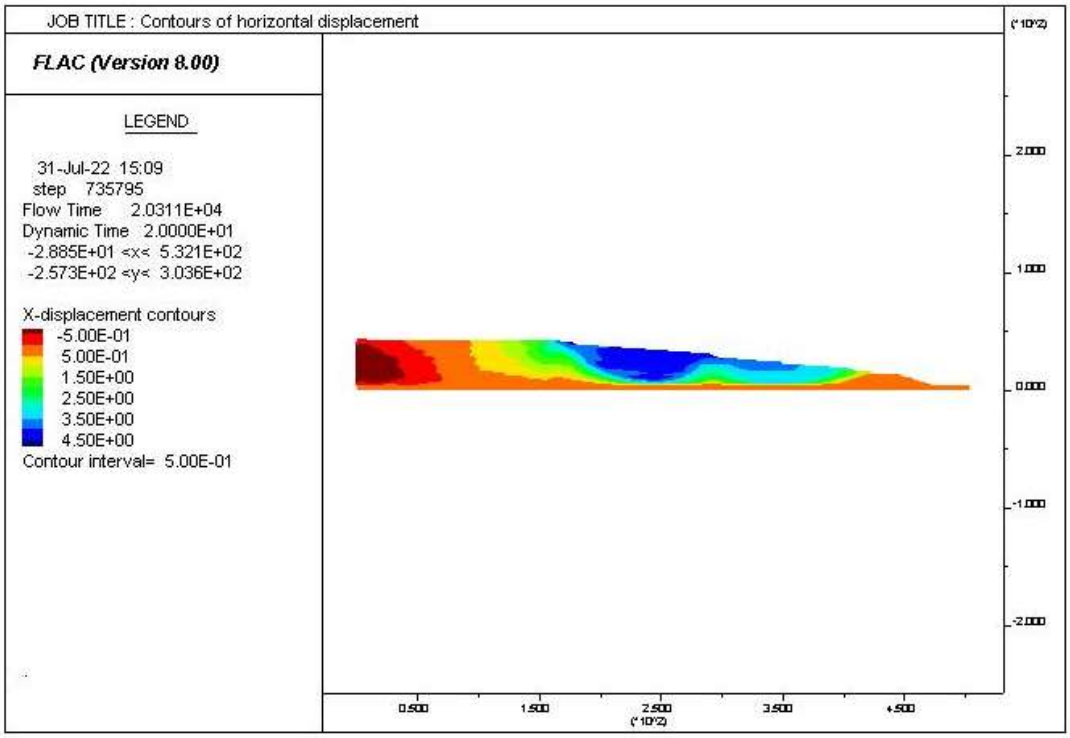

Figure A3. 48: Contours of horizontal displacement for the 16-110-40-8H- E_4Loma

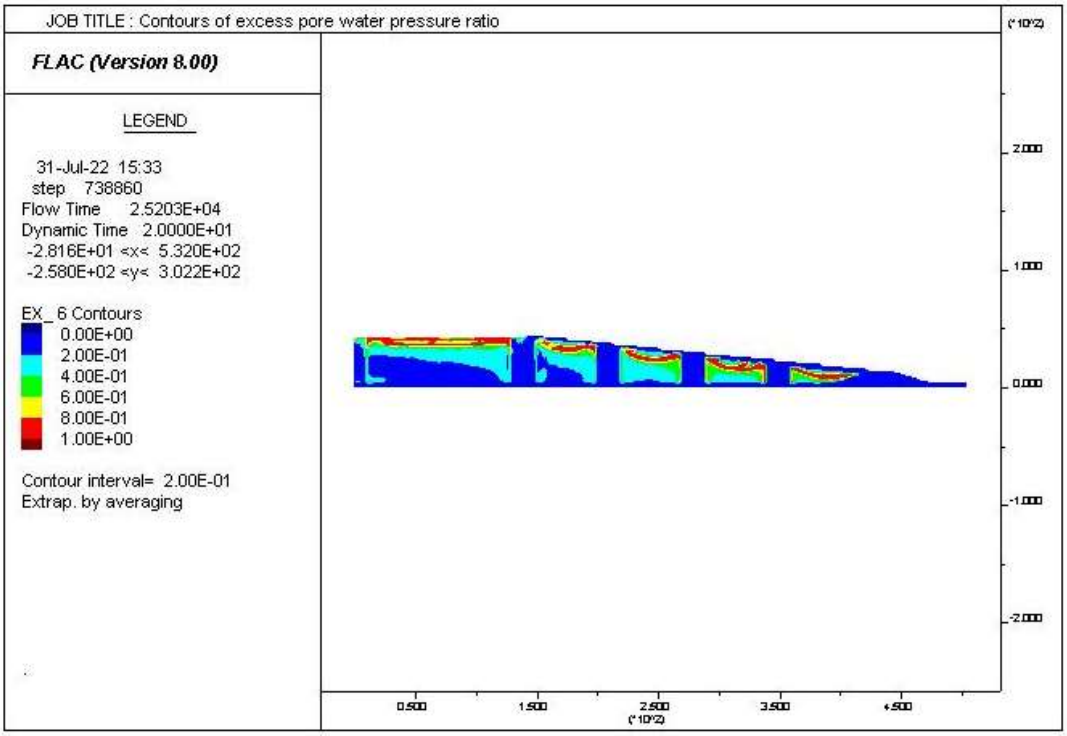

Figure A3. 49: Excess pore water pressure ratio distribution for the 20-50-40-8H- E_1 Loma

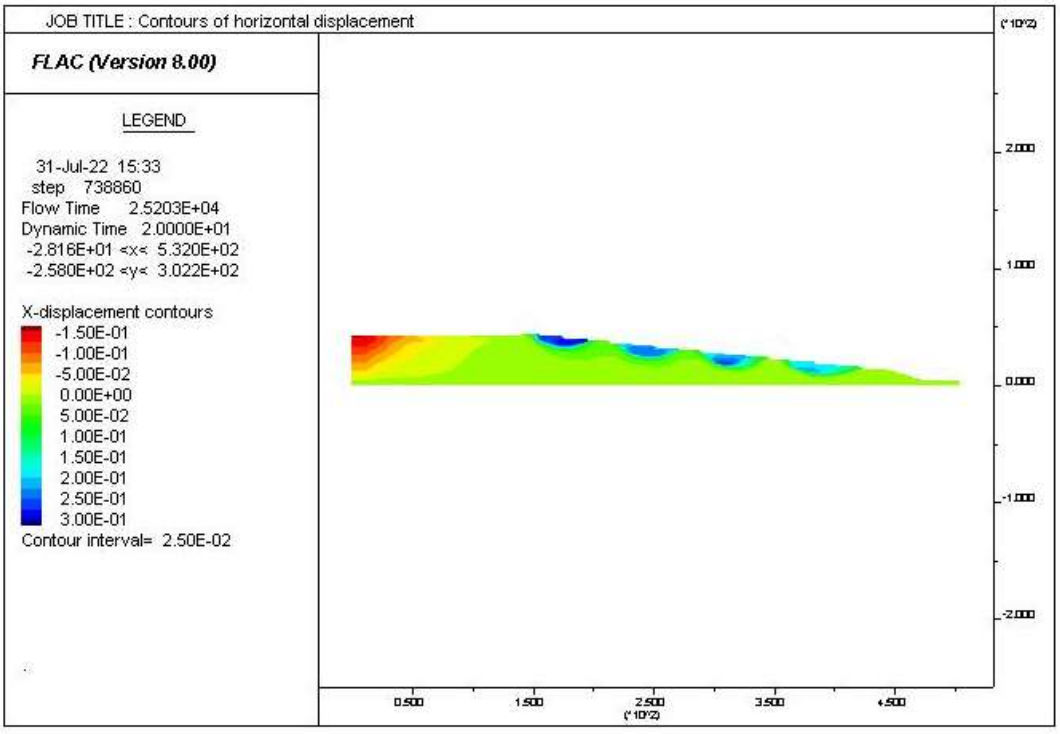

Figure A3. 50: Contours of horizontal displacement for the 20-50-40-8H- E_1Loma

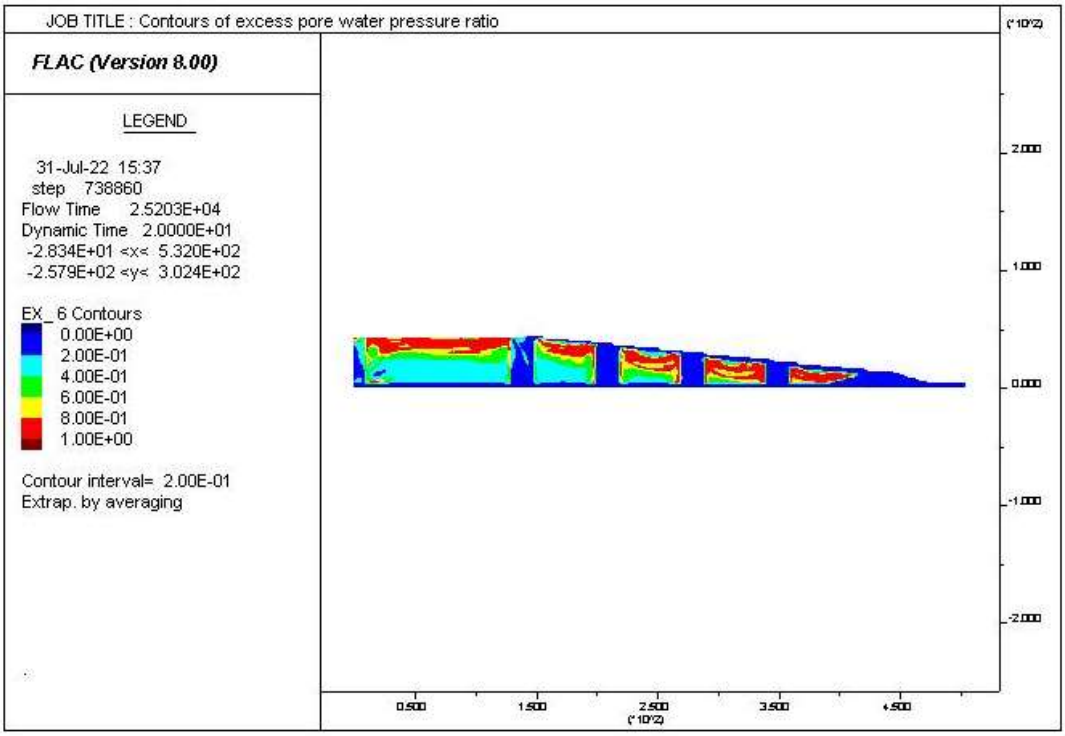

Figure A3. 51: Excess pore water pressure ratio distribution for the 20-50-40-8H- E_2 Loma

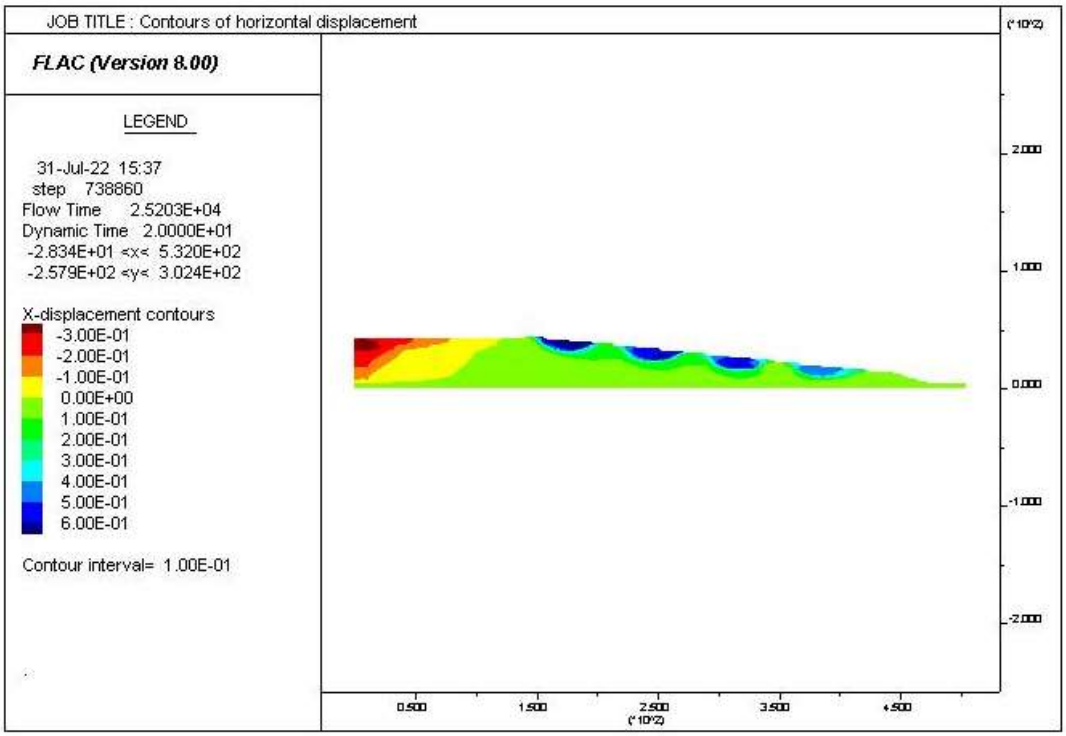

Figure A3. 52: Contours of horizontal displacement for the 20-50-40-8H- E_2Loma

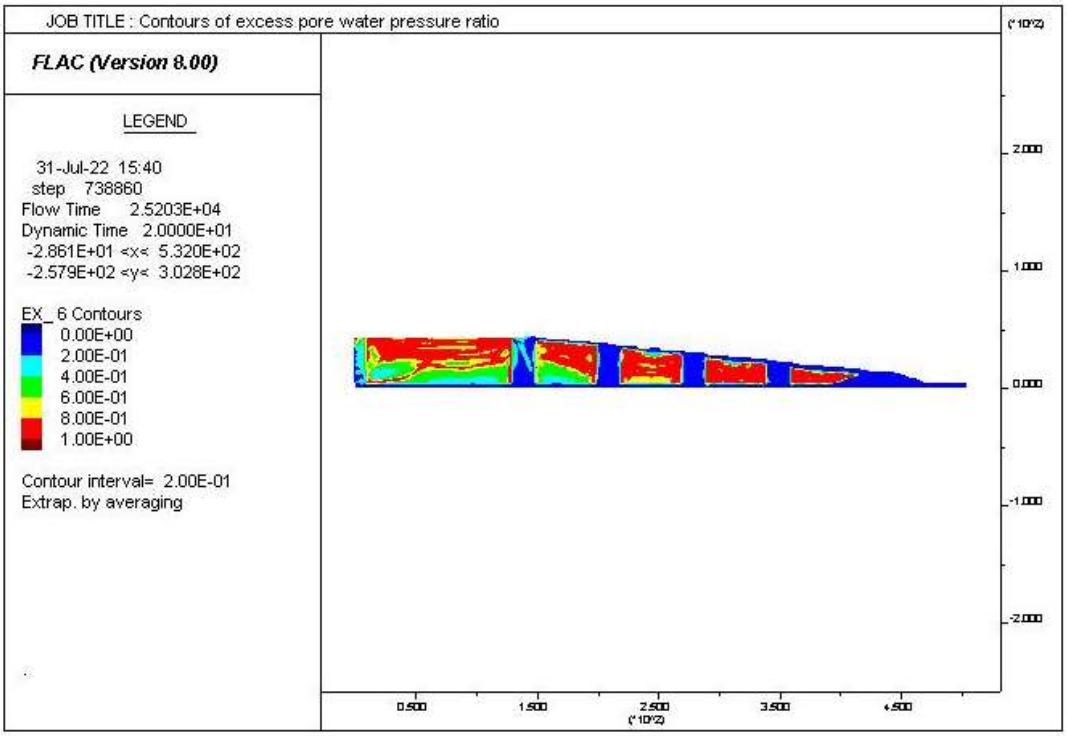

Figure A3. 53: Excess pore water pressure ratio distribution for the 20-50-40-8H- E_3 Loma

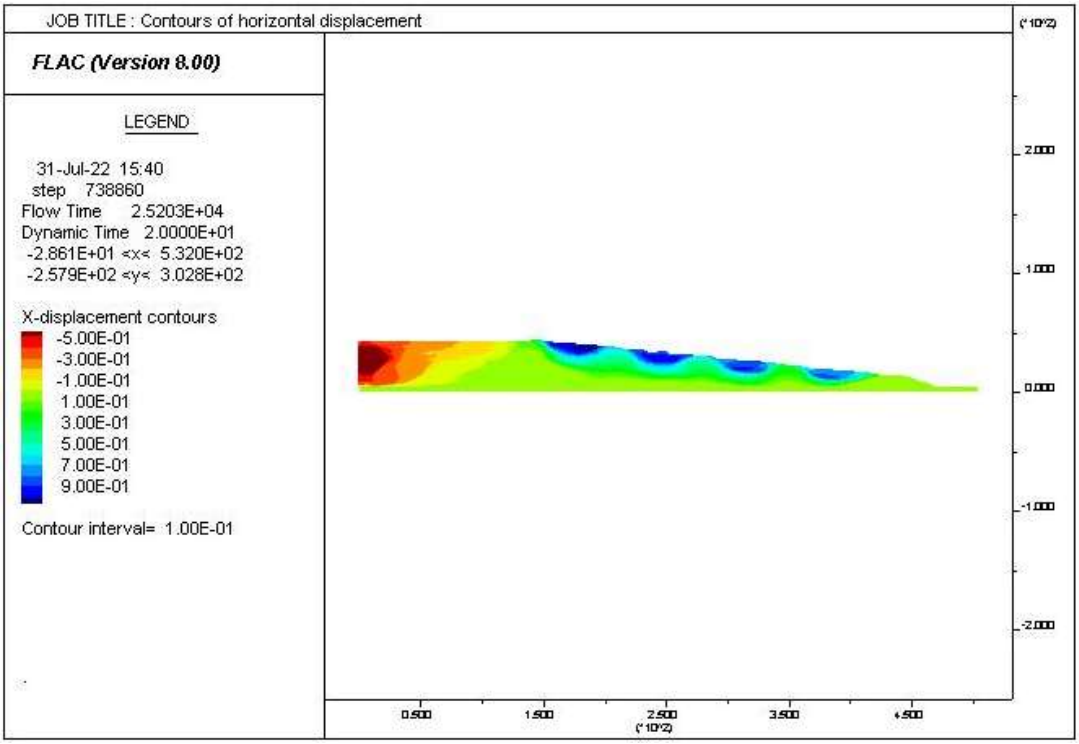

Figure A3. 54: Contours of horizontal displacement for the 20-50-40-8H- E_3Loma

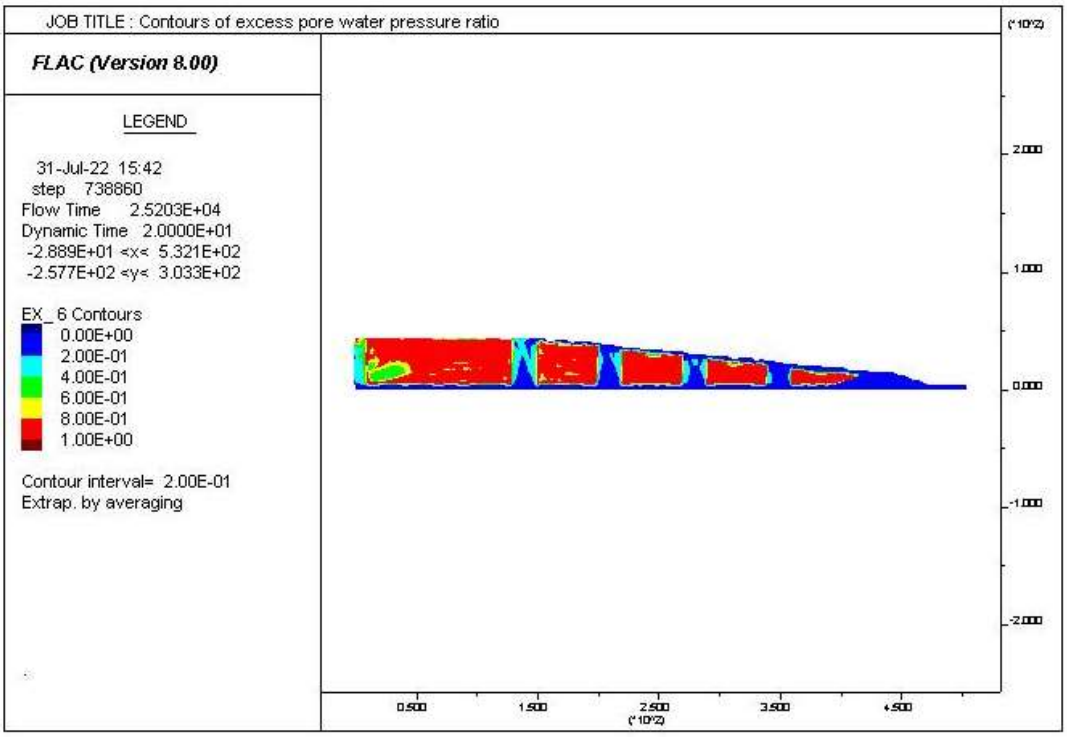

Figure A3. 55: Excess pore water pressure ratio distribution for the 20-50-40-8H- E_4 Loma

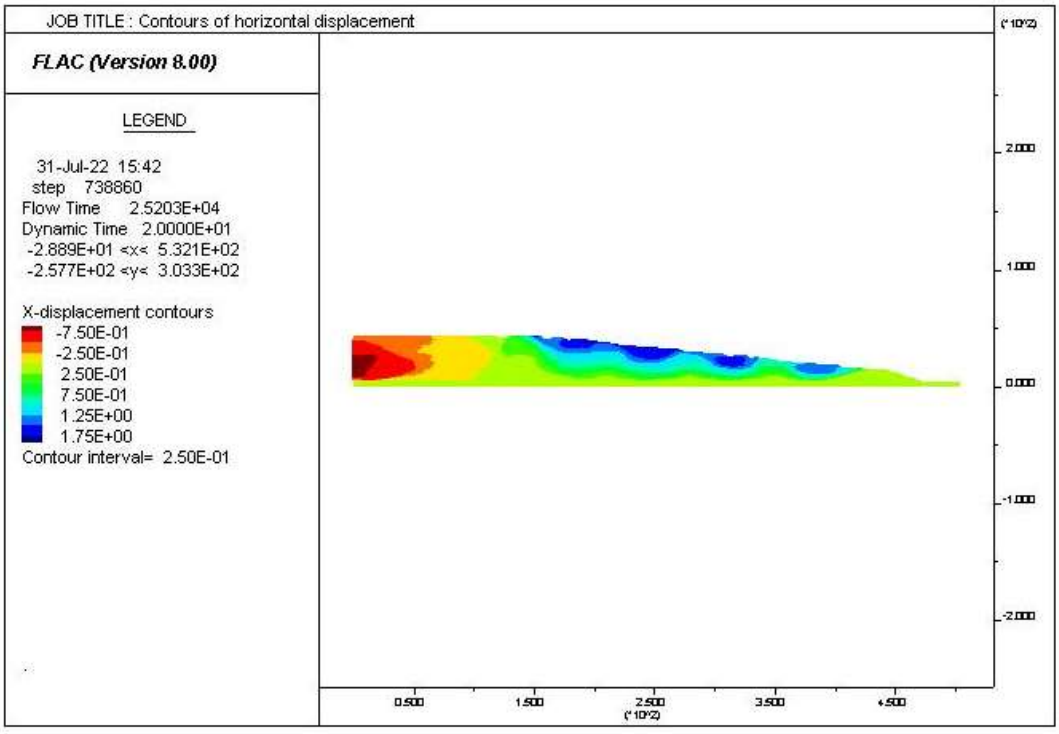

Figure A3. 56: Contours of horizontal displacement for the 20-50-40-8H- E_4Loma

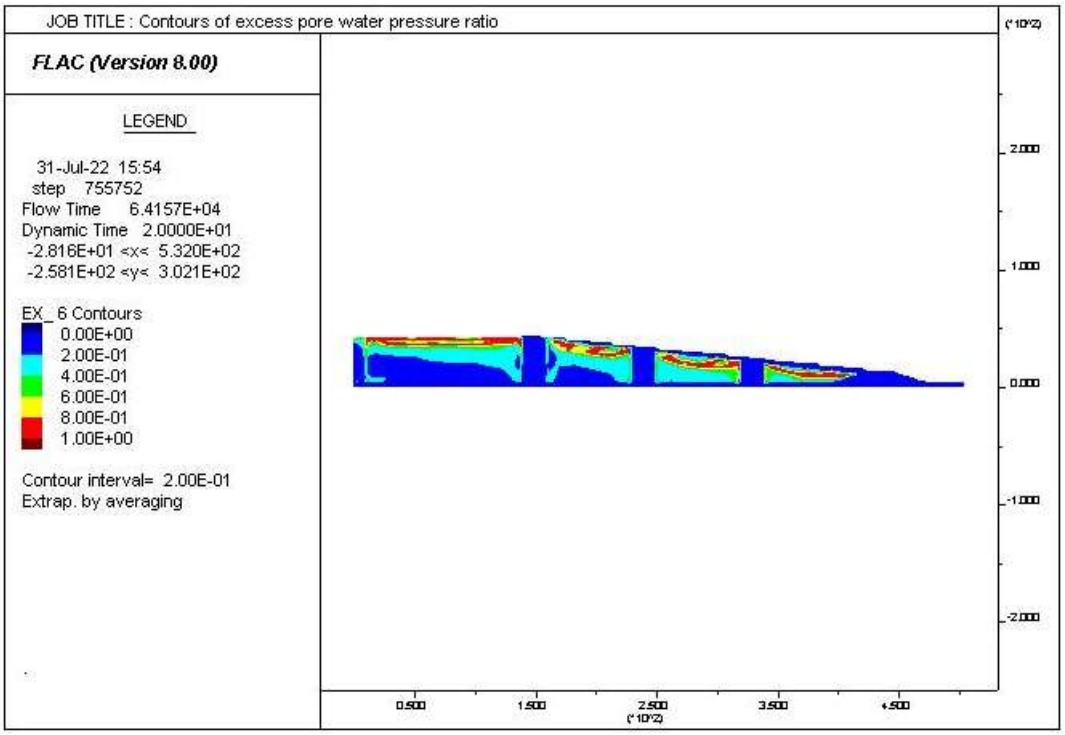

Figure A3. 57: Excess pore water pressure ratio distribution for the 20-70-40-8H- E_1 Loma

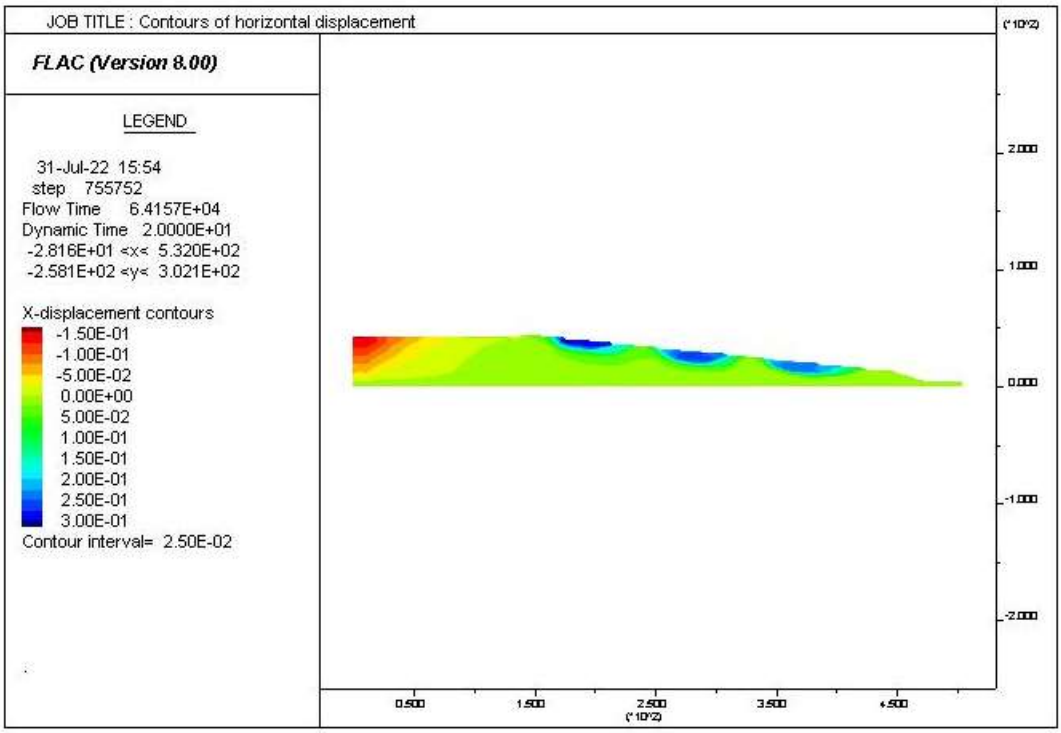

Figure A3. 58: Contours of horizontal displacement for the 20-70-40-8H- E_1Loma

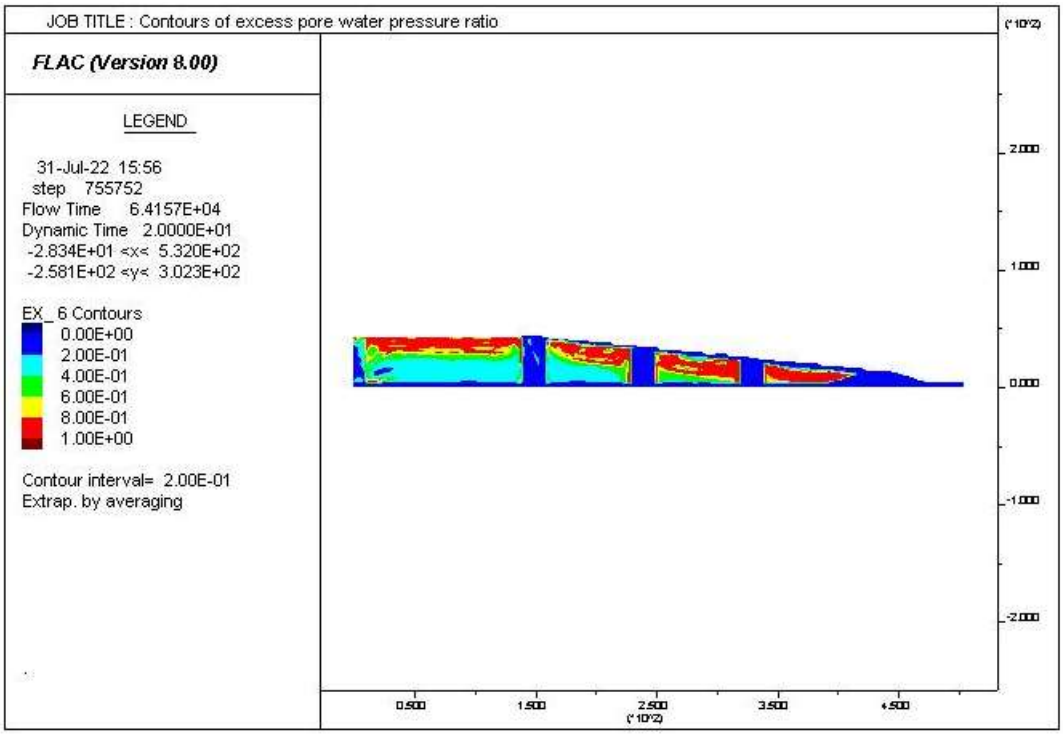

Figure A3. 59: Excess pore water pressure ratio distribution for the 20-70-40-8H- E_2 Loma

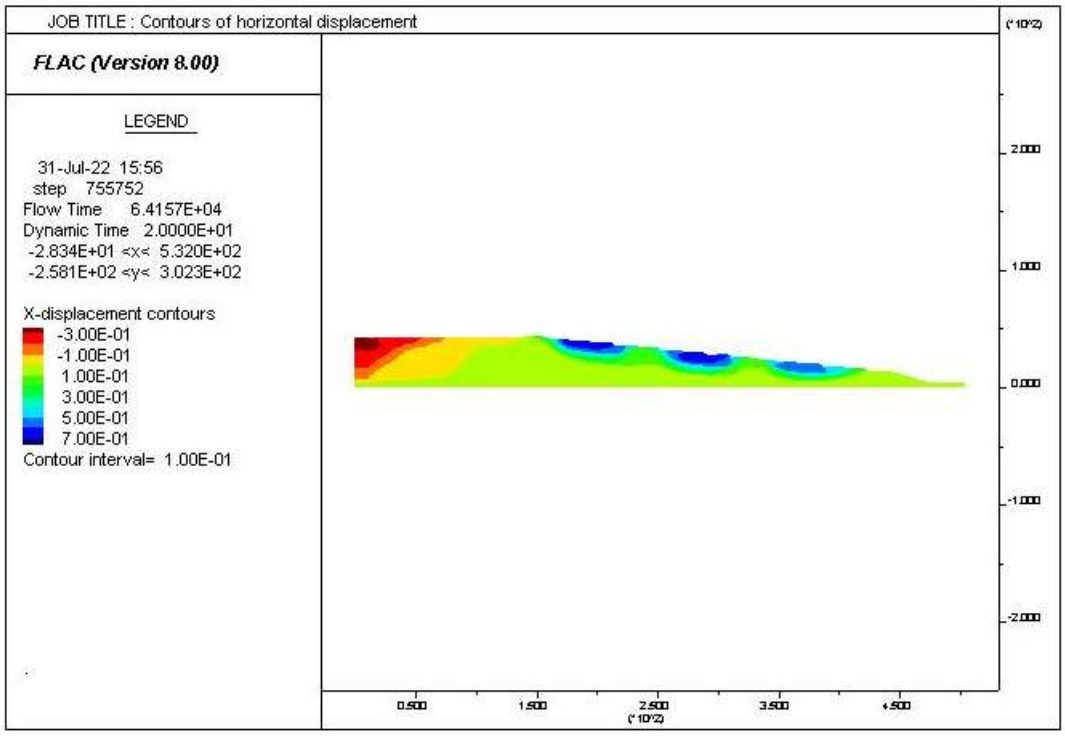

Figure A3. 60: Contours of horizontal displacement for the 20-70-40-8H- E_2Loma

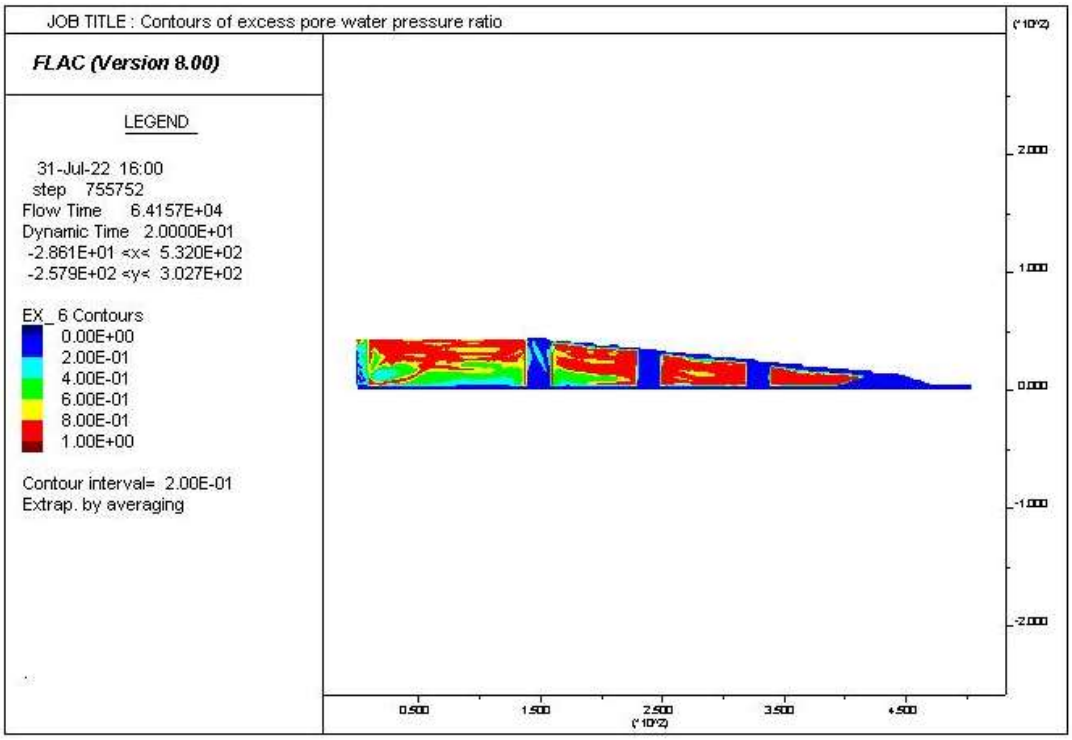

Figure A3. 61: Excess pore water pressure ratio distribution for the 20-70-40-8H- E_3 Loma

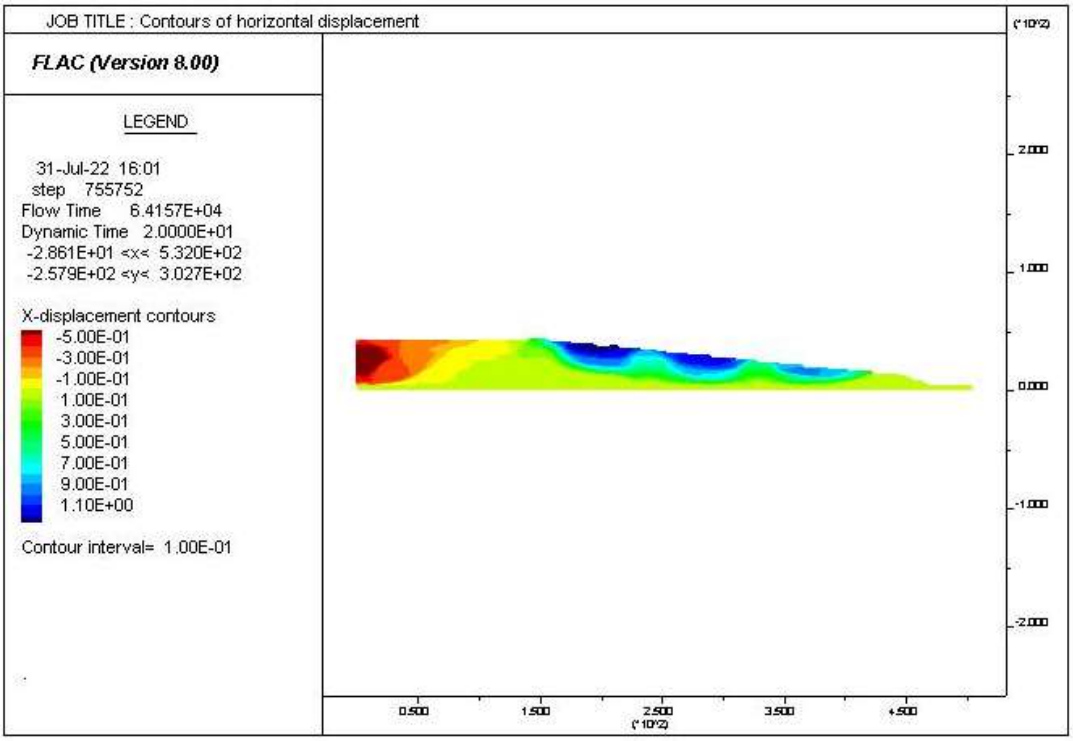

Figure A3. 62: Contours of horizontal displacement for the 20-70-40-8H- E_3 Loma

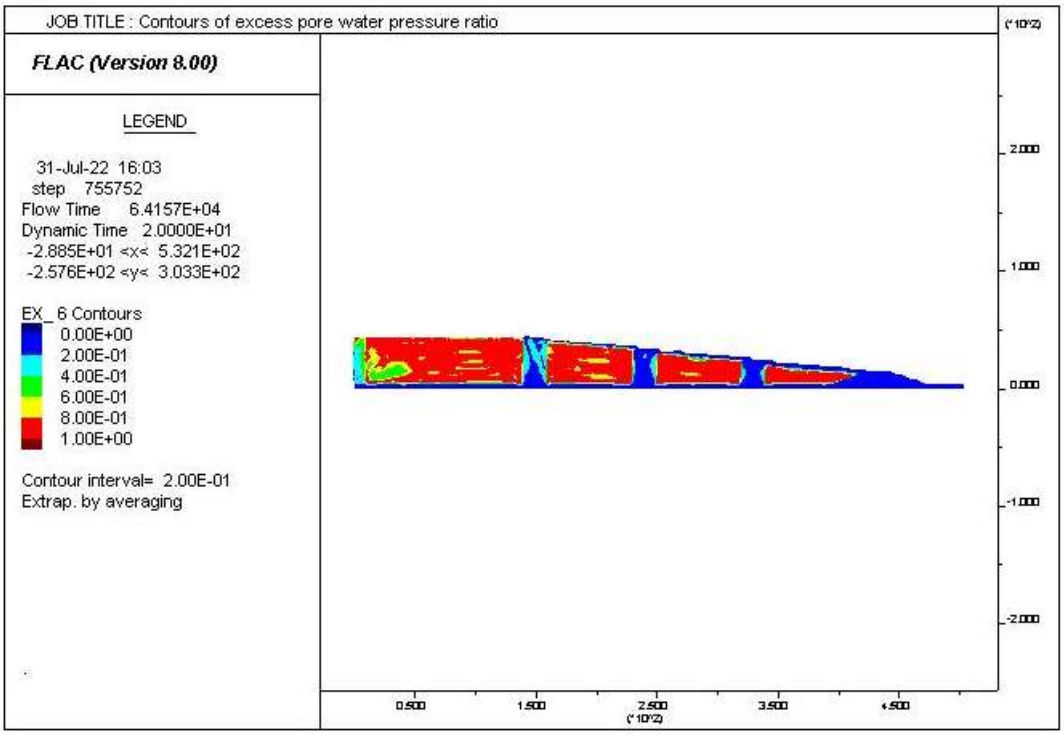

Figure A3. 63: Excess pore water pressure ratio distribution for the 20-70-40-8H- E_4 Loma

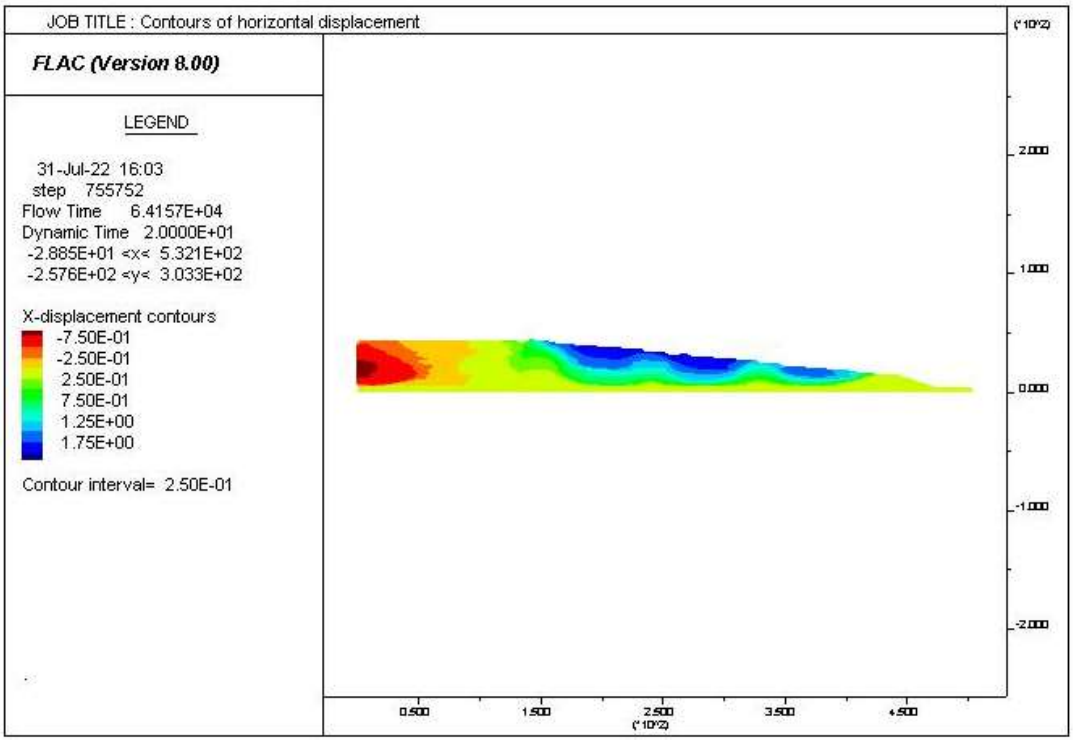

Figure A3. 64: Contours of horizontal displacement for the 20-70-40-8H- E_4Loma

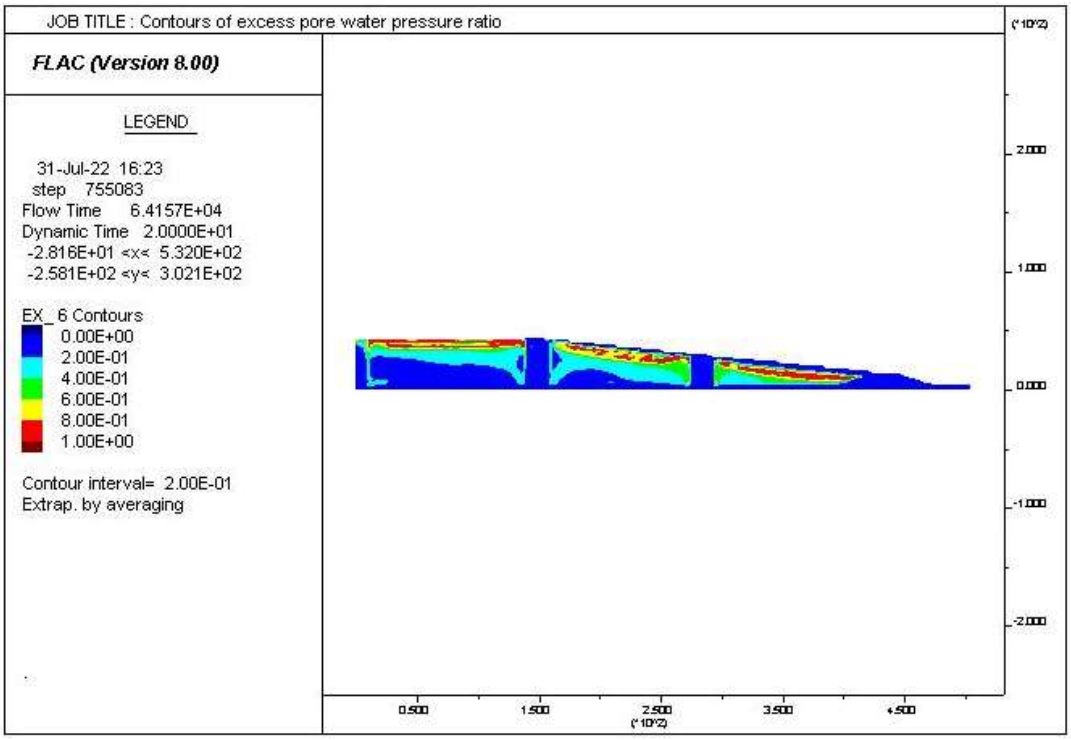

Figure A3. 65: Excess pore water pressure ratio distribution for the 20-115-40-8H- E_1 Loma

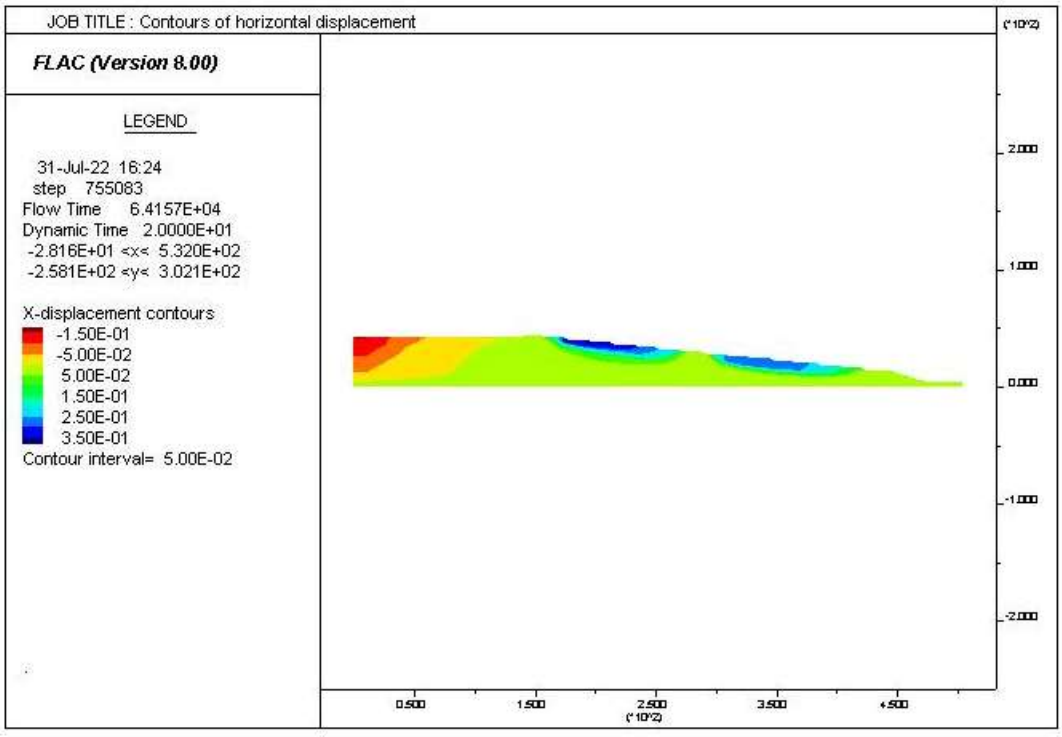

Figure A3. 66: Contours of horizontal displacement for the 20-115-40-8H- E_1Loma

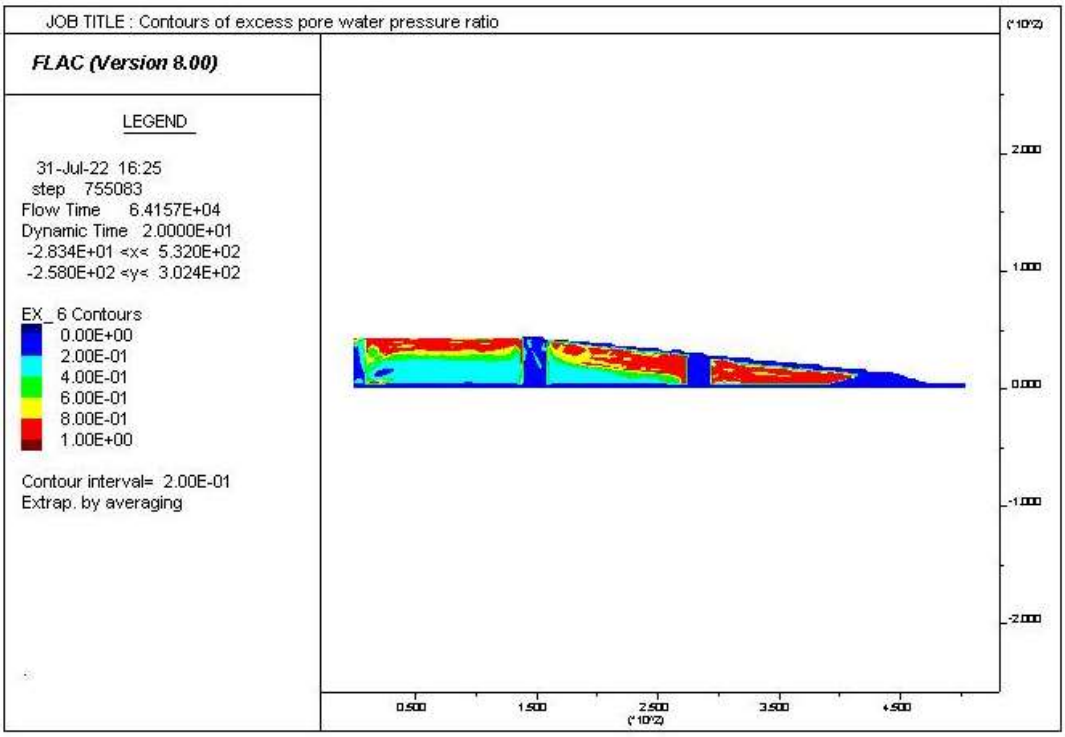

Figure A3. 67: Excess pore water pressure ratio distribution for the 20-115-40-8H- E_2 Loma

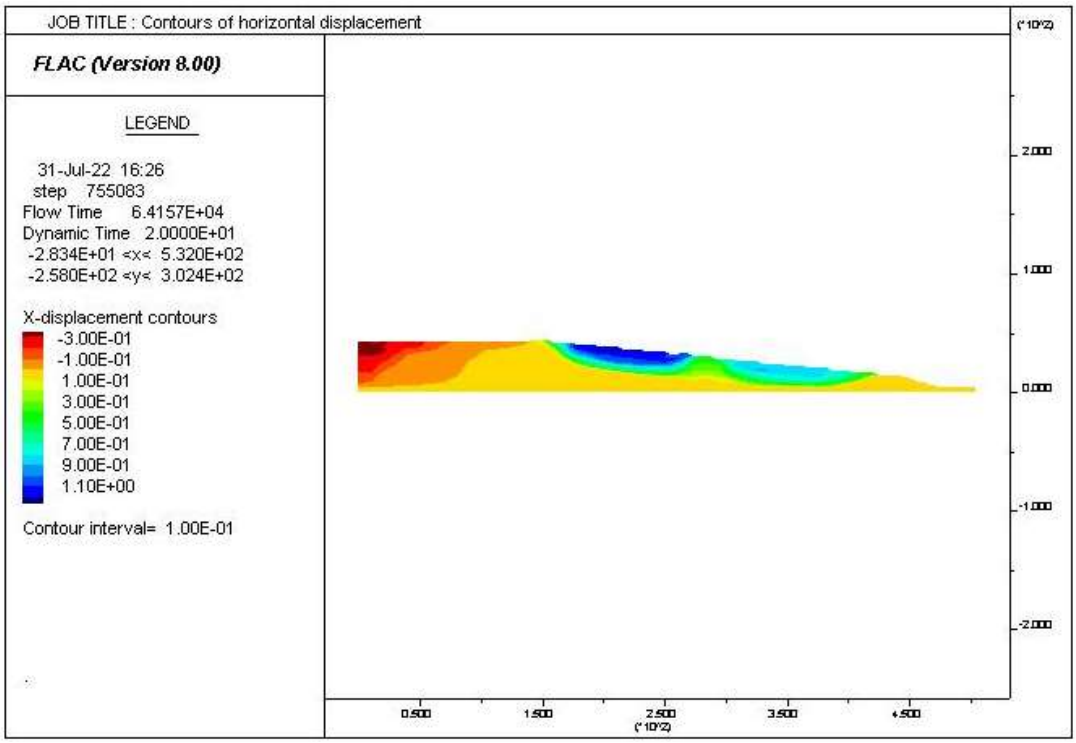

Figure A3. 68: Contours of horizontal displacement for the 20-115-40-8H- E_2Loma

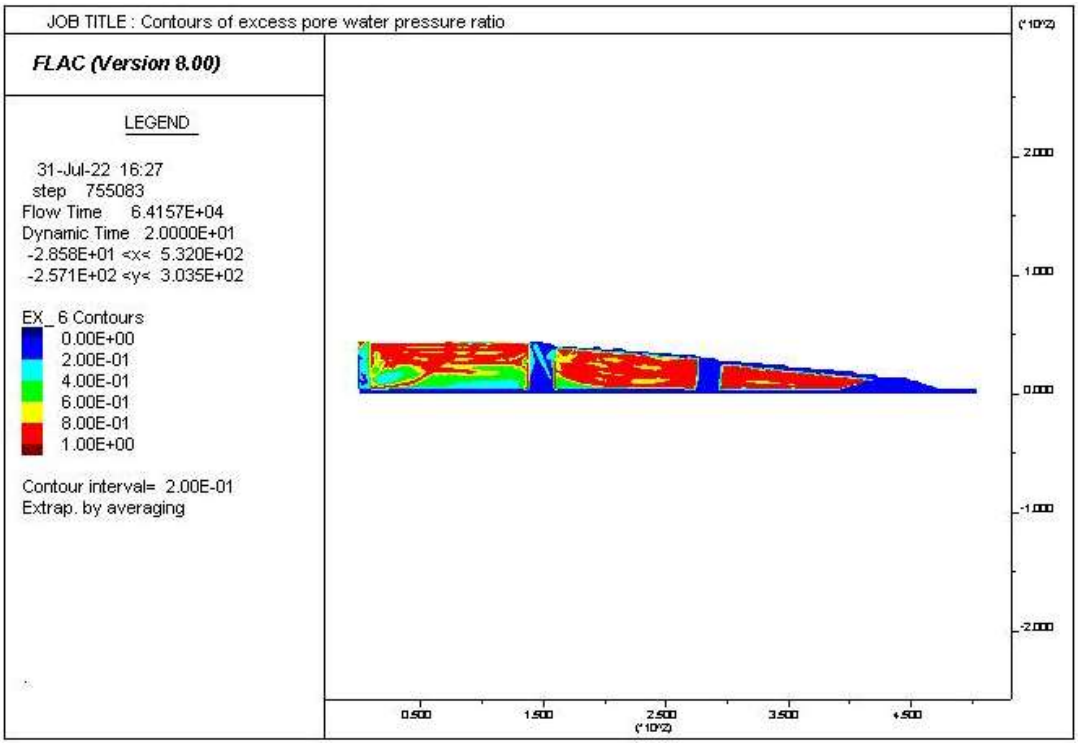

Figure A3. 69: Excess pore water pressure ratio distribution for the 20-115-40-8H- E_3 Loma

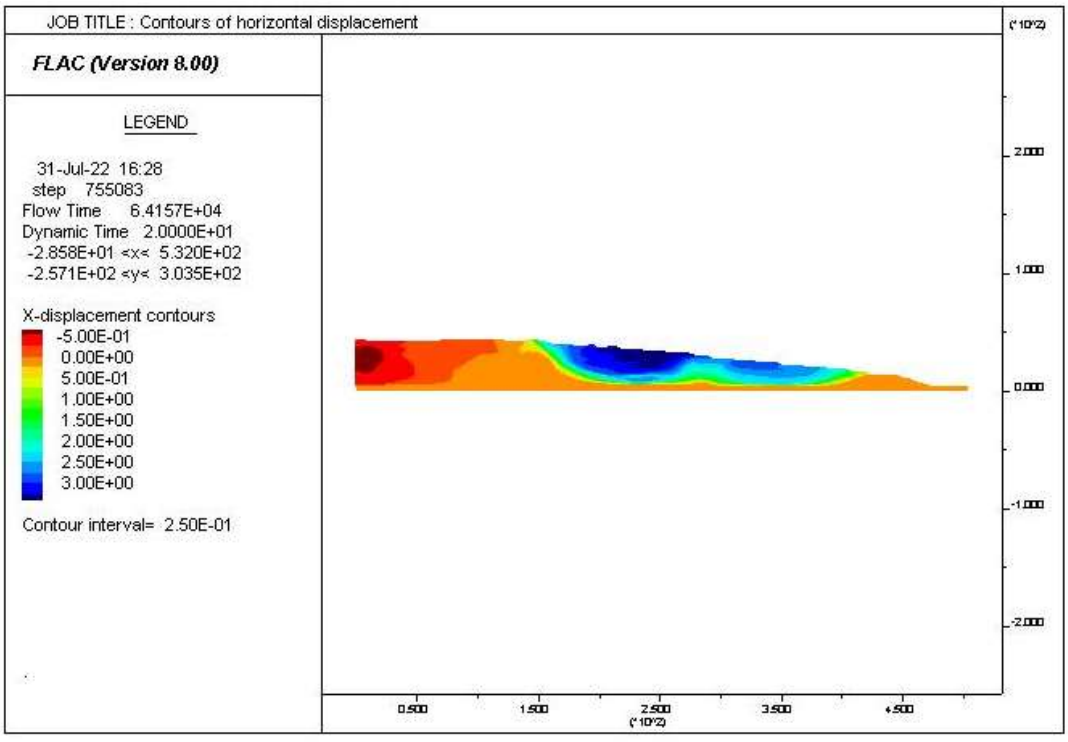

Figure A3. 70: Contours of horizontal displacement for the 20-115-40-8H- E_3 Loma

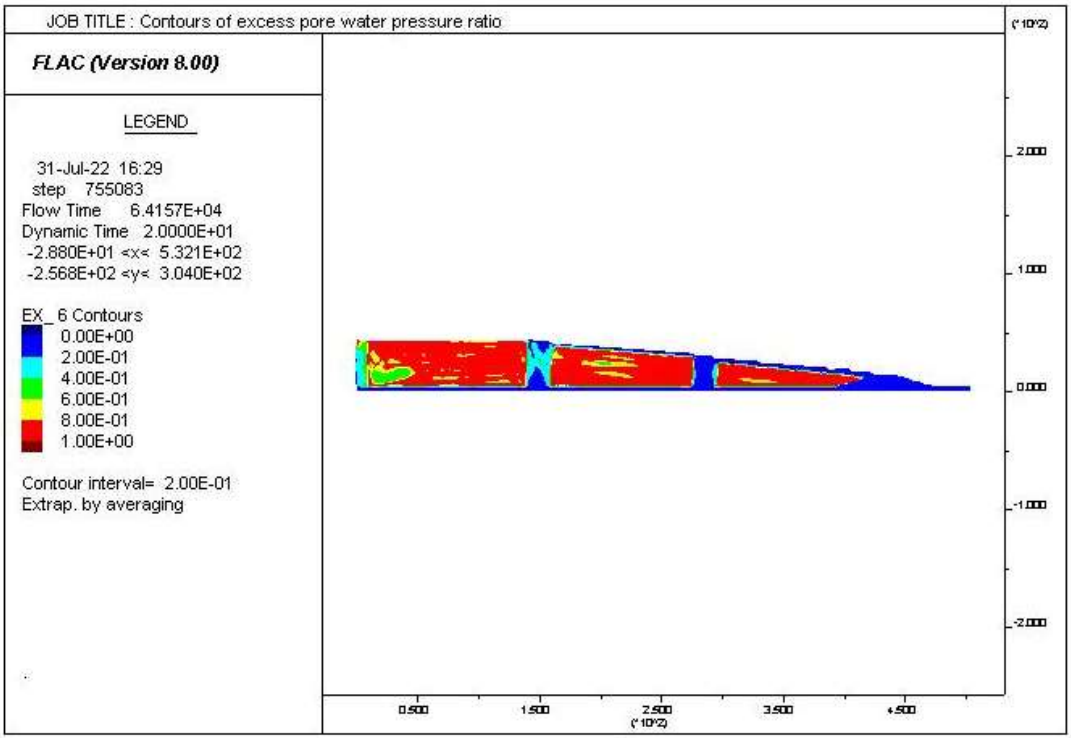

Figure A3. 71: Excess pore water pressure ratio distribution for the 20-115-40-8H- E_4 Loma

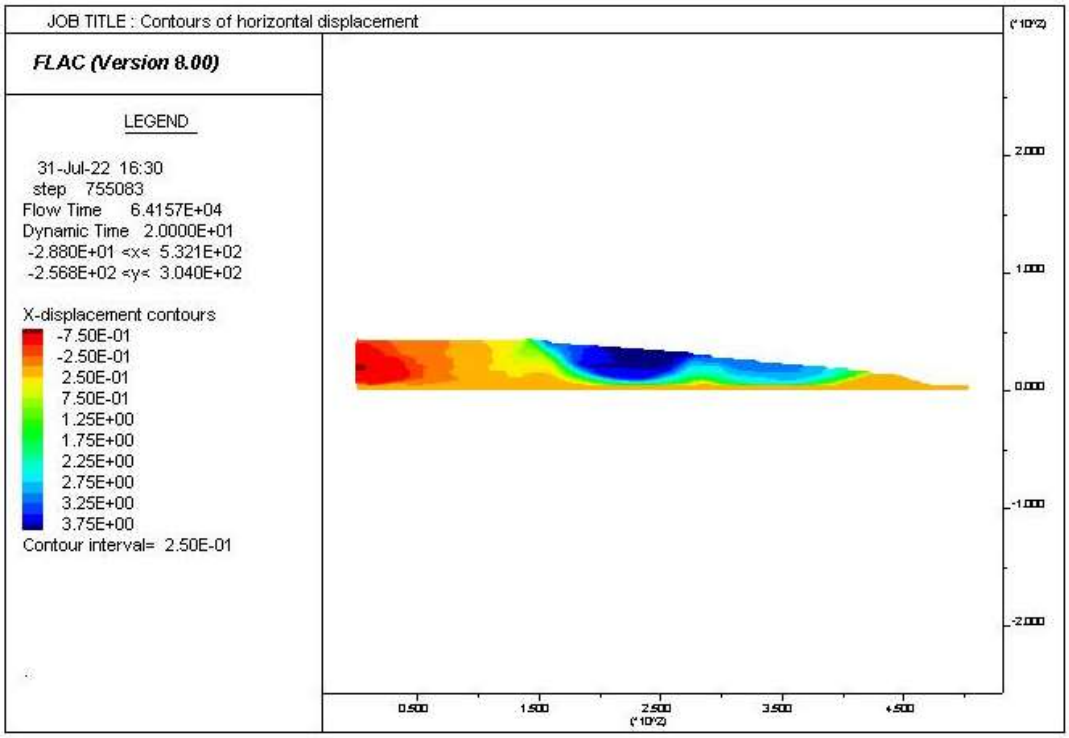

Figure A3. 72: Contours of horizontal displacement for the 20-115-40-8H- E_4 Loma

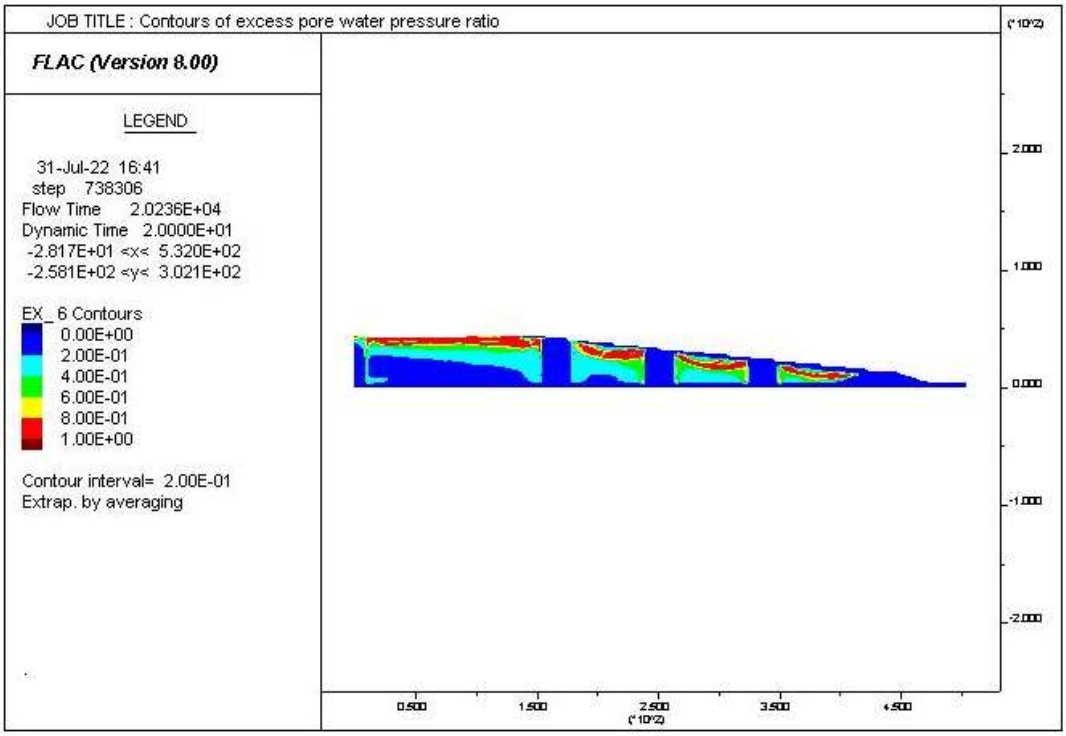

Figure A3. 73: Excess pore water pressure ratio distribution for the 25-60-40-8H- E_1 Loma

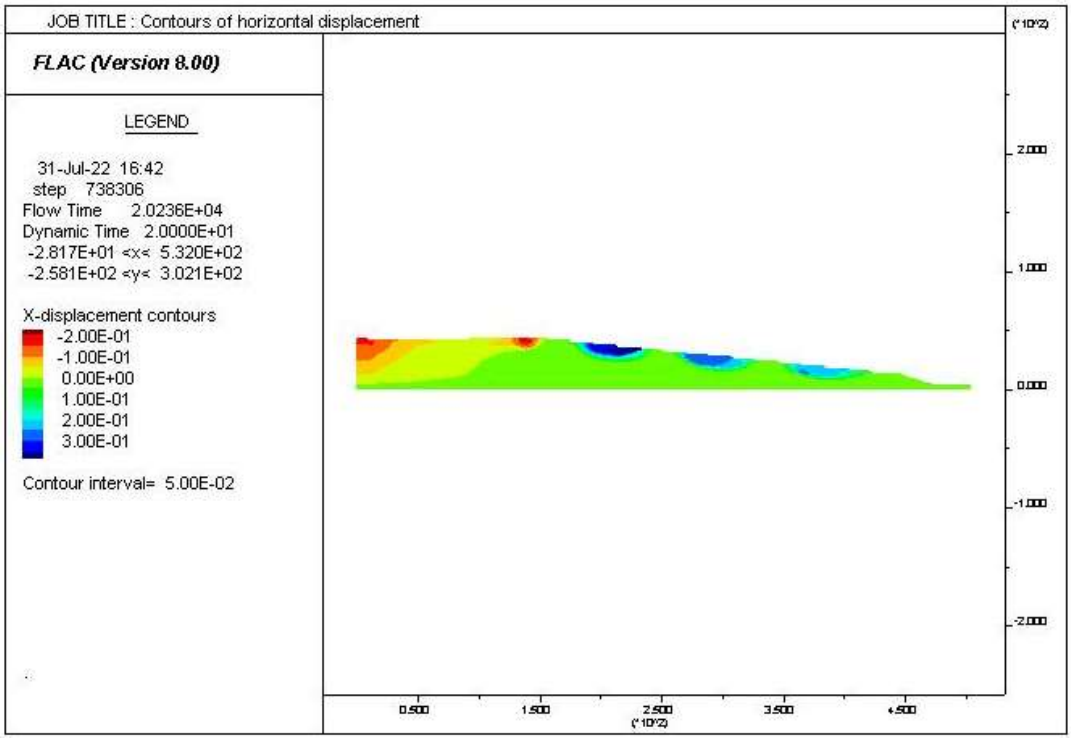

Figure A3. 74: Contours of horizontal displacement for the 25-60-40-8H- E_1Loma

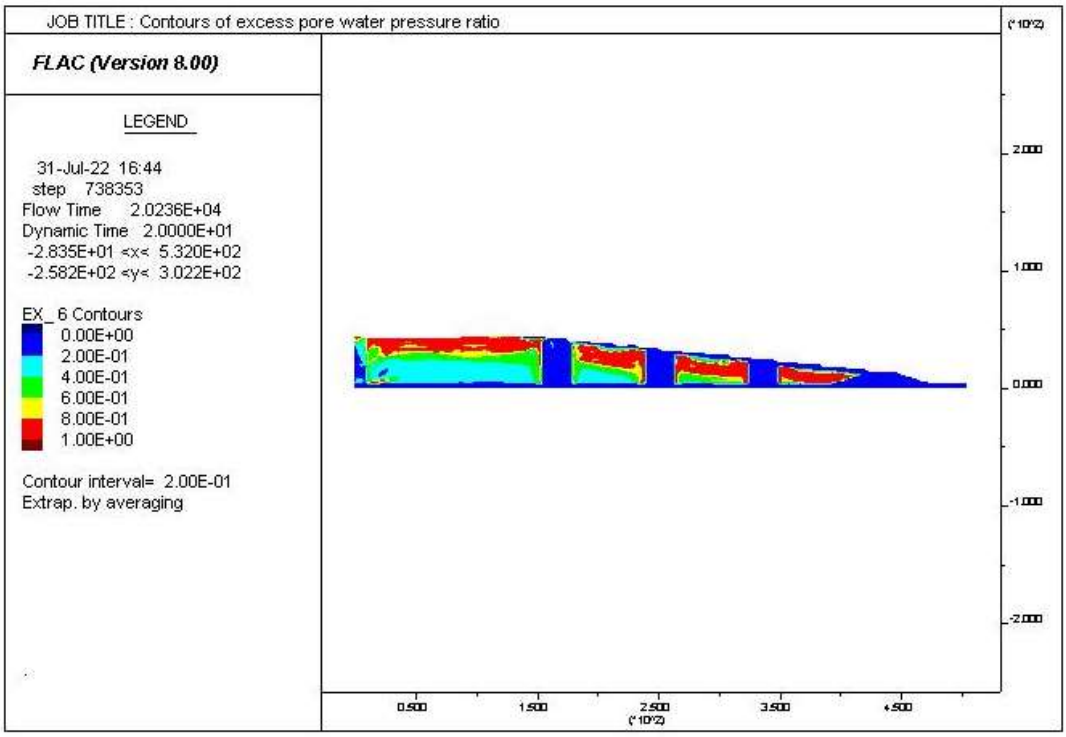

Figure A3. 75: Excess pore water pressure ratio distribution for the 25-60-40-8H- E_2 Loma

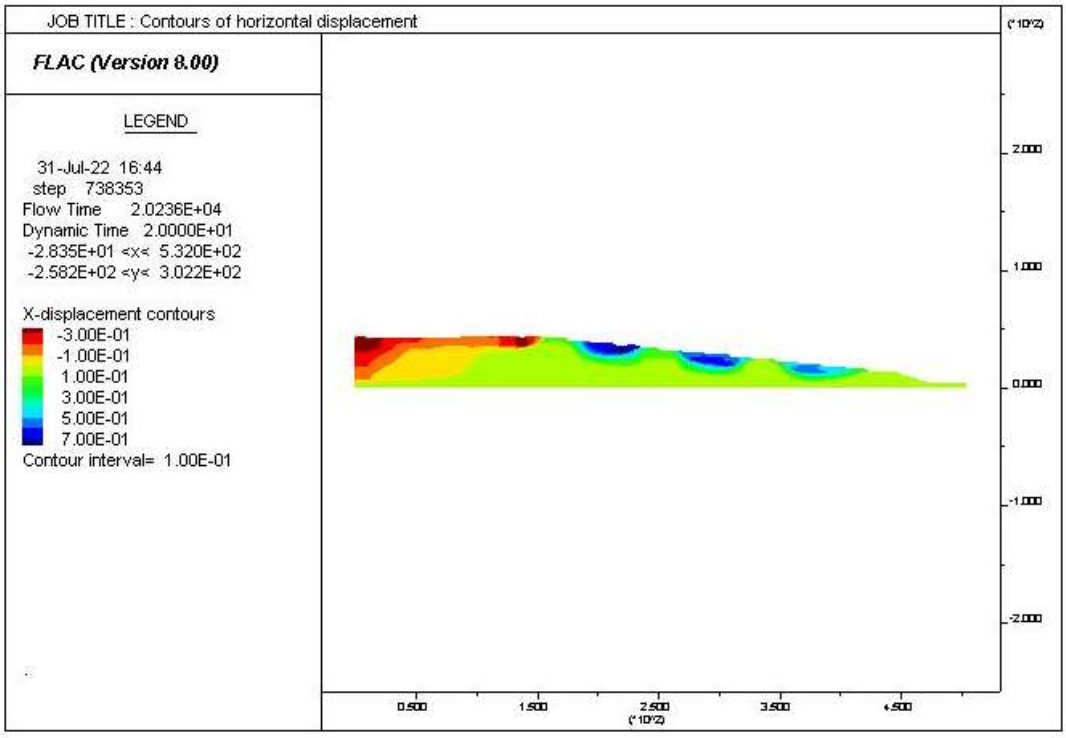

Figure A3. 76: Contours of horizontal displacement for the 25-60-40-8H- E_2Loma

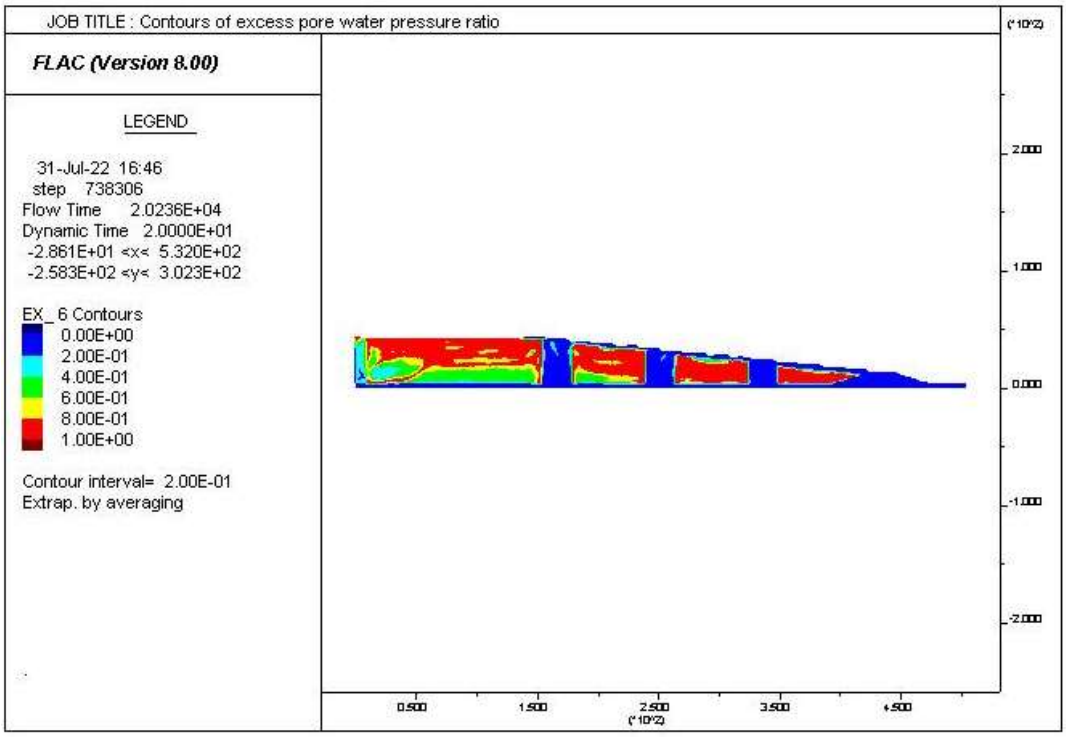

Figure A3. 77: Excess pore water pressure ratio distribution for the 25-60-40-8H- E_3 Loma

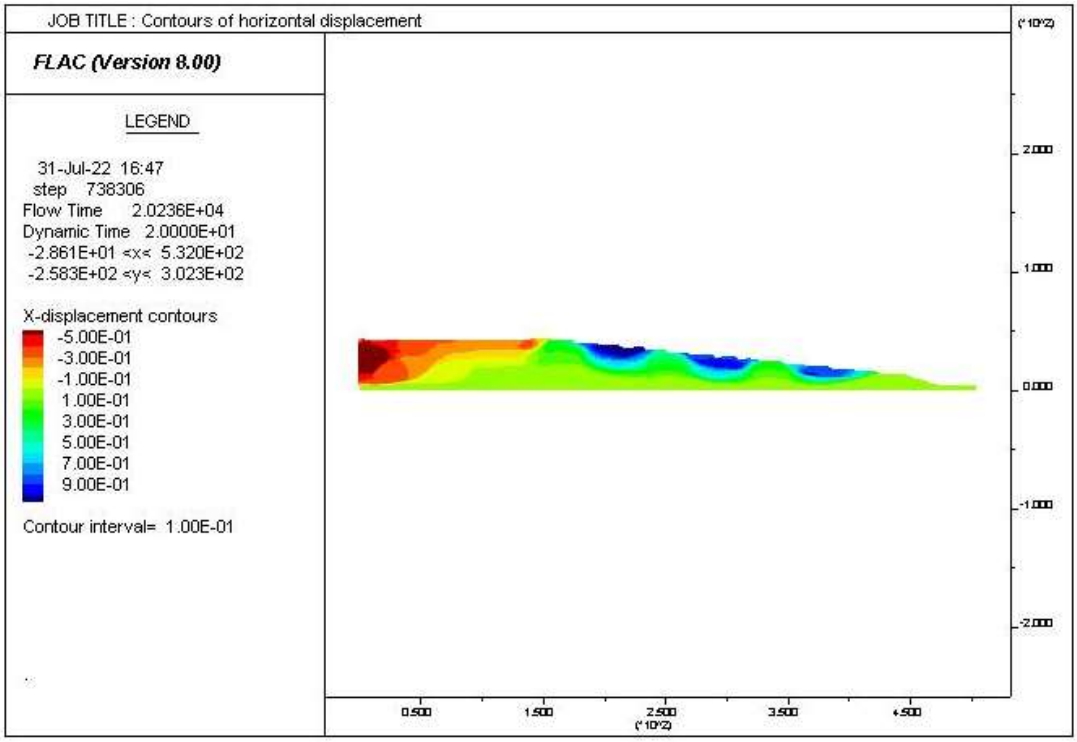

Figure A3. 78: Contours of horizontal displacement for the 25-60-40-8H- E_3Loma

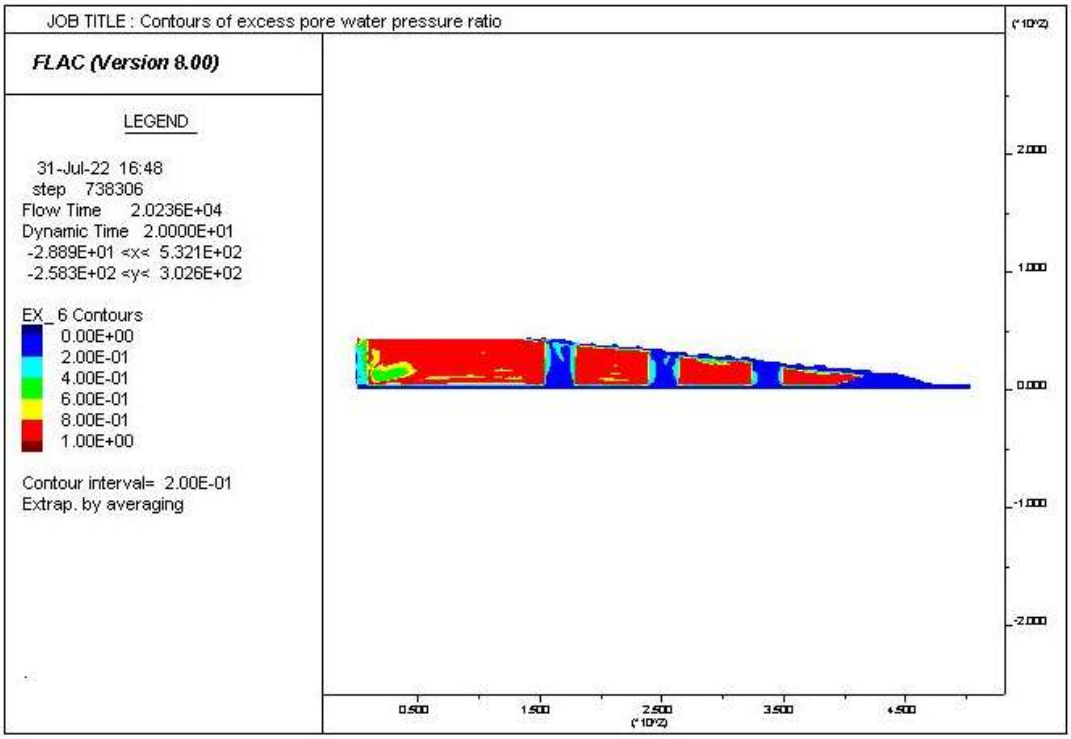

Figure A3. 79: Excess pore water pressure ratio distribution for the 25-60-40-8H- E_4 Loma

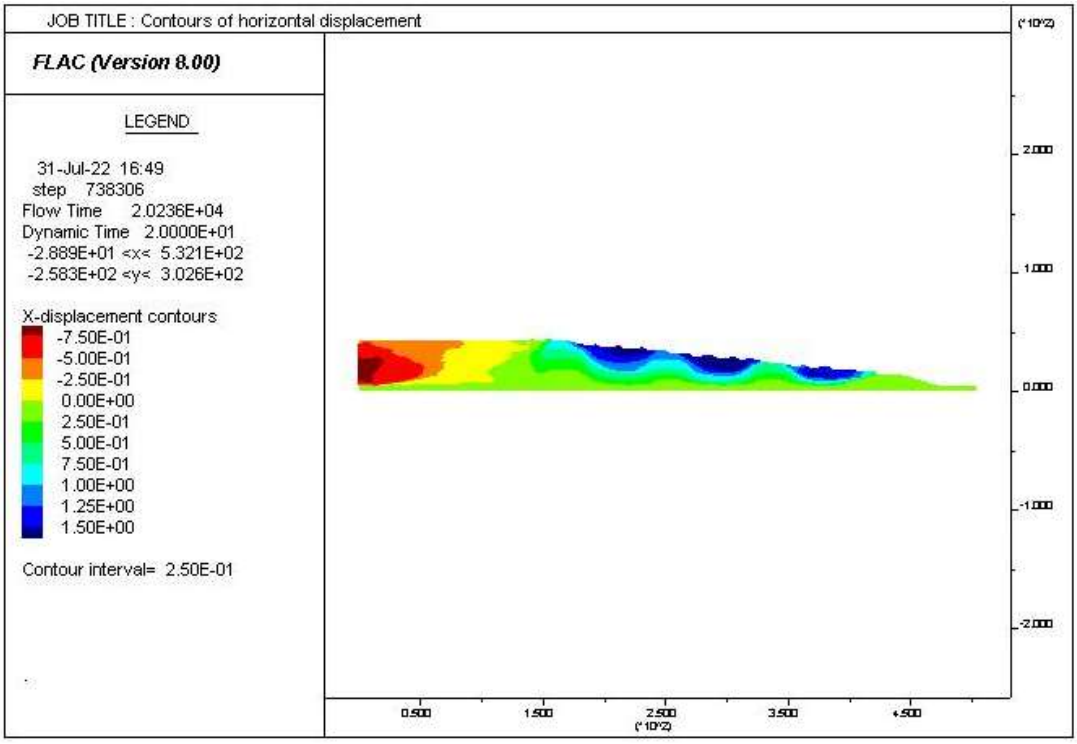

Figure A3. 80: Contours of horizontal displacement for the 25-60-40-8H- E_4Loma

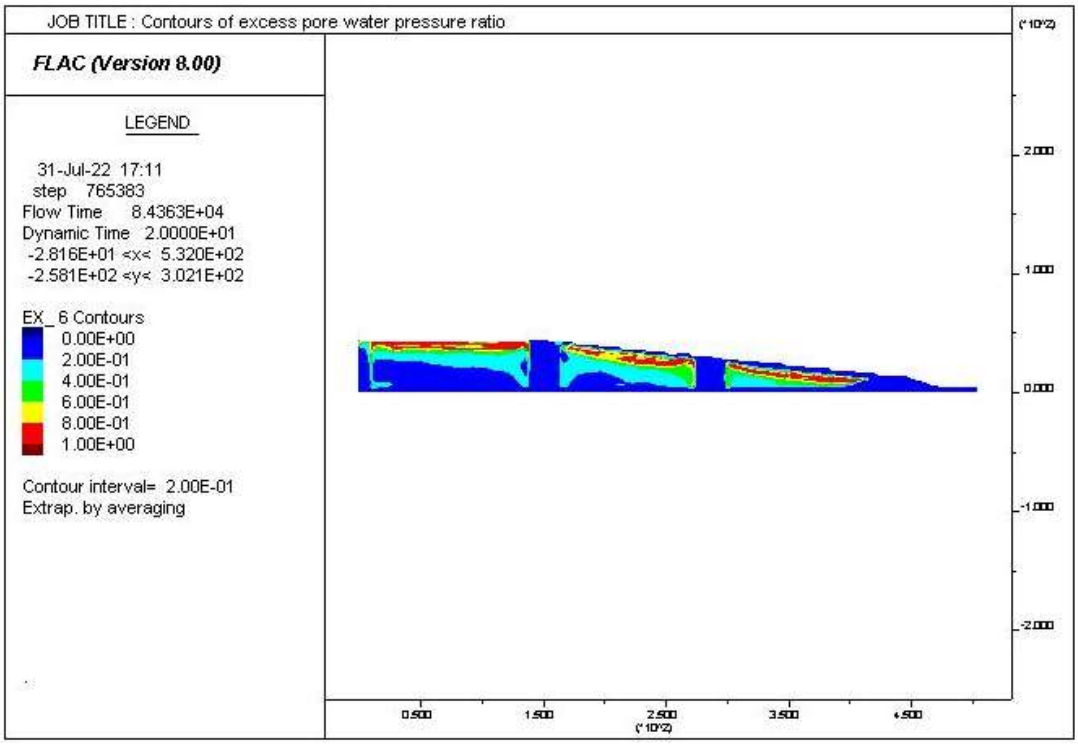

Figure A3. 81: Excess pore water pressure ratio distribution for the 25-110-40-8H- E_1 Loma

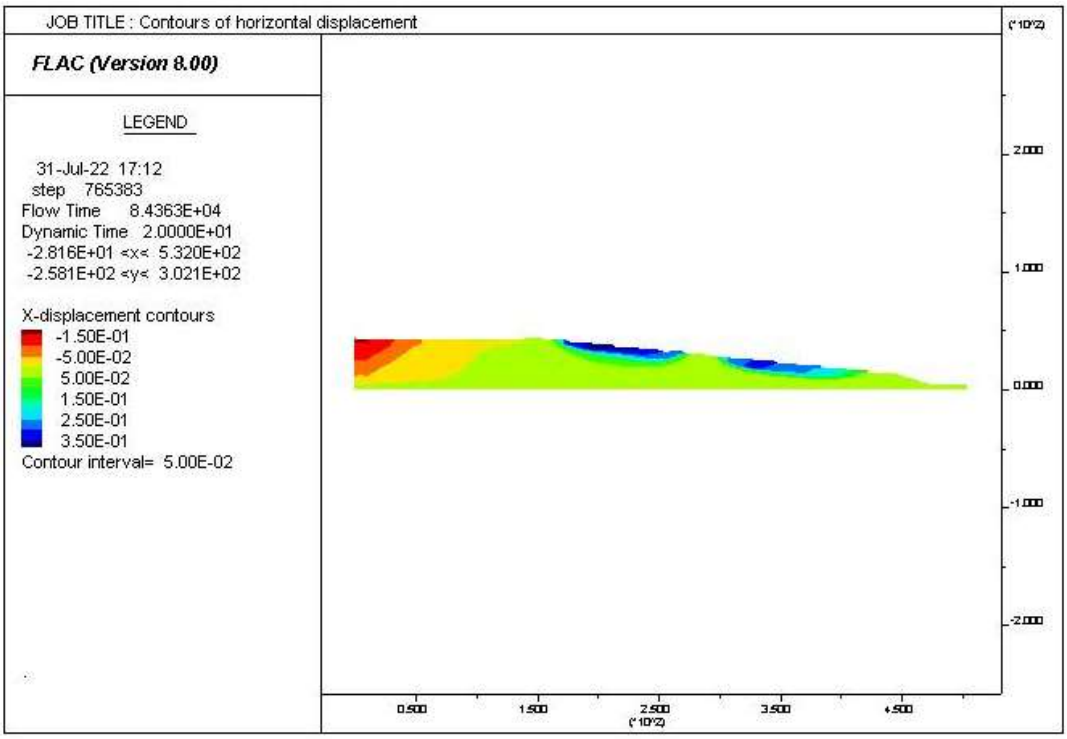

Figure A3. 82: Contours of horizontal displacement for the 25-110-40-8H- E_1Loma

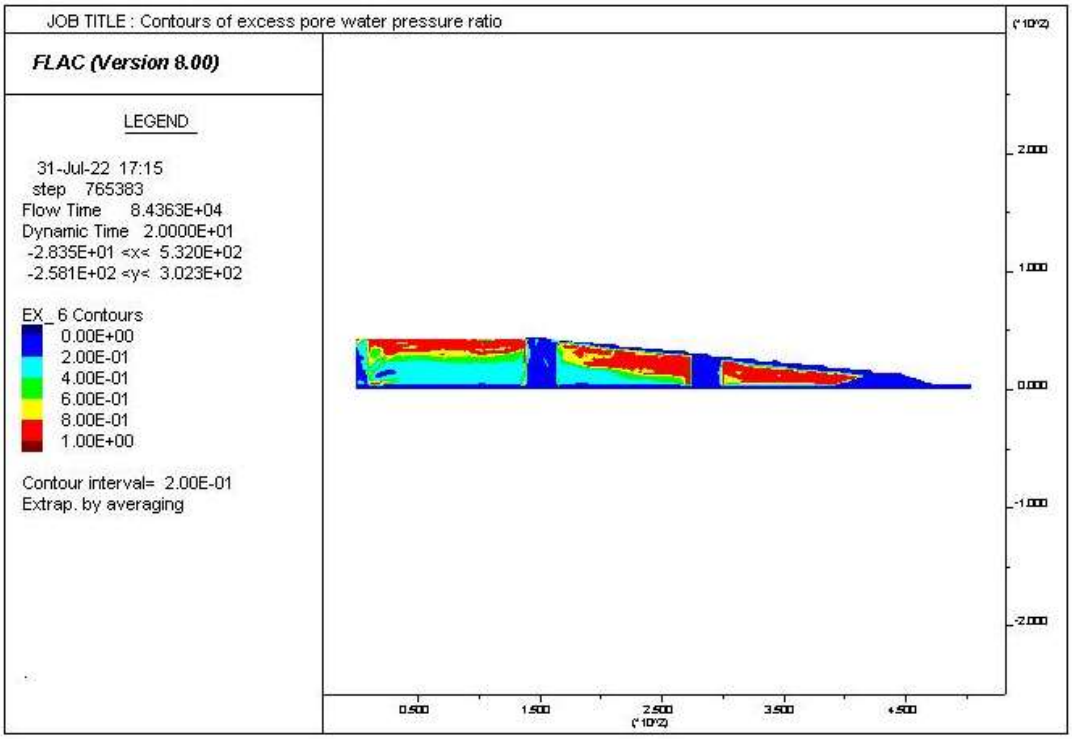

Figure A3. 83: Excess pore water pressure ratio distribution for the 25-110-40-8H- E_2 Loma

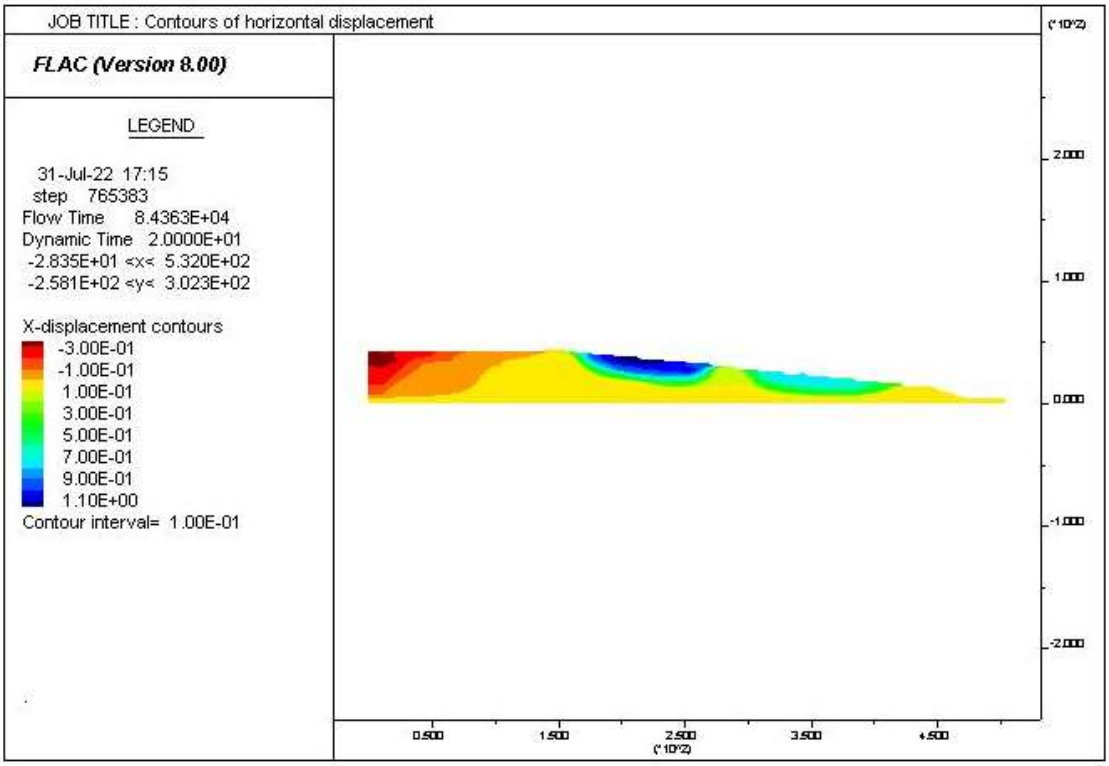

Figure A3. 84: Contours of horizontal displacement for the 25-110-40-8H- E_2Loma

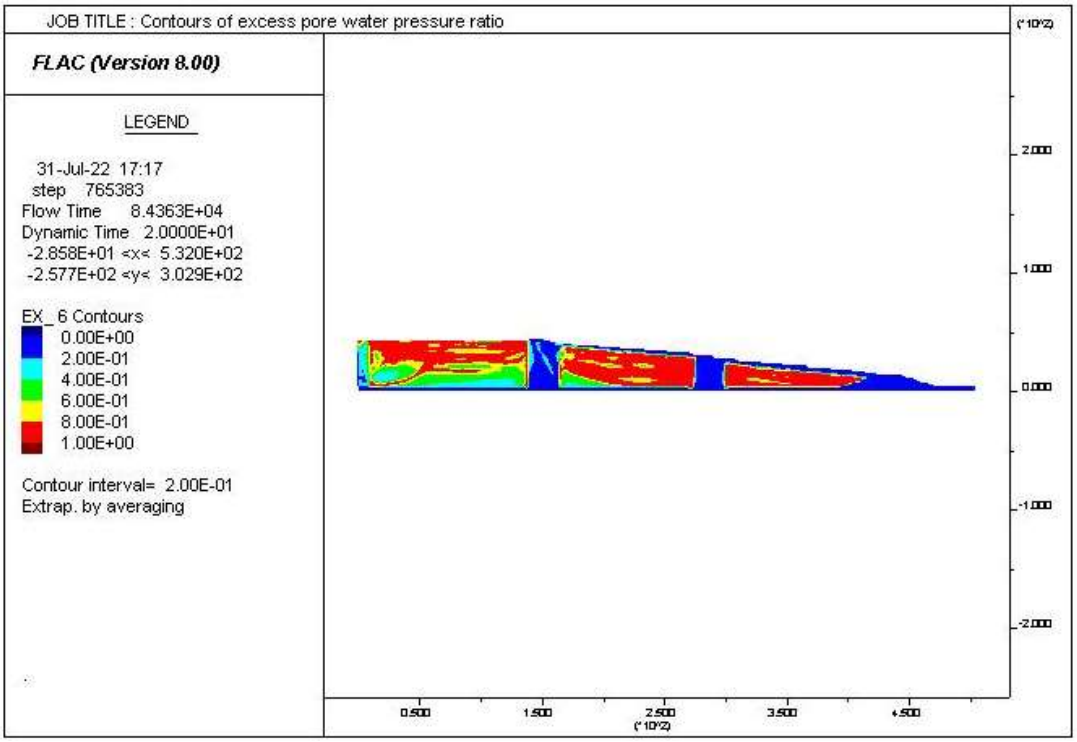

Figure A3. 85: Excess pore water pressure ratio distribution for the 25-110-40-8H- E_3 Loma

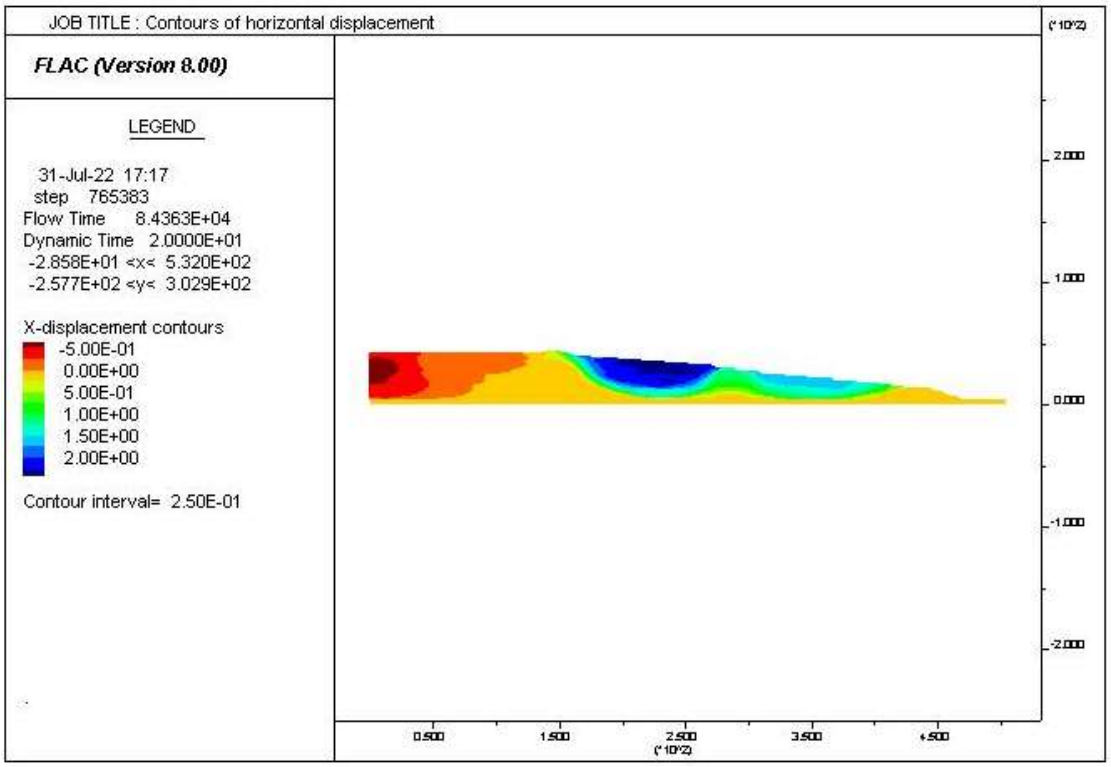

Figure A3. 86: Contours of horizontal displacement for the 25-110-40-8H- E_3Loma

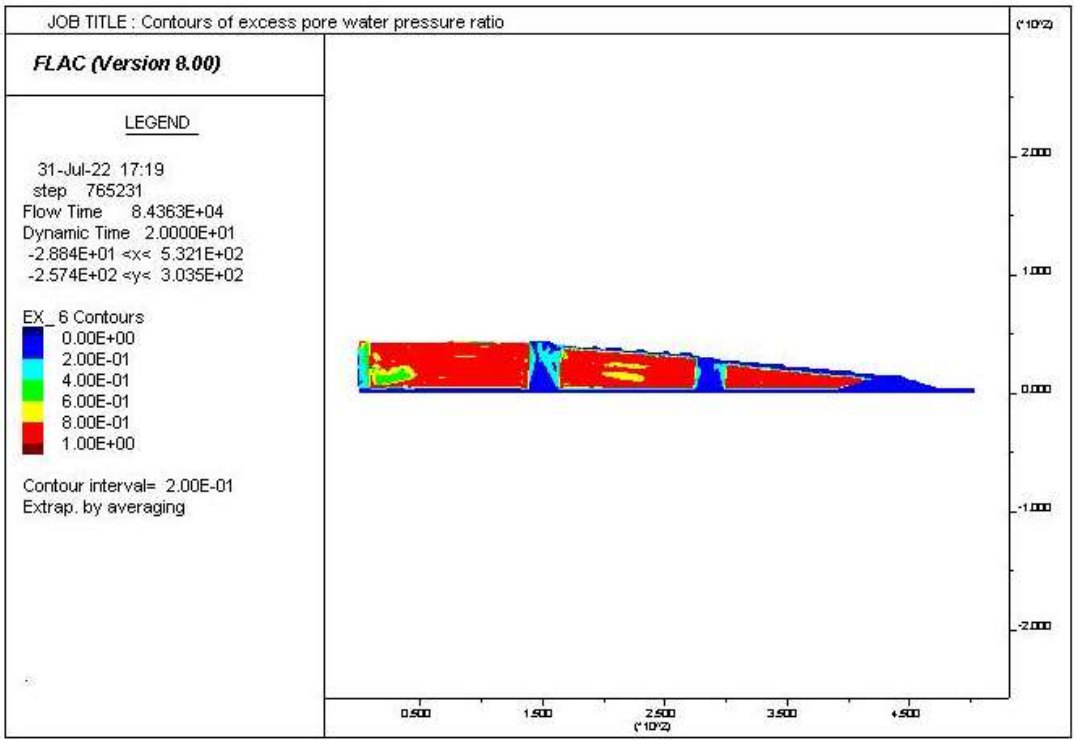

Figure A3. 87: Excess pore water pressure ratio distribution for the 25-110-40-8H- E_4 Loma

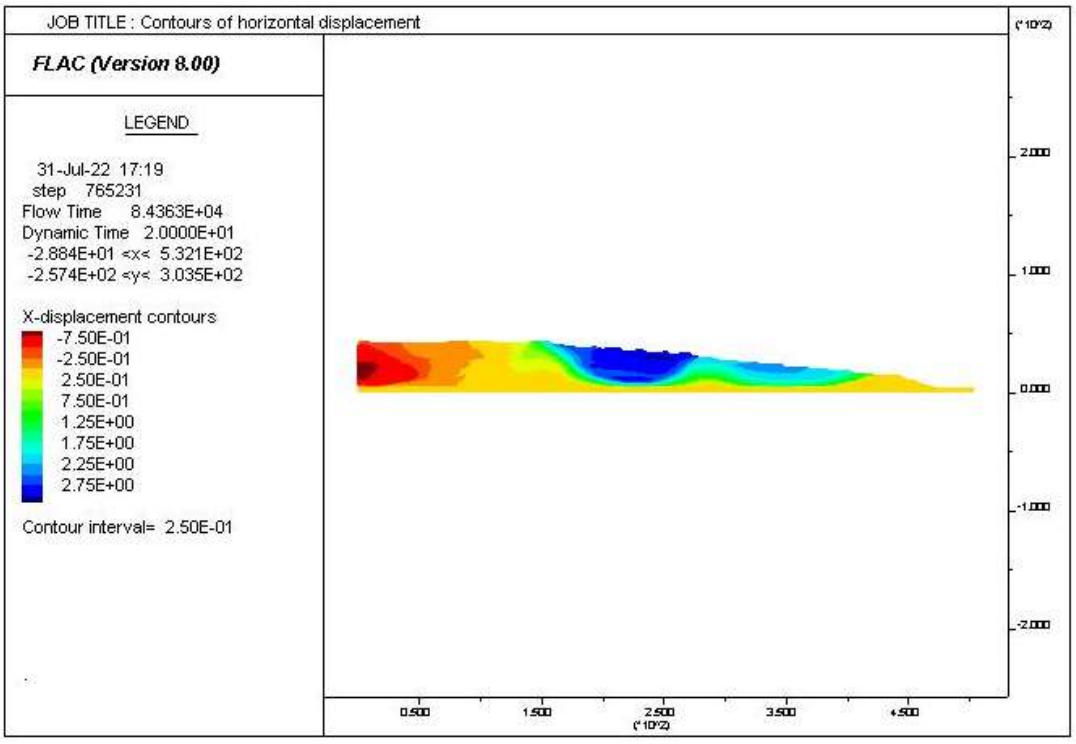

Figure A3. 88: Contours of horizontal displacement for the 25-110-40-8H- E_4Loma

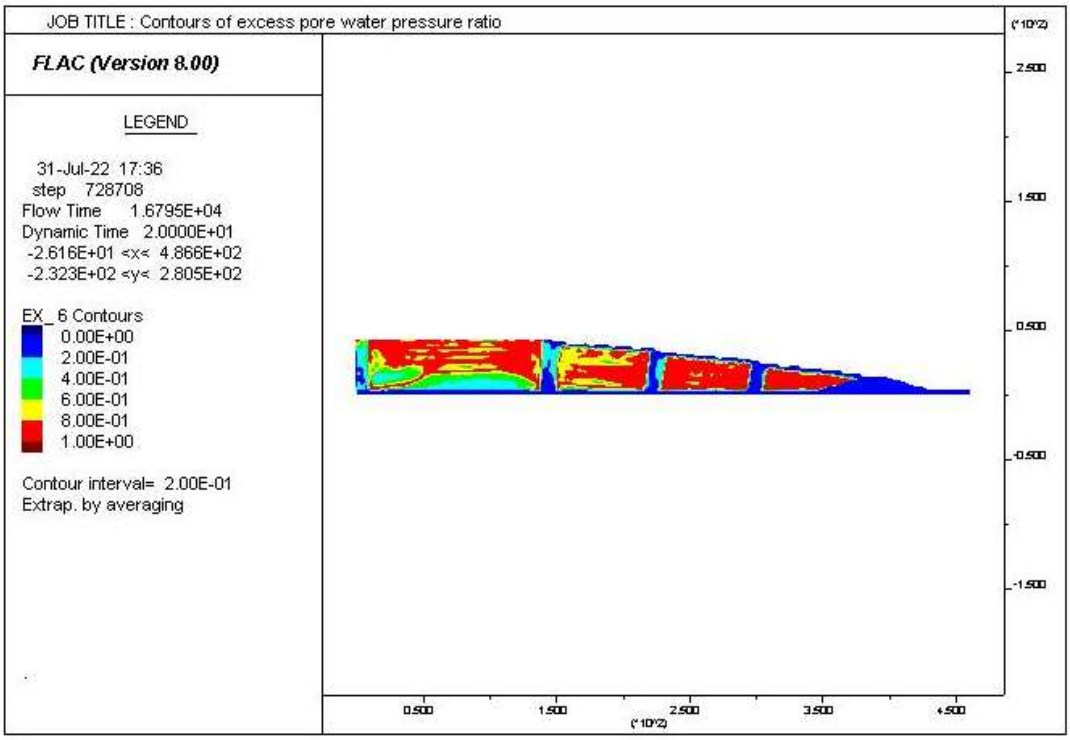

Figure A3. 89: Excess pore water pressure ratio distribution for the 12-65-40-7H- E_3 Loma

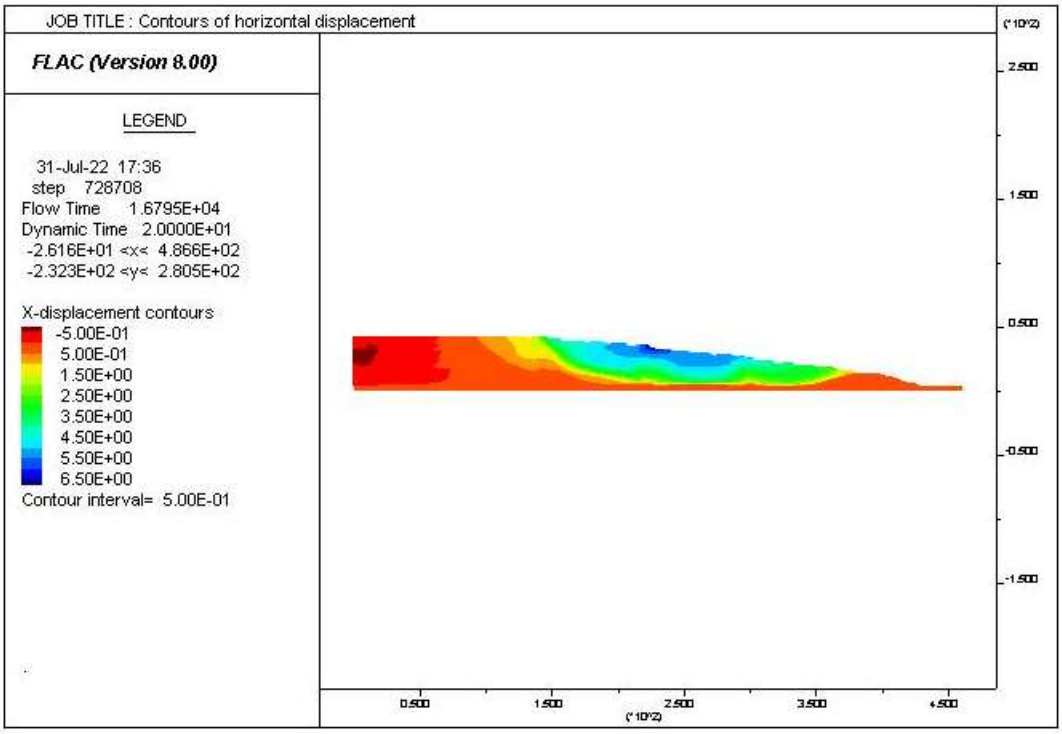

Figure A3. 90: Contours of horizontal displacement for the 12-65-40-7H- E_3Loma

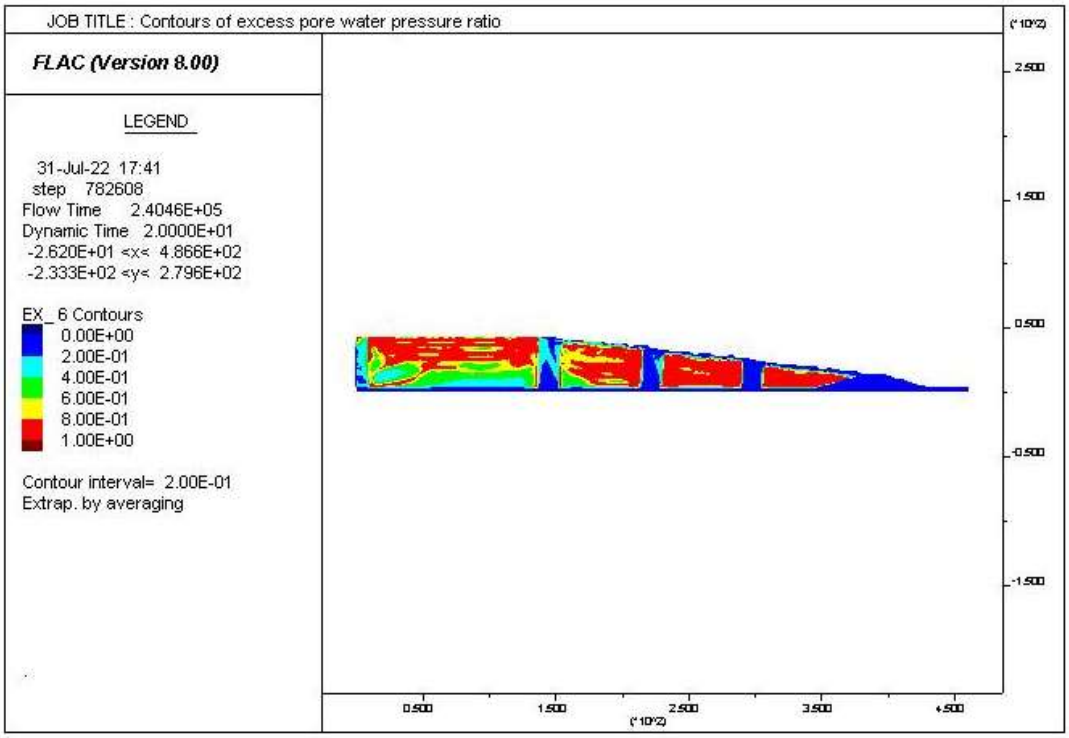

Figure A3. 91: Excess pore water pressure ratio distribution for the 16-60-40-7H- E_3 Loma

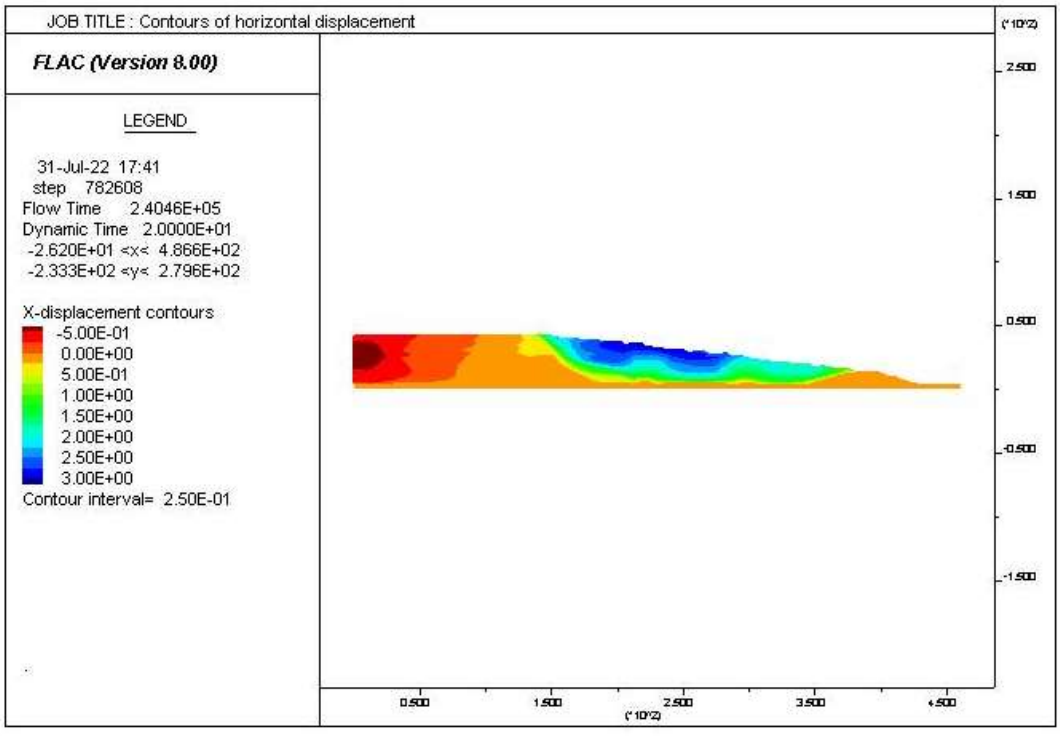

Figure A3. 92: Contours of horizontal displacement for the 16-60-40-7H- E_3Loma

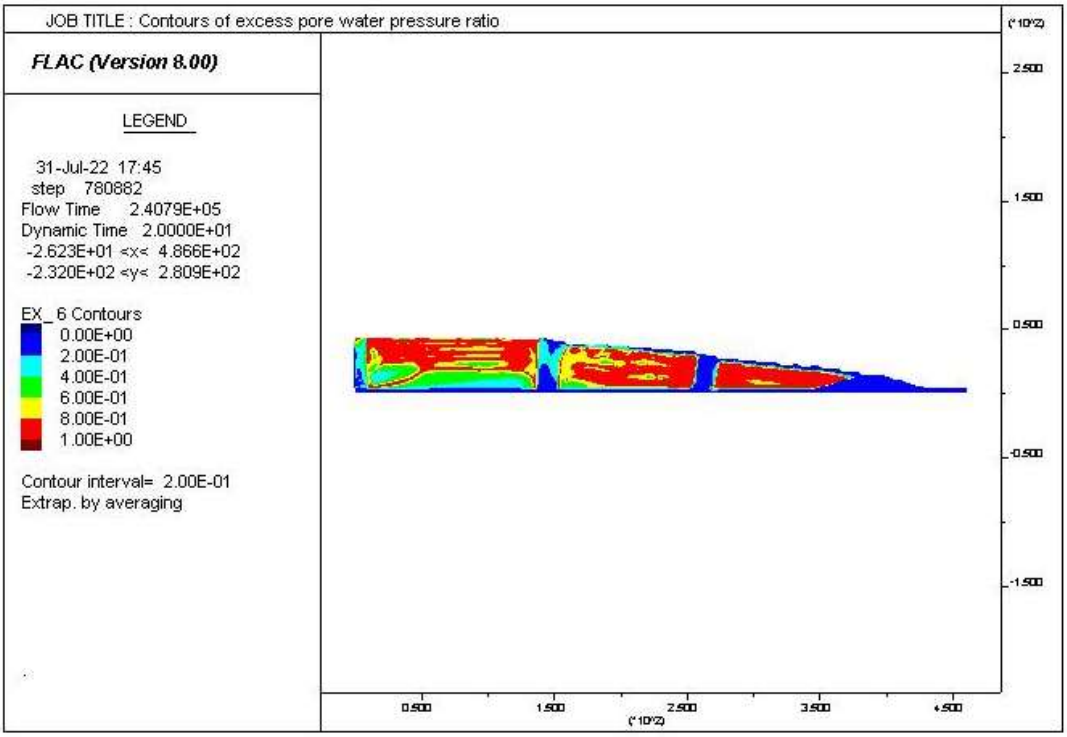

Figure A3. 93: Excess pore water pressure ratio distribution for the 16-100-40-7H- E_3 Loma

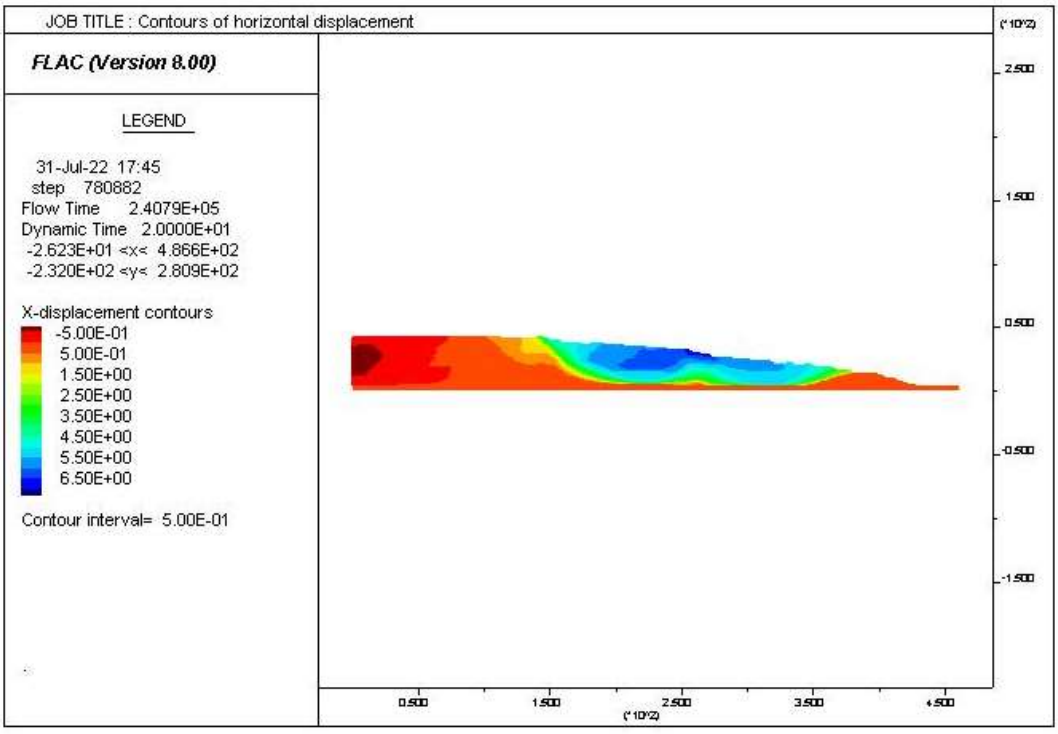

Figure A3. 94: Contours of horizontal displacement for the 16-100-40-7H- E_3Loma

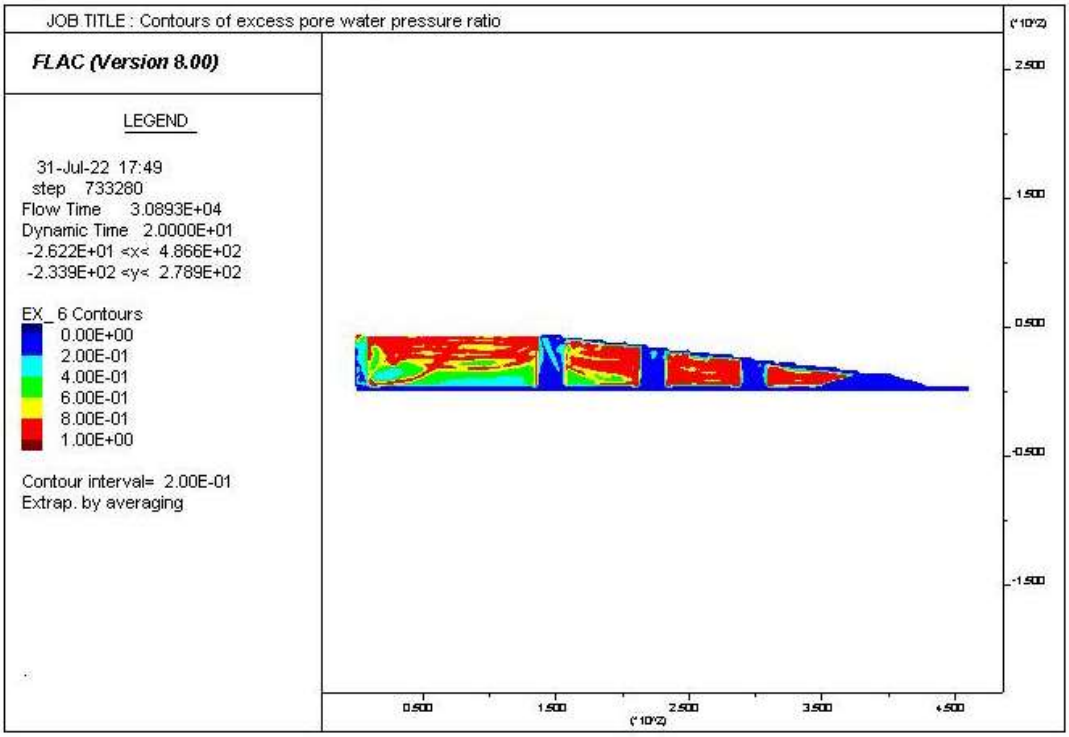

Figure A3. 95: Excess pore water pressure ratio distribution for the 20-56-40-7H- E_3 Loma

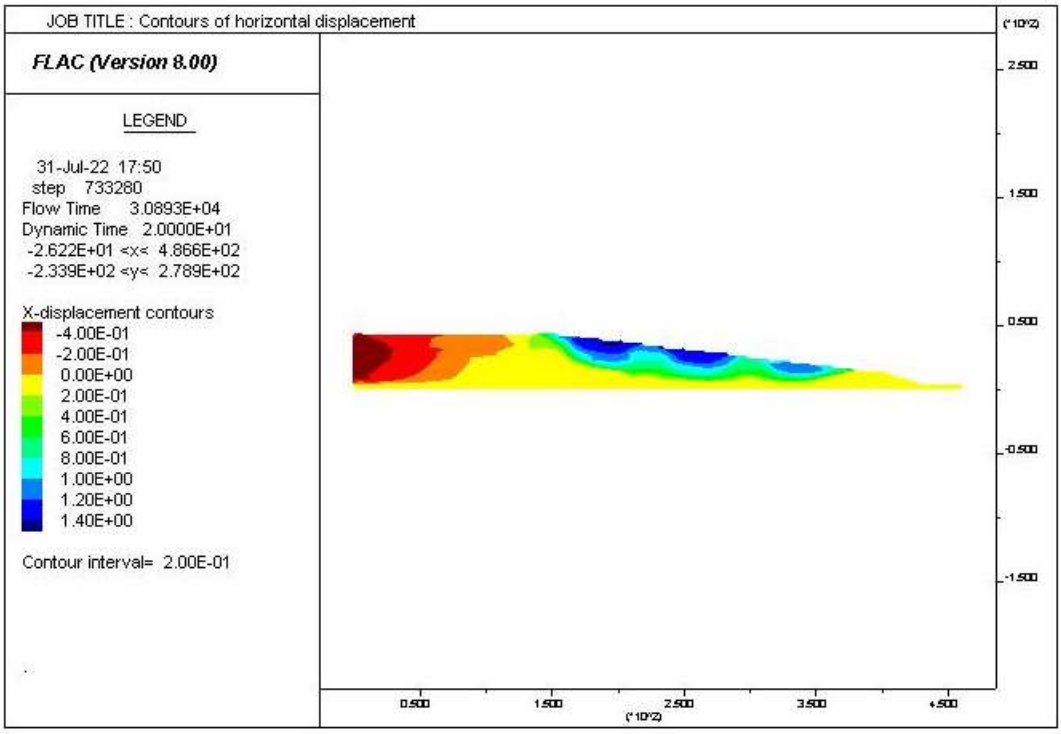

Figure A3. 96: Contours of horizontal displacement for the 20-56-40-7H- E_3Loma

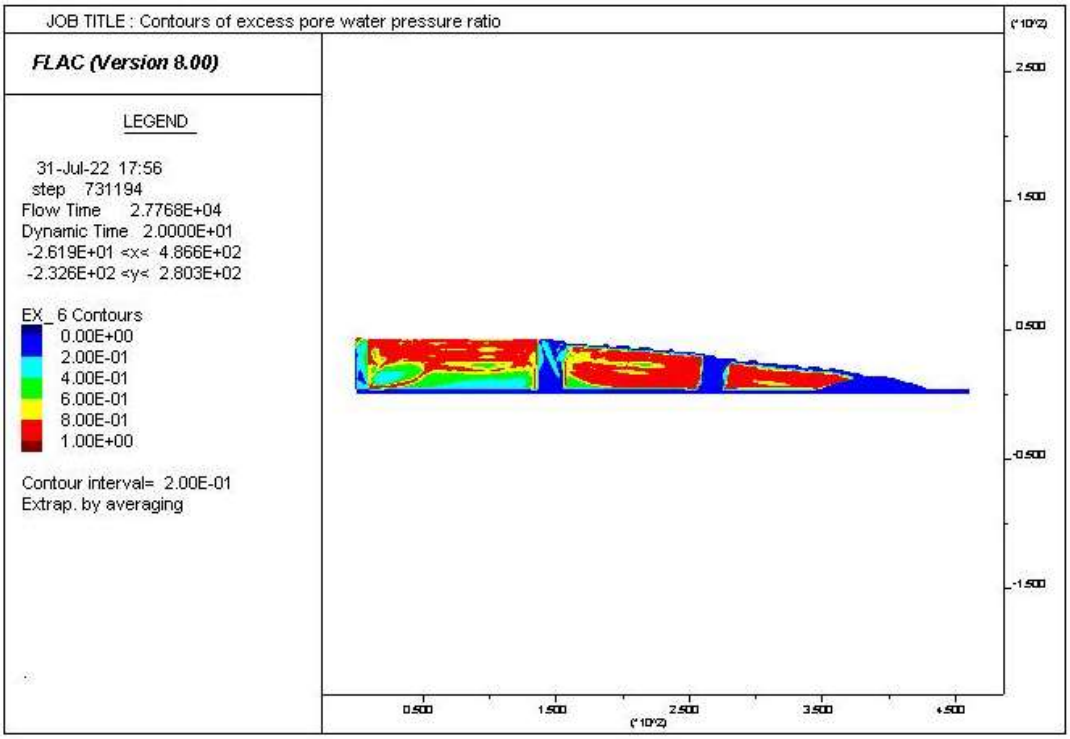

Figure A3. 97: Excess pore water pressure ratio distribution for the 20-100-40-7H- E_3 Loma

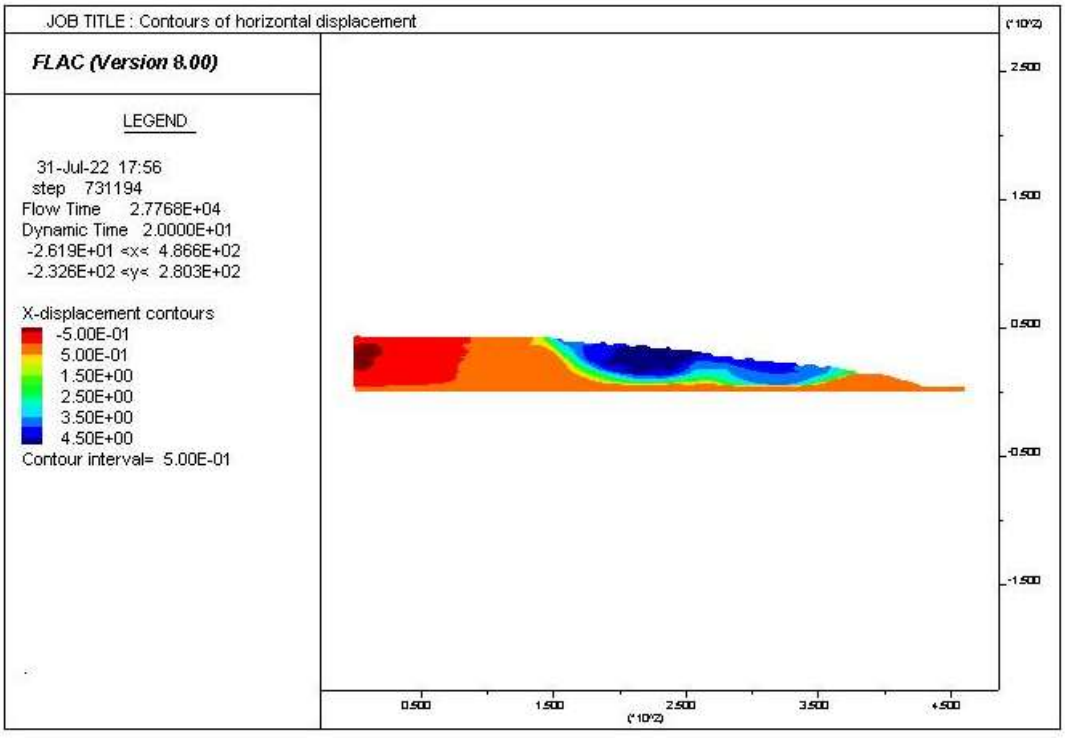

Figure A3. 98: Contours of horizontal displacement for the 20-100-40-7H- E_3Loma

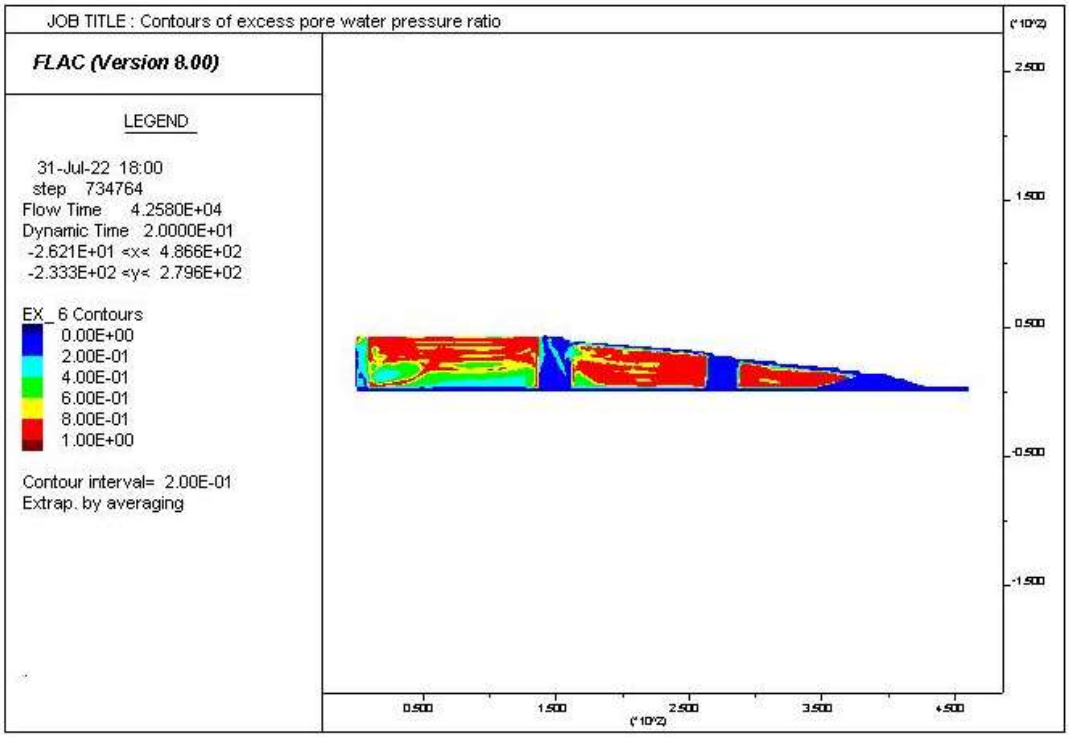

Figure A3. 99: Excess pore water pressure ratio distribution for the 25-100-40-7H- E_3 Loma

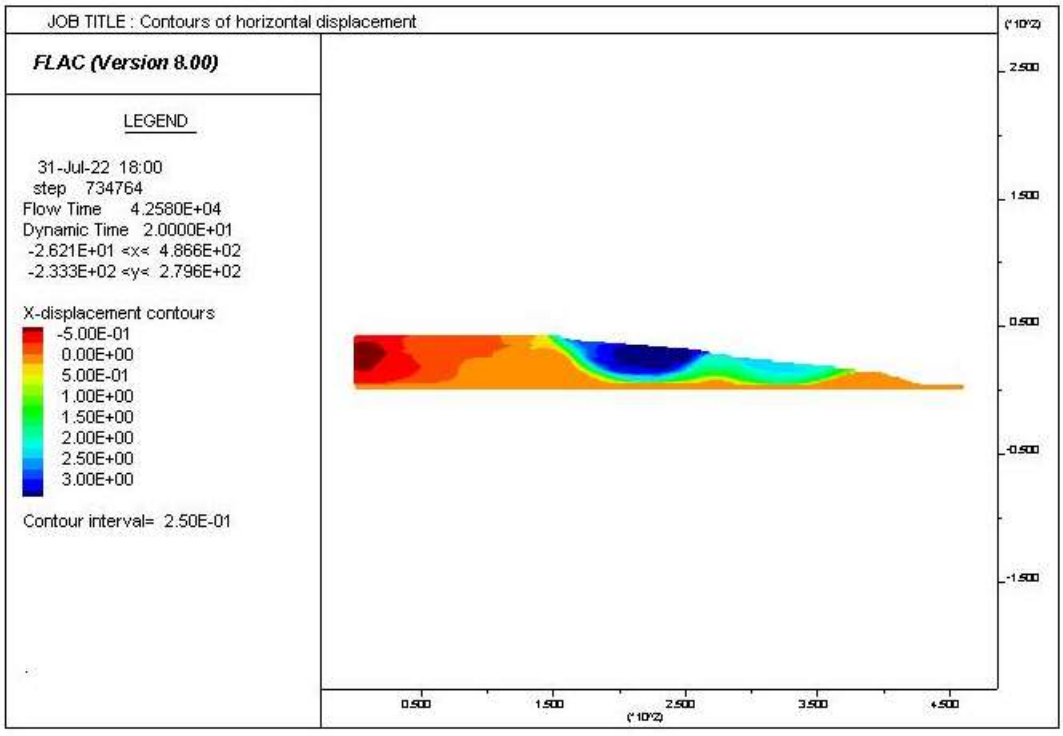

Figure A3. 100: Contours of horizontal displacement for the 25-100-40-7H- E_3Loma

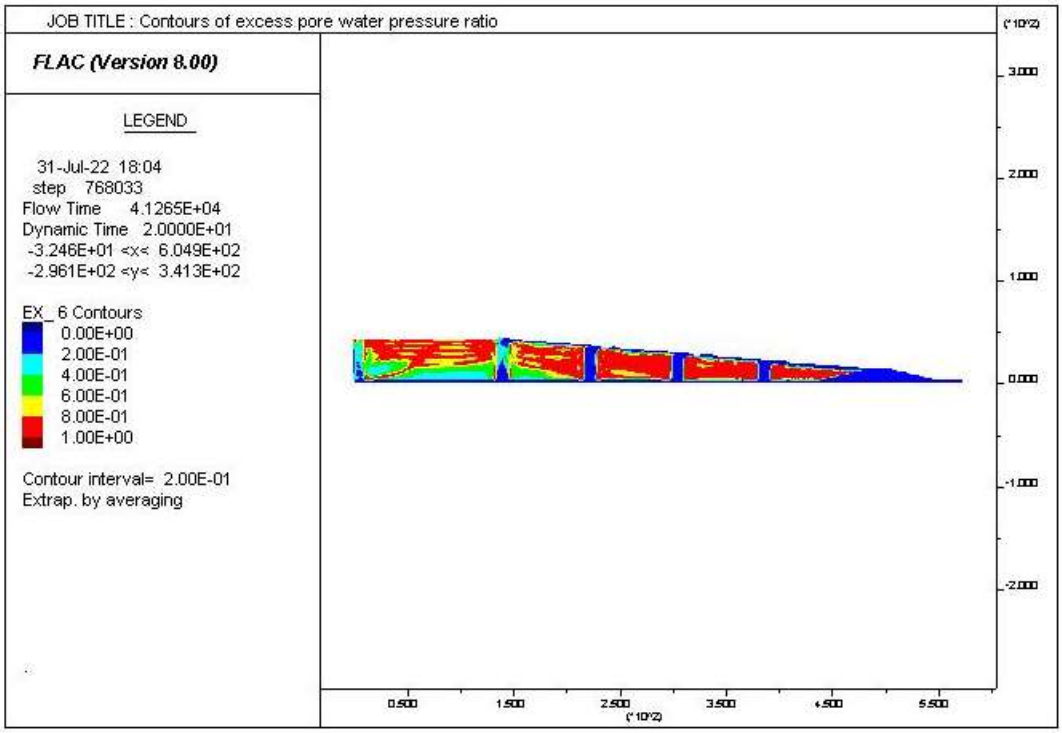

Figure A3. 101: Excess pore water pressure ratio distribution for the 12-70-40-10H- E_3 Loma

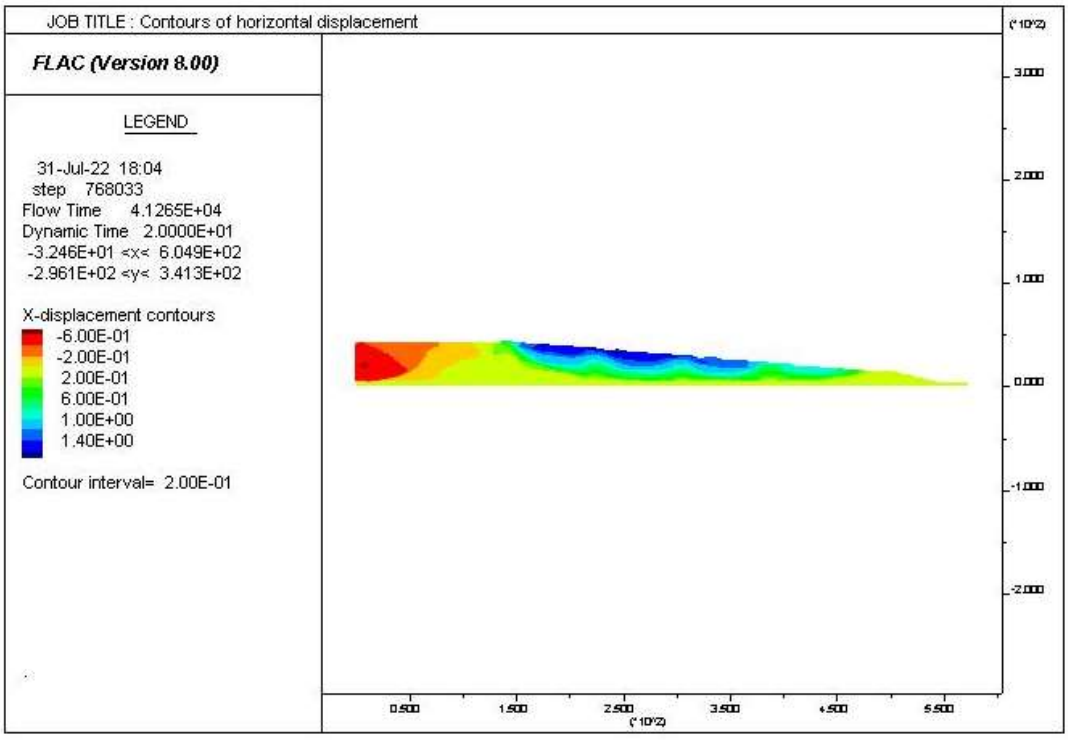

Figure A3. 102: Contours of horizontal displacement for the 12-70-40-10H- E_3Loma

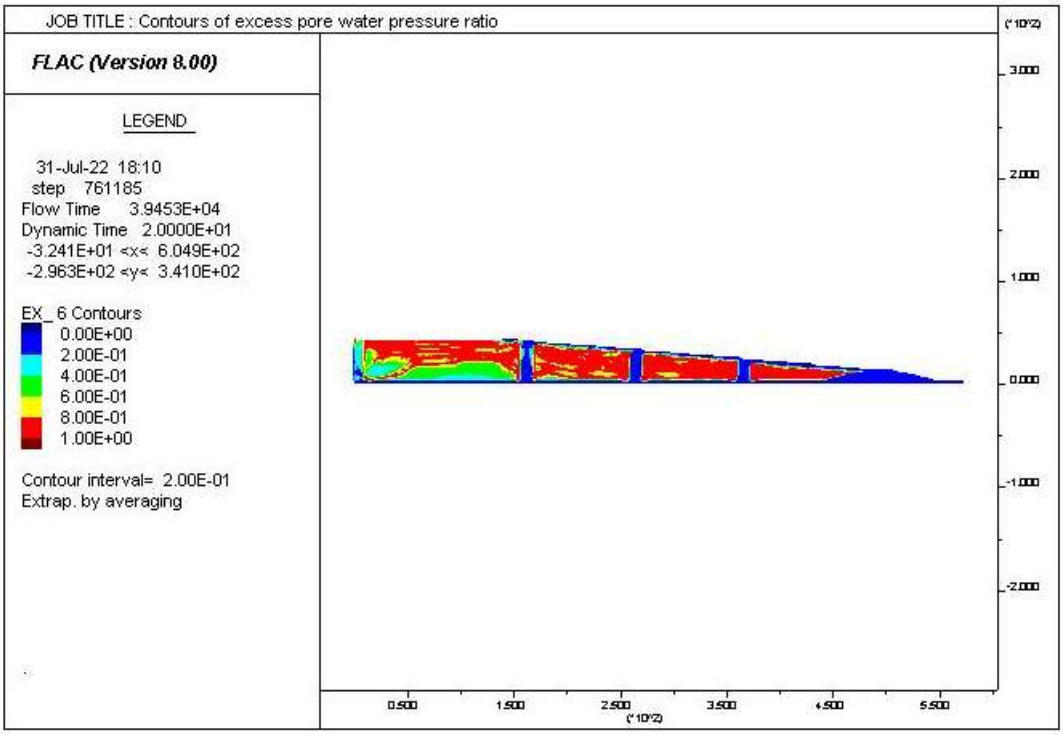

Figure A3. 103: Excess pore water pressure ratio distribution for the 12-90-40-10H- E_3 Loma

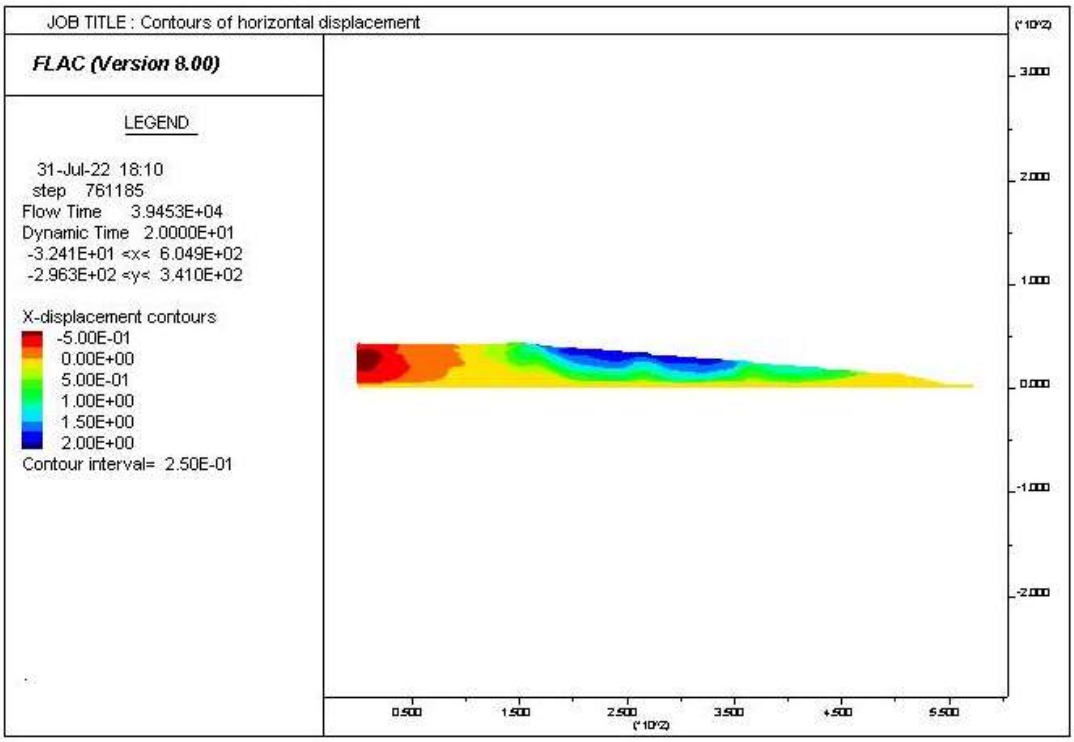

Figure A3. 104: Contours of horizontal displacement for the 12-90-40-10H- E_3Loma

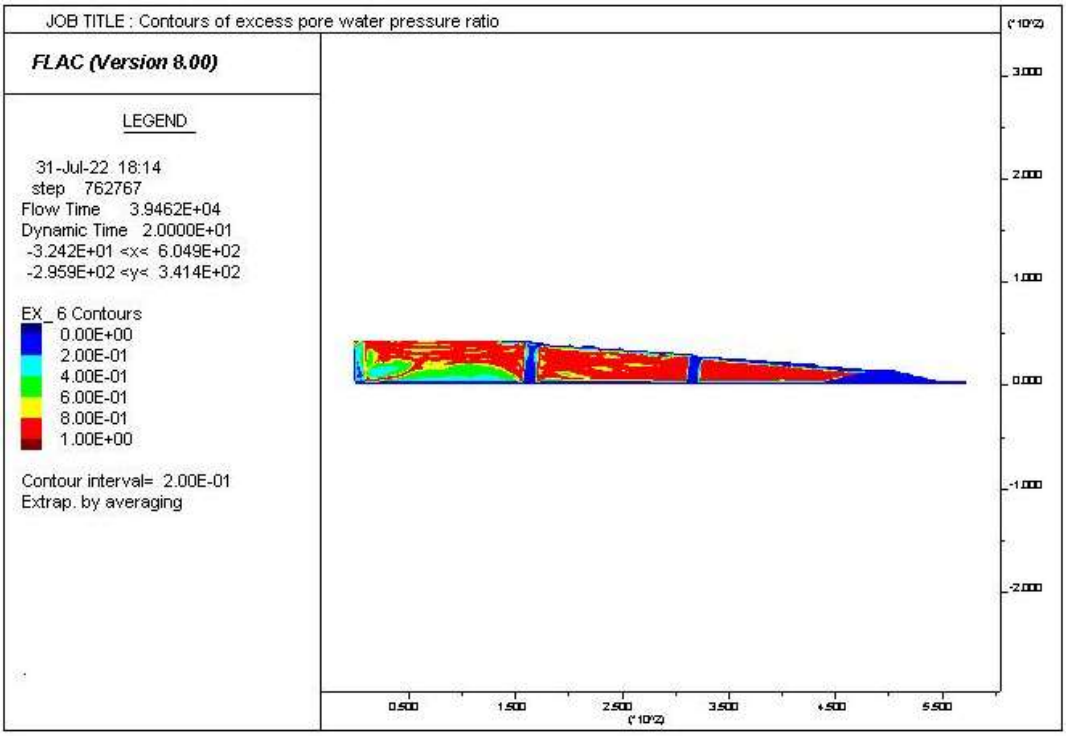

Figure A3. 105: Excess pore water pressure ratio distribution for the 12-140-40-10H- E_3 Loma

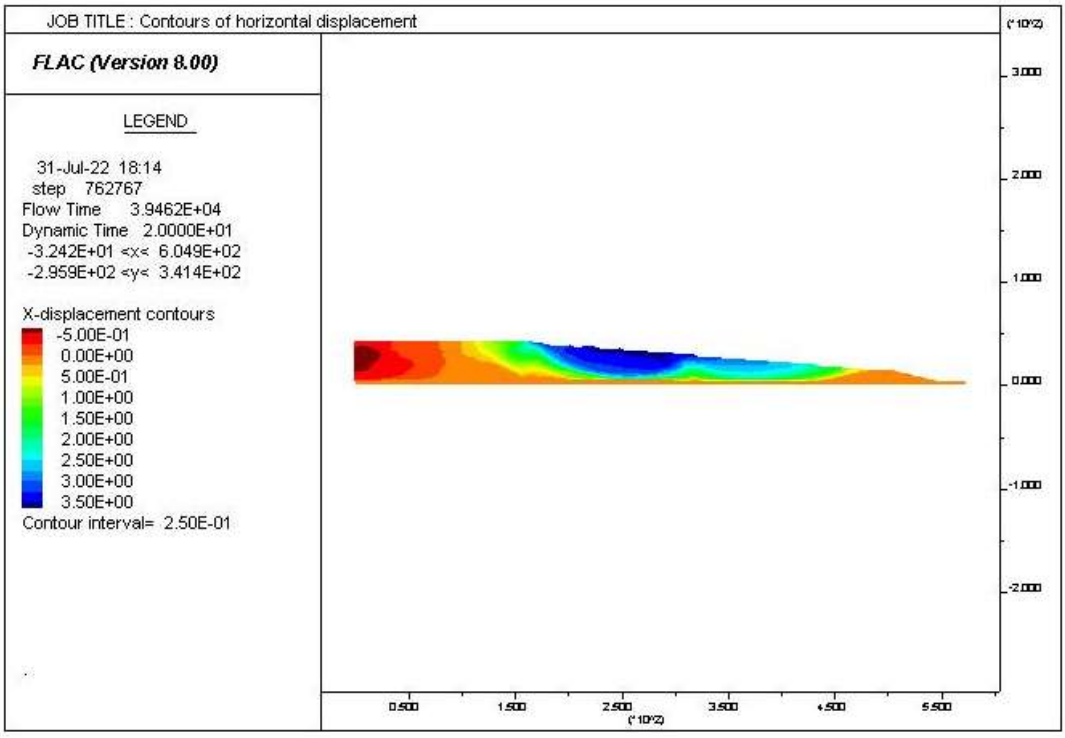

Figure A3. 106: Contours of horizontal displacement for the 12-140-40-10H- E_3Loma

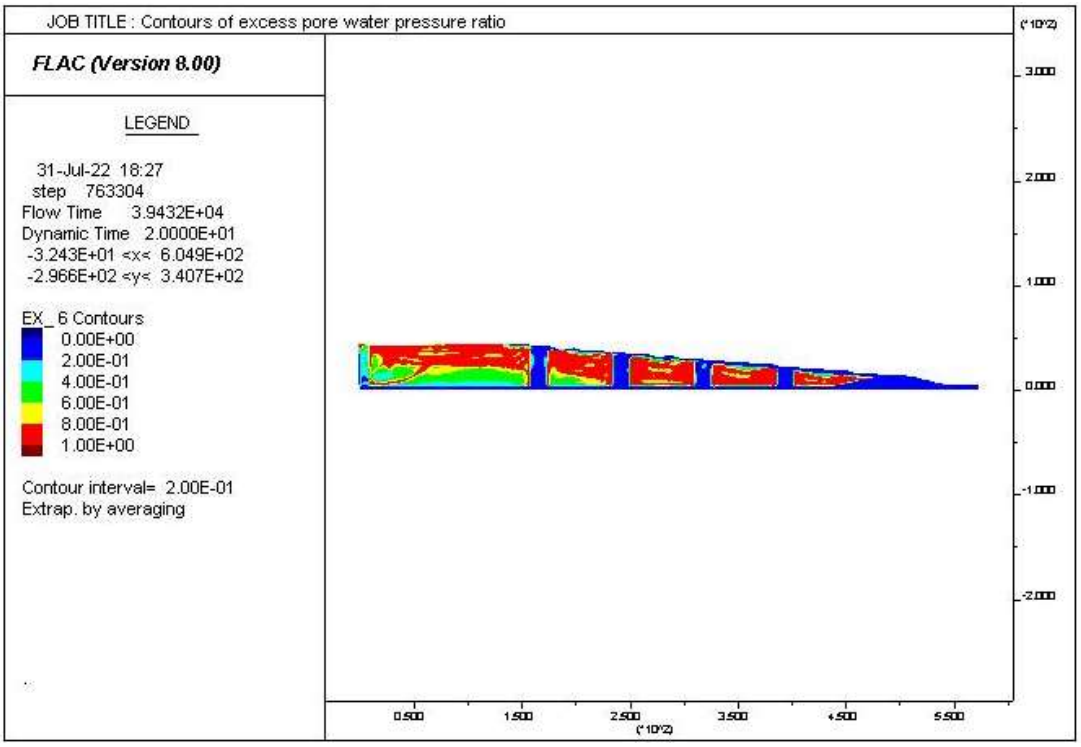

Figure A3. 107: Excess pore water pressure ratio distribution for the 16-60-40-10H- E_3 Loma

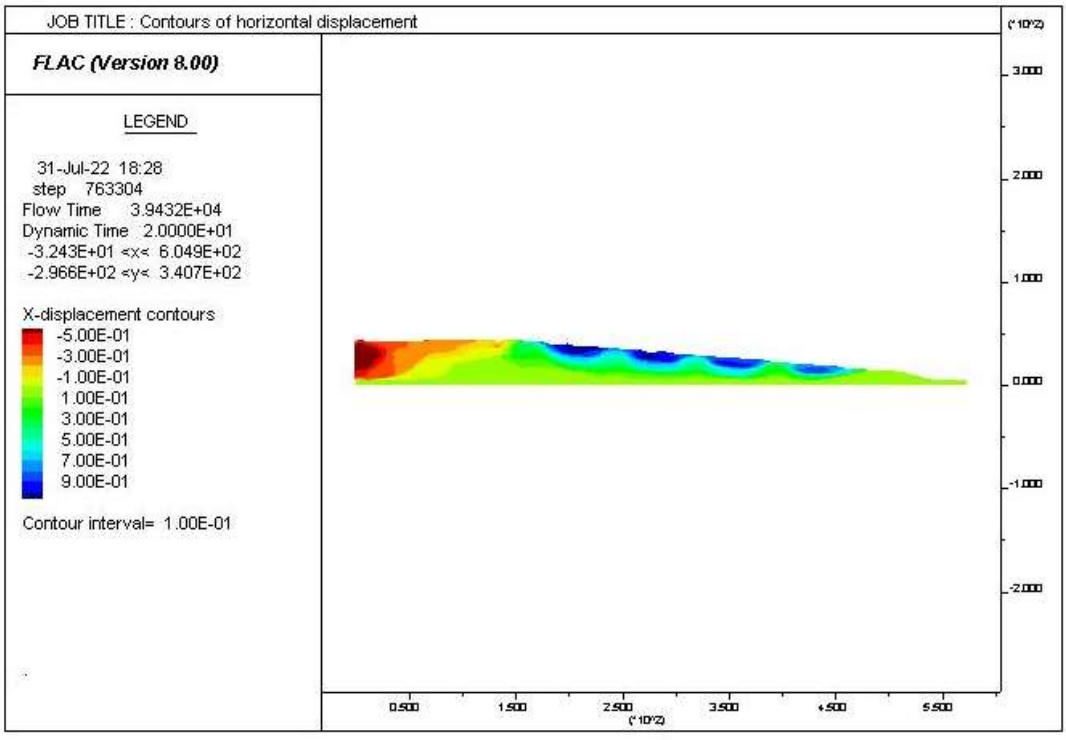

Figure A3. 108: Contours of horizontal displacement for the 16-60-40-10H- E_3Loma

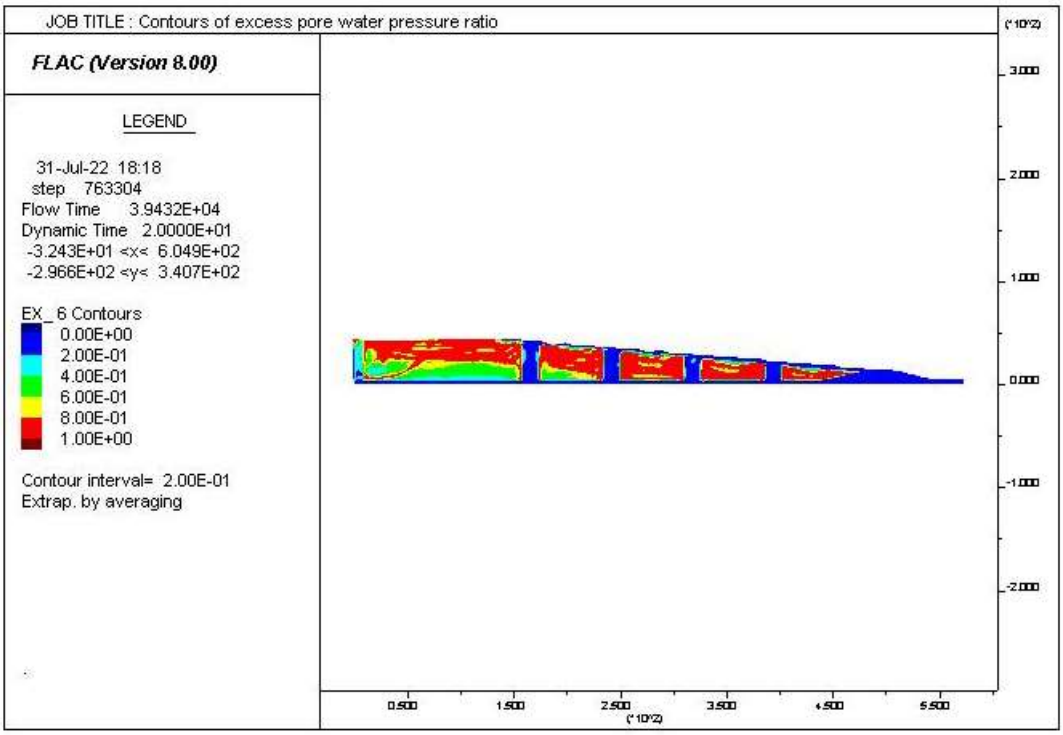

Figure A3. 109: Excess pore water pressure ratio distribution for the 16-90-40-10H- E_3 Loma

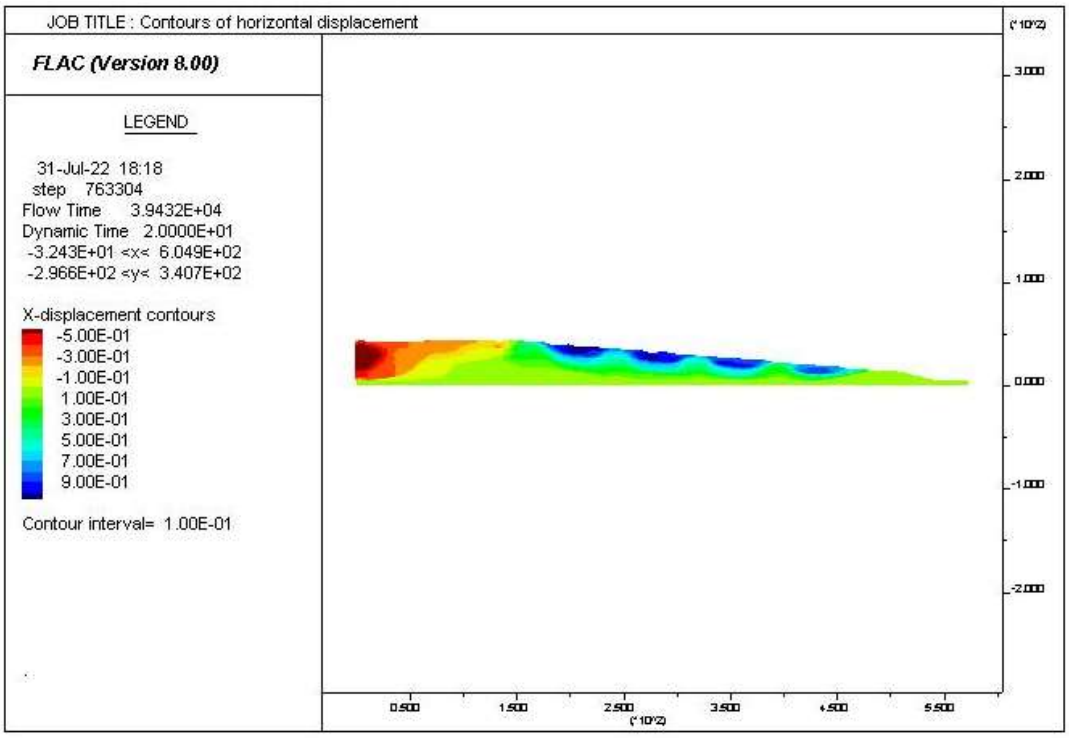

Figure A3. 110: Contours of horizontal displacement for the 16-90-40-10H- E_3Loma

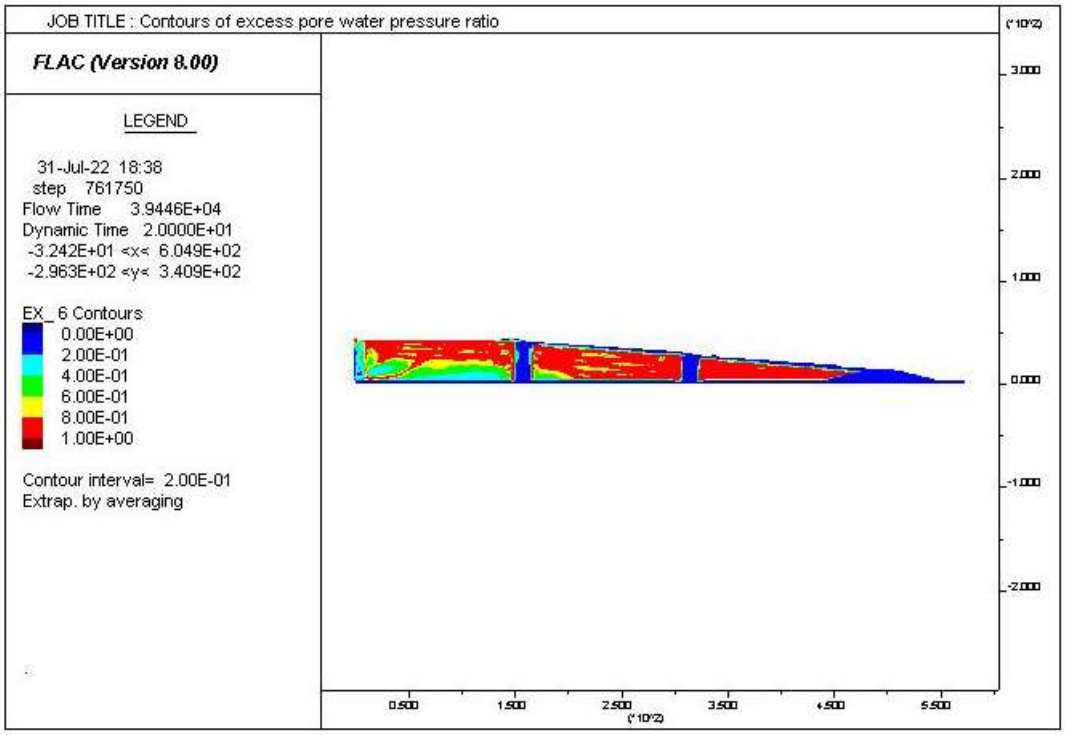

Figure A3. 111: Excess pore water pressure ratio distribution for the 16-140-40-10H- E_3 Loma

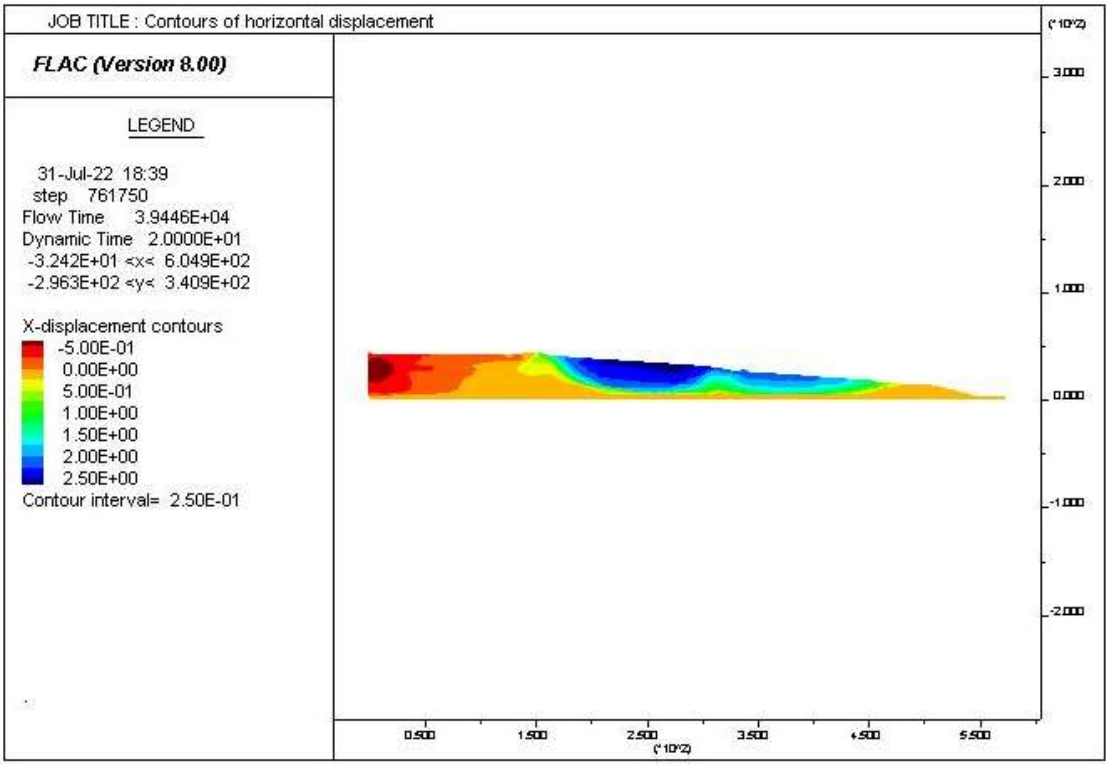

Figure A3. 112: Contours of horizontal displacement for the 16-140-40-10H- E_3Loma

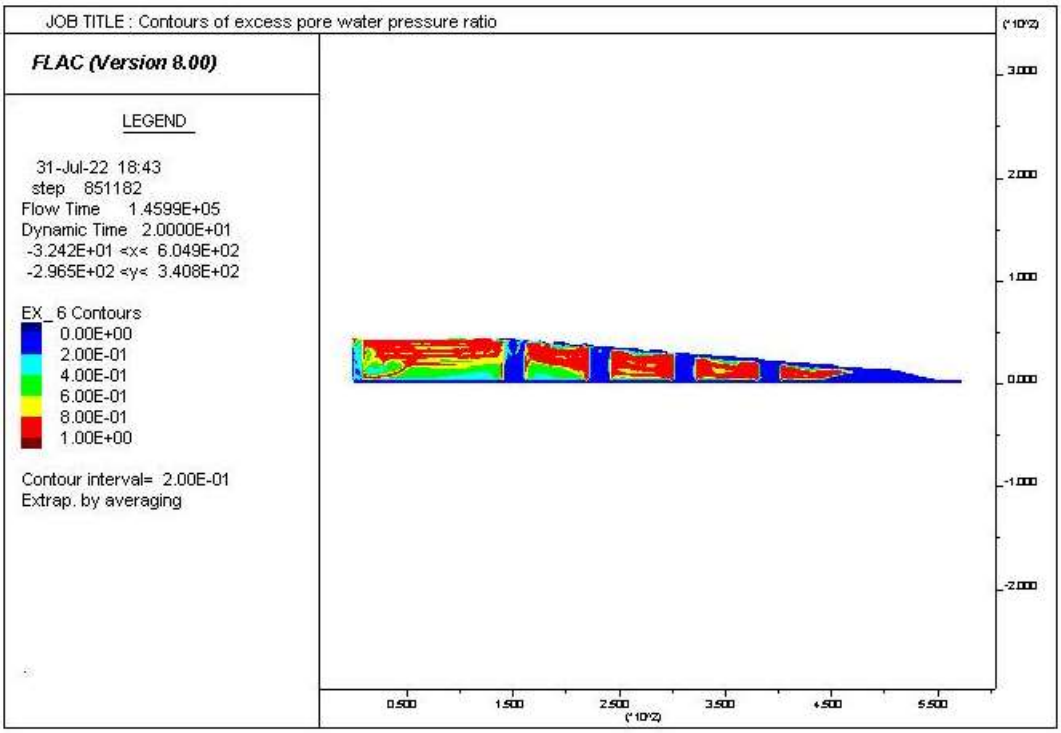

Figure A3. 113: Excess pore water pressure ratio distribution for the 20-60-40-10H- E_3 Loma

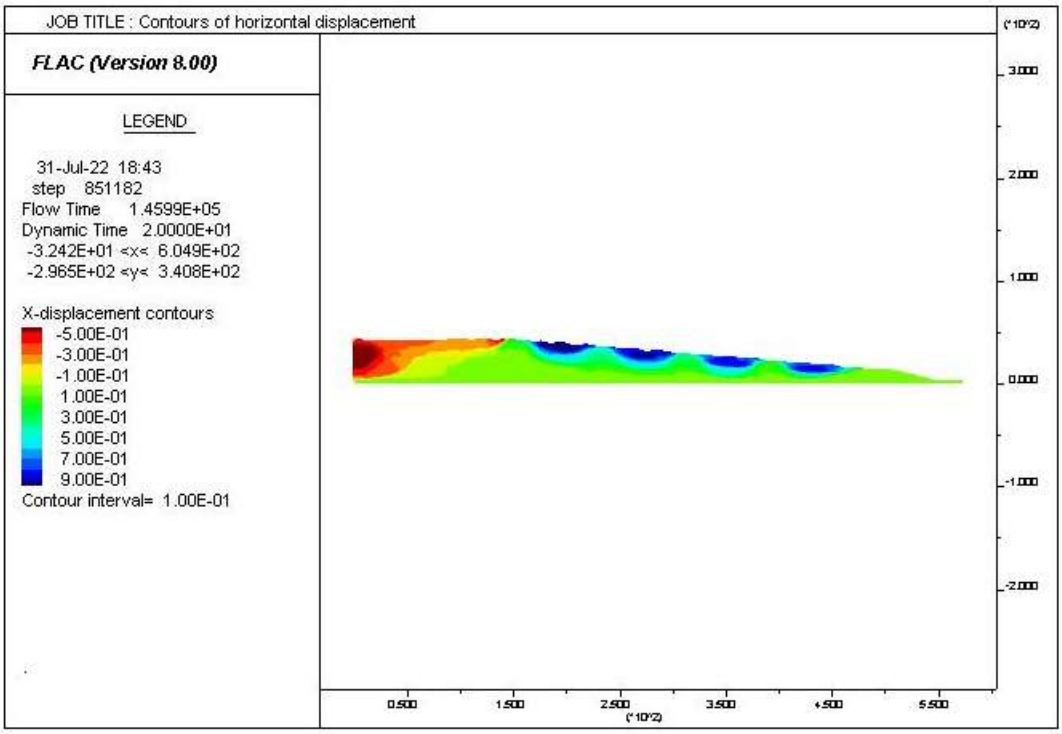

Figure A3. 114: Contours of horizontal displacement for the 20-60-40-10H- E_3Loma

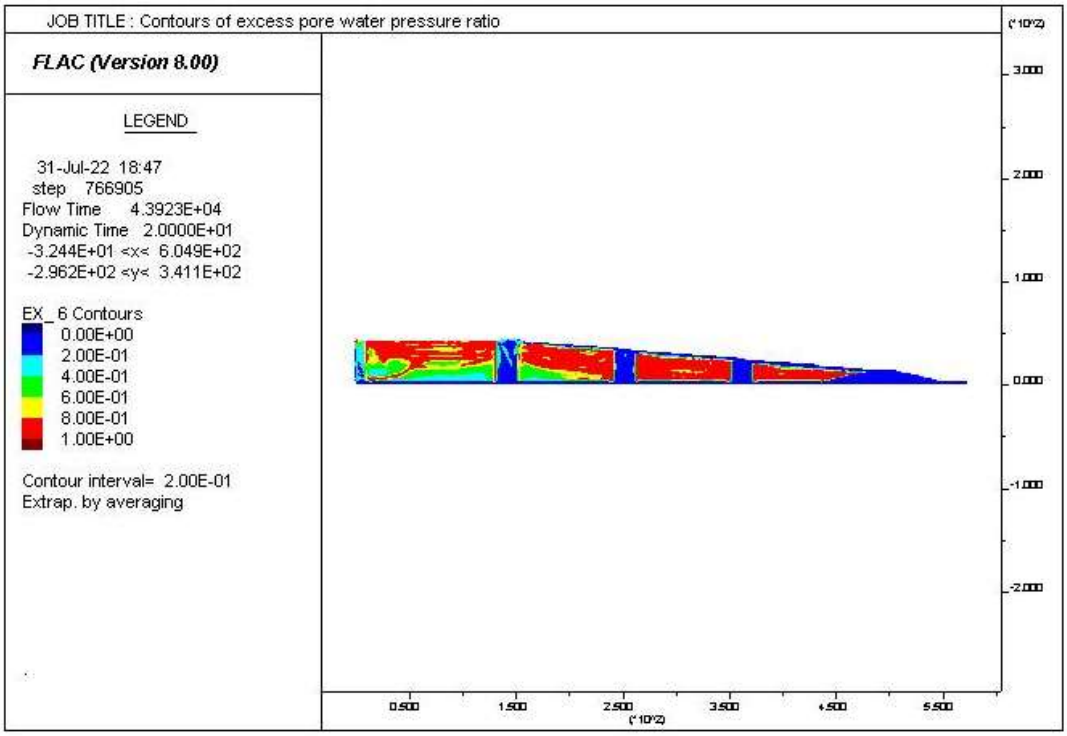

Figure A3. 115: Excess pore water pressure ratio distribution for the 20-90-40-10H- E_3 Loma

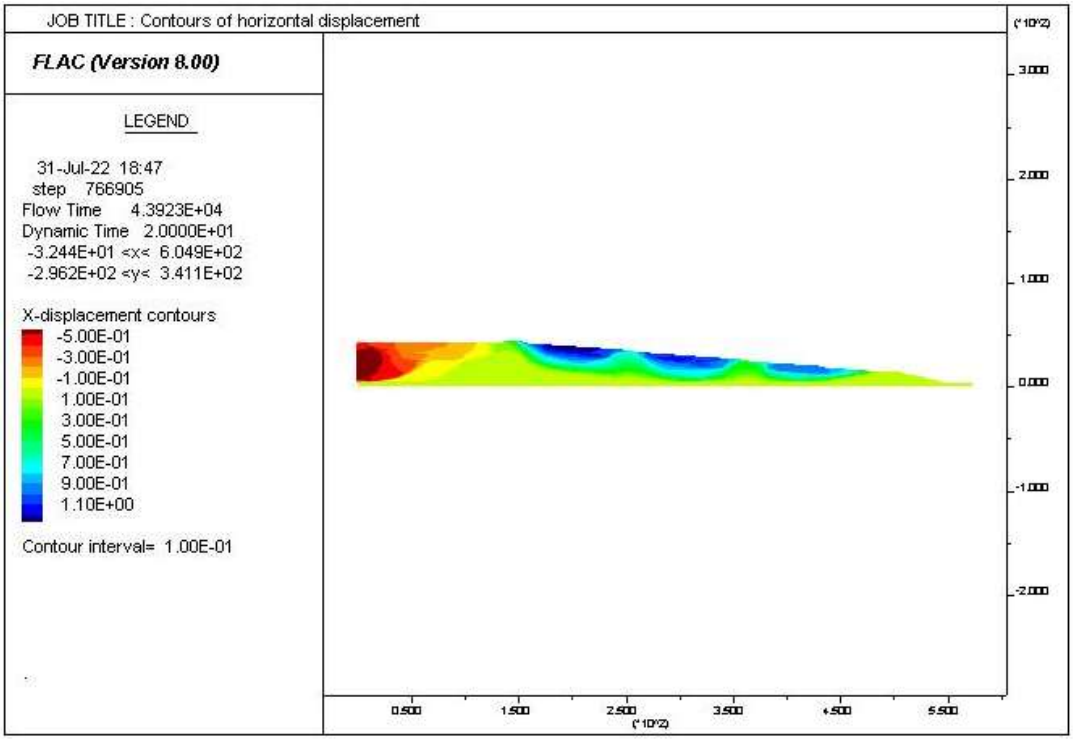

Figure A3. 116: Contours of horizontal displacement for the 20-90-40-10H- E_3Loma

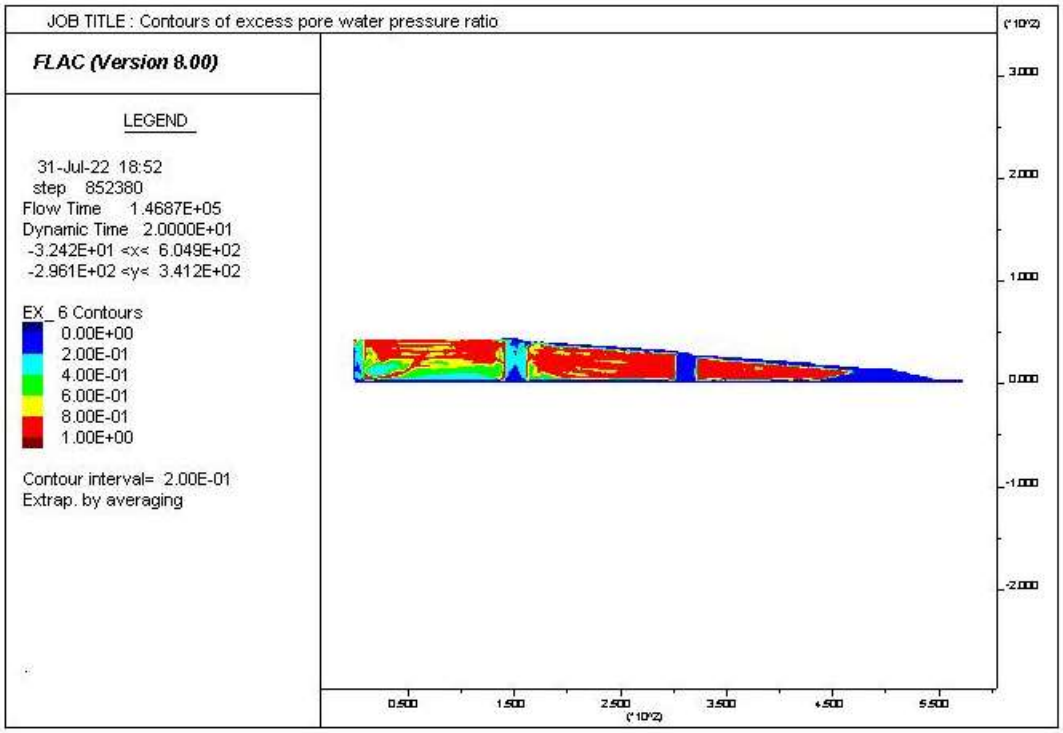

Figure A3. 117: Excess pore water pressure ratio distribution for the 20-140-40-10H- E_3 Loma

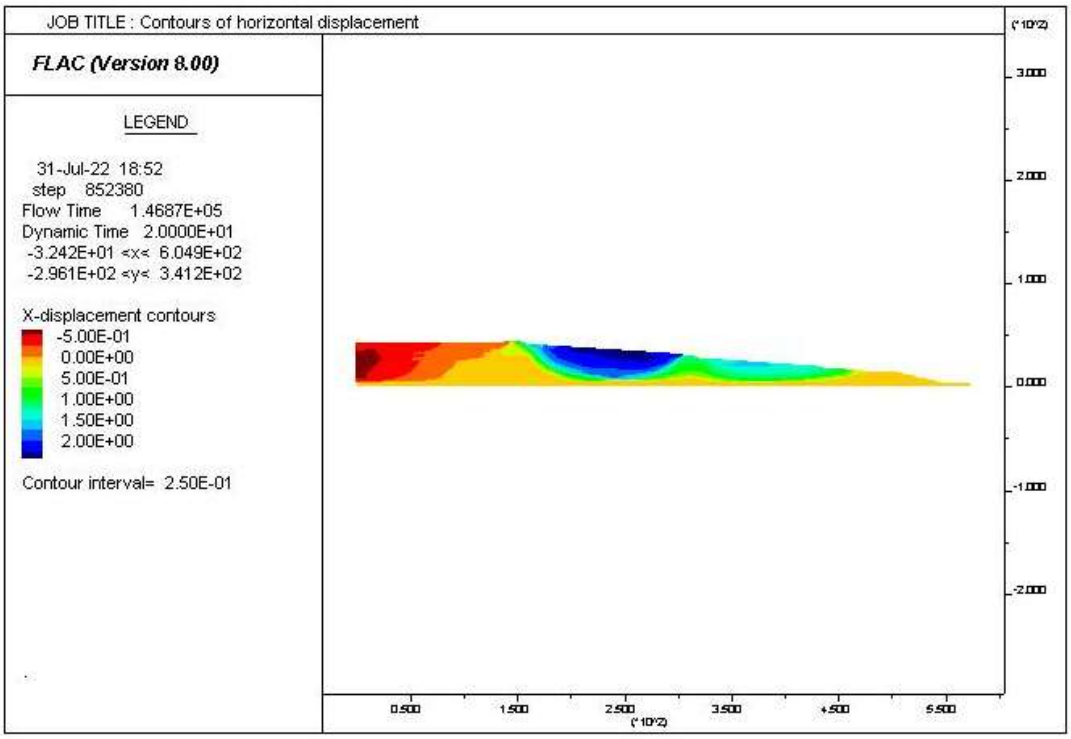

Figure A3. 118: Contours of horizontal displacement for the 20-140-40-10H- E_3Loma

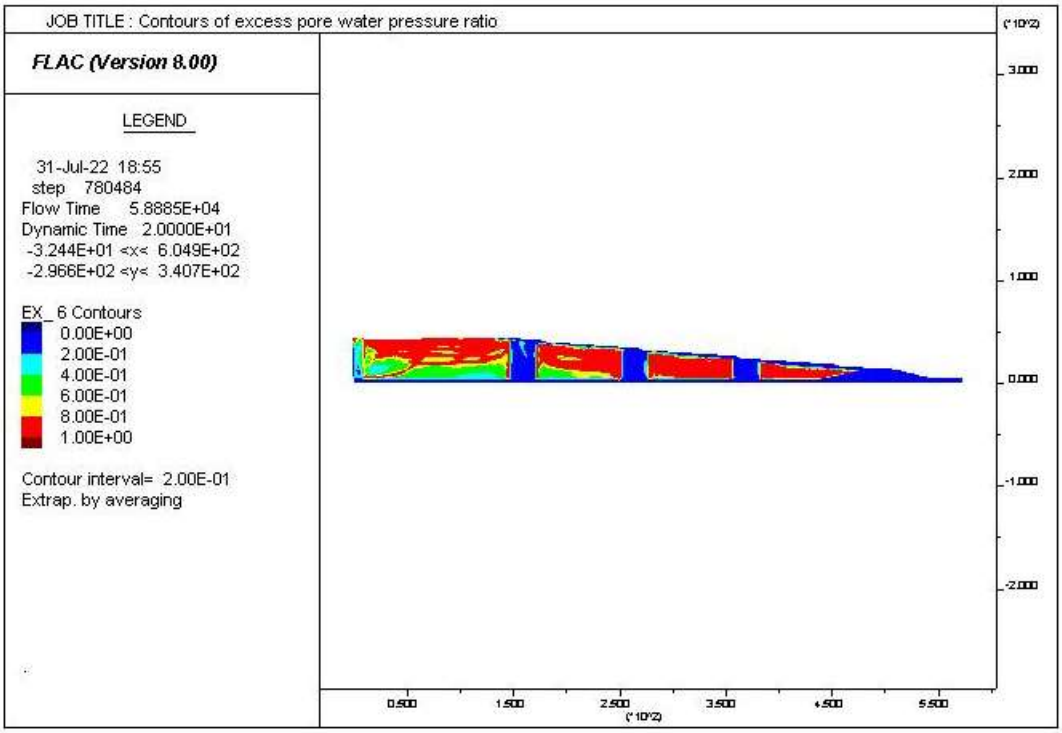

Figure A3. 119: Excess pore water pressure ratio distribution for the 25-80-40-10H- E_3 Loma

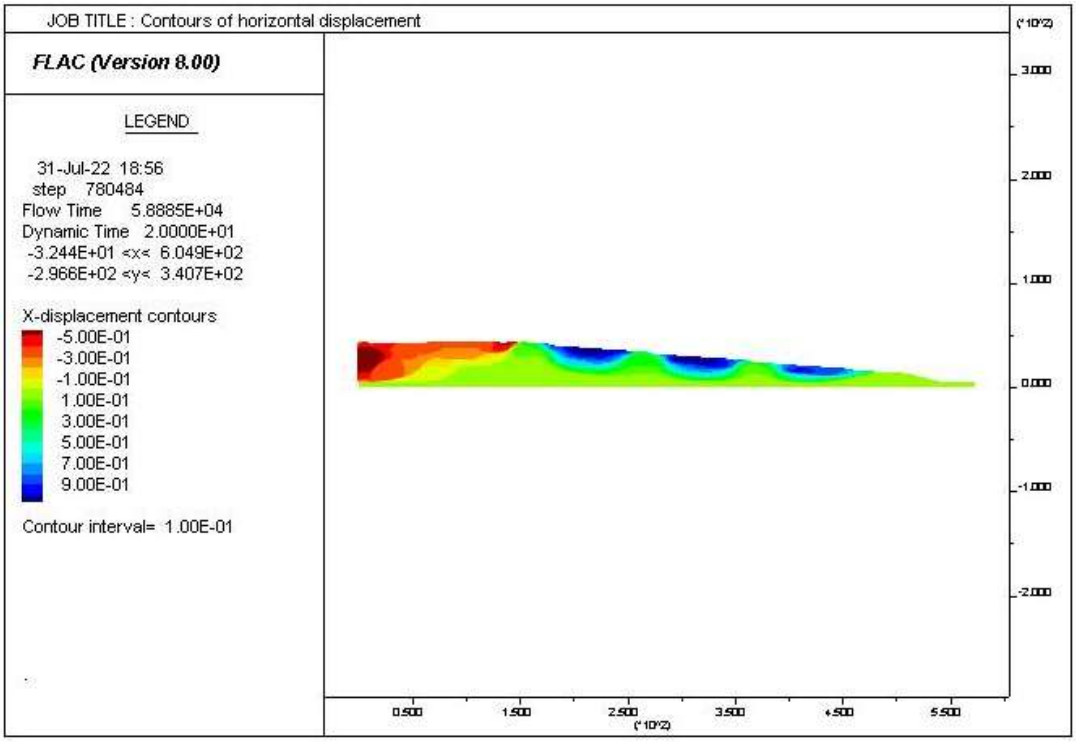

Figure A3. 120: Contours of horizontal displacement for the 25-80-40-10H- E_3Loma

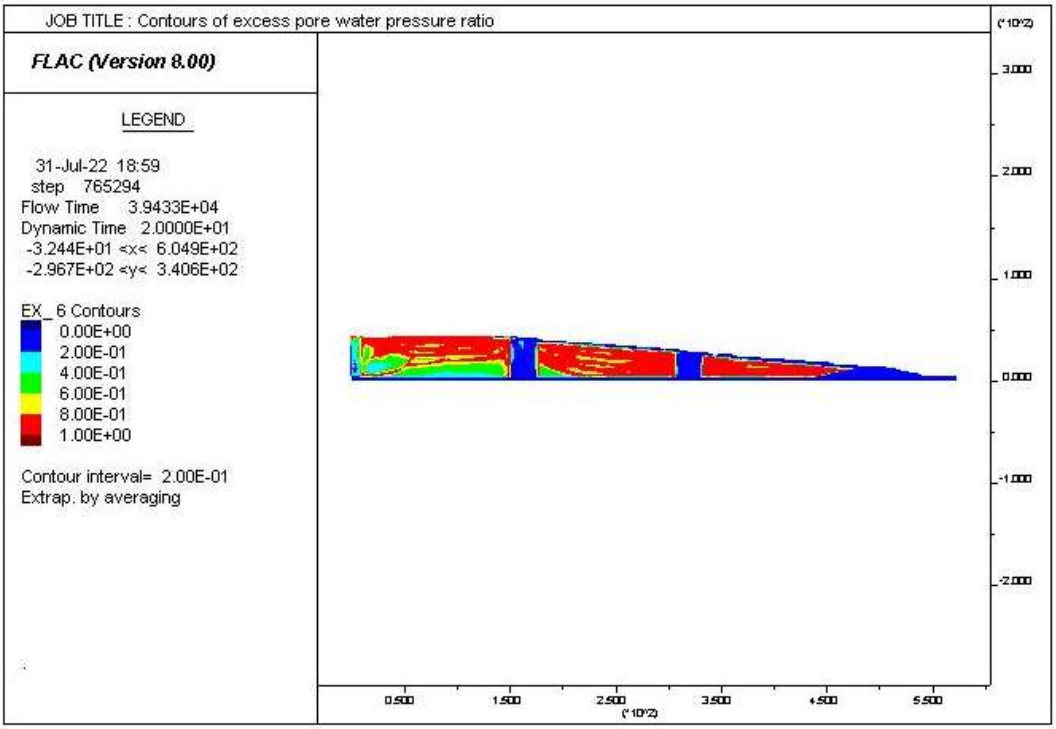

Figure A3. 121: Excess pore water pressure ratio distribution for the 25-130-40-10H- E_3 Loma

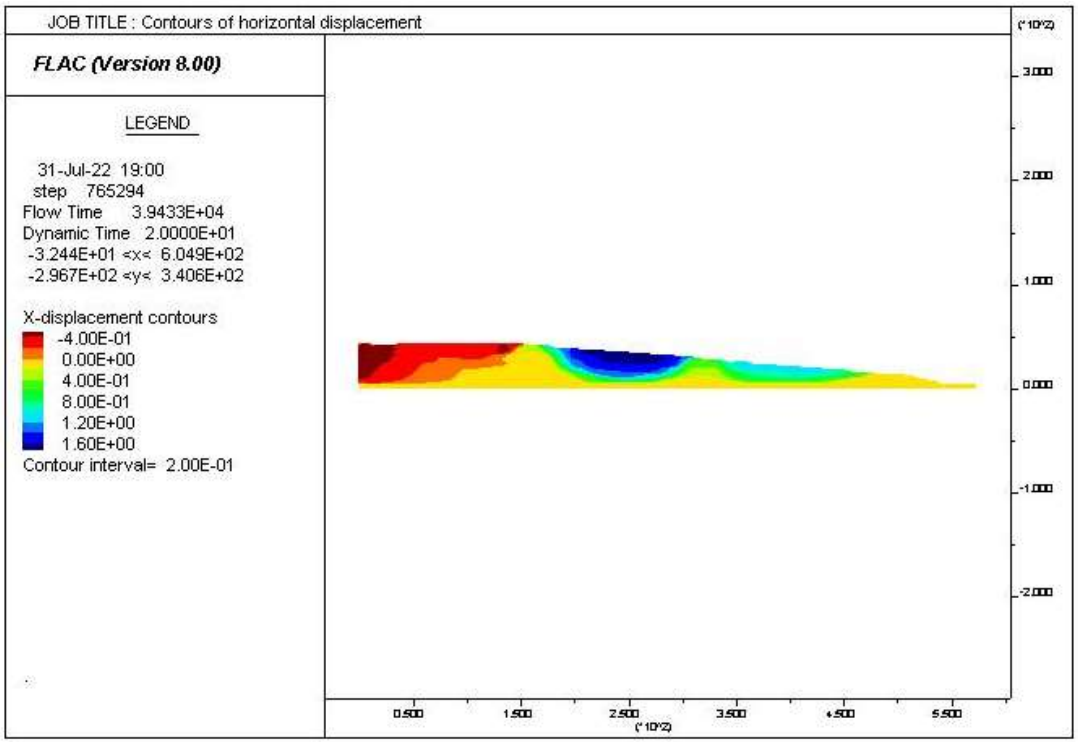

Figure A3. 122: Contours of horizontal displacement for the 25-130-40-10H- E_3Loma

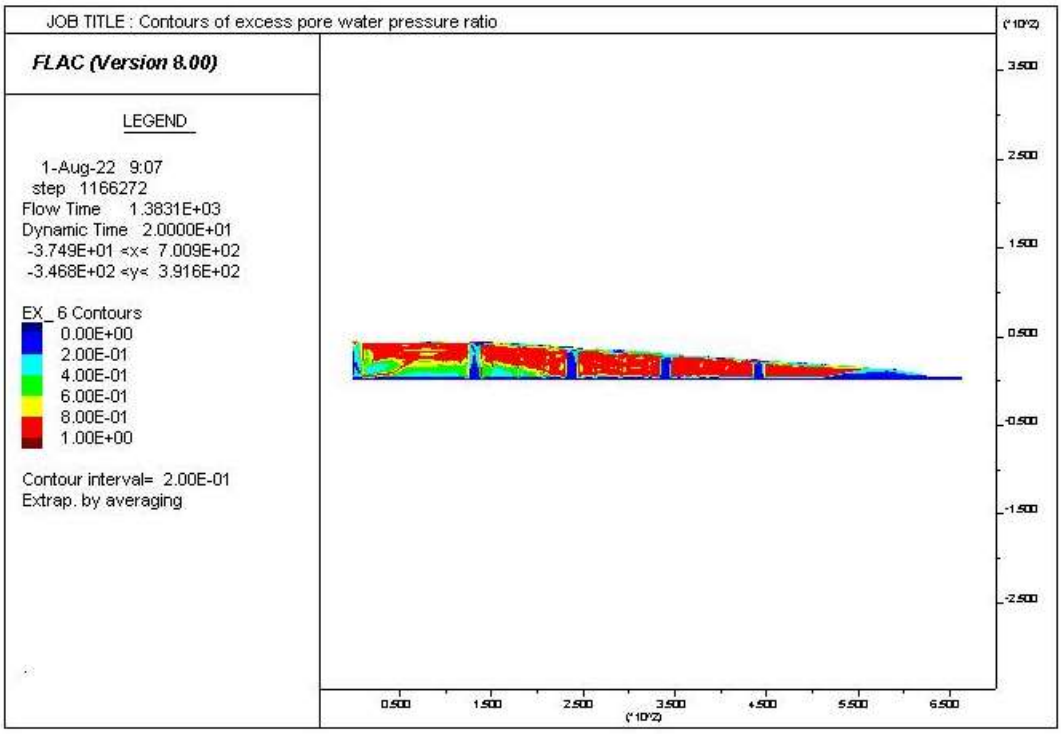

Figure A3. 123: Excess pore water pressure ratio distribution for the 12-90-40-12H- E_3 Loma

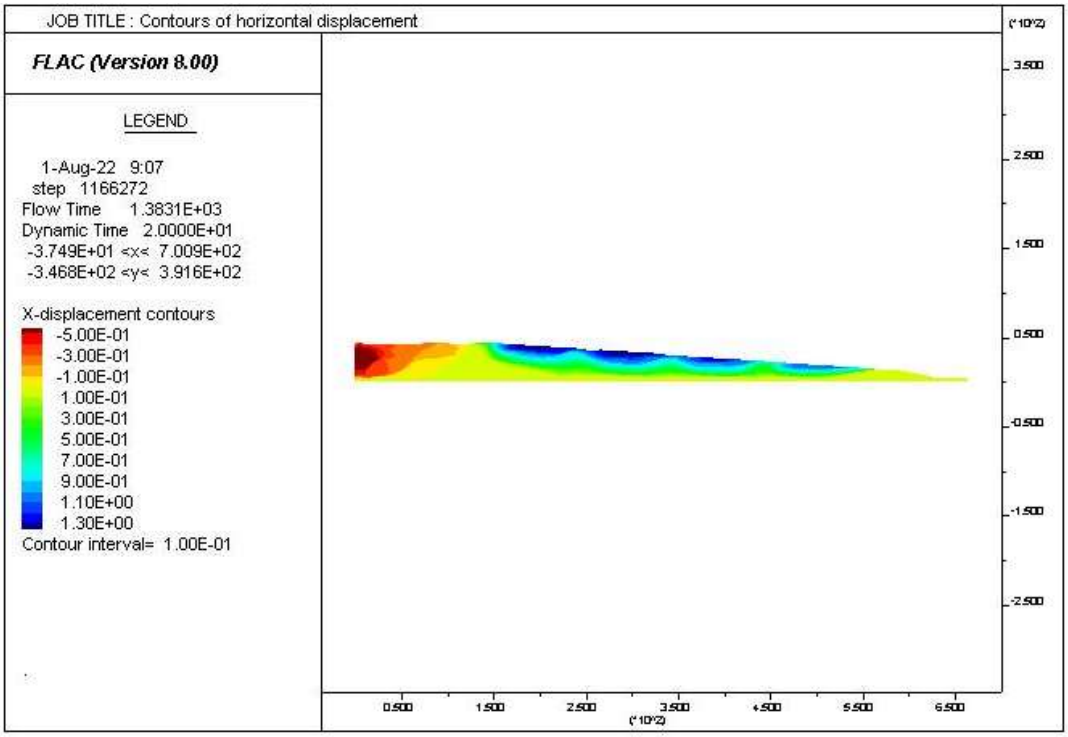

Figure A3. 124: Contours of horizontal displacement for the 12-90-40-12H- E_3Loma

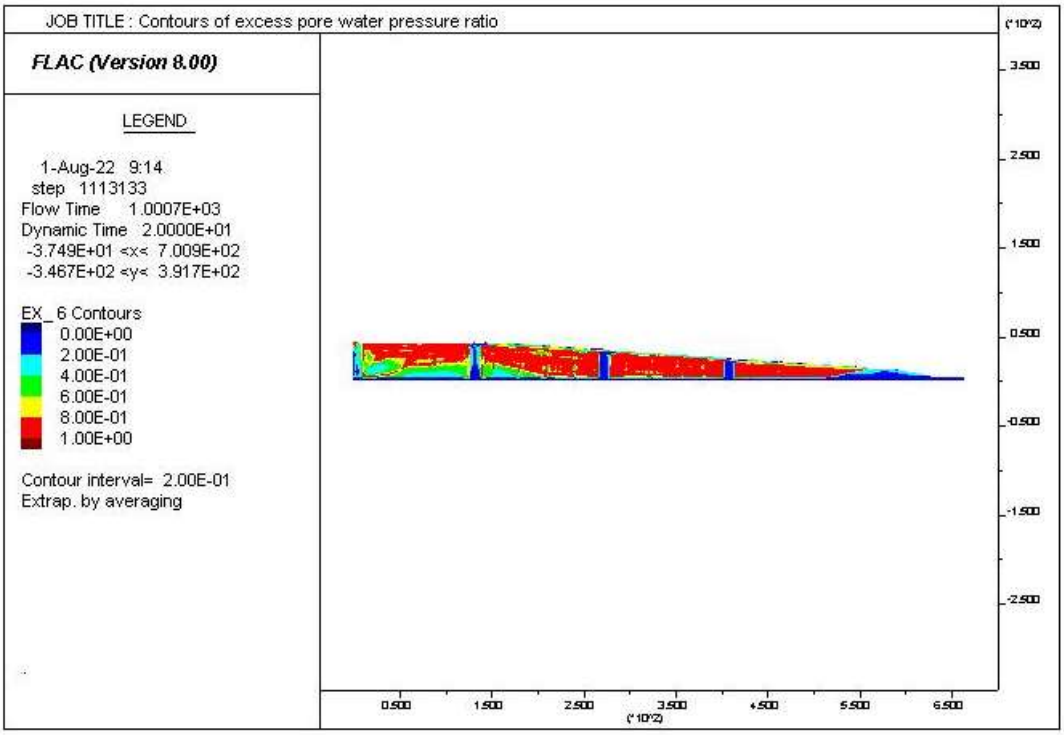

Figure A3. 125: Excess pore water pressure ratio distribution for the 12-125-40-12H- E_3 Loma

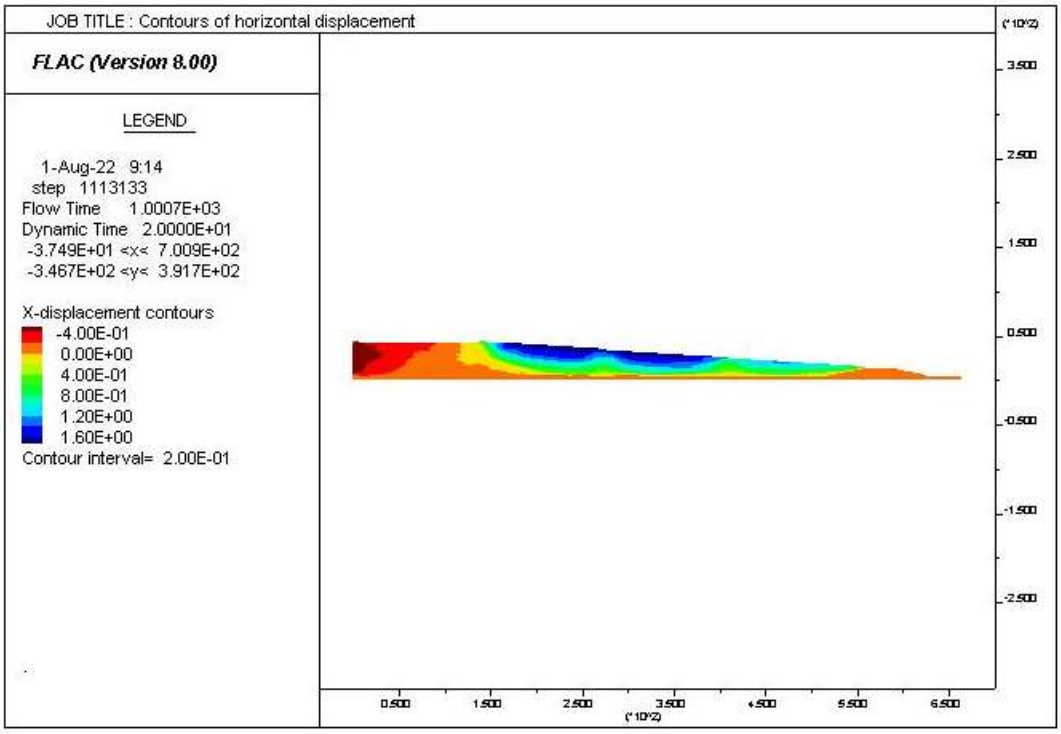

Figure A3. 126: Contours of horizontal displacement for the 12-125-40-12H- E_3Loma

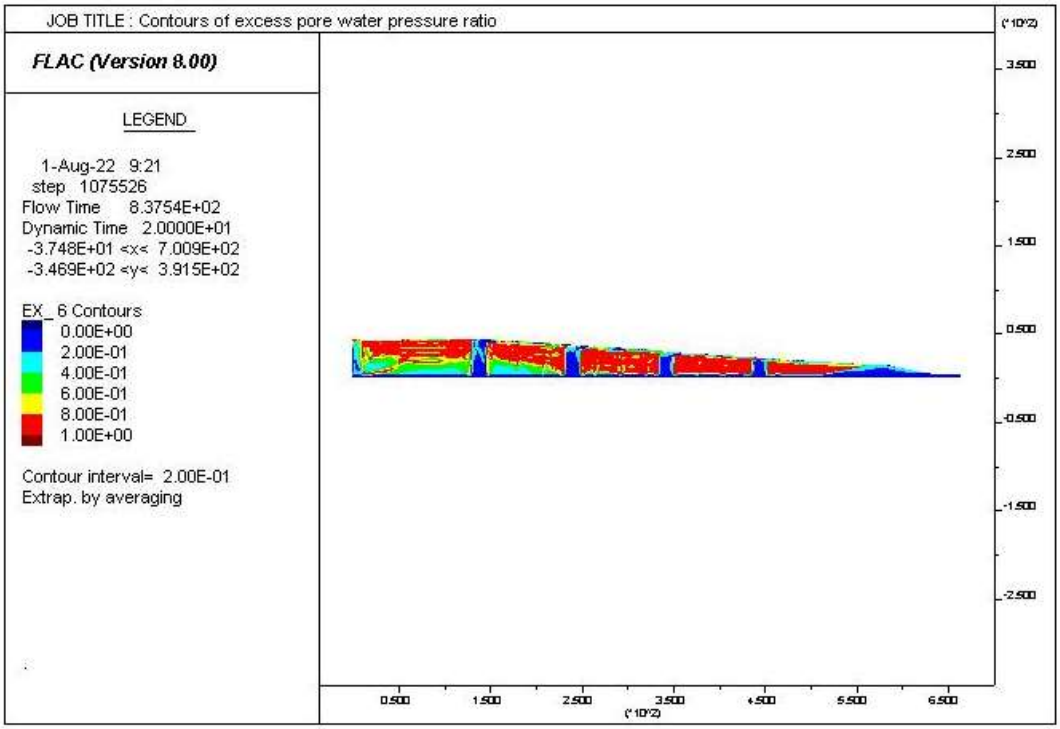

Figure A3. 127: Excess pore water pressure ratio distribution for the 16-86-40-12H- E_3 Loma

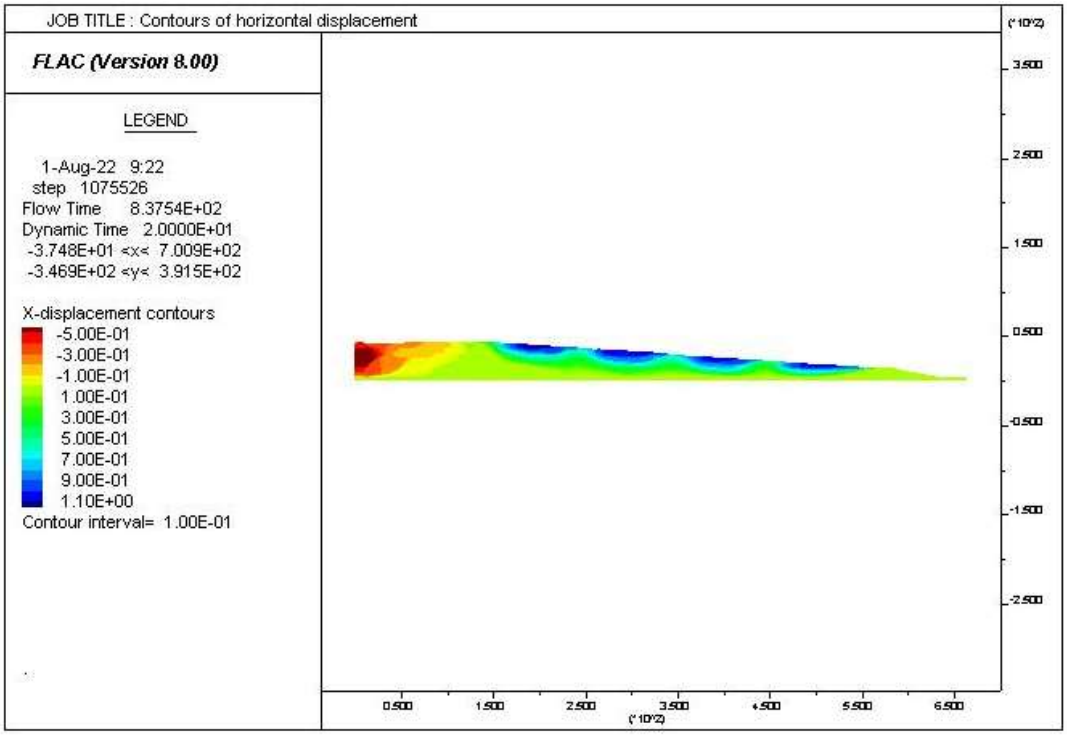

Figure A3. 128: Contours of horizontal displacement for the 16-86-40-12H- E_3Loma

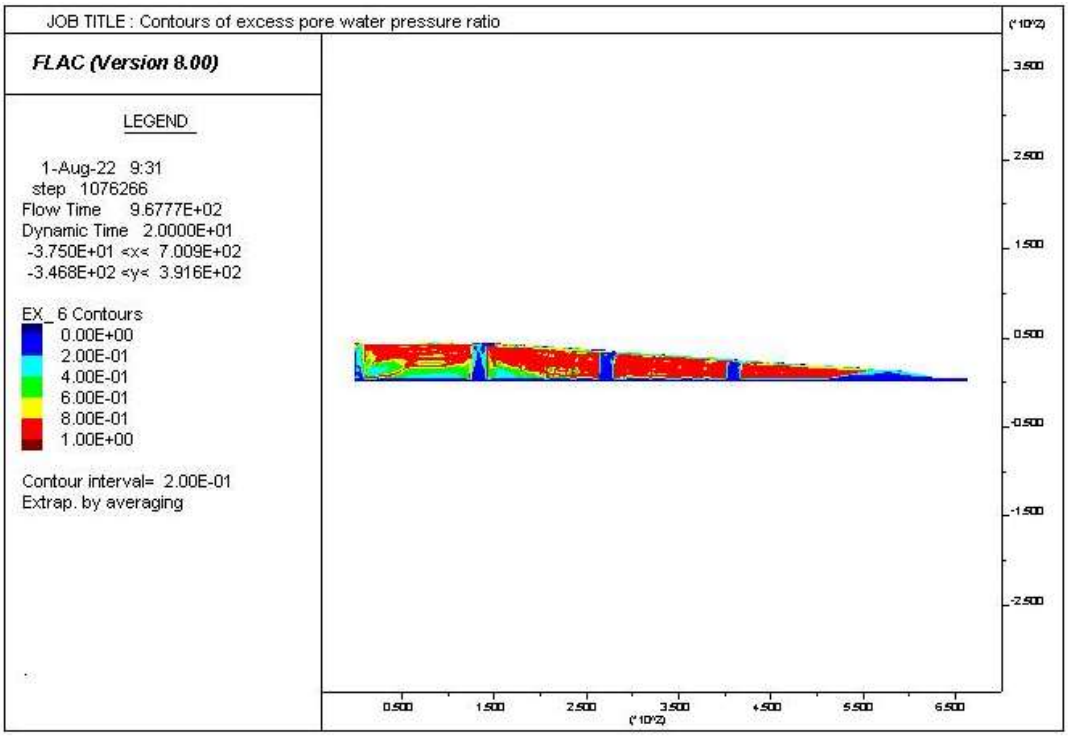

Figure A3. 129: Excess pore water pressure ratio distribution for the 16-121-40-12H- E_3 Loma

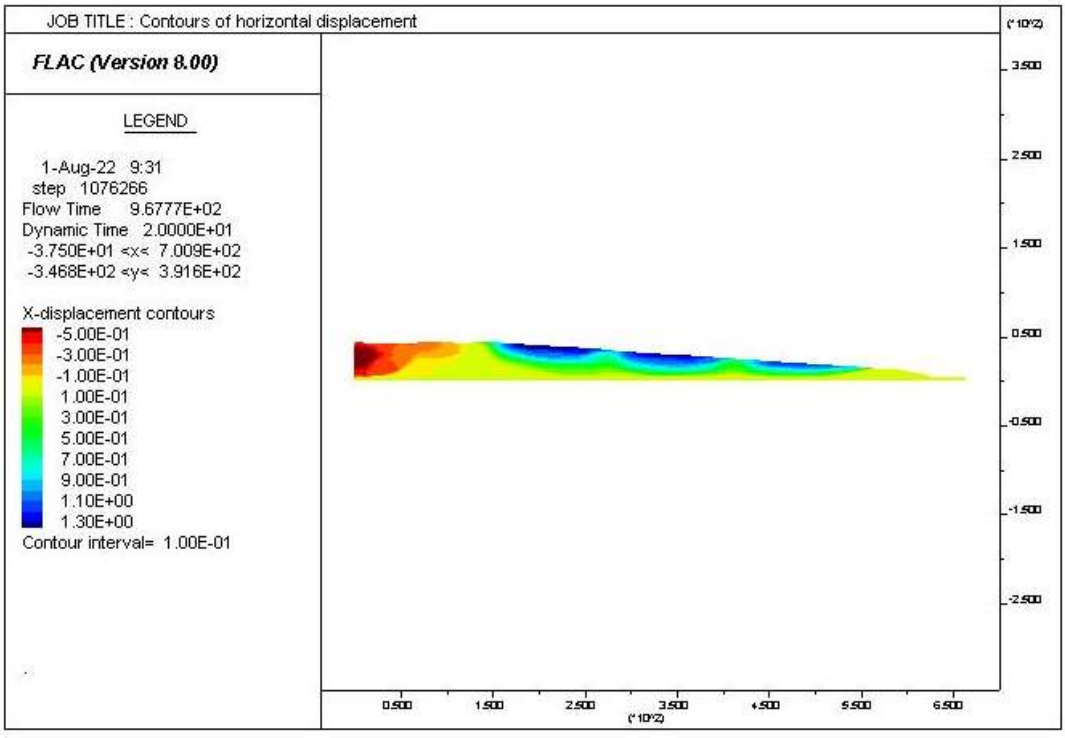

Figure A3. 130: Contours of horizontal displacement for the 16-121-40-12H- E_3Loma

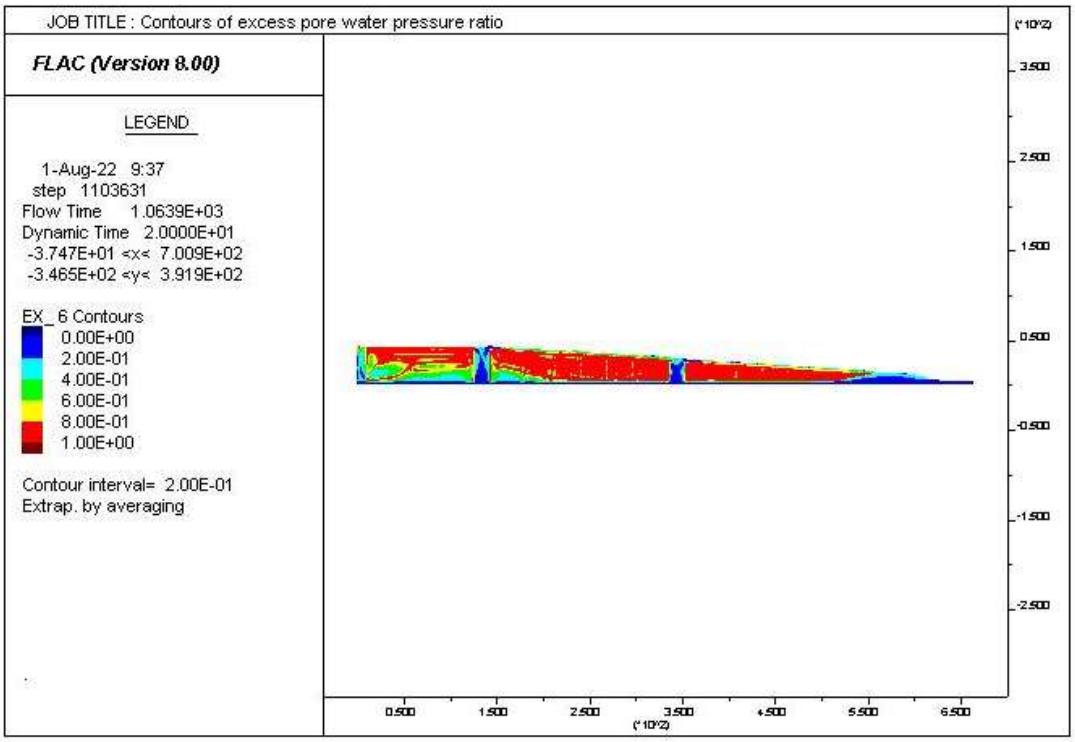

Figure A3. 131: Excess pore water pressure ratio distribution for the 16-186-40-12H- E_3 Loma

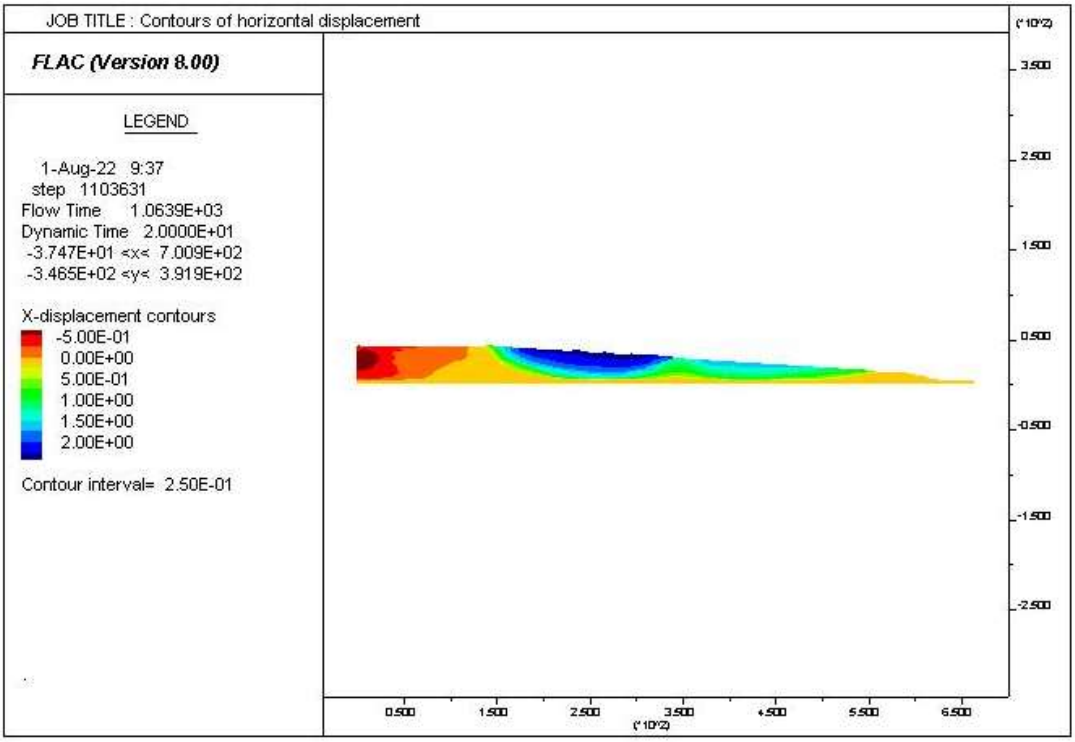

Figure A3. 132: Contours of horizontal displacement for the 16-186-40-12H- E_3Loma

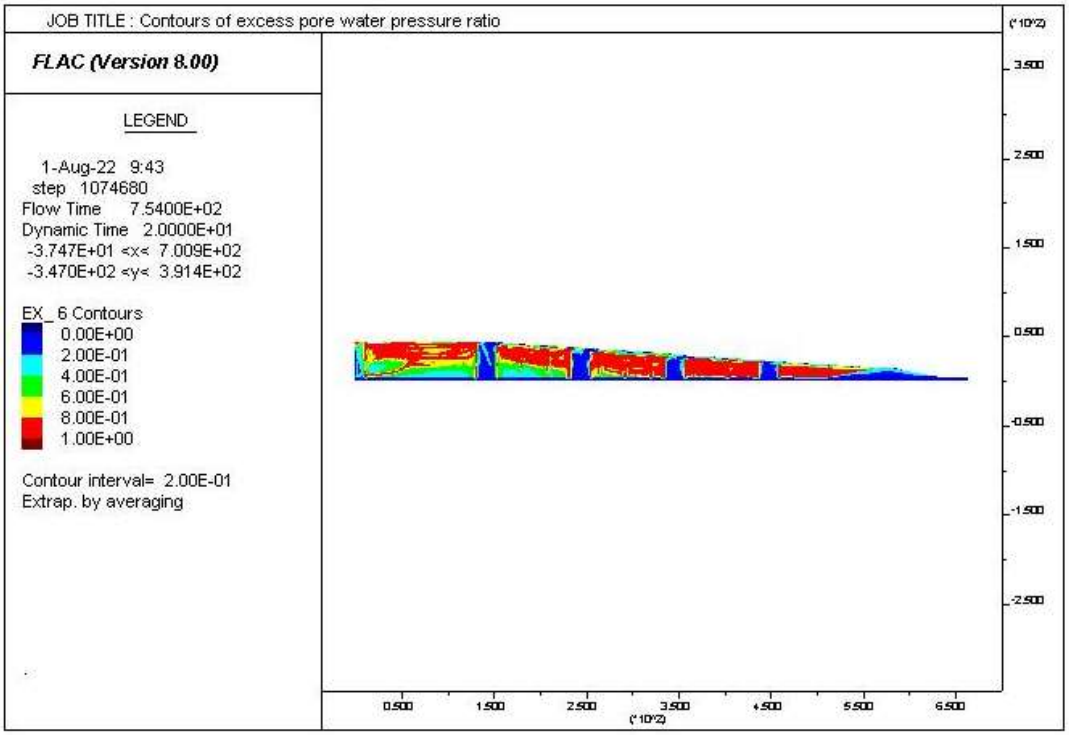

Figure A3. 133: Excess pore water pressure ratio distribution for the 20-82-40-12H- E_3 Loma

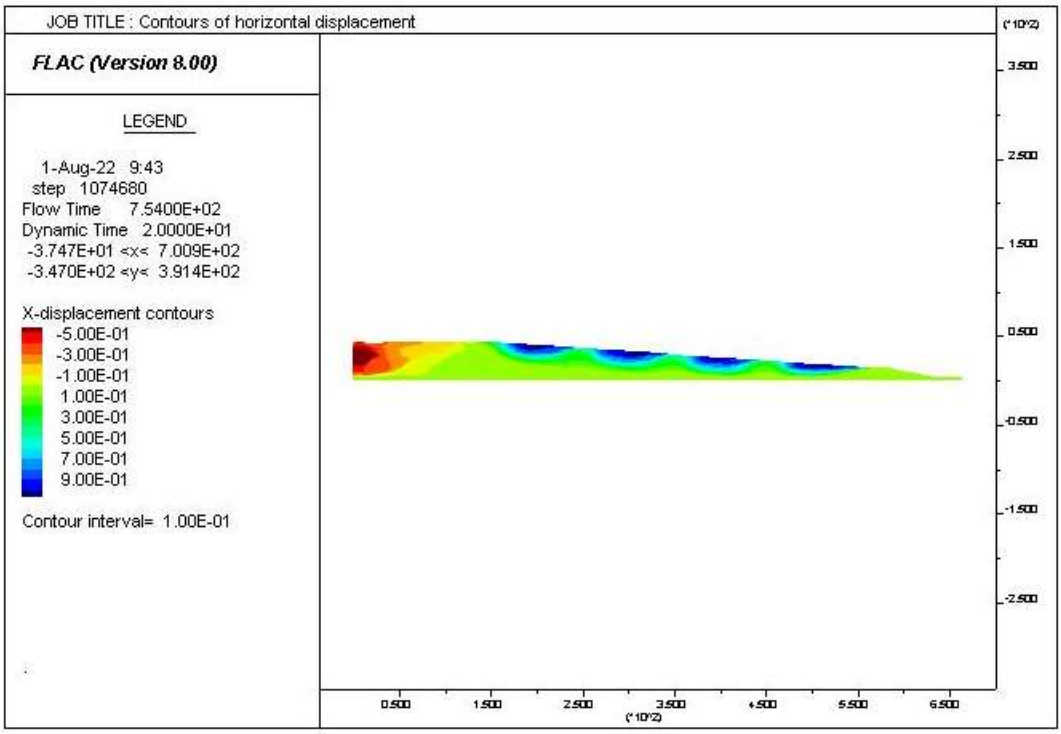

Figure A3. 134: Contours of horizontal displacement for the 20-82-40-12H- E_3Loma

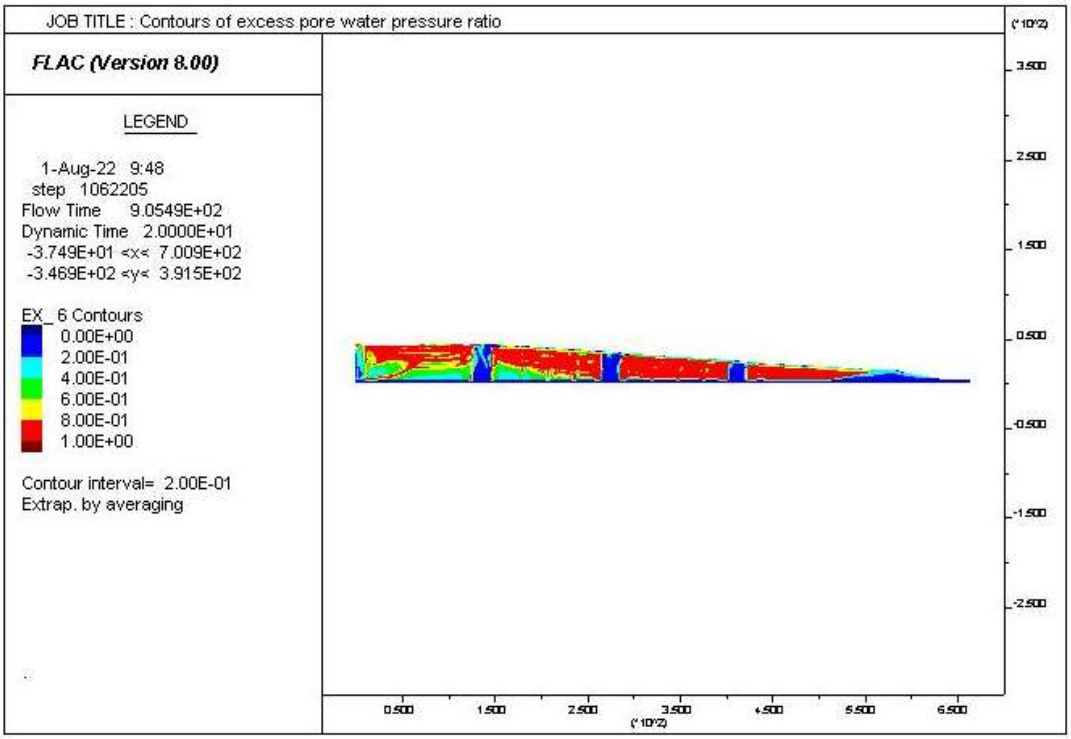

Figure A3. 135: Excess pore water pressure ratio distribution for the 20-117-40-12H- E_3 Loma

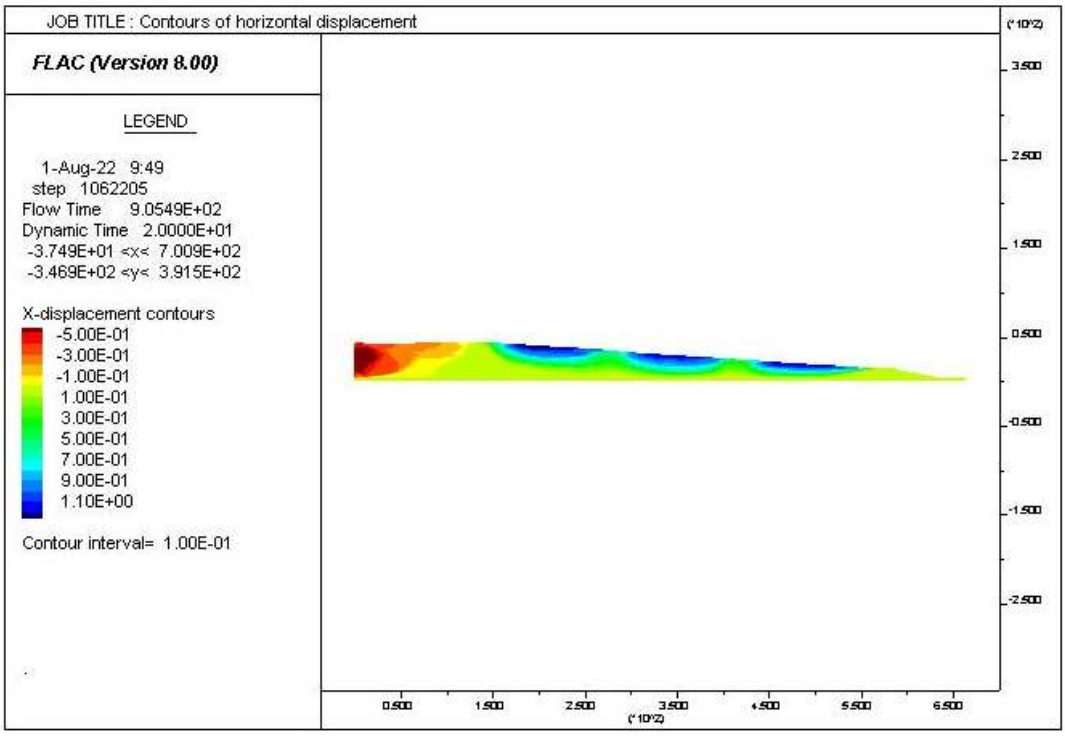

Figure A3. 136: Contours of horizontal displacement for the 20-117-40-12H- E_3Loma

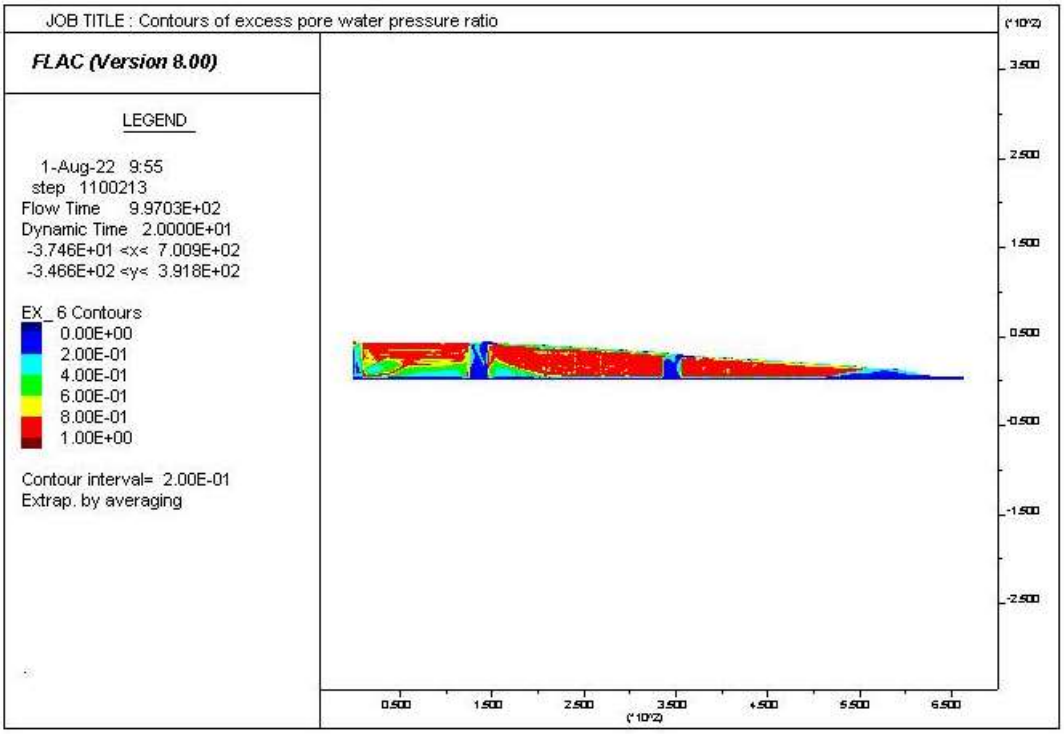

Figure A3. 137: Excess pore water pressure ratio distribution for the 20-182-40-12H- E_3 Loma

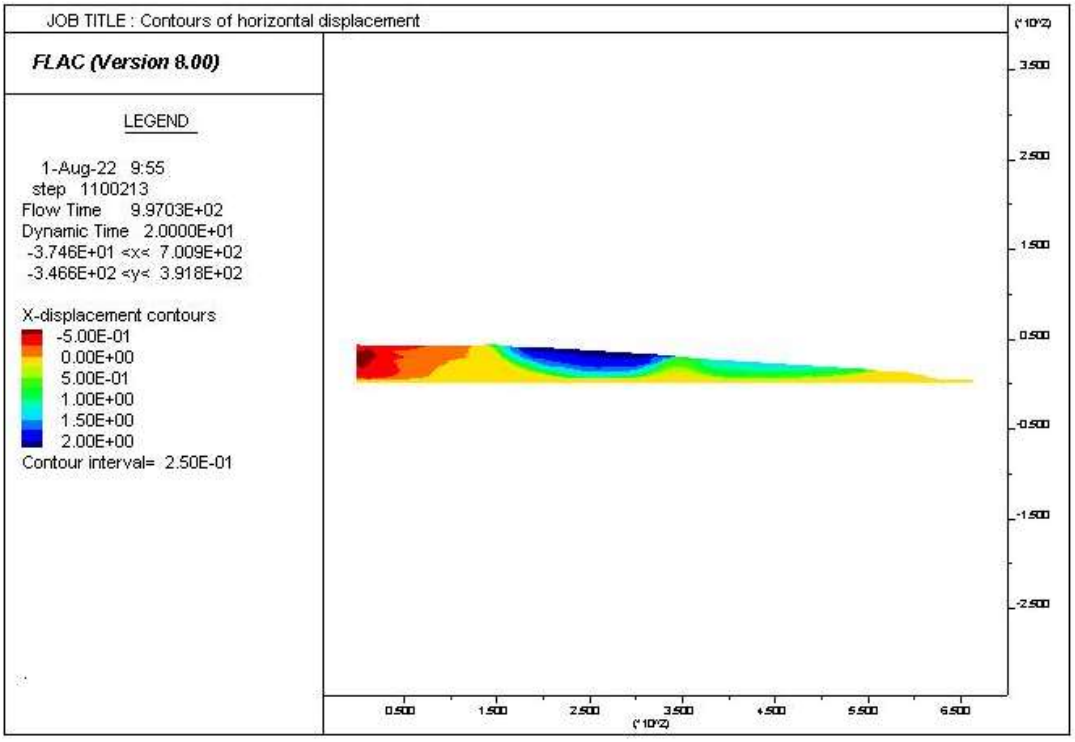

Figure A3. 138: Contours of horizontal displacement for the 20-182-40-12H- E_3Loma

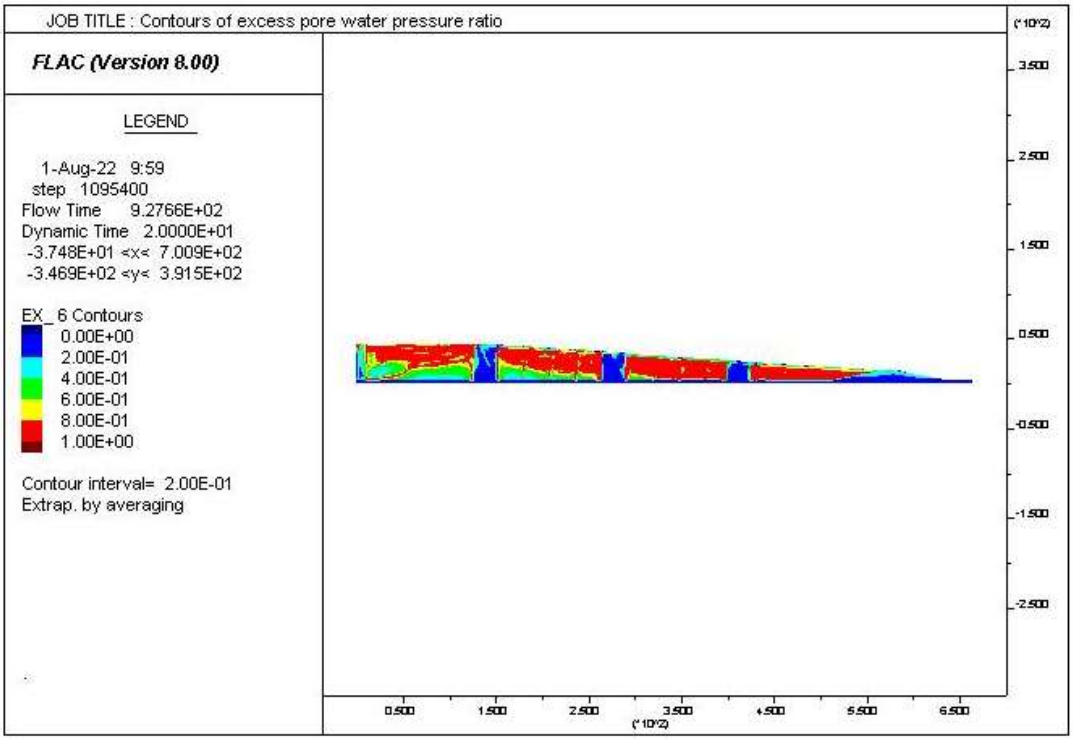

Figure A3. 139: Excess pore water pressure ratio distribution for the 25-110-40-12H- E_3 Loma

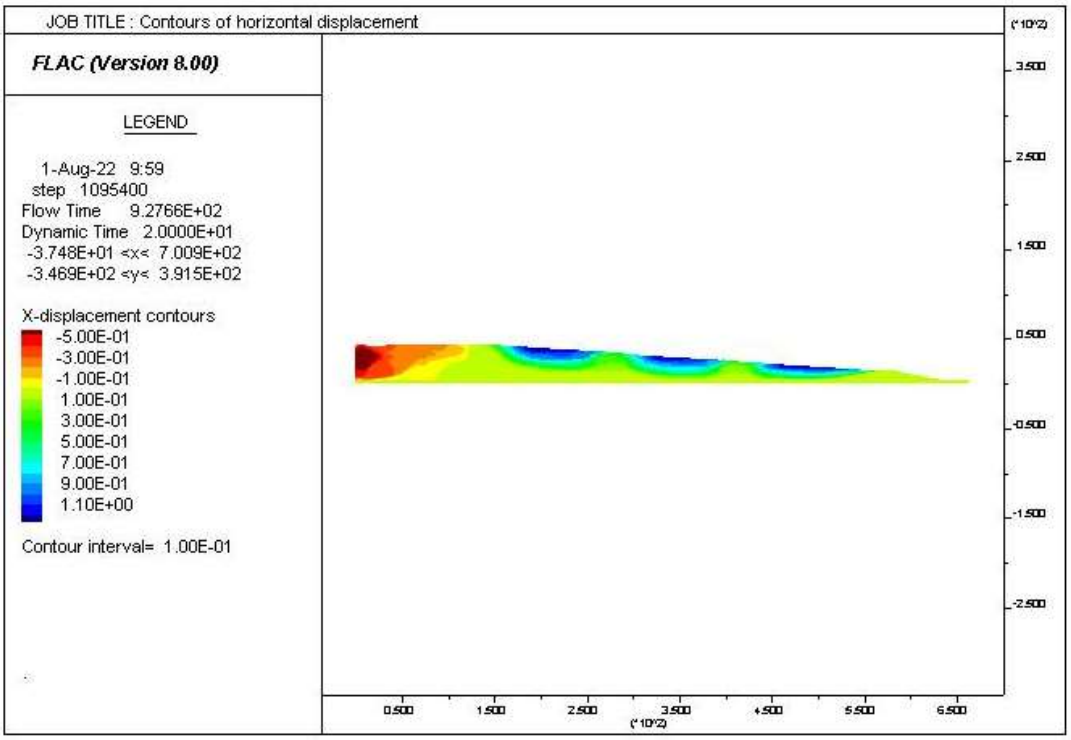

Figure A3. 140: Contours of horizontal displacement for the 25-110-40-12H- E_3Loma

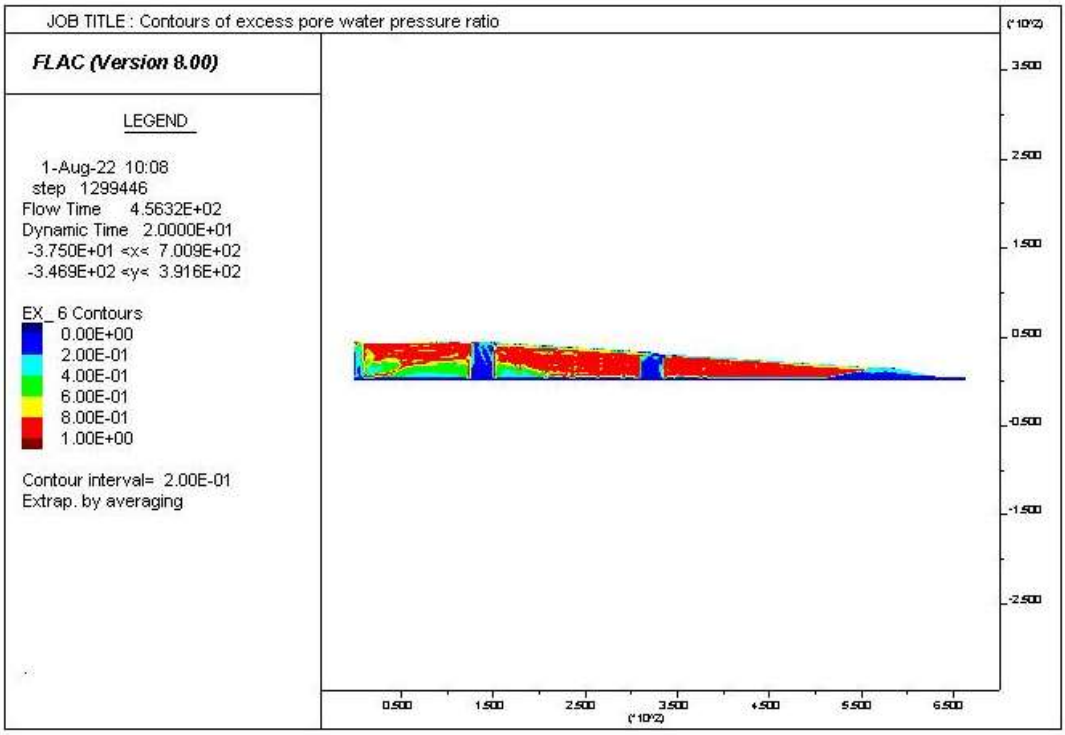

Figure A3. 141: Excess pore water pressure ratio distribution for the 25-150-40-12H- E_3 Loma

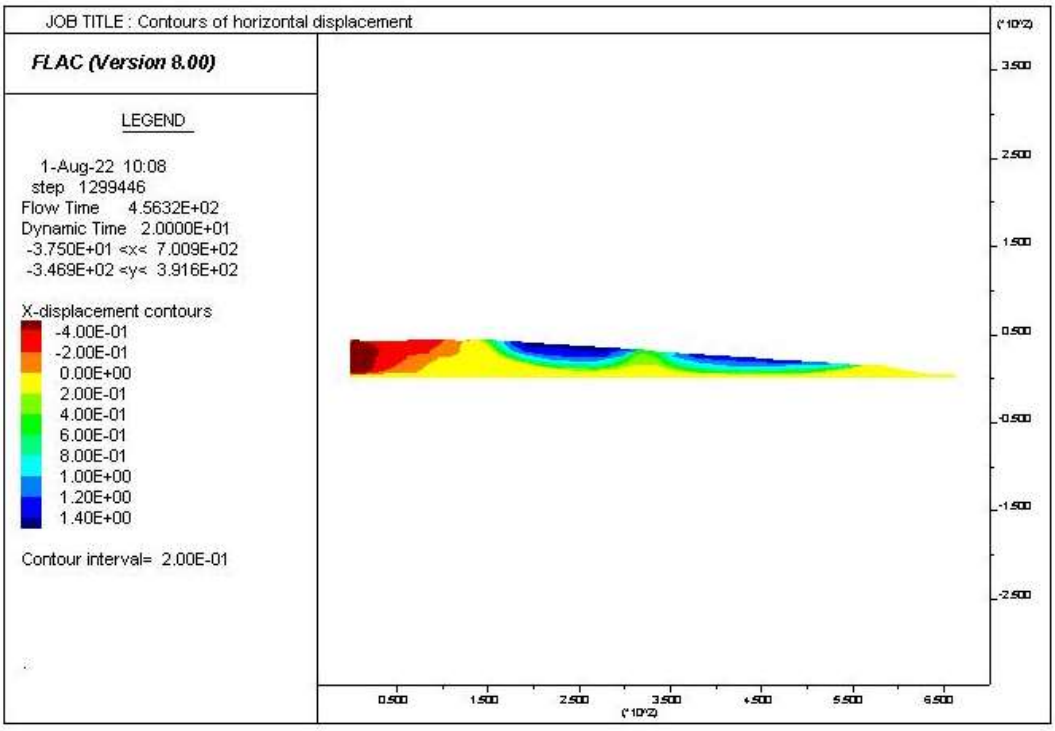

Figure A3. 142: Contours of horizontal displacement for the 25-150-40-12H- E_3Loma

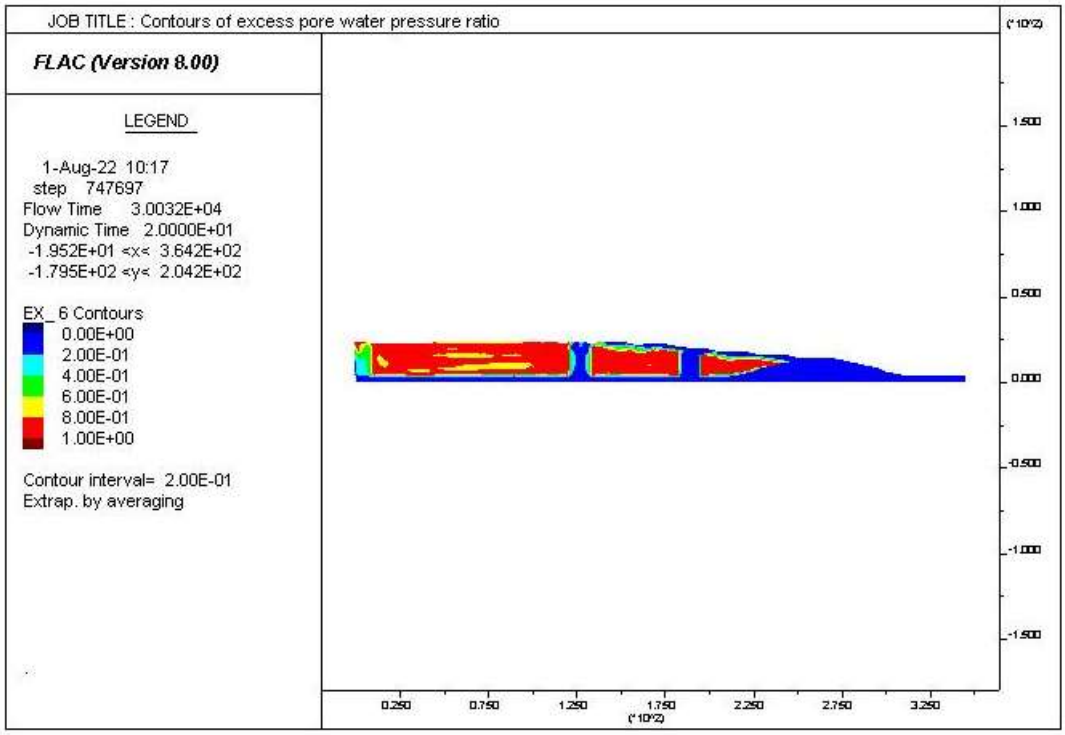

Figure A3. 143: Excess pore water pressure ratio distribution for the 12-50-20-8H- E_3 Loma

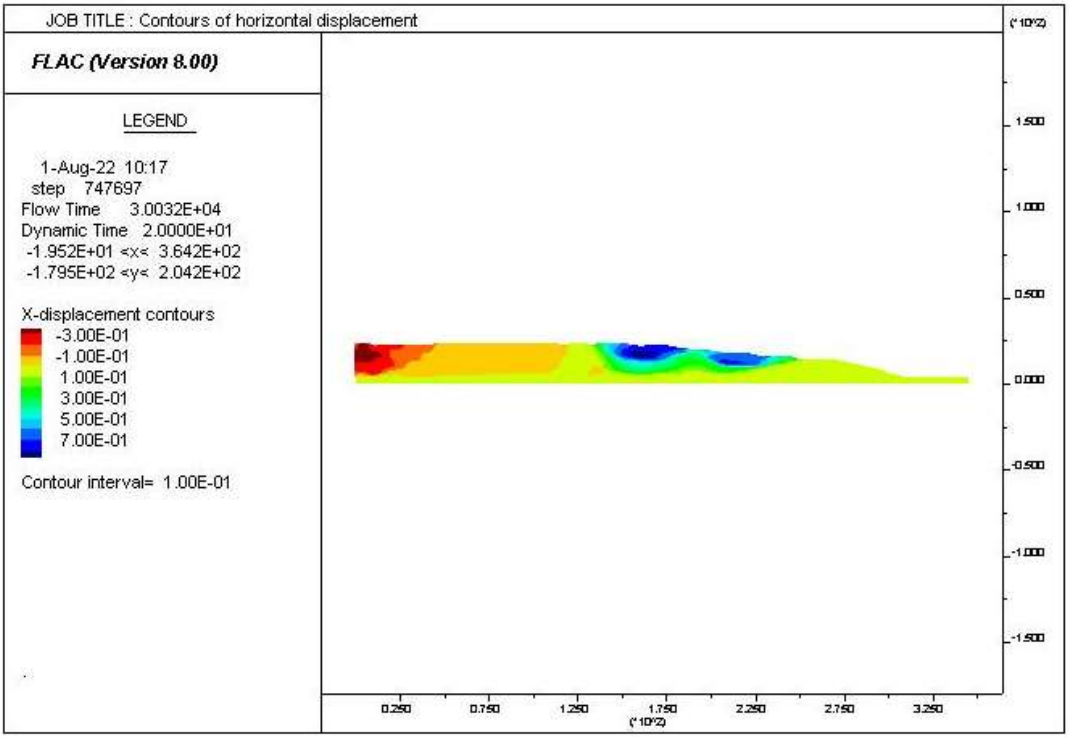

Figure A3. 144: Contours of horizontal displacement for the 12-50-20-8H- E_3Loma

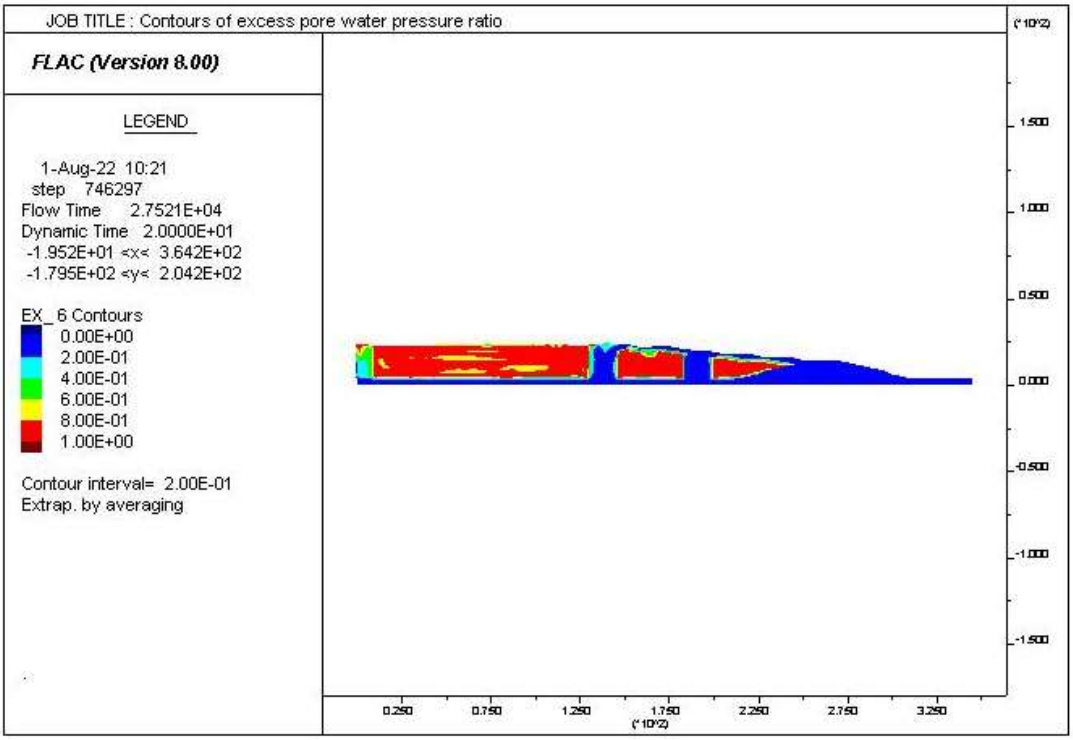

Figure A3. 145: Excess pore water pressure ratio distribution for the 16-37-20-8H- E_3 Loma

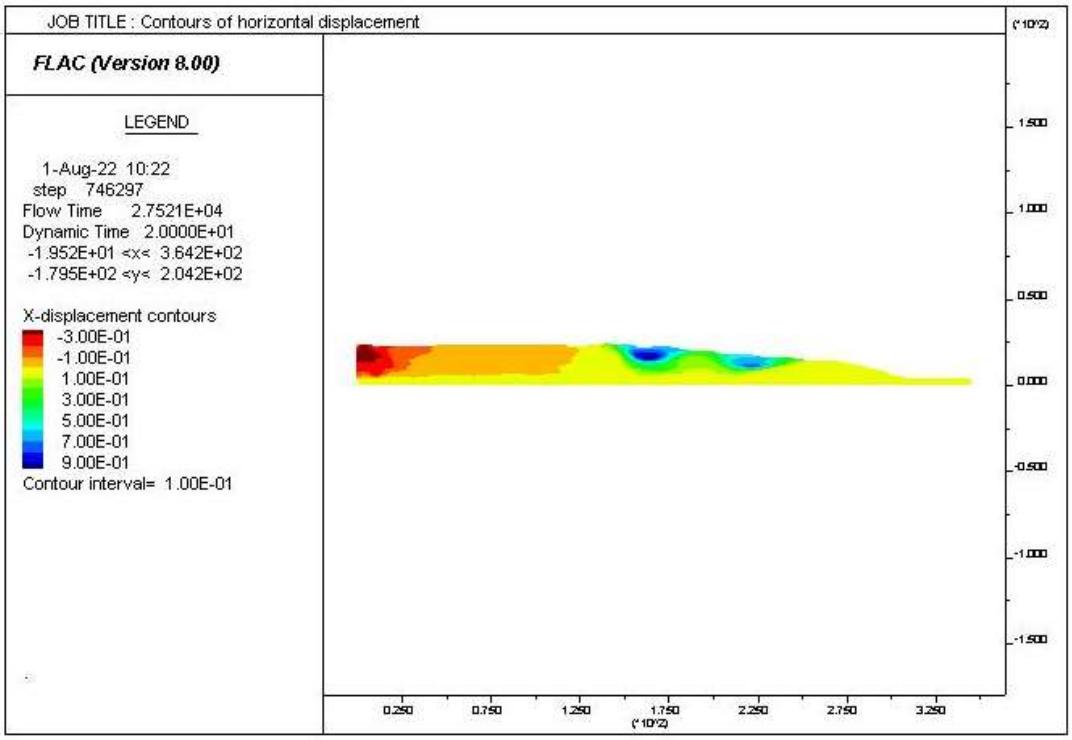

Figure A3. 146: Contours of horizontal displacement for the 16-37-20-8H- E_3Loma

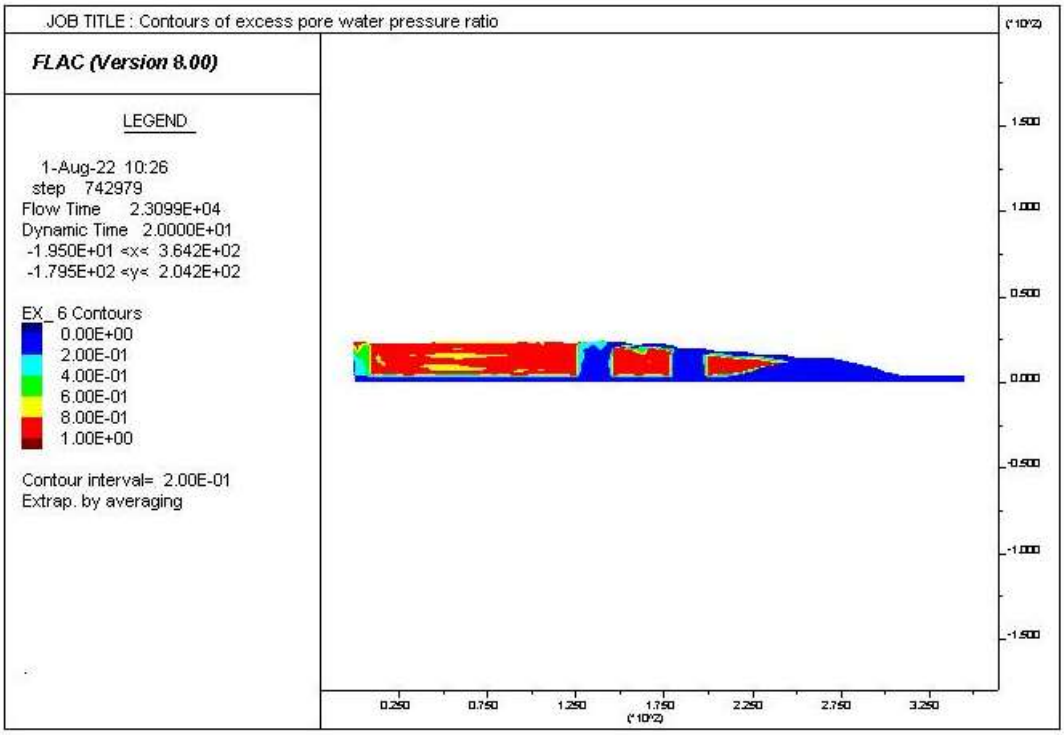

Figure A3. 147: Excess pore water pressure ratio distribution for the 20-33-20-8H- E_3 Loma

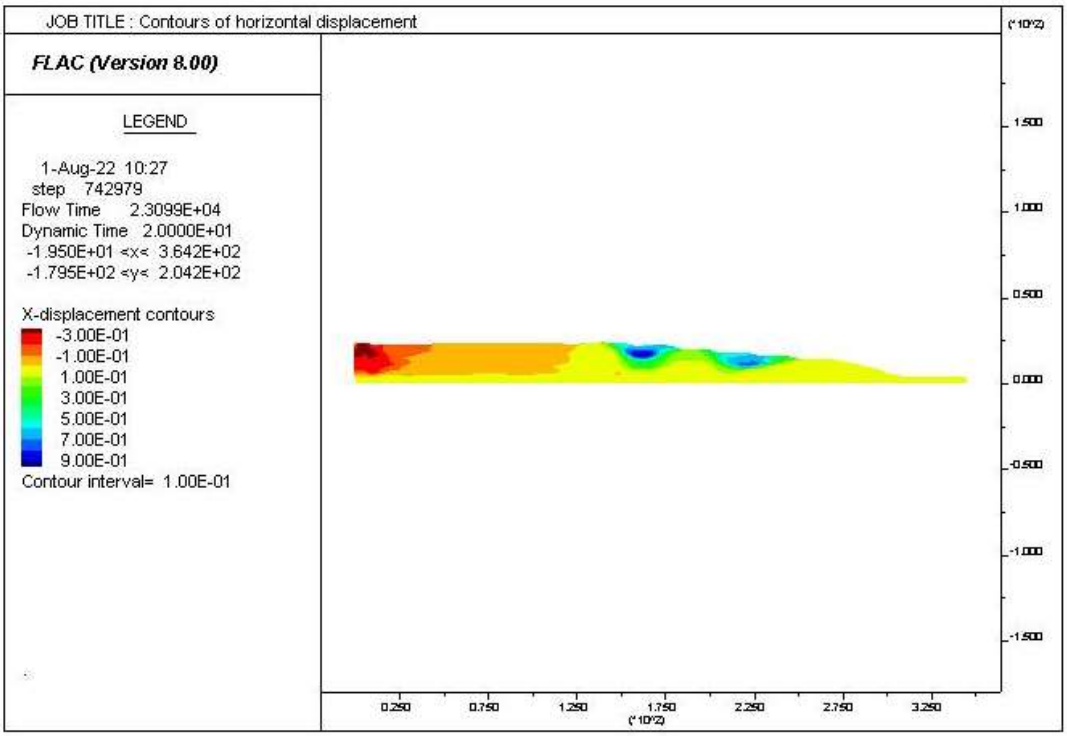

Figure A3. 148: Contours of horizontal displacement for the 20-33-20-8H- E_3Loma

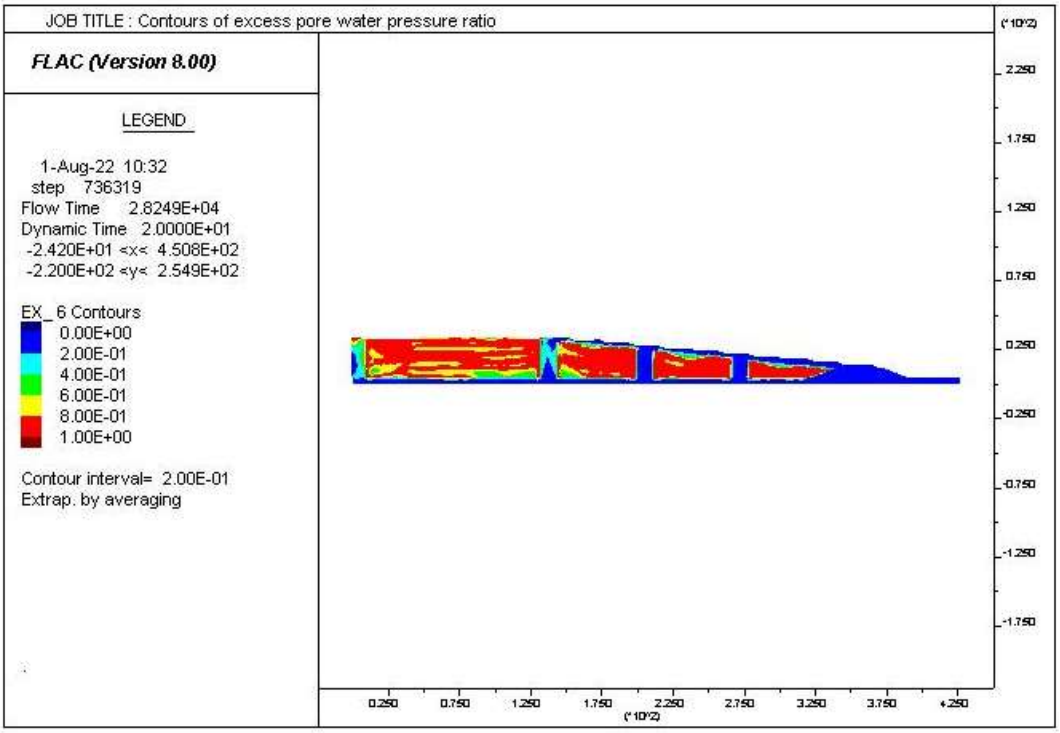

Figure A3. 149: Excess pore water pressure ratio distribution for the 12-55-30-8H- E_3 Loma

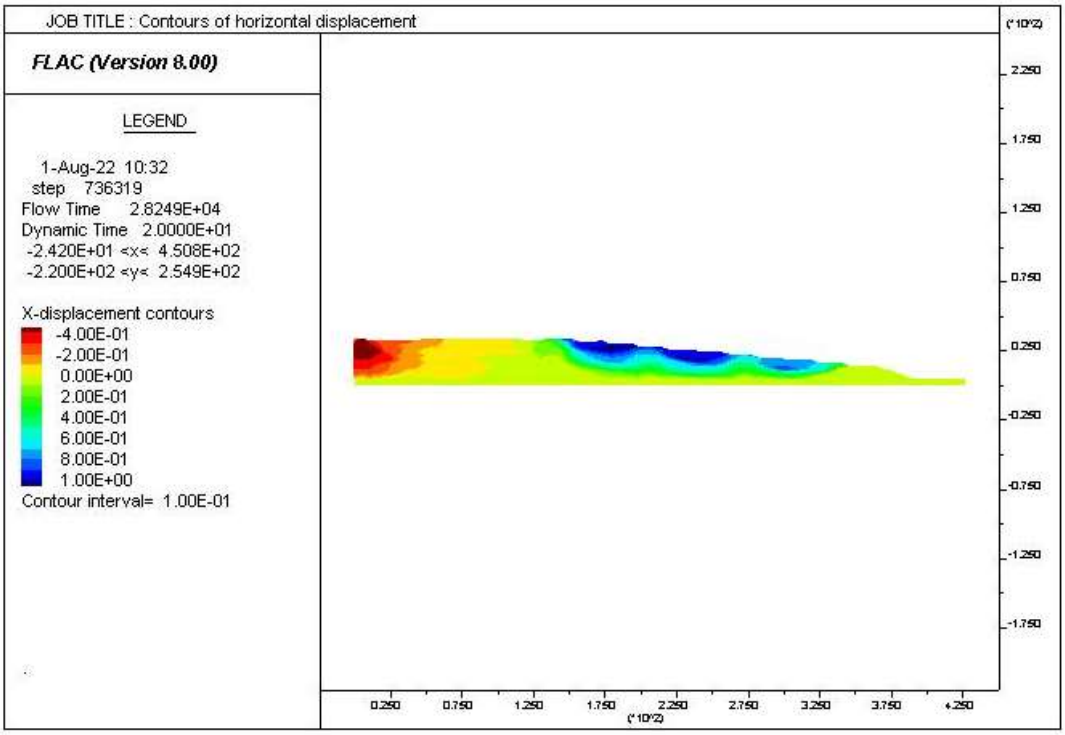

Figure A3. 150: Contours of horizontal displacement for the 12-55-30-8H- E_3Loma

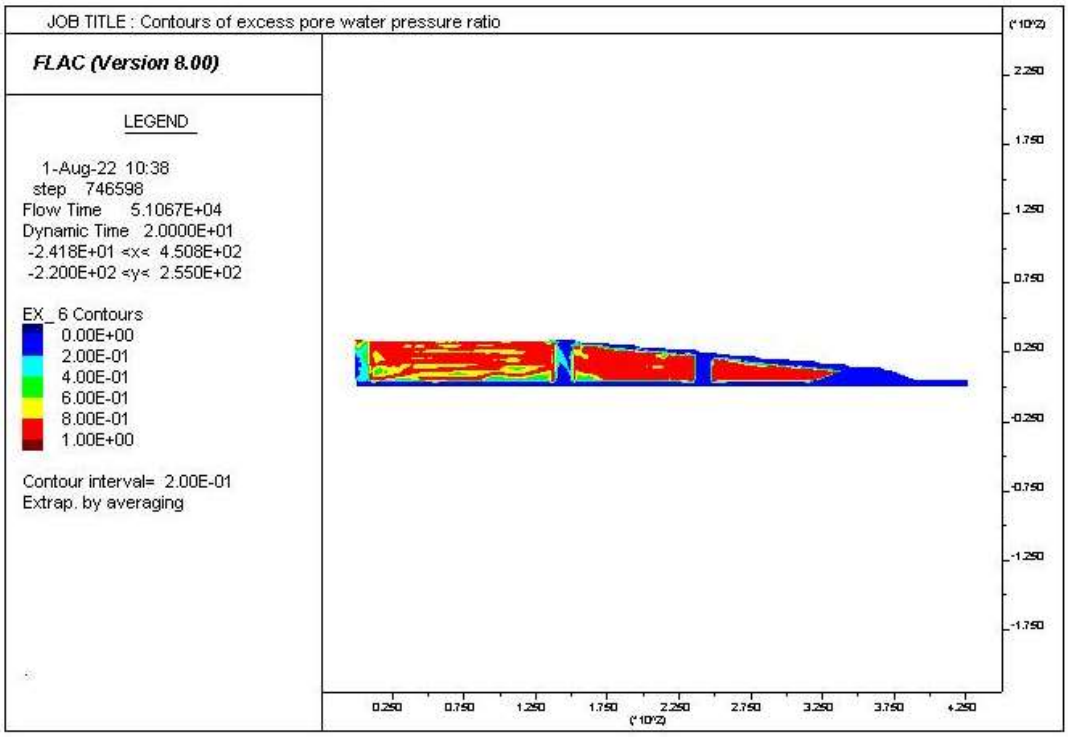

Figure A3. 151: Excess pore water pressure ratio distribution for the 12-85-30-8H- E_3 Loma

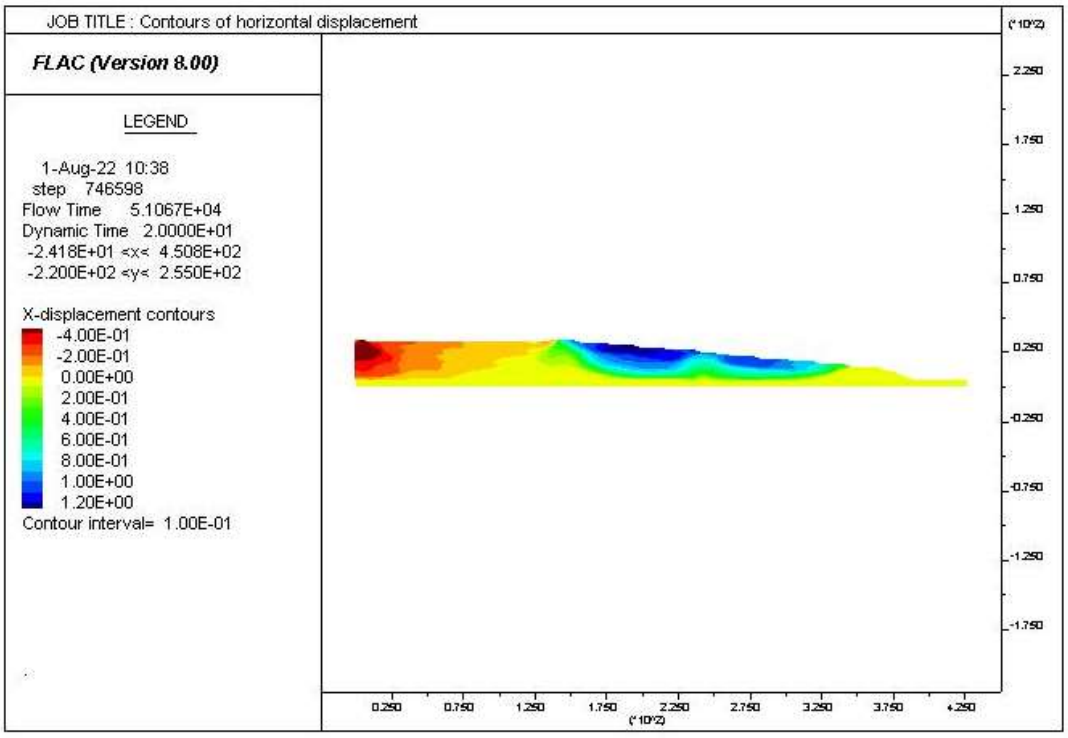

Figure A3. 152: Contours of horizontal displacement for the 12-85-30-8H- E_3Loma

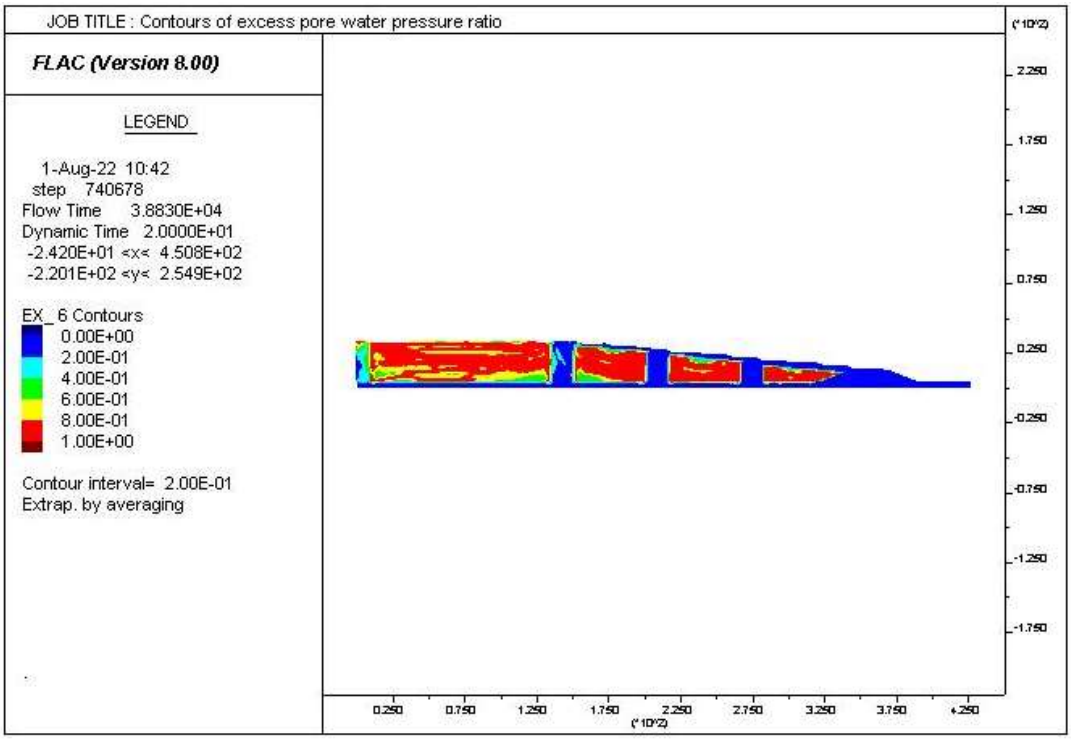

Figure A3. 153: Excess pore water pressure ratio distribution for the 16-50-30-8H- E_3 Loma

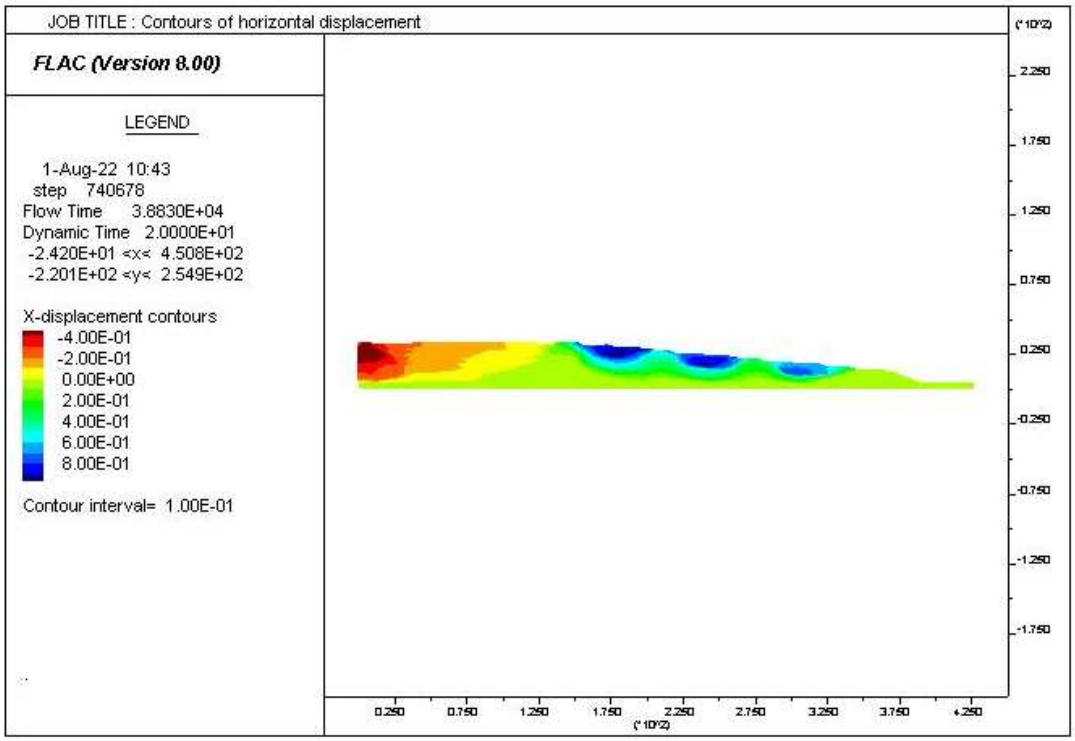

Figure A3. 154: Contours of horizontal displacement for the 16-50-30-8H- E_3Loma

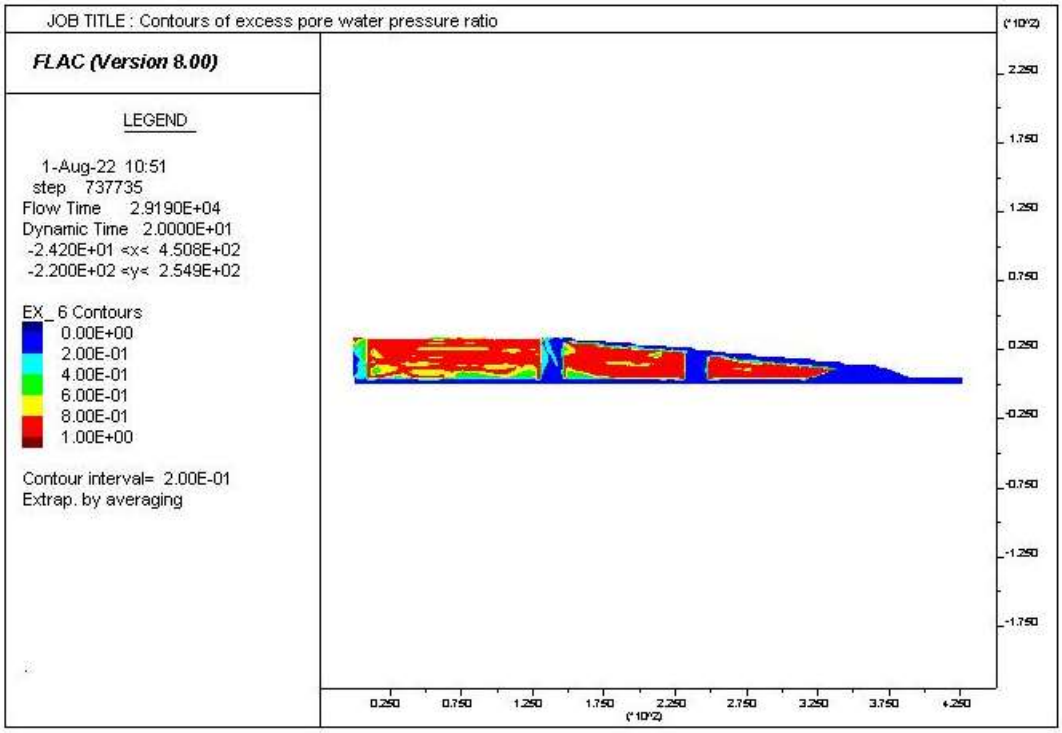

Figure A3. 155: Excess pore water pressure ratio distribution for the 16-85-30-8H- E_3 Loma

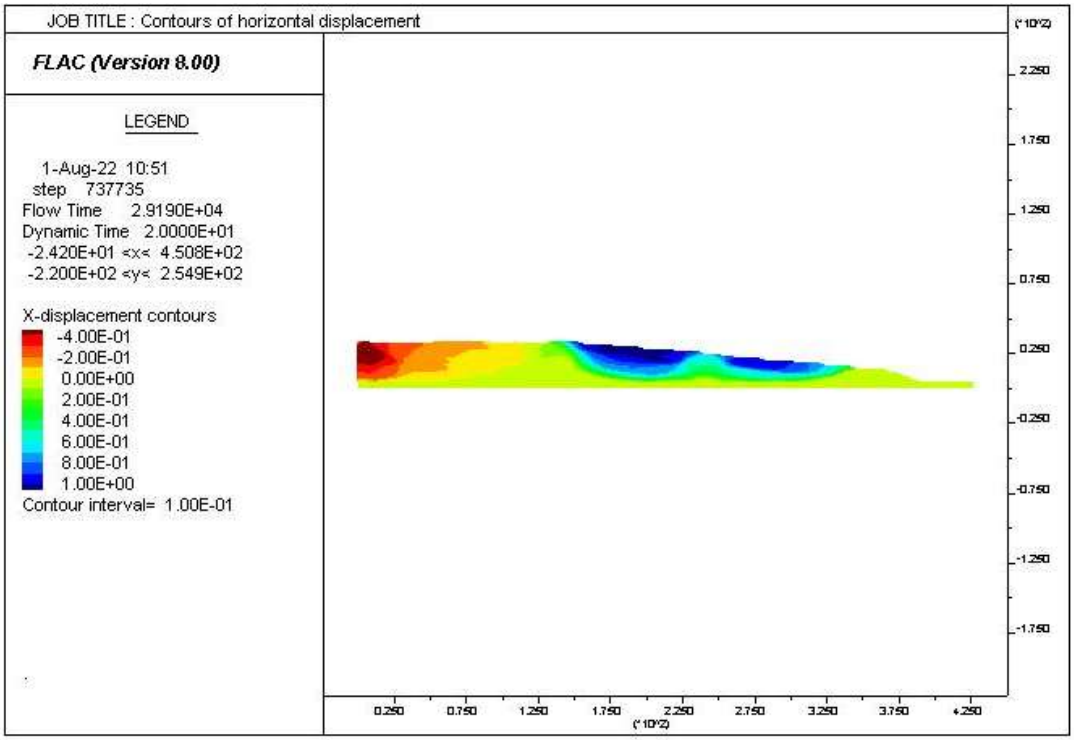

Figure A3. 156: Contours of horizontal displacement for the 16-85-30-8H- E_3Loma

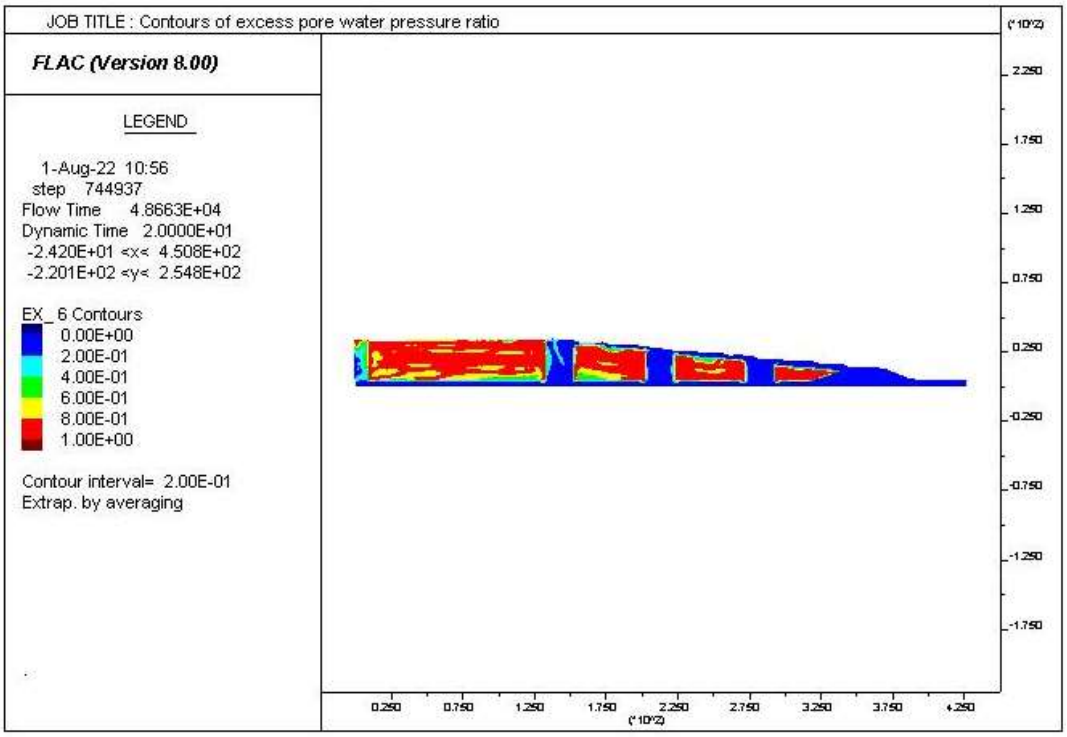

Figure A3. 157: Excess pore water pressure ratio distribution for the 20-50-30-8H- E_3 Loma

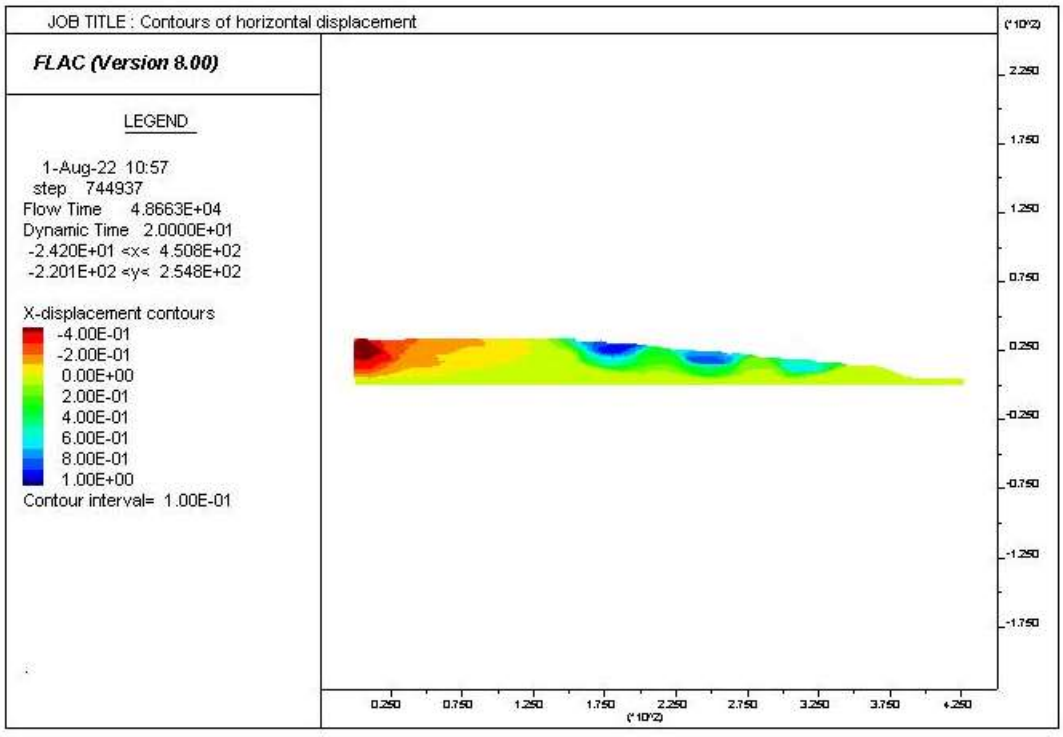

Figure A3. 158: Contours of horizontal displacement for the 20-50-30-8H- E_3 Loma

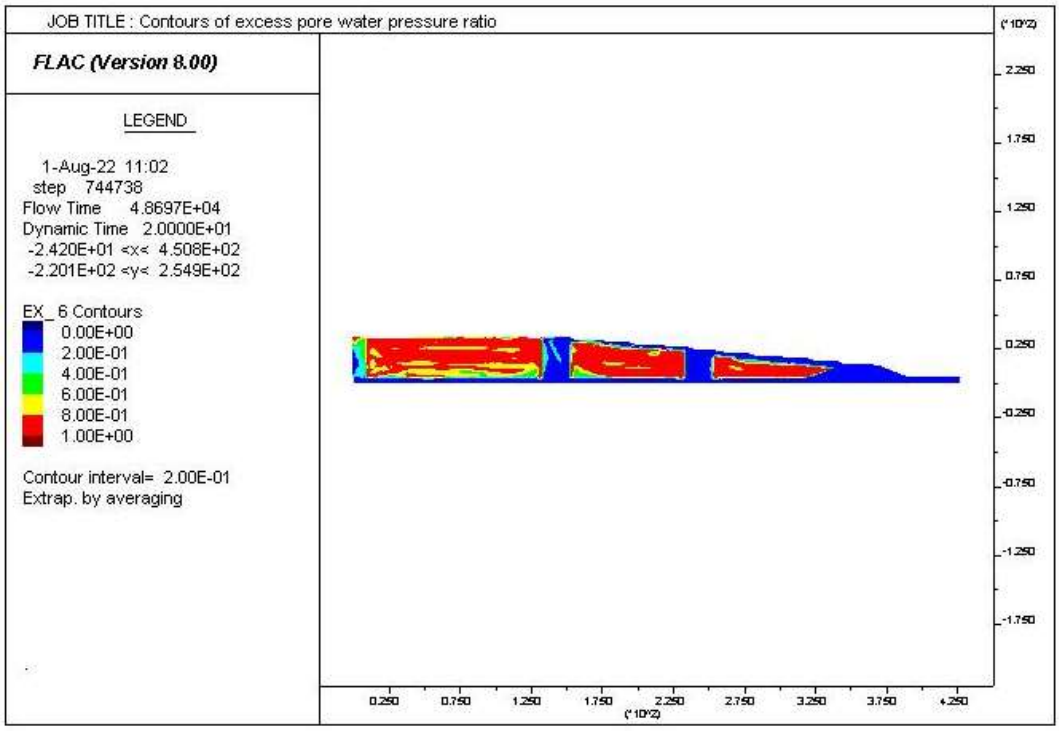

Figure A3. 159: Excess pore water pressure ratio distribution for the 20-80-30-8H- E_3 Loma

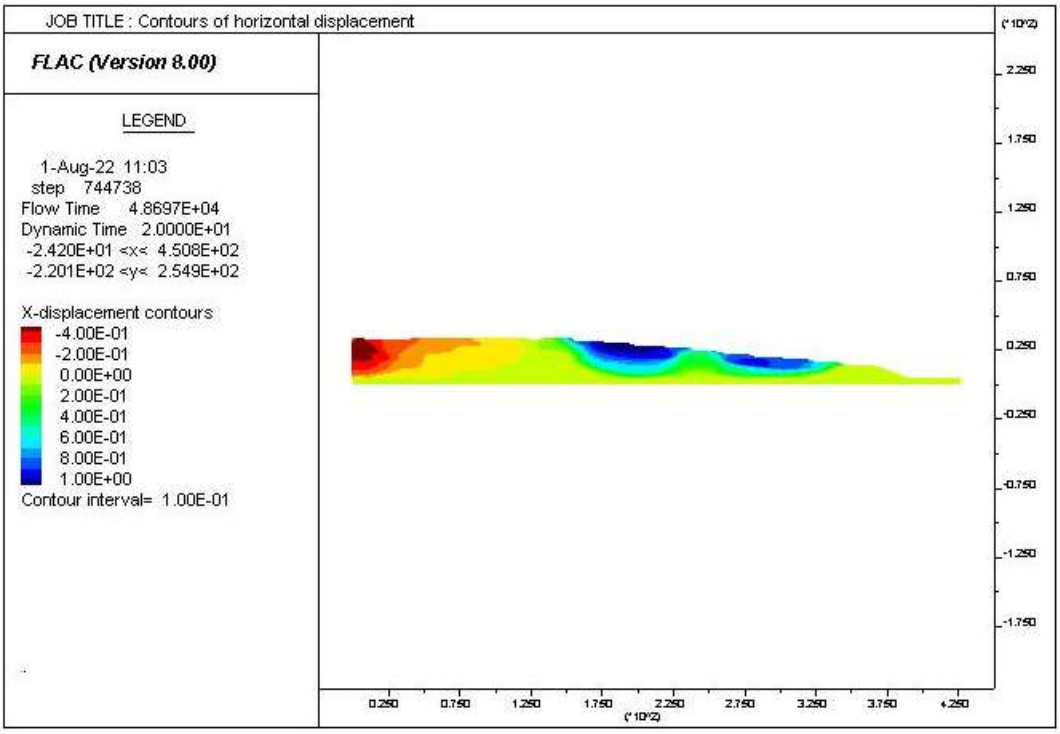

Figure A3. 160: Contours of horizontal displacement for the 20-80-30-8H- E_3 Loma

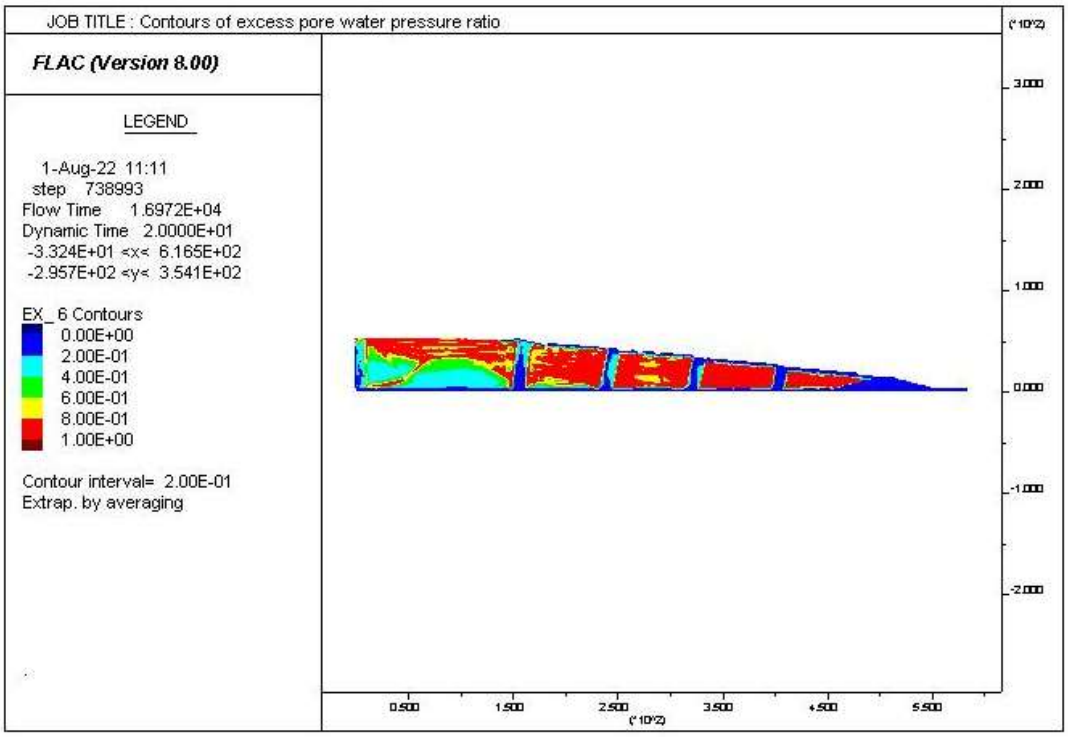

Figure A3. 161: Excess pore water pressure ratio distribution for the 12-70-50-8H- E_3 Loma

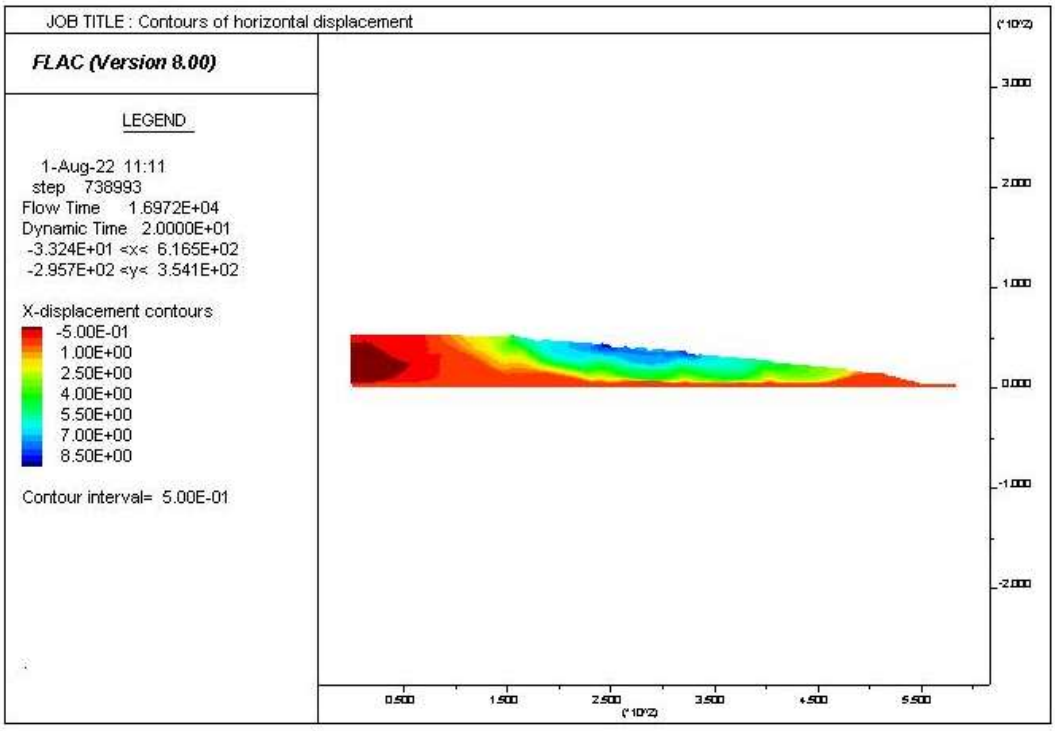

Figure A3. 162: Contours of horizontal displacement for the 12-70-50-8H- E_3 Loma

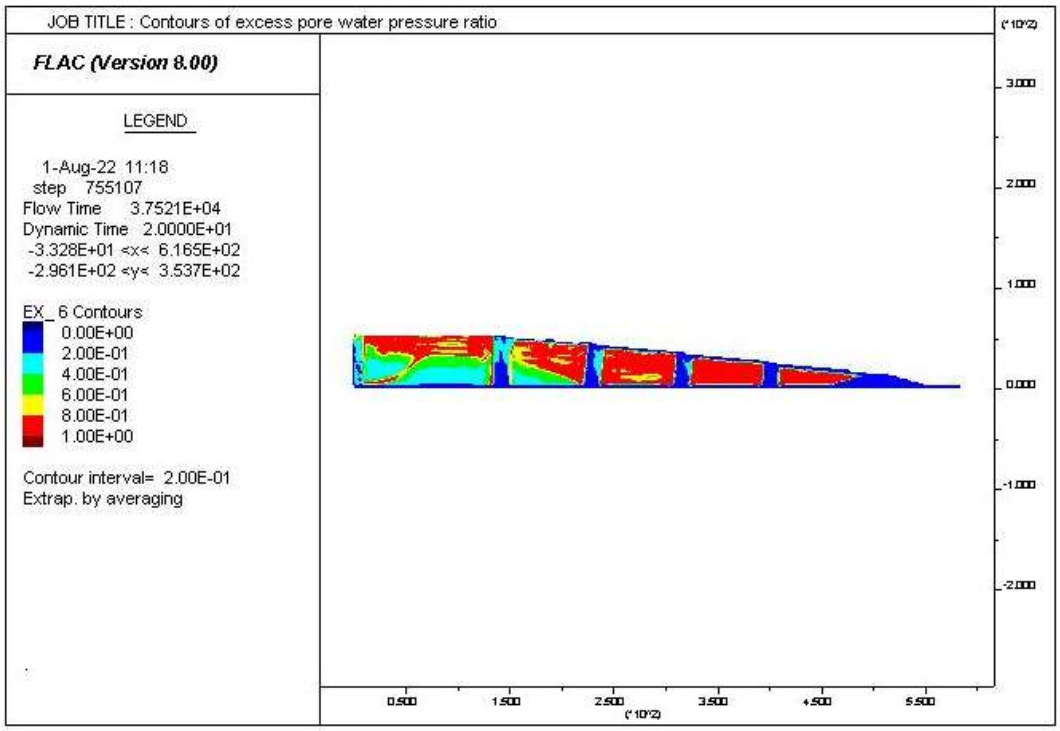

Figure A3. 163: Excess pore water pressure ratio distribution for the 16-70-50-8H- E_3 Loma

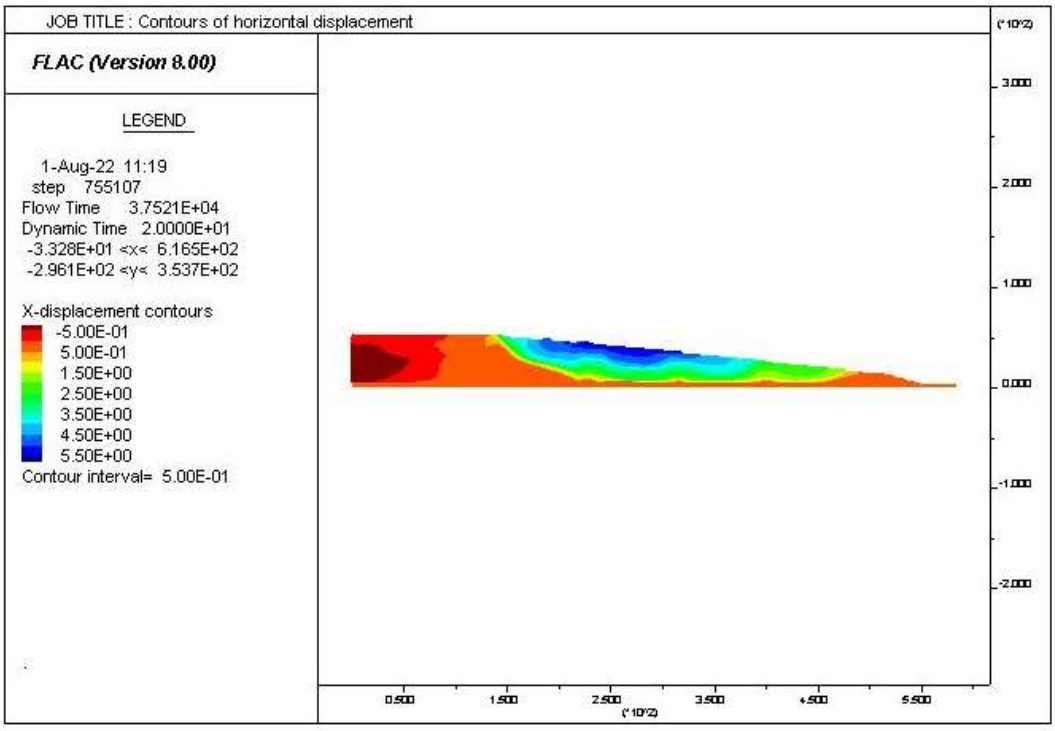

Figure A3. 164: Contours of horizontal displacement for the 16-70-50-8H- E_3Loma

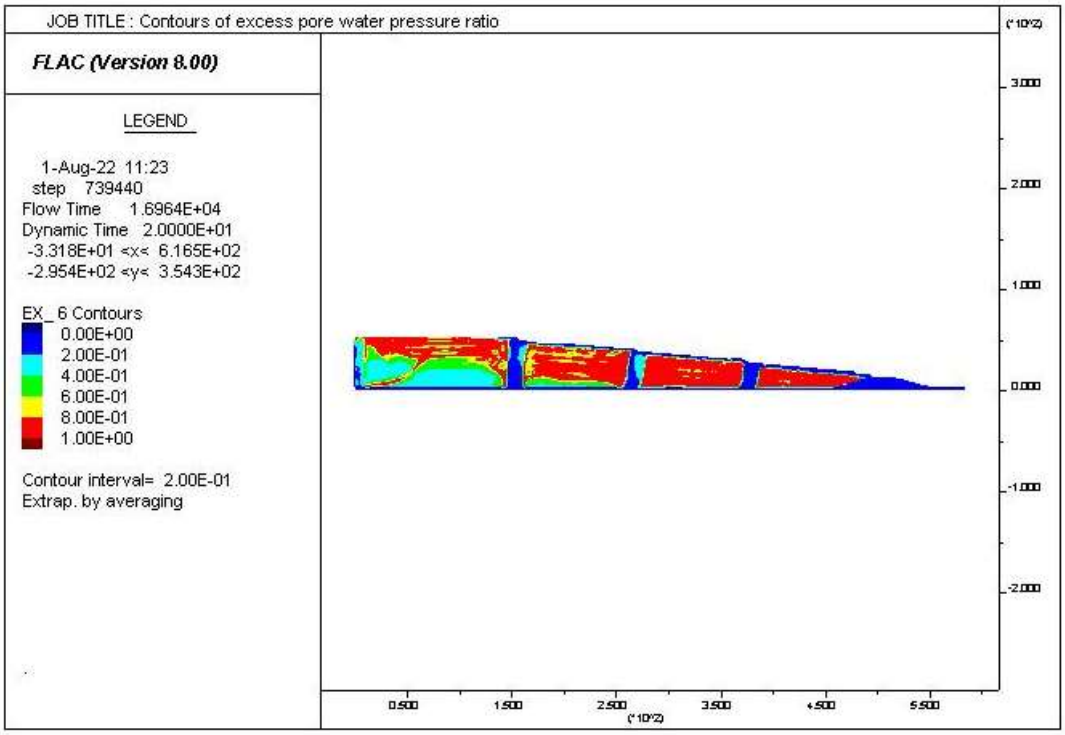

Figure A3. 165: Excess pore water pressure ratio distribution for the 16-95-50-8H- E_3 Loma

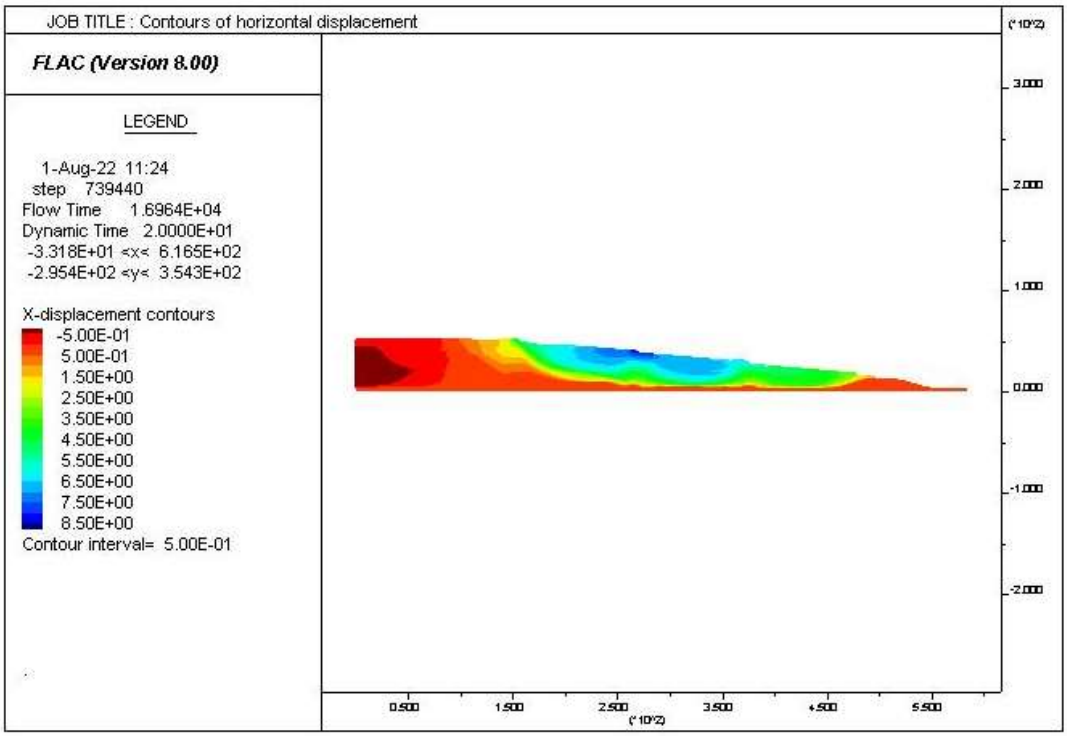

Figure A3. 166: Contours of horizontal displacement for the 16-95-50-8H- E_3Loma

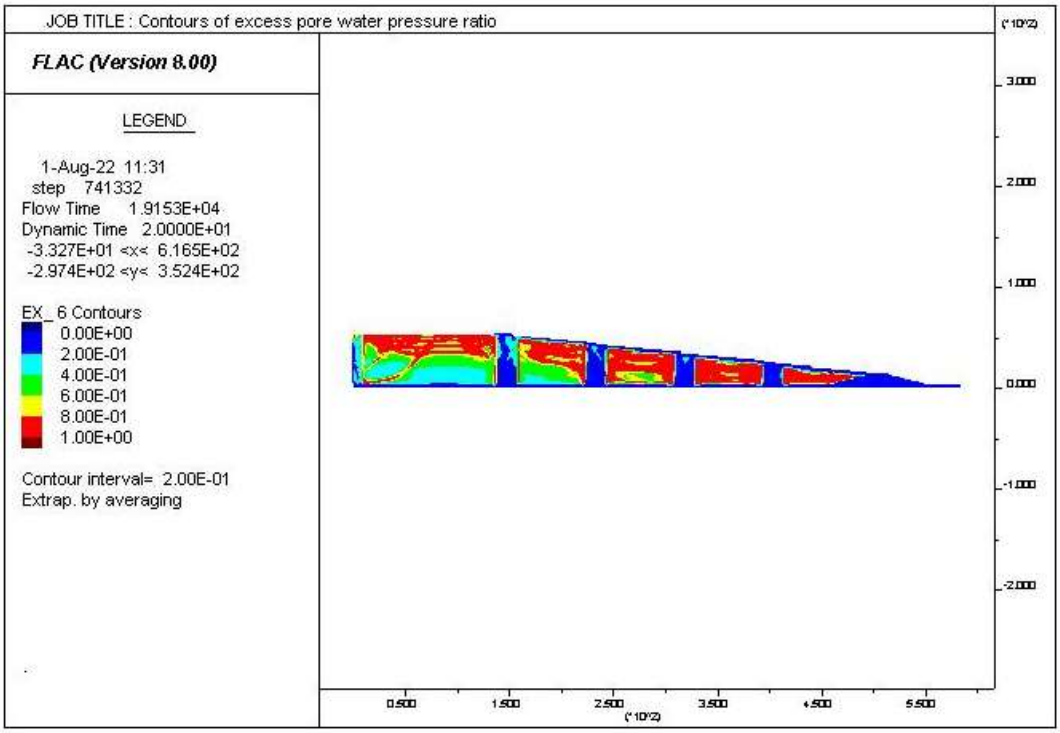

Figure A3. 167: Excess pore water pressure ratio distribution for the 20-65-50-8H- E_3 Loma

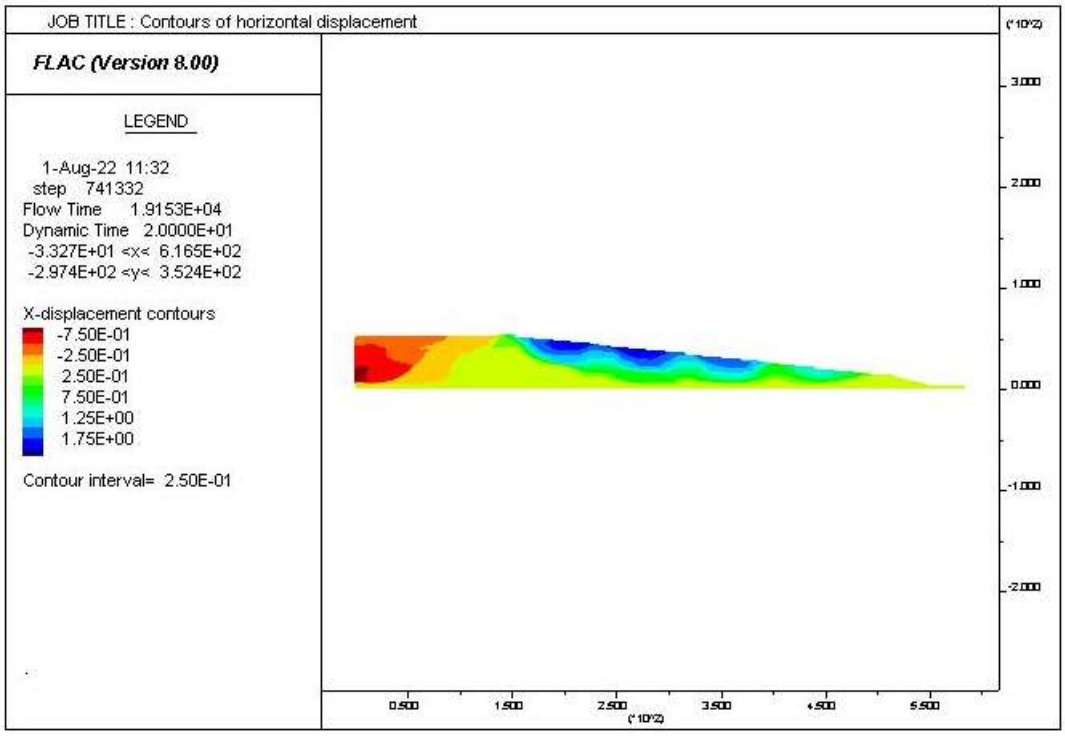

Figure A3. 168: Contours of horizontal displacement for the 20-65-50-8H- E_3Loma

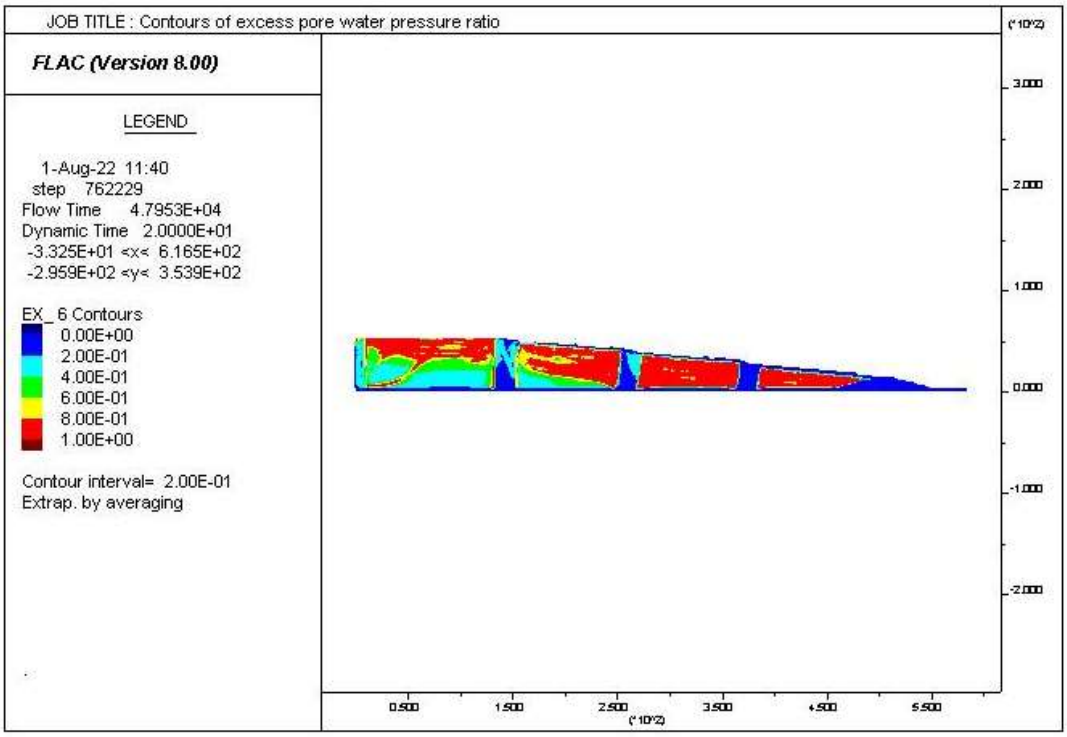

Figure A3. 169: Excess pore water pressure ratio distribution for the 20-95-50-8H- E_3 Loma

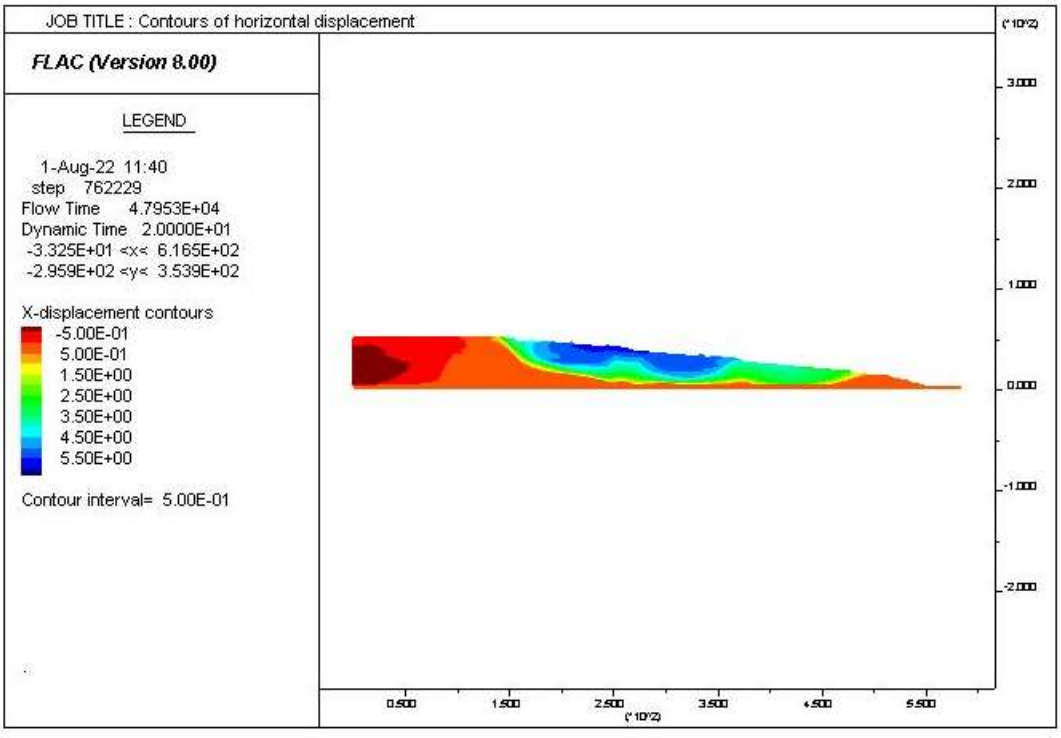

Figure A3. 170: Contours of horizontal displacement for the 20-95-50-8H- E_3Loma

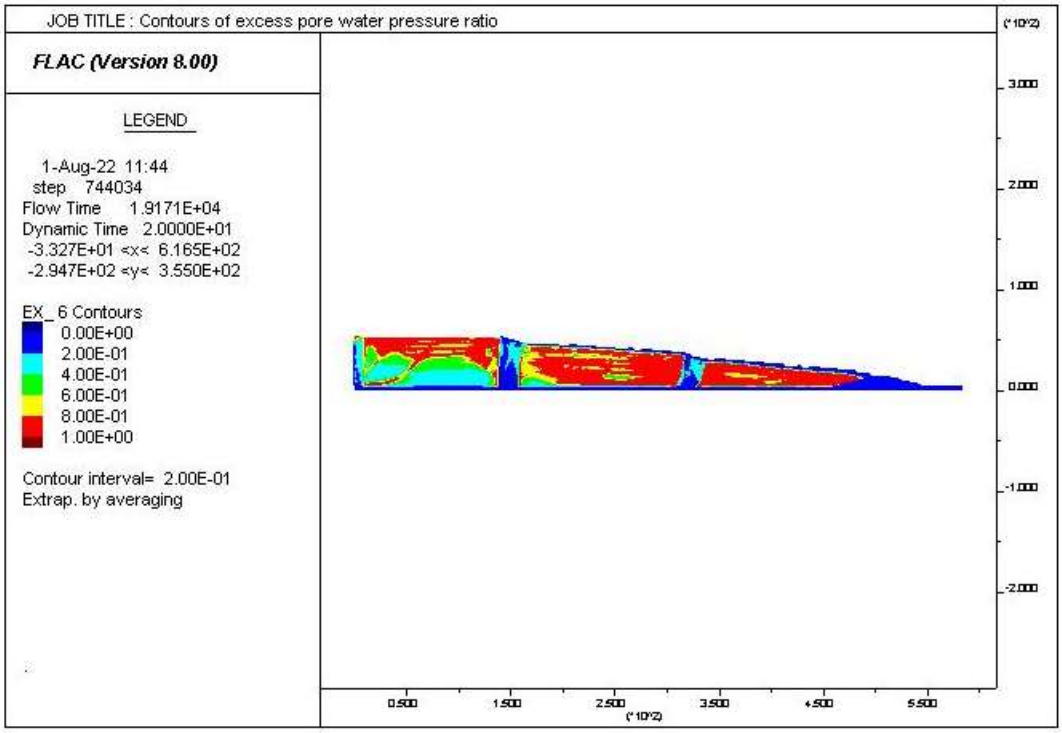

Figure A3. 171: Excess pore water pressure ratio distribution for the 20-150-50-8H- E_3 Loma

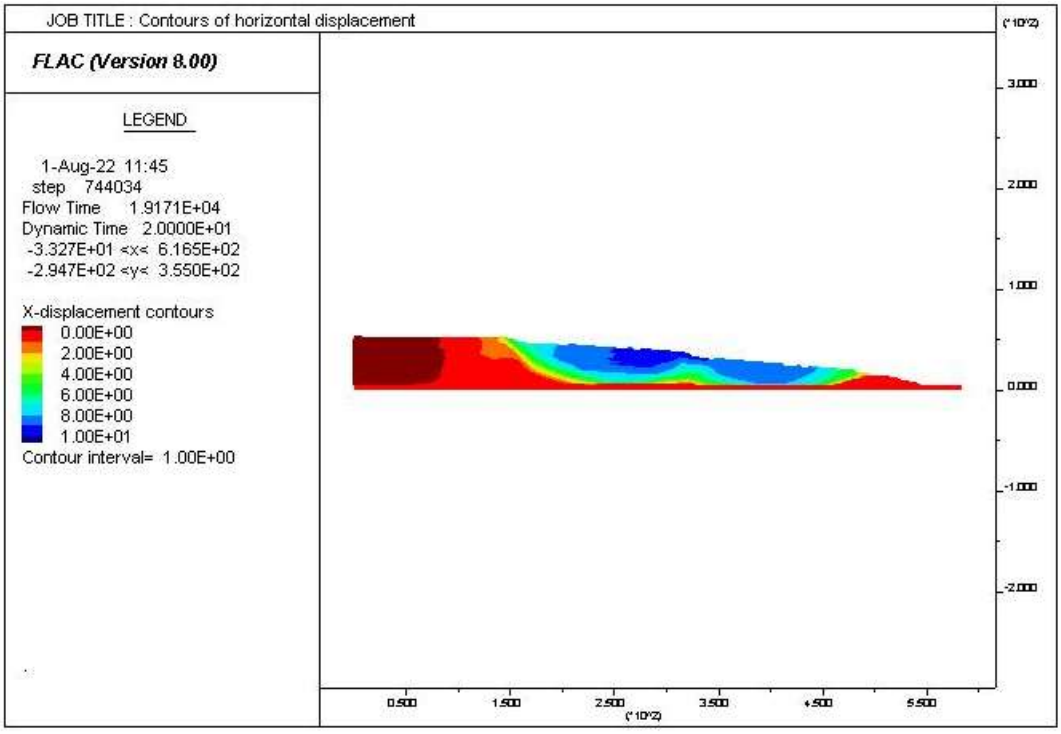

Figure A3. 172: Contours of horizontal displacement for the 20-150-50-8H- E_3Loma

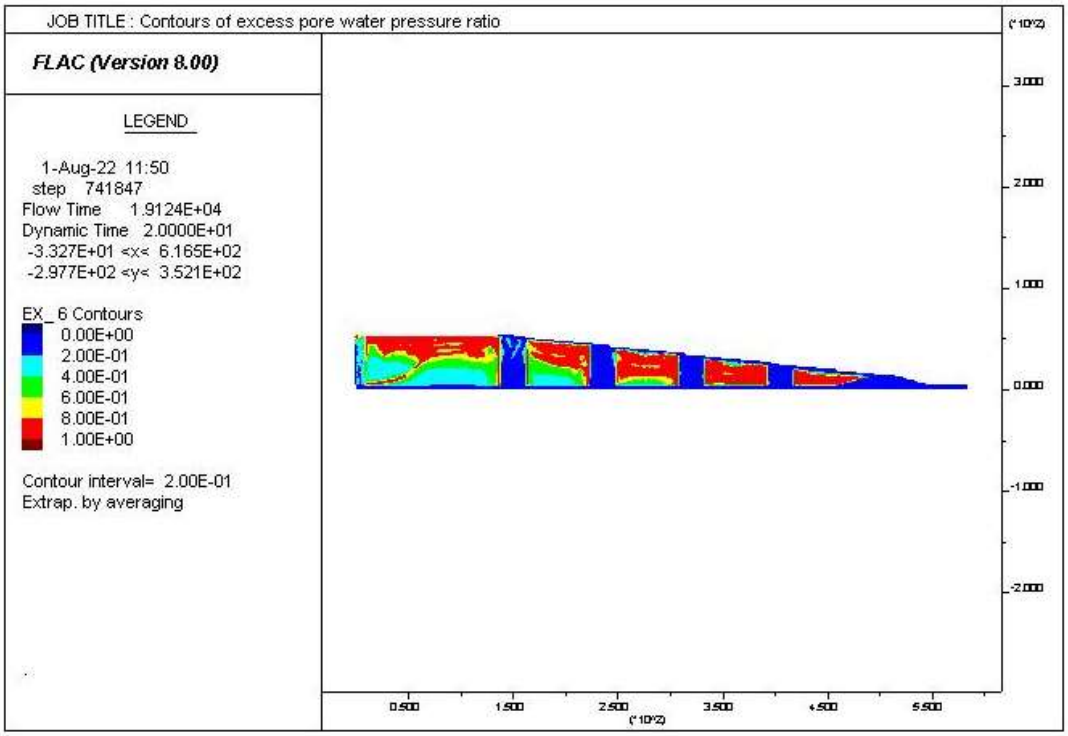

Figure A3. 173: Excess pore water pressure ratio distribution for the 25-60-50-8H- E_3 Loma

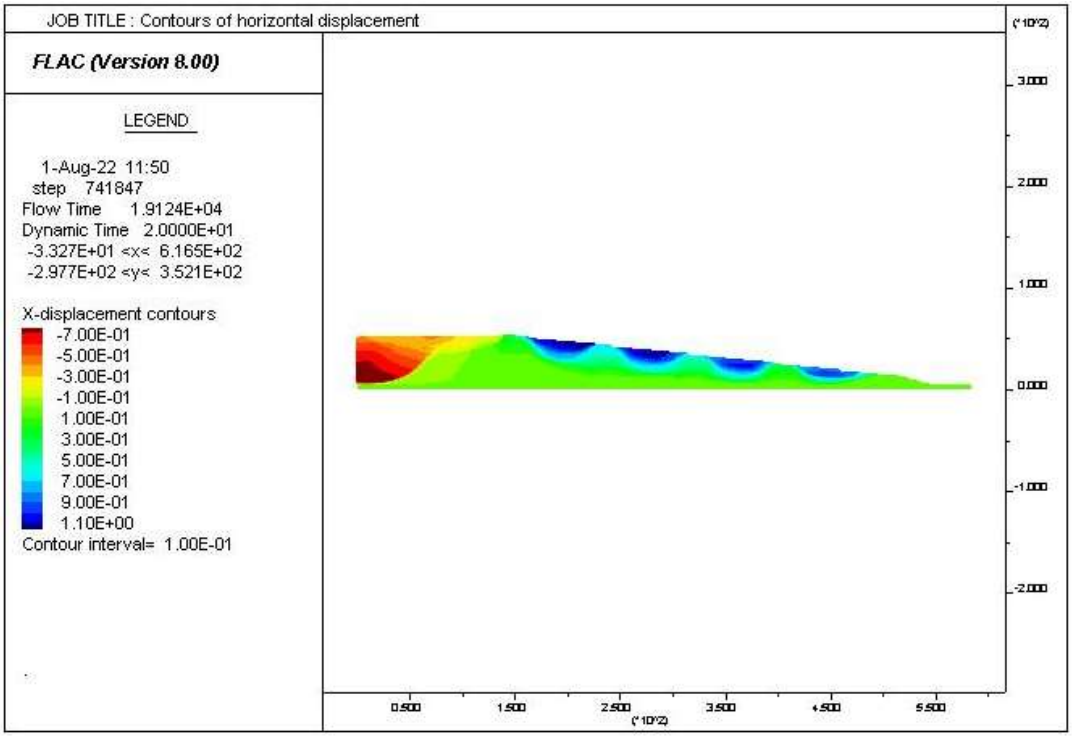

Figure A3. 174: Contours of horizontal displacement for the 25-60-50-8H- E_3Loma

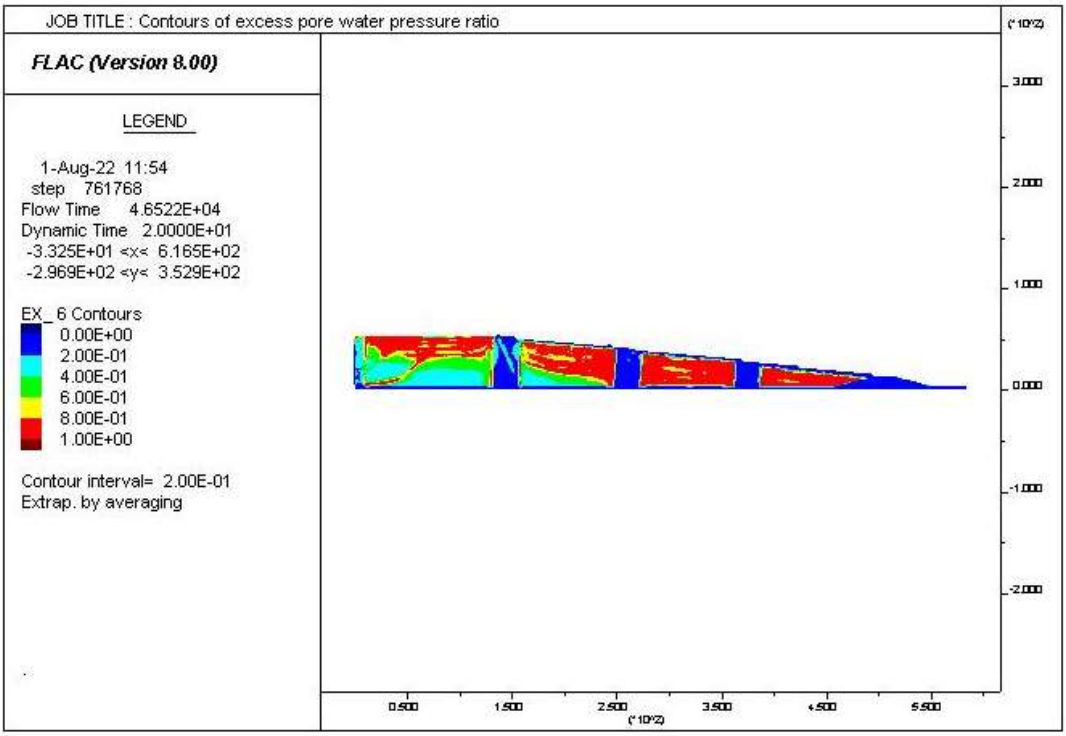

Figure A3. 175: Excess pore water pressure ratio distribution for the 25-90-50-8H- E_3 Loma

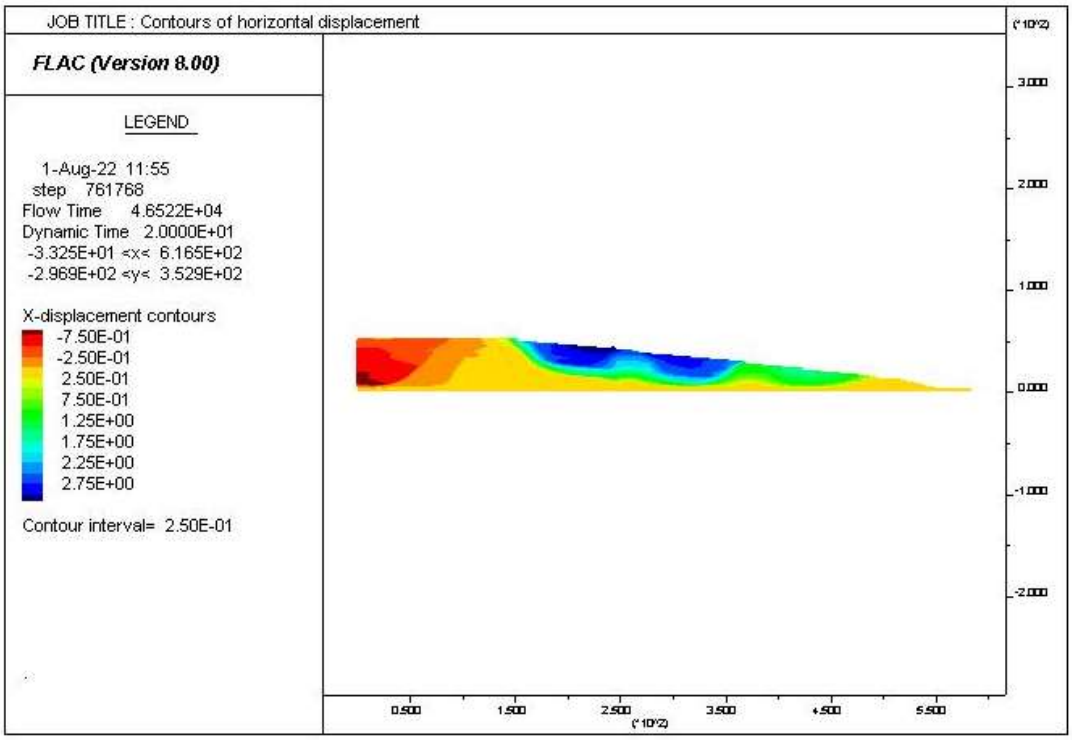

Figure A3. 176: Contours of horizontal displacement for the 25-90-50-8H- E_3Loma

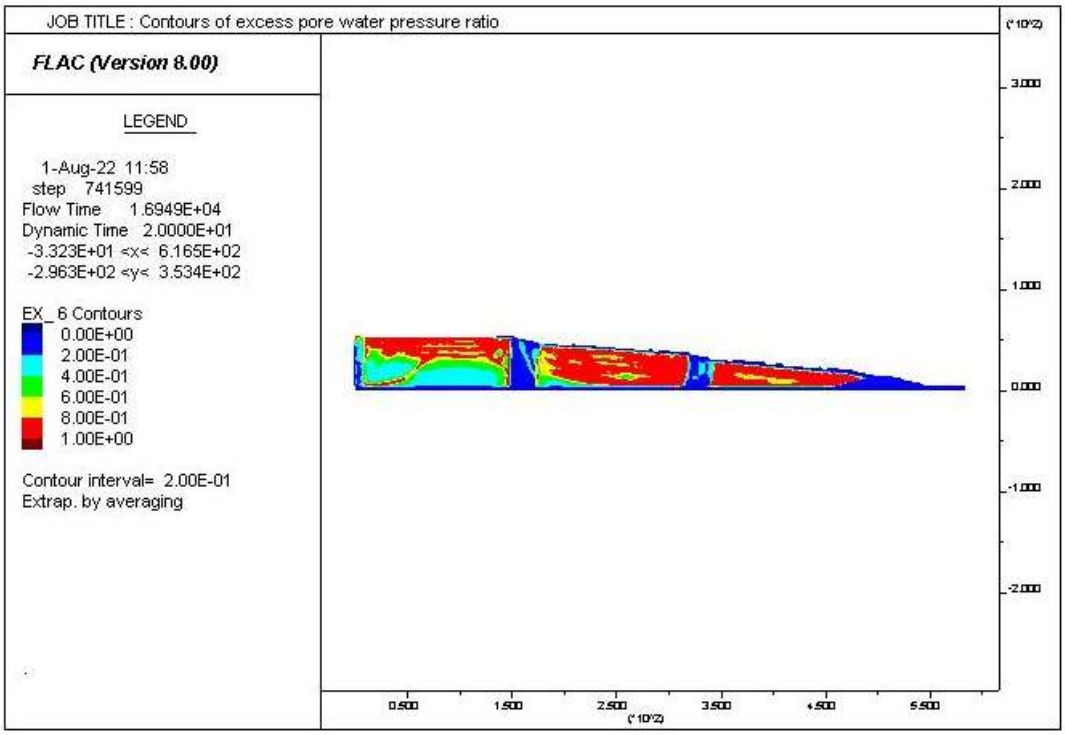

Figure A3. 177: Excess pore water pressure ratio distribution for the 25-140-50-8H- E_3 Loma

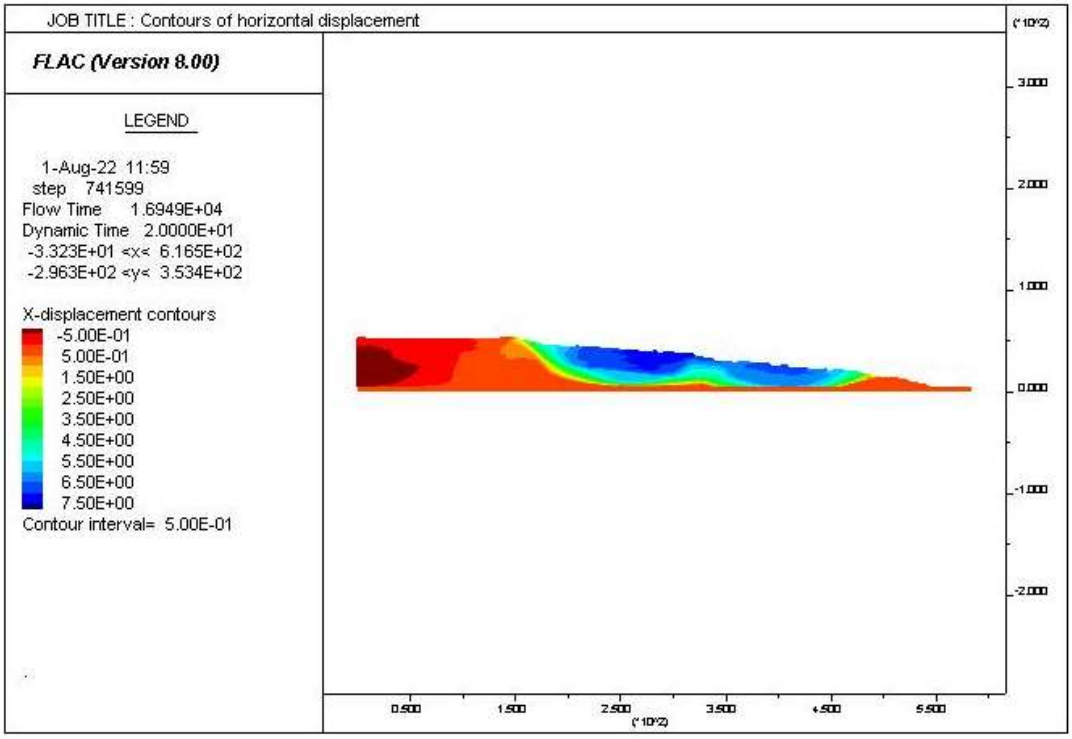

Figure A3. 178: Contours of horizontal displacement for the 25-140-50-8H- E_3Loma

A4 Performance indicators

The response of the various reinforced model impoundments is quantified with two performance indicators: the critically displaced volume of tailings (*CDV*) and the horizontal displacement of the downstream slope. These indicators are described in the following.

Critically displaced volume

The critically displaced volume (*CDV*), defined as the percentage volume of tailings (over the total volume) displaced horizontally more than 100 cm is used to analyse simulation results. A FISH function was written to capture elements with more than 100 cm displacement during the earthquake. Figure A4. 1 shows the critical displaced volume (in red color) for a reinforced model using three 16-m wide inclusions with an edge-to-edge spacing of 70 m under the E_3-Loma Prieta ground motion as an example. The ground motion caused 29% of the model's volume to displace critically at the end of the ground motion.

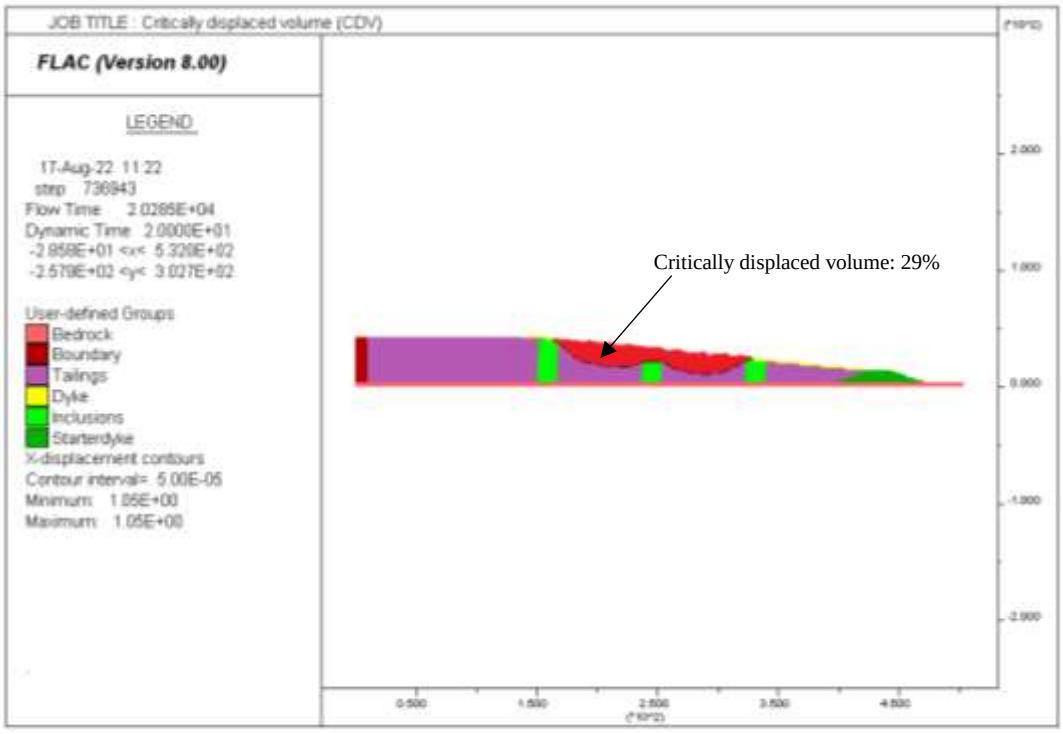

Figure A4. 1: Critically displaced volume under the E_3-Loma earthquake of the reinforced model using three 16-m wide inclusions with an edge-to-edge spacing of 70 m

Horizontal displacement of the downstream slope

The horizontal displacement is computed at the end of shaking at each nodal point along the downstream slope of tailings impoundment. The normalized horizontal displacement at each nodal point is then calculated by dividing its horizontal displacement at the end of shaking by its initial height above the bedrock layer. The average value of the normalized horizontal displacement of all the nodal points along the downstream slope (SAR_x) can be defined by the following equation:

$$\mathrm{SAR_x} = \mathrm{Average}\left(\frac{\mathrm{X_{disp_i}}}{\mathrm{H_i}}\right) \quad \text{(A4.1)}$$

Where X_{disp_i} is the horizontal displacement at nodal point *i* along the downstream slope at the end of the shaking, and H_i is the initial height above the bedrock layer at said nodal point. Table A4.1 presents the SAR_x calculation approach for the configuration 16-70-40-8H-E_3 Loma using the contours of the horizontal displacement presented in Figure A3. 38.

Table A4. 1: SAR_x calculation approach for the configuration 16-70-40-8H-E_3 Loma

H_i (m)	$Xdisp_i$ (m)	$(Xdisp_i/H_i)$ %	SAR_x %
40.00	0.82	2.05	5.06
39.00	0.92	2.36	
38.00	0.93	2.45	
38.00	1.36	3.58	
37.00	1.37	3.70	
36.00	1.39	3.86	
36.00	1.44	4.00	
35.00	1.48	4.23	
34.00	1.52	4.47	
34.00	1.60	4.71	
33.00	1.63	4.94	
32.00	1.64	5.13	
32.00	1.60	5.00	
31.00	1.68	5.42	
30.00	1.72	5.73	
30.00	1.56	5.20	
29.00	1.55	5.34	
28.00	1.52	5.43	
28.00	1.52	5.43	
27.00	1.57	5.81	

26.00	1.58	6.08
26.00	1.52	5.85
25.00	1.53	6.12
24.00	1.51	6.29
24.00	1.46	6.08
23.00	1.47	6.39
22.00	1.37	6.23
22.00	1.27	5.77
21.00	1.20	5.71
20.00	0.89	4.45
20.00	0.95	4.75
19.00	0.97	5.11
18.00	0.98	5.44
18.00	0.99	5.50
17.00	1.00	5.88
16.00	1.00	6.25
16.00	0.97	6.06
15.00	0.98	6.53
14.00	0.91	6.50
14.00	0.85	6.07
13.00	0.85	6.54
12.00	0.74	6.17
12.00	0.41	3.42
11.00	0.38	3.45
10.00	0.24	2.40

APPENDIX B OPTIMUM INTENSITY MEASURE EVALUATION APPROACH

B1 Input ground motions

An analysis of IMs is conducted to identify the most optimum intensity measures for evaluating the seismic response of tailings impoundments. Thirteen different ground motion intensity measures have been used to analyze earthquake-induced displacements, as presented in Table B1. 1.

Table B1. 1: Intensity Measures (IMs) considered for the numerical simulations

Type	IMs (identification, source)	Definition or formula
Peak	Peak ground acceleration, *PGA* (Kramer, 1996)	$PGA = \max\ \lvert a(t) \rvert$
	Peak ground velocity, *PGV* (Kramer, 1996)	$PGV = \max\ \lvert v(t) \rvert$
	Sustained maximum acceleration, *SMA* Sustained maximum velocity, *SMV* (Nuttli, 1979)	Third highest absolute value of acceleration/velocity in the time-history.
Compound	Ratio of *PGV* over *PGA* (Kramer, 1996)	$\frac{PGV}{PGA} = \frac{\max \lvert v_{(t)} \rvert}{\max \lvert a_{(t)} \rvert}$
Integral	Arias Intensity, *AI* (Arias, 1970)	$AI = \frac{\pi}{2g} \int_0^{tf} a^2(t) dt$
	Cumulative absolute velocity, *CAV* (Kramer, 1996)	$CAV = \int_0^{tf} \lvert a(t) \rvert dt$

	Root-mean-square acceleration, a_{rms} (Housner and Jennings, 1964)	$a_{rms} = \sqrt{\frac{1}{t_d}\int_{t_5}^{t_{95}} a^2(t)dt}$
	Root-mean-square velocity, v_{rms} (Housner and Jennings, 1964)	$v_{rms} = \sqrt{\frac{1}{t_d}\int_{t_5}^{t_{95}} v^2(t)dt}$
	Characteristic intensity, C_I (Park et al., 1985)	$C_I = {a_{rms}}^{1.5}.(t_{95} - t_5)^{0.5}$
Spectrum	Acceleration spectrum intensity, *ASI* (Housner, 1952)	$ASI = \int_{0.1}^{0.5} s_a(\xi = 5\%, T)dT$
	Velocity spectrum intensity, *VSI* (Housner, 1952)	$VSI = \int_{0.1}^{0.5} s_v(\xi = 5\%, T)dT$
	Housner's spectral intensity, H_I (Housner, 1952)	$H_I = \int_{0.1}^{2.5} S_{pv}(\xi = 5\%, T)\,dT$

Definition of symbols: $a(t)$ and $v(t)$ are acceleration and velocity time histories, in m/s^2 and m/s, respectively; t_f is duration of a ground motion in seconds; t_d is the relative duration ($t_d = t_{95} - t_5$) in seconds; t_5 and t_{95} are times at which 5% and 95% of Arias intensity of the motion are reached in seconds, respectively; T is the dominant period of response spectrum in seconds, defined as the period of maximum spectral acceleration (Rathje at al., 1998).; s_a and s_v are the acceleration and velocity spectra, in m/s^2 and m/s, respectively; S_{pv} is the pseudo velocity spectrum in m/s; and ξ is the damping ratio.

Table B1.2 presents the ground motions from the NGA-West2 (Ancheta et al. 2013) and NGA-East (Goulet et al. 2014) databases with the various intensity measures.

Table B1. 2: Input ground motion parameters (Ancheta et al. 2013; Goulet et al. 2014)

#	Earthquake	PGA (m/s^2)	AI (m/s)	PGV (m/s)	PGV/PGA (s)	VSI (m)	ASI (m/s)	CAV (m/s)	SMA (m/s^2)	SMV (m/s)	a_{rms} (m/s^2)	v_{rms} (m/s)	C_I	H_I (m)
1	Northridge	3.23	2.04	0.35	0.11	1.6	2.9	15.35	2.45	0.277	0.6	0.1	2.77	1.41
2	Saguenay	4.38	2.05	0.08	0.02	0.3	1.63	12.52	3.49	0.07	0.72	0.01	3.03	0.17
3	E_1-Loma Prieta	1.21	0.19	0.06	0.05	0.24	1.18	3.25	0.94	0.06	0.24	0.01	0.54	0.19
4	E_2-Loma Prieta	2.04	0.54	0.10	0.05	0.41	1.99	5.48	1.59	0.09	0.41	0.024	1.18	0.32
5	E_3-Loma Prieta	3.04	1.20	0.15	0.05	0.61	2.95	8.15	2.37	0.14	0.61	0.03	2.14	0.48
6	E_4-Loma Prieta	4.87	3.09	0.25	0.05	0.98	4.73	13.06	3.79	0.23	0.98	0.06	4.36	0.77
7	Au Sable Forks	1.96	0.47	0.06	0.03	0.22	1.50	5.60	1.6	0.03	0.32	0.008	0.98	0.14
8	Cape Mendocino	3.68	1.71	0.09	0.24	2.5	2.95	10.62	2.25	0.32	0.61	0.15	2.55	2.4
9	San Fernando	3.13	0.7	0.17	0.05	0.66	2.71	7.60	1.95	0.1	0.27	0.02	1.08	0.53
10	Mineral	1.02	0.05	0.04	0.03	0.17	0.43	1.30	0.62	0.03	0.14	0.007	0.2	0.13

B2 Evaluation of optimum scalar IMs

The optimum IMs for the seismic stability evaluation of tailings impoundments is evaluated based on two seismic performance indicators: the normalized horizontal displacement of the downstream slope (SAR_x) and the critically displaced volume (*CDV*) of tailings. This section presents the evaluation of these indicators to identify the optimum IMs using efficiency (Shome and Cornell, 1999), practicality (Nielson, 2007), and proficiency criteria.

B2. 1 Optimum Scalar IMs using SAR_x

The following equation can be used to represent the relationship between the SAR_x and IMs.

$$ln(SAR_x) = a + b\,.\ ln(IM) \quad \text{(B2.1)}$$

Practicality analysis

To characterize the sensitivity of a given IM to the seismic performance indicator (SAR_x), the regression parameter b in Eq. (B2.1.1) is used to define practicality, based on Nielson (2005). The assumption is that a greater value of *b* corresponds to a more sensitive relationship and to a more practical *IM*. Figure B2. 1 compares the practicality for the considered IMs and WRI configurations. The legend in this figure gives the configuration of the waste rock inclusions: the first number is the width of the inclusions and the second is the spacing between the inclusions (in meters). Results indicate that the coefficients for *PGV*, *SMV*, *Vrms*, and *VSI* are all higher compared to other IMs. Therefore, these four IMs are deemed more practical.

Proficiency analysis

The proficiency index (ζ) combines the efficiency (σ_ε) and the practicality (*b*) parameters as follows:

$$\zeta = {}^{\sigma_\varepsilon}/_{b} \quad \text{(B2.1)}$$

The lower the value of ζ is, the more proficient is the *IM*. The ζ values obtained for the candidate *IM*s and various configurations of the WRI are plotted in Figure B2. 2. According to the results, the *IM*s that have lower ζ values are *PGV, SMV,* and *VSI*; *VSI* has the best proficiency.

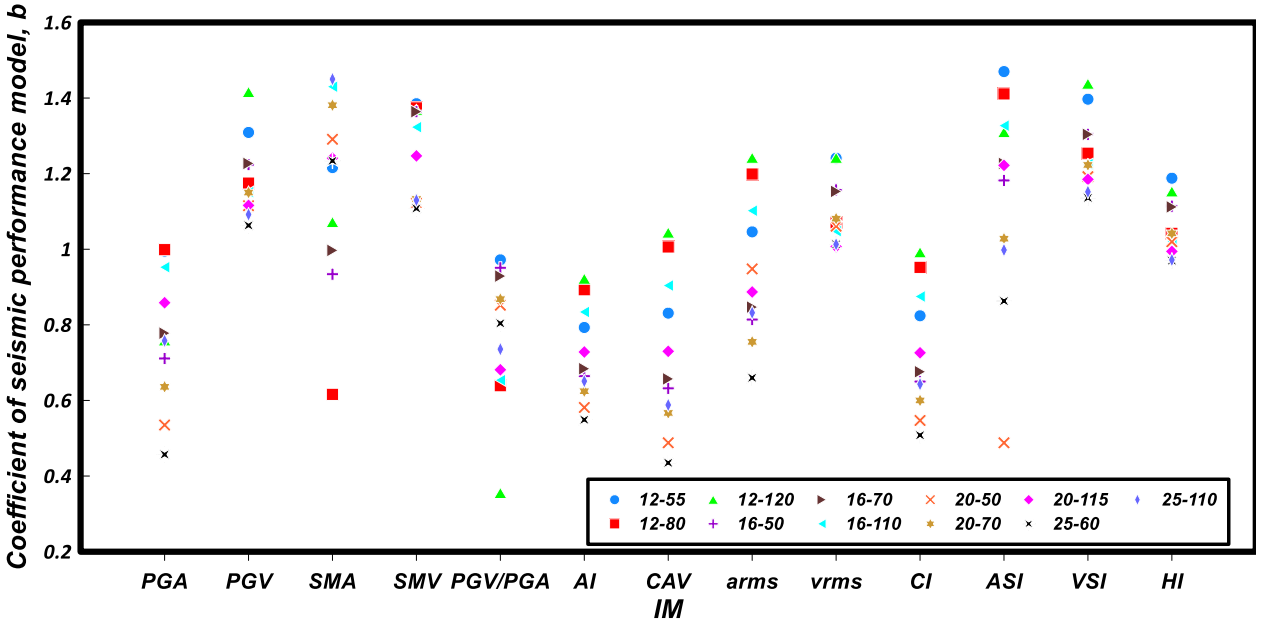

Figure B2. 1: Regression parameter (exponent) b of the seismic performance relationship (Eq. B2.1) for the candidate IMs and various configurations of the WRI (identified in the inserted legend)

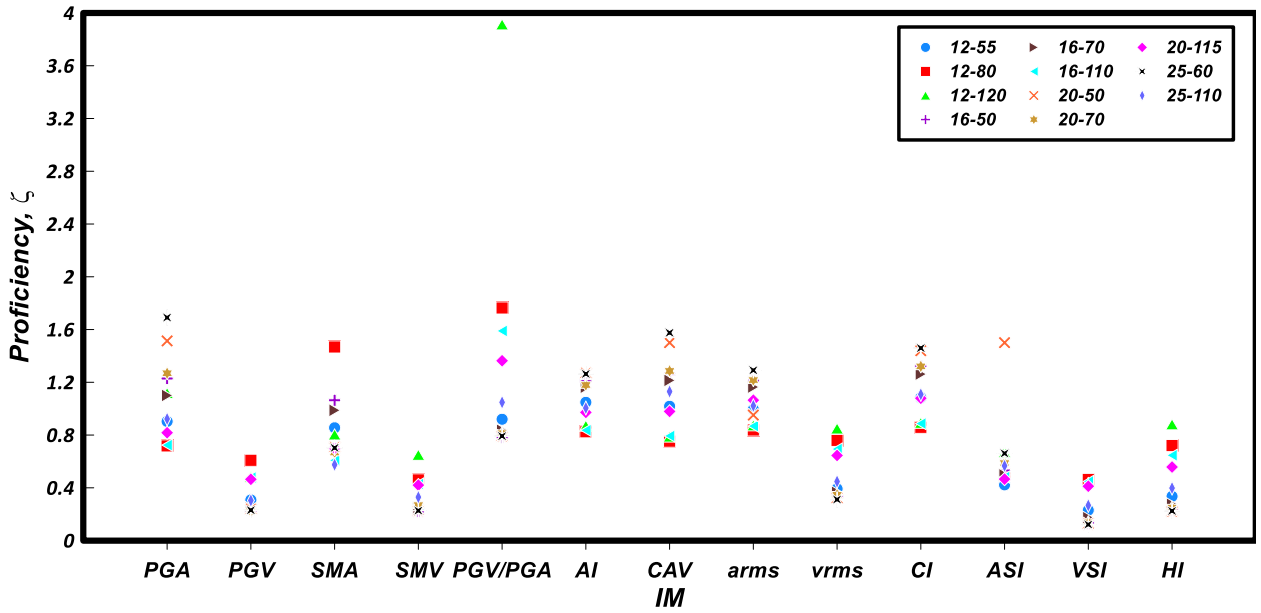

Figure B2. 2: The proficiency index, ζ of the candidate IMs for various configurations of the WRI (identified in the inserted legend)

B2. 2 Optimum Scalar IMs using CDV

The relationship between the CDV and IMs can be represented by the following equation.

$$ln(CDV) = a + b\,.\ ln(IM) \quad \text{(B2.2)}$$

The standard deviation of residuals, σ_ε and the coefficient of determination (R^2) are used for determining the optimum IM. A higher value of σ_ε indicating a lower efficiency, however the IM is inefficient when σ_ε is higher than 0.4.

Figure B2. 3 to Figure B2. 13 show the values of the σ_ε (a) and R^2 (b) for the considered IMs and different impoundment model configurations with waste rock inclusions. The results show that *VSI* and *PGV* are the *IM*s with the lowest values of σ_ε for all the configurations of WRI. However, all of the calculated values of σ_ε are higher than 0.4, indicating that all of the candidate IMs have a limited efficiency. The practicality and proficiency analyses were not performed for the performance model presented by *CDV*.

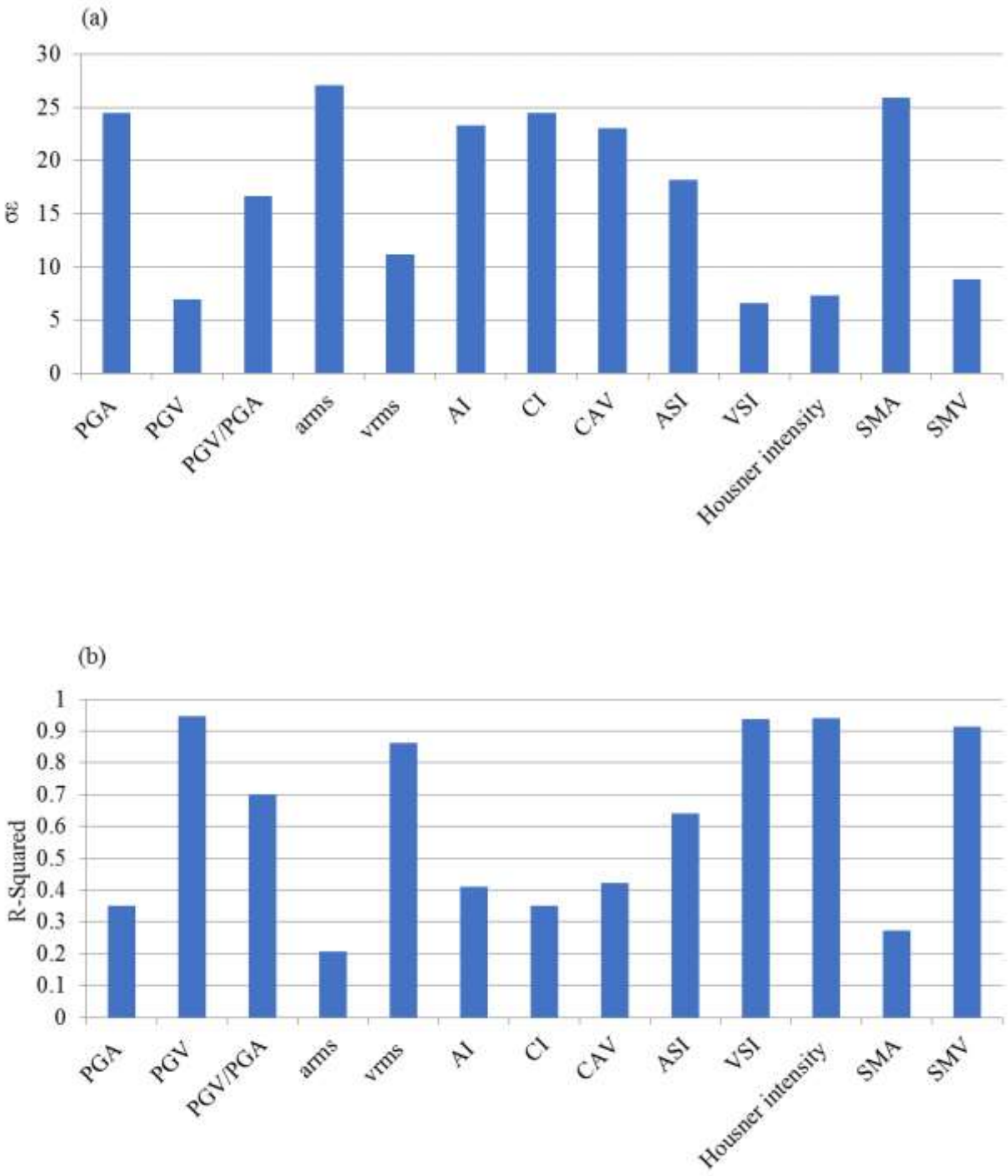

Figure B2. 3: Standard deviation of residuals, σ_ε (a) and coefficient of determination, R^2 (b) for the configuration 12-55 and candidate IMs

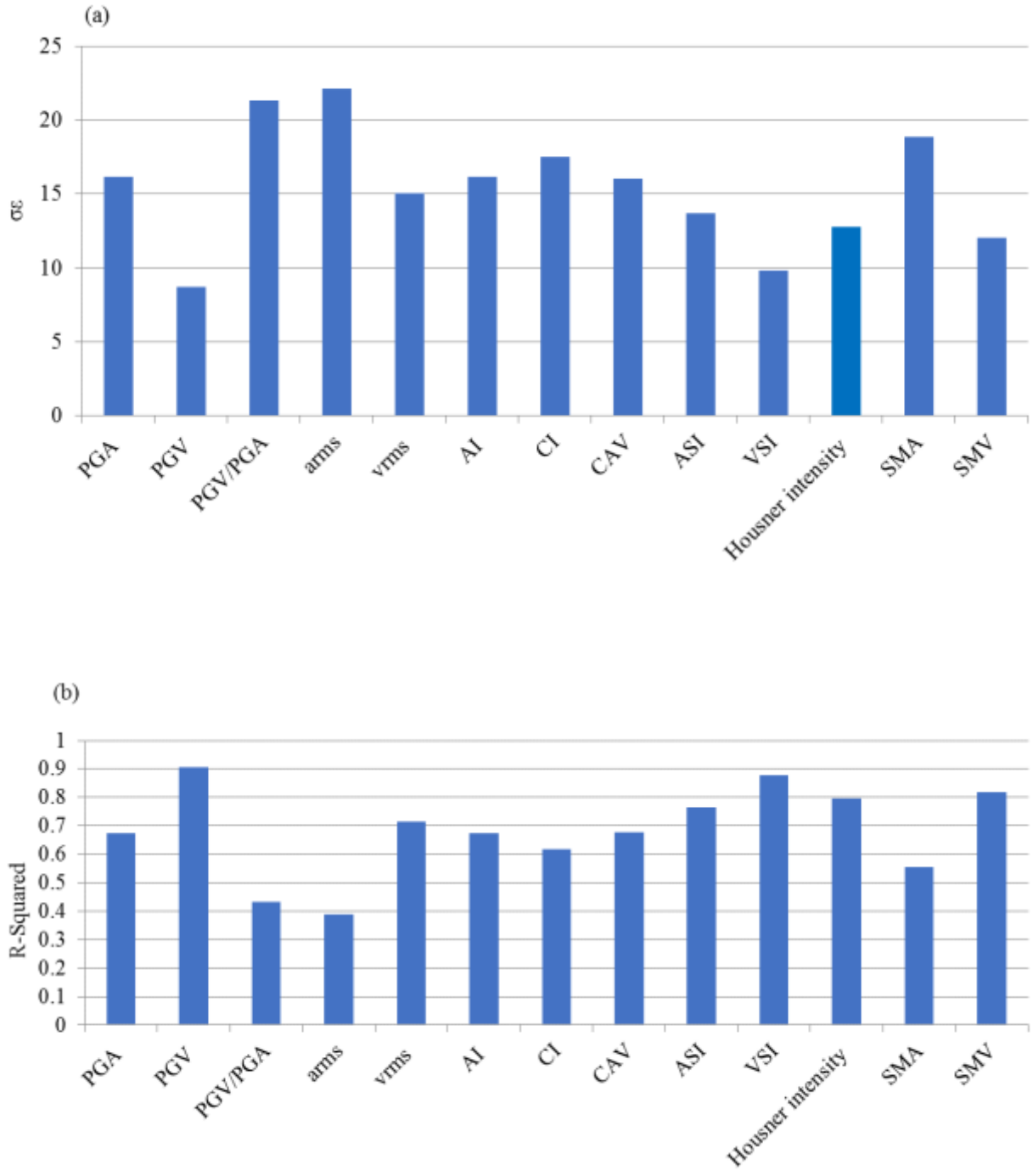

Figure B2. 4: Standard deviation of residuals, σ_{ε} (a) and coefficient of determination, R^2 (b) for the configuration 12-80 and candidate IMs

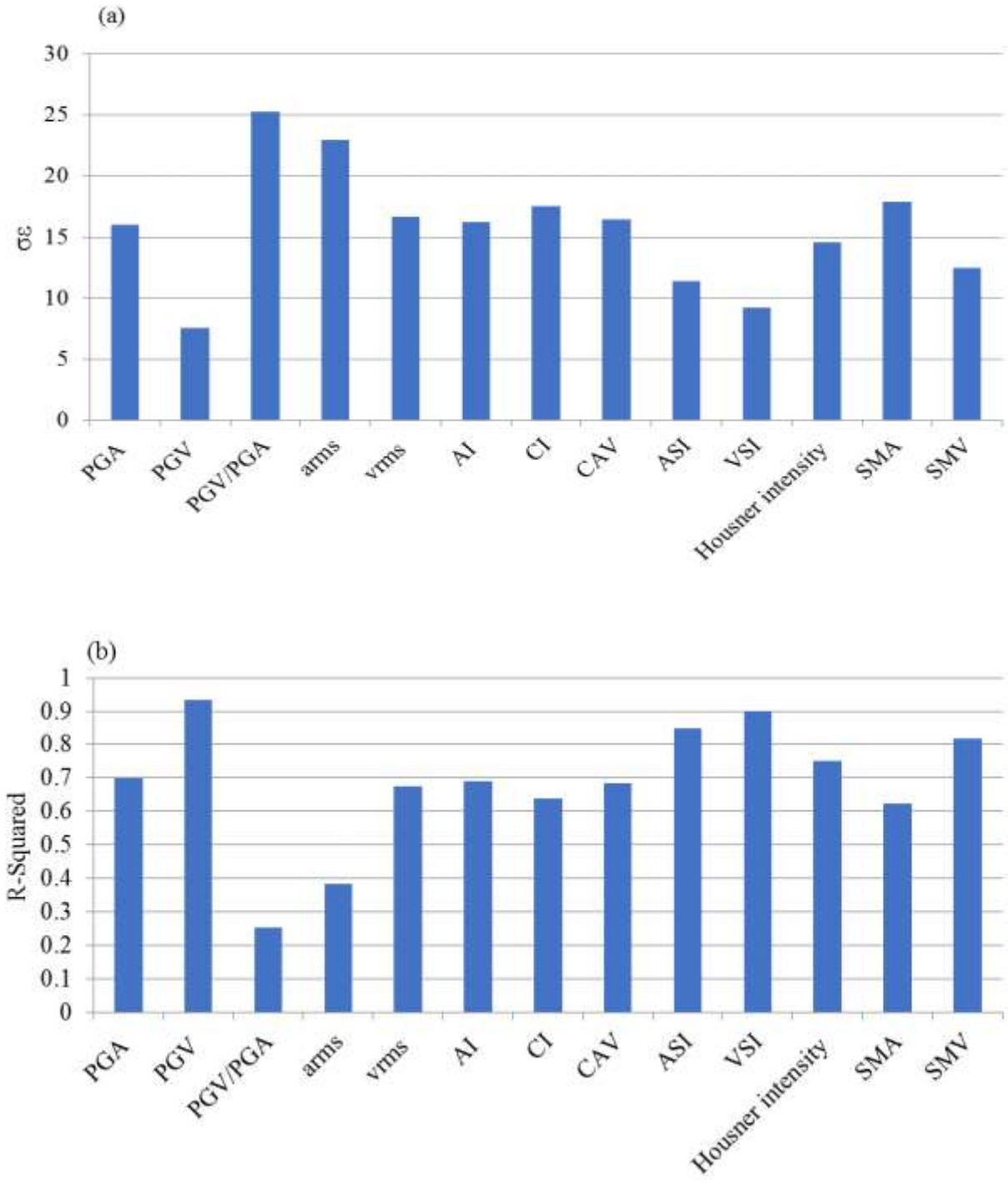

Figure B2. 5: Standard deviation of residuals, σ_ε (a) and coefficient of determination, R^2 (b) for the configuration 12-120 and candidate IMs

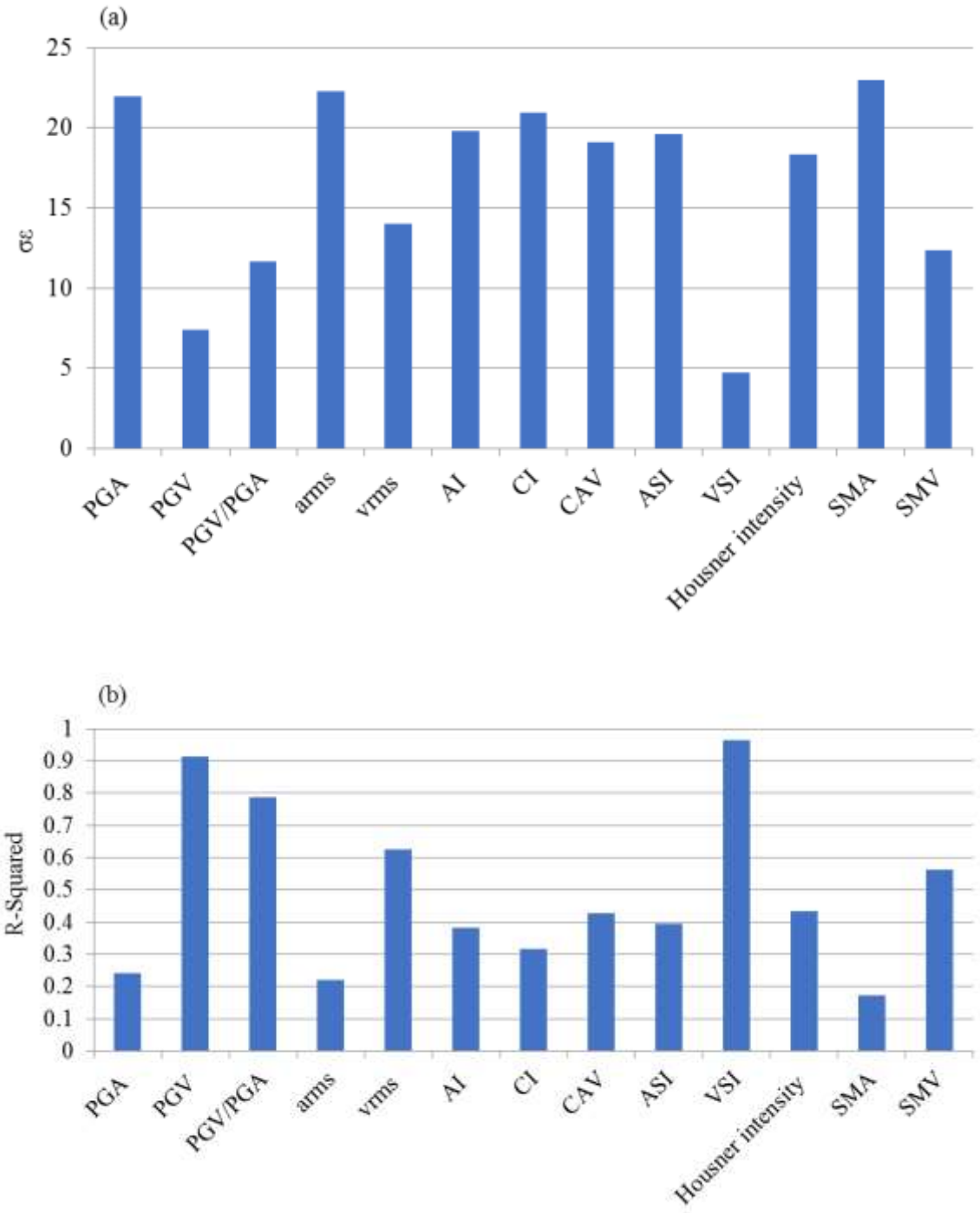

Figure B2. 6: Standard deviation of residuals, σ_ε (a) and coefficient of determination, R^2 (b) for the configuration 16-50 and candidate IMs

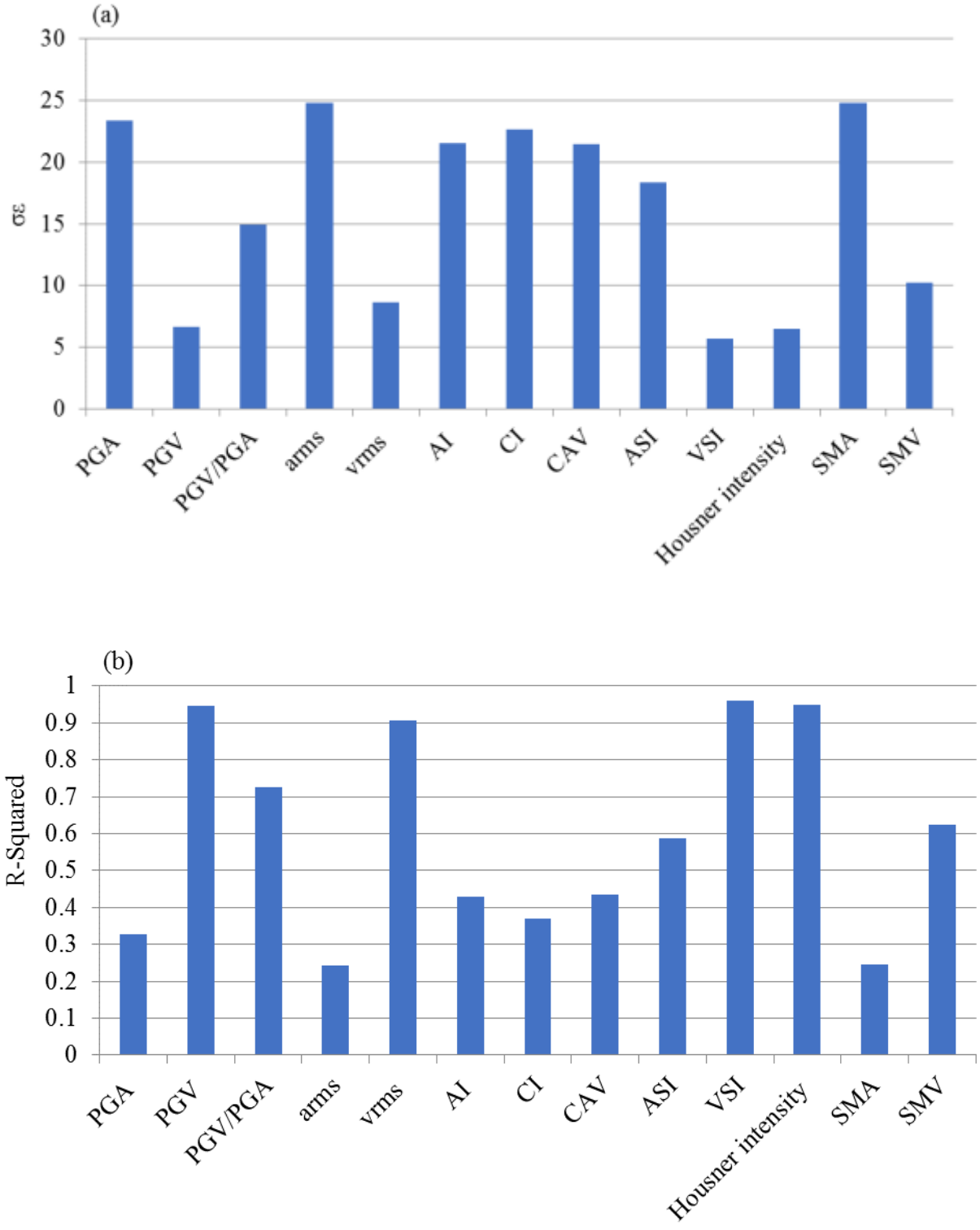

Figure B2. 7: Standard deviation of residuals, σ_ε (a) and coefficient of determination, R^2 (b) for the configuration 16-70 and candidate IMs

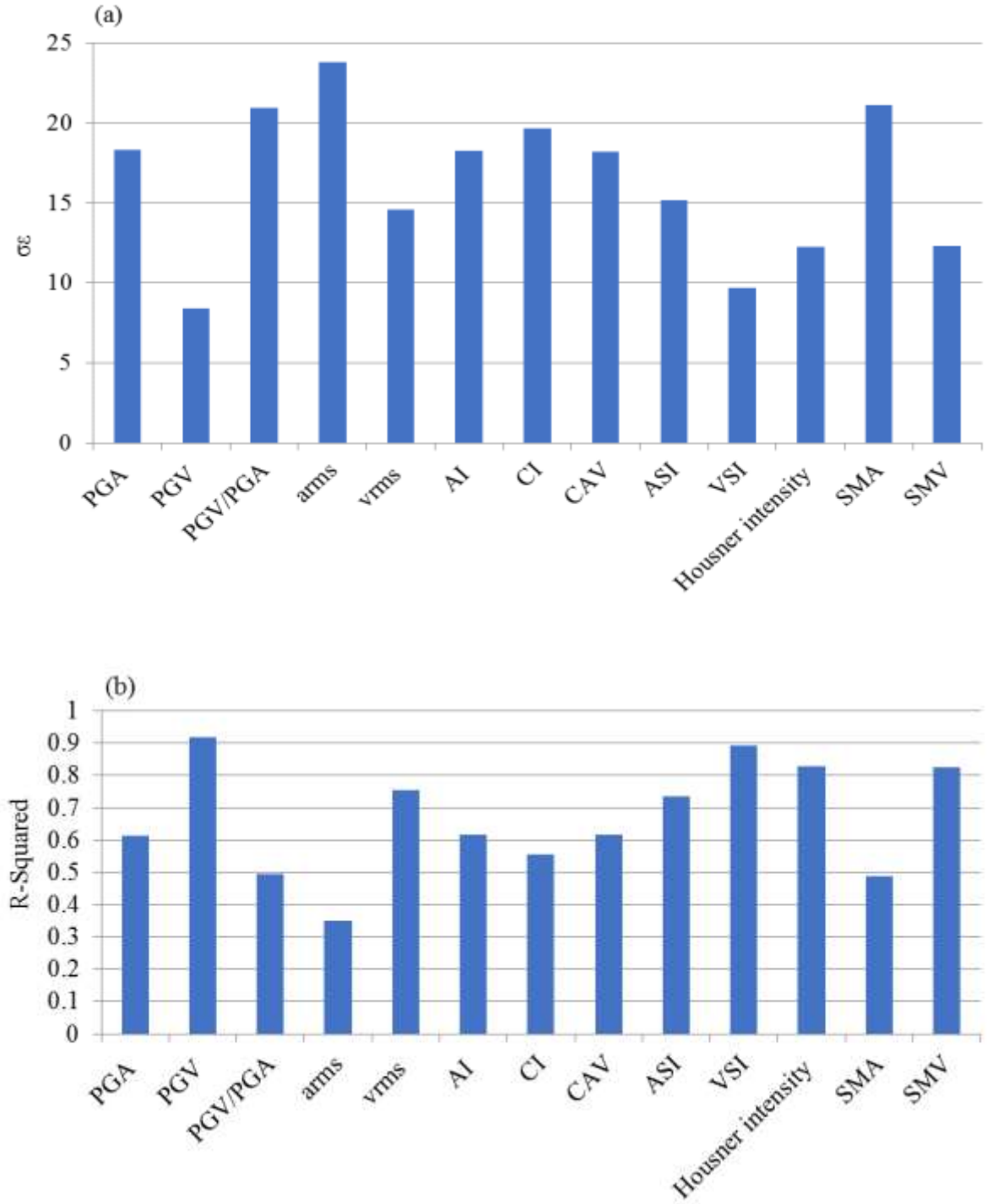

Figure B2. 8: Standard deviation of residuals, σ_ε (a) and coefficient of determination, R^2 (b) for the configuration 16-110 and candidate IMs

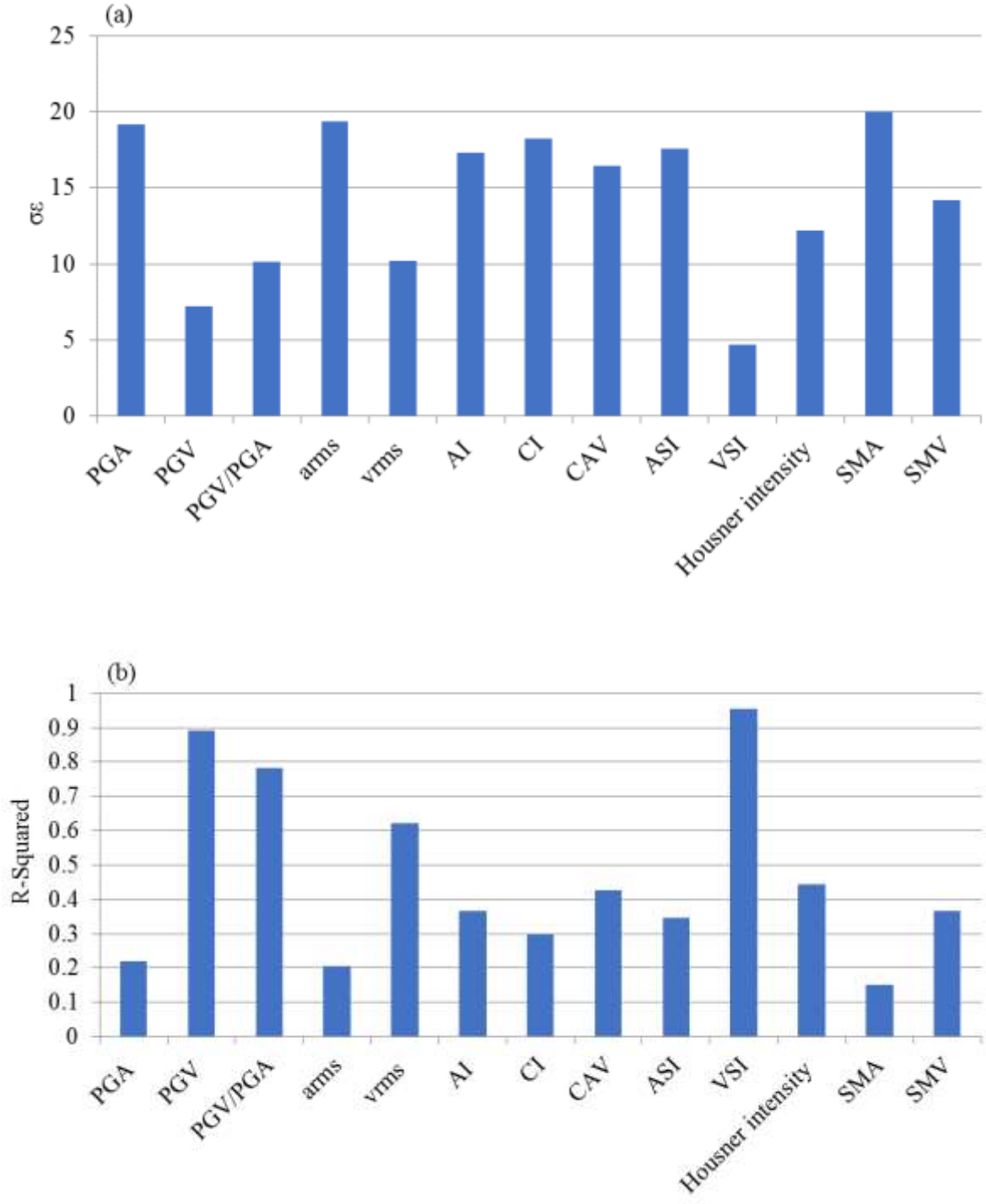

Figure B2. 9: Standard deviation of residuals, σ_ε (a) and coefficient of determination, R^2 (b) for the configuration 20-50 and candidate IMs

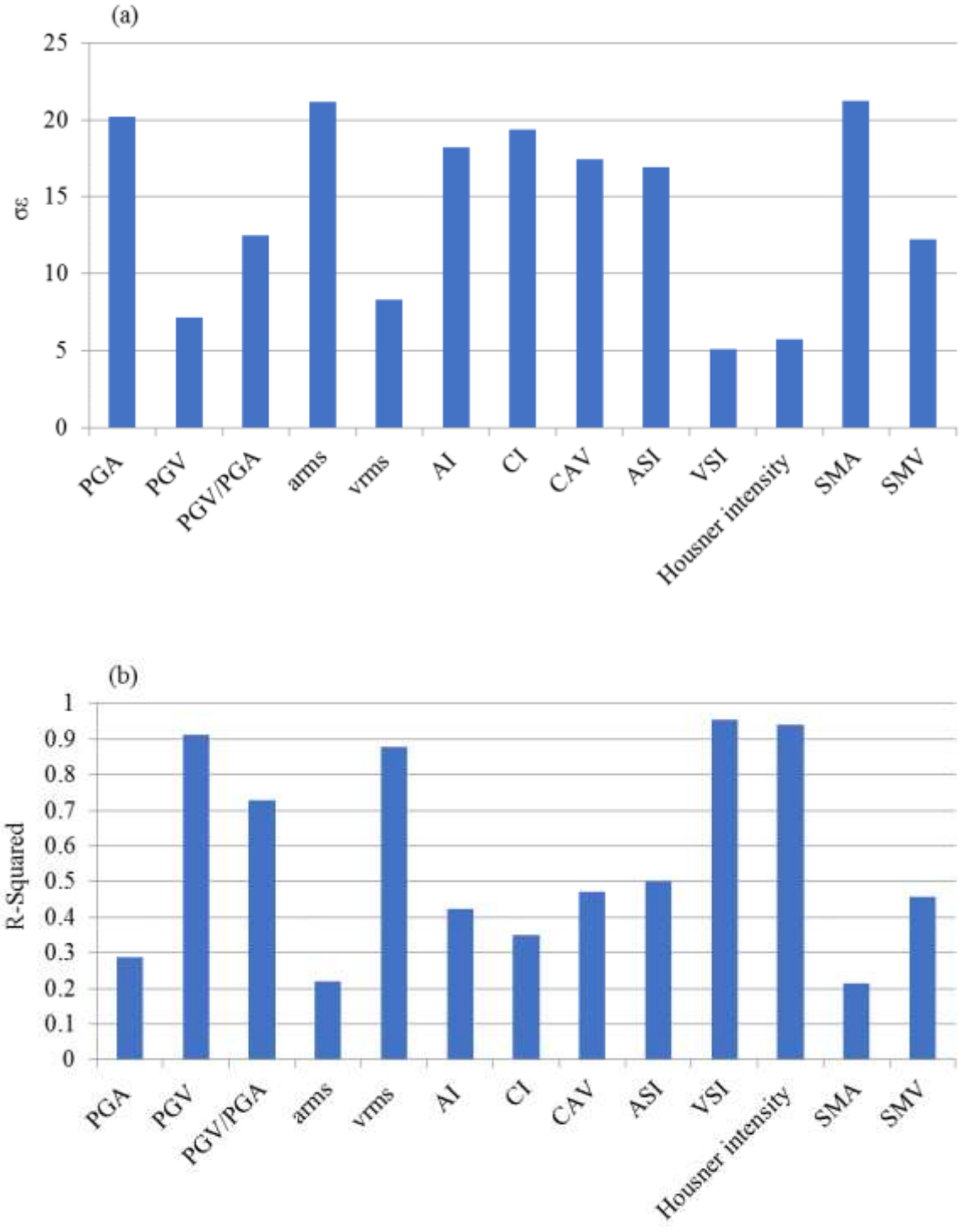

Figure B2. 10: Standard deviation of residuals, σ_ε (a) and coefficient of determination, R^2 (b) for the configuration 20-70 and candidate IMs

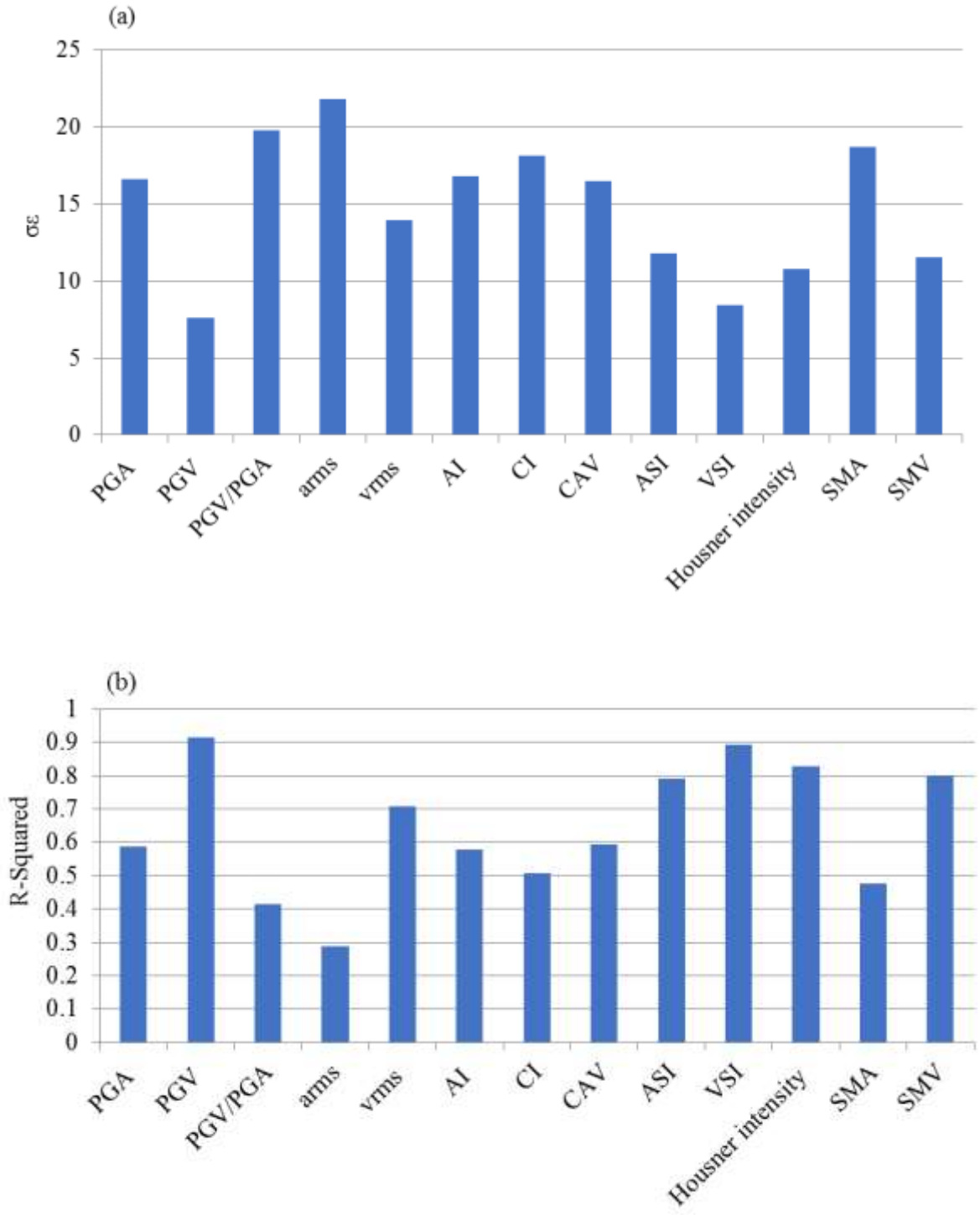

Figure B2. 11: Standard deviation of residuals, σ_ε (a) and coefficient of determination, R^2 (b) for the configuration 20-115 and candidate IMs

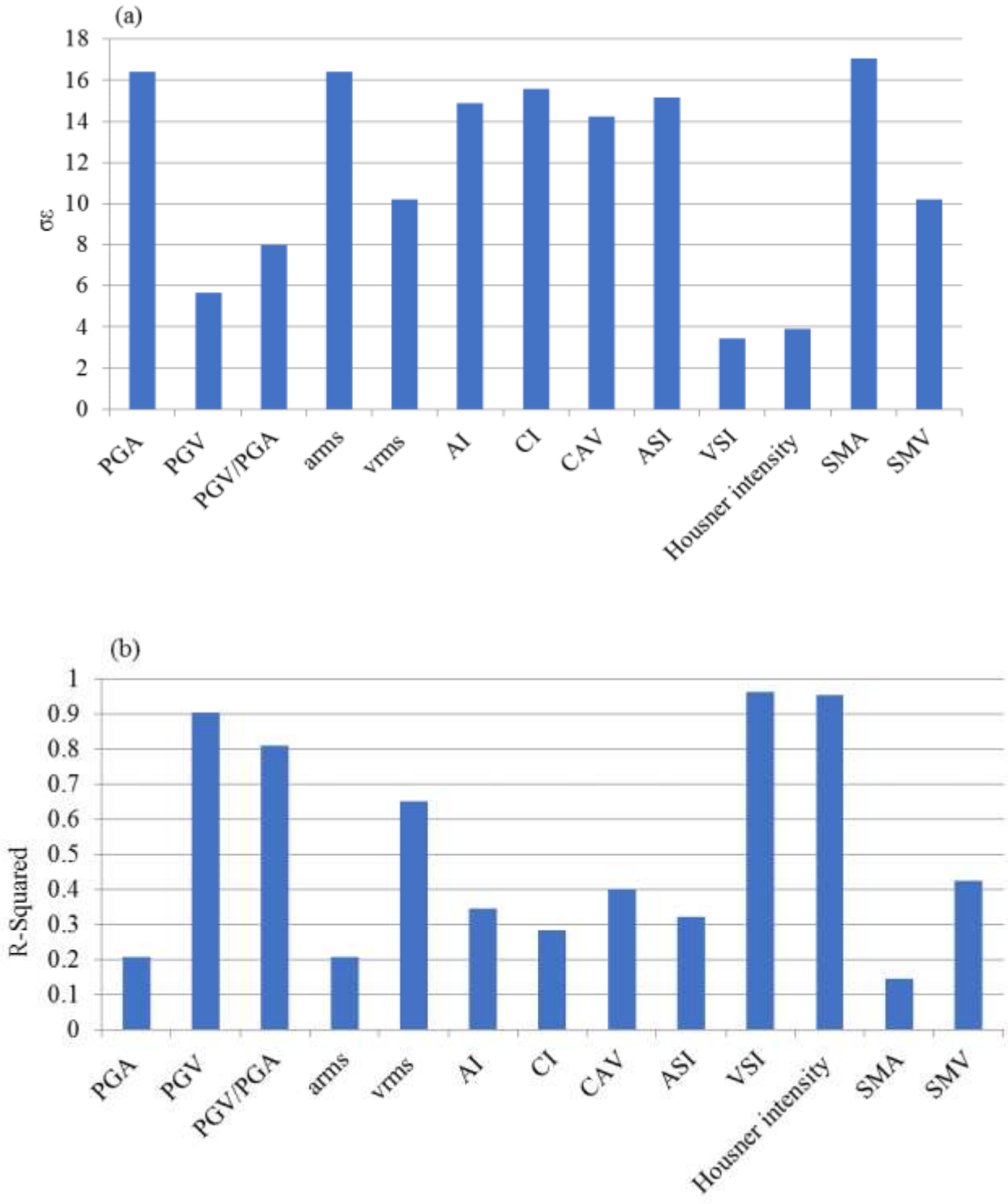

Figure B2. 12: Standard deviation of residuals, σ_ε (a) and coefficient of determination, R^2 (b) for the configuration 25-60 and candidate IMs

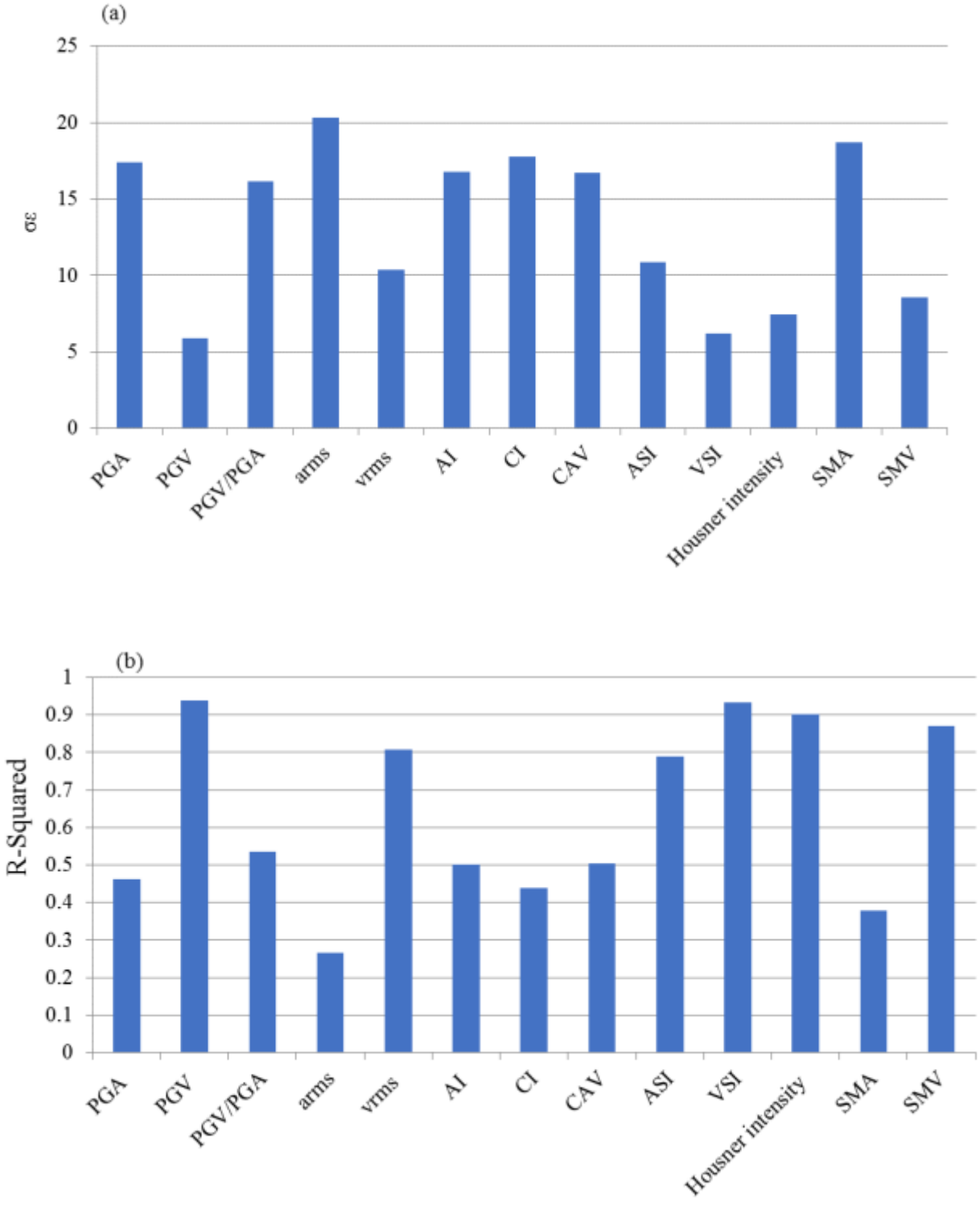

Figure B2. 13: Standard deviation of residuals, σ_ε (a) and coefficient of determination, R^2 (b) for the configuration 25-110 and candidate IMs

APPENDIX C DESIGN CORRELATION STATISTICAL ANALYSIS

Based on concepts developed to assess liquefaction-induced deformations of earth structures (e.g., Travasarou and Bray, 2003; Bray and Travasarou, 2007; Bray and Macedo, 2018) and on the results of the simulation, several functional forms were investigated to correlate the earthquake-induced horizontal displacement of downstream slope of reinforced tailings impoundments (SAR_x) with the various parameters. The results of the residuals study are presented in this section to evaluate the performance of the regression models and assess any potential bias for each case. The definition of various parameters and the units are presented in Table C. 1. Figure C. 1 to Figure C. 5 show the calculated residuals for the parameters included in each functional form evaluated here.

Table C. 1: Definition of the parameters in the regression models

Parameter	Definition	Unit
$\boldsymbol{\theta}$	Slope inclination	(˚)
H	Tailings thickness	(m)
VSI	Velocity spectrum intensity	(m)
PGA	Peak ground acceleration	(m/s^2)
W_{vs}	Volume spacing index	--
$CRR_{MW=7.5}$	Normalized cyclic resistance ratio at an effective stress of 100 kPa for an earthquake of magnitude 7.5	--
PGV	Peak ground velocity	(m/s)
V_n	Volume under the slope	m^3
I_d	Density index	--

$$\ln(SARx) = (-35.8673) + 1.5754.\ln(\theta) + 0.8639.\ln(H) + 0.9856\,.\ln(VSI) + 0.7988.\ln(PGA) + (-0.9953).\ln(W_{vs}) + (-11.2152).\ln(CRR_{Mw=7.5})$$

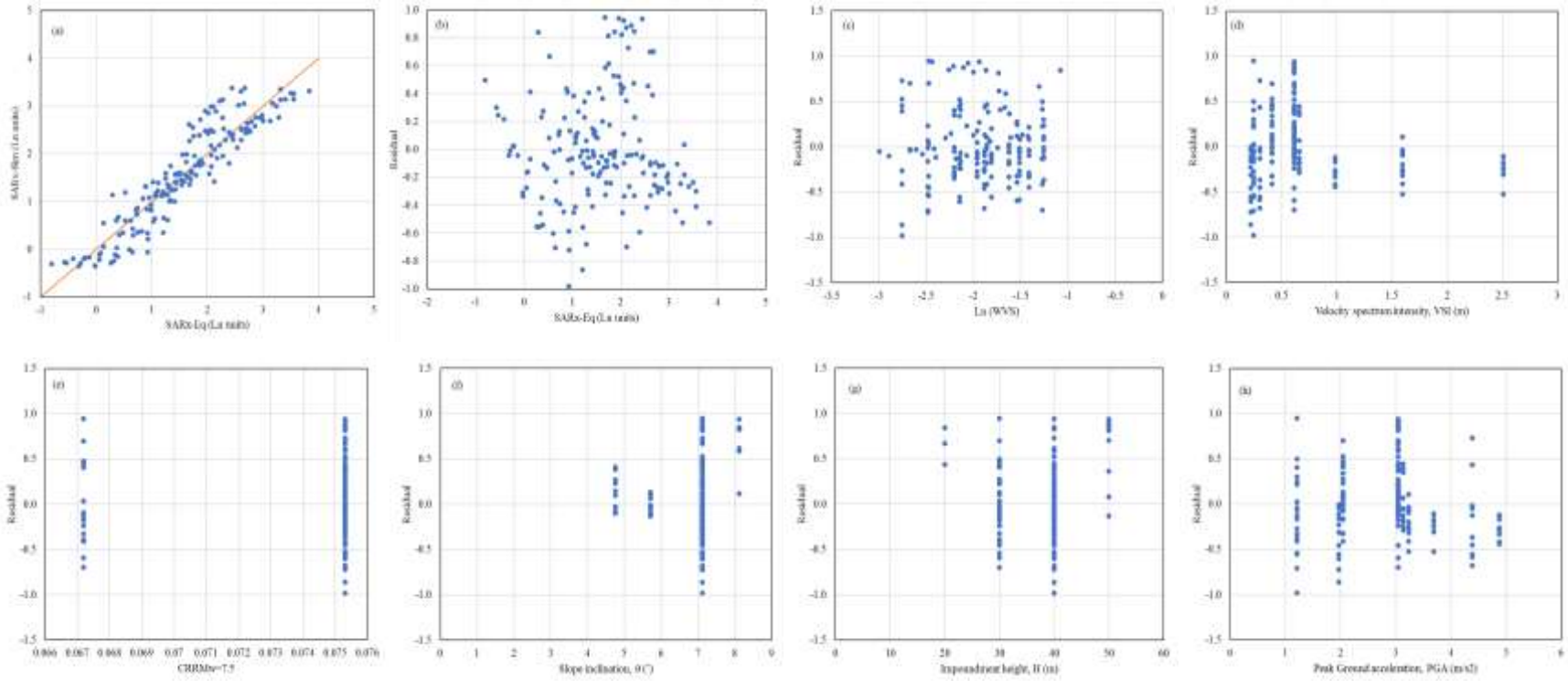

Figure C. 1: Comparison of SAR_x value estimated and calculated through numerical simulations (a), and distribution of residuals versus (b) estimated SAR_x, (c) Wvs, (d) VSI, (e) CRR $_{Mw=7.5}$, (f) slope inclination, (g) impoundment height, and (h) PGA

$$\ln(SARx) = (-34.7685) + 1.5.\ln(\theta) + 0.8337.\ln(H) + 0.9028\,.\ln(PGV) + 0.8535.\ln(PGA) + (-1.0002).\ln(W_{vs}) + (-11.3177).\ln(CRR_{Mw=7.5})$$

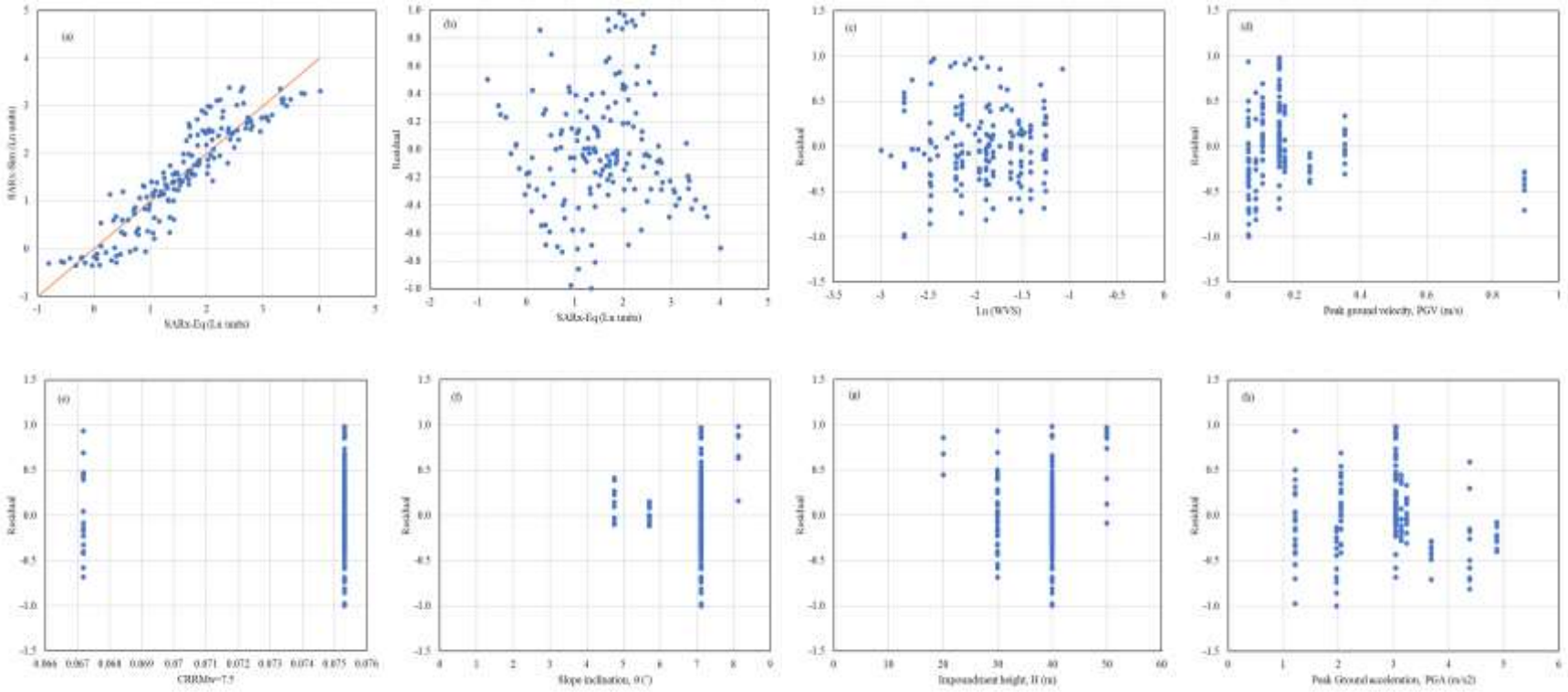

Figure C. 2: Comparison of SAR_x value estimated and calculated through numerical simulations (a), and distribution of residuals versus (b) estimated SAR_x, (c) Wvs, (d) PGV, (e) CRR $_{Mw=7.5}$, (f) slope inclination, (g) impoundment height, and (h) PGA

$$\ln(SARx) = (-27.0891) + 0.1013.\ln(V_n) + 0.9158\,.\ln(PGV) + 0.8489.\ln(PGA) + (-0.9333).\ln(W_{vs}) + (-10.3616).\ln(CRR_{Mw=7.5})$$

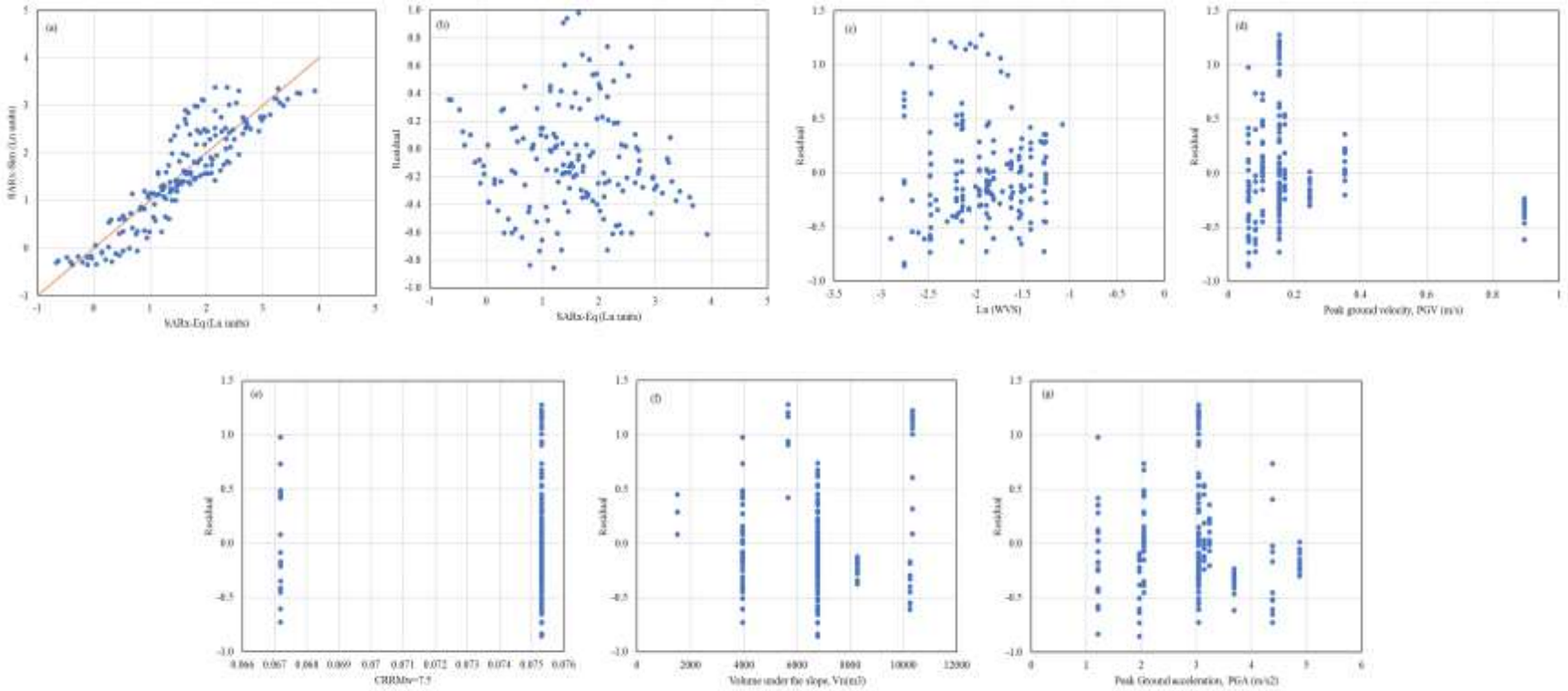

Figure C. 3: Comparison of SAR_x value estimated and calculated through numerical simulations (a), and distribution of residuals versus (b) estimated SAR_x, (c) Wvs, (d) PGV, (e) $CRR_{Mw=7.5}$, (f) volume under the slope, and (g) PGA

$$\ln(SARx) = (-27.9013) + 0.1049.\ln(V_n) + 0.9916\,.\ln(VSI) + 0.8022.\ln(PGA) + (-0.9243).\ln(W_{vs}) + (-10.2265).\ln(CRR_{Mw=7.5})$$

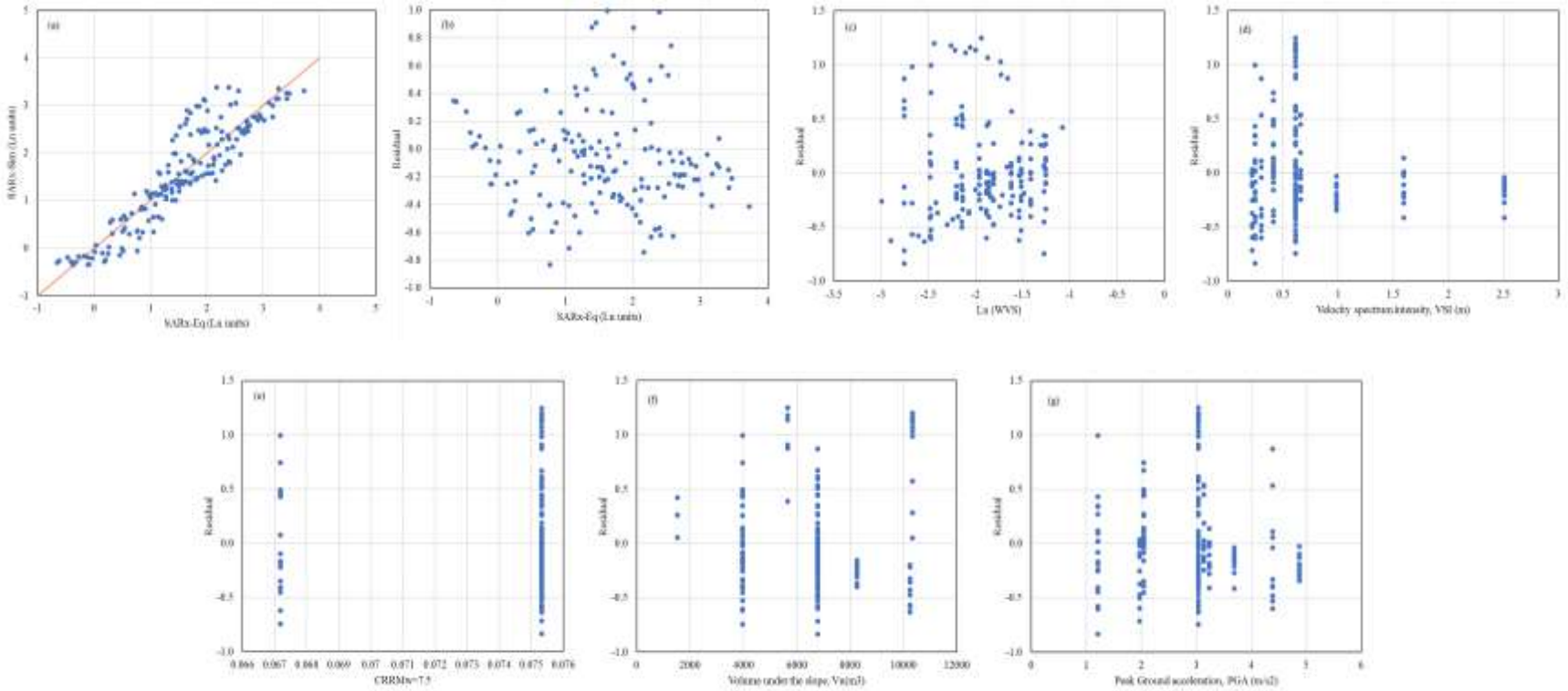

Figure C. 4: Comparison of SAR_x value estimated and calculated through numerical simulations (a), and distribution of residuals versus (b) estimated SAR_x, (c) Wvs, (d) VSI, (e) CRR $_{Mw=7.5}$, (f) volume under the slope, and (g) PGA

$$\ln(\text{SARx}) = 37.0991 + 0.1049.\ln(V_n) + 0.9916\,.\ln(VSI) + 0.8022.\ln(PGA) + (-0.9243).\ln(W_{vs}) + (-9.4164).\ln(I_d)$$

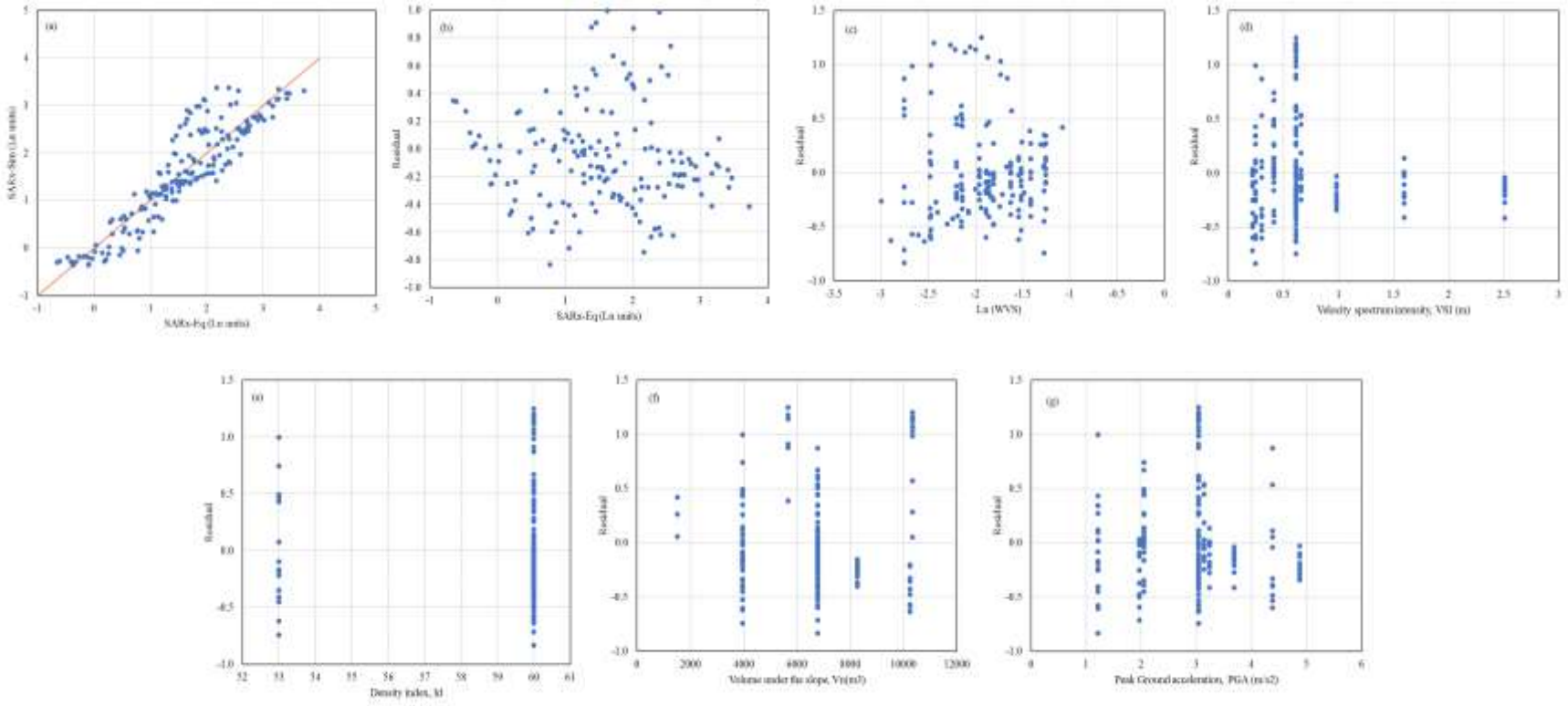

Figure C. 5: Comparison of SAR_x value estimated and calculated through numerical simulations (a), and distribution of residuals versus (b) estimated SAR_x, (c) Wvs, (d) VSI, (e) I_d, (f) volume under the slope, and (g) PGA